# Reactive Crystallization of Chiral Molecules

## Asymmetric Amplification and Deracemization

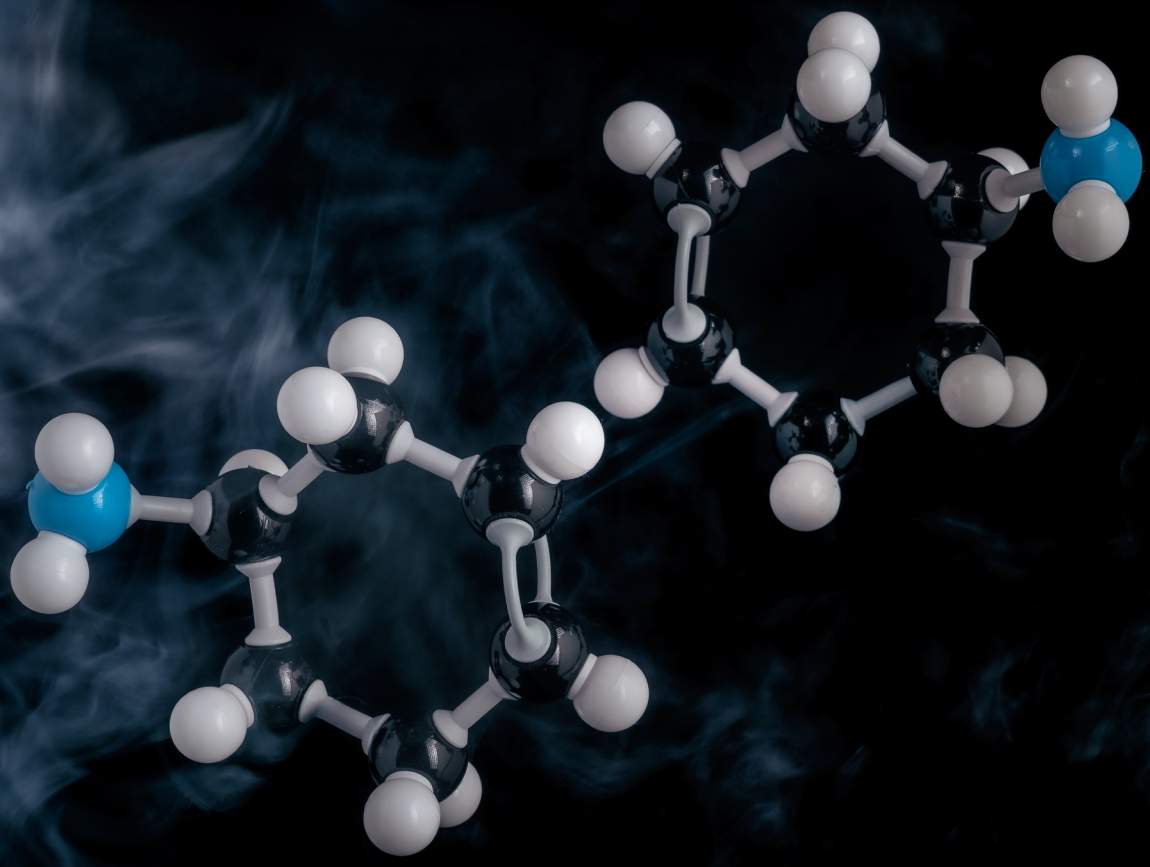

Sjoerd van Dongen

# Reactive Crystallization of Chiral Molecules

Asymmetric Amplification and Deracemization

Sjoerd van Dongen



Ph.D. Thesis, University of Amsterdam, April 2026.
*Reactive Crystallization of Chiral Molecules: Asymmetric Amplification and Deracemization*
Sjoerd W. van Dongen

Cover: *Photograph of Chiral Molecules* by Stef de Graauw and Sjoerd van Dongen

ISBN: 978-94-92323-94-1

The work described in this thesis was performed between June 2020 and March 2025 in the Self-Organizing Matter group of prof. dr. W.L. Noorduin at AMOLF, Science Park 104, 1098 XG Amsterdam, The Netherlands.

The work in this thesis was partially funded by the Dutch Research Council (NWO) as part of OCENW.KLEIN.155.

A digital version of this thesis is available at the AMOLF Institutional Repository, which can be reached at https://ir.amolf.nl.
The author can be reached at sjoerdvandongen@gmail.com.



Printed by Ridderprint | www.ridderprint.nl

Reactive Crystallization of Chiral Molecules
Asymmetric Amplification and Deracemization

ACADEMISCH PROEFSCHRIFT

ter verkrijging van de graad van doctor
aan de Universiteit van Amsterdam
op gezag van de Rector Magnificus
prof. dr. ir. P.P.C.C. Verbeek
ten overstaan van een door het College voor Promoties ingestelde commissie,
in het openbaar te verdedigen in de Agnietenkapel
op dinsdag 14 april 2026, te 16.00 uur

door Sjoerd Willem van Dongen
geboren te Eindhoven

***Promotiecommissie***

| | | |
|---|---|---|
| *Promotor:* | prof. dr. W.L. Noorduin | Universiteit van Amsterdam |
| *Copromotores:* | dr. B. Kaptein | InnoSyn B.V. |
| | prof. dr. R.M. Kellogg | Rijksuniversiteit Groningen |
| *Overige leden:* | prof. dr. J.H. van Maarseveen | Universiteit van Amsterdam |
| | prof. dr. H.M. Cuppen | Universiteit van Amsterdam |
| | prof. dr. G.J.M. Gruter | Universiteit van Amsterdam |
| | prof. dr. J.H. ter Horst | Tiofarma |
| | prof. dr. C. Viedma Molero | Universidad Complutense de Madrid |
| | prof. dr. A.R.A. Palmans | TU Eindhoven |

Faculteit der Natuurwetenschappen, Wiskunde en Informatica

# Table of Contents.

# Chapter 1
# Introduction.



The science set out in this thesis pertains to the reactive crystallization of chiral molecules. First, we will introduce the concept of chirality and explain the unique handles crystallization offers to control the symmetry of molecules. Following these introductions, this thesis will explore the fascinating processes that occur when the crystallization of chiral—i.e. asymmetric—molecules is combined with chemical reactions. As it turns out, such reactive chiral crystallization can convert an initially racemic solid-state—i.e. containing both molecular mirror-images—into an enantiopure end-state. This work aims to elucidate further the inner workings of such reactive chiral crystallizations and exploit these fundamental insights to expand its scope and applications.

Individually, chirality and crystallization increasingly feature in chemistry and engineering and both are central to a few of the pressing technological and societal challenges of this century.[1–3] Chirality is central to discussions on the origin of life and of critical importance to the effectiveness and safety of pharmaceuticals. Indeed, over the past decades, advances in chirality control have claimed numerous Nobel prizes.[4–11] Yet wider in scope, crystallization and crystal growth are key to separation and purification processes, geology and geochemistry, semiconductor manufacturing, chips and electronics, batteries and solar cells, next-generation materials.[12–19]

Perhaps not so notorious is the long history that the fields of crystallization and chirality dually share. After Biot discovered the optical activity of organic compounds in 1815, Pasteur deduced its molecular basis in chirality in 1848 by observing the distinct morphologies of the crystals of tartaric acid sodium ammonium salts.[20] Here began a fascinating and fruitful experimental journey, sealing the intricate connection between crystallization and chirality. Crystallization has been essential in the study and resolution of chiral molecules ever since. What is more elegant than an intrinsically stereoselective natural process that only incorporates molecules of a particular three-dimensional orientation? Combined, chiral crystallization indeed makes for a highly dynamic and multi-facetted field, at the interface where solids and liquids meet and physics and chemistry join forces.

This thesis will build on this intricate connection between crystallization and chirality and will feature crystallization as a tool to separate and convert molecular mirror-images. Before we embark on this journey, this chapter will shortly introduce chirality, while a substantial background on crystallization will be presented in the next.

*Note that this introduction and the following two chapters aim to discuss many terms and technical concepts in varying degrees of detail. Because the reader might be familiar with some, but not with others, the text supports both comprehensive study and selective reading. Sections may be read non-sequentially, in recognition of the diverse backgrounds and prior knowledge of the intended audience.*



# Chirality

The year is 1893 and William Thomson, who has just gained the title of Lord Kelvin, lectures on the 'Molecular Tactics of a Crystal'.[21] Addressing the geometry of molecular arrangements within crystals, he states that any figure of which the mirror image cannot be brought to coincide with itself, must be called 'chiral'. Recalling the Greek word for hand (χείρ), this concept of chirality can easily be understood when rephrased as 'handedness'. Indeed, our hands are two mirror images and no matter how you turn or twist them, no rotation or translation will allow you to superimpose or stack them (Fig. 1.1a).

## Molecular chirality

So how does the concept of chirality manifest on the molecular level? The answer to this question emerged halfway the 19$^{th}$ century. Sometime during 1848, famous biochemist Louis Pasteur was experimenting with crystals of tartaric acid salts as he noticed that these crystals exhibited hemihedral facets under the microscope: tiny flat faces on the edge of the crystal that sometimes oriented to the right, and sometimes to the left. Pasteur was able to separate these crystal mirror images using tweezers and showed that both types of crystals showed the opposite interaction with light: one crystal rotated plane-polarized light in the left direction, the other crystal turned light right.[22] Indeed, Pasteur not only achieved the first documented chiral resolution, but also linked macroscopic chirality to individual molecular chirality.[23]

So how exactly do such individual molecules determine chirality? It was not until 1874 that this pressing question was first answered by Van 't Hoff and Le Bel.[24] Building on seminal work by Kekulé, the duo founded the field of stereochemistry by introducing the concept of tetrahedral coordination of carbon atoms and the possibility to thus achieve asymmetric molecular centres.

To appreciate this view on molecular chirality, we consider Figure 1.1b, which shows a tetrahedral carbon atom ($sp^3$-hybridized) bearing four different substituents that exhibits a chirality very similar to our hands. Although often overlooked and understudied, also phosphorus (P-chiral phophines), sulfur (sulfoxides and sulfonium salts), and silicon (tetrasubstituted organosilanes) may yield chiral centres, akin to tetrahedral carbon. Tertiary amines provides a similar possibility for

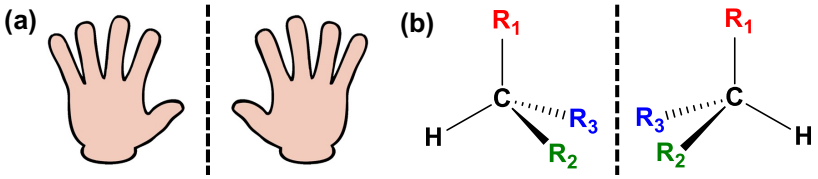


**Figure 1.1.** A view on chirality. (a) The macroscopic image of chirality: mirror images of our hands. (b) The molecular image of (point) chirality: tetrahedral carbons with four different substituents.

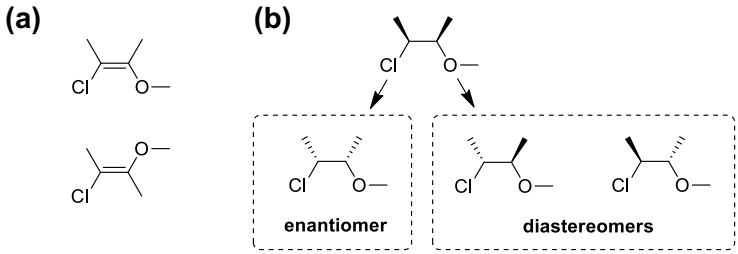


**Figure 1.2.** Configurational isomerism. Different three-dimensional structures of the same molecule can arise, for example through (a) cis-trans isomerism around a double bond or ring or (b) differing point chirality at chiral centres. Enantiomers are perfect mirror-images, while diastereomers are not.

chirality, but pyramidal inversion of the lone pair generally renders the molecules kinetically racemic (i.e. they exist in equal amounts of both mirror images).

Terminology in stereochemistry can be confusing and a short summary is warranted.[25] Stereochemistry not only pertains to chirality, but encompasses the broader realm of isomerism: the different ways in which the same atoms can be organized into different molecules. We discriminate between constitutional isomers (differing in nature and sequence of bonding) and stereoisomers (differing in three-dimensional arrangement). Molecules can switch between many possible configurations through free rotation around each single bond. In contrast, the rotations of some atoms can be confined, leading to configurational isomers (Fig. 1.2). Double bonds cause one type of restriction, where atoms are locked into planes, yielding cis-trans isomers (Fig. 1.2a). Tetrahedral carbons, that feature four different substituents, are also limited in their possible structural interconversions, breaking symmetry. These configurational isomers must now be narrowed down to stereoisomers which are not mirror images of each other (i.e. diastereomers) and those that are (Fig. 1.2b). Importantly, these mirror-images of chiral molecules are called enantiomers. Labelling enantiomers can proceed according to their natural interaction with light (+ and -), their correlation to D-(+)-glyceraldehyde according to Emiel Fischer (D and L), or by the weight of substituents (*R* and *S*). The latter system, initially proposed by Cahn, Ingold, and Prelog,[26] has now emerged as the standard for simple molecular chirality at a single chiral centre and is also the standard in this thesis.

Besides point chirality, as featured in tetrahedral carbons with four unique substituents, molecules can also exhibit axial and helical chirality.[27] Helical chirality is a very imaginative term: the molecule contains a screw axis, such as the aptly named class of helicenes. Axial chirality is often induced by different substituents on either sides of a single bond that are too bulky to allow rotation, locking three-dimensional configurations in place. The stereoisomers resulting from such hindered rotation are called atropisomers (biphenyls, binaphthyls, etc.). In some cases, the configuration of the molecule is not locked due to rotational impediments, but due to covalent bonds (cf. also twistanes). Special and interesting cases are chiral mechanically interlocked molecules such as rotaxanes and catenanes.[28] Molecular machines, featured in the Nobel Prize in Chemistry in 2016, build on these kinds of chirality.[29]

Beyond the realm of small molecules, one can also find chirality in polymers and metal complexes. Chiral supramolecular polymers can be formed from both achiral and chiral building blocks.[30] When assembling supramolecular polymers under regimes close to equilibrium, enthalpic mismatch penalties allow growing pristine helices that incorporate uniquely one type of enantiomeric building block.[31] The so-called majority rule also allows achiral building blocks to assemble into helical polymers, often due to cooperative effects and the presence of some initial symmetry breaking in the environment (sergeant and soldiers model).[32] Similarly, in the case of metal complexes, chirality can both be induced straightforwardly by chiral ligands or, in a more complicated fashion, through point chirality at the metal itself (e.g. unique substituents in tetrahedral and octahedral complexes or twisted complexes with bidentate or tridentate ligands).[33,34]

Finally, chiral nanostructures make up a special sort of chiral chemistry that is rapidly gaining attention. Due to their potentially strong interactions with polarized light, they may have significant applications in biosensing, asymmetric (photo)catalysis, and optoelectronics.[35,36] These nanostructures can acquire chirality through intrinsically asymmetric growth (autonomously or under external stimuli), assembly on chiral surfaces, the use of chiral ligands, or the assembly of achiral units into twisted superstructures.[37] For example, cysteine, a chiral amino acid that strongly binds gold surfaces, owing to its thiol functionality, can be used to induce twisted spikes and other morphologies during the assembly of gold nanoplatelets.[38] Chiral nanostructures are not only formed from inorganic and metallic cores, but can also be obtained from assembling organic building blocks, exemplified by the assembly of helical cysteine chains into nanoribbons and bowties (the chains are assembled through coordination with $Cd^{2+}$ ions).[39] A final example are chiral nanocrystals of tellurium, where screw dislocations induce a chiral polyhedral shape, even in the absence of any chiral ligands or other forms of applied symmetry breaking.[40] As these examples show, there is plenty of opportunity in the chain of

chirality transfer from molecule to nanostructure and the field is primed to produce exciting innovations.

This section on molecular chirality would not be complete without describing the way this thesis quantifies chirality. The main metric we will use is the enantiomeric excess (*ee*), defined as

$$ee = \frac{[R] - [S]}{[R] + [S]} \qquad \text{(eq. 1.1)}$$

where [R] and [S] are the concentrations or relative abundancies of each enantiomer in a system. In short, the *ee* yields an indication of the extent of enantioenrichment: 0 is racemic, 1 is enantiopure. Multiple approaches can determine the *ee* of a system. For organic molecules, chiral chromatography and circular dichroism are used most often. In theory, however, one could also use NMR, mass spectrometry, and even infrared spectroscopy.[41–44] Recently, with AI-driven experimentation and self-driven labs on the rise, increased attention has been given to optical techniques that allow high-throughput screening for enantiomeric excess.[45]

## Chirality and life

Chirality is part and parcel to life.[46,47] Our bodies are not only macroscopically asymmetrical, but their fundamental building blocks also exhibit chirality: the genetic material that encodes life (i.e. RNA and DNA) shows helical chirality (Fig. 1.3a), and the amino acids and sugars that form the metabolic factories producing our constituting biomaterials bear one or multiple chiral centres (i.e. carbon atoms with four different substituents; Fig. 1.3b).

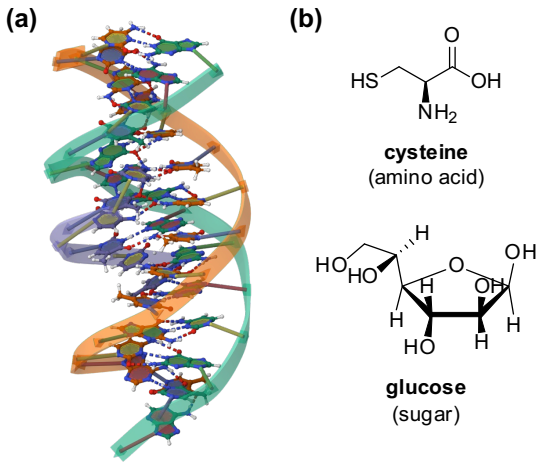


**Figure 1.3.** Examples of molecular chirality in biology. (a) DNA and RNA are helical polymers, built from ribonucleotides which containing a chiral sugar core (graphic from Wikimedia). (b) Fundamental molecular building blocks like amino acids (monomers of proteins) and sugar molecules contain point chirality through tetrahedral carbons. Such point chirality is conferred onto larger chiral superstructures.

Remarkably, it turns out that life is not just chiral; it is in fact homochiral. Indeed, the amino acids that make up all proteins are almost exclusively L-enantiomers, leading to right-handed α-helices and chiral folded superstructures. In turn, the carbohydrates that life's enzymes construct and consume appear mainly as D-enantiomers. Ever since the discovery of biological homochirality, both its origin and purpose have been the subject of much research.[48–50]

Although a full discussion of the particular properties chirality can give to a system is beyond the scope of this introduction, calculations on chiral fluids show that chirality, already in its most simple form, can furnish an abundance of nontrivial behaviours.[51] In biological systems, however, a particularly interesting argument has been made by Ron Naaman, who has become known for his work on Chiral-Induced Spin Selectivity (CISS).[52] Simply put, through spin-orbit coupling, spin-polarized electrons scatter asymmetrically from chiral molecules such that chiral molecules can bring forth polarized currents and interact selectively with polarized magnetic and electrical fields.[53,54] Naaman argues that electron spin plays a critical role in chemical reactions and chemical bonding and that the CISS-effect can control interactions and reaction pathways. Specifically, he conjectures that "electron spin can act as a chiral bias to enantiospecifically facilitate chemical reactions" in enzymes and strengthen the allosteric interactions between peptides and substrates, and may also "increase the specificity and sensitivity of biorecognition elements", such as in the replication of genetic material. The key argument underlying this reasoning is that homochirality must have strong benefits to biochemical processes to justify the enormous amount of energy organisms spend in preserving it.[55,56] Others have made the reverse argument: chiral mismatches cause kinetic stalling when creating chains of molecules so that a chiral cross-inhibition mechanism favours homochirality.[57,58]

## Chiral amplification

Besides the yet enigmatic function of chirality, much focus has been on its genesis: the initial breaking of symmetry and the subsequent amplification of an initial enantioenrichment.[59]

The origin of homochirality thus starts with the origin of broken symmetry. The question of breaking symmetry knows many answers and plausible theories: extraterrestrial sources, circularly polarized light, the magnetic field, chiral mineral surfaces, and bare stochasticity—to name a few.[60–66] Recent studies of asteroids, however, have sought to question the delivery of an initial enantioenrichment from beyond earth.[67] Reasonings based on parity violation also seem increasingly unlikely.[68] Some authors have actually reversed the question and argued, supported by mathematical analysis, that the racemic state of a system becomes increasingly less stable as the number of chiral molecules that are produced from achiral building

blocks grows, and any sufficiently large system thus inherently strives to break symmetry in whichever way possible.[69]

Once symmetry is broken, the asymmetry needs to be amplified to reach homochirality. In the 1950s, Frank postulated that chiral amplification can occur when (i) enantiomers can self-replicate and (ii) enantiomers inhibit the replication of their counterpart, e.g. through inactivation of racemic dimers.[70] Such mutual inhibition is required, as replication alone does not increase an initial enrichment but merely consolidates it (Fig. 1.4a). Also, without mutual inhibition, the broken symmetry could possibly be shattered through a spontaneous enrichment towards the other mirror-image and thus is statistically unstable.[71] It is this latter aspect of mutual inhibition that is often missing from seemingly autocatalytic systems. Ribo and co-workers challenge the mutual-inhibition requirement, by arguing that first-order autocatalysis together with mutual cross-catalysis is also feasible.[72] A number of realizations have been proposed to achieve such amplification of chirality: chiral poisoning, surface packing, nonlinear effects in asymmetric catalysis, chiral recognition in self-replicators—all are among viable routes.[73–75] Recently, building on nonlinear effects observed in synthesis and catalysis, Feringa and co-workers have even proposed the self-enantioresolving properties of amino acid derivatives through diastereomeric homo- and heterochiral association in solution.[76,77]

In this thesis, however, the mechanism explored for chiral amplification is asymmetric crystallization. Seminal and famous demonstrations of spontaneous chiral amplification through crystallization were given by Havinga, Kondepudi, McBride and Viedma (Fig. 1.4b).[78–81] Sodium chlorate, an achiral salt, crystallizes into

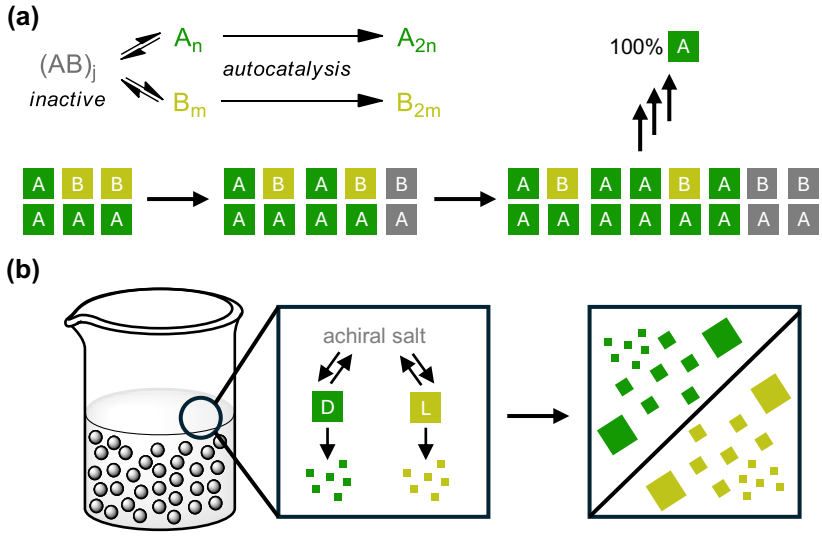


**Figure 1.4.** Asymmetric amplification (a) as postulated through the mechanism of Frank, by means of autocatalysis and mutual inhibition, and (b) as demonstrated for the stochastic deracemization of achiral salts that crystallize into enantiopure crystals under grinding (glass beads) and secondary nucleation.

two populations of chiral crystals of opposite handedness. Spontaneous crystallization of such solutions can yield only a single handedness in the crystals, provided they are stirred vigorously. The rationale is an initial stochastic breaking of symmetry, e.g. through nucleation, which then is amplified. Viedma observed that—after some time—also a racemic mixture of crystals self-converts into a single handedness. The mechanism of this amplification remains poorly understood, is a matter investigated in this very thesis, and a number of theories will be introduced in chapter 3. Part of the answer lies in the stereoselective nature of these crystals—they only incorporate their own—and effects reminiscent of the mutual inhibition described by Frank have been reported.[82–84]

This concept of chiral amplification can also be translated from self-sorting crystals to supramolecular systems.[85–87]

In Eindhoven, Meijer and Palmans studied enantiomeric building blocks that can assemble into chiral supramolecular polymers.[32,88] They recognized the potential for cooperative effects in self-assembly and the subsequent amplification of chirality. Indeed, even small amounts of chiral building blocks or other chiral stimuli can induce handedness in supramolecular aggregates of otherwise predominantly achiral components, possibly evoking a self-selection and transfer mechanism.[89,90] Such inductive effects are rooted in cooperativity, where noncovalent interactions such as hydrogen bonding or π–π stacking behave in a non-additive manner: neighbouring interactions strongly affect new bonding, providing a selection mechanism and possibly enabling the long-range amplification of chirality down a chain.[91] To demonstrate the supramolecular effects of cooperativity, they created a common solute resource pool through a racemization reaction that continuously flips the chirality of the enantiomeric building blocks.[92] They found that significant enantiomeric excess emerges under enantiomeric interconversion of the building blocks, with the effectiveness of chiral amplification determined by the energy penalty associated to the mismatch of incorporating a building block of the opposite handedness and mediation by a chiral sergeant.[92]

In Groningen, Otto introduced self-replicating stacking macrocycles that spontaneously arise from achiral aromatic molecules through dynamic disulfide bonds.[93] Similar to β-sheet formation, this provides the basis for populations of stacks of different structure or chirality. Although multiple confirmations initially arise, continuous cycles of breakage and re-assembly cause the product distribution shifts towards the most stable confirmation—a phenomenon reminiscent of cycles of asymmetric crystallization.[94] Ultimately, chiral amino-acid precursors can lead to enantioselective self-replication through the preferred incorporation of one handedness into the stack.[95] Crucially, the growth of fibres from racemic building blocks was reported to be much slower, providing the potential mechanism for relative mutual inhibition theoretically required for amplification. Otto's self-

replicators were later adapted to catalyse retro-aldol reactions,[96] illustrating the starting point for a cascade of metabolic chiral induction.[97,98]

These examples of chiral amplification through an interplay of thermodynamic and kinetic processes inspire many possible pathways for chiral induction to establish full homochirality.[82] A key denominator is that chiral structures are known to preferentially bond and adsorb other chiral molecules in a stereoselective manner.[99–102] This can, in turn, also induce asymmetric catalysis by a chemically active structure or surface.[49,103] Inspired by these concepts, Ozturk and co-workers have proposed a five-step cascade to achieve biological homochirality from a singularly enriched molecule: (i) an initial chiral amplification mechanism yields the chiral RNA-precursor ribose-aminooxazoline predominantly as D-enantiomer; (ii) D-ribonucleotides are therefrom formed; (iii) the D-ribonucleotides polymerize as D-tRNA; (iv) D-tRNA asymmetrically catalyses the synthesis of L-peptides; (v) L-peptides become L-enzymes that stereoselectively recycle and replicate amino acids; (vi) and a true homochiral metabolism is born.[104] Hein and Blackmond have made similar arguments to transfer chirality from amino acids to carbohydrates via transamination and asymmetric formose reactions.[105] Ultimately, the propagation of homochirality from one system to the next is self-consistent: a universal adoption of single handedness makes for a much more efficient and versatile building blocks—analogous to the universal adoption of right-handed screws in engineering.[106] A similar principle curtailing diversity was also recently demonstrated for the previously mentioned macrocyclic self-replicators.[107] Perhaps homochirality is an inevitable norm rather than a striking enigma after all.

## Turning the tables

Regardless of its origins, homochirality also prompts another interesting question: can the opposing handedness be an unexpected advantage for biological survival? Indeed, mirror-life would enjoy immunity from many proteins and toxins that cannot metabolize their mirrored-sugars or bind their mirrored-receptors.[108] Advances in the field of synthesis and biology have already allowed incorporating D-amino acids into peptides or even making entirely mirror-image proteins.[109,110] Inverted biological structures can feature as surprisingly potent ligands for naturally occurring peptides, while enjoying high biological stability.[111,112] Such properties can provide valuable biochemical mechanisms that can serve as unprecedented therapeutic tools.[113,114] A number of important antibiotics incorporate D-amino acids and may be an effective tool in combatting increasing antimicrobial resistance.[115]

Several scientists have cautioned against these developments and have even warned for mirror-life risking human extinction:[116,117] mirror bacteria could broadly evade many immune defences of humans, animals, plants, and other organisms. Invasive ecological and pathological effects like those can pose serious risks, as the mere

counter-argument that mirror-life faces a disadvantage when acquiring nutrients is insufficient as it could quickly adapt.[118] It is a misconception, however, that D-amino acids do not occur naturally. In fact, they feature ubiquitously—in bacteria, in plants, in mammals.[119] Some have been linked to pathological processes, like Alzheimer's, and they have been effective as biomarkers or to treat disease.[120,121] Others have been linked to regulatory and signalling functions or structural biology roles.[122,123] Marine microorganisms have recently been found to exhibit unique enantiomers and chiral processes, with distinct metabolic strategies, which has remained relatively underexplored so far.[124]

## Chirality as a challenge

Chirality also plays a role beyond biology, from spiral galaxies in astronomy,[125] to spintronics and optoelectronics.[126] Having established the universality of chirality and its interactions with light in particular, it follows naturally that mankind has also embarked upon a quest to capitalize on chirality: nanosphere lithography for asymmetric plasmonic metasurfaces, patterning with chiral nanoparticles, and applications featuring chiral photonic structures and waveguides—to name a few—are well underway.[37,127–133]

To some, chirality may be a niche curiosity or an exciting opportunity for technological innovation. In the field of agrochemicals and drug development, however, chirality is of vital importance and a key challenge. Whereas biological homochirality yields biochemical receptors with high degree of selectivity, regular chemical synthesis suffers from a lower degree of stereochemical control. What this means was painfully illustrated in the late 1950s: the chiral drug thalidomide was prescribed as sleeping drug and cure for morning sickness. Unfortunately, it was marketed as racemate, a one-to-one mixture of its two enantiomers, and it turned out that both enantiomers had very different biological properties. The (*R*)-enantiomer has the desired clinical effects, but the (*S*)-enantiomer proved teratogenic and led to birth defects in children.[134] Sadly, in the case of thalidomide and as with many other drugs, both enantiomers racemize—i.e. interconvert—in the body naturally, so that administering merely its (*R*)-enantiomer would be to no avail—showing a fundamental impediment for drug development.[135] Nonetheless, the case of thalidomide marks the relevance of considering the chirality of bioactive molecules. Ever since, the challenge of asymmetric synthesis has been on the forefront of drug development as the majority of approved pharmaceuticals today is chiral and almost all are supplied as a single enantiomer (Fig. 1.5).[136,137]

Increasing access to pure enantiomers of existing chiral compounds would take away major difficulties in the development of new pharmaceuticals and agrochemicals. Moreover, an advent of straightforward paths to enantiopurity would allow for repurposing existing drugs, so-called 'chiral switches': remarketing a single

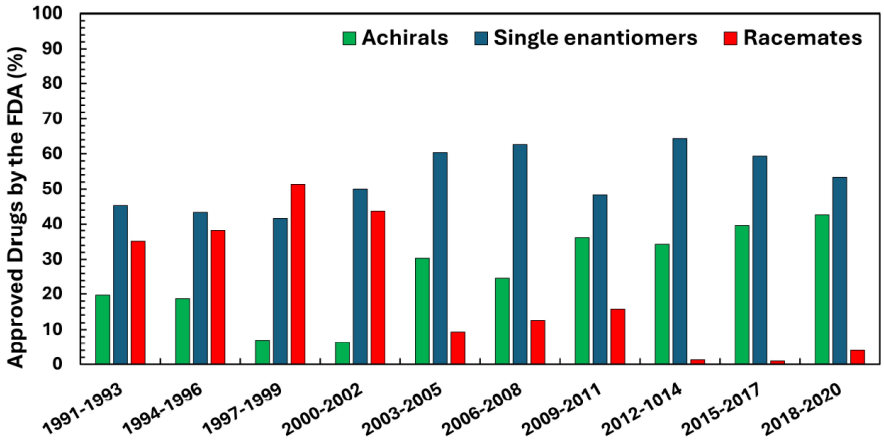


**Figure 1.5.** Chirality of FDA-approved drugs in the period 1991-2020, as summarized and binned by Pinetre (2024) [138]. For statistics, diastereomeric mixtures have been classified as racemates.

enantiomer of drugs currently or previously on the market as racemates.[44] Commercial arguments for using only one of the enantiomers can be increased therapeutical effectiveness, better bioavailability, or reduced toxicity or side-effects.[136] Notably, some single enantiomers may even have totally new therapeutic applications and then benefit from renewed market exclusivity under both European and US legislation. The case of such 'chiral switches' not merely serves to stress the challenge of chirality but especially the opportunities that loom at the end of an effective path to enantiopurity.

## Paths to enantiopurity

So how do we obtain enantiopure molecules? The physical and chemical properties of enantiomers are identical and their difference is only revealed if they interact with a chiral environment itself. Reactions therefore naturally produce racemic mixtures and many conventional separation methods cannot discriminate between the mirror-images of chiral molecules. In short, one can either start with a chiral building block, use chiral reagents or catalysts, or perform separation of racemic mixtures through complex chromatographical techniques, or through chiral crystallization (Fig. 1.6a).

The most straightforward method to integrate a chiral centre in a molecule is to start from the chiral pool. This chiral pool collectively entails all commercially or potentially readily available chiral molecules already in the desired configuration. With the advent of bio-based chemistry, the engineering of this pool is especially attractive.[139] For instance, yeasts like *Yarrowia lipolytica* can be engineered to produce a wide array of chiral acids and metabolites through fermentation of sunflower oil.[140,141] Especially the bioproduction of α-hydroxy acids has been successful, and many optically pure stereoisomers of such acids can be obtained from plants or large scale microbial factories.[142,143]

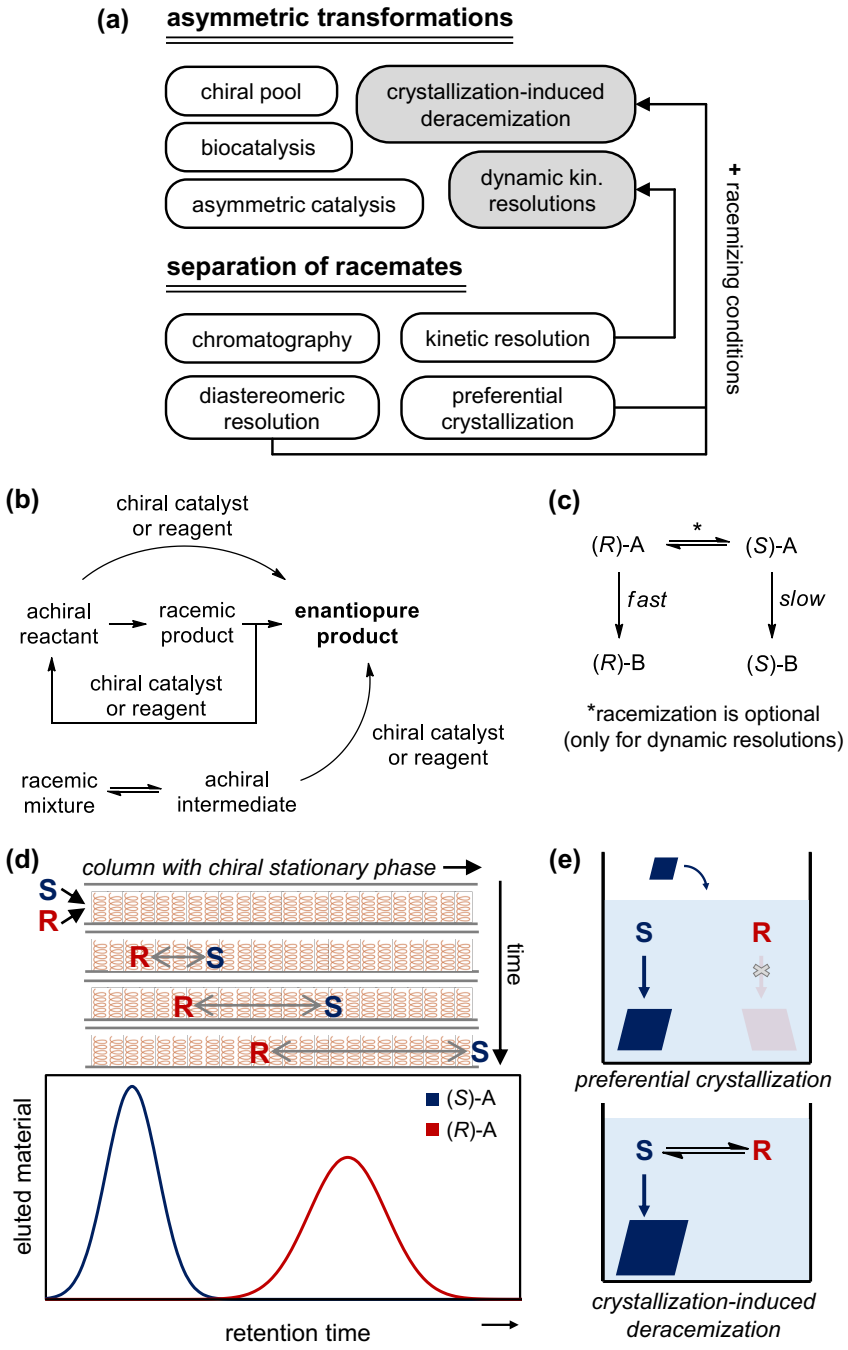


**Figure 1.6.** Paths to enantiopurity. (a) Summarized and classified into asymmetric transformations, that yield a single enantiomer (~100% yield), and separations, that allow obtaining both enantiomer from a racemic or enriched mixture (~50% yield). A visual explanation is further given of (b) the asymmetric synthesis of enantiopure products from achiral reactants or racemic mixtures, (c) kinetic and dynamic kinetic resolutions of racemates, (d) chiral chromatography, and (e) preferential crystallization and crystallization-induced deracemization.

If the starting reactants are achiral and the enantiomeric reaction product needs to be of a specific stereochemistry, one truly enters the field of asymmetric synthesis. In asymmetric synthesis, chirality is induced through a chiral catalyst or a chiral auxiliary (Fig. 1.6b). Some of the most famous examples of asymmetric catalysis have been provided by Nobel Prize winners Knowles, Noyori and Sharpless (2001), and List and MacMillan (2021).

The first catalytic asymmetric syntheses featured transition metal complexes used for hydrogenations bearing chiral ligands.[4,144] First, the prochiral reactant unpreferentially binds the catalyst. Then, as with hands in a handshake, one of the two enantiomeric products has a more favourable diastereomeric transition state and therefore is preferentially formed.[145] Kagan has studied the effect of using enantiomerically impure catalysts, discovering fascinating non-linear effects (e.g. product *ee* exceeding catalyst *ee*).[146] Similar discoveries also feature in this thesis, when the effects of chiral amplification through crystal growth with enantiomerically impure seeds are detailed (esp. Chapter 4). Besides the work by Knowles and Noyori, the Sharpless epoxidation is the other seminal instance of asymmetric catalysis, an innovation immediately relevant for industrial scale processes.[6] In contrast with hydrogenation, Sharpless' process allows for the stereoselective addition of an oxygen to a double bond, forming a reactive epoxide.

The second major innovation in asymmetric synthesis was the use of organic molecules at catalysts. It turns out that not just chiral transition metal catalyst complexes are suitable to perform asymmetric synthesis, but chiral organic molecules can also directly catalyse reactions stereoselectively.[147] List is famous for his use of L- or D-proline, as an amino acid taken from the chiral pool, to stereoselectively catalyse intermolecular aldol reactions.[9] Shortly after, MacMillan reported on amine-catalysed enantioselective Dies-Alder reactions.[10] These two reactions were later respectively classified as enamine and iminium organocatalysis. The impacts of these work was heightened by their mechanistic discussions and the more generic concept of substrate activation presented. Later work by MacMillan merged the initial ideas from organocatalysis with photoredox catalysis, giving access to novel intermediates sustainably.[148]

Taking inspiration from nature, the use of biocatalysis for asymmetric synthesis has also seen a steady rise. These enzymes are often isolated from engineered thermophilic microbes and optimized for desired conversions and stability in suitable industrial reaction conditions.[149] After optimization and expression, immobilization of the enzymes provides an effective heterogeneous chiral catalyst with good industrial performance.[150] Artificial intelligence allows engineering and adapting enzymes for metabolic engineering with increasing facility, significantly shortening the development timeline.[151] Commonly cited pitfalls in asymmetric biocatalysis are large-scale enzyme production, enzymatic stability, and the frequent

need for cofactors—although work-arounds and solutions on the industrial scale have been established.[152]

The field of asymmetric catalysis contains a special subset of reactions called catalytic deracemizations.[153] These reactions form a fall-back strategy: a racemic mixture can be chemically deracemized post-synthesis. This type of catalytic deracemization strategy is conceptually closely related to kinetic resolutions, which will be discussed shortly. In catalytic deracemizations, there are two general strategies: (i) only of the two enantiomers reacts and its stereochemistry is inverted, or (ii) both enantiomers are turned into a prochiral intermediate that is subsequently converted to single enantiomer of choice. Harnessing existing asymmetric transformations, the exact place in the process where a chiral catalyst or auxiliary is required differs. Recently, much attention has been paid to the use of light as means of delivering the activation energy required for catalytic deracemizations.[154]

An anticipated special trick to resolve enantiomers is called kinetic resolution (Fig. 1.6c). This concept is closely related to the first class of catalytic deracemizations: In a kinetic resolution enantiomers react with different reaction rates, yielding enantioenrichment in the less reactive enantiomer. One could argue that kinetic resolution is a kind of separation based on asymmetric reaction rates, often those of enzymatic catalysts. Kinetic resolution not seldomly requires a subsequent separation step in which reacted enantiomers are separated from the unreacted enantiomers.

More conceptually related to this thesis is the *dynamic* kinetic resolution (DKR). In this variation, a second reaction is introduced that allows racemization of the enantiomers (i.e. fast interconversion).[155] The concept here is very much distinct from that of a classic kinetic resolution: the product is now of interest, rather than the enantiomer that lags kinetically behind. Indeed, in DKR, an enantiomeric excess of the slowly reacting enantiomer builds up, which in turns means that this minor enantiomer is first converted to the more reactive major enantiomer and subsequently also to the product. Viewed in this way, a DKR perfectly combines catalytic deracemization and asymmetric synthesis. Unsurprisingly therefore, DKR has been successful in the enantiopure synthesis of many classes of compounds.[156,157] The idea of coupling racemization in solution with other kinetic processes will feature heavily in this thesis.

Having discussed methods reliant on asymmetric chemical reactions, which aim to synthetically obtain only the desired enantiomer, we turn to the first major technique to separate enantiomeric mixtures: chiral chromatography (Fig. 1.6d). Chiral chromatography typically relies on chiral stationary phases that bind one the two enantiomers more strongly. The two enantiomers consequently elute from the column at different times as isolated fractions.[158] Many different chiral stationary

phases exist and the method has seen wide application, especially at the laboratory scale. The use of chiral mobile phases is also possible, creating a chiral column environment whilst permitting the use of established achiral stationary phases.[159] Besides a chiral mobile or stationary phase, one can also use derivatization: chiral derivatizing reagents can yield diastereomers that may be separated conventionally. Due to the high amount of solvent used and the high cost associated with development and procurement of the stationary phase, chiral liquid chromatography is not a very economical or green approach. A benefit of chiral chromatography is that, besides chiral resolution, the chromatography step may simultaneously also get rid of other impurities left over from synthesis. At production scale, simulated moving bed chromatography has been a breakthrough in scaling and productivity.[160]

The second major class of techniques to separate enantiomers is chiral crystallization (Fig. 1.6e). In principle, crystallization from solution can be used to separate species that behave independently in their crystallization behaviour.[161] Separation then ultimately occurs through filtration: one component is crystallized as a solid, while the other remains dissolved in solution. For chiral molecules, however, this oftentimes poses a problem: in 90-95% of cases racemic compounds crystallize as racemic crystals, i.e. solids containing both enantiomers in a 1:1 ratio. Therefore, crystallization is only effective in the special cases when the enantiomers crystallize into separate enantiopure crystals (5-10%) or when they can be brought to do so. In such cases, one enantiomer can for instance be isolated by seeded crystallization and the mother liquor evaporated to recover a mixture enriched in the other.[162,163] This approach is called ‘preferential crystallization’ or ‘resolution by entrainment’.

Besides classical direct crystallization, preferential crystallization can also be combined with solution-phase racemization. If so, one can (partially) deracemize rather than just separate a racemic mixture.[164] Similar to the case of dynamic kinetic resolution, the enantiomer seeds grow at the expense of the other enantiomer, since the crystallization driving forces are coupled through the racemization reaction. Especially effective are cycles of crystal growth and dissolution under racemizing conditions, allowing the full deracemization of slightly enriched (i.e. scalemic) mixtures of enantiomers.[81] Such cycles can be implemented in many ways, such as through grinding or temperature cycling.[165,166] These processes are at the core of this thesis and chapter 3 will introduce chiral crystallization in detail.

As stated before, only few chiral compounds crystallize naturally in a fashion permitting separation or deracemization through crystallization. Two major approaches to further broaden the scope of using crystallization are: (i) the formation of diastereomeric salts, and (ii) the use of co-crystallization. The first case entails combining a chiral target (X; acid or base) with an enantiomerically pure

resolving agent (A; base or acid).[167] The resulting two complexes (R-X:A and S-X:A), stemming from the ionic counter-interactions, are diastereomeric and can thus be separated based on different solubilities. In some variants, a racemic solution of the chiral target is exposed to a library of resolving agents to screen for a combination that has a sufficiently large difference in metastable zone (i.e. a kind of effective kinetic solubility) and thus resolving power.[168,169] This concept is at the core of an approach called Dutch resolution, which will be explained in Chapter 3. When the chiral target is not acidic or basic, either covalent derivatizations with chiral auxiliaries or achiral basic or acidic moieties can be considered, though further increasing process complexity. In the second case, the goal is to mimic conglomerate behaviour through co-crystallization. There, one aims to find an achiral molecule (i.e. A)—called the co-former—that, when combined with a racemic solution of the chiral molecule of interest (i.e. XR and XS), induces the formation of analogous conglomerate co-crystals (i.e. A-XR and A-XS).[170,171] Both these approaches can again be combined with racemization in solution to turn chiral resolution into deracemization processes.[172–175]

As they have little particular relevance for this thesis, other separation methods, such as enantiospecific liquid-liquid extraction and membrane separation, will not be discussed in this introduction. Similarly, methods based on host-guest chemistry and MOFs—notwithstanding their most recent Nobel Prize—are beyond the scope.[176,177]

## Taking stock

The diversity in approaches to cope with chiral challenges in synthesis now compels us to take stock: which of these paths towards enantiopurity are actually chosen in industry when manufacturing enantiopure molecules? And what are the bottlenecks? Having reviewed over 150 synthetic steps wherein chiral centres were introduced in drug molecules brought to market over the last 15 years, a clear picture emerges.[137,178–180] In approximately half of the cases, the chiral centres were imported from the chiral pool. Another 30% involved chiral resolution, mainly crystallization or chromatography. The final 20% comprised asymmetric syntheses, with an equal propensity to using chiral catalysts or chiral auxiliaries. Interestingly, the survey did not provide compelling evidence to conclude a clear shift to indicate that one or more methods are particularly increasing or decreasing in popularity.

Although conceptually ideal, applying asymmetric synthesis at scale and in commercial processes poses a number of concrete challenges.[181] Most stem from transferring the problem of enantiopurity from starting material to catalyst or auxiliary. Chiral ligands and catalysts are not widely available for each transformation, while an industrial process may easily require many kilograms of such catalysts or auxiliaries. Besides crude availability, intellectual property rights

further limit the availability and economics of the most popular and scalable catalysts and auxiliaries. Ignoring these two key concerns, the implementation of formulaic asymmetric syntheses often requires detours in the synthetic route. Such constraints impact the efficiency of the final process and, as a result, its economy. This analysis explains why asymmetric syntheses form an attractive proposition on paper, but may often be cumbersome to realize at scale.

Within the realm of chiral resolutions, the use of supercritical fluid chromatography is surely on the rise. This can be explained through the limited occurrence of racemic conglomerates (i.e. self-sorting enantiopure crystals), so that resolving agents for diastereomeric salt formation are often required for resolution via crystallization. Indeed, chromatography is more expensive in operation but nevertheless more versatile and easier in development. The growing use of $CO_2$ as mobile phase limits its footprint and solvent use.

Whether to choose an asymmetric process in synthesis or whether to perform a resolution is ultimately determined by two factors: (i) overall cost-of-goods and (ii) development risk.[182] From a practical standpoint, a more elaborate route using the chiral pool can be preferred over an efficient route involving asymmetric synthesis. Indeed, the high rate of attrition in pharmaceutical development is an important argument in favour of generic paths that are easy to implement (~90% of developed drugs do not reach the market).[183] Resolutions often imply discarding 50% or more of the synthesized material and this issue becomes more costly each step the resolution is delayed. However, the implementation of an effective racemization and recycling step can tip the balance in the favour of classical resolutions. An example is the synthesis of duloxetine,[184] a dual inhibitor of serotonin and norepinephrine uptake used to treat depressive and anxiety disorders. The route developed during R&D and scaled to pilot scale introduces the chiral centre (i.e. the reduction from ketone to secondary alcohol) using a Li(*ent*-Chirald®)$_2$AlH$_2$ complex with 90% yield and 85-90% enantiomeric excess. However, similar efficiency at scale could be obtained using crystallization (diastereomeric resolution combined with racemization), which was chosen for the final industrial production of duloxetine.[184]

The preceding analysis shows that, when feasible, crystallization-based processes for chiral resolution or deracemization are clearly appealing to industry. Although the poor statistics of conglomerate occurrence and a myriad of other practical problems are often cited as barriers to widely opt for and implement crystallization processes for chiral resolution and deracemization,[158,185,186] the reality is that crystallization process development and the design of the synthesis pathway of a molecule are two very distinct disciplines that are often executed by different parts of an organization.[187] Due to said poor statistics, it often occurs that the final racemic product of the synthesis is indeed not a conglomerate. One proposed remedy would be to integrate crystal form considerations in the choice and design of a synthetic

pathway—an approach we will also recommend in Chapter 8. Several intermediates in pathways neglected for other reasons might indeed have been (racemizable) conglomerates or suitable for Dutch resolution or co-crystal formation, enabling the application of chiral crystallization to obtain a final enantiopure product.

Unfortunately, as a consequence of its poor statistics and isolated position in R&D, chiral crystallization often has a niche reputation and is left to specialists, deterring integration in the standard toolkit of organic chemists and the wider chemistry curriculum. One goal of this thesis is to lower the threshold to apply chiral crystallization, expand its scope, and advocate for its use. Within the reach of any chemist, and not confined to the mystic methods of crystallization-experts, chiral crystallization will prove to be a powerful and very economical approach that often allows getting to grips with the challenge of chirality.

## Outline of this thesis

This thesis expands our fundamental understanding of crystallization-induced deracemizations (CIDs) and then proceeds to distil lessons that can guide the practical development of deracemization processes. The last chapter puts these findings in a broader context: it reflects on the commonly perceived thermodynamic boundaries that limit the application of CIDs. Every chapter has been written as to allow a self-contained reading thereof.

Having introduced the concept of chirality and the general topic of this thesis in **Chapter 1**, we provide further theoretical background in the subsequent two chapters. First, **Chapter 2** provides theoretical foundations of crystallization. After introducing basic thermodynamic concepts, the chapter focuses on dynamic processes of crystal growth, dissolution, and nucleation, as well as related phenomena such as polymorphism, defects, impurities, and inhibition. It concludes with an introduction to reactive crystallization as a topic central to this thesis. **Chapter 3** then proceeds to translate these concepts to the context of chiral crystallization. We start by considering chiral crystal forms and basic preferential crystallization. Next, we discuss the idea of racemizing conditions in the liquid phase, which opens a complex network and enables mass transfer between enantiomeric solids through the liquid phase. Finally, we will examine deracemization through cycles of preferential crystal growth and dissolution under such racemizing conditions and provide a perspective on the main mechanistic questions.

Having provided the theoretical background, we will proceed to the experimental core of this thesis. So far, studies of crystallization-induced deracemization tend to only consider full cycles of crystal growth and dissolution. By now, it has been well established that such cycles indeed allow for enantioenrichment of an initially scalemic (i.e. enriched) solid phase. The contributions of the individual processes,

however, has not been studied systematically. Although experimental work is lacking, crystal growth by itself has commonly been assumed as a source of enantiomeric erosion and discounted as a potential source of enantiomeric amplification. **Chapter 4** challenges this assumption. In this chapter, we study if, and how, crystal growth under racemizing conditions by itself can lead to any form of enantioenrichment. From preferential crystallization, one would perhaps expect—at best—that any initial enantioenrichment is preserved during growth. We investigate whether growth under racemizing conditions can drive enantioenrichment. Counterintuitively, we demonstrate that growth can amplify chirality, an effect arising from the interplay between racemization and growth rates. We also show how the strength of this effect is modulated by the relative amount of crystallized material. As in every chapter, we reflect on how these mechanistic insights can inform process design.

After having demonstrated striking non-linear chiral amplification during crystal growth in Chapter 4, we proceed to examine the effects of crystal size and number on such asymmetric amplification phenomena in **Chapter 5**. Indeed, we hypothesize that amplification phenomena hinge on subtle asymmetries in crystal populations and resulting kinetic drivers. In this chapter, we scrutinize how imbalances in size and mass between two enantiomeric crystal populations translate to asymmetric growth rates which, in turn, determine the outcome of asymmetric crystallization. We will show that a minority population of small crystals can collectively outgrow and ultimately dominate a majority of larger crystals and the resulting imbalances in growth rates can yield positive, linear or even negative, non-linear chiral amplification. Finally, we will also exploit an understanding of crystal growth mechanisms to modulate the effect of size-disparities on the outcome of asymmetric crystallizations.

Besides crystal growth, dissolution is the other key component of cycles driving crystallization-induced deracemization. In **Chapter 6**, we therefore systematically investigate the relative induvial contributions of crystal growth and dissolution for chiral amplification under racemizing conditions. We use a mass balance to expose crystal dynamics and demonstrate that liquid-phase racemization during growth enhances chiral amplification, while racemization during dissolution is counterproductive as the major enantiomer molecules are effectively racemized. We also reveal that there is a persistent dissymmetry between the growth and dissolution of the enantiomer populations—regardless of racemization rate. Indeed, over a full cycle, growth-driven amplification outweighs dissolution-induced erosion. From these experiments, we conclude that it is the fundamental difference between the mechanisms of crystal growth and dissolution that enables a ratchet effect that drives chiral amplification. We reflect on the possible roots of this mechanistic dissymmetry and harness these insights to present an optimal approach

to deracemization that switches racemization selectively on and off during growth and dissolution respectively. This chapter identifies the key practical challenges ahead in the field.

**Chapter 7** applies some of the fundamental lessons learned in this thesis and describes a wholly new process for crystallization-induced deracemization: Deracemization through Solvent Cycling. Solvent Cycling achieves cycles of crystal growth and dissolution by removing solvent, inducing growth, and re-adding solvent, inducing dissolution. Having established in earlier chapters that the combination of slow growth and fast dissolution of crystals is ideal for rapid deracemization, we repurpose a Soxhlet apparatus to realize the slow evaporation and fast re-addition of solvent autonomously. Moreover, we show that Solvent Cycling enables deep cycles and achieves deracemization of a clopidogrel precursor in 3.5 hours—much faster than state-of-the-art methods. As the process mirrors the natural rain cycle, it may also shed light on the origins of biohomochirality.

So far, this thesis has studied the deracemization of conglomerates—i.e. chiral molecules that crystallize into separate enantiomerically pure crystals. Unfortunately, only 5-10% of compounds naturally crystallizes as such a conglomerate. These thermodynamic statistics are a major bottleneck in the practical implementation of crystallization-induced deracemizations. In **Chapter 8**, we open new previously unconsidered possibilities for isolating enantiopure molecules by considering nonequilibrium conditions to address this thermodynamic bottleneck. We systematically analyze the energy differences ($\Delta G^{\Phi}$) between racemic and enantiopure crystal phases for libraries of target molecules (phenylglycine, praziquantel) with different chemical modifications. We show that these libraries reveal wide but similar continuous distributions of $\Delta G^{\Phi}$, wherein similar chemical modifications group together. We realize that such a grouping would allow a directed evolution strategy to quickly discover racemic crystals with a low $\Delta G^{\Phi}$, for which the desired enantiomer might be isolated through nonequilibrium crystallization. Comparing our results with literature data, we also conjecture that as many as half of all chiral molecules may kinetically form enantiopure crystals (~50%), significantly improving our odds of applying chiral crystallization for practically obtaining the single enantiomer of choice.

## References

(1) Desiraju, G. R. Crystal Engineering: A Holistic View. *Angew. Chem. Int. Ed.* **2007**, *46* (44), 8342–8356. https://doi.org/10.1002/anie.200700534.

(2) Sholl, D. S.; Lively, R. P. Seven Chemical Separations to Change the World. *Nature* **2016**, *532* (7600), 435–437. https://doi.org/10.1038/532435a.

(3) Aspuru-Guzik, A.; Baik, M.-H.; Balasubramanian, S.; Banerjee, R.; Bart, S.; Borduas-Dedekind, N.; Chang, S.; Chen, P.; Corminboeuf, C.; Coudert, F.-X.; Cronin, L.; Crudden, C.; Cuk, T.; Doyle, A. G.; Fan, C.; Feng, X.;

Freedman, D.; Furukawa, S.; Ghosh, S.; Glorius, F.; Jeffries-EL, M.; Katsonis, N.; Li, A.; Linse, S. S.; Marchesan, S.; Maulide, N.; Milo, A.; Narayan, A. R. H.; Naumov, P.; Nevado, C.; Nyokong, T.; Palacin, R.; Reid, M.; Robinson, C.; Robinson, G.; Sarpong, R.; Schindler, C.; Schlau-Cohen, G. S.; Schmidt, T. W.; Sessoli, R.; Shao-Horn, Y.; Sleiman, H.; Sutherland, J.; Taylor, A.; Tezcan, A.; Tortosa, M.; Walsh, A.; Watson, A. J. B.; Weckhuysen, B. M.; Weiss, E.; Wilson, D.; Yam, V. W.-W.; Yang, X.; Ying, J. Y.; Yoon, T.; You, S.-L.; Zarbin, A. J. G.; Zhang, H. Charting a Course for Chemistry. *Nat. Chem.* **2019**, *11* (4), 286–294. https://doi.org/10.1038/s41557-019-0236-7.

(4) Knowles, W. S.; Sabacky, M. J. Catalytic Asymmetric Hydrogenation Employing a Soluble, Optically Active, Rhodium Complex. *Chem. Commun. Lond.* **1968**, No. 22, 1445. https://doi.org/10.1039/c19680001445.

(5) Prelog, V. Chirality in Chemistry. *Science* **1976**, *193* (4247), 17–24. https://doi.org/10.1126/science.935852.

(6) Katsuki, T.; Sharpless, K. B. The First Practical Method for Asymmetric Epoxidation. *J. Am. Chem. Soc.* **1980**, *102* (18), 5974–5976. https://doi.org/10.1021/ja00538a077.

(7) Noyori, R.; Kitamura, M. Enantioselective Addition of Organometallic Reagents to Carbonyl Compounds: Chirality Transfer, Multiplication, and Amplification. *Angew. Chem. Int. Ed. Engl.* **1991**, *30* (1), 49–69. https://doi.org/10.1002/anie.199100491.

(8) Bonner, W. A. The Quest for Chirality. In *AIP Conference Proceedings*; AIP: Santa Monica, California (USA), 1996; Vol. 379, pp 17–49. https://doi.org/10.1063/1.51234.

(9) List, B.; Lerner, R. A.; Barbas, C. F. Proline-Catalyzed Direct Asymmetric Aldol Reactions. *J. Am. Chem. Soc.* **2000**, *122* (10), 2395–2396. https://doi.org/10.1021/ja994280y.

(10) Ahrendt, K. A.; Borths, C. J.; MacMillan, D. W. C. New Strategies for Organic Catalysis: The First Highly Enantioselective Organocatalytic Diels–Alder Reaction. *J. Am. Chem. Soc.* **2000**, *122* (17), 4243–4244. https://doi.org/10.1021/ja000092s.

(11) Noyori, R. Asymmetric Catalysis: Science and Opportunities (Nobel Lecture) Copyright© The Nobel Foundation 2002. We Thank the Nobel Foundation, Stockholm, for Permission to Print This Lecture. *Angew. Chem. Int. Ed.* **2002**, *41* (12), 2008. https://doi.org/10.1002/1521-3773(20020617)41:12%253C2008::AID-ANIE2008%253E3.0.CO;2-4.

(12) Buonsanti, R.; Cossairt, B. The Future of Colloidal Semiconductor Nanocrystals. *Chem. Mater.* **2025**, *37* (4), 1333–1334. https://doi.org/10.1021/acs.chemmater.5c00023.

(13) Yang, M.; Liu, Y.; Mo, Y. Lithium Crystallization at Solid Interfaces. *Nat. Commun.* **2023**, *14* (1), 2986. https://doi.org/10.1038/s41467-023-38757-2.

(14) Sekar, S.; Thamotharan, K.; Manickam, S.; Murugesan, B.; Kakimoto, K.; Perumalsamy, R. A Critical Review of The Process and Challenges of Silicon Crystal Growth for Photovoltaic Applications. *Cryst. Res. Technol.* **2024**, *59* (1), 2300131. https://doi.org/10.1002/crat.202300131.

(15) Aarts, J.; Fischer, H.; Adan, O.; Huinink, H. Towards Stable Performance of Salt Hydrates in Thermochemical Energy Storage: A Review. *J. Energy Storage* **2025**, *114*, 115726. https://doi.org/10.1016/j.est.2025.115726.

(16) Walsh, F. C.; Herron, M. E. Electrocrystallization and Electrochemical Control of Crystal Growth: Fundamental Considerations and Electrodeposition of Metals. *J. Phys. Appl. Phys.* **1991**, *24* (2), 217–225. https://doi.org/10.1088/0022-3727/24/2/019.

(17) Hulliger, J. Chemistry and Crystal Growth. *Angew. Chem. Int. Ed. Engl.* **1994**, *33* (2), 143–162. https://doi.org/10.1002/anie.199401431.

(18) García-Ruiz, J. M.; Otálora, F. Crystal Growth in Geology. In *Handbook of Crystal Growth*; Elsevier, 2015; pp 1–43. https://doi.org/10.1016/B978-0-444-63303-3.00001-8.

(19) Arkhipov, S. G.; Bekker, T. B.; Gaydamaka, A. A.; Likhacheva, A. Y.; Losev, E. A.; Boldyreva, E. V. From Geology to Biology: An Interdisciplinary Course in Crystal Growth. *J. Appl. Crystallogr.* **2022**, *55* (5), 1368–1376. https://doi.org/10.1107/S1600576722008032.
(20) Moseley, H. W. Pasteur: The Chemist. *J. Chem. Educ.* **1928**, *5* (1), 50. https://doi.org/10.1021/ed005p50.
(21) Thomson, W. *The Molecular Tactics of a Crystal*; Clarendon Press: Oxford, 1894.
(22) Pasteur, L. Recherches Sur Les Relations Qui Peuvent Exister Entre La Forme Cristalline, La Composition Chimique et Les Sens de La Polarisation Rotatoire. *Ann Chim Phys* **1848**, *24* (3), 442–460.
(23) Vantomme, G.; Crassous, J. Pasteur and Chirality: A Story of How Serendipity Favors the Prepared Minds. *Chirality* **2021**, *33* (10), 597–601. https://doi.org/10.1002/chir.23349.
(24) Grossman, R. B. Van't Hoff, Le Bel, and the Development of Stereochemistry: A Reassessment. *J. Chem. Educ.* **1989**, *66* (1), 30. https://doi.org/10.1021/ed066p30.
(25) Garbacz, P. Introduction to Molecular Chirality. In *Physical Principles of Chirality in NMR*; Garbacz, P., Ed.; Royal Society of Chemistry, 2024; pp 1–32. https://doi.org/10.1039/BK9781839169588-00001.
(26) Cahn, R. S.; Ingold, C.; Prelog, V. Spezifikation Der Molekularen Chiralität. *Angew. Chem.* **1966**, *78* (8), 413–447. https://doi.org/10.1002/ange.19660780803.
(27) *Physical Principles of Chirality in NMR*; Garbacz, P., Ed.; Royal Society of Chemistry, 2024. https://doi.org/10.1039/9781839169588.
(28) Jamieson, E. M. G.; Modicom, F.; Goldup, S. M. Chirality in Rotaxanes and Catenanes. *Chem. Soc. Rev.* **2018**, *47* (14), 5266–5311. https://doi.org/10.1039/C8CS00097B.
(29) Buriak, J. M. 2016 Chemistry Nobel Prize - Molecular Machines Are Real. *Chem. Mater.* **2016**, *28* (20), 7179–7180. https://doi.org/10.1021/acs.chemmater.6b04254.
(30) García, F.; Gómez, R.; Sánchez, L. Chiral Supramolecular Polymers. *Chem. Soc. Rev.* **2023**, *52* (21), 7524–7548. https://doi.org/10.1039/D3CS00470H.
(31) Ten Eikelder, H. M. M.; Markvoort, A. J.; De Greef, T. F. A.; Hilbers, P. A. J. An Equilibrium Model for Chiral Amplification in Supramolecular Polymers. *J. Phys. Chem. B* **2012**, *116* (17), 5291–5301. https://doi.org/10.1021/jp300622m.
(32) Palmans, A. R. A.; Meijer, E. W. Amplification of Chirality in Dynamic Supramolecular Aggregates. *Angew. Chem. Int. Ed.* **2007**, *46* (47), 8948–8968. https://doi.org/10.1002/anie.200701285.
(33) Cao, Z.-Y.; Brittain, W. D. G.; Fossey, J. S.; Zhou, F. Recent Advances in the Use of Chiral Metal Complexes with Achiral Ligands for Application in Asymmetric Catalysis. *Catal. Sci. Technol.* **2015**, *5* (7), 3441–3451. https://doi.org/10.1039/C5CY00182J.
(34) Yao, L.; Zhang, Q.; Li, M.; Chen, C.; Gu, H.; Liu, S.; Long, G.; Liu, F.; Yang, W.; Tang, J. Amplification of Chirality in Self-Assembled Chiral Perovskite Superstructure Films. *J. Am. Chem. Soc.* **2025**, *147* (40), 36420–36427. https://doi.org/10.1021/jacs.5c10609.
(35) Kotov, N. A.; Liz-Marzán, L. M.; Weiss, P. S. Chiral Nanostructures: New Twists. *ACS Nano* **2021**, *15* (8), 12457–12460. https://doi.org/10.1021/acsnano.1c06959.
(36) Kwon, J.; Park, K. H.; Choi, W. J.; Kotov, N. A.; Yeom, J. Chiral Spectroscopy of Nanostructures. *Acc. Chem. Res.* **2023**, *56* (12), 1359–1372. https://doi.org/10.1021/acs.accounts.2c00756.
(37) Ma, W.; Xu, L.; De Moura, A. F.; Wu, X.; Kuang, H.; Xu, C.; Kotov, N. A. Chiral Inorganic Nanostructures. *Chem. Rev.* **2017**, *117* (12), 8041–8093. https://doi.org/10.1021/acs.chemrev.6b00755.
(38) Jiang, W.; Qu, Z.; Kumar, P.; Vecchio, D.; Wang, Y.; Ma, Y.; Bahng, J. H.; Bernardino, K.; Gomes, W. R.; Colombari, F. M.; Lozada-Blanco, A.; Veksler, M.; Marino, E.; Simon, A.; Murray, C.; Muniz, S. R.; De Moura, A. F.; Kotov, N. A. Emergence of Complexity in Hierarchically Organized Chiral Particles. *Science* **2020**, *368* (6491), 642–648. https://doi.org/10.1126/science.aaz7949.
(39) Kumar, P.; Vo, T.; Cha, M.; Visheratina, A.; Kim, J.-Y.; Xu, W.; Schwartz, J.; Simon, A.; Katz, D.; Nicu, V. P.; Marino, E.; Choi, W. J.; Veksler, M.; Chen, S.; Murray, C.; Hovden, R.; Glotzer, S.; Kotov, N. A. Photonically

Active Bowtie Nanoassemblies with Chirality Continuum. *Nature* **2023**, *615* (7952), 418–424. https://doi.org/10.1038/s41586-023-05733-1.

(40) Ben-Moshe, A.; Da Silva, A.; Müller, A.; Abu-Odeh, A.; Harrison, P.; Waelder, J.; Niroui, F.; Ophus, C.; Minor, A. M.; Asta, M.; Theis, W.; Ercius, P.; Alivisatos, A. P. The Chain of Chirality Transfer in Tellurium Nanocrystals. *Science* **2021**, *372* (6543), 729–733. https://doi.org/10.1126/science.abf9645.

(41) Finn, M. G. Emerging Methods for the Rapid Determination of Enantiomeric Excess. *Chirality* **2002**, *14* (7), 534–540. https://doi.org/10.1002/chir.10101.

(42) Yu, X.; Yao, Z.-P. Chiral Recognition and Determination of Enantiomeric Excess by Mass Spectrometry: A Review. *Anal. Chim. Acta* **2017**, *968*, 1–20. https://doi.org/10.1016/j.aca.2017.03.021.

(43) Leung, D.; Kang, S. O.; Anslyn, E. V. Rapid Determination of Enantiomeric Excess: A Focus on Optical Approaches. *Chem Soc Rev* **2012**, *41* (1), 448–479. https://doi.org/10.1039/C1CS15135E.

(44) Calcaterra, A.; D'Acquarica, I. The Market of Chiral Drugs: Chiral Switches versus de Novo Enantiomerically Pure Compounds. *J. Pharm. Biomed. Anal.* **2018**, *147*, 323–340. https://doi.org/10.1016/j.jpba.2017.07.008.

(45) Herrera, B. T.; Pilicer, S. L.; Anslyn, E. V.; Joyce, L. A.; Wolf, C. Optical Analysis of Reaction Yield and Enantiomeric Excess: A New Paradigm Ready for Prime Time. *J. Am. Chem. Soc.* **2018**, *140* (33), 10385–10401. https://doi.org/10.1021/jacs.8b06607.

(46) Barron, L. D. An Introduction to Chirality at the Nanoscale. In *Chirality at the Nanoscale*; Amabilino, D. B., Ed.; Wiley, 2009; pp 1–27. https://doi.org/10.1002/9783527625345.ch1.

(47) Riehl, J. P. *Mirror-Image Asymmetry: An Introduction to the Origin and Consequences of Chirality*, 1st ed.; Wiley, 2010. https://doi.org/10.1002/9780470588888.

(48) Calvin, M. *Chemical Evolution and the Origin of Life*; Clarendon Press: Oxford, 1969.

(49) Cintas, P. Chirality of Living Systems: A Helping Hand from Crystals and Oligopeptides. *Angew. Chem. Int. Ed.* **2002**, *41* (7), 1139–1145. https://doi.org/10.1002/1521-3773(20020402)41:7%253C1139::AID-ANIE1139%253E3.0.CO;2-9.

(50) Devínsky, F. Chirality and the Origin of Life. *Symmetry* **2021**, *13* (12), 2277. https://doi.org/10.3390/sym13122277.

(51) Debets, V. E.; Löwen, H.; Janssen, L. M. C. Glassy Dynamics in Chiral Fluids. *Phys. Rev. Lett.* **2023**, *130* (5), 058201. https://doi.org/10.1103/PhysRevLett.130.058201.

(52) Bloom, B. P.; Paltiel, Y.; Naaman, R.; Waldeck, D. H. Chiral Induced Spin Selectivity. *Chem. Rev.* **2024**, *124* (4), 1950–1991. https://doi.org/10.1021/acs.chemrev.3c00661.

(53) Ray, K.; Ananthavel, S. P.; Waldeck, D. H.; Naaman, R. Asymmetric Scattering of Polarized Electrons by Organized Organic Films of Chiral Molecules. *Science* **1999**, *283* (5403), 814–816. https://doi.org/10.1126/science.283.5403.814.

(54) Carmeli, I.; Gefen, Z.; Vager, Z.; Naaman, R. Alternation between Modes of Electron Transmission through Organized Organic Layers. *Phys. Rev. B* **2003**, *68* (11), 115418. https://doi.org/10.1103/PhysRevB.68.115418.

(55) Bloom, B. P.; Waldeck, A. R.; Waldeck, D. H. Homochirality and Chiral-Induced Spin Selectivity: A New Spin on the Origin of Life. *Proc. Natl. Acad. Sci.* **2022**, *119* (34), e2210505119. https://doi.org/10.1073/pnas.2210505119.

(56) Gonda, Y.; Matsuda, A.; Adachi, K.; Ishii, C.; Suzuki, M.; Osaki, A.; Mita, M.; Nishizaki, N.; Ohtomo, Y.; Shimizu, T.; Yasui, M.; Hamase, K.; Sasabe, J. Mammals Sustain Amino Acid Homochirality against Chiral Conversion by Symbiotic Microbes. *Proc. Natl. Acad. Sci.* **2023**, *120* (15), e2300817120. https://doi.org/10.1073/pnas.2300817120.

(57) Kondepudi, D. K.; Nelson, G. W. Chiral Symmetry Breaking in Nonequilibrium Systems. *Phys. Rev. Lett.* **1983**, *50* (14), 1023–1026. https://doi.org/10.1103/PhysRevLett.50.1023.

(58) Laurent, G.; Göppel, T.; Lacoste, D.; Gerland, U. Emergence of Homochirality via Template-Directed Ligation in an RNA Reactor. *PRX Life* **2024**, *2* (1), 013015. https://doi.org/10.1103/PRXLife.2.013015.

(59) Bada, J. L. Origins of Homochirality. *Nature* **1995**, *374* (6523), 594–595. https://doi.org/10.1038/374594a0.

(60) Pizzarello, S. Identifying Chiral Molecules and Their Enantiomeric Excesses in Extraterrestrial Samples: An Experimental Journey. *Isr. J. Chem.* **2016**, *56* (11–12), 1027–1035. https://doi.org/10.1002/ijch.201600039.

(61) Bocková, J.; Jones, N. C.; Topin, J.; Hoffmann, S. V.; Meinert, C. Uncovering the Chiral Bias of Meteoritic Isovaline through Asymmetric Photochemistry. *Nat. Commun.* **2023**, *14* (1), 3381. https://doi.org/10.1038/s41467-023-39177-y.

(62) Noorduin, W. L.; Bode, A. A. C.; Van Der Meijden, M.; Meekes, H.; Van Etteger, A. F.; Van Enckevort, W. J. P.; Christianen, P. C. M.; Kaptein, B.; Kellogg, R. M.; Rasing, T.; Vlieg, E. Complete Chiral Symmetry Breaking of an Amino Acid Derivative Directed by Circularly Polarized Light. *Nat. Chem.* **2009**, *1* (9), 729–732. https://doi.org/10.1038/nchem.416.

(63) Shoji, M.; Kitazawa, Y.; Sato, A.; Watanabe, N.; Boero, M.; Shigeta, Y.; Umemura, M. Enantiomeric Excesses of Aminonitrile Precursors Determine the Homochirality of Amino Acids. *J. Phys. Chem. Lett.* **2023**, *14* (13), 3243–3248. https://doi.org/10.1021/acs.jpclett.2c03862.

(64) Rikken, G. L. J. A.; Raupach, E. Enantioselective Magnetochiral Photochemistry. *Nature* **2000**, *405* (6789), 932–935. https://doi.org/10.1038/35016043.

(65) Li, R.; Deng, Q.; Han, L.; Ouyang, T.; Che, S.; Fang, Y. Prebiotic Formation of Enantiomeric Excess D-Amino Acids on Natural Pyrite. *Nat. Commun.* **2024**, *15* (1), 10130. https://doi.org/10.1038/s41467-024-54481-x.

(66) Hazen, R. M.; Filley, T. R.; Goodfriend, G. A. Selective Adsorption of L - and D -Amino Acids on Calcite: Implications for Biochemical Homochirality. *Proc. Natl. Acad. Sci.* **2001**, *98* (10), 5487–5490. https://doi.org/10.1073/pnas.101085998.

(67) Glavin, D. P.; Dworkin, J. P.; Alexander, C. M. O.; Aponte, J. C.; Baczynski, A. A.; Barnes, J. J.; Bechtel, H. A.; Berger, E. L.; Burton, A. S.; Caselli, P.; Chung, A. H.; Clemett, S. J.; Cody, G. D.; Dominguez, G.; Elsila, J. E.; Farnsworth, K. K.; Foustoukos, D. I.; Freeman, K. H.; Furukawa, Y.; Gainsforth, Z.; Graham, H. V.; Grassi, T.; Giuliano, B. M.; Hamilton, V. E.; Haenecour, P.; Heck, P. R.; Hofmann, A. E.; House, C. H.; Huang, Y.; Kaplan, H. H.; Keller, L. P.; Kim, B.; Koga, T.; Liss, M.; McLain, H. L.; Marcus, M. A.; Matney, M.; McCoy, T. J.; McIntosh, O. M.; Mojarro, A.; Naraoka, H.; Nguyen, A. N.; Nuevo, M.; Nuth, J. A.; Oba, Y.; Parker, E. T.; Peretyazhko, T. S.; Sandford, S. A.; Santos, E.; Schmitt-Kopplin, P.; Seguin, F.; Simkus, D. N.; Shahid, A.; Takano, Y.; Thomas-Keprta, K. L.; Tripathi, H.; Weiss, G.; Zheng, Y.; Lunning, N. G.; Righter, K.; Connolly, H. C.; Lauretta, D. S. Abundant Ammonia and Nitrogen-Rich Soluble Organic Matter in Samples from Asteroid (101955) Bennu. *Nat. Astron.* **2025**, *9* (2), 199–210. https://doi.org/10.1038/s41550-024-02472-9.

(68) Hawbaker, N. A.; Blackmond, D. G. Energy Threshold for Chiral Symmetry Breaking in Molecular Self-Replication. *Nat. Chem.* **2019**, *11* (10), 957–962. https://doi.org/10.1038/s41557-019-0321-y.

(69) Laurent, G.; Lacoste, D.; Gaspard, P. Emergence of Homochirality in Large Molecular Systems. *Proc. Natl. Acad. Sci.* **2021**, *118* (3), e2012741118. https://doi.org/10.1073/pnas.2012741118.

(70) Frank, F. C. On Spontaneous Asymmetric Synthesis. *Biochim. Biophys. Acta* **1953**, *11*, 459–463. https://doi.org/10.1016/0006-3002(53)90082-1.

(71) Blackmond, D. G. Asymmetric Autocatalysis and Its Implications for the Origin of Homochirality. *Proc. Natl. Acad. Sci.* **2004**, *101* (16), 5732–5736. https://doi.org/10.1073/pnas.0308363101.

(72) Ribó, J. M.; Crusats, J.; El-Hachemi, Z.; Moyano, A.; Hochberg, D. Spontaneous Mirror Symmetry Breaking in Heterocatalytically Coupled Enantioselective Replicators. *Chem. Sci.* **2017**, *8* (1), 763–769. https://doi.org/10.1039/C6SC02446G.

(73) Fenwick, D. R.; Kagan, H. B. Asymmetric Amplification. In *Topics in Stereochemistry*; Denmark, S. E., Ed.; Wiley, 1999; Vol. 22, pp 257–296. https://doi.org/10.1002/9780470147313.ch5.

(74) Feringa, B. L.; Van Delden, R. A. Absolute Asymmetric Synthesis: The Origin, Control, and Amplification of Chirality. *Angew. Chem. Int. Ed.* **1999**, *38* (23), 3418–3438. https://doi.org/10.1002/(SICI)1521-3773(19991203)38:23%253C3418::AID-ANIE3418%253E3.0.CO;2-V.

(75) Zepik, H.; Shavit, E.; Tang, M.; Jensen, T. R.; Kjaer, K.; Bolbach, G.; Leiserowitz, L.; Weissbuch, I.; Lahav, M. Chiral Amplification of Oligopeptides in Two-Dimensional Crystalline Self-Assemblies on Water. *Science* **2002**, *295* (5558), 1266–1269. https://doi.org/10.1126/science.1065625.

(76) Wynberg, H.; Feringa, B. Enantiomeric Recognition and Interactions. *Tetrahedron* **1976**, *32* (22), 2831–2834. https://doi.org/10.1016/0040-4020(76)80131-7.

(77) Hagelschuer, A.; Padín, D.; Dašková, V.; Feringa, B. L. Toward Chiral Recognition by Design: Uncovering the Self-Enantioresolving Properties of Chiral Amine Derivatives. *J. Am. Chem. Soc.* **2025**, *147* (22), 18662–18673. https://doi.org/10.1021/jacs.5c01251.

(78) Havinga, E. Spontaneous Formation of Optically Active Substances. *Biochim. Biophys. Acta* **1954**, *13*, 171–174. https://doi.org/10.1016/0006-3002(54)90300-5.

(79) Kondepudi, D. K.; Kaufman, R. J.; Singh, N. Chiral Symmetry Breaking in Sodium Chlorate Crystallization. *Science* **1990**, *250* (4983), 975–976. https://doi.org/10.1126/science.250.4983.975.

(80) McBride, J. M.; Carter, R. L. Spontaneous Resolution by Stirred Crystallization. *Angew. Chem. Int. Ed. Engl.* **1991**, *30* (3), 293–295. https://doi.org/10.1002/anie.199102931.

(81) Viedma, C. Chiral Symmetry Breaking During Crystallization: Complete Chiral Purity Induced by Nonlinear Autocatalysis and Recycling. *Phys. Rev. Lett.* **2005**, *94* (6), 065504. https://doi.org/10.1103/PhysRevLett.94.065504.

(82) Blackmond, D. G.; Klussmann, M. Spoilt for Choice: Assessing Phase Behavior Models for the Evolution of Homochirality. *Chem. Commun.* **2007**, No. 39, 3990. https://doi.org/10.1039/b709314b.

(83) Blackmond, D. G. The Origin of Biological Homochirality. *Cold Spring Harb. Perspect. Biol.* **2010**, *2* (5), a002147–a002147. https://doi.org/10.1101/cshperspect.a002147.

(84) Baglai, I.; Leeman, M.; Wurst, K.; Kellogg, R. M.; Noorduin, W. L. Enantiospecific Solid Solution Formation Triggers the Propagation of Homochirality. *Angew. Chem. Int. Ed.* **2020**, *59* (47), 20885–20889. https://doi.org/10.1002/anie.202009719.

(85) Safont-Sempere, M. M.; Fernández, G.; Würthner, F. Self-Sorting Phenomena in Complex Supramolecular Systems. *Chem. Rev.* **2011**, *111* (9), 5784–5814. https://doi.org/10.1021/cr100357h.

(86) Liu, M.; Zhang, L.; Wang, T. Supramolecular Chirality in Self-Assembled Systems. *Chem. Rev.* **2015**, *115* (15), 7304–7397. https://doi.org/10.1021/cr500671p.

(87) Ribó, J. M.; Hochberg, D.; Buhse, T.; Micheau, J.-C. Viedma Deracemization Mechanisms in Self-Assembly Processes. *Phys. Chem. Chem. Phys.* **2025**, *27* (5), 2516–2527. https://doi.org/10.1039/D4CP03910F.

(88) Smulders, M. M. J.; Stals, P. J. M.; Mes, T.; Paffen, T. F. E.; Schenning, A. P. H. J.; Palmans, A. R. A.; Meijer, E. W. Probing the Limits of the Majority-Rules Principle in a Dynamic Supramolecular Polymer. *J. Am. Chem. Soc.* **2010**, *132* (2), 620–626. https://doi.org/10.1021/ja9080875.

(89) Micali, N.; Engelkamp, H.; Van Rhee, P. G.; Christianen, P. C. M.; Scolaro, L. M.; Maan, J. C. Selection of Supramolecular Chirality by Application of Rotational and Magnetic Forces. *Nat. Chem.* **2012**, *4* (3), 201–207. https://doi.org/10.1038/nchem.1264.

(90) van Dijken, D. J.; Beierle, J. M.; Stuart, M. C. A.; Szymański, W.; Browne, W. R.; Feringa, B. L. Autoamplification of Molecular Chirality through the Induction of Supramolecular Chirality. *Angew. Chem. Int. Ed.* **2014**, *53* (20), 5073–5077. https://doi.org/10.1002/anie.201311160.

(91) Mahadevi, A. S.; Sastry, G. N. Cooperativity in Noncovalent Interactions. *Chem. Rev.* **2016**, *116* (5), 2775–2825. https://doi.org/10.1021/cr500344e.
(92) Cantekin, S.; Ten Eikelder, H. M. M.; Markvoort, A. J.; Veld, M. A. J.; Korevaar, P. A.; Green, M. M.; Palmans, A. R. A.; Meijer, E. W. Consequences of Cooperativity in Racemizing Supramolecular Systems. *Angew. Chem. Int. Ed.* **2012**, *51* (26), 6426–6431. https://doi.org/10.1002/anie.201201701.
(93) Carnall, J. M. A.; Waudby, C. A.; Belenguer, A. M.; Stuart, M. C. A.; Peyralans, J. J.-P.; Otto, S. Mechanosensitive Self-Replication Driven by Self-Organization. *Science* **2010**, *327* (5972), 1502–1506. https://doi.org/10.1126/science.1182767.
(94) Altay, Y.; Tezcan, M.; Otto, S. Emergence of a New Self-Replicator from a Dynamic Combinatorial Library Requires a Specific Pre-Existing Replicator. *J. Am. Chem. Soc.* **2017**, *139* (39), 13612–13615. https://doi.org/10.1021/jacs.7b07346.
(95) Yang, S.; Geiger, Y.; Geerts, M.; Eleveld, M. J.; Kiani, A.; Otto, S. Enantioselective Self-Replicators. *J. Am. Chem. Soc.* **2023**, *145* (30), 16889–16898. https://doi.org/10.1021/jacs.3c05472.
(96) Ottelé, J.; Hussain, A. S.; Mayer, C.; Otto, S. Chance Emergence of Catalytic Activity and Promiscuity in a Self-Replicator. *Nat. Catal.* **2020**, *3* (7), 547–553. https://doi.org/10.1038/s41929-020-0463-8.
(97) Palmans, A. R. A. Deracemisations under Kinetic and Thermodynamic Control. *Mol. Syst. Des. Eng.* **2017**, *2* (1), 34–46. https://doi.org/10.1039/C6ME00088F.
(98) Singh, A.; Goswami, S.; Singh, P.; Das, D. Exploitation of Catalytic Dyads by Short Peptide-Based Nanotubes for Enantioselective Covalent Catalysis. *Angew. Chem. Int. Ed.* **2023**, *62* (51), e202315716. https://doi.org/10.1002/anie.202315716.
(99) Ortega Lorenzo, M.; Baddeley, C. J.; Muryn, C.; Raval, R. Extended Surface Chirality from Supramolecular Assemblies of Adsorbed Chiral Molecules. *Nature* **2000**, *404* (6776), 376–379. https://doi.org/10.1038/35006031.
(100) Kühnle, A.; Linderoth, T. R.; Hammer, B.; Besenbacher, F. Chiral Recognition in Dimerization of Adsorbed Cysteine Observed by Scanning Tunnelling Microscopy. *Nature* **2002**, *415* (6874), 891–893. https://doi.org/10.1038/415891a.
(101) Crassous, J. Chiral Transfer in Coordination Complexes: Towards Molecular Materials. *Chem. Soc. Rev.* **2009**, *38* (3), 830. https://doi.org/10.1039/b806203j.
(102) Ozturk, S. F.; Liu, Z.; Sutherland, J. D.; Sasselov, D. D. Origin of Biological Homochirality by Crystallization of an RNA Precursor on a Magnetic Surface. *Sci. Adv.* **2023**, *9* (23), eadg8274. https://doi.org/10.1126/sciadv.adg8274.
(103) Raynal, M.; Portier, F.; Van Leeuwen, P. W. N. M.; Bouteiller, L. Tunable Asymmetric Catalysis through Ligand Stacking in Chiral Rigid Rods. *J. Am. Chem. Soc.* **2013**, *135* (47), 17687–17690. https://doi.org/10.1021/ja408860s.
(104) Ozturk, S. F.; Sasselov, D. D.; Sutherland, J. D. The Central Dogma of Biological Homochirality: How Does Chiral Information Propagate in a Prebiotic Network? *J. Chem. Phys.* **2023**, *159* (6), 061102. https://doi.org/10.1063/5.0156527.
(105) Hein, J. E.; Blackmond, D. G. On the Origin of Single Chirality of Amino Acids and Sugars in Biogenesis. *Acc. Chem. Res.* **2012**, *45* (12), 2045–2054. https://doi.org/10.1021/ar200316n.
(106) MacDermott, A. J.; Barron, L. D.; Brack, A.; Buhse, T.; Drake, A. F.; Emery, R.; Gottarelli, G.; Greenberg, J. M.; Haberle, R.; Hegstrom, R. A.; Hobbs, K.; Kondepudi, D. K.; McKay, C.; Moorbath, S.; Raulin, F.; Sandford, M.; Schwartzman, D. W.; Thiemann, W. H.-P.; Tranter, G. E.; Zarnecki, J. C. Homochirality as the Signature of Life: The SETH Cigar. *Planet. Space Sci.* **1996**, *44* (11), 1441–1446. https://doi.org/10.1016/S0032-0633(96)00057-8.

(107) Eleveld, M. J.; Geiger, Y.; Wu, J.; Kiani, A.; Schaeffer, G.; Otto, S. Competitive Exclusion among Self-Replicating Molecules Curtails the Tendency of Chemistry to Diversify. *Nat. Chem.* **2025**, *17* (1), 132–140. https://doi.org/10.1038/s41557-024-01664-0.

(108) Brewster, J. H.; Laskowski, M. Left-Handed Comments. *Science* **1992**, *258* (5086), 1289–1289. https://doi.org/10.1126/science.1455216.

(109) Xu, Y.; Zhu, T. F. Mirror-Image T7 Transcription of Chirally Inverted Ribosomal and Functional RNAs. *Science* **2022**, *378* (6618), 405–412. https://doi.org/10.1126/science.abm0646.

(110) Harrison, K.; Mackay, A. S.; Kambanis, L.; Maxwell, J. W. C.; Payne, R. J. Synthesis and Applications of Mirror-Image Proteins. *Nat. Rev. Chem.* **2023**, *7* (6), 383–404. https://doi.org/10.1038/s41570-023-00493-y.

(111) Schumacher, T. N. M.; Mayr, L. M.; Minor, D. L.; Milhollen, M. A.; Burgess, M. W.; Kim, P. S. Identification of D -Peptide Ligands Through Mirror-Image Phage Display. *Science* **1996**, *271* (5257), 1854–1857. https://doi.org/10.1126/science.271.5257.1854.

(112) Klußmann, S.; Nolte, A.; Bald, R.; Erdmann, V. A.; Fürste, J. P. Mirror-Image RNA That Binds D-Adenosine. *Nat. Biotechnol.* **1996**, *14* (9), 1112–1115. https://doi.org/10.1038/nbt0996-1112.

(113) Mandal, K.; Uppalapati, M.; Ault-Riché, D.; Kenney, J.; Lowitz, J.; Sidhu, S. S.; Kent, S. B. H. Chemical Synthesis and X-Ray Structure of a Heterochiral {D-Protein Antagonist *plus* Vascular Endothelial Growth Factor} Protein Complex by Racemic Crystallography. *Proc. Natl. Acad. Sci.* **2012**, *109* (37), 14779–14784. https://doi.org/10.1073/pnas.1210483109.

(114) Feng, Z.; Xu, B. Inspiration from the Mirror: D-Amino Acid Containing Peptides in Biomedical Approaches. *Biomol. Concepts* **2016**, *7* (3), 179–187. https://doi.org/10.1515/bmc-2015-0035.

(115) Kapil, S.; Sharma, V. D -Amino Acids in Antimicrobial Peptides: A Potential Approach to Treat and Combat Antimicrobial Resistance. *Can. J. Microbiol.* **2021**, *67* (2), 119–137. https://doi.org/10.1139/cjm-2020-0142.

(116) Adamala, K. P.; Agashe, D.; Belkaid, Y.; Bittencourt, D. M. D. C.; Cai, Y.; Chang, M. W.; Chen, I. A.; Church, G. M.; Cooper, V. S.; Davis, M. M.; Devaraj, N. K.; Endy, D.; Esvelt, K. M.; Glass, J. I.; Hand, T. W.; Inglesby, T. V.; Isaacs, F. J.; James, W. G.; Jones, J. D. G.; Kay, M. S.; Lenski, R. E.; Liu, C.; Medzhitov, R.; Nicotra, M. L.; Oehm, S. B.; Pannu, J.; Relman, D. A.; Schwille, P.; Smith, J. A.; Suga, H.; Szostak, J. W.; Talbot, N. J.; Tiedje, J. M.; Venter, J. C.; Winter, G.; Zhang, W.; Zhu, X.; Zuber, M. T. Confronting Risks of Mirror Life. *Science* **2024**, *386* (6728), 1351–1353. https://doi.org/10.1126/science.ads9158.

(117) ÓhÉigeartaigh, S. Extinction of the Human Species: What Could Cause It and How Likely Is It to Occur? *Camb. Prisms Extinction* **2025**, *3*, e4. https://doi.org/10.1017/ext.2025.4.

(118) Adamala, K.; Agashe, D.; Binder, D.; Cai, Y.; Cooper, V.; Duncombe, R.; Esvelt, K.; Glass, J.; Hand, T.; Inglesby, T.; Isaacs, F.; Jones, J.; Lenski, R.; Lewis, G.; Medzhitov, R.; Nicotra, M.; Oehm, S.; Pannu, J.; Relman, D.; Suga, H.; Sweere, J.; Szostak, J.; Talbot, N.; Wang, B. Technical Report on Mirror Bacteria: Feasibility and Risks. **2025**. https://doi.org/10.25740/CV716PJ4036.

(119) Genchi, G. An Overview on D-Amino Acids. *Amino Acids* **2017**, *49* (9), 1521–1533. https://doi.org/10.1007/s00726-017-2459-5.

(120) Shi, Y.; Hussain, Z.; Zhao, Y. Promising Application of D-Amino Acids toward Clinical Therapy. *Int. J. Mol. Sci.* **2022**, *23* (18), 10794. https://doi.org/10.3390/ijms231810794.

(121) Fisher, G. H.; D'Aniello, A.; Vetere, A.; Padula, L.; Cusano, G. P.; Man, E. H. Free D-Aspartate and D-Alanine in Normal and Alzheimer Brain. *Brain Res. Bull.* **1991**, *26* (6), 983–985. https://doi.org/10.1016/0361-9230(91)90266-M.

(122) Satoh, S.; Esashi, Y. D-Amino-Acid-Stimulated Ethylene Production in Seed Tissues. *Planta* **1980**, *149* (1), 64–68. https://doi.org/10.1007/BF00386229.

(123) Cava, F.; Lam, H.; De Pedro, M. A.; Waldor, M. K. Emerging Knowledge of Regulatory Roles of D-Amino Acids in Bacteria. *Cell. Mol. Life Sci.* **2011**, *68* (5), 817–831. https://doi.org/10.1007/s00018-010-0571-8.

(124) Liu, L.; Zhong, M.; Chen, Q.; Tang, K. The Hidden Hand of Molecular Chirality in Marine Biogeochemistry. *Trends Chem.* **2025**, *7* (3), 149–162. https://doi.org/10.1016/j.trechm.2025.01.007.

(125) Kondepudi, D. K.; Durand, D. J. Chiral Asymmetry in Spiral Galaxies? *Chirality* **2001**, *13* (7), 351–356. https://doi.org/10.1002/chir.1044.

(126) Matassa, R.; Ray, S. C.; Zheng, Y. Chirality in Nanomaterials. *Sci. Rep.* **2024**, *14* (1), 26268, s41598-024-77887–5. https://doi.org/10.1038/s41598-024-77887-5.

(127) Zhou, Y.; Marson, R. L.; Van Anders, G.; Zhu, J.; Ma, G.; Ercius, P.; Sun, K.; Yeom, B.; Glotzer, S. C.; Kotov, N. A. Biomimetic Hierarchical Assembly of Helical Supraparticles from Chiral Nanoparticles. *ACS Nano* **2016**, *10* (3), 3248–3256. https://doi.org/10.1021/acsnano.5b05983.

(128) Valev, V. K.; Govorov, A. O.; Pendry, J. Chirality and Nanophotonics: Chirality and Nanophotonics (Advanced Optical Materials 16/2017). *Adv. Opt. Mater.* **2017**, *5* (16), adom.201770069. https://doi.org/10.1002/adom.201770069.

(129) Wu, Z.; Chen, X.; Wang, M.; Dong, J.; Zheng, Y. High-Performance Ultrathin Active Chiral Metamaterials. *ACS Nano* **2018**, *12* (5), 5030–5041. https://doi.org/10.1021/acsnano.8b02566.

(130) Lin, L.; Lepeshov, S.; Krasnok, A.; Jiang, T.; Peng, X.; Korgel, B. A.; Alù, A.; Zheng, Y. All-Optical Reconfigurable Chiral Meta-Molecules. *Mater. Today* **2019**, *25*, 10–20. https://doi.org/10.1016/j.mattod.2019.02.015.

(131) Di Giuseppe, G.; Vitali, D. Entangled Light Enhances Force Sensing. *Nat. Photonics* **2023**, *17* (6), 465–466. https://doi.org/10.1038/s41566-023-01215-y.

(132) Petronijevic, E.; Cesca, T.; Scian, C.; Mattei, G.; Voti, R. L.; Sibilia, C.; Belardini, A. Demonstration of Extrinsic Chirality in Self-Assembled Asymmetric Plasmonic Metasurfaces and Nanohole Arrays. *Sci. Rep.* **2024**, *14* (1), 17210. https://doi.org/10.1038/s41598-024-68007-4.

(133) Vlasov, E.; Heyvaert, W.; Ni, B.; Van Gordon, K.; Girod, R.; Verbeeck, J.; Liz-Marzán, L. M.; Bals, S. High-Throughput Morphological Chirality Quantification of Twisted and Wrinkled Gold Nanorods. *ACS Nano* **2024**, *18* (18), 12010–12019. https://doi.org/10.1021/acsnano.4c02757.

(134) Tokunaga, E.; Yamamoto, T.; Ito, E.; Shibata, N. Understanding the Thalidomide Chirality in Biological Processes by the Self-Disproportionation of Enantiomers. *Sci. Rep.* **2018**, *8* (1), 17131. https://doi.org/10.1038/s41598-018-35457-6.

(135) Ballard, A.; Narduolo, S.; Ahmed, H. O.; Keymer, N. I.; Asaad, N.; Cosgrove, D. A.; Buurma, N. J.; Leach, A. G. Racemisation in Chemistry and Biology. *Chem. – Eur. J.* **2020**, *26* (17), 3661–3687. https://doi.org/10.1002/chem.201903917.

(136) McVicker, R. U.; O'Boyle, N. M. Chirality of New Drug Approvals (2013–2022): Trends and Perspectives. *J. Med. Chem.* **2024**, *67* (4), 2305–2320. https://doi.org/10.1021/acs.jmedchem.3c02239.

(137) Senkuttuvan, N.; Komarasamy, B.; Krishnamoorthy, R.; Sarkar, S.; Dhanasekaran, S.; Anaikutti, P. The Significance of Chirality in Contemporary Drug Discovery-a Mini Review. *RSC Adv.* **2024**, *14* (45), 33429–33448. https://doi.org/10.1039/D4RA05694A.

(138) Pinètre, C. Achieving Enantiopurity Through Directed Evolution and Crystallization under Non-Equilibrium Conditions, Normandie Université, Rouen, 2024.

(139) Jang, Y.; Kim, B.; Shin, J. H.; Choi, Y. J.; Choi, S.; Song, C. W.; Lee, J.; Park, H. G.; Lee, S. Y. Bio-based Production of C2–C6 Platform Chemicals. *Biotechnol. Bioeng.* **2012**, *109* (10), 2437–2459. https://doi.org/10.1002/bit.24599.

(140) Heretsch, P.; Thomas, F.; Aurich, A.; Krautscheid, H.; Sicker, D.; Giannis, A. Syntheses with a Chiral Building Block from the Citric Acid Cycle: (2 *R* ,3 *S* )-Isocitric Acid by Fermentation of Sunflower Oil. *Angew. Chem. Int. Ed.* **2008**, *47* (10), 1958–1960. https://doi.org/10.1002/anie.200705000.

(141) Liu, H.-H.; Ji, X.-J.; Huang, H. Biotechnological Applications of Yarrowia Lipolytica: Past, Present and Future. *Biotechnol. Adv.* **2015**, *33* (8), 1522–1546. https://doi.org/10.1016/j.biotechadv.2015.07.010.

(142) Aurich, A.; Specht, R.; Müller, R. A.; Stottmeister, U.; Yovkova, V.; Otto, C.; Holz, M.; Barth, G.; Heretsch, P.; Thomas, F. A.; Sicker, D.; Giannis, A. Microbiologically Produced Carboxylic Acids Used as Building Blocks in Organic Synthesis. In *Reprogramming Microbial Metabolic Pathways*; Wang, X., Chen, J., Quinn, P., Eds.; Subcellular Biochemistry; Springer Netherlands: Dordrecht, 2012; Vol. 64, pp 391–423. https://doi.org/10.1007/978-94-007-5055-5_19.

(143) Haleema, S.; Sasi, P. V.; Ibnusaud, I.; Polavarapu, P. L.; Kagan, H. B. Enantiomerically Pure Compounds Related to Chiral Hydroxy Acids Derived from Renewable Resources. *RSC Adv.* **2012**, *2* (25), 9257. https://doi.org/10.1039/c2ra21205f.

(144) Miyashita, A.; Yasuda, A.; Takaya, H.; Toriumi, K.; Ito, T.; Souchi, T.; Noyori, R. Synthesis of 2,2'-Bis(Diphenylphosphino)-1,1'-Binaphthyl (BINAP), an Atropisomeric Chiral Bis(Triaryl)Phosphine, and Its Use in the Rhodium(I)-Catalyzed Asymmetric Hydrogenation of .Alpha.-(Acylamino)Acrylic Acids. *J. Am. Chem. Soc.* **1980**, *102* (27), 7932–7934. https://doi.org/10.1021/ja00547a020.

(145) Halpern, J. Mechanism and Stereoselectivity of Asymmetric Hydrogenation. *Science* **1982**, *217* (4558), 401–407. https://doi.org/10.1126/science.217.4558.401.

(146) Guillaneux, D.; Zhao, S.-H.; Samuel, O.; Rainford, D.; Kagan, H. B. Nonlinear Effects in Asymmetric Catalysis. *J. Am. Chem. Soc.* **1994**, *116* (21), 9430–9439. https://doi.org/10.1021/ja00100a004.

(147) Garg, A.; Rendina, D.; Bendale, H.; Akiyama, T.; Ojima, I. Recent Advances in Catalytic Asymmetric Synthesis. *Front. Chem.* **2024**, *12*, 1398397. https://doi.org/10.3389/fchem.2024.1398397.

(148) Nicewicz, D. A.; MacMillan, D. W. C. Merging Photoredox Catalysis with Organocatalysis: The Direct Asymmetric Alkylation of Aldehydes. *Science* **2008**, *322* (5898), 77–80. https://doi.org/10.1126/science.1161976.

(149) Zhang, Z.-J.; Pan, J.; Ma, B.-D.; Xu, J.-H. Efficient Biocatalytic Synthesis of Chiral Chemicals. In *Bioreactor Engineering Research and Industrial Applications I*; Ye, Q., Bao, J., Zhong, J.-J., Eds.; Advances in Biochemical Engineering/Biotechnology; Springer Berlin Heidelberg: Berlin, Heidelberg, 2014; Vol. 155, pp 55–106. https://doi.org/10.1007/10_2014_291.

(150) Nanba, H.; Yasohara, Y.; Hasegawa, J.; Takahashi, S. Bioreactor Systems for the Production of Optically Active Amino Acids and Alcohols. *Org. Process Res. Dev.* **2007**, *11* (3), 503–508. https://doi.org/10.1021/op060129e.

(151) Jang, W. D.; Kim, G. B.; Kim, Y.; Lee, S. Y. Applications of Artificial Intelligence to Enzyme and Pathway Design for Metabolic Engineering. *Curr. Opin. Biotechnol.* **2022**, *73*, 101–107. https://doi.org/10.1016/j.copbio.2021.07.024.

(152) Devine, P. N.; Howard, R. M.; Kumar, R.; Thompson, M. P.; Truppo, M. D.; Turner, N. J. Extending the Application of Biocatalysis to Meet the Challenges of Drug Development. *Nat. Rev. Chem.* **2018**, *2* (12), 409–421. https://doi.org/10.1038/s41570-018-0055-1.

(153) Huang, M.; Pan, T.; Jiang, X.; Luo, S. Catalytic Deracemization Reactions. *J. Am. Chem. Soc.* **2023**, *145* (20), 10917–10929. https://doi.org/10.1021/jacs.3c02622.

(154) Großkopf, J.; Bach, T. Catalytic Photochemical Deracemization via Short-Lived Intermediates. *Angew. Chem. Int. Ed.* **2023**, *62* (50), e202308241. https://doi.org/10.1002/anie.202308241.

(155) Huerta, F. F.; Minidis, A. B. E.; Bäckvall, J.-E. Racemisation in Asymmetric Synthesis. Dynamic Kinetic Resolution and Related Processes in Enzyme and Metal Catalysis. *Chem. Soc. Rev.* **2001**, *30* (6), 321–331. https://doi.org/10.1039/b105464n.

(156) Blacker, A. J.; Stirling, M. J.; Page, M. I. Catalytic Racemisation of Chiral Amines and Application in Dynamic Kinetic Resolution. *Org. Process Res. Dev.* **2007**, *11* (3), 642–648. https://doi.org/10.1021/op060233w.

(157) Yang, L.-C.; Deng, H.; Renata, H. Recent Progress and Developments in Chemoenzymatic and Biocatalytic Dynamic Kinetic Resolution. *Org. Process Res. Dev.* **2022**, *26* (7), 1925–1943. https://doi.org/10.1021/acs.oprd.1c00463.

(158) Sui, J.; Wang, N.; Wang, J.; Huang, X.; Wang, T.; Zhou, L.; Hao, H. Strategies for Chiral Separation: From Racemate to Enantiomer. *Chem. Sci.* **2023**, *14* (43), 11955–12003. https://doi.org/10.1039/D3SC01630G.

(159) Pettersson, C. Chromatographic Separation of Enantiomers of Acids with Quinine as Chiral Counter Ion. *J. Chromatogr. A* **1984**, *316*, 553–567. https://doi.org/10.1016/S0021-9673(00)96183-1.

(160) Lorenz, H.; Seidel-Morgenstern, A. Processes To Separate Enantiomers. *Angew. Chem. Int. Ed.* **2014**, *53* (5), 1218–1250. https://doi.org/10.1002/anie.201302823.

(161) Cisternas, L. A.; Vásquez, C. M.; Swaney, R. E. On the Design of Crystallization-based Separation Processes: Review and Extension. *AIChE J.* **2006**, *52* (5), 1754–1769. https://doi.org/10.1002/aic.10768.

(162) Levilain, G.; Coquerel, G. Pitfalls and Rewards of Preferential Crystallization. *CrystEngComm* **2010**, *12* (7), 1983. https://doi.org/10.1039/c001895c.

(163) Gänsch, J.; Huskova, N.; Kerst, K.; Temmel, E.; Lorenz, H.; Mangold, M.; Janiga, G.; Seidel-Morgenstern, A. Continuous Enantioselective Crystallization of Chiral Compounds in Coupled Fluidized Beds. *Chem. Eng. J.* **2021**, *422*, 129627. https://doi.org/10.1016/j.cej.2021.129627.

(164) Rougeot, C.; Hein, J. E. Application of Continuous Preferential Crystallization to Efficiently Access Enantiopure Chemicals. *Org. Process Res. Dev.* **2015**, *19* (12), 1809–1819. https://doi.org/10.1021/acs.oprd.5b00141.

(165) Noorduin, W. L.; Izumi, T.; Millemaggi, A.; Leeman, M.; Meekes, H.; Van Enckevort, W. J. P.; Kellogg, R. M.; Kaptein, B.; Vlieg, E.; Blackmond, D. G. Emergence of a Single Solid Chiral State from a Nearly Racemic Amino Acid Derivative. *J. Am. Chem. Soc.* **2008**, *130* (4), 1158–1159. https://doi.org/10.1021/ja7106349.

(166) Suwannasang, K.; Flood, A. E.; Rougeot, C.; Coquerel, G. Using Programmed Heating–Cooling Cycles with Racemization in Solution for Complete Symmetry Breaking of a Conglomerate Forming System. *Cryst. Growth Des.* **2013**, *13* (8), 3498–3504. https://doi.org/10.1021/cg400436r.

(167) Kellogg, R. M.; Kaptein, B.; Vries, T. R. Dutch Resolution of Racemates and the Roles of Solid Solution Formation and Nucleation Inhibition. In *Novel Optical Resolution Technologies*; Sakai, K., Hirayama, N., Tamura, R., Eds.; Topics in Current Chemistry; Springer Berlin Heidelberg: Berlin, Heidelberg, 2007; Vol. 269, pp 159–197. https://doi.org/10.1007/128_2006_095.

(168) Vries, T.; Wynberg, H.; Van Echten, E.; Koek, J.; Ten Hoeve, W.; Kellogg, R. M.; Broxterman, Q. B.; Minnaard, A.; Kaptein, B.; Van Der Sluis, S.; Hulshof, L.; Kooistra, J. The Family Approach to the Resolution of Racemates. *Angew. Chem. Int. Ed.* **1998**, *37* (17), 2349–2354. https://doi.org/10.1002/(SICI)1521-3773(19980918)37:17%253C2349::AID-ANIE2349%253E3.0.CO;2-I.

(169) Dalmolen, J.; Tiemersma-Wegman, T. D.; Nieuwenhuijzen, J. W.; Van Der Sluis, M.; Van Echten, E.; Vries, T. R.; Kaptein, B.; Broxterman, Q. B.; Kellogg, R. M. The Dutch Resolution Variant of the Classical Resolution of Racemates by Formation of Diastereomeric Salts: Family Behaviour in Nucleation Inhibition. *Chem. – Eur. J.* **2005**, *11* (19), 5619–5624. https://doi.org/10.1002/chem.200500440.

(170) Charpentier, M. D.; Devogelaer, J.-J.; Tijink, A.; Meekes, H.; Tinnemans, P.; Vlieg, E.; De Gelder, R.; Johnston, K.; Ter Horst, J. H. Comparing and Quantifying the Efficiency of Cocrystal Screening Methods for Praziquantel. *Cryst. Growth Des.* **2022**, *22* (9), 5511–5525. https://doi.org/10.1021/acs.cgd.2c00615.

(171) Rapeenun, P.; Gerard, C. J. J.; Pinètre, C.; Cartigny, Y.; Tinnemans, P.; De Gelder, R.; Flood, A. E.; Ter Horst, J. H. Searching for Conglomerate Cocrystals of the Racemic Compound Praziquantel. *Cryst. Growth Des.* **2024**, *24* (1), 480–490. https://doi.org/10.1021/acs.cgd.3c01158.

(172) Brands, K. M. J.; Davies, A. J. Crystallization-Induced Diastereomer Transformations. *Chem. Rev.* **2006**, *106* (7), 2711–2733. https://doi.org/10.1021/cr0406864.

(173) Engwerda, A. H. J.; Mertens, J. C. J.; Tinnemans, P.; Meekes, H.; Rutjes, F. P. J. T.; Vlieg, E. Solid-Phase Conversion of Four Stereoisomers into a Single Enantiomer. *Angew. Chem. Int. Ed.* **2018**, *57* (47), 15441–15444. https://doi.org/10.1002/anie.201808913.

(174) Guillot, M.; De Meester, J.; Huynen, S.; Collard, L.; Robeyns, K.; Riant, O.; Leyssens, T. Cocrystallization-Induced Spontaneous Deracemization: A General Thermodynamic Approach to Deracemization. *Angew. Chem. Int. Ed.* **2020**, *59* (28), 11303–11306. https://doi.org/10.1002/anie.202002464.

(175) Lerdwiriyanupap, T.; Belletti, G.; Tinnemans, P.; Meekes, H.; Rutjes, F. P. J. T.; Vlieg, E.; Flood, A. E. Combining Diastereomeric Resolution and Viedma Ripening by Using a Racemic Resolving Agent. *Eur. J. Org. Chem.* **2021**, *2021* (44), 5975–5980. https://doi.org/10.1002/ejoc.202101193.

(176) Liu, J.; Mukherjee, S.; Wang, F.; Fischer, R. A.; Zhang, J. Homochiral Metal–Organic Frameworks for Enantioseparation. *Chem. Soc. Rev.* **2021**, *50* (9), 5706–5745. https://doi.org/10.1039/D0CS01236J.

(177) Boun, P.; Songsermsawad, S.; Saothayanun, T. K.; Bureekaew, S.; Flood, A. E. Enantiopure-Grafted Metal–Organic Framework for the Separation of the Enantiomers of Baclofen. *ChemSusChem* **2025**, e202501467. https://doi.org/10.1002/cssc.202501467.

(178) Liu, K. K.-C.; Sakya, S. M.; O'Donnell, C. J.; Flick, A. C.; Ding, H. X. Synthetic Approaches to the 2010 New Drugs. *Bioorg. Med. Chem.* **2012**, *20* (3), 1155–1174. https://doi.org/10.1016/j.bmc.2011.12.049.

(179) Tamatam, R.; Shin, D. Asymmetric Synthesis of US-FDA Approved Drugs over Five Years (2016–2020): A Recapitulation of Chirality. *Pharmaceuticals* **2023**, *16* (3), 339. https://doi.org/10.3390/ph16030339.

(180) Yuan, S.; Wang, D.-S.; Liu, H.; Zhang, S.-N.; Yang, W.-G.; Lv, M.; Zhou, Y.-X.; Zhang, S.-Y.; Song, J.; Liu, H.-M. New Drug Approvals for 2021: Synthesis and Clinical Applications. *Eur. J. Med. Chem.* **2023**, *245*, 114898. https://doi.org/10.1016/j.ejmech.2022.114898.

(181) Shimizu, H.; Sayo, N.; Saito, T. Eliminating Barriers in Large-Scale Asymmetric Synthesis. In *Asymmetric Catalysis on Industrial Scale*; Blaser, H., Federsel, H., Eds.; Wiley, 2010; pp 207–218. https://doi.org/10.1002/9783527630639.ch12.

(182) Federsel, H.-J. Asymmetry on Large Scale: The Roadmap to Stereoselective Processes. *Nat. Rev. Drug Discov.* **2005**, *4* (8), 685–697. https://doi.org/10.1038/nrd1798.

(183) Federsel, H.-J. Facing Chirality in the 21st Century: Approaching the Challenges in the Pharmaceutical Industry. *Chirality* **2003**, *15* (S1), S128–S142. https://doi.org/10.1002/chir.10274.

(184) Liu, R.; Behrens, C.; Ni, C. Industrial Application of Chiral Technologies. In *Chiral Drugs*; Lin, G., You, Q., Cheng, J., Eds.; Wiley, 2011; pp 253–296. https://doi.org/10.1002/9781118075647.ch6.

(185) Cote, A.; Erdemir, D.; Girard, K. P.; Green, D. A.; Lovette, M. A.; Sirota, E.; Nere, N. K. Perspectives on the Current State, Challenges, and Opportunities in Pharmaceutical Crystallization Process Development. *Cryst. Growth Des.* **2020**, *20* (12), 7568–7581. https://doi.org/10.1021/acs.cgd.0c00847.

(186) Aprile, G.; Devos, C.; Vetter, T.; Capellades, G.; Girard, K. P.; Burcham, C. L.; Bhamidi, V.; Green, D.; Stelzer, T.; Braatz, R. D.; Myerson, A. S. Reflecting on Barriers to Continuous Pharmaceutical Crystallization. *Nat. Chem. Eng.* **2025**, *2* (9), 520–523. https://doi.org/10.1038/s44286-025-00268-w.

(187) Pinetre, C.; Van Dongen, S. W.; Brandel, C.; Léonard, A.-S.; Charpentier, M. D.; Dupray, V.; Oosterling, K.; Kaptein, B.; Leeman, M.; Kellogg, R. M.; Ter Horst, J. H.; Noorduin, W. L. Enantiopurity by Directed Evolution of Crystal Stabilities and Nonequilibrium Crystallization. *J. Am. Chem. Soc.* **2025**, *147* (10), 8864–8870. https://doi.org/10.1021/jacs.5c00569.

# Chapter 2
# Crystals and Crystal Dynamics.



We start by introducing the key player in this thesis and addressing crystals and their dynamics. As opposed to the rather abstract concept of molecular chirality, crystals and crystallization are not foreign to us. Indeed, table salt is formed when seawater evaporates, quartz and other minerals abound in nature and furnish jewellery and electronics, and honey slowly transitions from a delicious liquid to a grainy mess through crystal nucleation, growth and the ripening of sugar crystals.

The word 'crystal' is derived from the Ancient Greek 'κρύσταλλος', often taken to mean 'ice' specifically, but is perhaps much more iconic and descriptive of the hard material with shiny appearance that characterizes many crystals. One of the first mentions is found in Homer's Odyssey, entrusted to the forefathers of paper in the 8th century B.C., where—nearing the end of the fourteenth book—the hero Odysseus recounts.*

> ... αὐτὰρ ὕπερθε χιὼν γένετ' ἠΰτε πάχνη,
> ψυχρή, καὶ σακέεσσι περιτρέφετο κρύσταλλος.
>
> "... but then from above snow came like rime,
> cold, and around our shields grew ice." [Hom. *Od.* 14.476-477]

## The Solid State

Crystals are solids, but not all solids are crystals. A hallmark of the solid state is the positional confinement of its constituent particles.[1] Contrary to gases or liquids, wherein atoms, molecules or ions have the freedom to move around, the solid imposes strict boundaries on their mobility and essentially fixes them in space. It is an important result from statistical physics that particles have an intrinsic disposition to kinetic motion, the degree of which scales with temperature.[2,3] As a consequence, increasing the supply of (thermal) energy will ultimately allow particles to break free of their solid-state arrangement and transition to one of the other states of matter. The reverse is also true: the solid state is classically of lower energy and therefore energetically more stable (Fig. 2.1).

Although this work is not so much concerned with the internal make-up of crystals, we should perhaps more generally point out that solids, when classed by their intrinsic order, come in three main forms:

(1) crystalline structures,
(2) glasses and amorphous solids, and
(3) semi-solids, such as gels, waxes, butter, and many plastics.

* Unless stated otherwise, all translations are my own.

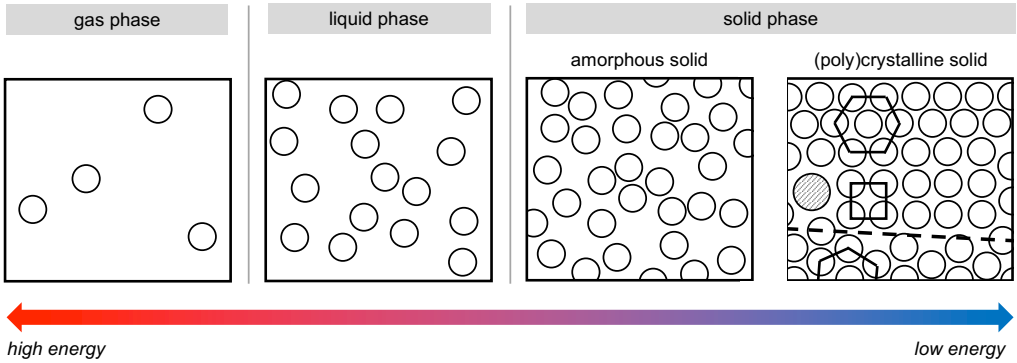


**Figure 2.1.** Classical view of the states of matter: gas phase, liquid phase, and solid phase. The solid phase generally has a lower energy and can be realized as a liquid kinetically frozen in place (amorphous solid) or as a highly ordered phase ((poly)crystalline solid). A crystalline solid can feature defects, impurities, polymorphism, and grain boundaries, examples of which are indicated by the black lines and grey-shaded circle.

The third category, that of semi-solids, is expertly introduced in textbooks on soft condensed matter physics but unfortunately beyond the scope of this thesis.[4,5] It is sufficient to say that these semi-solids macroscopically perhaps behave like solids under certain conditions, but microscopically would be best described as slow-flowing liquids. Their extreme viscosity or viscoelasticity can be deceiving.

The second category is that of amorphous solids, which are solids that have typically formed in much haste. Indeed, when a solidification process proceeds very rapidly, the particles do not have sufficient time to find an optimal and structured arrangement and prematurely 'freeze in place' (Fig. 2.1).[6]

Amorphous solids are isotropic: they have the same properties in all directions. In contrast, crystals are inherently anisotropic. Jammed but without long-range order, amorphous solids have properties both reminiscent of the solid and liquid states and show long-range stress correlations.[7] Another unique property is the possibility for plastic deformation through transitions between jammed and flowing behaviour, a phenomenon currently under scrutiny and reminiscent of macroscopic granular media.[8]

Glasses are a class of amorphous solids whose study is particularly rife with debate.[9,10] They form in nature under conditions where thermal shocks quickly cool down molten materials, such as lava exiting a volcano forming Obsidian. There is much evidence that, before the discovery of metals, these natural vitreous materials played an important role to early humans, as decorative objects, mirrors, and weapons.[11]

An instructive example of the counterintuitive but exciting properties of non-equilibrium materials such as glasses is that of the Rupert's drop (Fig. 2.2). Possibly brought to light by Dutch engineer Cornelis Drebbel, but more probably already known since Roman times, Rupert's drops are little glass bubbles with liquid inclusions prepared through thermal quenching by dripping molten glass into cold

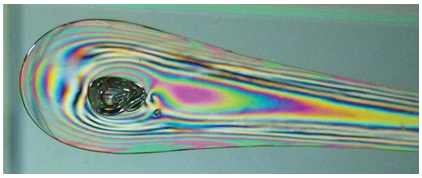

**Figure 2.2.** Isochromatic fringes indicating stress in a glass called Prince Rupert's drop, visually apparent through an effect coined 'photoelasticity', reproduced from ref. [13].



water.[12] Such thermal quenching greatly favours kinetics over thermodynamics and leads to highly amorphous solid droplets. Such drops are incredibly strong glasses because their surface is under high compressive stress. To break the drop, a crack must penetrate the interior tension zone, but doing so requires overcoming the immense compressive forces on the surface, making the drop extremely tough.[13] The study and understanding of these Rupert's drops has greatly contributed to the production of toughened glass and development of appropriate quenching methods.[12]

Amorphous materials are not only fascinating curiosities, but also gain increased traction in industry.[14–16] Amorphous nanomaterials, for example, may outperform their crystalline counterparts in catalysis and as electrode materials due to their increased number of active side, owing to surface-to-volume effects and the larger abundance of coordinatively dangling atoms on the surface.[14,16,17] Moreover, the disordered atomic arrangement can afford a continuous charge transport pathway and aid in ion diffusion.[15] In optical materials, disorder allows tuning the band-gap and enhances electron transition probability, leading to stronger fluorescence,[18,19] while defects and metastable electronic states can improve e.g. SERS sensitivity.[15,20] In the pharmaceutical industry, amorphous drug formulations are of interest for they can enhance drug solubility by a factor of 10 to 1600.[21] Like many organic molecules, pharmaceuticals often have poor aqueous solubility, rendering amorphous formulations especially advantageous for bioavailability.[22] One typical method for the preparation of amorphous dispersions from otherwise crystalline ingredients, is the use of polymer carriers: a mixture of the active pharmaceutical ingredient (API) and a carrier (e.g. PVP(A), PEG or HP(M)C) is melted or dissolved and then solidified through cooling or precipitation.[23] Alternatively, quench-crystallization can be directly performed on the API without a carrier present. Particularly attractive are the use of freeze-drying, spray-drying and anti-solvent crystallization, due to their fast precipitation kinetics and degree of process control.[24] Grinding (i.e. mechanical attrition) can also lead to amorphous solid-phases and may even be combined with synthesis into a one-pot procedure,[25–28] although stability can be an issue both during the grinding process, due to thermal effects originating in collisions and friction,[29,30] as well as during storage, as ground particles are prone to caking and ripening, decreasing shelf-life of the amorphous formulation.[31]

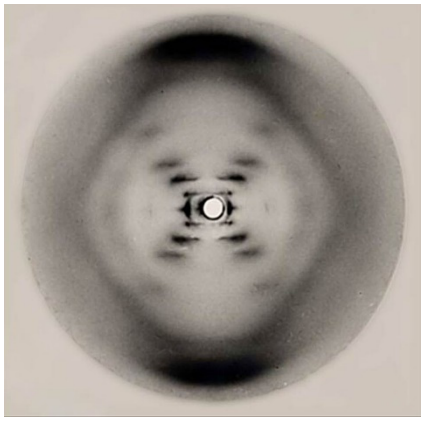

**Figure 2.3.** X-ray diffraction image of the double helix structure of the DNA molecule. The image was made in 1952 by Raymond Gosling and Rosalind Franklin (ref. [33]). X-ray diffraction is often used to elucidate the molecular structure of crystals.

Obviously, there is a wide and continuous range in 'crystallinity' and 'ordering' among the host of materials we daily come across, and the distinction between disorder and order sometimes borders the philosophical. This transition, however, is of great interest. Although both a blessing and a curse, the high number of degrees of freedom in polymer chains, proteins, and other large macromolecules, combined with their relatively weak intermolecular interactions, often prevent their natural solidification as crystals. It is an active topic of research to develop methods to nonetheless achieve this,[32] the relevance of which is perhaps illustrated by the elucidation of the DNA double-helix model through X-ray crystallography in the 1950s (Fig. 2.3) and the many other subsequent Nobel Prizes awarded for the glimpse that crystallizing biomolecules can give us into the structure of biology.[33–35]

Having discussed semi-solids, glasses and amorphous solids, we return to crystals, the first category of solid forms. In fact, they have already been defined by exclusion: crystals are ordered solid structures with proper packing of its constituent particles to populate a low energy state that is both thermodynamically and kinetically stable (Fig. 2.1). Often crystals exhibit a sharp solid-liquid transition with well-defined melting point. Morphologically, crystals are characterized by a particular shape with distinct facets and edges.

The next sections will briefly explore the internal arrangements of crystals, the rules governing their stability, and the dynamics of crystal growth and dissolution. Finally, we will discuss the practical use of crystallization in industrial processes and conclude with introducing reactive crystallization—a topic central to this thesis.

## Crystal Stability and Crystallization Driving Force

Crystallization is the process by which ordered solids emerge from disordered phases such as gasses, liquids (melts) or solutions. At its core, crystallization is governed by

a subtle interplay between thermodynamic stability and kinetic accessibility. A crystal is only thermodynamically favoured to form under suitable energetic conditions, yet its emergence and subsequent growth are also governed by kinetics: its constituent molecules or ions physically need to arrange themselves into the crystal lattice. This process does not occur instantaneously, but unfolds through distinct stages—most notably nucleation and growth—each governed by a combination of driving forces and rate-determining barriers. We will briefly examine the fundamental principles that dictate when and how crystals form and the mechanisms by which they grow. The first question to consider is that of thermodynamic stability: when are crystals energetically favourable to form or remain?

In mechanics, we find a particle's ideal path by minimizing its action (the integral of kinetic minus potential energy).[36] Similarly, thermodynamics holds that its stable state (i.e. equilibrium) is found by minimizing its free energy $F$, defined as

$$F = U - T \cdot S \qquad \text{(eq. 2.1)}$$

where $U$ is the internal energy of a system, $T$ is its temperature and $S$ is its entropy.[37] This definition immediately exposes a balancing act between the internal energy of a system and its entropy. This famously enigmatic concept of entropy is formally defined by Boltzmann as

$$S = k_B \ln \Omega \qquad \text{(eq. 2.2)}$$

where $\Omega$ is the number of possible microscopic realizations of the systems, often called configurations or microstates, and $k_B$ is Boltzmann's constant. In short, we can either make a system more stable by optimizing its internal energy, or by increasing its configurational degrees of freedom. Which of the two dominates is defined by temperature, establishing temperature as the critical parameter for defining phase transitions.

Traditionally, crystallization has mainly been considered to result from the packing of particles with attractive energetic potentials. Simulations halfway the 20$^{th}$ century, however, also showed freezing transitions for hard spheres that bear no interaction beyond an exclusion principle (i.e. infinite repulsion at contact).[38,39] For such hard-sphere systems, crystallization does not occur due to attractive forces but, counterintuitively, due to entropy maximization.[40,41] While densely packed, the ordered crystal arrangement actually provides particles more free volume to move within their local environments. The crystal thus exhibits a higher number of possible microstates (and thus higher entropy) than the disordered dense fluid. Experimental studies on colloidal suspensions have confirmed that crystallization indeed also has entropic drivers, rather than only those based on interaction energies and it has been established that even repulsive particles can therefore pack

and crystallize into highly ordered phases.[42,43] Such entropic packing mechanisms can even result in nematic chiral phases.[44]

Now, to now understand the general driving force for crystallization and assess crystal stability through crystallization driving force, we need to consider a crystal in its surroundings. Indeed, the question which is more stable, a crystallized or non-crystallized state, can only be answered through comparing the free energies of these different states. The difference between states is most conveniently given by the Gibbs free energy difference (ΔG) and its corresponding chemical potential difference (Δμ):

$$\Delta G = \Delta H - T\Delta S \quad \text{(eq. 2.3)}$$

$$\Delta \mu = \left(\frac{\partial \Delta G}{\partial N}\right)_{T,P} \quad \text{(eq. 2.4)}$$

where $H$ is enthalpy and $N$ is number. In the Gibbs free energy difference, total internal energy ($U$) is thus replaced by enthalpy ($H$) to add contributions of pressure and volume ($pV$):

$$H = U + p \cdot V \quad \text{(eq. 2.5)}$$

Because this thesis mainly considers crystal growth and dissolution in solution, we consider a simple crystal in a solution of its building blocks (Fig. 2.4). First, let us take stock of the main interactions: (i) interactions between building blocks, (ii) interactions between solvent molecules, and (iii) interactions between building blocks and solvent molecules.

(i) Interactions between building blocks mainly occur within the crystal. Considering ideal solution thermodynamics, we normally assume no interactions between building blocks in the solution.

(ii) Interactions between solvent molecules do not differ between a solvent with or without a crystal present, so that these can be ignored when considering the difference in free energy between a crystallized and fully dissolved system.

(iii) Interactions between building blocks and solvent molecules occur in terms of solvation (shell of solvent around a dissolved building block) and on the interface of the crystal (outer layer of building blocks). The latter group of interactions leads to the interfacial energy, an energy penalty paid by the crystal for its total surface area. The former group of non-ideal interactions is of key importance in determining the equilibrium solubility for an infinite bulk crystal (with negligible surface-to-volume ratio).

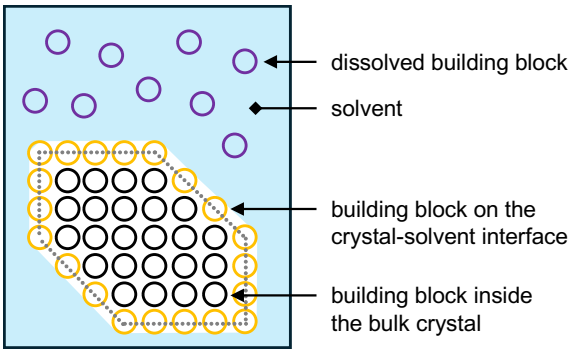




**Figure 2.4.** A building block (e.g. a crystallizing molecule, depicted as spheres) can experience different interactions when crystallizing in a solvent (blue): with the solution (as dissolved building block, purple), with other building blocks (inside of the bulk crystal, black), or both (as adatom on the crystal-solvent interface, yellow).

The difference between a crystallized state and fully dissolved state is most easily described from the liquid-phase perspective by the ideal solution model (i.e. akin to an ideal gas) based on the entropy of mixing. This yields the liquid chemical potential ($\mu_L$)

$$\mu_L = \mu_L^* + RT \ln c \qquad \text{(eq. 2.6)}$$

with R the gas constant, $c$ the solute concentration (amount dissolved building block), and $\mu_L^*$ the base chemical potential of the liquid without any building blocks dissolved.

At equilibrium $\Delta\mu = 0$: the crystal must have a chemical potential equal to that of the liquid phase. Equilibrium occurs at a concentration at which there is no driving force for any building blocks to detach or attach to the crystal. This is the concentration of a saturated solution, and is more commonly known as the solubility ($c^*$). The chemical potential of the solid therefore is

$$\mu_S = \mu_L^* + RT \ln c^* \qquad \text{(eq. 2.7)}$$

and the thermodynamic driving force for crystallization ($\Delta\mu$) is

$$\Delta\mu = RT \ln \frac{c}{c^*} \qquad \text{(eq. 2.8)}$$

wherein the fraction $c/c^*$ is known as the supersaturation $\sigma$. Whenever $\sigma > 1$, crystal growth is thermodynamically favourable. Whenever $\sigma < 1$, crystal dissolution is thermodynamically favourable. The supersaturation $\sigma$ is thus the key driving force for crystallization.

The contribution of interfacial energy, i.e. the building block-solvent interactions on the crystal surface, has not yet been considered. If one accounts for an energy penalty for each unit of interfacial surface area (A), through the interfacial energy or surface tension ($\gamma$), the chemical potential is given by

$$\mu = \mu_{\text{bulk}} + \frac{\partial A}{\partial N}\gamma \qquad \text{(eq. 2.9)}$$

When one considers the crystal surface as locally curved like a sphere with radius $r$ and defines the spherical volume as $Nv$ (i.e. a building block has volume $v$), we find

$$\mu = \mu_{\text{bulk}} + \frac{2v}{r}\gamma \qquad \text{(eq. 2.10)}$$

This relation implies that the chemical potential of the crystal decreases with increasing curvature (1/r), making the crystal phase less stable at smaller size. Indeed, it turns out that crystal stability is dependent on its shape and size, a phenomenon coined the Gibbs-Thomson effect. Smaller crystals are thermodynamically less stable than larger crystals, and there is a thermodynamic driving force to increase crystal size and minimize its surface-to-volume ratio. This ultimately leads to Ostwald ripening, wherein larger crystals grow at the expense of smaller crystals. In the end, enhanced by thermal fluctuations induced by opening and closing the freezer, thermodynamics dictates that any smooth ice cream will inevitably turn crunchy.

## Phase Transitions and Nucleation

Having considered the main components that define crystal stability and the driving force for crystallization, we can proceed to discuss the actual birth of a crystallite from a clear supersaturated liquid.

So far, we have identified temperature and concentration (through supersaturation) to be the key parameters in determining phase transition behaviour of matter between crystalline and liquid (solution) phases. Let us thus establish the regions that exist in the two-dimensional space of solute concentration and temperature (Fig. 2.5). At equilibrium ($\Delta\mu = \Delta G = 0$), the concentration is that of the crystal solubility ($c = c^*$). When $c > c^*$, $\sigma > 1$ and the system is supersaturated. There is a driving force for crystallization. When no crystals exist, however, a nucleus must first be formed. The supersaturated region can thus be further subdivided in a supersaturated region that shows spontaneous nucleation, and a supersaturated region that is metastable because the conditions for the formation of a nucleus (i.e. the primary formation of a new thermodynamic phase) are not met and crystallization is impeded. When $c < c^*$, $\sigma < 1$ and the system is undersaturated. This implies a driving force for dissolution of any crystals that may be present.

First, let us consider how the solubility depends on temperature. The equilibrium constant $K$ for the phase transition between solute and crystal is given directly by the solubility

$$K = \prod_i \{i\}^{\alpha_i} = c^* \qquad \text{(eq. 2.11)}$$

because the activity ($\{i\}$) of a solid is 1. Invoking the Van 't Hoff-equation, we can relate the equilibrium solubility to the enthalpy ($\Delta H$) and entropy ($\Delta S$) of crystallization as

$$\Delta G = -RT \ln K = \Delta H - T\Delta S \qquad \text{(eq. 2.12)}$$

and construct the archetypical description of temperature dependent solubility as

$$c^* = \exp\left(\frac{\Delta S}{R} - \frac{\Delta H}{RT}\right) \qquad \text{(eq. 2.13)}$$

We note that this description is typically used when ΔH and ΔS are temperature-independent and solution behaviour is ideal. When ΔH and ΔS are temperature-dependent, however, engineers prefer to fit data to the empirical Apelblat-equation, for which a theoretical underpinning was provided jointly by Apelblat and Cuevas-Valenzuela:[45,46]

$$\ln c^* = A + B \cdot T + C \cdot \ln T \qquad \text{(eq. 2.14)}$$

Second, let us consider the nucleation process for the formation of a primary crystallite. Classically, the formation of a nucleus entails two important aspects: (i) the stochastic collisions of solute molecules to form a collection of molecules and (ii) the critical step in which the collection grows into a crystal and does not redissolve (Fig. 2.6a). Kinetically, the probability of formation of such a viable nucleus thus is the product of stochastic collisions and the probability of passing a critical energy barrier. So what is the origin of this critical energy barrier?

Previously, we derived the size and shape dependence of crystal stability and noted that a very small crystal is very unstable due to its high surface-to-volume ratio and

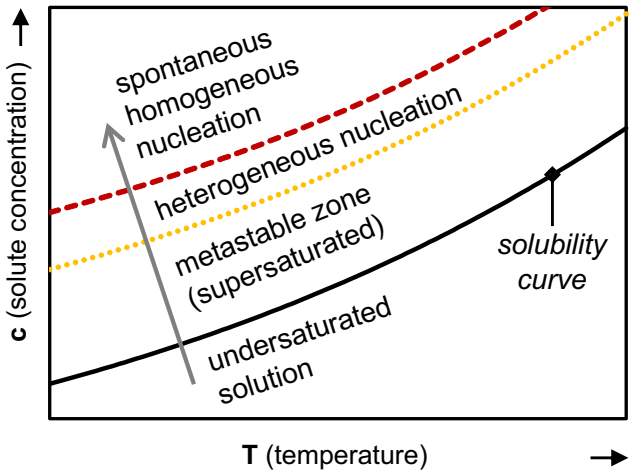


**Figure 2.5.** 2D phase diagram of solute concentration (c) and temperature (T) showing the crystallization driving force at different levels of supersaturation (indicated by the grey arrow): undersaturated solution (dissolution driving force), supersaturated solution in the metastable zone (crystal growth driving force), heterogeneous nucleation zone (nucleation and growth onto foreign surfaces), and homogeneous nucleation zone (spontaneous nucleation and growth). The solubility curve defines the saturation point, at which there is no net driving force for dissolution or growth. In the absence of seed crystals, no crystal growth will take place in the metastable zone. In the absence of foreign surfaces, no nucleation and growth will take place in the heterogeneous nucleation zone.

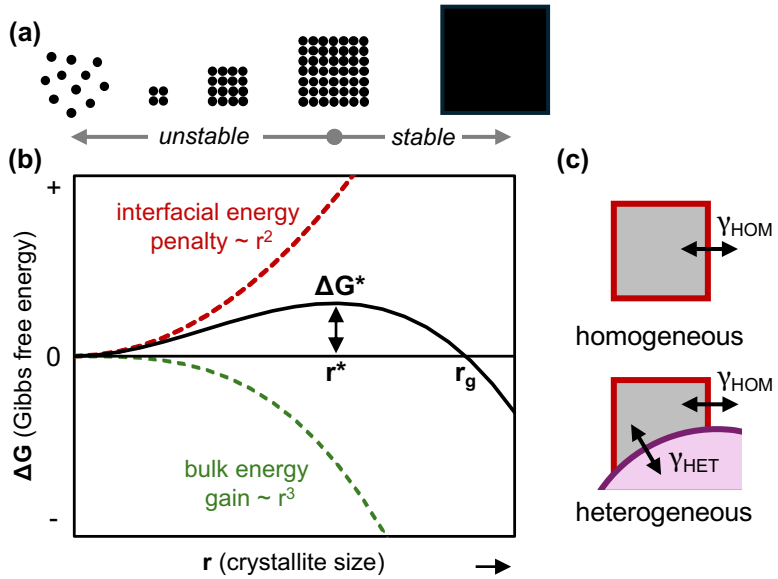


**Figure 2.6.** Nucleation: the birth of a crystallite. (a) During nucleation (classical perspective) a few solute molecules find each other and pack together, slowly expanding the emerging crystallite by incorporating more solute molecules. (b) Thermodynamic stability of an emerging crystallite is determined by a trade-off in energy paid for solid-liquid interface and bulk energy gained by removing molecules from solution and gaining enthalpy. A small crystallite is thermodynamically unstable and kinetically tends to dissolve. From a critical size (r*), the energy barrier from nucleation is passed (ΔG*) and the nucleus becomes more stable by expanding rather than dissolving, until a thermodynamically stable crystal is achieved (i.e. when r = $r_g$). (c) Heterogeneous nucleation requires a lower energy penalty than homogeneous nucleation and thus occurs spontaneously at lower supersaturations, since the energy penalty associated to solid-solid interface ($\gamma_{HET}$) is generally lower.

the subsequent energy penalty paid for its interfacial tension (Fig. 2.6b). We find a resulting energy barrier for nucleation (ΔG*)

$$\Delta G^* = \frac{16\pi}{3} \cdot \left(\frac{v}{RT \ln \sigma}\right)^2 \cdot \gamma^3 \qquad \text{(eq. 2.15)}$$

which corresponds to a critical nucleus size (r*) of

$$r^* = \frac{2v\gamma}{RT \ln \sigma} \qquad \text{(eq. 2.16)}$$

From Arrhenius, we then straightforwardly define the nucleation rate $J$ (through the critical rate-limiting step) as:

$$J = k_c \exp\left(-\frac{\Delta G^*}{RT}\right) \qquad \text{(eq. 2.17)}$$

with $k_c$ as a parameter representing collision frequency.

This result stresses the stochastic nature of nucleation. While the partial metastable nature of the supersaturated region in the phase diagram is now evident (recall Fig. 2.5), it remains unclear at exactly what supersaturation one would draw the line between 'metastable' (i.e. no nucleation) and 'unstable' (i.e. primary nucleation

occurs). Indeed, this question is almost philosophical in nature, because it is a matter of timescales, nucleation conditions, and the manner of observation. From the seemingly simple nucleation rate $J$, we can calculate the cumulative probability of nucleation during a time-interval $t$ in a volume $V$ by using the Poisson distribution:[47]

$$P(t) = 1 - \exp(-JVt) \qquad \text{(eq. 2.18)}$$



First, the nucleation rate increases with volume and the metastable zone width (MSZW, shown in Fig. 2.5) accordingly decreases, but at large volumes a plateau is reached.[48] When volume initially increases, both the number of nucleation events (statistics) and the probability of formation of initial collections of building blocks through collisions increase.[49] When volumes become sufficiently large, however, the stochastic nature of crossing the energy barrier for nucleation disappears according to the central limit theory and there is no longer a limiting factor in the collision events for the formation of initial collections through random collisions. At very low volumes, a very different nucleation behaviour is observed than at medium or large volumes, and translating nucleation rates across experimental conditions is non-trivial. In fact, in some microfluidic droplets with nanolitre volume, metastable zones grow enormous, as both the probability of stochastically collecting sufficient solute molecules to reach the critical size and the number of viable nucleation sites become severely limited.[50–52] Similar arguments regarding concentration fluctuations and homogenization also affect observed nucleation rates across experimental set-ups and systems. In properly homogenized systems crystal growth is no longer diffusion limited, so that a nucleus can grow more easily, thereby increasing its stability and shortening its time to detection. The definition of the metastable zone thus depends on reactor geometry, volume, and homogenization.

Second, the above analysis shows that the metastable zone is defined by the observation method and time (or rather: patience). If one only observes for several minutes, one will determine a very different supersaturation at which nuclei are spontaneously formed, compared to stirring a reactor for multiple days. Also, whether nuclei are detected by eye or through laser diffraction or Raman will change the sizes at which nuclei will first be detected. Again, the methodology here affects the determination of the metastable zone.[53] In practice, it is important to establish at least that the metastable zone is truly metastable over the course of an experiment—if indeed only growth but no nucleation is desired. The metastable zone should thus be determined as much as possible under the conditions of the actual crystal growth experiment.

Besides primary homogeneous nucleation, where the nucleus randomly appears somewhere in a solution, heterogeneous nucleation is also an important source of nuclei. In that case, an existing surface acts as the seed for nucleation (Fig. 2.6c). This existing surface can be unrelated to the crystallizing species (e.g. the reactor wall, dust, or impellor), but can also be another crystal (e.g. a crystal form of the same

molecule or a crystal of a similar molecule, impurity or salt). The nucleation barrier for heterogeneous nucleation is often much lower, because the presence of an existing foreign surface reduces the energetic penalty associated with forming a new interface between the nucleus and the surrounding phase: the crystal–solvent interface is partly replaced by a crystal–substrate interface, which typically has a lower interfacial free energy. As a result, the critical nucleus size decreases and nucleation occurs more readily, often at lower supersaturations compared to homogeneous nucleation. The extent of this reduction in interfacial tension typically depends on the degree of lattice match and chemical affinity between the substrate and the nucleating phase. Specific foreign surfaces can, akin to heterogeneous catalysts, also act as pre-absorption substrates, facilitating the bringing together of a collection of molecules to form an initial nucleus. In fact, closely matching surfaces can even template the crystallization process, strongly favouring the formation of specific crystal orientations or polymorphs.[54]

Because the total surface area of foreign surfaces available for heterogeneous nucleation in a crystallizer is limited compared to the voluminous space available for homogeneous nucleation, homogeneous nucleation would be the dominating nucleation mode at higher supersaturations, while heterogeneous nucleation would be more prevalent at lower supersaturation. In theory, at least two metastable zones can therefore be discriminated: a homogeneous and heterogeneous metastable zone. In practice, though, mainly the homogeneous metastable zone is reported as a system's metastable zone.

Next to the classical nucleation primary mechanism described above (coined CNT), more and more non-classical modes of nucleation are being established.[53,55–57] With increasing supersaturation, the energetic barrier for nucleus formation starts to lower and initial pre-nuclei can form and do occur in high amounts. Through collisions with other such pre-nuclei, these can coalesce and form full stable nuclei that continue to grow into mature crystals.[58,59] Although the assembly of thermodynamically stable prenucleation clusters is perhaps nonclassical, its underlying theory and the principles for their formation and coalescence are well-established.[60,61] Increasing supersaturation even further, nucleation can occur through spinodal decomposition as the energy barrier for nucleation is comparable with the thermal energy ($k_BT$).[62,63] Intuitively related is a mechanism reported for the crystallization of certain enzymes (e.g. lysozyme and deoxy-hemoglobin S) based on a two-step process: an initial fluctuation of the solute concentration produces a dense, metastable liquid droplet, within which a subsequent structural ordering event gives rise to the crystalline nucleus.[64,65]

Besides these various primary nucleation mechanisms, new nuclei readily appear in systems that already contain mature crystals. In an approach advocated by Estrin and Youngquist, a mature crystal was impaled on a rotating rod.[66] Many new nuclei

are formed under such conditions, through a phenomenon labelled secondary nucleation: new nuclei can be formed by breeding at existing crystals or through attrition and shear.[67,68] Indeed, fines on the surface of seed crystals can be dislodged and act as nuclei, small parts of crystals can shear off or crystals can be broken into multiple segments. Evidently, such effects are especially prevalent for fragile crystal morphologies, like needles or thin plates. Importantly, these various mechanisms of secondary nucleation can all lead to very different types of nuclei and result in wide dispersity in shape, polymorph and sizes through anomalous growth modes.[69] Secondary nucleation is often considered a very efficient way to speed up crystallization, as it is inherently autocatalytic.[70]

## Crystal-Size Dependence of Solubility

Prompted by the consequences of size-dependence of crystal stability during our discussion on nucleation, we should also revisit the concept of equilibrium solubility. Because the stability of small crystals is lower, their equilibrium solubility will be higher. In fact, this other consequence of the Gibbs-Thomson effect can be captured to correct equilibrium solubility for bulk crystals ($c^*_\infty$) as follows

$$c^* = c^*_\infty \exp\left(\frac{\gamma}{RT} \cdot \frac{2v}{r}\right) \qquad \text{(eq. 2.19)}$$

with $r$ as the crystallite size (conformal spherical radius). In slurries that are subjected to attrition, which causes breaking down larger crystals into smaller ones, one therefore routinely observes higher apparent 'equilibrium' solubilities.[71,72]

## Kinetics and Modes of Crystal Growth

Having established the critical parameters that drive crystal growth and dissolution (temperature, supersaturation, and crystal size and shape), we can now investigate these processes more closely and dive into their mechanisms. The rate and pathway of crystal growth and dissolution—both are highly dynamic processes that proceed through various microscopic steps—depend on driving force as well as kinetic barriers. It is important to point out that crystal growth and dissolution virtually always and continuously occur on a molecular level; it is the net balance of these two counteracting processes that ultimately defines whether the crystals are 'growing' or 'dissolving' macroscopically.[73]

In 1927, Kossel and Stranski separately developed a basic crystal growth model, in which a cubic growth unit attaches to the surface of an existing crystal (Fig. 2.7a).[74,75] In this so-called terrace-step-kink model, the key consideration is the number of interactions of the growth unit to neighbouring units on the Kossel-crystal surface. The model identifies kink sites, where the adatom has two neighbouring units, and holds that these kink sites are the most favourable to incorporate a new growing unit onto the crystal surface. The reasoning is simple: kink sites provide the strongest net

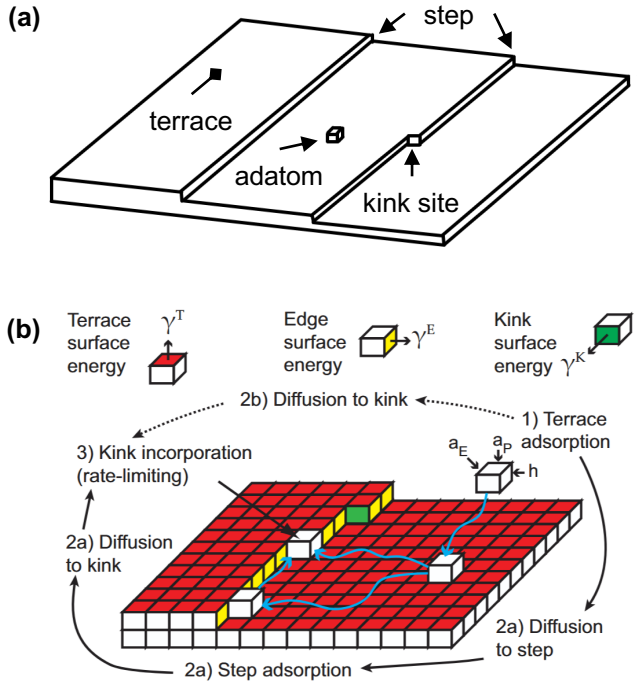


**Figure 2.7.** Terrace-step-kink model for crystal growth. (a) The layering of crystals gives rise to terraces and steps. A building block on the surface of a crystal is called an adatom. Building blocks may have up to four lateral neighbours. In a kink site the building block has two lateral neighbours, making it the determining growth site of a crystal where an adatom is incorporated. (b) Depiction of the sequential events in layer-by-layer growth through the incorporation of adatoms at kink sites, reproduced from ref. [77].

bonding energy. Given incorporation at kink sites as preferred mode of growth, one can imagine the emergence of so-called steps and terraces: crystal layers develop laterally as growth units attach preferentially to kink positions, gradually filling in each layer before starting the next (Fig. 2.7b). This sequential process creates flat terraces separated by molecular steps. As one layer completes, a new step is created through nucleation on the crystal surface. In practice, as pointed out by Frenkel, the inherent roughness of crystals is a potent source of kink sites and facilitates the emergence of new steps.[76]

This idea of emerging steps and terraces was the starting point for Burton, Cabrera and Frank to formulate their BCF-model for crystal growth through step flow in 1951.[78] Unsatisfied by the lack of a quantitative description of step-growth dynamics and puzzled by the exact origin of new steps, the trio set out to improve the qualitative model by Kossel and Stranski. The key insight that underpins the BCF-model, is the quantitative description of step dynamics through considering adatoms on surfaces as mobile. The displacement and mobility of adatoms was conveniently described through diffusion kinetics and equations for the flow of adatoms towards steps could be derived. These diffusion equations were coupled to the exchange between the surface layer (adsorbed state) and the surrounding (gas vapour). The

result was the seminal analytic continuous model of step flow dynamics describing crystal growth.

Interested in the free diffusion of adatoms on crystal surfaces, Ehrlich and Schwöbel then experimentally studied the direction from which adsorbed atoms approach the kink-sites of a step.[79,80] It turns out that an additional energy barrier exists that inhibits mobile adatoms from descending to lower terraces, because the descent temporarily lowers the bonding energy. As a result, adatoms are more likely to attach to ascending steps, a phenomenon coined the ES-effect. The asymmetric nature of the ES-effect leads to a preferential accumulation of material at ascending steps, causing them to advance more rapidly than their trailing neighbours.[81] Over time, this difference in step velocities gives rise to step bunching, where steps cluster together, producing uneven surface morphologies with wide terraces and closely spaced step regions.[82] The ES-effect has been observed for many crystals, amongst which Cu, Si, and W.[83,84]

In the semiconductor industry, where many materials are produced through epitaxial growth of thin consecutive crystalline layers, molecular beam epitaxy and related techniques yield conditions of crystal growth very well described by the BCF-model and ES-effect.[85–87] Recent work in the field still puts the BCF-model central to our understanding and descriptions of the growth of many semiconductor materials.[88–94]

Although the BCF-model made leaps in the quantitative description of growth through describing the mobility of adatoms on crystal surfaces, the formation of new steps was still a bottleneck in crystal growth kinetics. When one considers 2D-nucleation on a crystal surface as a primary origin of new steps, it remained a mystery why experiments showed crystals to grow at very low supersaturation.[95] Indeed, at such low supersaturation the driving force for nucleation is insufficient, as we have previously examined, so crystals would be expected to face a metastable dead-zone for growth. The breakthrough in understanding the growth that is nonetheless observed at low supersaturation was made by Frank.[96] Experimentally, he observed pyramidal morphologies at the tips of crystals and the BCF-model was able to explain these observations by introducing so-called screw-dislocations.[78] A screw dislocation is a particular kind of defect in a crystal, where the atoms of the crystal lattice are misaligned and some atoms are out of position so that a step emerges (Fig. 2.8a). Critically, the resulting step never terminates, forming a spiral (Fig. 2.8b). The existence of such screw dislocations thus removes the need for successive nucleation for the emergence of new steps and allows for continuous layer growth at low supersaturations (Fig. 2.8c).

At elevated supersaturations, however, heterogeneous nucleation does become a feasible pathway towards the formation of new steps.[98–100] In a growth mode coined

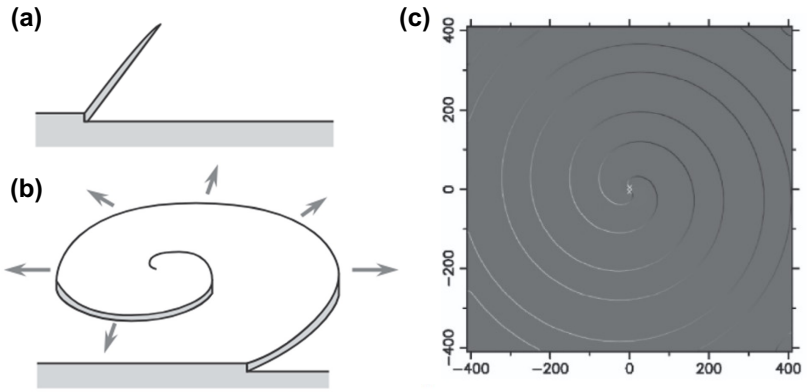


**Figure 2.8.** Spiral growth is enabled by a screw dislocation (panel a) which allows a form of layer-by-layer growth on a continuously evolving spiral step (panel b; schematics adapted from ref. [95]). Phase field simulation of spiral growth (panel c, reproduced from ref. [97]).

'birth-and-spread', adatoms form a 2D nucleus on the crystal surface (i.e. birth), creating an island that serves as a round step for further growth (i.e. spread).[101,102] Increasing supersaturation even further means increasing the nucleation rate. Consequently, these nucleation events become so common, that the formation of these islands is the dominant driver for growth.[103] This regime of nucleation-driven growth is called 'polynuclear' growth and is often evident from microscopy as well as more detailed growth-rate analysis.[104]

Finally, the supersaturation may be such that the critical nucleus size is on the order of the crystal unit cell. In these conditions, there is no longer an effective energy barrier for attachment to the crystal surface. Adatoms can thus freely adsorb to the crystal surface and only the kinetics of successful collisions between solute molecules and crystal surface are limiting. In this regime, the growth rate can thus be expressed as a direct combination of the crystallization driving force and mass transport. Wilson and Frenkel thus give the growth rate ($R$) for rough growth as

$$R = k_g \cdot \left(\frac{c}{c^*} - 1\right) \qquad \text{(eq. 2.20)}$$

with $k_g$ the intrinsic rate of incorporation of the system.[73]

Ultimately, it is the crystallization driving force that determines the crystallization mechanism. But how are the different regimes connected? Tilbury and Doherty presented an elaborate quantitative description in 2017, where they connected all previously described growth regimes to form a continuous perspective (Fig. 2.9a).[105] In conclusion, as supersaturation increases, the progression in mechanisms would move from spiral growth, to 2D birth-and-spread, to 2D polynuclear, to rough growth, to mass-transport-limited growth. Engineers therefore often describe the crystal growth rate (G) through the empirical power law

$$G = k_g \cdot \left(\frac{c}{c^*} - 1\right)^g \qquad \text{(eq. 2.21)}$$

where fitting the exponent $g$ (usually a value between 1 and 2) is aimed to capture the changing growth dynamics.[106] Note that c* should ideally consider size-dependence of solubility as well. Some authors explicitly multiply $G$ by $c$, to indicate the rate depends on the frequency of collisions between crystal surface and solute. The total amount of available surface area of the crystals should also be considered.



By now, it may be evident that the kinetics of crystal growth are a combination of mass transport, the number of attachment opportunities afforded by collisions and the crystal growth mechanism, and the kinetics of attachment, given by the

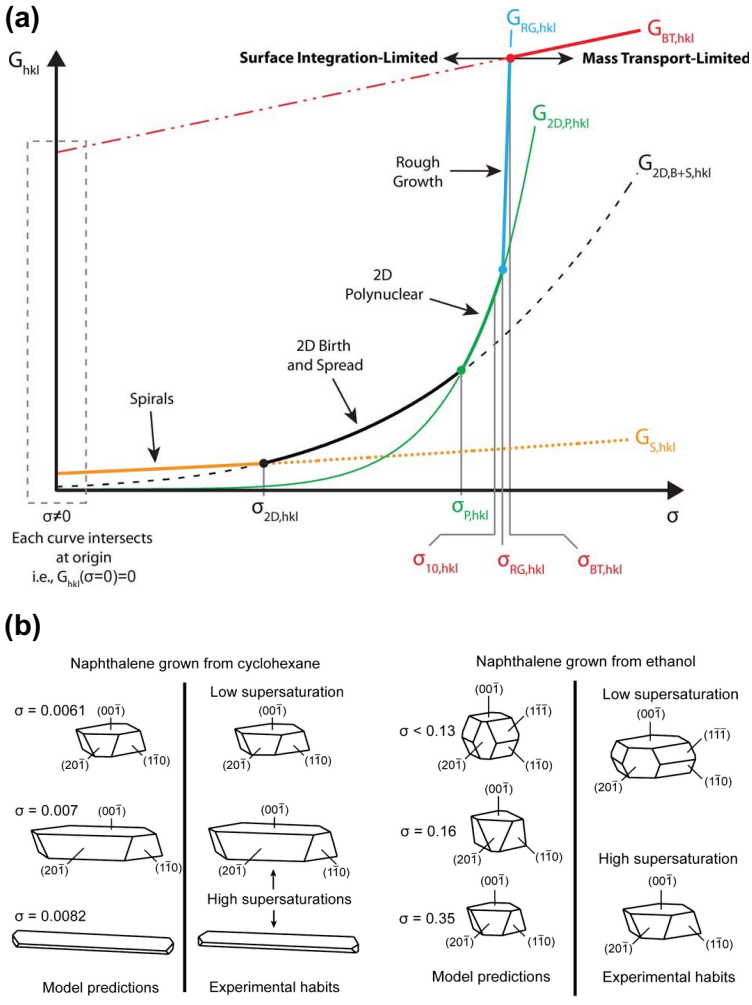


**Figure 2.9.** Supersaturation and solvent can affect both the crystal growth mechanism as well as the crystal habit: (a) Overview by Tilbury and Doherty of the transitions between crystal growth mechanisms as function of supersaturation;[105] (b) Predicted and experimental effect of supersaturation and solvent on the habit of naphthalene from refs. [77,105,110,111].

crystallization driving force. Besides the crystallization driving force, we have now established how the supersaturation also dictates the growth rate mechanism. It is important to note, though, that a crystal has multiple facets and that each facet has distinct interfacial energies and thus features distinct growth mechanisms and kinetics.[77] The interfacial energy of a facet is shaped, amongst other things, by its unique interactions with the solvent.[107,108] After realizing that the fastest-growing facets of a crystal generally disappear, we can appreciate that choosing different solvents and supersaturations will affect crystal habit and morphology by stabilizing different surfaces and favouring different growth mechanisms (Fig. 2.9b). This result is not only key in understanding the shapes that crystals naturally take, but also engineering crystals to take the forms we want[109]—an important problem in industrial crystallization, as will be discussed in a later section.

Notably, seemingly random but significant growth rate fluctuations are routinely observed for crystals in crystallizers, leading to a phenomenon called 'growth rate dispersion'.[112] This stochastic variation in crystal growth rates is often ascribed to differing internal lattice perfections between crystals and surface effects induced by the crystal's growth history.[113–115] Unfortunately, the phenomenon remains enigmatic yet today. This observation, however, does prompts us to discuss defects in crystals and an important phenomenon called polymorphism.

## Defects and Polymorphism

Crystals inevitably exhibit defects (i.e. molecular imperfections) and can also be formed through different internal arrangements of the crystallizing molecules in the crystal unit cells. This arrangement of the same building block into different crystals structures is called polymorphism (vide Fig. 2.1). Both defects and polymorphism impact crystal stability, nucleation kinetics, growth mechanisms, crystal habit and other properties.

Defects in crystals are often categorized per their dimensionality and can be summarized as point defects (0D), line defects (1D), planar or surface defects (2D), and lastly macroscopic or bulk defects (3D).[116] Point defects concern a mutation only in a unit cell: a normally occupied site can be unoccupied (termed vacancy), occupied by the wrong species (anti-site or substitute), or an otherwise unoccupied site can be occupied (termed interstitial). Line defects, also termed dislocations, originate from a local misalignment of the crystal lattice (a so-called slip or glide). At a dislocation, the lattice is shifted by a unit, which enables specific growth modes, such as the discussed spiral growth mode. Planar defects comprise larger scale grain or antiphase boundaries (sifts of the lattice arrangement or crystallographic direction) and similar phenomena, where actual lines are visible, marking the differing crystal domains. Bulk defects comprise gaps, pores, cavities, and inclusion of foreign matter

within the crystal. All defects cause stress and strain in the crystal and generally lower its thermodynamic stability.[117,118]

Besides variation within a single crystal, a single molecule or crystallizing species can also show a wide variety of polymorphs. For example, biominerals of CaCO3 have been widely studied for orthopaedic, drug delivery and biomedical applications and have been found to exist in three distinct anhydrous polymorphs: vaterite (hexagonal), aragonite (orthorhombic) and calcite (rhombohedral).[119] A few of the shapes these polymorphs can take are shown in Figure 2.10a. In nature, these forms often originate by transformation of the amorphous form.[120] All polymorphs can have very different properties and solubilities (Fig. 2.10b) and tend to form at different temperatures (Fig. 2.10c). For instance, Hadjittofis et al. monitored CaCO3 polymorphism via XRPD during crystallization (Fig. 2.10d), revealing a sequential transformation: vaterite emerged initially, then gradually dissolved as aragonite precipitated, with calcite ultimately appearing when the system reached the $CaCO_3$ solubility limit.[121]

The latter observation is an example of the Ostwald-Lussac rule of phases:[123] Which polymorph appears during crystallization is not solely dictated by thermodynamic stability; kinetic factors play an equally vital role. According to the Ostwald-Lussac rule, a system does not necessarily crystallize directly into the most stable

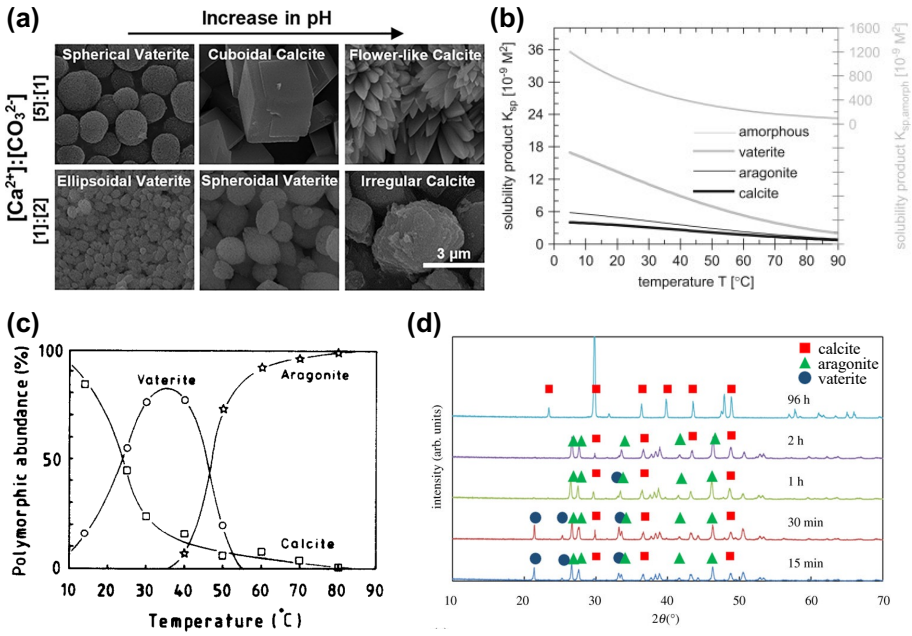


**Figure 2.10.** Polymorphs and the rule of Ostwald-Lussac as illustrated by the case of $CaCO_3$. The different polymorphs of have very different crystal structures and morphological appearance (panel a, reproduced from ref. [119]) and also differ in their thermodynamic stability, as evidenced from solubility curves (panel b, reproduced from [120]) and enantiotropy (panel c, reproduced from [122]). During crystallization of CaCO3, the polymorphs may appear in sequence, nucleating as the lesser stable aragonite and vaterite and then transforming to the most stable form calcite (panel d, reproduced from [121]).

polymorph. Rather, it typically passes through one or more metastable (kinetically accessible but thermodynamically disadvantaged) forms before eventually converting to the most stable phase.[124,125] This sequential emergence is not universal, but often reflects the fact that energy barriers for nucleation are often lower for less stable forms, allowing them to typically appear first.[126] The initial formation of such less-stable phases can be explained by slightly lower interfacial free energies, which translate into lower nucleation energy barriers.[127] Experimental observations have primarily focused on colloid and protein systems, which exhibit relatively slow crystallization kinetics and comparatively large particle dimensions. Recently, however, in situ high-resolution electron microscopy for metal phosphates and single-shot XFEL diffraction studies of Xe nanoparticles have both revealed the Ostwald-Lussac rule operating at the atomic scale.[128,129] Outside crystallization, a similar mechanism has also been shown responsible for structural transitions and morphology of dipeptide supramolecular polymers and quantum dots.[130,131]

Polymorphism is practically important for crystalline products; it directly impacts product performance, shelf life, intellectual property protection, and manufacturing.[132–134] When selecting and screening for polymorphism, exploiting the Ostwald-Lussac rule is one possible approach.[135,136] Other approaches for polymorph screening and selection that directly target crystal interfacial energies and nucleation-growth mechanisms are based on additives,[137–142] solvent selection,[143–145] templating,[146–148] and—naturally—seeding.[149,150] Alternatively, one can attempt to induce the formation of metastable structures through impeding crystallization: sublimation, melt quenching, attrition through grinding, freeze drying and spray drying, and crystallization in confinement can all limit the kinetic pathways to the stable form and induce the formation of metastable polymorphs.[132–134,151,152]

Often, the various polymorphs of organic molecules are close in energy (usually less than a few kJ/mol) and one in three compounds in the CSD is known to have one or more polymorphs.[153] Interesting in the context of this thesis, is to note that chiral molecules are usually less prone to polymorphism than their achiral counterparts.[153] From a kinetic perspective, it is worthwhile to note that some metastable polymorphs in fact grow much faster than their stable counterparts, providing unexpected pathways to their further growth and domination after seeding or spontaneous formation.[154,155] This observation may have far-reaching implications for reactive crystallizations, as will be discussed in several outlook sections of thesis (esp. Chapter 8).

Not only producing the right polymorph is important, knowledge of the entire polymorph landscape is essential. The case of ritonavir illustrates the critical importance of polymorphism in pharmaceutical development: Abbott Laboratories faced a market crisis in 1998 when an unexpected, less soluble polymorph (Form II) emerged in their HIV-drug Norvir, causing product failures as the more stable form

of the drug with lower solubility precipitated out of solution, contaminating manufacturing facilities so severely that entire facilities had to be shut down and decontaminated. This ultimately required both reformulation and new bulk drug production processes to address the crisis.[156,157] McCrone famously said that every compound has different polymorphic forms, and that, in general, the number of forms known for that compound is proportional to the time and money spent researching it,[134,158] a position strongly defended by Dunitz and Bernstein.[159,160]

Today, advanced computational methods aid research and development by providing a prediction of the possible crystal structures of a crystallizing species—a technique coined Crystal Structure Prediction (CSP).[161] In CSP, one first generates many possible ordered crystal structures of a given species (~$10^3$–$10^6$) and then estimates their lattice energy in vacuum and at 0 K (thus ignoring solute or solvent interactions, flexibility, and vibrations). The result are so-called crystal energy landscapes, that show the stability and density of the top candidates (Fig. 2.11). Typically, these results are compared with experimental results from screening and extra effort is geared towards trying to isolate the most stable polymorphs.[162,163] A difficulty in using CSP, is deciding when to give up if the predicted stable polymorph is never found. Indeed, our current *ab initio* modelling of crystallization kinetics, nucleation mechanisms, and the influence of experimental conditions insufficient to determine whether a given structure is genuinely kinetically inaccessible or simply has not been realized due to subtle experimental or environmental factors.[164] The next step in CSP will be to also predict which polymorphs will form under which conditions and incorporate elements such as solvent-interactions, impurities, and surface templating.

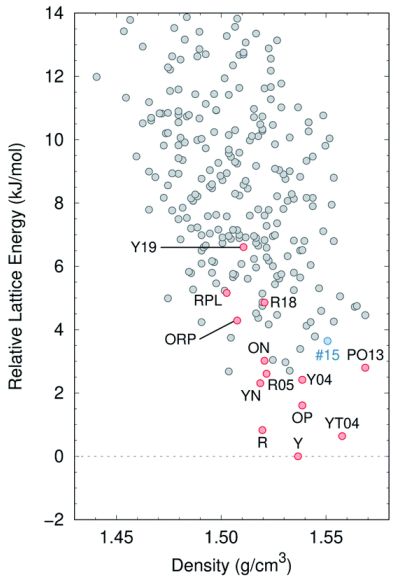


**Figure 2.11.** An example a polymorphic energy landscape reproduced from ref. [162], which shows the polymorphs of ROY predicted by CSP. The polymorphs that have been successfully experimentally isolated are shaded pink or blue.

## Impurities and Inhibition

The presence of impurities modulates both nucleation and growth, often leading to inhibition effects or defect incorporation. Impurities are commonly defined as any foreign (i.e. other) species than the crystallizing species. In principle, the study of impurities is mainly undertaken with regard to the quality of the resulting crystals, both in shape and in purity. In contrast, inhibitors are a specific kind of species that in principle bind to the surface of crystals and modulate (often negatively) the rate of growth. When the foreign molecule is incorporated into the crystal, it is an impurity. When the foreign molecule affects the growth process (e.g. shape or kinetics), it is an impurity and an inhibitor.

Traditionally, inhibitors were seen as species purposely added to affect crystallization dynamics or that were inadvertently present (often as impurities). Recently, however, research has shown that inhibitors are not necessarily foreign to a system. For instance, isomers that show interconversion (such as tautomers) can give cross-inhibition, where one of the isomers inhibits the crystallization of the other.[165,166] A similar situation can also exist for polymorphism or situations where the components of a system can crystallize into different (co)crystal structures.[167–171] Such self-poisoning phenomena are oftentimes counterintuitive and therefore overlooked, although sometimes key to explain distinctive characteristics of crystal shape and growth dynamics.[172] Especially further away from equilibrium, self-poisoning of even otherwise seemingly normal systems can become an increasingly common occurrence—an effect often scaling with the frequency of heterogeneous nucleation.[173]

In their must-read paper "Principles of Crystal Nucleation and Growth", DeYoreo and Vekilov have summarized the three main pathways of growth inhibition:[174] step-pinning, incorporation, and kink-blocking—schematically shown in Figure 2.12. Although all three are closely related, there are some key differences that ought to be discussed.

Step-pinning is the first inhibition mechanism, which describes the situation where a foreign molecule adsorbs at a step and impedes its advance. The only way for a pinned step to continue is either by growing around or over the pinning impurity (leading to defect incorporation), or through the formation of a protruding front. Both remedies are subject to the energy penalties of heterogeneous nucleation. It follows then, that crystal growth of affected facets is fully halted at low crystallization driving force. Only at supersaturations under which the interfacial energy penalty associated with the remedy can be overcome, will crystallization recommence. At this point, the crystal growth rate will quickly recover to the value without step-pinning, akin to the polynuclear and rough growth mechanisms discussed before. Notably, the impact of step-pinning is strongly dependent on the density of impurities on the step, which normally scale with the impurity concentration in solution (cf. Langmuir adsorption isotherm).

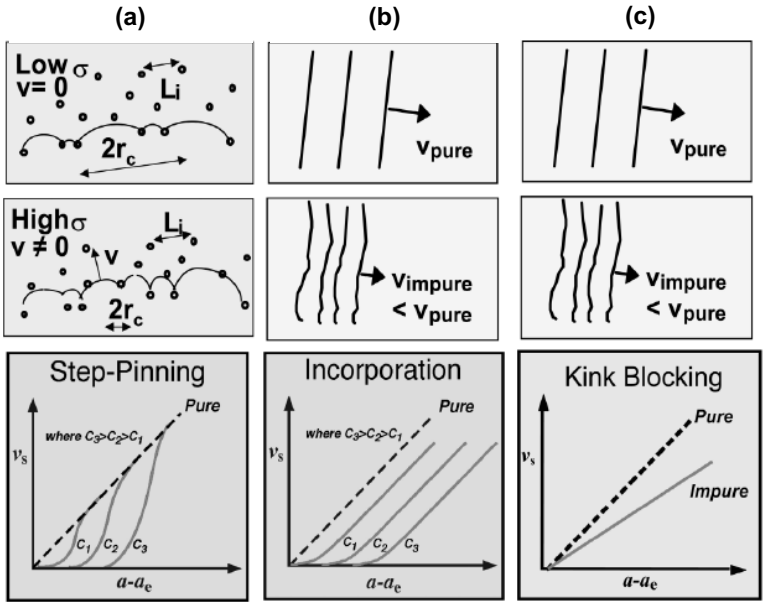


**Figure 2.12.** Depiction of crystal growth inhibition by impurities, reproduced from ref. [174]: (a) step-pinning, in which an adsorbed inhibitor impedes step advance and forces high-energy inclusion or 2D nucleation to protrude; (b) incorporation, in which the resulting defects cause strain and lower crystal stability, leading to a lower crystallization driving force; (c) kink-blocking, in which the transient occupation of kink sites by inhibitors slows the kinetics of incorporating building blocks into the crystal.

After an impurity has been incorporated into the crystal structure, the second inhibition mechanism occurs. As discussed in the section on defects, the incorporation of an impurity leads to local internal stress and decreased thermodynamic stability. However, also the entropy of the crystal is locally increased. The net result can thus be either an increase or decrease in growth rate, although the negative energetic contributions often outweigh the entropic advantages. Effectively, due to a shift in chemical potential, the solubility of the crystal is shifted linearly with respect to its unaffected equilibrium.

Besides step-pinning, an impurity can also transiently block a kink-site. In this third inhibition mechanism, there is merely a kinetic delay. The net number of kink-sites is effectively reduced, because some sites are unavailable due to the presence of an adsorbed impurity. The result is no clear shift in thermodynamic stability or growth mechanism, but a kinetic decrease of growth rate. Evidently, the supersaturations at which the system transitions from one growth mechanism to the next can be affected by a transient inhibition phenomenon as kink-blocking. The difference between step-pinning and kink-blocking is deceivingly small and resides only in the residence time of the impurity. Note that a transiently blocked step is immaterial, as long as the kink-site is not blocked, hence the difference in name between the two mechanisms.

Intriguingly, besides forming impediments, impurities can also promote nucleation and growth by lowering the interfacial energy penalty for heterogeneous nucleation on the crystal surface.[175] In such a scenario, the regular crystal growth mechanism might be slowed down, but a transition can be made to more rough-growth mechanisms and appreciable rates of growth can be conserved. Counterintuitively, through such a mechanism, the special case may even arise in which impurities can speed up the net growth rate of a crystal.

Characterizing the growth rate as a function of supersaturation in the presence and absence of inhibitors is often a good way to diagnose the inhibition mechanism at play. Supplementing such kinetic analysis, the incorporation of impurities will often leave microscopically visible marks through etch-pits upon dissolution: the region surrounding the incorporated impurity will often exhibit lower chemical potential and will thus preferentially dissolve.[176–178] As with all discussions on crystallization mechanisms, the effect of inhibition can again by very much facet-dependent. Consequently, inhibition of selected facets is one of the tools crystal engineering offers to achieve specific crystal shapes and morphologies.[179–182]

Having discussed the effect of inhibitors on growth, we should also briefly consider their effect on nucleation. An additive can adsorb to one or more facets of a small (pre-)nucleation cluster and thereby block or stall its further growth.[183] Because of size-dependent solubility effects (eq. 2.19), the nucleus is then prone to redissolve and nucleation is effectively inhibited.

The reverse, nucleation promotion, can be achieved through templating, essentially using inhibitors in a different role where they present a lower barrier for nucleation rather than binding to an existing crystal surface.[184] A legitimate question is whether this is essentially just heterogeneous nucleation and a very particular kind of non-solid 'seeding'. In terms of mechanism, the considerations are at least very similar: a molecular template can lower the nucleation barrier through minimizing the interfacial energy. An argument for retaining the term 'inhibition' for such species holds when they impact the polymorph that nucleates and grows, as one could then argue the natural polymorph is kinetically slower to nucleate and grow and thus practically inhibited. For example, the nucleation of (*RS*)-mandelic acid can be inhibited by the addition of e.g. 2-phenylpropionic acid, allowing the preferential nucleation of the pure enantiomer.[185,186] Similar findings were reported for proxyphylline, where the nucleation of the stable racemic compound was inhibited by the achiral solvent (isobutyl alcohol) and the conglomerate could be obtained through seeded growth.[187]

Indeed, inhibitors do not only affect nucleation and growth dynamics, but can also direct the crystal forms that are observed in a system. By selectively inhibiting the

growth of stable polymorphs, metastable polymorphs of L-glutamic acid and paracetamol could be obtained.[141,188]

As evident from the examples before, the employ of inhibitors is also of interest in the resolution of enantiomers, as such resolution requires the growth of frequently relatively unstable enantiopure crystals.[139] Addadi, Lahav and Leiserowitz showed for example how a racemic solution of the amino acid asparagine crystallized in the presence of several other enantiopure amino acids as additives.[189] They found that the additive binds stereoselectively at the surface and differently affects the growth of the D and L crystals. Such effects can arguably also lead to the cross-inhibition by opposing enantiomers.[168] This groundwork inspired later work in which growth inhibition of a stable racemic compound allowed the crystallization of the enantiopure conglomerate form.[190,191] These so-called 'tailor-made' inhibitors were in fact closely related compounds that originated from synthesis (reagents or by-products) or comprised other entries from structurally-related libraries. Nonetheless, the potential of such approaches is clear and inhibition can be an important tool to crystallize otherwise thermodynamically disfavoured crystal forms.

A final interesting question is the effect of inhibition on the dissolution of crystals, a question which has hardly been studied and presents a relative lacuna in our knowledge of crystallization dynamics.[192] More generally, in fact, crystal dissolution has been given relatively little public study as compared to crystal growth. While the production of high-quality single crystals has seen relevance for many applications, the interest in making crystals disappear is perhaps often regarded as merely an academic curiosity or only relevant for selected mineralogists. This thesis will certainly challenge such views (esp. Chapters 6 and 8). One would expect that inhibition (and impurities in general) have pronounced effect also on the dissolution of crystals. First, the emergence of etch-pits should be recalled as a clear morphological marker of certain kinds of impurities and inhibitions.[193,194] Second, the dynamics of dissolution can be considered in the presence of inhibitors. Dissolution classically occurs through adatom-by-adatom dissociation at step-edges, although particle-by-particle detachment is also possible.[195,196] Mobile inhibitors can traverse the crystal surface, facilitate the nucleation of kink-sites, and thereby speed up dissolution.[197] Depending on the mechanism of inhibition, the presence of low amounts of inhibitor can also induce crystal dissolution even in a supersaturated growth environment—possibly with strain-reduction as driving force.[198,199] Dissolution can, however, also be halted by inhibition, as is observed for calcite dissolution in the presence of magnesium ions.[200] In such cases, step velocities are halted (in either direction: dissolution or growth) and step-pinning is considered the underlying mechanism of action.[201,202]

The rational design of crystal growth inhibitors is arguably not yet routine, but expected to pick up significantly with progress in computational chemistry, enabling unprecedented levels of design.[203–206] Currently, preventing the crystallization of ice,[207–209] calcium carbonate (the cause of scaling),[210] and calcium oxalate (the primary component of kidney stones)[199] are among the most actively studied. When our fundamental understanding on molecular inhibition mechanisms has become more satisfactory and such rational design of crystal growth inhibitors prove routinely accessible, this particular side of crystal engineering has the potential for big impact on particle engineering and the development of separation processes.[211]

## Industrial Crystallization Processes

Besides the enticing appearance and fascinating properties of crystals, crystallization is also one of the most versatile and oldest separation techniques in the whole of chemical engineering.[1] Back around 3500 B.C., breakthroughs in applied chemistry were realized in Egypt, Ancient Mesopotamia and Crete.[212] Already there and then, advanced metallurgy was practiced and high quality copper was purified through melt crystallization.[213] The controlled evaporative crystallization of salts from seawater was already depicted in China in 2700 B.C, and the recrystallization of sugar from sugar cane extracts is reported to have been developed in India in 327 B.C.[214] Indeed, crystallization is, and ever since the earliest industrial processes has been, an instrumental tool for producing, purifying, and giving one's desired properties to chemical products.

Today, industrial crystallization is part and parcel to separating, recycling and purifying many essential feedstocks and producing high quality salts, pharmaceuticals and fine chemicals.[215–221] In the EU alone, over 50 million tonnes per annum of sugar and NaCl are produced through crystallization processes. Worldwide, many thousands of tonnes of pharmaceuticals and fine chemicals are likewise purified (e.g. ascorbic acid and acetylsalicylic acid). Prominently emerging is hydrometallurgical recycling through crystallization, wherein rare earth metals are precipitated from leachates and recycled and purified through solution-based crystallization processes.[222,223] Besides applications in semiconductors and energy storage, the increased call for intensified recycling efforts, biobased feedstocks, and green chemistry will only increase the importance of crystallization in the chemical industry.[224–226]

While laboratory-scale crystallization allows for easy, fast and precise control of parameters such as temperature, concentration, and mixing in small, homogeneous environments, industrial crystallization must contend with significantly larger volumes and complex equipment where maintaining uniform conditions is much more challenging.[1,227] At the research scale, crystallization is typically used to study fundamental principles, optimize conditions, or screen crystal forms. In contrast,

industrial crystallization processes require robust and reproducible operation using non-ideal feedstocks and with stricter economic, environmental, and safety constraints.

Besides cooling crystallization, anti-solvent crystallization is widely adopted in pharmaceutical manufacturing due to its compatibility with ambient operating temperatures, its homogeneity, and its ability to deliver high product yields, owing to its large accessible phase-space.[228–230] In anti-solvent crystallization, the compound to be crystallized in normally dissolved in a good solvent, to which a poor solvent is added that mixes with the good solvent. The result is a decrease in solubility and a driving force for crystallization. Molecularly, the anti-solvent initially penetrates the solvation shell, after which a rearrangement occurs, ultimately leading to the expulsion of an anti-solvent/solvent pair from the shell as repulsive forces dominate—effectively leading to desolvation.[231] Besides anti-solvents, changing pH to affect the solubility of species is also a common means of crystallization control.



Lab-scale crystallization processes often occur in batch-mode, while industry often prefers continuous processes. For crystallization, many specific reactor types have been developed to achieve continuous crystallization processes, uniquely designed to enable initial seeding and steady-state process output parameters.[232–234] Well-known reactor types for continuous crystallization are mixed suspension mixed product removal (MSMPR) crystallizers and tubular or plug flow crystallizers (PFC): laminar-flow tubular crystallizers (LFTC), coiled flow inverter (CFI) crystallizers, segmented/slug flow crystallizers, and continuous oscillatory baffled crystallizers (COBC).[221] A further discussion of these reactor types is beyond the scope of this thesis.

The transition from lab to industrial scale does introduce numerous challenges, including mass and heat transport, non-uniform mixing, temperature gradients, fouling, nucleation behaviour, and inconsistent crystal size distributions—all of which can impact product quality and process efficiency.[235] Successfully scaling up crystallization thus demands careful consideration of these complexities and requires accurate control and online monitoring to ensure consistent product quality in form, size, shape, and purity. A number of these aspects are worthwhile to address here, as they will also feature—to various degrees—in the work presented in this thesis.

With respect to size, a small crystal size distribution can lead to fine powders that easily cake (i.e. form lumps which may trap mother liquor or water from humid air) and can clog filters. With respect to shape, needle-like crystals are hard to filter and shape affects the flow properties of the final powder, which in turn is important for processing the product. Considering these two parameters already shows a clear link

between crystallization fundamentals and industrial concerns.[217,236] The final size distribution is very much an outcome of the interplay between nucleation (primary and secondary), attrition, homogenization, and growth.[237] Often, real-time monitoring of concentration of the crystallizing species is employed to obtain control of the supersaturation as a generic handle for a number of these crystallization parameters. Focused beam reflectance can also be used to monitor the number of crystals, although some studies have also successfully tracked crystallization through simple turbidity measurements.[238–241] In the preceding sections of this introduction, the shape of crystals has already been related to crystallization conditions (solvent and supersaturation) and the presence of impurities and inhibitors.

Beyond a one-step crystallization experiment, primarily aimed at purification and isolation of a product, successive (re)crystallizations may be required to transform the crystals into a population with a desired size and shape. One method, particularly interesting in the context of this thesis, is that of temperature cycling.[242] During temperature cycling, a suspension of crystals is consecutively heated and cooled, which consecutively increases and decreases solubility, thereby inducing cycles of crystal dissolution and growth (Fig. 2.13a).[243] In a way, such a procedure can be seen as an enhanced ripening process, as fines have a lower solubility and thus dissolve early and disappear (Fig. 2.13b).[244,245] Temperature cycling therefore results a narrower crystal size distribution but a larger average crystal size.

Temperature cycles can lead to particularly interesting results in terms of crystal shape. Below a thermodynamic roughening transition, the equilibrium shape of crystals is principally determined by the so-called Wulff-construction, which minimizes the interfacial energy.[248] In actual growth processes, however, interfacial kinetic processes can naturally lead to deviations from this classical Wulff-shape.[249] In contrast to the equilibrium crystal shape, face-specific rates of growth and dissolution drive the evolution of shape during temperature cycling (Fig. 2.13c).[247] Indeed, whenever a facet's rates of growth and dissolution are unequal, temperature cycling drives the shape of a crystal away from its equilibrium. If a face dissolves faster than it grows, it recedes; if a face grows faster than it dissolves, it expands. In essence, the process thus depends on the hysteretic nature of combining growth and dissolution.[247] The appearance of virtual faces is also a hallmark of temperature cycling, whereby edges and vertices bifurcate into new planes that enable unusual morphological pathways.[250] Although the results of shape due to temperature cycling are hard to predict and quite detailed knowledge of crystal growth and dissolution behaviour is required, 2D population balance modelling has been effectively applied.[251–253]

Naturally, all complexities involved with regular seeded cooling crystallization are equally extant during the growth segment of a temperature cycle and require effective control. Solvent choice, heating-cooling rates, and the depth of temperature swings are the critical parameters in temperature cycling.[250,254] Practically, three distinct variants of implementing temperature cycling exist: splitting growth and dissolution processes between two reactors (pumping cycling),[244,255,256] successively heating and cooling one reactor (temporal cycling),[254,257,258] and constant temperature gradients within one reactor (spatial cycling).[259,260] During the development of such processes, accurate monitoring is essential to ensure effective crystal shape and size engineering.[243,261,262]

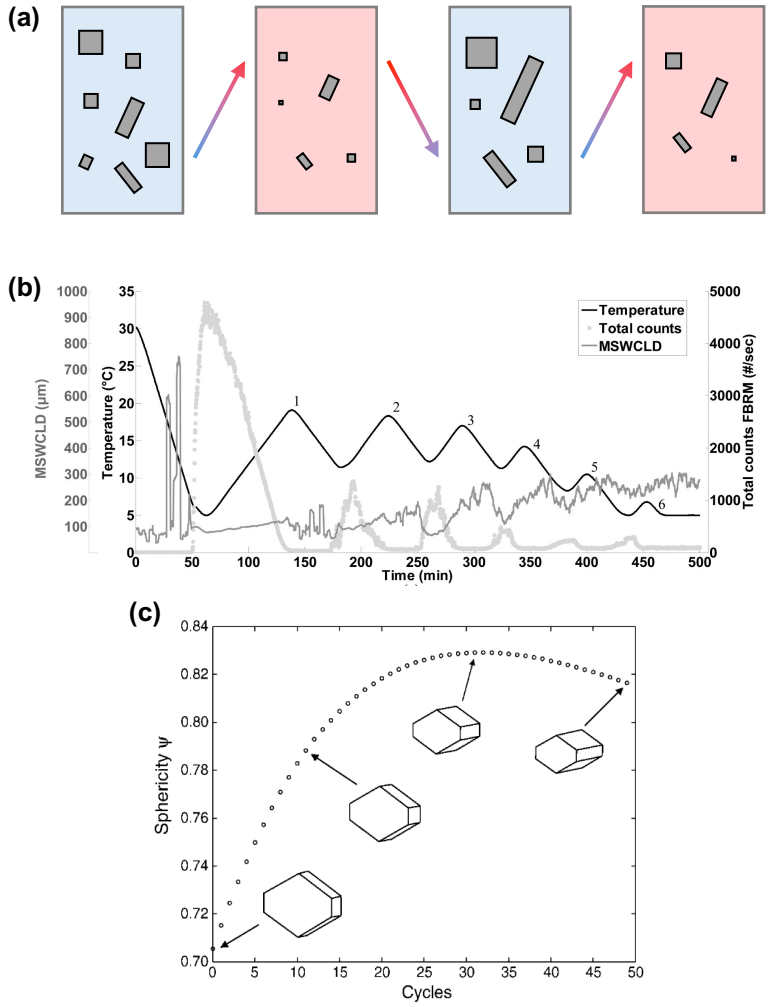


**Figure 2.13.** Temperature cycling uses consecutive heating and cooling to elicit solubility swings resulting in cycles of crystal growth and dissolution that can affect the average size and shape of the crystals (panel a). Examples are shown of experimental crystal size evolution (panel b, reproduced from ref. [246]) and crystal shape evolution (panel c, reproduced from ref. [247]).

The seeding of crystallization processes naturally is another a crucial aspect that should not be overlooked.[263,264] For one, it eliminates dependence on primary nucleation and gives much greater control over the amount of crystallizing particles.[265] Control over the crystallization mechanism and the extent of secondary nucleation are the challenges that then remain. Seeding also allows speeding up the productivity by enhancing crystallization rates. The preparation of seeds, however, is often ignored.[266] Important aspects seeds are their size and stability, their propensity to growth rate dispersion, and crystal surface roughness (which relates to secondary nucleation rates). Unfortunately, not much research has been published so far that discusses seed preparation extensively and thoroughly. Controlling seed-size (and thereby crystal surface area) has received most attention, as it is the most straightforward handle to control a product's final crystal size distribution.

Besides control over size and shape, control over polymorphism can pose serious challenges—especially in the pharmaceutical industry. Polymorphism is notorious: over 50% of the molecules in Roche and Lilly's library that were screened for polymorphism readily showed polymorphism, and more than 75% of molecules could be crystallized in at least one different polymorph when this was seriously attempted.[153] We should note here that the solvent is not only a critical factor in the crystallization dynamics, but can actually also be incorporated into the crystal structure.[267] If so, one speaks of solvates. In the case of included water, a solvate is termed a hydrate. Often solvates are particularly unwanted crystal forms due to their instability.[268] In contrast, co-crystals—where an ancillary co-former is present in the crystal structure—have recently gained substantial attention as a route toward adjustable and improved solid-state properties of pharmaceutical compounds.[269,270] Solvates and co-crystals are not strictly polymorphs of a crystallizing compound, because both composition and arrangement of the crystal structure differ. Regardless, solvates and co-crystals are always part of discussions on controlling crystal form.

Classically, temperature and supersaturation are considered the primary control factors for polymorphism.[151] Temperature affects relative polymorph stability and thermodynamics dictates which polymorph is preferred at which absolute temperature—different crystal forms appearing as function temperature is called enantiotropy.[271] Because different polymorphs have different thermodynamic stability, supersaturation dictates whether each will grow or dissolve and is also critical in each phase's nucleation kinetics. The nucleation bottleneck can sometimes be overcome by seeding a system with the desired polymorph.[132] To aid the stability of the desired polymorph and suppress the nucleation of undesired forms, solvent choice is another essential factor.[272,273] This relates back to the interactions between the solvent and the crystal on the interface, where the molecular interactions between a solvent and any possible facet differs. In addition, differences in

conformational distributions in solution can give rise to different nucleation behaviour.[274] As discussed previously, additives can also be very effective in controlling the nucleation and growth of crystal forms.

Besides thermodynamic stability, the compatibility of metastable zones of the various possible crystal forms should be carefully considered. The biggest enemy of metastable polymorphs is the solution-mediated polymorph transformation, during which solvent molecules essentially facilitate recrystallization of the stable form.[154] Such a procedure can also be employed advantageously to convert solvates to anhydrous forms or to convert polymorphs in systems where relative stability is a strong function of solvent choice.



Another technique for polymorph control that has recently picked up attention is mechanical grinding, for which the input of mechanical energy through collisions of hard spheres shapes unique nonequilibrium conditions that may drive the appearance of otherwise hard-to-grow polymorphs.[275,276] Unfortunately, the details of mechanochemistry are not well understood, but size-dependent stability, interfacial solvation effects, increased nucleation events, enhanced accessibility of growth sites and surface roughening might all play a role.[277–279] Strikingly, some polymorphic transformations only appear after long induction times—from hours to days—an unparalleled levering of kinetic over thermodynamic stability.[280] The likelihood of co-crystal formation has especially been increased through mechanochemical means.[281,282] It remains to be seen how this innovation will be integrated into more conventional crystallization process pipelines.

Anti-solvent crystallization is of special interest for polymorph control, for it yields access to a broad range of possible supersaturations, nucleation conditions and thermodynamic phase-regimes.[283] Indeed, ternary phase diagrams increase the number of viable pathways under which a certain polymorph is stable without nucleating unwanted polymorphs.[228] Solvent addition potentially suffers less from inhomogeneities stemming from delayed transport phenomena on large scales than conventional reactor temperature controls. The specific choice of solvents can also lower the detachment kinetics of adatoms, in turn lowering solvent-mediated polymorph transformations which are antagonistic for polymorph control.[284] By now, diverse strategies have been developed for high-throughput screening and the development of ternary phase diagrams to guide polymorph control.[285]

A recently emerging research trend is crystallization in confinement. Nanoscale pores offer a powerful platform for screening and controlling polymorphism by stabilizing metastable forms, suppressing undesired crystallization, and enabling the discovery of new polymorphs that are inaccessible through bulk methods.[286,287] While this strategy shows strong potential for industrial polymorph control, it currently remains primarily at the research stage due to challenges with scalability and crystal

recovery. Notably, however, pores and confinements naturally occur within many components used in crystallization, so that consideration and knowledge of crystallization in confinement is desirable.

Reflecting on the complexity of modern industrial crystallization, Ter Horst emphasizes that we can only really advance the design and development of robust crystallization processes that meet industrial demands by studying and understanding the molecular underpinnings of crystallization.[288] This foundational knowledge becomes even more critical when crystallization is coupled to chemical reactions — a strategy that greatly complexifies the crystallization process but also widely expands its scope and potential for chemical synthesis. In the following section, we will explore the unique challenges and opportunities presented by reactive crystallization, the focus this thesis.

## Reactive Crystallization

Reactive crystallization is a complex process, where the kinetics and thermodynamics of crystallization are combined with chemical reactions involving the crystallizing species.[289] In reactive crystallization, supersaturation is commonly not seen to be principally generated through cooling (or other means of lowering net solubility), but through the in-situ formation of the crystallizing species as a product of a chemical reaction. Product formation increases concentration and thereby can result in supersaturation (Fig. 2.14a). Compared to conventional (i.e. non-reactive) crystallization, reactive crystallization has the intrinsic potential to pull on a chemical equilibrium by removing a species from the solution, gas or melt (cf. Chatelier's principle) to increase the yield of a reaction. Reactive crystallization can also be a useful strategy to isolate or protect otherwise transient intermediates that form part of a larger reaction network. Although reactive crystallization may sound very similar to conventional crystallization, it often serves different goals, elicits other considerations, and presents us with new handles and control mechanisms. By now, a wide array of reactive crystallization strategies has already been implemented as continuous processes on an industrial scale, which generally show much improved yield compared to stand-alone chemical procedures.[290,291,289]

In essence, reactive crystallization stems from the concept of coupled equilibria. A chemical equilibrium involves a reversible back-and-forth reaction, e.g. A ⇌ B. At equilibrium, the forward and reverse rates are equal (but non-zero). This means that that the net reaction rate at equilibrium is zero and the concentrations of the reactants ([A] and [B]) are constant. We can define an equilibrium constant $K$ for the equilibrium reaction A ⇌ B as

$$K = \frac{[B]}{[A]} \qquad \text{(eq. 2.22)}$$

Note that the position of this equilibrium is very much dependent on temperature, following Van 't Hoff's equation, and also on other conditions affecting the chemical reaction rates (such as solvent).

An interesting case of equilibrium reactions coupled to crystallization involves the presence of seed crystals of all crystallizing species, as was studied by Kuhn and Dimroth (Fig. 2.14b).[292,293] They showed that the solubility equilibria for all species should also be considered (e.g. [A]* and [B]*), coupling the equilibrium of the reaction with those of crystallization. They demonstrated how, when $K \cdot [A]^* > [B]^*$, the coupled equilibria drive the conversion of solid A into solid B. One especially common misconception about reactive crystallization is that the desired product should be less soluble than the reactant(s). The analysis above shows, however, that it is not solubility by itself that matters, but the product of solubility with the reaction equilibrium. Besides, from a practical perspective, the relative solubilities of reactants and products can be tuned in many ways, such as by the choice of solvent, or by adding co-formers to yield co-crystals to lower the solubility of the product.

In developing a reactive crystallization process, there is always more than one species that must be considered.[294] One must take stock of the solubility of all species

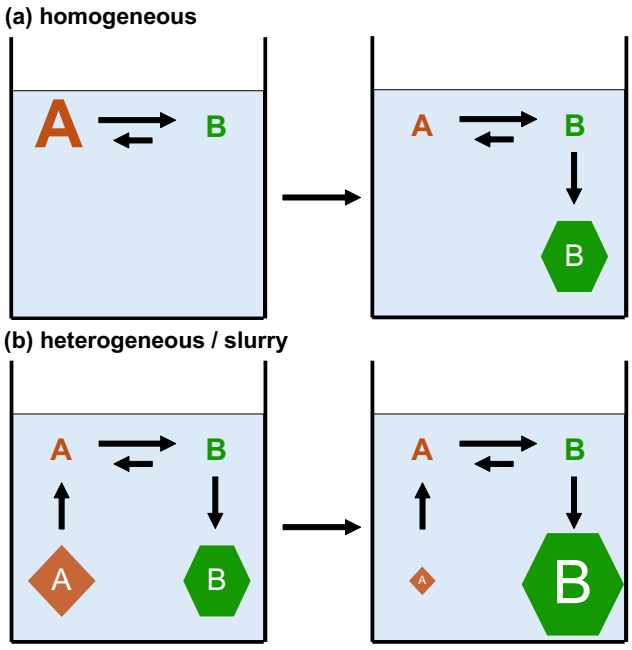


**Figure 2.14.** Two main modes of reactive crystallization processes for a reaction from A to B for which the reaction equilibrium limits the yield of B, which has a much lower solubility than A: (a) Homogeneous starting conditions (solution of A), from which spontaneously formed B nucleates and crystallization drives the equilibrium towards a high yield in solid B; (b) Heterogeneous starting conditions (e.g. slurry of equal amounts of A and B), for which the coupled equilibria of dissolution, reaction and crystallization effectively convert the solid A into solid B.

and the rates and equilibria of the chemical reactions between those species. Naturally, conditions are selected whereby the desired compound experiences a driving force to crystallize, but reactants and byproducts remain in solution or and can dissolve (from a solid feed). Note that such a heterogeneous approach is at odds with what is habitual in many (organic) syntheses, where the critical components are oftentimes fully dissolved and the product is isolated later. Often, it may be beneficial to design a custom solvent mixture that balances the desired solubilities of the various species and allows for efficient chemical conversions. An additional complexity might be faced when the reagent concentrations also affect each other's solubility or when they act as an inhibitor to crystallization.[295–299]

Well-known applications of reactive crystallization stem from instantaneous ionic reactions in hydrometallurgy and $CO_2$-sequestration. With recent research mainly being concentrated in Asia, reactive crystallization processes have been successfully developed to extract and recycle metals from Li, Ni, Al, to Ba and Sc.[300–304] Much attention has also been given to the precipitation of $CO_2$ as carbonate salt by bubbling the gas through a solution of lithium, calcium, or magnesium chloride or hydroxide.[305] Building on these seminal ionic applications, reactive crystallization has also been expanded to the more complicated realm of non-instantaneous covalent reactions. Initially, acid-base chemistry, condensations, and substitutions (e.g. acid chlorides and anhydrides) presented a fruitful starting point because of the stark solubility effects of protonation and deprotonation on organic substrates and reactive crystallization was mainly applied to increase reaction yield and conveniently isolate products.[306–309] Later, fermentations and biocatalytic processes were reworked into reactive crystallizations, allowing the mitigation of poor selectivity, inconvenient equilibrium constants, and intrinsically limited yield (due to biocatalyst stability) through in-situ product removal.[310] Following these developments, strides were made in using immobilized enzymes and catalysts for reactive crystallization and even electrochemically-induced reactive crystallization was successfully attempted.[311–313]

An inherent challenge in reactive crystallization is compatibility between reaction and crystallization conditions. Sometimes, it may be necessary to separate the reaction and crystallization conditions in space or time. This can be performed sequentially, in which a reactor is first exposed to reaction conditions, and then the conditions are altered to favour crystallization (e.g. addition of an anti-solvent, change of pH, change of temperature—post-removal of any unstable catalyst). In such a scenario, however, key benefits of reactive crystallization may be lost. Therefore, a cyclic approach could be preferred, such that a process is split between multiple reactors and pumped from one to the next or back-and-forth. Tubular reactors with a gradient in conditions can achieve spatial separation of crystallization and reaction conditions, akin to multi-step processes in flow-

chemistry.[314–316] Although hardly explored, one can envision oscillations between reaction-geared and crystallization-geared conditions of the reactor-line in both of these scenarios, through which a continuous reactive crystallization process is ultimately obtained.

Besides chemical compatibility, also a need for catalysis to drive the reaction may cause problems. A heterogeneous catalyst can serve as a platform for heterogeneous nucleation and be blocked by crystallization. Specifically, the highly active catalyst pores are ideal confinements for crystallization. In terms of separation, immobilization of catalysts may be preferred to more easily discriminate between crystallized product and catalyst—especially in the context of (semi-)continuous processes. When the chemical reaction is too fast for the crystallization process to consume the product, large supersaturations can ensue and control over the crystallization process will diminish. Crystallization as a productivity limit is undesirable, and can sometimes be mitigated by milling to maximize the available surface area and enhance autocatalytic secondary nucleation.[317,318]

Reactive crystallization can also be applied for the deracemization of interconverting diastereomers, a process known as crystallization-induced diastereomer transformation.[319] In this chiral variant of reactive crystallization, the more soluble diastereomer is converted into the less soluble diastereomer. Strikingly, reactive crystallization even works when the solubilities of two crystallizing species are equal and their reaction equilibrium constant is unity. This is the case of racemizing enantiomers and will be the basis for our discussion of deracemization through reactive crystallization presented in the next chapter.[320–323]

## References


(1) Mullin, J. W. *Crystallization*, 4th ed.; Butterworth-Heinemann: Oxford Boston, 2001.

(2) Greiner, W.; Neise, L.; Stöcker, H. *Thermodynamics and Statistical Mechanics*; Springer New York: New York, NY, 1995. https://doi.org/10.1007/978-1-4612-0827-3.

(3) Goodstein, D. *Thermal Physics: Energy and Entropy*, 1st ed.; Cambridge University Press, 2015. https://doi.org/10.1017/CBO9781139942539.

(4) Jones, R. A. L. *Soft Condensed Matter*; Oxford University PressOxford, 2002. https://doi.org/10.1093/oso/9780198505907.001.0001.

(5) Doi, M. *Soft Matter Physics*; Oxford University Press, 2013. https://doi.org/10.1093/acprof:oso/9780199652952.001.0001.

(6) Berthier, L.; Biroli, G. Theoretical Perspective on the Glass Transition and Amorphous Materials. *Rev. Mod. Phys.* **2011**, *83* (2), 587–645. https://doi.org/10.1103/RevModPhys.83.587.

(7) Tong, H.; Sengupta, S.; Tanaka, H. Emergent Solidity of Amorphous Materials as a Consequence of Mechanical Self-Organisation. *Nat. Commun.* **2020**, *11* (1), 4863. https://doi.org/10.1038/s41467-020-18663-7.

(8) Regev, I.; Weber, J.; Reichhardt, C.; Dahmen, K. A.; Lookman, T. Reversibility and Criticality in Amorphous Solids. *Nat. Commun.* **2015**, *6* (1), 8805. https://doi.org/10.1038/ncomms9805.

(9) Anderson, P. W. Through the Glass Lightly. *Science* **1995**, *267* (5204), 1615–1616. https://doi.org/10.1126/science.267.5204.1615.f.
(10) Sastry, S.; Debenedetti, P. G.; Stillinger, F. H. Signatures of Distinct Dynamical Regimes in the Energy Landscape of a Glass-Forming Liquid. *Nature* **1998**, *393* (6685), 554–557. https://doi.org/10.1038/31189.
(11) Heide, K.; Heide, G. Vitreous State in Nature—Origin and Properties. *Geochemistry* **2011**, *71* (4), 305–335. https://doi.org/10.1016/j.chemer.2011.10.001.
(12) Prince Rupert's Drops. *Notes Rec. R. Soc. Lond.* **1986**, *41* (1), 1–26. https://doi.org/10.1098/rsnr.1986.0001.
(13) Aben, H.; Anton, J.; Õis, M.; Viswanathan, K.; Chandrasekar, S.; Chaudhri, M. M. On the Extraordinary Strength of Prince Rupert's Drops. *Appl. Phys. Lett.* **2016**, *109* (23), 231903. https://doi.org/10.1063/1.4971339.
(14) Zhai, W.; Sakthivel, T.; Chen, F.; Du, C.; Yu, H.; Dai, Z. Amorphous Materials for Elementary-Gas-Involved Electrocatalysis: An Overview. *Nanoscale* **2021**, *13* (47), 19783–19811. https://doi.org/10.1039/D1NR06764H.
(15) Kang, J.; Yang, X.; Hu, Q.; Cai, Z.; Liu, L.-M.; Guo, L. Recent Progress of Amorphous Nanomaterials. *Chem. Rev.* **2023**, *123* (13), 8859–8941. https://doi.org/10.1021/acs.chemrev.3c00229.
(16) Jia, B.; Liu, G.; Zhang, B.; Zheng, J.; Yin, K.; Lin, J.; Han, C.; Fan, X.; Xu, M.; Ye, L. General Modification Strategy on Amorphous Materials to Boost Catalytic Performance. *Adv. Funct. Mater.* **2024**, *34* (44), 2405867. https://doi.org/10.1002/adfm.202405867.
(17) Hendrikse, H. C.; Aguirre, A.; Van Der Weijden, A.; Meeussen, A. S.; Neira D'Angelo, F.; Noorduin, W. L. Rational Design of Bioinspired Nanocomposites with Tunable Catalytic Activity. *Cryst. Growth Des.* **2021**, *21* (8), 4299–4304. https://doi.org/10.1021/acs.cgd.1c00165.
(18) Wang, X.; Shi, W.; Wang, S.; Zhao, H.; Lin, J.; Yang, Z.; Chen, M.; Guo, L. Two-Dimensional Amorphous $TiO_2$ Nanosheets Enabling High-Efficiency Photoinduced Charge Transfer for Excellent SERS Activity. *J. Am. Chem. Soc.* **2019**, *141* (14), 5856–5862. https://doi.org/10.1021/jacs.9b00029.
(19) Gurbatov, S. O.; Modin, E.; Puzikov, V.; Tonkaev, P.; Storozhenko, D.; Sergeev, A.; Mintcheva, N.; Yamaguchi, S.; Tarasenka, N. N.; Chuvilin, A.; Makarov, S.; Kulinich, S. A.; Kuchmizhak, A. A. Black Au-Decorated $TiO_2$ Produced via Laser Ablation in Liquid. *ACS Appl. Mater. Interfaces* **2021**, *13* (5), 6522–6531. https://doi.org/10.1021/acsami.0c20463.
(20) Yu, J.; Chen, C.; Zhang, Q.; Lin, J.; Yang, X.; Gu, L.; Zhang, H.; Liu, Z.; Wang, Y.; Zhang, S.; Wang, X.; Guo, L. Au Atoms Anchored on Amorphous $C_3N_4$ for Single-Site Raman Enhancement. *J. Am. Chem. Soc.* **2022**, *144* (48), 21908–21915. https://doi.org/10.1021/jacs.2c07413.
(21) Hancock, B. C.; Parks, M. What Is the True Solubility Advantage for Amorphous Pharmaceuticals? *Pharm. Res.* **2000**, *17* (4), 397–404. https://doi.org/10.1023/A:1007516718048.
(22) Chiou, W. L.; Riegelman, S. Pharmaceutical Applications of Solid Dispersion Systems. *J. Pharm. Sci.* **1971**, *60* (9), 1281–1302. https://doi.org/10.1002/jps.2600600902.
(23) Janssens, S.; Van Den Mooter, G. Review: Physical Chemistry of Solid Dispersions. *J. Pharm. Pharmacol.* **2009**, *61* (12), 1571–1586. https://doi.org/10.1211/jpp.61.12.0001.
(24) Yu, L. Amorphous Pharmaceutical Solids: Preparation, Characterization and Stabilization. *Adv. Drug Deliv. Rev.* **2001**, *48* (1), 27–42. https://doi.org/10.1016/S0169-409X(01)00098-9.
(25) Hancock, B. C.; Zografi, G. Characteristics and Significance of the Amorphous State in Pharmaceutical Systems. *J. Pharm. Sci.* **1997**, *86* (1), 1–12. https://doi.org/10.1021/js9601896.
(26) Noorduin, W. L.; Kaptein, B.; Meekes, H.; van Enckevort, W. J. P.; Kellogg, R. M.; Vlieg, E. Fast Attrition-Enhanced Deracemization of Naproxen by a Gradual In Situ Feed. *Angew. Chem. Int. Ed.* **2009**, *48* (25), 4581–4583. https://doi.org/10.1002/anie.200901386.
(27) Noorduin, W. L.; Van Der Asdonk, P.; Bode, A. A. C.; Meekes, H.; Van Enckevort, W. J. P.; Vlieg, E.; Kaptein, B.; Van Der Meijden, M. W.; Kellogg, R. M.; Deroover, G. Scaling Up Attrition-Enhanced Deracemization

by Use of an Industrial Bead Mill in a Route to Clopidogrel (Plavix). *Org. Process Res. Dev.* **2010**, *14* (4), 908–911. https://doi.org/10.1021/op1001116.
(28) Reynes, J. F.; Leon, F.; García, F. Mechanochemistry for Organic and Inorganic Synthesis. *ACS Org. Inorg. Au* **2024**, *4* (5), 432–470. https://doi.org/10.1021/acsorginorgau.4c00001.
(29) Fantozzi, N.; Volle, J.-N.; Porcheddu, A.; Virieux, D.; García, F.; Colacino, E. Green Metrics in Mechanochemistry. *Chem. Soc. Rev.* **2023**, *52* (19), 6680–6714. https://doi.org/10.1039/D2CS00997H.
(30) Aydonat, S.; Hergesell, A. H.; Seitzinger, C. L.; Lennarz, R.; Chang, G.; Sievers, C.; Meisner, J.; Vollmer, I.; Göstl, R. Leveraging Mechanochemistry for Sustainable Polymer Degradation. *Polym. J.* **2024**, *56* (4), 249–268. https://doi.org/10.1038/s41428-023-00863-9.
(31) Sun, Y.; Zhu, L.; Wu, T.; Cai, T.; Gunn, E. M.; Yu, L. Stability of Amorphous Pharmaceutical Solids: Crystal Growth Mechanisms and Effect of Polymer Additives. *AAPS J.* **2012**, *14* (3), 380–388. https://doi.org/10.1208/s12248-012-9345-6.
(32) Luft, J. R.; Newman, J.; Snell, E. H. Crystallization Screening: The Influence of History on Current Practice. *Acta Crystallogr. Sect. F Struct. Biol. Commun.* **2014**, *70* (7), 835–853. https://doi.org/10.1107/S2053230X1401262X.
(33) Franklin, R. E.; Gosling, R. G. Molecular Configuration in Sodium Thymonucleate. *Nature* **1953**, *171* (4356), 740–741. https://doi.org/10.1038/171740a0.
(34) Watson, J. D.; Crick, F. H. C. Molecular Structure of Nucleic Acids: A Structure for Deoxyribose Nucleic Acid. *Nature* **1953**, *171* (4356), 737–738. https://doi.org/10.1038/171737a0.
(35) Shi, Y. A Glimpse of Structural Biology through X-Ray Crystallography. *Cell* **2014**, *159* (5), 995–1014. https://doi.org/10.1016/j.cell.2014.10.051.
(36) Landau, L. D.; Lifšic, E. M. *Mechanics*, 3d ed.; Course of theoretical physics; Pergamon Press: Oxford New York, 1976.
(37) Landau, L. D.; Lifšic, E. M.; Pitaevskij, L. P. *Statistical Physics*, 3d ed.; Course of theoretical physics; Elsevier Butterworth Heinemann: Amsterdam Heidelberg, 2011.
(38) Alder, B. J.; Wainwright, T. E. Phase Transition for a Hard Sphere System. *J. Chem. Phys.* **1957**, *27* (5), 1208–1209. https://doi.org/10.1063/1.1743957.
(39) Hutchinson, P. The Phase Transition of the Hard Sphere Fluid. *Mol. Phys.* **1967**, *13* (5), 495–499. https://doi.org/10.1080/00268976700101411.
(40) Onsager, L. The Effects of Shape on the Interaction of Colloidal Particles. *Ann. N. Y. Acad. Sci.* **1949**, *51* (4), 627–659. https://doi.org/10.1111/j.1749-6632.1949.tb27296.x.
(41) Frenkel, D. Entropy-Driven Phase Transitions. *Phys. Stat. Mech. Its Appl.* **1999**, *263* (1–4), 26–38. https://doi.org/10.1016/S0378-4371(98)00501-9.
(42) Pusey, P. N.; Van Megen, W. Phase Behaviour of Concentrated Suspensions of Nearly Hard Colloidal Spheres. *Nature* **1986**, *320* (6060), 340–342. https://doi.org/10.1038/320340a0.
(43) Piazza, R. Settled and Unsettled Issues in Particle Settling. *Rep. Prog. Phys.* **2014**, *77* (5), 056602. https://doi.org/10.1088/0034-4885/77/5/056602.
(44) Dussi, S.; Dijkstra, M. Entropy-Driven Formation of Chiral Nematic Phases by Computer Simulations. *Nat. Commun.* **2016**, *7* (1), 11175. https://doi.org/10.1038/ncomms11175.
(45) Apelblat, A.; Manzurola, E. Solubilities Ofo-Acetylsalicylic, 4-Aminosalicylic, 3,5-Dinitrosalicylic, Andp-Toluic Acid, and Magnesium- -Aspartate in Water fromT=(278 to 348) K. *J. Chem. Thermodyn.* **1999**, *31* (1), 85–91. https://doi.org/10.1006/jcht.1998.0424.
(46) Cuevas-Valenzuela, J.; González-Rojas, Á.; Wisniak, J.; Apelblat, A.; Pérez-Correa, J. R. Solubility of (+)-Catechin in Water and Water-Ethanol Mixtures within the Temperature Range 277.6–331.2K: Fundamental Data to Design Polyphenol Extraction Processes. *Fluid Phase Equilibria* **2014**, *382*, 279–285. https://doi.org/10.1016/j.fluid.2014.09.013.

(47) Jiang, S.; Ter Horst, J. H. Crystal Nucleation Rates from Probability Distributions of Induction Times. *Cryst. Growth Des.* **2011**, *11* (1), 256–261. https://doi.org/10.1021/cg101213q.
(48) Kubota, N. Analysis of the Effect of Volume on Induction Time and Metastable Zone Width Using a Stochastic Model. *J. Cryst. Growth* **2015**, *418*, 15–24. https://doi.org/10.1016/j.jcrysgro.2015.02.021.
(49) Devos, C.; Van Gerven, T.; Kuhn, S. A Review of Experimental Methods for Nucleation Rate Determination in Large-Volume Batch and Microfluidic Crystallization. *Cryst. Growth Des.* **2021**, *21* (4), 2541–2565. https://doi.org/10.1021/acs.cgd.0c01606.
(50) Hammadi, Z.; Candoni, N.; Grossier, R.; Ildefonso, M.; Morin, R.; Veesler, S. Small-Volume Nucleation. *Comptes Rendus Phys.* **2013**, *14* (2–3), 192–198. https://doi.org/10.1016/j.crhy.2012.12.004.
(51) Ildefonso, M.; Candoni, N.; Veesler, S. Heterogeneous Nucleation in Droplet-Based Nucleation Measurements. *Cryst. Growth Des.* **2013**, *13* (5), 2107–2110. https://doi.org/10.1021/cg4001686.
(52) Yang, F. Nucleation in a Liquid Droplet. *Phys. Chem. Chem. Phys.* **2020**, *22* (18), 9990–9997. https://doi.org/10.1039/D0CP00559B.
(53) Li, J.; Deepak, F. L. *In Situ* Kinetic Observations on Crystal Nucleation and Growth. *Chem. Rev.* **2022**, *122* (23), 16911–16982. https://doi.org/10.1021/acs.chemrev.1c01067.
(54) Vekilov, P. G. Nucleation. *Cryst. Growth Des.* **2010**, *10* (12), 5007–5019. https://doi.org/10.1021/cg1011633.
(55) De Yoreo, J. A Perspective on Multistep Pathways of Nucleation. In *ACS Symposium Series*; Zhang, X., Ed.; American Chemical Society: Washington, DC, 2020; Vol. 1358, pp 1–17. https://doi.org/10.1021/bk-2020-1358.ch001.
(56) Karthika, S.; Radhakrishnan, T. K.; Kalaichelvi, P. A Review of Classical and Nonclassical Nucleation Theories. *Cryst. Growth Des.* **2016**, *16* (11), 6663–6681. https://doi.org/10.1021/acs.cgd.6b00794.
(57) Vekilov, P. G. Nonclassical Nucleation. In *ACS Symposium Series*; Zhang, X., Ed.; American Chemical Society: Washington, DC, 2020; Vol. 1358, pp 19–46. https://doi.org/10.1021/bk-2020-1358.ch002.
(58) Voorhees, P. W. The Theory of Ostwald Ripening. *J. Stat. Phys.* **1985**, *38* (1–2), 231–252. https://doi.org/10.1007/BF01017860.
(59) De Yoreo, J. J.; Gilbert, P. U. P. A.; Sommerdijk, N. A. J. M.; Penn, R. L.; Whitelam, S.; Joester, D.; Zhang, H.; Rimer, J. D.; Navrotsky, A.; Banfield, J. F.; Wallace, A. F.; Michel, F. M.; Meldrum, F. C.; Cölfen, H.; Dove, P. M. Crystallization by Particle Attachment in Synthetic, Biogenic, and Geologic Environments. *Science* **2015**, *349* (6247), aaa6760. https://doi.org/10.1126/science.aaa6760.
(60) Gebauer, D.; Völkel, A.; Cölfen, H. Stable Prenucleation Calcium Carbonate Clusters. *Science* **2008**, *322* (5909), 1819–1822. https://doi.org/10.1126/science.1164271.
(61) Smeets, P. J. M.; Finney, A. R.; Habraken, W. J. E. M.; Nudelman, F.; Friedrich, H.; Laven, J.; De Yoreo, J. J.; Rodger, P. M.; Sommerdijk, N. A. J. M. A Classical View on Nonclassical Nucleation. *Proc. Natl. Acad. Sci.* **2017**, *114* (38). https://doi.org/10.1073/pnas.1700342114.
(62) Bray, A. J. Theory of Phase-Ordering Kinetics. *Adv. Phys.* **2002**, *51* (2), 481–587. https://doi.org/10.1080/00018730110117433.
(63) Scheifele, B.; Saika-Voivod, I.; Bowles, R. K.; Poole, P. H. Heterogeneous Nucleation in the Low-Barrier Regime. *Phys. Rev. E* **2013**, *87* (4), 042407. https://doi.org/10.1103/PhysRevE.87.042407.
(64) Vekilov, P. G. Dense Liquid Precursor for the Nucleation of Ordered Solid Phases from Solution. *Cryst. Growth Des.* **2004**, *4* (4), 671–685. https://doi.org/10.1021/cg049977w.
(65) Loh, N. D.; Sen, S.; Bosman, M.; Tan, S. F.; Zhong, J.; Nijhuis, C. A.; Král, P.; Matsudaira, P.; Mirsaidov, U. Multistep Nucleation of Nanocrystals in Aqueous Solution. *Nat. Chem.* **2017**, *9* (1), 77–82. https://doi.org/10.1038/nchem.2618.
(66) Sung, C. Y.; Estrin, J.; Youngquist, G. R. Secondary Nucleation of Magnesium Sulfate by Fluid Shear. *AIChE J.* **1973**, *19* (5), 957–962. https://doi.org/10.1002/aic.690190511.

(67) Agrawal, S. G.; Paterson, A. H. J. Secondary Nucleation: Mechanisms and Models. *Chem. Eng. Commun.* **2015**, *202* (5), 698–706. https://doi.org/10.1080/00986445.2014.969369.
(68) Xu, S.; Hou, Z.; Chuai, X.; Wang, Y. Overview of Secondary Nucleation: From Fundamentals to Application. *Ind. Eng. Chem. Res.* **2020**, *59* (41), 18335–18356. https://doi.org/10.1021/acs.iecr.0c03304.
(69) Garside, J.; Davey, R. J. Secondary Contact Nucleation: Kinetics, Growth, and Scale-Up. *Chem. Eng. Commun.* **1980**, *4* (4–5), 393–424. https://doi.org/10.1080/00986448008935918.
(70) Steendam, R. R. E.; Frawley, P. J. Secondary Nucleation of Sodium Chlorate: The Role of Initial Breeding. *Cryst. Growth Des.* **2019**, *19* (6), 3453–3460. https://doi.org/10.1021/acs.cgd.9b00317.
(71) Noorduin, W. L.; van Enckevort, W. J. P.; Meekes, H.; Kaptein, B.; Kellogg, R. M.; Tully, J. C.; McBride, J. M.; Vlieg, E. The Driving Mechanism Behind Attrition-Enhanced Deracemization. *Angew. Chem. Int. Ed.* **2010**, *49* (45), 8435–8438. https://doi.org/10.1002/anie.201002036.
(72) Köllges, T.; Vetter, T. Model-Based Analysis of Continuous Crystallization/Reaction Processes Separating Conglomerate Forming Enantiomers. *Cryst. Growth Des.* **2017**, *17* (1), 233–247. https://doi.org/10.1021/acs.cgd.6b01487.
(73) Weeks, J. D.; Gilmer, G. H. Dynamics of Crystal Growth. In *Advances in Chemical Physics*; Prigogine, I., Rice, S. A., Eds.; Wiley, 1979; Vol. 40, pp 157–228. https://doi.org/10.1002/9780470142592.ch4.
(74) Kossel, W. Zur Theorie Des Kristallwachstums. *Nachrichten Von Ges. Wiss. Zu Gött. Math.-Phys. Kl.* **1927**, *1927*, 135–143.
(75) Stranski, I. N. Zur Theorie Des Kristallwachstums. *Z. Für Phys. Chem.* **1928**, *136U* (1), 259–278. https://doi.org/10.1515/zpch-1928-13620.
(76) Frenkel, J. On the Surface Motion of Particles in Crystals and the Natural Roughness of Crystalline Faces. *J Phys USSR* **1945**, *9*, 392.
(77) Tilbury, C. J.; Green, D. A.; Marshall, W. J.; Doherty, M. F. Predicting the Effect of Solvent on the Crystal Habit of Small Organic Molecules. *Cryst. Growth Des.* **2016**, *16* (5), 2590–2604. https://doi.org/10.1021/acs.cgd.5b01660.
(78) Burton, W. K.; Cabrera, N.; Frank, F. C. The Growth of Crystals and the Equilibrium Structure of Their Surfaces. *Philos. Trans. R. Soc. Lond. Ser. Math. Phys. Sci.* **1951**, *243* (866), 299–358. https://doi.org/10.1098/rsta.1951.0006.
(79) Ehrlich, G.; Hudda, F. G. Atomic View of Surface Self-Diffusion: Tungsten on Tungsten. *J. Chem. Phys.* **1966**, *44* (3), 1039–1049. https://doi.org/10.1063/1.1726787.
(80) Schwoebel, R. L.; Shipsey, E. J. Step Motion on Crystal Surfaces. *J. Appl. Phys.* **1966**, *37* (10), 3682–3686. https://doi.org/10.1063/1.1707904.
(81) Sato, M.; Uwaha, M. Growth Law of Step Bunches Induced by the Ehrlich–Schwoebel Effect in Growth. *Surf. Sci.* **2001**, *493* (1–3), 494–498. https://doi.org/10.1016/S0039-6028(01)01258-4.
(82) Politi, P.; Villain, J. Ehrlich-Schwoebel Instability in Molecular-Beam Epitaxy: A Minimal Model. *Phys. Rev. B* **1996**, *54* (7), 5114–5129. https://doi.org/10.1103/PhysRevB.54.5114.
(83) Saúl, A.; Métois, J.-J.; Ranguis, A. Experimental Evidence for an Ehrlich-Schwoebel Effect on Si(111). *Phys. Rev. B* **2002**, *65* (7), 075409. https://doi.org/10.1103/PhysRevB.65.075409.
(84) Xiang, S. K.; Huang, H. *Ab Initio* Determination of Ehrlich–Schwoebel Barriers on Cu{111}. *Appl. Phys. Lett.* **2008**, *92* (10), 101923. https://doi.org/10.1063/1.2891106.
(85) Venables, J. A.; Spiller, G. D. T.; Hanbucken, M. Nucleation and Growth of Thin Films. *Rep. Prog. Phys.* **1984**, *47* (4), 399–459. https://doi.org/10.1088/0034-4885/47/4/002.
(86) Verschuren, C. A.; Leys, M. R.; Marschner, T.; Vonk, H.; Wolter, J. H. A Modified BCF Model to Quantitatively Describe the (100)InP Growth Rate in Chemical Beam Epitaxy. *J. Cryst. Growth* **1998**, *188* (1–4), 11–16. https://doi.org/10.1016/S0022-0248(98)00045-1.

(87) Muller, P. Elastic Effects on Surface Physics. *Surf. Sci. Rep.* **2004**, *54* (5–8), 157–258. https://doi.org/10.1016/j.surfrep.2004.05.001.
(88) Andersen, T. K.; Cook, S.; Wan, G.; Hong, H.; Marks, L. D.; Fong, D. D. Layer-by-Layer Epitaxial Growth of Defect-Engineered Strontium Cobaltites. *ACS Appl. Mater. Interfaces* **2018**, *10* (6), 5949–5958. https://doi.org/10.1021/acsami.7b16970.
(89) Redkov, A. V.; Kukushkin, S. A. Development of Burton–Cabrera–Frank Theory for the Growth of a Non-Kossel Crystal via Chemical Reaction. *Cryst. Growth Des.* **2020**, *20* (4), 2590–2601. https://doi.org/10.1021/acs.cgd.9b01721.
(90) Bellet-Amalric, E.; André, R.; Bougerol, C.; Den Hertog, M.; Jaffal, A.; Cibert, J. Controlling the Shape of a Tapered Nanowire: Lessons from the Burton-Cabrera-Frank Model. *Nanotechnology* **2020**, *31* (27), 274004. https://doi.org/10.1088/1361-6528/ab849e.
(91) Ju, G.; Xu, D.; Thompson, C.; Highland, M. J.; Eastman, J. A.; Walkosz, W.; Zapol, P.; Stephenson, G. B. Burton-Cabrera-Frank Theory for Surfaces with Alternating Step Types. *Phys. Rev. B* **2022**, *105* (5), 054312. https://doi.org/10.1103/PhysRevB.105.054312.
(92) Redkov, A. Impact of Schwoebel Barriers on the Step-Flow Growth of a Multicomponent Crystal. *Crystals* **2023**, *14* (1), 25. https://doi.org/10.3390/cryst14010025.
(93) Rost, M. J.; Jacobse, L.; Koper, M. T. M. Non-Random Island Nucleation in the Electrochemical Roughening on Pt(111). *Angew. Chem. Int. Ed.* **2023**, *62* (27), e202216376. https://doi.org/10.1002/anie.202216376.
(94) Ju, G.; Xu, D.; Thompson, C.; Highland, M. J.; Eastman, J. A.; Walkosz, W.; Zapol, P.; Shen, B.; Stephenson, G. B. Burton-Cabrera-Frank Theory for the Influence of off-Cut Direction on the Growth of Hcp Crystals. *Phys. Rev. B* **2024**, *110* (19), 195303. https://doi.org/10.1103/PhysRevB.110.195303.
(95) Uwaha, M. Introduction to the BCF Theory. *Prog. Cryst. Growth Charact. Mater.* **2016**, *62* (2), 58–68. https://doi.org/10.1016/j.pcrysgrow.2016.04.002.
(96) Frank, F. C. The Influence of Dislocations on Crystal Growth. *Discuss. Faraday Soc.* **1949**, *5*, 48. https://doi.org/10.1039/df9490500048.
(97) Miura, H.; Kobayashi, R. Phase-Field Modeling of Step Dynamics on Growing Crystal Surface: Direct Integration of Growth Units to Step Front. *Cryst. Growth Des.* **2015**, *15* (5), 2165–2175. https://doi.org/10.1021/cg501806d.
(98) Veesler, S.; Boistelle, R. Growth Kinetics of Hydrargillite Al(OH)3 from Caustic Soda Solutions. *J. Cryst. Growth* **1994**, *142* (1–2), 177–183. https://doi.org/10.1016/0022-0248(94)90286-0.
(99) Mahajan, A. J.; Kirwan, D. J. Nucleation and Growth Kinetics of Biochemicals Measured at High Supersaturations. *J. Cryst. Growth* **1994**, *144* (3–4), 281–290. https://doi.org/10.1016/0022-0248(94)90468-5.
(100) Lee, M.; Parkinson, G. M. Growth Rates of Gibbsite Single Crystals Determined Using in Situ Optical Microscopy. *J. Cryst. Growth* **1999**, *198–199*, 270–274. https://doi.org/10.1016/S0022-0248(98)01187-7.
(101) Frank, F. C. Nucleation-Controlled Growth on a One-Dimensional Growth of Finite Length. *J. Cryst. Growth* **1974**, *22* (3), 233–236. https://doi.org/10.1016/0022-0248(74)90100-6.
(102) Higgins, S. R.; Jordan, G.; Eggleston, C. M.; Knauss, K. G. Dissolution Kinetics of the Barium Sulfate (001) Surface by Hydrothermal Atomic Force Microscopy. *Langmuir* **1998**, *14* (18), 4967–4971. https://doi.org/10.1021/la9806606.
(103) Nielsen, A. E. Electrolyte Crystal Growth Mechanisms. *J. Cryst. Growth* **1984**, *67* (2), 289–310. https://doi.org/10.1016/0022-0248(84)90189-1.
(104) Sweegers, C.; Meekes, H.; Van Enckevort, W. J. P.; Hiralal, I. D. K.; Rijkeboer, A. Growth Rate Analysis of Gibbsite Single Crystals Growing from Aqueous Sodium Aluminate Solutions. *Cryst. Growth Des.* **2004**, *4* (1), 185–198. https://doi.org/10.1021/cg030004q.

(105) Tilbury, C. J.; Doherty, M. F. Modeling Layered Crystal Growth at Increasing Supersaturation by Connecting Growth Regimes. *AIChE J.* **2017**, *63* (4), 1338–1352. https://doi.org/10.1002/aic.15617.
(106) Deck, L.-T.; Mazzotti, M. Conceptual Validation of Stochastic and Deterministic Methods To Estimate Crystal Nucleation Rates. *Cryst. Growth Des.* **2023**, *23* (2), 899–914. https://doi.org/10.1021/acs.cgd.2c01133.
(107) Winn, D.; Doherty, M. F. A New Technique for Predicting the Shape of Solution-grown Organic Crystals. *AIChE J.* **1998**, *44* (11), 2501–2514. https://doi.org/10.1002/aic.690441117.
(108) Snyder, R. C.; Doherty, M. F. Predicting Crystal Growth by Spiral Motion. *Proc. R. Soc. Math. Phys. Eng. Sci.* **2009**, *465* (2104), 1145–1171. https://doi.org/10.1098/rspa.2008.0234.
(109) Lovette, M. A.; Browning, A. R.; Griffin, D. W.; Sizemore, J. P.; Snyder, R. C.; Doherty, M. F. Crystal Shape Engineering. *Ind. Eng. Chem. Res.* **2008**, *47* (24), 9812–9833. https://doi.org/10.1021/ie800900f.
(110) Grimbergen, R. F. P.; Reedijk, M. F.; Meekes, H.; Bennema, P. Growth Behavior of Crystal Faces Containing Symmetry-Related Connected Nets: A Case Study of Naphthalene and Anthracene. *J. Phys. Chem. B* **1998**, *102* (15), 2646–2653. https://doi.org/10.1021/jp980040d.
(111) Wells, A. F. XXI. Crystal Habit and Internal Structure. *Lond. Edinb. Dublin Philos. Mag. J. Sci.* **1946**, *37* (266), 184–199. https://doi.org/10.1080/14786444608561072.
(112) Zumstein, R. C.; Rousseau, R. W. Growth Rate Dispersion in Batch Crystallization with Transient Conditions. *AIChE J.* **1987**, *33* (11), 1921–1925. https://doi.org/10.1002/aic.690331123.
(113) Pantaraks, P.; Flood, A. E. Effect of Growth Rate History on Current Crystal Growth: A Second Look at Surface Effects on Crystal Growth Rates. *Cryst. Growth Des.* **2005**, *5* (1), 365–371. https://doi.org/10.1021/cg049863k.
(114) Ulrich, J. Growth Rate Dispersion — a Review. *Cryst. Res. Technol.* **1989**, *24* (3), 249–257. https://doi.org/10.1002/crat.2170240302.
(115) Srisanga, S.; Flood, A. E.; Galbraith, S. C.; Rugmai, S.; Soontaranon, S.; Ulrich, J. Crystal Growth Rate Dispersion versus Size-Dependent Crystal Growth: Appropriate Modeling for Crystallization Processes. *Cryst. Growth Des.* **2015**, *15* (5), 2330–2336. https://doi.org/10.1021/acs.cgd.5b00126.
(116) Li, M.; Zhang, C.; Li, M.; Liu, F.; Zhou, L.; Gao, Z.; Sun, J.; Han, D.; Gong, J. Growth Defects of Organic Crystals: A Review. *Chem. Eng. J.* **2022**, *429*, 132450. https://doi.org/10.1016/j.cej.2021.132450.
(117) Chen, N.; Wang, Y.; He, H.; Lin, L. Effects of Point Defects on Lattice Parameters of Semiconductors. *Phys. Rev. B* **1996**, *54* (12), 8516–8521. https://doi.org/10.1103/PhysRevB.54.8516.
(118) Dolabella, S.; Borzì, A.; Dommann, A.; Neels, A. Lattice Strain and Defects Analysis in Nanostructured Semiconductor Materials and Devices by High-Resolution X-Ray Diffraction: Theoretical and Practical Aspects. *Small Methods* **2022**, *6* (2), 2100932. https://doi.org/10.1002/smtd.202100932.
(119) Oral, Ç. M.; Ercan, B. Influence of pH on Morphology, Size and Polymorph of Room Temperature Synthesized Calcium Carbonate Particles. *Powder Technol.* **2018**, *339*, 781–788. https://doi.org/10.1016/j.powtec.2018.08.066.
(120) Beck, R.; Andreassen, J.-P. The Onset of Spherulitic Growth in Crystallization of Calcium Carbonate. *J. Cryst. Growth* **2010**, *312* (15), 2226–2238. https://doi.org/10.1016/j.jcrysgro.2010.04.037.
(121) Hadjittofis, E.; Vargas, S. M.; Litster, J. D.; Campbell, K. L. S. Exploring the Role of Crystal Habit in the Ostwald Rule of Stages. *Proc. R. Soc. Math. Phys. Eng. Sci.* **2022**, *478* (2258), 20210601. https://doi.org/10.1098/rspa.2021.0601.
(122) Ogino, T.; Suzuki, T.; Sawada, K. The Formation and Transformation Mechanism of Calcium Carbonate in Water. *Geochim. Cosmochim. Acta* **1987**, *51* (10), 2757–2767. https://doi.org/10.1016/0016-7037(87)90155-4.
(123) Ostwald, W. Studien Über Die Bildung Und Umwandlung Fester Körper: 1. Abhandlung: Übersättigung Und Überkaltung. *Z. Für Phys. Chem.* **1897**, *22U* (1), 289–330. https://doi.org/10.1515/zpch-1897-2233.

(124) Van Santen, R. A. The Ostwald Step Rule. *J. Phys. Chem.* **1984**, *88* (24), 5768–5769. https://doi.org/10.1021/j150668a002.
(125) Cardew, P. T. Ostwald Rule of Stages—Myth or Reality? *Cryst. Growth Des.* **2023**, *23* (6), 3958–3969. https://doi.org/10.1021/acs.cgd.2c00141.
(126) Threlfall, T. Structural and Thermodynamic Explanations of Ostwald's Rule. *Org. Process Res. Dev.* **2003**, *7* (6), 1017–1027. https://doi.org/10.1021/op030026l.
(127) De Yoreo, J. J. Casting a Bright Light on Ostwald's Rule of Stages. *Proc. Natl. Acad. Sci.* **2022**, *119* (7), e2121661119. https://doi.org/10.1073/pnas.2121661119.
(128) Chung, S.-Y.; Kim, Y.-M.; Kim, J.-G.; Kim, Y.-J. Multiphase Transformation and Ostwald's Rule of Stages during Crystallization of a Metal Phosphate. *Nat. Phys.* **2009**, *5* (1), 68–73. https://doi.org/10.1038/nphys1148.
(129) Niozu, A.; Kumagai, Y.; Hiraki, T. N.; Fukuzawa, H.; Motomura, K.; Bucher, M.; Asa, K.; Sato, Y.; Ito, Y.; You, D.; Ono, T.; Li, Y.; Kukk, E.; Miron, C.; Neagu, L.; Callegari, C.; Di Fraia, M.; Rossi, G.; Galli, D. E.; Pincelli, T.; Colombo, A.; Owada, S.; Tono, K.; Kameshima, T.; Joti, Y.; Katayama, T.; Togashi, T.; Yabashi, M.; Matsuda, K.; Bostedt, C.; Ueda, K.; Nagaya, K. Crystallization Kinetics of Atomic Crystals Revealed by a Single-Shot and Single-Particle X-Ray Diffraction Experiment. *Proc. Natl. Acad. Sci.* **2021**, *118* (51), e2111747118. https://doi.org/10.1073/pnas.2111747118.
(130) Washington, A. L.; Foley, M. E.; Cheong, S.; Quffa, L.; Breshike, C. J.; Watt, J.; Tilley, R. D.; Strouse, G. F. Ostwald's Rule of Stages and Its Role in CdSe Quantum Dot Crystallization. *J. Am. Chem. Soc.* **2012**, *134* (41), 17046–17052. https://doi.org/10.1021/ja302964e.
(131) Levin, A.; Mason, T. O.; Adler-Abramovich, L.; Buell, A. K.; Meisl, G.; Galvagnion, C.; Bram, Y.; Stratford, S. A.; Dobson, C. M.; Knowles, T. P. J.; Gazit, E. Ostwald's Rule of Stages Governs Structural Transitions and Morphology of Dipeptide Supramolecular Polymers. *Nat. Commun.* **2014**, *5* (1), 5219. https://doi.org/10.1038/ncomms6219.
(132) Llinàs, A.; Goodman, J. M. Polymorph Control: Past, Present and Future. *Drug Discov. Today* **2008**, *13* (5–6), 198–210. https://doi.org/10.1016/j.drudis.2007.11.006.
(133) Bernstein, J. Polymorphism – A Perspective. *Cryst. Growth Des.* **2011**, *11* (3), 632–650. https://doi.org/10.1021/cg1013335.
(134) Lee, E. H. A Practical Guide to Pharmaceutical Polymorph Screening & Selection. *Asian J. Pharm. Sci.* **2014**, *9* (4), 163–175. https://doi.org/10.1016/j.ajps.2014.05.002.
(135) Black, J. F. B.; Cardew, P. T.; Cruz-Cabeza, A. J.; Davey, R. J.; Gilks, S. E.; Sullivan, R. A. Crystal Nucleation and Growth in a Polymorphic System: Ostwald's Rule, *p* -Aminobenzoic Acid and Nucleation Transition States. *CrystEngComm* **2018**, *20* (6), 768–776. https://doi.org/10.1039/C7CE01960B.
(136) Germann, L. S.; Arhangelskis, M.; Etter, M.; Dinnebier, R. E.; Friščić, T. Challenging the Ostwald Rule of Stages in Mechanochemical Cocrystallisation. *Chem. Sci.* **2020**, *11* (37), 10092–10100. https://doi.org/10.1039/D0SC03629C.
(137) Van Mil, J.; Gati, E.; Addadi, L.; Lahav, M. Useful Impurities for Optical Resolutions. 1. Crystallization of Photopolymerizing Dienes in the Presence of Their Chiral Topochemical Products. *J. Am. Chem. Soc.* **1981**, *103* (5), 1248–1249. https://doi.org/10.1021/ja00395a058.
(138) Addadi, L.; Weinstein, S.; Gati, E.; Weissbuch, I.; Lahav, M. Resolution of Conglomerates with the Assistance of Tailor-Made Impurities. Generality and Mechanistic Aspects of the "Rule of Reversal". A New Method for Assignment of Absolute Configuration. *J. Am. Chem. Soc.* **1982**, *104* (17), 4610–4617. https://doi.org/10.1021/ja00381a018.
(139) Addadi, L.; Berkovitch-Yellin, Z.; Weissbuch, I.; Van Mil, J.; Shimon, L. J. W.; Lahav, M.; Leiserowitz, L. Growth and Dissolution of Organic Crystals with "Tailor-Made" Inhibitors—Implications in

Stereochemistry and Materials Science. *Angew. Chem. Int. Ed. Engl.* **1985**, *24* (6), 466–485. https://doi.org/10.1002/anie.198504661.

(140) Addadi, L.; Weiner, S. Control and Design Principles in Biological Mineralization. *Angew. Chem. Int. Ed. Engl.* **1992**, *31* (2), 153–169. https://doi.org/10.1002/anie.199201531.

(141) Davey, R. J.; Blagden, N.; Potts, G. D.; Docherty, R. Polymorphism in Molecular Crystals: Stabilization of a Metastable Form by Conformational Mimicry. *J. Am. Chem. Soc.* **1997**, *119* (7), 1767–1772. https://doi.org/10.1021/ja9626345.

(142) Lee, E. H.; Byrn, S. R.; Carvajal, M. T. Additive-Induced Metastable Single Crystal of Mefenamic Acid. *Pharm. Res.* **2006**, *23* (10), 2375–2380. https://doi.org/10.1007/s11095-006-9045-y.

(143) Almarsson, Ö.; Hickey, M. B.; Peterson, M. L.; Morissette, S. L.; Soukasene, S.; McNulty, C.; Tawa, M.; MacPhee, J. M.; Remenar, J. F. High-Throughput Surveys of Crystal Form Diversity of Highly Polymorphic Pharmaceutical Compounds. *Cryst. Growth Des.* **2003**, *3* (6), 927–933. https://doi.org/10.1021/cg034058b.

(144) Morissette, S. L.; Soukasene, S.; Levinson, D.; Cima, M. J.; Almarsson, Ö. Elucidation of Crystal Form Diversity of the HIV Protease Inhibitor Ritonavir by High-Throughput Crystallization. *Proc. Natl. Acad. Sci.* **2003**, *100* (5), 2180–2184. https://doi.org/10.1073/pnas.0437744100.

(145) Florence, A. J.; Johnston, A.; Price, S. L.; Nowell, H.; Kennedy, A. R.; Shankland, N. An Automated Parallel Crystallisation Search for Predicted Crystal Structures and Packing Motifs of Carbamazepine. *J. Pharm. Sci.* **2006**, *95* (9), 1918–1930. https://doi.org/10.1002/jps.20647.

(146) Hiremath, R.; Basile, J. A.; Varney, S. W.; Swift, J. A. Controlling Molecular Crystal Polymorphism with Self-Assembled Monolayer Templates. *J. Am. Chem. Soc.* **2005**, *127* (51), 18321–18327. https://doi.org/10.1021/ja0565119.

(147) Case, D. H.; Srirambhatla, V. K.; Guo, R.; Watson, R. E.; Price, L. S.; Polyzois, H.; Cockcroft, J. K.; Florence, A. J.; Tocher, D. A.; Price, S. L. Successful Computationally Directed Templating of Metastable Pharmaceutical Polymorphs. *Cryst. Growth Des.* **2018**, *18* (9), 5322–5331. https://doi.org/10.1021/acs.cgd.8b00765.

(148) Penha, F. M.; Gopalan, A.; Meijlink, J. C.; Ibis, F.; Eral, H. B. Selective Crystallization of D -Mannitol Polymorphs Using Surfactant Self-Assembly. *Cryst. Growth Des.* **2021**, *21* (7), 3928–3935. https://doi.org/10.1021/acs.cgd.1c00243.

(149) Beckmann, W.; Nickisch, K.; Budde, U. Development of a Seeding Technique for the Crystallization of the Metastable A Modification of Abecarnil. *Org. Process Res. Dev.* **1998**, *2* (5), 298–304. https://doi.org/10.1021/op980029b.

(150) Friščić, T.; MacGillivray, L. R. Engineering Cocrystal and Polymorph Architecture via Pseudoseeding. *Chem. Commun.* **2009**, No. 7, 773. https://doi.org/10.1039/b820120j.

(151) Kitamura, M. Strategy for Control of Crystallization of Polymorphs. *CrystEngComm* **2009**, *11* (6), 949. https://doi.org/10.1039/b809332f.

(152) Belenguer, A. M.; Lampronti, G. I.; Michalchuk, A. A. L.; Emmerling, F.; Sanders, J. K. M. Quantitative Reversible One Pot Interconversion of Three Crystalline Polymorphs by Ball Mill Grinding. *CrystEngComm* **2022**, *24* (23), 4256–4261. https://doi.org/10.1039/D2CE00393G.

(153) Cruz-Cabeza, A. J.; Reutzel-Edens, S. M.; Bernstein, J. Facts and Fictions about Polymorphism. *Chem. Soc. Rev.* **2015**, *44* (23), 8619–8635. https://doi.org/10.1039/C5CS00227C.

(154) Mangin, D.; Puel, F.; Veesler, S. Polymorphism in Processes of Crystallization in Solution: A Practical Review. *Org. Process Res. Dev.* **2009**, *13* (6), 1241–1253. https://doi.org/10.1021/op900168f.

(155) Sacchi, P.; Neoptolemou, P.; Davey, R. J.; Reutzel-Edens, S. M.; Cruz-Cabeza, A. J. Do Metastable Polymorphs Always Grow Faster? Measuring and Comparing Growth Kinetics of Three Polymorphs of Tolfenamic Acid. *Chem. Sci.* **2023**, *14* (42), 11775–11789. https://doi.org/10.1039/D3SC02040A.

(156) Chemburkar, S. R.; Bauer, J.; Deming, K.; Spiwek, H.; Patel, K.; Morris, J.; Henry, R.; Spanton, S.; Dziki, W.; Porter, W.; Quick, J.; Bauer, P.; Donaubauer, J.; Narayanan, B. A.; Soldani, M.; Riley, D.; McFarland, K. Dealing with the Impact of Ritonavir Polymorphs on the Late Stages of Bulk Drug Process Development. *Org. Process Res. Dev.* **2000**, *4* (5), 413–417. https://doi.org/10.1021/op000023y.

(157) Bauer, J.; Spanton, S.; Henry, R.; Quick, J.; Dziki, W.; Porter, W.; Morris, J. Ritonavir: An Extraordinary Example of Conformational Polymorphism. *Pharm. Res.* **2001**, *18* (6), 859–866. https://doi.org/10.1023/A:1011052932607.

(158) Fox, D.; Labes, M. M.; Weissberger, A. *Physics and Chemistry of the Organic Solid State*; Interscience: New York, NY, 1965; Vol. 2.

(159) Dunitz, J. D.; Bernstein, J. Disappearing Polymorphs. *Acc. Chem. Res.* **1995**, *28* (4), 193–200. https://doi.org/10.1021/ar00052a005.

(160) Kahr, B.; Tan, M.; Ye, H.-M.; Shtukenberg, A. G. Polymorphism and Morphology Folklore. *Cryst. Growth Des.* **2019**, *19* (11), 5999–6003. https://doi.org/10.1021/acs.cgd.9b00910.

(161) Price, S. L. Predicting Crystal Structures of Organic Compounds. *Chem Soc Rev* **2014**, *43* (7), 2098–2111. https://doi.org/10.1039/C3CS60279F.

(162) Beran, G. J. O.; Sugden, I. J.; Greenwell, C.; Bowskill, D. H.; Pantelides, C. C.; Adjiman, C. S. How Many More Polymorphs of ROY Remain Undiscovered. *Chem. Sci.* **2022**, *13* (5), 1288–1297. https://doi.org/10.1039/D1SC06074K.

(163) Weatherston, J.; Probert, M. R.; Hall, M. J. Polymorphic ROYalty: The 14th ROY Polymorph Discovered via High-Throughput Crystallization. *J. Am. Chem. Soc.* **2025**, *147* (14), 11949–11954. https://doi.org/10.1021/jacs.4c17826.

(164) Price, S. L. Why Don't We Find More Polymorphs? *Acta Crystallogr. Sect. B Struct. Sci. Cryst. Eng. Mater.* **2013**, *69* (4), 313–328. https://doi.org/10.1107/S2052519213018861.

(165) Derdour, L.; Skliar, D. A Review of the Effect of Multiple Conformers on Crystallization from Solution and Strategies for Crystallizing Slow Inter-Converting Conformers. *Chem. Eng. Sci.* **2014**, *106*, 275–292. https://doi.org/10.1016/j.ces.2013.11.025.

(166) Tang, W.; Yang, T.; Morales-Rivera, C. A.; Geng, X.; Srirambhatla, V. K.; Kang, X.; Chauhan, V. P.; Hong, S.; Tu, Q.; Florence, A. J.; Mo, H.; Calderon, H. A.; Kisielowski, C.; Hernandez, F. C. R.; Zou, X.; Mpourmpakis, G.; Rimer, J. D. Tautomerism Unveils a Self-Inhibition Mechanism of Crystallization. *Nat. Commun.* **2023**, *14* (1), 561. https://doi.org/10.1038/s41467-023-35924-3.

(167) Stoica, C.; Tinnemans, P.; Meekes, H.; Van Enckevort, W. J. P.; Vlieg, E. Rough Growth Behavior of a Polar Steroid Crystal: A Case of Polymorphic Self-Poisoning? *Cryst. Growth Des.* **2006**, *6* (6), 1311–1317. https://doi.org/10.1021/cg0505416.

(168) Robin, A.; Iavicoli, P.; Wurst, K.; Dyer, M. S.; Haq, S.; Amabilino, D. B.; Raval, R. A Racemic Conglomerate Nipped in the Bud: A Molecular View of Enantiomer Cross-Inhibition of Conglomerate Nucleation at a Surface. *Cryst. Growth Des.* **2010**, *10* (10), 4516–4525. https://doi.org/10.1021/cg100806w.

(169) Liu, Y.; Black, J. F. B.; Boon, K. F.; Cruz-Cabeza, A. J.; Davey, R. J.; Dowling, R. J.; George, N.; Hutchinson, A.; Montis, R. When Crystals Do Not Grow: The Growth Dead Zone. *Cryst. Growth Des.* **2019**, *19* (8), 4579–4587. https://doi.org/10.1021/acs.cgd.9b00478.

(170) Gerard, C. J. J.; Pinetre, C.; Cercel, H.; Charpentier, M. D.; Sanselme, M.; Couvrat, N.; Brandel, C.; Cartigny, Y.; Dupray, V.; Ter Horst, J. H. Phase Diagrams of Praziquantel and Vanillic Acid Cocrystals: Racemic Compound and Conglomerate System. *Cryst. Growth Des.* **2024**, *24* (8), 3378–3387. https://doi.org/10.1021/acs.cgd.4c00114.

(171) Liu, Y.; Marinova, V.; Davey, R. J.; Gabriele, B.; Salvalaglio, M.; Cruz-Cabeza, A. J. Conformational Self-Poisoning in Crystal Growth. *JACS Au* **2025**, *5* (4), 1781–1790. https://doi.org/10.1021/jacsau.5c00043.

(172) Weissbuch, I.; Leiserowitz, L.; Lahav, M. Self-Poisoning at {011} Faces of α-Resorcinol Crystals May Explain Its Unidirectional Growth in the Vapor Phase: A Molecular Modeling Study. *Cryst. Growth Des.* **2006**, *6* (3), 625–628. https://doi.org/10.1021/cg050424a.

(173) Lasaga, A. C.; Lüttge, A. Mineralogical Approaches to Fundamental Crystal Dissolution Kinetics. *Am. Mineral.* **2004**, *89* (4), 527–540. https://doi.org/10.2138/am-2004-0407.

(174) De Yoreo, J. J. Principles of Crystal Nucleation and Growth. *Rev. Mineral. Geochem.* **2003**, *54* (1), 57–93. https://doi.org/10.2113/0540057.

(175) Sangwal, K. Effects of Impurities on Crystal Growth Processes. *Prog. Cryst. Growth Charact. Mater.* **1996**, *32* (1–3), 3–43. https://doi.org/10.1016/0960-8974(96)00008-3.

(176) Van Der Hoek, B.; Van Enckevort, W. J. P.; Van Der Linden, W. H. Dissolution Kinetics and Etch Pit Studies of Potassium Aluminium Sulphate. *J. Cryst. Growth* **1983**, *61* (2), 181–193. https://doi.org/10.1016/0022-0248(83)90353-6.

(177) Sangwal, K.; Zaniewska, G. Influence of Impurities on the Etching of NaCl Crystals. *J. Mater. Sci.* **1984**, *19* (4), 1131–1144. https://doi.org/10.1007/BF01120022.

(178) Kurumathoor, R.; Franz, G. Etch Pits on Beryl as Indicators of Dissolution Behaviour. *Eur. J. Mineral.* **2018**, *30* (1), 107–124. https://doi.org/10.1127/ejm/2018/0030-2703.

(179) Chen, S.; Carroll, D. L. Silver Nanoplates: Size Control in Two Dimensions and Formation Mechanisms. *J. Phys. Chem. B* **2004**, *108* (18), 5500–5506. https://doi.org/10.1021/jp031077n.

(180) Yasnikov, I. S.; Denisova, D. A. Specific Features of the Evolution of Electrolytic Copper Microcrystals with Inhibition of the Growth of Low-Energy Facets. *Phys. Solid State* **2013**, *55* (3), 642–647. https://doi.org/10.1134/S1063783413030335.

(181) Mader, A. V.; Helmbrecht, L.; Noorduin, W. L. Multi-Layered Barium and Strontium Carbonate Structures Induced by the Small Organic Dye Acid Orange 7. *Cryst. Growth Des.* **2021**, *21* (11), 6349–6356. https://doi.org/10.1021/acs.cgd.1c00823.

(182) Su, Y.; Li, S.; Li, X.; Zhou, J.; Chauhan, V. P.; Li, M.; Su, Y.; Liu, C.; Ren, Y.; Yin, W.; Rimer, J. D.; Cai, T. Tartronic Acid as a Potential Inhibitor of Pathological Calcium Oxalate Crystallization. *Adv. Sci.* **2024**, *11* (21), 2400642. https://doi.org/10.1002/advs.202400642.

(183) Weissbuch, I.; Addadi, L.; Lahav, M.; Leiserowitz, L. Molecular Recognition at Crystal Interfaces. *Science* **1991**, *253* (5020), 637–645. https://doi.org/10.1126/science.253.5020.637.

(184) Weissbuch, I.; Lahav, M.; Leiserowitz, L. Toward Stereochemical Control, Monitoring, and Understanding of Crystal Nucleation. *Cryst. Growth Des.* **2003**, *3* (2), 125–150. https://doi.org/10.1021/cg0200560.

(185) Mughal, R. K.; Davey, R. J.; Blagden, N. Application of Crystallization Inhibitors to Chiral Separations. 1. Design of Additives to Discriminate between the Racemic Compound and the Pure Enantiomer of Mandelic Acid. *Cryst. Growth Des.* **2007**, *7* (2), 218–224. https://doi.org/10.1021/cg0605638.

(186) Mughal, R. K.; Davey, R. J.; Black, S. N. Application of Crystallization Inhibitors to Chiral Separations. 2. Enhancing the Chiral Purity of Mandelic Acid by Crystallization. *Cryst. Growth Des.* **2007**, *7* (2), 225–228. https://doi.org/10.1021/cg060565s.

(187) Harfouche, L. C.; Brandel, C.; Cartigny, Y.; Ter Horst, J. H.; Coquerel, G.; Petit, S. Enabling Direct Preferential Crystallization in a Stable Racemic Compound System. *Mol. Pharm.* **2019**, *16* (11), 4670–4676. https://doi.org/10.1021/acs.molpharmaceut.9b00805.

(188) Liu, Y.; Gabriele, B.; Davey, R. J.; Cruz-Cabeza, A. J. Concerning Elusive Crystal Forms: The Case of Paracetamol. *J. Am. Chem. Soc.* **2020**, *142* (14), 6682–6689. https://doi.org/10.1021/jacs.0c00321.

(189) Addadi, L.; Berkovitch-Yellin, Z.; Domb, N.; Gati, E.; Lahav, M.; Leiserowitz, L. Resolution of Conglomerates by Stereoselective Habit Modifications. *Nature* **1982**, *296* (5852), 21–26. https://doi.org/10.1038/296021a0.

(190) Belletti, G.; Meekes, H.; Rutjes, F. P. J. T.; Vlieg, E. Role of Additives during Deracemization Using Temperature Cycling. *Cryst. Growth Des.* **2018**, *18* (11), 6617–6620. https://doi.org/10.1021/acs.cgd.8b00856.

(191) Engwerda, A. H. J.; van Schayik, P.; Jagtenberg, H.; Meekes, H.; Rutjes, F. P. J. T.; Vlieg, E. Deracemization of a Racemic Compound by Using Tailor-Made Additives. *Chem. – Eur. J.* **2018**, *24* (12), 2863–2867. https://doi.org/10.1002/chem.201706088.

(192) Biber, M. V.; Dos Santos Afonso, M.; Stumm, W. The Coordination Chemistry of Weathering: IV. Inhibition of the Dissolution of Oxide Minerals. *Geochim. Cosmochim. Acta* **1994**, *58* (9), 1999–2010. https://doi.org/10.1016/0016-7037(94)90280-1.

(193) MacInnis, I. N.; Brantley, S. L. Development of Etch Pit Size Distributions on Dissolving Minerals. *Chem. Geol.* **1993**, *105* (1–3), 31–49. https://doi.org/10.1016/0009-2541(93)90117-2.

(194) Motzer, C.; Reichling, M. Morphological Classification and Quantitative Analysis of Etch Pits. *J. Appl. Phys.* **2010**, *108* (11), 113523. https://doi.org/10.1063/1.3510535.

(195) Zhu, G.; Legg, B. A.; Sassi, M.; Liang, X.; Zong, M.; Rosso, K. M.; De Yoreo, J. J. Crystal Dissolution by Particle Detachment. *Nat. Commun.* **2023**, *14* (1), 6300. https://doi.org/10.1038/s41467-023-41443-y.

(196) Dove, P. M.; Han, N.; De Yoreo, J. J. Mechanisms of Classical Crystal Growth Theory Explain Quartz and Silicate Dissolution Behavior. *Proc. Natl. Acad. Sci.* **2005**, *102* (43), 15357–15362. https://doi.org/10.1073/pnas.0507777102.

(197) Ives, M. B. On Kink Kinetics in Crystal Dissolution. *J. Phys. Chem. Solids* **1963**, *24* (2), 275–281. https://doi.org/10.1016/0022-3697(63)90132-X.

(198) Lutsko, J. F.; González-Segredo, N.; Durán-Olivencia, M. A.; Maes, D.; Van Driessche, A. E. S.; Sleutel, M. Crystal Growth Cessation Revisited: The Physical Basis of Step Pinning. *Cryst. Growth Des.* **2014**, *14* (11), 6129–6134. https://doi.org/10.1021/cg501307y.

(199) Chung, J.; Granja, I.; Taylor, M. G.; Mpourmpakis, G.; Asplin, J. R.; Rimer, J. D. Molecular Modifiers Reveal a Mechanism of Pathological Crystal Growth Inhibition. *Nature* **2016**, *536* (7617), 446–450. https://doi.org/10.1038/nature19062.

(200) Compton, R. G.; Brown, C. A. The Inhibition of Calcite Dissolution/Precipitation: Mg2+ Cations. *J. Colloid Interface Sci.* **1994**, *165* (2), 445–449. https://doi.org/10.1006/jcis.1994.1248.

(201) Christoffersen, J.; Christoffersen, M. R. Kinetics of Dissolution of Calcium Hydroxyapatite. *J. Cryst. Growth* **1981**, *53* (1), 42–54. https://doi.org/10.1016/0022-0248(81)90054-3.

(202) Arvidson, R. S.; Collier, M.; Davis, K. J.; Vinson, M. D.; Amonette, J. E.; Luttge, A. Magnesium Inhibition of Calcite Dissolution Kinetics. *Geochim. Cosmochim. Acta* **2006**, *70* (3), 583–594. https://doi.org/10.1016/j.gca.2005.10.005.

(203) Bromley, L. A.; Cottier, D.; Davey, R. J.; Dobbs, B.; Smith, S.; Heywood, B. R. Interactions at the Organic/Inorganic Interface: Molecular Design of Crystallization Inhibitors for Barite. *Langmuir* **1993**, *9* (12), 3594–3599. https://doi.org/10.1021/la00036a040.

(204) De Leeuw, N. H.; Cooper, T. G. A Computer Modeling Study of the Inhibiting Effect of Organic Adsorbates on Calcite Crystal Growth. *Cryst. Growth Des.* **2004**, *4* (1), 123–133. https://doi.org/10.1021/cg0341003.

(205) Deij, M. A.; Vissers, T.; Meekes, H.; Vlieg, E. Toward Rational Design of Tailor-Made Additives Using Growth Site Statistics. *Cryst. Growth Des.* **2007**, *7* (4), 778–786. https://doi.org/10.1021/cg060885b.

(206) Van Enckevort, W. J. P.; Los, J. H. "Tailor-Made" Inhibitors in Crystal Growth: A Monte Carlo Simulation Study. *J. Phys. Chem. C* **2008**, *112* (16), 6380–6389. https://doi.org/10.1021/jp7099543.

(207) Balcerzak, A. K.; Capicciotti, C. J.; Briard, J. G.; Ben, R. N. Designing Ice Recrystallization Inhibitors: From Antifreeze (Glyco)Proteins to Small Molecules. *RSC Adv* **2014**, *4* (80), 42682–42696. https://doi.org/10.1039/C4RA06893A.

(208) Warren, M. T.; Galpin, I.; Bachtiger, F.; Gibson, M. I.; Sosso, G. C. Ice Recrystallization Inhibition by Amino Acids: The Curious Case of Alpha- and Beta-Alanine. *J. Phys. Chem. Lett.* **2022**, *13* (9), 2237–2244. https://doi.org/10.1021/acs.jpclett.1c04080.

(209) Wu, X.; Qiu, Y.; Chen, C.; Gao, Y.; Wang, Y.; Yao, F.; Zhang, H.; Li, J. Polysaccharide-Derived Ice Recrystallization Inhibitors with a Modular Design: The Case of Dextran-Based Graft Polymers. *Langmuir* **2022**, *38* (46), 14097–14108. https://doi.org/10.1021/acs.langmuir.2c02032.

(210) Dobberschütz, S.; Nielsen, M. R.; Sand, K. K.; Civioc, R.; Bovet, N.; Stipp, S. L. S.; Andersson, M. P. The Mechanisms of Crystal Growth Inhibition by Organic and Inorganic Inhibitors. *Nat. Commun.* **2018**, *9* (1), 1578. https://doi.org/10.1038/s41467-018-04022-0.

(211) Shtukenberg, A. G.; Lee, S. S.; Kahr, B.; Ward, M. D. Manipulating Crystallization with Molecular Additives. *Annu. Rev. Chem. Biomol. Eng.* **2014**, *5* (1), 77–96. https://doi.org/10.1146/annurev-chembioeng-061312-103308.

(212) Chemistry in the Ancient World. *Nature* **1937**, *140* (3554), 1006–1006. https://doi.org/10.1038/1401006a0.

(213) Moorey, P. R. S.; Moorey, P. R. S. *Ancient Mesopotamian Materials and Industries: The Archaeological Evidence*; Clarendon Press: Oxford, 1994.

(214) Schoen, H. M.; Grove, C. S.; Palermo, J. A. The Early History of Crystallization. *J. Chem. Educ.* **1956**, *33* (8), 373. https://doi.org/10.1021/ed033p373.

(215) *Crystallization: Basic Concepts and Industrial Applications*, 1st ed.; Beckmann, W., Ed.; Wiley, 2013. https://doi.org/10.1002/9783527650323.

(216) Weingaertner, D. A.; Lynn, S.; Hanson, D. N. Extractive Crystallization of Salts from Concentrated Aqueous Solution. *Ind. Eng. Chem. Res.* **1991**, *30* (3), 490–501. https://doi.org/10.1021/ie00051a009.

(217) Yu, Z. Q.; Chew, J. W.; Chow, P. S.; Tan, R. B. H. Recent Advances in Crystallization Control. *Chem. Eng. Res. Des.* **2007**, *85* (7), 893–905. https://doi.org/10.1205/cherd06234.

(218) Tung, H.-H. Industrial Perspectives of Pharmaceutical Crystallization. *Org. Process Res. Dev.* **2013**, *17* (3), 445–454. https://doi.org/10.1021/op3002323.

(219) Gao, Z.; Rohani, S.; Gong, J.; Wang, J. Recent Developments in the Crystallization Process: Toward the Pharmaceutical Industry. *Engineering* **2017**, *3* (3), 343–353. https://doi.org/10.1016/J.ENG.2017.03.022.

(220) Mauriaucourt, M.; Jiang, S.; Soare, A.; Zwijnenburg, A.; Shahidzadeh, N. Multiscale Study on the Mechanism of a Bio-Based Anticaking Agent for NaCl Crystals. *ACS Omega* **2020**, *5* (49), 31575–31583. https://doi.org/10.1021/acsomega.0c03776.

(221) Orehek, J.; Teslić, D.; Likozar, B. Continuous Crystallization Processes in Pharmaceutical Manufacturing: A Review. *Org. Process Res. Dev.* **2021**, *25* (1), 16–42. https://doi.org/10.1021/acs.oprd.0c00398.

(222) Ma, Y.; Svärd, M.; Xiao, X.; Gardner, J. M.; Olsson, R. T.; Forsberg, K. Precipitation and Crystallization Used in the Production of Metal Salts for Li-Ion Battery Materials: A Review. *Metals* **2020**, *10* (12), 1609. https://doi.org/10.3390/met10121609.

(223) Neumann, J.; Petranikova, M.; Meeus, M.; Gamarra, J. D.; Younesi, R.; Winter, M.; Nowak, S. Recycling of Lithium-Ion Batteries—Current State of the Art, Circular Economy, and Next Generation Recycling. *Adv. Energy Mater.* **2022**, *12* (17), 2102917. https://doi.org/10.1002/aenm.202102917.

(224) Yu, L.; Dean, K.; Li, L. Polymer Blends and Composites from Renewable Resources. *Prog. Polym. Sci.* **2006**, *31* (6), 576–602. https://doi.org/10.1016/j.progpolymsci.2006.03.002.

(225) Orjuela, A.; Orjuela, A. D. P. Production of Biofuels and Biobased Chemicals in Biorefineries and Potential Use of Intensified Technologies. In *Biofuels and Biorefining*; Elsevier, 2022; pp 305–359. https://doi.org/10.1016/B978-0-12-824117-2.00007-7.

(226) Singh, S.; Shreyash, N.; Kode, V. R.; Qian, X.; Wickramasinghe, S. R. Review of Separation and Purification of Biobased Derivatives Produced from Food Waste for Industrial Use. *Circ. Econ. Sustain.* **2024**, *4* (2), 905–928. https://doi.org/10.1007/s43615-023-00312-y.

(227) *Handbook of Industrial Crystallization*, 2nd ed.; Myerson, A. S., Ed.; Butterworth-Heinemann: Boston, 2002.

(228) Minamisono, T.; Takiyama, H. Control of Polymorphism in the Anti-Solvent Crystallization with a Particular Temperature Profile. *J. Cryst. Growth* **2013**, *362*, 135–139. https://doi.org/10.1016/j.jcrysgro.2011.11.091.

(229) Tulcidas, A.; Nascimento, S.; Santos, B.; Alvarez, C.; Pawlowski, S.; Rocha, F. Statistical Methodology for Scale-up of an Anti-Solvent Crystallization Process in the Pharmaceutical Industry. *Sep. Purif. Technol.* **2019**, *213*, 56–62. https://doi.org/10.1016/j.seppur.2018.12.019.

(230) Jia, S.; Yang, P.; Gao, Z.; Li, Z.; Fang, C.; Gong, J. Recent Progress in Antisolvent Crystallization. *CrystEngComm* **2022**, *24* (17), 3122–3135. https://doi.org/10.1039/D2CE00059H.

(231) Dighe, A. V.; Podupu, P. K. R.; Coliaie, P.; Singh, M. R. Three-Step Mechanism of Antisolvent Crystallization. *Cryst. Growth Des.* **2022**, *22* (5), 3119–3127. https://doi.org/10.1021/acs.cgd.2c00014.

(232) Plumb, K. Continuous Processing in the Pharmaceutical Industry. *Chem. Eng. Res. Des.* **2005**, *83* (6), 730–738. https://doi.org/10.1205/cherd.04359.

(233) Zhang, D.; Xu, S.; Du, S.; Wang, J.; Gong, J. Progress of Pharmaceutical Continuous Crystallization. *Engineering* **2017**, *3* (3), 354–364. https://doi.org/10.1016/J.ENG.2017.03.023.

(234) Wang, J.; Li, F.; Lakerveld, R. Process Intensification for Pharmaceutical Crystallization. *Chem. Eng. Process. - Process Intensif.* **2018**, *127*, 111–126. https://doi.org/10.1016/j.cep.2018.03.018.

(235) Ter Horst, J. H.; Schmidt, C.; Ulrich, J. Fundamentals of Industrial Crystallization. In *Handbook of Crystal Growth*; Elsevier, 2015; pp 1317–1349. https://doi.org/10.1016/B978-0-444-63303-3.00032-8.

(236) Nagy, Z. K.; Braatz, R. D. Advances and New Directions in Crystallization Control. *Annu. Rev. Chem. Biomol. Eng.* **2012**, *3* (1), 55–75. https://doi.org/10.1146/annurev-chembioeng-062011-081043.

(237) Sang-Il Kwon, J.; Nayhouse, M.; Orkoulas, G.; Christofides, P. D. Crystal Shape and Size Control Using a Plug Flow Crystallization Configuration. *Chem. Eng. Sci.* **2014**, *119*, 30–39. https://doi.org/10.1016/j.ces.2014.07.058.

(238) Harner, R. S.; Ressler, R. J.; Briggs, R. L.; Hitt, J. E.; Larsen, P. A.; Frank, T. C. Use of a Fiber-Optic Turbidity Probe to Monitor and Control Commercial-Scale Unseeded Batch Crystallizations. *Org. Process Res. Dev.* **2009**, *13* (1), 114–124. https://doi.org/10.1021/op8001504.

(239) Triger, A.; Pic, J.-S.; Cabassud, C. Determination of Struvite Crystallization Mechanisms in Urine Using Turbidity Measurement. *Water Res.* **2012**, *46* (18), 6084–6094. https://doi.org/10.1016/j.watres.2012.08.030.

(240) Dai, Z.; Zhang, F.; Kan, A. T.; Ruan, G.; Yan, F.; Bhandari, N.; Zhang, Z.; Liu, Y.; Lu, A. Y.-T.; Deng, G.; Tomson, M. B. Two-Stage Model Reveals Barite Crystallization Kinetics from Solution Turbidity. *Ind. Eng. Chem. Res.* **2019**, *58* (25), 10864–10874. https://doi.org/10.1021/acs.iecr.9b01707.

(241) Coles, S. J.; Threlfall, T. L. A Practical Guide to the Measurement of Turbidity Curves of Cooling Crystallisations from Solution. *CrystEngComm* **2020**, *22* (10), 1865–1874. https://doi.org/10.1039/C9CE01622H.

(242) Wu, Z.; Yang, S.; Wu, W. Application of Temperature Cycling for Crystal Quality Control during Crystallization. *CrystEngComm* **2016**, *18* (13), 2222–2238. https://doi.org/10.1039/C5CE02522B.

(243) Kim, S.; Wei, C.; Kiang, S. Crystallization Process Development of an Active Pharmaceutical Ingredient and Particle Engineering via the Use of Ultrasonics and Temperature Cycling. *Org. Process Res. Dev.* **2003**, *7* (6), 997–1001. https://doi.org/10.1021/op034107t.

(244) Saeman, W. C. Crystal-size Distribution in Mixed Suspensions. *AIChE J.* **1956**, *2* (1), 107–112. https://doi.org/10.1002/aic.690020122.
(245) Shtukenberg, A. G.; García-Ruiz, J. M.; Kahr, B. Punin Ripening and the Classification of Solution-Mediated Recrystallization Mechanisms. *Cryst. Growth Des.* **2021**, *21* (2), 1267–1277. https://doi.org/10.1021/acs.cgd.0c01545.
(246) Simone, E.; Klapwijk, A. R.; Wilson, C. C.; Nagy, Z. K. Investigation of the Evolution of Crystal Size and Shape during Temperature Cycling and in the Presence of a Polymeric Additive Using Combined Process Analytical Technologies. *Cryst. Growth Des.* **2017**, *17* (4), 1695–1706. https://doi.org/10.1021/acs.cgd.6b01683.
(247) Snyder, R. C.; Studener, S.; Doherty, M. F. Manipulation of Crystal Shape by Cycles of Growth and Dissolution. *AIChE J.* **2007**, *53* (6), 1510–1517. https://doi.org/10.1002/aic.11174.
(248) Schulz, H. J. Equilibrium Shape of Crystals. *J. Phys.* **1985**, *46* (2), 257–269. https://doi.org/10.1051/jphys:01985004602025700.
(249) Sekerka, R. F. Equilibrium and Growth Shapes of Crystals: How Do They Differ and Why Should We Care? *Cryst. Res. Technol.* **2005**, *40* (4–5), 291–306. https://doi.org/10.1002/crat.200410342.
(250) Neugebauer, P.; Cardona, J.; Besenhard, M. O.; Peter, A.; Gruber-Woelfler, H.; Tachtatzis, C.; Cleary, A.; Andonovic, I.; Sefcik, J.; Khinast, J. G. Crystal Shape Modification via Cycles of Growth and Dissolution in a Tubular Crystallizer. *Cryst. Growth Des.* **2018**, *18* (8), 4403–4415. https://doi.org/10.1021/acs.cgd.8b00371.
(251) Rosenbaum, T.; Mbachu, V.; Mitchell, N. A.; Gamble, J. F.; Cho, P.; Engstrom, J. D. Comparison of One-Dimensional and Two-Dimensional Population Balance Models for Optimization of a Crystallization Process for a Needle-Shaped Active Pharmaceutical Ingredient. *Org. Process Res. Dev.* **2022**, *26* (4), 1094–1105. https://doi.org/10.1021/acs.oprd.1c00344.
(252) Zhang, Y.; Doherty, M. F. Simultaneous Prediction of Crystal Shape and Size for Solution Crystallization. *AIChE J.* **2004**, *50* (9), 2101–2112. https://doi.org/10.1002/aic.10182.
(253) Briesen, H. Simulation of Crystal Size and Shape by Means of a Reduced Two-Dimensional Population Balance Model. *Chem. Eng. Sci.* **2006**, *61* (1), 104–112. https://doi.org/10.1016/j.ces.2004.11.062.
(254) Jiang, M.; Zhu, X.; Molaro, M. C.; Rasche, M. L.; Zhang, H.; Chadwick, K.; Raimondo, D. M.; Kim, K.-K. K.; Zhou, L.; Zhu, Z.; Wong, M. H.; O'Grady, D.; Hebrault, D.; Tedesco, J.; Braatz, R. D. Modification of Crystal Shape through Deep Temperature Cycling. *Ind. Eng. Chem. Res.* **2014**, *53* (13), 5325–5336. https://doi.org/10.1021/ie400859d.
(255) Suwannasang, K.; Flood, A. E.; Coquerel, G. A Novel Design Approach To Scale Up the Temperature Cycle Enhanced Deracemization Process: Coupled Mixed-Suspension Vessels. *Cryst. Growth Des.* **2016**, *16* (11), 6461–6467. https://doi.org/10.1021/acs.cgd.6b01139.
(256) Zipp, G. L.; Randolph, A. D. Selective Fines Destruction in Batch Crystallization. *Ind. Eng. Chem. Res.* **1989**, *28* (9), 1446–1448. https://doi.org/10.1021/ie00093a027.
(257) Suwannasang, K.; Flood, A. E.; Rougeot, C.; Coquerel, G. Using Programmed Heating–Cooling Cycles with Racemization in Solution for Complete Symmetry Breaking of a Conglomerate Forming System. *Cryst. Growth Des.* **2013**, *13* (8), 3498–3504. https://doi.org/10.1021/cg400436r.
(258) Seki, H.; Su, Y. Robust Optimal Temperature Swing Operations for Size Control of Seeded Batch Cooling Crystallization. *Chem. Eng. Sci.* **2015**, *133*, 16–23. https://doi.org/10.1016/j.ces.2014.12.027.
(259) Shan, G. Production of Large Crystals with a Narrow Crystal Size Distribution by a Novel WWDJ Batch Crystallizer. *Chem. Eng. J.* **2002**, *85* (2–3), 161–167. https://doi.org/10.1016/S1385-8947(01)00153-X.
(260) Majumder, A.; Nagy, Z. K. Fines Removal in a Continuous Plug Flow Crystallizer by Optimal Spatial Temperature Profiles with Controlled Dissolution. *AIChE J.* **2013**, *59* (12), 4582–4594. https://doi.org/10.1002/aic.14196.

(261) Eisenschmidt, H.; Bajcinca, N.; Sundmacher, K. Optimal Control of Crystal Shapes in Batch Crystallization Experiments by Growth-Dissolution Cycles. *Cryst. Growth Des.* **2016**, *16* (6), 3297–3306. https://doi.org/10.1021/acs.cgd.6b00288.

(262) Bakar, M. R. A.; Nagy, Z. K.; Rielly, C. D. Seeded Batch Cooling Crystallization with Temperature Cycling for the Control of Size Uniformity and Polymorphic Purity of Sulfathiazole Crystals. *Org. Process Res. Dev.* **2009**, *13* (6), 1343–1356. https://doi.org/10.1021/op900174b.

(263) He, Y.; Gao, Z.; Zhang, T.; Sun, J.; Ma, Y.; Tian, N.; Gong, J. Seeding Techniques and Optimization of Solution Crystallization Processes. *Org. Process Res. Dev.* **2020**, *24* (10), 1839–1849. https://doi.org/10.1021/acs.oprd.0c00151.

(264) Zhang, F.; Shan, B.; Wang, Y.; Zhu, Z.; Yu, Z.-Q.; Ma, C. Y. Progress and Opportunities for Utilizing Seeding Techniques in Crystallization Processes. *Org. Process Res. Dev.* **2021**, *25* (7), 1496–1511. https://doi.org/10.1021/acs.oprd.1c00103.

(265) Qamar, S.; Peter Elsner, M.; Hussain, I.; Seidel-Morgenstern, A. Seeding Strategies and Residence Time Characteristics of Continuous Preferential Crystallization. *Chem. Eng. Sci.* **2012**, *71*, 5–17. https://doi.org/10.1016/j.ces.2011.12.030.

(266) Aamir, E.; Nagy, Z. K.; Rielly, C. D. Evaluation of the Effect of Seed Preparation Method on the Product Crystal Size Distribution for Batch Cooling Crystallization Processes. *Cryst. Growth Des.* **2010**, *10* (11), 4728–4740. https://doi.org/10.1021/cg100305w.

(267) Nangia, A.; Desiraju, G. R. Pseudopolymorphism: Occurrences of Hydrogen Bonding Organic Solvents in Molecular Crystals. *Chem. Commun.* **1999**, No. 7, 605–606. https://doi.org/10.1039/a809755k.

(268) Veith, H.; Luebbert, C.; Sadowski, G. Correctly Measuring and Predicting Solubilities of Solvates, Hydrates, and Polymorphs. *Cryst. Growth Des.* **2020**, *20* (2), 723–735. https://doi.org/10.1021/acs.cgd.9b01145.

(269) Aitipamula, S.; Banerjee, R.; Bansal, A. K.; Biradha, K.; Cheney, M. L.; Choudhury, A. R.; Desiraju, G. R.; Dikundwar, A. G.; Dubey, R.; Duggirala, N.; Ghogale, P. P.; Ghosh, S.; Goswami, P. K.; Goud, N. R.; Jetti, R. R. K. R.; Karpinski, P.; Kaushik, P.; Kumar, D.; Kumar, V.; Moulton, B.; Mukherjee, A.; Mukherjee, G.; Myerson, A. S.; Puri, V.; Ramanan, A.; Rajamannar, T.; Reddy, C. M.; Rodriguez-Hornedo, N.; Rogers, R. D.; Row, T. N. G.; Sanphui, P.; Shan, N.; Shete, G.; Singh, A.; Sun, C. C.; Swift, J. A.; Thaimattam, R.; Thakur, T. S.; Kumar Thaper, R.; Thomas, S. P.; Tothadi, S.; Vangala, V. R.; Variankaval, N.; Vishweshwar, P.; Weyna, D. R.; Zaworotko, M. J. Polymorphs, Salts, and Cocrystals: What's in a Name? *Cryst. Growth Des.* **2012**, *12* (5), 2147–2152. https://doi.org/10.1021/cg3002948.

(270) Fleischman, S. G.; Kuduva, S. S.; McMahon, J. A.; Moulton, B.; Bailey Walsh, R. D.; Rodríguez-Hornedo, N.; Zaworotko, M. J. Crystal Engineering of the Composition of Pharmaceutical Phases: Multiple-Component Crystalline Solids Involving Carbamazepine. *Cryst. Growth Des.* **2003**, *3* (6), 909–919. https://doi.org/10.1021/cg034035x.

(271) Henck, J.; Kuhnert-Brandstatter, M. Demonstration of the Terms Enantiotropy and Monotropy in Polymorphism Research Exemplified by Flurbiprofen. *J. Pharm. Sci.* **1999**, *88* (1), 103–108. https://doi.org/10.1021/js9801945.

(272) Kitamura, M. Controlling Factors and Mechanism of Polymorphic Crystallization. *Cryst. Growth Des.* **2004**, *4* (6), 1153–1159. https://doi.org/10.1021/cg0497795.

(273) Lee, A. Y.; Erdemir, D.; Myerson, A. S. Crystal Polymorphism in Chemical Process Development. *Annu. Rev. Chem. Biomol. Eng.* **2011**, *2* (1), 259–280. https://doi.org/10.1146/annurev-chembioeng-061010-114224.

(274) Abramov, Y. A.; Zell, M.; Krzyzaniak, J. F. Toward a Rational Solvent Selection for Conformational Polymorph Screening. In *Chemical Engineering in the Pharmaceutical Industry*; Ende, M. T., Ende, D. J., Eds.; Wiley, 2019; pp 519–532. https://doi.org/10.1002/9781119600800.ch23.

(275) Linberg, K.; Sander, P. C.; Emmerling, F.; Michalchuk, A. A. L. *In Situ* Investigation of Controlled Polymorphism in Mechanochemistry at Elevated Temperature. *RSC Mechanochemistry* **2024**, *1* (1), 43–49. https://doi.org/10.1039/D3MR00019B.

(276) James, S. L.; Adams, C. J.; Bolm, C.; Braga, D.; Collier, P.; Friščić, T.; Grepioni, F.; Harris, K. D. M.; Hyett, G.; Jones, W.; Krebs, A.; Mack, J.; Maini, L.; Orpen, A. G.; Parkin, I. P.; Shearouse, W. C.; Steed, J. W.; Waddell, D. C. Mechanochemistry: Opportunities for New and Cleaner Synthesis. *Chem Soc Rev* **2012**, *41* (1), 413–447. https://doi.org/10.1039/C1CS15171A.

(277) Lampronti, G. I.; Michalchuk, A. A. L.; Mazzeo, P. P.; Belenguer, A. M.; Sanders, J. K. M.; Bacchi, A.; Emmerling, F. Changing the Game of Time Resolved X-Ray Diffraction on the Mechanochemistry Playground by Downsizing. *Nat. Commun.* **2021**, *12* (1), 6134. https://doi.org/10.1038/s41467-021-26264-1.

(278) Sacchi, P.; Wright, S. E.; Neoptolemou, P.; Lampronti, G. I.; Rajagopalan, A. K.; Kras, W.; Evans, C. L.; Hodgkinson, P.; Cruz-Cabeza, A. J. Crystal Size, Shape, and Conformational Changes Drive Both the Disappearance and Reappearance of Ritonavir Polymorphs in the Mill. *Proc. Natl. Acad. Sci.* **2024**, *121* (15), e2319127121. https://doi.org/10.1073/pnas.2319127121.

(279) Belenguer, A. M.; Lampronti, G. I.; De Mitri, N.; Driver, M.; Hunter, C. A.; Sanders, J. K. M. Understanding the Influence of Surface Solvation and Structure on Polymorph Stability: A Combined Mechanochemical and Theoretical Approach. *J. Am. Chem. Soc.* **2018**, *140* (49), 17051–17059. https://doi.org/10.1021/jacs.8b08549.

(280) Linberg, K.; Szymoniak, P.; Schönhals, A.; Emmerling, F.; Michalchuk, A. A. L. The Origin of Delayed Polymorphism in Molecular Crystals Under Mechanochemical Conditions. *Chem. – Eur. J.* **2023**, *29* (71), e202302150. https://doi.org/10.1002/chem.202302150.

(281) Trzeciak, K.; Dudek, M. K.; Potrzebowski, M. J. Mechanochemical Transformations of Pharmaceutical Cocrystals: Polymorphs and Coformer Exchange. *Chem. – Eur. J.* **2024**, *30* (71), e202402683. https://doi.org/10.1002/chem.202402683.

(282) Kulla, H.; Becker, C.; Michalchuk, A. A. L.; Linberg, K.; Paulus, B.; Emmerling, F. Tuning the Apparent Stability of Polymorphic Cocrystals through Mechanochemistry. *Cryst. Growth Des.* **2019**, *19* (12), 7271–7279. https://doi.org/10.1021/acs.cgd.9b01158.

(283) Ostergaard, I.; Szilagyi, B.; De Diego, H. L.; Qu, H.; Nagy, Z. K. Polymorphic Control and Scale-Up Strategy for Antisolvent Crystallization Using a Sequential Supersaturation and Direct Nucleation Control Approach. *Cryst. Growth Des.* **2020**, *20* (8), 5538–5550. https://doi.org/10.1021/acs.cgd.0c00716.

(284) Gu, C.-H.; Young, V.; Grant, D. J. W. Polymorph Screening: Influence of Solvents on the Rate of Solvent-Mediated Polymorphic Transformation. *J. Pharm. Sci.* **2001**, *90* (11), 1878–1890. https://doi.org/10.1002/jps.1137.

(285) Thorson, M. R.; Goyal, S.; Gong, Y.; Zhang, G. G. Z.; Kenis, P. J. A. Microfluidic Approach to Polymorph Screening through Antisolvent Crystallization. *CrystEngComm* **2012**, *14* (7), 2404. https://doi.org/10.1039/c2ce06167h.

(286) Meldrum, F. C.; O'Shaughnessy, C. Crystallization in Confinement. *Adv. Mater.* **2020**, *32* (31), 2001068. https://doi.org/10.1002/adma.202001068.

(287) Hamilton, B. D.; Ha, J.-M.; Hillmyer, M. A.; Ward, M. D. Manipulating Crystal Growth and Polymorphism by Confinement in Nanoscale Crystallization Chambers. *Acc. Chem. Res.* **2012**, *45* (3), 414–423. https://doi.org/10.1021/ar200147v.

(288) Ter Horst, J. H. Industrial Crystallization: Fundamental Understanding for Challenges Ahead. *Chem. Eng. Technol.* **2012**, *35* (6), 965–965. https://doi.org/10.1002/ceat.201290037.

(289) McDonald, M. A.; Salami, H.; Harris, P. R.; Lagerman, C. E.; Yang, X.; Bommarius, A. S.; Grover, M. A.; Rousseau, R. W. Reactive Crystallization: A Review. *React. Chem. Eng.* **2021**, *6* (3), 364–400. https://doi.org/10.1039/D0RE00272K.

(290) Zhang, H.; Lakerveld, R.; Heider, P. L.; Tao, M.; Su, M.; Testa, C. J.; D'Antonio, A. N.; Barton, P. I.; Braatz, R. D.; Trout, B. L.; Myerson, A. S.; Jensen, K. F.; Evans, J. M. B. Application of Continuous Crystallization in an Integrated Continuous Pharmaceutical Pilot Plant. *Cryst. Growth Des.* **2014**, *14* (5), 2148–2157. https://doi.org/10.1021/cg401571h.

(291) Xu, K.; Xu, P. Efficient Calcium Lactate Production by Fermentation Coupled with Crystallization-Based in Situ Product Removal. *Bioresour. Technol.* **2014**, *163*, 33–39. https://doi.org/10.1016/j.biortech.2014.04.002.

(292) Kuhn, R.; Deutsch, A. Bildung Aromatischer Kohlenwasserstoffe Aus Dien-carbonsäuren (Über Konjugierte Doppelbindungen, XXI. Mitteil.). *Berichte Dtsch. Chem. Ges. B Ser.* **1932**, *65* (1), 43–49. https://doi.org/10.1002/cber.19320650108.

(293) Dimorth, O. Über Intramolekulare Umlagerungen. Fünfte Abhandlung. Der Einfluß Des Lösungsmittels Auf Reaktionsgeschwindigkeit Und Gleichgewicht. Der Einfluß Des Lösungsmittels Auf Reaktionsgeschwindigkeit Und Gleichgewicht. *Justus Liebigs Ann. Chem.* **1910**, *377* (2), 127–163. https://doi.org/10.1002/jlac.19103770202.

(294) Teychené, S.; Rodríguez-Ruiz, I.; Ramamoorthy, R. K. Reactive Crystallization: From Mixing to Control of Kinetics by Additives. *Curr. Opin. Colloid Interface Sci.* **2020**, *46*, 1–19. https://doi.org/10.1016/j.cocis.2020.01.003.

(295) Kubota, N. Effect of Impurities on the Growth Kinetics of Crystals. *Cryst. Res. Technol.* **2001**, *36* (8–10), 749–769. https://doi.org/10.1002/1521-4079(200110)36:8/10%253C749::AID-CRAT749%253E3.0.CO;2-%2523.

(296) Wang, T.-C.; Hu, W.-H. Solid–Liquid Equilibria of Nine Binary Systems with Dicarboxylic Acids. *J. Chem. Eng. Data* **2017**, *62* (3), 931–937. https://doi.org/10.1021/acs.jced.6b00628.

(297) McDonald, M. A.; Marshall, G. D.; Bommarius, A. S.; Grover, M. A.; Rousseau, R. W. Crystallization Kinetics of Cephalexin Monohydrate in the Presence of Cephalexin Precursors. *Cryst. Growth Des.* **2019**, *19* (9), 5065–5074. https://doi.org/10.1021/acs.cgd.9b00429.

(298) Urwin, S. J.; Levilain, G.; Marziano, I.; Merritt, J. M.; Houson, I.; Ter Horst, J. H. A Structured Approach To Cope with Impurities during Industrial Crystallization Development. *Org. Process Res. Dev.* **2020**, *24* (8), 1443–1456. https://doi.org/10.1021/acs.oprd.0c00166.

(299) Chum, C. K.; Gladwell, I. R.; Marziano, I.; Salvalaglio, M. Unravelling the Impact of Process Impurities on the Crystallization of Ritlecitinib Tosylate Using Molecular Dynamics. *Org. Process Res. Dev.* **2024**, *28* (9), 3587–3593. https://doi.org/10.1021/acs.oprd.4c00106.

(300) Chen, P.-C.; Cheng, G. Y.; Kou, M. H.; Shia, P. Y.; Chung, P. O. Nucleation and Morphology of Barium Carbonate Crystals in a Semi-Batch Crystallizer. *J. Cryst. Growth* **2001**, *226* (4), 458–472. https://doi.org/10.1016/S0022-0248(01)01408-7.

(301) Li, Y.; Zhang, Y.; Yang, C.; Chen, L.; Zhang, Y. Crystallization of Aluminium Hydroxide from the Reactive NaAl(OH)4–NaHCO3 Solution: Experiment and Modeling. *Chem. Eng. Sci.* **2010**, *65* (16), 4906–4912. https://doi.org/10.1016/j.ces.2010.05.042.

(302) Cao, T.; Zhang, W.; Cheng, J.; Yang, C. Comparative Experimental Study on Reactive Crystallization of Ni(OH) 2 in an Airlift-Loop Reactor and a Stirred Reactor. *Chin. J. Chem. Eng.* **2018**, *26* (1), 196–206. https://doi.org/10.1016/j.cjche.2017.03.007.

(303) Peters, E. M.; Kaya, Ş.; Dittrich, C.; Forsberg, K. Recovery of Scandium by Crystallization Techniques. *J. Sustain. Metall.* **2019**, *5* (1), 48–56. https://doi.org/10.1007/s40831-019-00210-4.

(304) Zhao, S.; Gao, J.; Ma, S.; Li, C.; Ma, Y.; He, Y.; Gong, J.; Zhou, F.; Zhang, B.; Tang, W. Mechanism and Modelling of Reactive Crystallization Process of Lithium Carbonate. *Processes* **2019**, *7* (5), 248. https://doi.org/10.3390/pr7050248.

(305) Ochonma, P.; Gao, X.; Gadikota, G. Tuning Reactive Crystallization Pathways for Integrated $CO_2$ Capture, Conversion, and Storage via Mineralization. *Acc. Chem. Res.* **2024**, *57* (3), 267–274. https://doi.org/10.1021/acs.accounts.3c00482.

(306) Noorduin, W. L.; Izumi, T.; Millemaggi, A.; Leeman, M.; Meekes, H.; Van Enckevort, W. J. P.; Kellogg, R. M.; Kaptein, B.; Vlieg, E.; Blackmond, D. G. Emergence of a Single Solid Chiral State from a Nearly Racemic Amino Acid Derivative. *J. Am. Chem. Soc.* **2008**, *130* (4), 1158–1159. https://doi.org/10.1021/ja7106349.

(307) Quon, J. L.; Zhang, H.; Alvarez, A.; Evans, J.; Myerson, A. S.; Trout, B. L. Continuous Crystallization of Aliskiren Hemifumarate. *Cryst. Growth Des.* **2012**, *12* (6), 3036–3044. https://doi.org/10.1021/cg300253a.

(308) Liu, R.; Huang, M.; Yao, X.; Chen, S.; Wang, S.; Suo, Z. Gas-Liquid Reactive Crystallization Kinetics of 2,4,6-Triamino-1,3,5-Trinitrobenzene in the Semi-Batch Procedure. *J. Cryst. Growth* **2018**, *491*, 6–15. https://doi.org/10.1016/j.jcrysgro.2018.03.006.

(309) Jiang, M.; Ni, X.-W. Effects of Solvents and Impurity on Crystallization Kinetics and Crystal Properties in a Reactive Crystallization of Paracetamol. *J. Cryst. Growth* **2019**, *523*, 125150. https://doi.org/10.1016/j.jcrysgro.2019.125150.

(310) Su, W.; Jiang, Y.; Zuo, X.; Li, C.; Wang, H. Engineering Nucleation/Crystallization to Intensify the Enzymatic Reactions and Fermentation: A Review. *Chem. Eng. J.* **2022**, *431*, 134186. https://doi.org/10.1016/j.cej.2021.134186.

(311) Urbanus, J.; Bisselink, R. J. M.; Nijkamp, K.; Ter Horst, J. H.; Verdoes, D.; Roelands, C. P. M. Integrated Product Removal of Slightly Water-Soluble Carboxylates from Fermentation by Electrochemically Induced Crystallization. *J. Membr. Sci.* **2010**, *363* (1–2), 36–47. https://doi.org/10.1016/j.memsci.2010.07.030.

(312) Fellechner, O.; Blatkiewicz, M.; Smirnova, I. Reactive Separations for In Situ Product Removal of Enzymatic Reactions: A Review. *Chem. Ing. Tech.* **2019**, *91* (11), 1522–1543. https://doi.org/10.1002/cite.201900027.

(313) Salami, H.; Lagerman, C. E.; Harris, P. R.; McDonald, M. A.; Bommarius, A. S.; Rousseau, R. W.; Grover, M. A. Model Development for Enzymatic Reactive Crystallization of β-Lactam Antibiotics: A Reaction–Diffusion-Crystallization Approach. *React. Chem. Eng.* **2020**, *5* (11), 2064–2080. https://doi.org/10.1039/D0RE00276C.

(314) McQuade, D. T.; Seeberger, P. H. Applying Flow Chemistry: Methods, Materials, and Multistep Synthesis. *J. Org. Chem.* **2013**, *78* (13), 6384–6389. https://doi.org/10.1021/jo400583m.

(315) Britton, J.; Raston, C. L. Multi-Step Continuous-Flow Synthesis. *Chem. Soc. Rev.* **2017**, *46* (5), 1250–1271. https://doi.org/10.1039/C6CS00830E.

(316) Wan, L.; Kong, G.; Liu, M.; Jiang, M.; Cheng, D.; Chen, F. Flow Chemistry in the Multi-Step Synthesis of Natural Products. *Green Synth. Catal.* **2022**, *3* (3), 243–258. https://doi.org/10.1016/j.gresc.2022.07.007.

(317) Cameli, F.; Ter Horst, J. H.; Steendam, R. R. E.; Xiouras, C.; Stefanidis, G. D. On the Effect of Secondary Nucleation on Deracemization through Temperature Cycles. *Chem. – Eur. J.* **2020**, *26* (6), 1344–1354. https://doi.org/10.1002/chem.201904239.

(318) McGinty, J.; Yazdanpanah, N.; Price, C.; Ter Horst, J. H.; Sefcik, J. Nucleation and Crystal Growth in Continuous Crystallization. In *The Handbook of Continuous Crystallization*; Yazdanpanah, N., Nagy, Z. K., Eds.; The Royal Society of Chemistry, 2020; pp 1–50. https://doi.org/10.1039/9781788013581-00001.

(319) Brands, K. M. J.; Davies, A. J. Crystallization-Induced Diastereomer Transformations. *Chem. Rev.* **2006**, *106* (7), 2711–2733. https://doi.org/10.1021/cr0406864.

(320) Boyle, W. J.; Sifniades, S.; Van Peppen, J. F. Asymmetric Transformation of .Alpha.-Amino-.Epsilon.-Caprolactam, a Lysine Precursor. *J. Org. Chem.* **1979**, *44* (26), 4841–4847. https://doi.org/10.1021/jo00394a021.

(321) Weinges, K.; Klotz, K.; Droste, H. Asymmetrische Synthesen, V. Optisch Aktive 5-Amino-4-phenyl-1,3-dioxane Und Deren Einfluß Auf Die Stereoselektivität Der Asymmetrischen Strecker-Synthese. *Chem. Ber.* **1980**, *113* (2), 710–721. https://doi.org/10.1002/cber.19801130228.

(322) Hongo, C.; Tohyama, M.; Yoshioka, R.; Yamada, S.; Chibata, I. Asymmetric Transformation of DL - *p* - Hydroxyphenylglycine by a Combination of Preferential Crystallization and Simultaneous Racemization of the *o* -Toluenesulfonate. *Bull. Chem. Soc. Jpn.* **1985**, *58* (2), 433–436. https://doi.org/10.1246/bcsj.58.433.

(323) Hassan, N. A.; Bayer, E.; Jochims, J. C. Syntheses of Optically Active α-Amino Nitriles by Asymmetric Transformation of the Second Kind Using a Principle of O. Dimroth. *J. Chem. Soc. Perkin 1* **1998**, No. 22, 3747–3758. https://doi.org/10.1039/a806337k.

# Chapter 3
# **Chiral Crystallization.**

Now that both the concepts of chirality and the fundamentals of crystallization have been introduced, we can examine how crystallization and chirality come together in the separation of enantiomers and diastereomers. Thereafter, we will explore how coupling chiral crystallization to chemical reactions can lead to enantioconvergent processes that rely on the intricate interplay of kinetics and the intrinsic enantioselectivity of crystals.



Before starting this chapter, we wish to point the reader to a few general resources in this field. The go-to guide is the seminal work by Jacques, Collet & Wilen.[1] Besides that handbook, a few recent reviews provide a good background and discuss notable advances in the field.[2–4]

## Packing problems

The topic of chiral crystallization can be understood to ask two different questions: (i) how do chiral molecules crystallize, and (ii) how do chiral crystals form? Both questions are not at all the same. Indeed, chiral molecules can form both achiral and chiral crystals, while chiral crystals can also be formed both from achiral and chiral molecules. Only the first question, that of crystallizing chiral molecules, may seem relevant in the context of this thesis. However, many historic and fundamental experiments in chiral amplification have actually featured achiral molecules that crystallize in chiral space groups. Hence, before diving into the crystallization of chiral molecules, briefly reflecting on the formation of chiral structures provides some very useful background knowledge.

The question why molecules such as $N_2$, $NH_3$, $NaClO_3$, and benzophenone crystallize as chiral crystals is a puzzling one.[5,6] Brock and Dunitz stressed the enigma, by clarifying that "inversion centres are especially favourable for crystal packing, because they diminish like-like interactions and are uniquely compatible with translation".[7] Indeed, inversion centres mediate strong molecular interactions and generally allow for very close packing.[8] So why would achiral molecules then pack into chiral unit cells that lack inversion symmetry (i.e. non-centrosymmetric unit cells)? Pidcock summarized a rationale depending on the rigidity of the molecule.[9] First, rigid molecules that contain inversion symmetry are seldomly found to crystallize in chiral space groups. Conformationally flexible molecules, however, can have steric barriers for interconversion between confirmations, rendering them effectively asymmetric. These molecules thus behave like enantiomers for crystallization purposes and may resolve spontaneously. For Pidcock, the question remained, though, why flexible molecules that are not sterically hindered would

then sometimes still prefer to pack "*via* screw axes rather than inversion centres and glide planes". An important factor to be considered in such cases proves to be intermolecular: strong, directional intermolecular forces can substitute for intrinsic or steric inflexibility by effectively locking molecules into a one-handed arrangement at the supramolecular level. Key examples of such forces are hydrogen bonding, halogen bonding, and π-interactions.[10,11] Indeed, one can imagine that helical or end-to-end columnar motifs can yield homochiral chains in the crystal lattice.[12] This also frequently occurs for molecules that can adopt propeller-like conformations, owing to $C_2$ or $C_3$ symmetry axes.[13] Finally, multimers of achiral molecules can also sometimes yield asymmetric supramolecular assemblies within a crystal unit-cell, much like chiral molecules themselves are built-up from achiral subunits.[14,15]



Very similar arguments can also be made for explaining the general emergence of chiral structures from achiral particles:[16,17] Directional interactions can suppress inversion-symmetric arrangements, local asymmetries (sergeants) can direct overall helicity (of the soldiers), and collective packing can propagate chirality into longe-range order. Stacking faults or imperfections in achiral building block assemblies can quickly lead to chiral induction.[18] Screw-dislocation-driven growth mechanisms are another frequent source of chirality, also at the nanoparticle level.[19–22]

Having discussed the crystallization of achiral building blocks into chiral structures, we now turn to the crystallization of chiral molecules. In principle, a pure enantiomer only crystallizes into a chiral space group, as its symmetry cannot be inverted. For a racemic mixture of enantiomers, it is also possible to obtain a racemic conglomerate, where enantiomers self-sort into enantiomerically pure crystals (Fig. 3.1a, about 5-10% of the time). In such a case, an enantiomer molecule only fits the glove of its corresponding crystal, providing a very strong source of separation and enantioselectivity. It is also possible, and actually much more frequent (about 90-95% of the time), that the two enantiomers combine into a centrosymmetric unit cell (Fig. 3.1b) and both enantiomers pack into one racemic crystal (called a racemic compound; Fig. 3.1c).[23] Besides these two most common forms of chiral crystallization of enantiomers, it is also possible to obtain a solid solution or false conglomerate behaviour—both occur an estimated less than 1% of the time and will not be discussed further here.[24–26]

Before we continue, we should discuss how one practically discriminates between conglomerate crystals and racemic crystals.[27] The first option is to compare the XRPD patterns or solid-state NMR spectra of crystals from the racemate and the pure enantiomer. If the patterns or spectra are the same, this is a strong indication for a conglomerate. In that case, a successful resolution through crystallization or the isolation of an enantiopure single crystal constitute the ultimate proof. If the patterns or spectra are different, one generally has racemic crystals, although as an

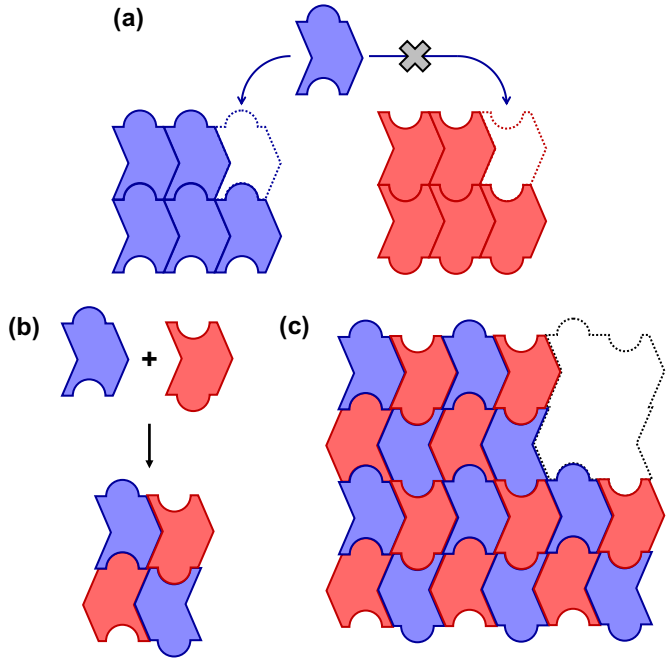


**Figure 3.1.** A mixture of two enantiomers can crystallize into enantiopure crystals, called conglomerates, which only stereoselectively incorporate its own handedness (panel a, 5-10% of cases) or crystallize together into racemic unit cells (panel b) to form racemic crystals (panel c, 90-95% of cases).



option would remain conglomerate polymorphism. It may be prudent to allow full (seeded) equilibration of crystal structures. One should also consider crystallization from different solvents and avoid the presence of solvates. This is to avoid, as it happens occasionally, any mischaracterization due to polymorphism or metastable phases. For full characterization of the solid-phase, single-crystal X-ray diffraction is required. Recently, state-of-the-art electron diffraction has likewise provided tools for conglomerate identification.[28] For quick screening, second harmonic generation can provide a first indication of non-centrosymmetric crystal unit cells.[29] Note, however, that racemic molecules occasionally also crystallize in chiral space groups.

Besides direct characterization of the solid-state arrangement, the thermodynamic stability of the crystal phases (through DSC) and their solubilities should be characterized. In the case of a conglomerate, a set energy-difference between a racemic mixture of crystals and enantiopure crystals exists purely originating from the entropy of mixing (resulting in a ~25 °C lower in melting point). DSC cycles can also provide indications of polymorphism, impurities and solvates. Solubility of the two crystal phases is another important characteristic. The solubilities of conglomerate crystals are independent, ideally giving a double solubility of the racemate compared to the pure enantiomer (for non-dissociating compounds). For a (stable) racemic compound, however, the stabilities of the enantiomerically pure crystal and the racemic crystal are not the same, causing different solubilities of a

pure enantiomer and the racemate. The phase diagram of scalemic mixtures (i.e. 0 < *ee* < 1) in the case of racemic compounds is therefore given by combining the equations of Schröder-Van Laar and Prigogine-Defay, and features a specific non-zero eutectic composition in *ee*.[1,30,31] Blackmond and colleagues have provided an easy equation for linking the solubility ratio (α) to the eutectic composition ($ee_{eu}$):[32]

$$ee_{eu} = \frac{1 - \frac{a^2}{4}}{1 + \frac{a^2}{4}} \qquad \text{(eq. 3.1)}$$



If the results from the solubility behaviour and/or DSC do not match the other characteristics, there may be non-ideal solution behaviour of the compound, as the equation is derived from ideal solution behaviour.

Conglomerate crystallization is remarkable, as it can be a very powerful tool for chiral separation and even an effective asset in asymmetric synthesis.[33–35] In chapter 1 we noted the central conundrum of chiral chemistry: the inherent difficulty in separating enantiomers due to their physical and chemical identical properties. Indeed, only in another chiral environment can enantiomers be discriminated. Conglomerate crystals provide such an enantioselective environment and uniquely do so themselves without requiring any outside source. This also brings us to the question of their unfortunate statistics: why do conglomerates form only in such a small percentage of cases? Understanding this impediment can inform crystal engineering to command this so-desired conglomerate behaviour at will.

Wallach—ahead of his time—explained the statistics by prospectively citing Kitaigorodskii's previously stated packing principle: inversion centres maximize close packing efficiency and therefore are preferred.[36] That argument appears generally strong, but exceptions are known where screw axes and helical packing achieve comparable densities and not all conglomerate structures are indeed less dense than their racemic counterparts.[37] The rule of thumb though holds: Racemic crystals are in principle preferred, owing to the generally more efficient packing of centrosymmetric space groups. Exemptions to the rule often recall the same principles as those described for achiral molecules crystallizing in chiral space groups: strong homochiral motifs induced by intermolecular interactions and propeller-like molecules predisposed to chiral packing.[38] Noteworthy counterexamples are carboxylic acids and amines that can easily form energetically favourable achiral dimers through H-bonding.[23] The rationale above explains why the chance of conglomerate formation is not homogeneous: Related structures and families of compounds can show distorted statistics, depending on the nature of their similarities.[39,40] This is an important realization for chemists that try to engineer conglomerates through covalent modifications, as is done to achieve a resolvable

intermediate.[41–47] Crystal structure prediction is increasingly able to predict possible conglomerate formation and can aid rational design.[48]

The crucial balance between intermolecular interactions and packing phenomena is especially evident on surfaces, providing insight into two-dimensional crystallization.[49,50] Computational 2D-studies have also shown that pre-nucleation clusters and supramolecular assemblies are good indications of final crystallization behaviour.[51] Moreover, they have confirmed that strongly heterogeneous interactions across molecules favour the spontaneous resolution of racemic mixtures into conglomerates.[52] Insights from computed energy landscapes have further shown that, in case of conglomerate formation, the energy difference between the conglomerate and the next-best racemic crystal is often actually very close.[53] These findings have raised the question whether kinetics may tip the balance in conglomerate formation, rather than crystal lattice energies alone—a question still open and in dire need of study.[54] Giving some clues, confinements should be studied as they may increase the likelihood of conglomerate formation through kinetic and 2D-templating pathways.[55–57]



An important exception with regard to the standard statistics of conglomerate formation are salts: Ionic crystals show much higher conglomerate rates (up to 2 or 3 times that of molecular crystals).[38] The strong electrostatic constraints may quickly trump packing efficiency considerations. This concept has been the inspiration of several crystal engineering endeavours, where enantiomers were either transformed into salts by introducing a counter-ion or co-crystallized with salts to induce conglomerate behaviour.[29,40,58–62]

Having explained the rationale behind the work on salt co-crystals to induce conglomerate behaviour, we can easily explain why other co-crystallization strategies have also seen increased interest (Fig. 3.2).[63–66] These strategies take full advantage of the possibilities of combinatorial chemistry without the need for covalent derivatization of the target. The only complications introduced are the supply of coformer and its separation and recycling after chiral resolution has been completed. Besides achiral coformers, the use of chiral coformers to force a diastereomeric-like resolution in the solid phase can also be effective, but does have the general disadvantage of requiring a chiral auxiliary.[67] In some cases, although very niche and perhaps more of a curiosity, two racemic compounds can be their respective coformer, allowing for their simultaneous resolution in the solid phase.[68] Finding the right coformer is the big challenge in co-crystallization and often requires more elaborate screening than covalent derivatization, increasing development time and cost. Fortunately, co-crystals prediction has seen much interest and they can be predicted increasingly well—although chiral crystal structure prediction (CSP) is notoriously difficult.[69–73]

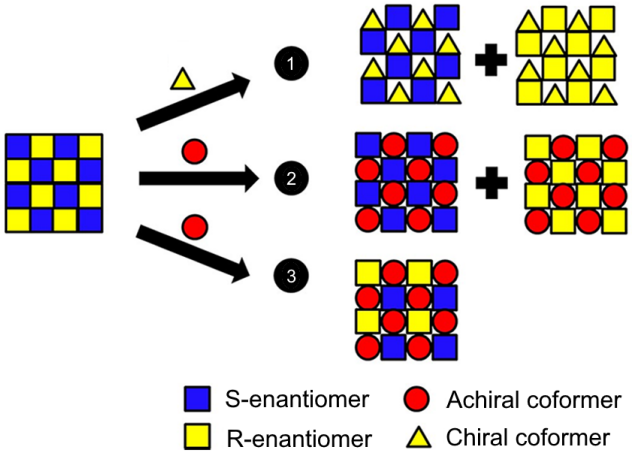


**Figure 3.2.** Co-crystallization for chiral resolution. Using coformers, a racemic mixture that would normally crystallize into racemic crystals can now crystallize together with a chiral coformer as (1) conglomerate co-crystals, or with a achiral coformer as either (2) conglomerate co-crystals or (3) racemic co-crystal or solid-solution. Indeed, a chiral coformer may effectively force enantioselective crystallization, breaking the racemic behaviour upon co-crystal formation. Schematic adapted from [65].

An alternative approach to chiral resolution that employs chiral crystallization is close in spirit to combinatorial co-crystallization with chiral coformers—albeit a much older strategy—but does not rely on conglomerate behaviour is that of diastereomeric salt formation.[74,75] In this approach of diastereomeric salt formation, a chiral resolving agent (X, in principle a base or acid) is added to a racemate (*RS*, acidic or basic respectively). The two enantiomeric ions can complex together to precipitate as a diastereomeric salt (*R*:X and *S*:X). As said in chapter 1, diastereomers do have different chemical and physical properties and thus in principle different crystal stabilities and solubilities. The diastereomers can then be separated by crystallization and the resolving agent recycled. Although sounding deceptively simple, a random choice of resolving agent can lead to no solid salt formation at all or the formation of salts with only minor solubility differences.

A key innovation in this technique, now known as Dutch Resolution, was made by Ton de Vries and co-workers, who employed a simultaneous family of resolving agents.[76] In that approach, a mix of closely related resolving agents (e.g. mix M: mandelic acid, *p*-methylmandelic acid, and *p*-bromomandelic acid) was added to one racemate (e.g. 1-(4-bromophenyl)ethanamine). The result was striking: "rapid precipitation of a crystalline diastereomeric salt in good to high enantiomeric purity and yield"—in the case of our example 96% *ee* was achieved after recrystallization. Notably, the resulting salts were usually composed of random distributions of the resolving agents from the mix and in unpredictable stoichiometries.

For a further discussion of diastereomeric salt formation and strategies therein, the reader is directed to the cited references in this paragraph and the guide by Faigl & Fogassy et al.[77]

## Preferential Crystallization

If one has a chiral compound crystallizing as a conglomerate, i.e. self-sorting into enantiopure crystals, one can apply preferential crystallization to separate a racemic mixture—a concept first demonstrated by Pasteur for left- and right-handed sodium ammonium tartrate crystals.[78] In a later demonstration, racemic methadone was separated into large crystals—each weighing multiple grams—of the opposite enantiomers through evaporation from a concentrated solution.[79] From a fundamental point of view, such preferential crystallization has also gained much attention as a route towards biological homochirality as advocated by Blackmond and others.[80,81] Interestingly, Noorduin and co-workers showed that polarized light can be used to preferentially crystallize one of the two enantiomers through photo-generating a tailor-made additive, serving as a transferable source of symmetry breaking.[82]

Relying on the manual picking of large crystals using tweezers is not ideal for the production of enantiomerically pure products. A more typical preferential crystallization process to separate two enantiomers is depicted in Figure 3.3 and generally works as follows.[1,83]

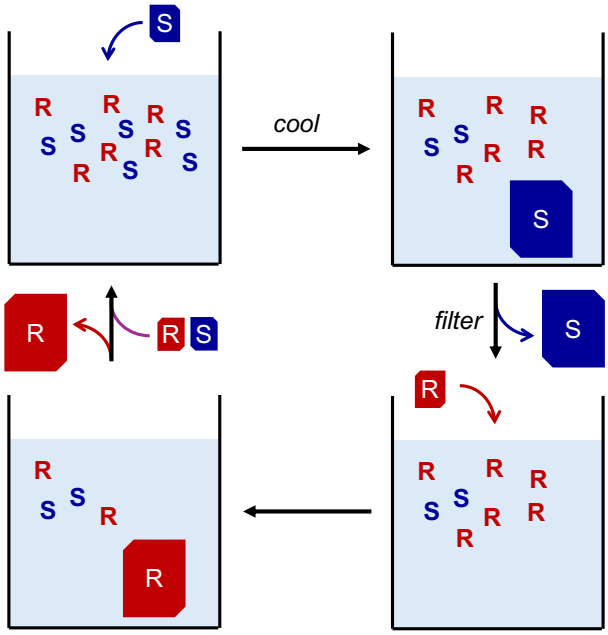


**Figure 3.3.** Preferential crystallization of a conglomerate. Through the independent solid-state behaviour of the two enantiomers, enantiopure crystals can be grown from seeded crystallization of conglomerates. Seeding with the *S*-enantiomer in a cooling crystallization that remains within the metastable zone of the *R*-enantiomer affords grown enantiopure crystals in *S*. The supersaturated solution can then be cooled further to nucleate and grow *R*. After adding fresh racemate, these consecutive steps can be repeated to exploit conglomerate crystallization as a pathway for chiral resolution, theoretically affording 50% yield in the desired enantiomer.

First, a racemic solution, i.e. containing both enantiomers in equal amounts, is exposed to an enantiopure seed crystal of one of the two enantiomers (here: *S*). Upon cooling, the solubility of the solution lowers and a crystallization driving force is induced. Because the enantiomers crystallize in separate crystals, they have independent solubilities and therefore independent supersaturations. The seeded enantiomer keeps growing, thereby continuously reducing its supersaturation to zero, while the unseeded enantiomer keeps building up supersaturation. The unseeded enantiomer does not automatically nucleate and growth, as long as its energy barrier for nucleation is not reached. Therefore, the cooling growth of the seeded enantiomer is stopped before nucleation of the other enantiomer is induced. Rather than cooling to induce preferential growth, it is of course also possible to use evaporation or the introduction of an anti-solvent as a driver for crystallization. Important is to stay within the metastable zone and prevent unwanted nucleation.

After growth of the first enantiomer, the solution is filtered or the grown enantiomerically pure solid phase removed otherwise. Now, the solution is perfectly saturated in one enantiomer (here: *S*) and well supersaturated in the other (here: *R*). Therefore, if one now adds an enantiomerically pure seed crystal of that enantiomer, one directly starts its preferential growth. No further cooling is required at this stage, although it can be implemented for higher absolute yield in the step. After removing the grown crystals, one can continue the process by again seeding with the first enantiomer until the solution is sufficiently depleted of material.[*]

The same process can also be executed for conglomerate co-crystals and even to some extent for diastereomeric salts, although those have distinct and coupled solubilities, complicating the phase diagram. Nevertheless, as long as the components of interest are situated in separate crystals, some variant of preferential crystallization can be implemented for their separation.

Rather than executing the rudimentary process described above in small batches, Rougeot and Hein have summarized recent developments aiming to implement continuous preferential crystallization processes to efficiently access enantiopure crystals.[84] Although continuous crystallization processes pose many particular engineering challenges,[85] three main approaches can be identified. The first, most basic approach, uses a single crystallizer with seeds of the desired enantiomer, through which a supersaturated solution is flown (outflow removed) and from which the pure enantiomer crystals are withdrawn.[86] A fluidized bed crystallizer is the most natural implementation of this approach.[87] The second approach uses two separated crystallizers, between which a crystal-free liquid is circulated—one crystallizer for each enantiomer.[88,89] In each reactor, the liquid gets enriched in the opposite enantiomer due to crystallization. Because of liquid-phase circulation, however,

[*] Note that, in industry, racemate is often added after each crystallization step to achieve identical cycles.

these unwanted liquid-phase enrichments are turned into solid-phase enantiopurity in the opposing reactor. A derived possibility is changing the second crystallizer to a dissolution rather than crystallization tank, using mother liquor from the crystallization tank that gets depleted in one enantiomer to enrich the solid phase in the dissolution-tank in the other enantiomer.[90–92] This second version of the two-reactor approach has a much higher theoretical productivity. The third approach features three reactors: one crystallizer for each enantiomer and a feed tank.[93–95] In essence this combines the first two approaches: a supersaturated racemic solution is supplied by the feed tank to two coupled crystallizers that balance each other's supersaturation.



A problem inevitably encountered in continuous preferential crystallization processes is the appearance of crystals of the unwanted enantiomer through nucleation and growth. Ter Horst and colleagues propose to combat that issue by flushing the system with an enantiopure solution of the desired enantiomer, effectively dissolving any undesired crystallites.[96] Rather than flushing periodically, they cleverly further propose to monitor the presence of unwanted crystallites through online polarimetry.

Having discussed the regular preferential crystallization of conglomerates, a few interesting cases remain. The first edge-case is that of so-called 'lamellar' or 'epitaxial' conglomerates.[97,98] Figure 3.4 shows how a single crystal is built up out of alternating layers of left- and right-handed crystals—epitaxy is an Ancient Greek term meaning '(sequential) ordering on top (of another layer)'. Indeed, although the individual crystalline domains are definitely enantiopure, the macroscopic crystals as a whole are often (near)-racemic. Such a situation makes the use of preferential crystallization moot, as macroscopic separation is not easily achieved by crystallization. Some solutions have been found, the most effective being crystallization-induced deracemization by grinding, which will be discussed later in this chapter. The only way to spot an epitaxial conglomerate is through special experiments (SHG, DSC and XRPD will not provide any clues): the crystals will often appear striated, are not enantiopure upon analysis, and will fall apart when exposed to enantiopure solution into thin flakes (since the alternating domains keeping the crystal together will be dissolved).[99]

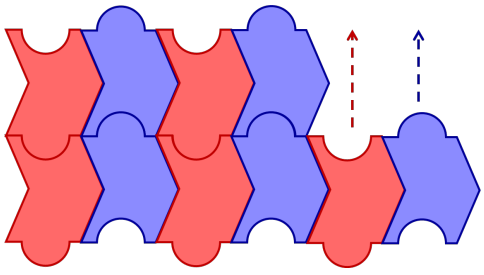

**Figure 3.4.** Lamellar or epitaxial conglomerates are macroscopically racemic crystals made up of enantiopure layers or domains. Such mere local conglomerate behaviour hinders chiral resolution.

The likely reason for the formation of epitaxial conglomerates is that the energy difference between the (fictitious) racemic crystal structure and the conglomerate crystal structure is very small. In such cases, it is energetically easy for one enantiomer to nucleate on top of the other one, sharing a 'racemic' layer. This reasoning points us to another possible complication: cross-inhibition. In that scenario, one enantiomer acts as an inhibitor for the nucleation or growth of the other one. In a preferential crystallization, such a scenario would be obviously fatal as both enantiomers are present in relative abundance. Although this phenomenon has, to the best of our knowledge, gained very little to no attention in conglomerate literature so far, the clues are clear.[74] An artificial study on a racemic compound has shown that the counter enantiomer will immediately block an enantiopure surface and form racemic patches.[100] Worryingly, studies have shown a preference for racemic compound formation in 2D over 3D, further lowering the threshold for cross-inhibition of conglomerates.[50,101] Indeed, when the racemic crystal structure is energetically close, it is far from unreasonable that enantiomers can act as their own 'tailor-made' inhibitors.[37,102,103]

Inhibition, however, can also be turned into a strength and used to apply preferential crystallization to racemic compounds, i.e. to chiral molecules that do not self-sort into enantiomerically pure crystals (Fig. 3.5). One option is that an additive inhibits the nucleation or crystal growth of the racemic crystal, but not that of the enantiomer.[104–108] In that way, it is possible to treat the system as conglomerate, because the racemic crystals are effectively put out of play. Another approach is using an additive to alter the stability of the enantiopure or racemic crystal phase or both.[109,110] If such an additive creates co-crystals that render an enantiopure co-crystal relatively more stable than the other possible solid phases, this flips the thermodynamic driving force to allow preferential crystallization as well.

Besides differences in crystal stability, intrinsic differences in nucleation and growth rates between the enantiopure and racemic crystals may sometimes also be exploited to allow for preferential crystallization of racemic compounds. Brandel and co-workers studied diprophylline and proxyphylline—both racemic compounds—and obtained surprising but inspiring results.[111–113] Their first observations pertained to

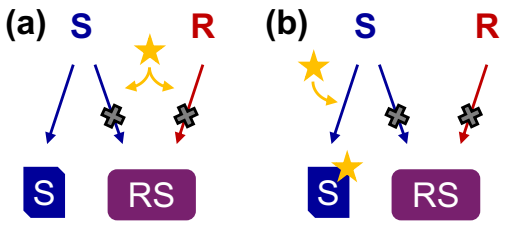


**Figure 3.5.** Additives in chiral crystallization: (a) an additive (illustrated with a yellow star) can inhibit the growth or nucleation of the racemic crystal form or (b) alter the relative stabilities of the conglomerate and racemic compound in favour of the conglomerate crystal form, for instance through co-crystallization. Both approaches may allow (pseudo-)conglomerate behaviour and thus (partial) preferential crystallization.

double polymorphism, i.e. the racemic and enantiopure crystal forms had multiple crystal forms. Harnessing the complicated solid-state landscape, that also featured solid-solution behaviour, they showed that the conformational variability of the crystal unit cells could be an effective kinetic inhibitor of racemate crystal growth. Later they also showed that careful solvent selection can lower nucleation rates so much that a supersaturated solution of the racemate is effectively only able to address its crystallization driving force by growing the provided enantiopure seeds, rather than nucleating and growing racemic crystals. So far, it is unclear whether these strategies can be generalized or are only applicable to very specific systems, but the concepts demonstrated can certainly offer much inspiration in the resolution of racemic compounds through preferential crystallization.



A final noteworthy strategy to apply preferential crystallization to racemic compounds involves the shifting of the eutectic.[114,115] In Magdeburg, Lorenz and colleagues extensively explored how shifts in solvent and temperature or the presence of additives can change the relative (kinetic) stability between the racemic and enantiopure crystal forms, effectively changing the eutectic composition of the system. Inspired by two-step processes in azeotropic distillation, this approach circumvents thermodynamic limitations by likewise splitting the crystallization process into two steps: (i) delivering initial enrichment through a liquid phase of high eutectic composition, and (ii) providing a pure enantiomer in the solid phase under a lower eutectic composition. This work builds on studies by Fogassy in Budapest, who documented how enantiopure solid phases could still be obtained from racemic compounds with appropriate eutectics.[116] Indeed, careful navigation of the phase diagram and eutectic line renders crystallization feasible as a technique to obtain pure enantiomers even from the racemates of racemic compounds.[117]

## Racemization Reactions

After chiral crystallization has been used for separating enantiomers, one still is left with 50% of undesired enantiomer material. One of the disadvantages most often propagated for separation methods, as compared to e.g. asymmetric synthesis or the use of the chiral pool, is this large amount of ‘waste’. One way to address this problem is by introducing a recycling step, implemented through a racemization reaction. The racemization reaction interconverts enantiomers—typically in solution—and allows for turning any leftover undesired enantiomer back into racemic material. At this point, separation can be repeated. After successive steps of separation and recycling, one could theoretically obtain almost 100% yield in the desired enantiomer (Fig. 3.6).

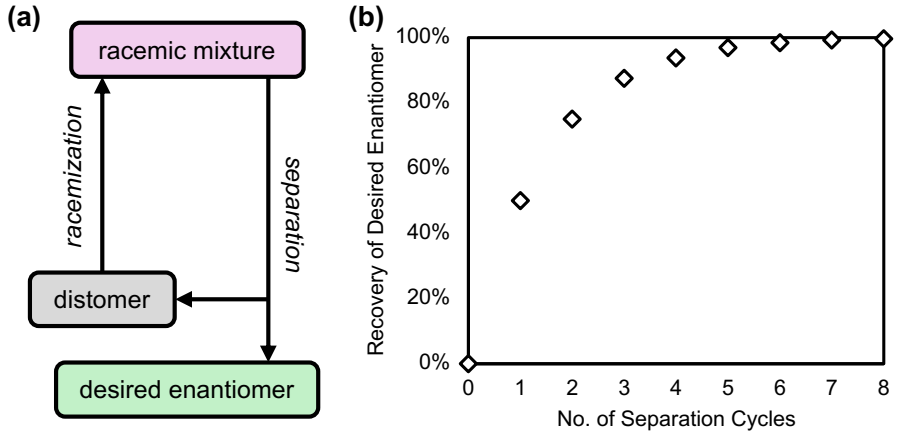


**Figure 3.6.** Through cycles of separation (chiral resolution) and racemization it is theoretically possible to achieve a 100% yield in the desired enantiomer. (a) After separation, the distomer (i.e. undesired enantiomer) is racemized and used as input for a sequential chiral resolution. (b) If a separation step affords the maximum yield of 50%, 8 cycles are required to fully deracemize a racemic mixture.

In 2006, Ebbers and co-workers collected a great number of instances in literature where organic molecules had been racemized.[118] A summary of the main strategies to racemize organic molecules is presented in Figure 3.7, inspired by the seminal overview by Ebbers et al. We will now discuss these four main classical approaches (Fig. 3.7).

First, the use of a base can catalyse the racemization of chiral centres through the abstraction of a proton, forming an achiral $sp^2$ intermediate. Such an intermediate can either be resonance-stabilized through a neighbouring group (e.g. keto, nitrile, or nitro moiety) or function as the first step in an elimination reaction (through the presence of a suitable leaving group). A second approach is the use of acid catalysis. This approach typically follows the formation of an achiral carbocation via a moiety that is a good leaving group upon protonation, or the formation of a double bond (proton rearrangement) through the presence of a heteroatom that can be protonated.

Derived from these basic two approaches are racemization reactions involving Schiff-bases and tautomerisms. A Schiff-base is a special case of imine and is most typically formed by reacting a chiral amine with an aromatic aldehyde (condensation reaction). Such a Schiff-base is especially prone to racemization under either basic or acidic conditions, due to the strong resonance-stabilization of either a carbanion on the chiral centre and the stability of the protonated bridging nitrogen (imine-enamine tautomerism). The Schiff-base approach is heavily used for racemizing amino acids and their derivatives. In fact, the vast majority of naturally occurring amino acids is readily racemized in the presence of catalytic amounts of salicylaldehyde and acetic acid.[119] A similarly effective approach to racemization is found for the keto-enol tautomerism, when a ketone is directly next to the chiral

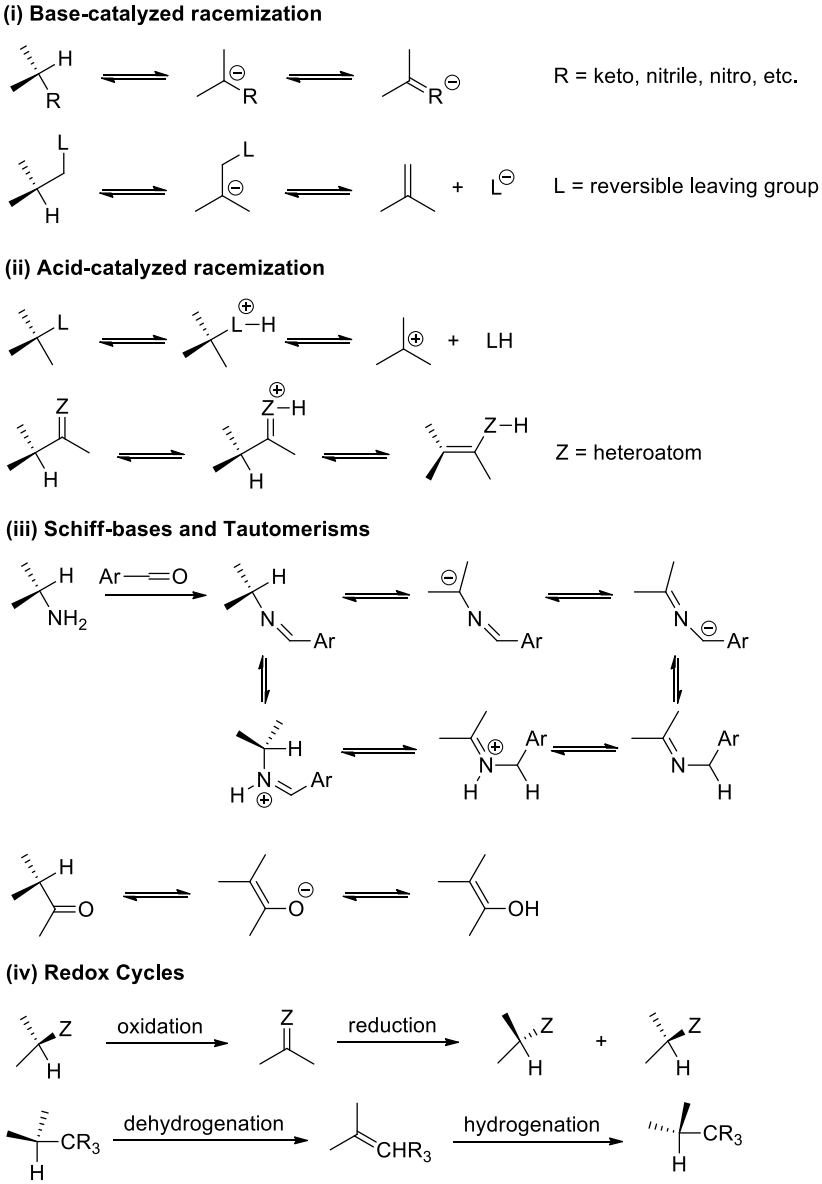


**Figure 3.7.** Overview of the main types of racemization reactions.

centre. Flanking aryl groups greatly aid activation and increase the acidity of the chiral proton, but the proton is also acidic in other variants like amino nitriles. Finally, both tautomerism and Schiff-base can be combined to achieve very efficient racemization under mild conditions, as illustrated by the case of benzodiazepinone.[120]

Having discussed tautomerisms, a related but interesting case is the racemization of ring derivatives that proceeds through resonance-stabilized structures that (i) break

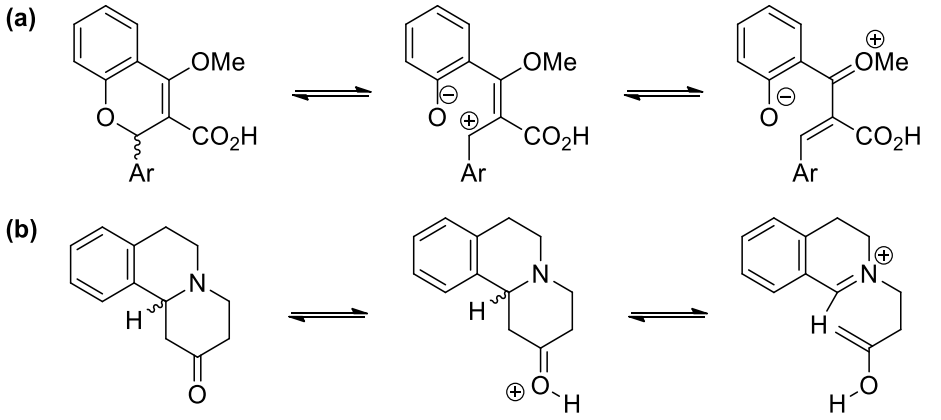


**Figure 3.8.** Examples of racemization reactions by reversible rearrangements involving the opening of chiral rings: (a) formation of a ring-opened zwitterionic intermediate in a cyclic ether; (b) formation of a ring-opened retro-Mannich-type intermediate.

the rotational confinements imposed by the ring and (ii) create an achiral $sp^2$-hybridized intermediate (Fig. 3.8a).[121] Quite similar in concept is racemization through a retro-Mannich-type intermediate (Fig. 3.8b).[122] Likewise, aldol/retro-aldol reactions can also constitute racemization.[123] Further typical classical reversible covalent organic reactions that can be applied in racemization may depend on the reversible formation of hemiacetals, hemiaminals, hemithioacetals, cyanohydrins, nitroaldols, nitrones, N,O-acetals, or N,S-acetals, and the similar aza-Henry or thia-Michael reactions.[124,125]

The fourth strategy has seen especially much development over the last decades and features a redox cycle to induce racemization. Most commonly, a hydrogen is abstracted from a chiral centre by forming a double bond with either an adjacent heteroatom or other carbon (oxidation/dehydrogenation), resulting in an achiral intermediate. Upon reduction or hydrogenation, the chiral centre is restored. When the second step is performed without any chiral catalyst, both enantiomers are formed in equal amounts, completing the racemization redox cycle. This approach is especially common for alcohols at the chiral centre. For many of these cycles, transition metal catalysis is used to achieve the redox cycle, employing Pt, Pd, Ru, or Rh catalysts.[126–128] For benzylic alcohols, however, acidic zeolites can also be effective racemization catalysts in water.[129] The use of two-phase systems is one way of combining both steps of the cycle within one pot.[130] The racemization of secondary alcohols can also be achieved electrocatalytically through iridium-catalysed anodic dehydrogenation and rhodium-catalysed cathodic hydrogenation.[131]

Besides these kind of redox cycles, more types cycles can be used for racemization. In fact, the most famous racemizing cycle is probably the Walden inversion (Fig. 3.9a).[132] In that cycle, two consecutive $S_N2$ reactions with $PCl_5$ and moist $Ag_2O$ invert the stereochemistry of the alcohol. Likewise, the stereochemistry of a halide can be

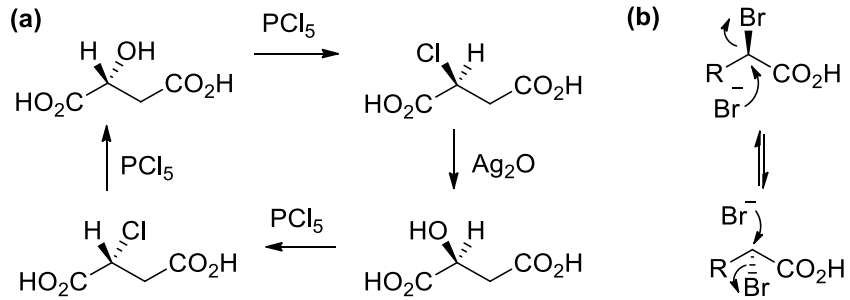


**Figure 3.9.** Racemization through cycles of stereochemical inversions: (a) Walden inversion; (b) consecutive $S_N2$-substitution.



inverted through consecutive $S_N2$ reactions in the presence of its halide salt (Fig. 3.9b).[133] A strategy derived from this principle was used to racemize an E/Z mixture in the presence of acid and bromine.[134] Indeed, many more variants of such continuous cycles of substitutions or elimination-addition reactions can be a viable racemization strategy—reminiscent of the previously mentioned retro-Mannich/Mannich sequence.[123,135,136]

A special case of racemization, that will not be discussed in detail here, is thermal racemization or racemization in the melt.[137] Such racemization is often prevalent for axially chiral structures. E/Z-Photoisomerization is a well-known similar strategy, allowing rotation around double bonds through an excited state. In both cases, however, it is important to note that some confirmations are energetically more favourable, often leading to unequal amounts of the stereoisomers being formed during isomerisation as the back-and-forth rates are not the same.[138,139]

Also worth discussing are the types of reactions featuring in asymmetric catalysis. When such reactions make use of catalysts with chiral ligands, it is often possible to replace those with achiral ligands. In such cases, the reaction can be repurposed to lead to symmetrical results and yield a counterintuitive tool to achieve racemization. Two recent examples of this idea, inspired by previous work on asymmetric photocatalysis, were given by Knowles, and Yamamoto and Akiyama (Fig. 3.10).[140,141] In these mechanisms, the use of light creates a radical that allows inversion of the chirality, either in an $S_N2$-like fashion as we have seen before or by freeing up the possibility to rotate around the bond. Although using light as an reaction ingredient, note that both these examples were developed for application in the context of reactive chiral crystallization. Photocatalysis is not in any way required, though, as evidenced by similar results provided through copper catalysis.[142]

Three main types of photoinduced dynamic radical processes are central to our current toolbox to be used for racemization: radical generation at a chiral centre through (i) C-H abstraction (HAT) or (ii) excited-state electron transfer (SET), and (iii) diradical formation at a double or triple bond (Fig. 3.11).[143] In these processes, a photocatalyst or photosensitizer facilitates electron and/or energy transfer of a

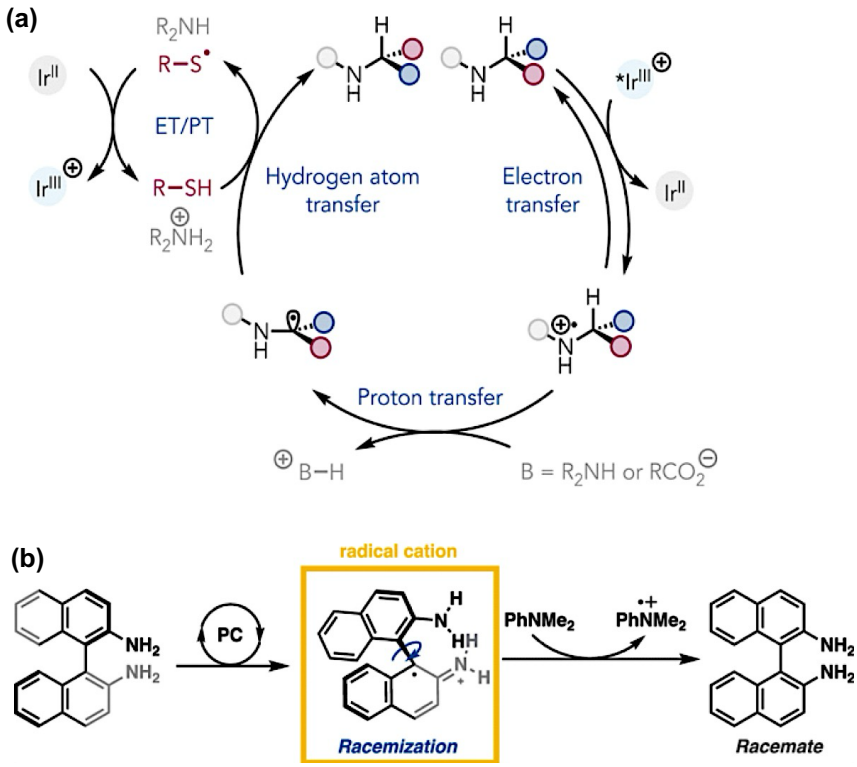


**Figure 3.10.** Racemization through achiral photocatalysis, featuring (a) racemizing α-stereogenic amines via a combination of hydrogen atom, electron and proton transfer with coupled catalysts, reproduced from [140]; and (b) racemizing BINAM derivatives via radical cation species, reproduced from [141].

molecule with another molecule or transfers its own electron to a molecule.[144] Allenes racemize as described previously, through either one of the three mechanisms. Indeed, apart from direct excitation of the allenes, it is also possible to initiate isomerisation of allenes with suitable templates (e.g. lactam) through energy transfer from a photosensitizer, as demonstrated by Bach.[145–147] Racemization of a chiral centre (tetrahedral carbon with C—H) in principle occurs via routes (ii) and (iii), and ultimately works because of a radical or resonant carbanion being formed at that centre, which ultimately allows for the re-addition of a hydrogen atom from either side.[148–152] Note that for chiral catalysis, in contrast, the hydrogen abstraction, re-addition or electron transfer is enantiospecific, leading to deracemization or asymmetric synthesis when using chiral auxiliaries or catalysts.

In these kinds of reactions suitable for racemization, much work has been done on—amongst others—urea derivatives, secondary alcohols, α- and β-ketones, and amines.[153–160] Visible-light-mediated photocatalysis is gaining traction and special reactor designs (including flow chemistry set-ups) are being developed and tested to allow cost-effective transformations at scale.[161] We therefore foresee that many

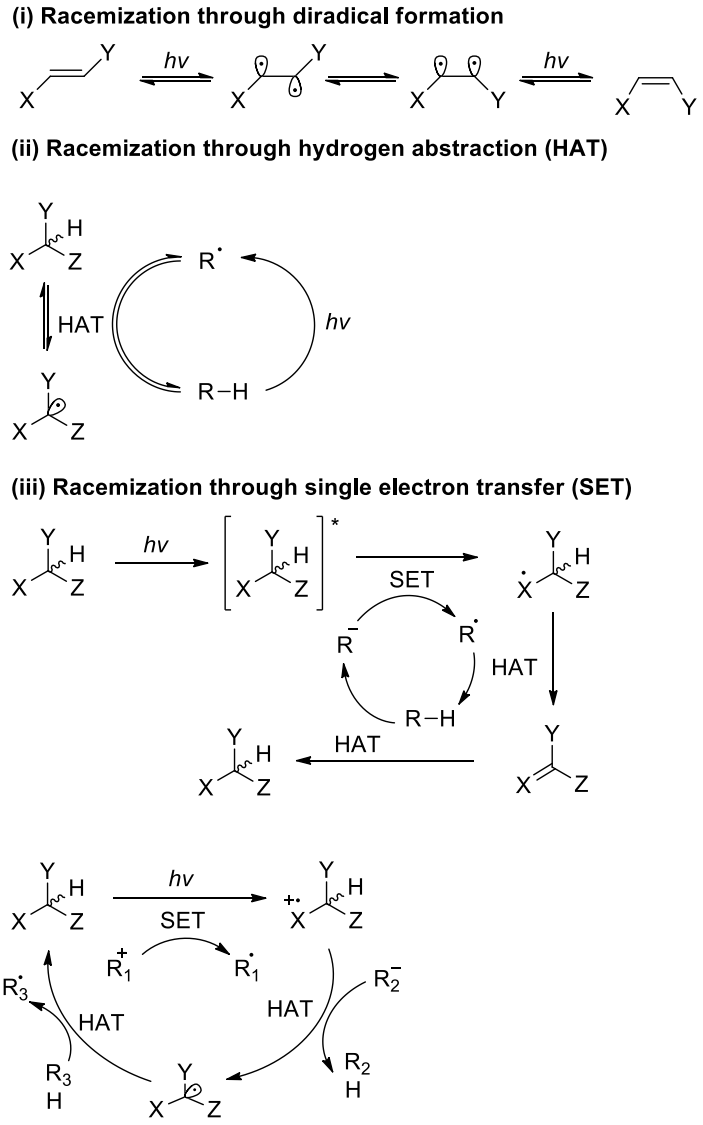


**Figure 3.11.** Main modes of photoinduced dynamic radical processes applied for racemization.

nonenzymatic chiral catalytic deracemizations can be adapted and repurposed as racemization reactions.[162–164] Analogous to inspiration from asymmetric catalytic deracemizations, the wide palette of reaction conditions developed for deuteration and triation of pharmaceutical compounds might likewise be repurposed.[165–168] Rather than using photons as (only) energy source, the use of electrochemistry is also an enticing thought that might broaden substrate scope, although its compatibility with crystallization and scaling-up might poses different challenges.[169–172]

Besides these classical chemical approaches, the use of biocatalysis for racemization has seen increased interest. Over the past decades, efficient mutagenesis methods have emerged that allow widely tuning conditions and substrate scope of enzymes for use in pharmaceutical synthesis.[173] Currently, enzymatic racemization is a common approach for racemizing carboxylic acids, especially a-hydroxy carboxylic acids, which can be racemized through the use of mandelate and lactate racemases.[174] Next to carboxylic acids, much work has naturally been published on the racemization of amino acids and their derivatives through amino acid racemases (AARs).[175] For other types of hydroxyl carbons, epimerases are particularly well known, racemizing specific chiral centres of carbohydrate-like backbones.[176] Besides those well-known biocatalytic racemizations, also several racemases occur in the break down of fatty acids, such as methylmalonyl-CoA epimerase.[177] More niche racemases have been isolated and engineered to racemize activated (e.g. α-hydroxy ketones and α-aminonitriles) and unactivated alcohols and amines.[178] Addressing a major concern, we note that combining enzymatic reactions and crystallization has seen great progress in the past decades.[179,180] In fact, special enzymatic reactors have been developed to combine immobilized enzymes with crystallization to allow biocatalysis as source of the racemization reaction in chiral crystallizations.[181,182]



Closing this section, we note that racemization reactions are also a key component of dynamic kinetic resolutions. Hence, a huge racemization toolbox has already been developed and multiple overviews exist in literature.[123,183–187] Particularly interesting is the fact that various orthogonal approaches have been studied to racemize the same chemical chiral centre, considering compatibility with other processes and reaction conditions. Referring back to such studies is therefore valuable when engineering a process that aims to combine racemization with crystallization conditions. In general, the state of affairs described in this chapter—already in its incomplete summary form—satisfies the conclusion that racemization of the chiral centre of interest does not need at all be the bottleneck in designing a reactive chiral crystallization process.

## Cyclic Preferential Crystallization

In the previous section on racemization reactions, we have already introduced the concept of sequential separation and racemization steps to realize effective deracemization cycles (refer back to Fig. 3.6). This section will briefly hone in on this idea and showcase some work that has been performed to combine racemization reactions and preferential crystallization. This will be the preliminary to discussing direct crystallization-induced deracemizations (CIDs)—which is the focus of the final two sections of this chapter and the core process studied in this thesis.

Early adoption of the combination of crystallization and racemization featured a sequential implementation of preferential crystallization for separation and

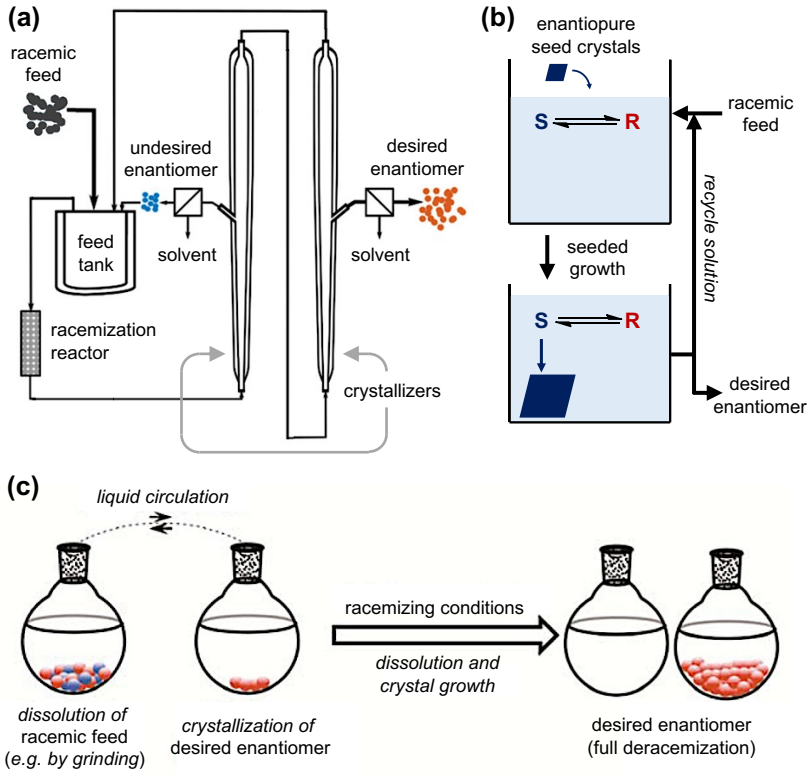


**Figure 3.12.** Combining racemization and preferential crystallization: (a) sequential steps of separation and racemization for recycling of the undesired enantiomer in a modern continuous implementation (adapted from [194]); (b) preferential crystallization under racemizing conditions allows direct partial deracemization; (c) adding the in-situ dissolution of the racemic feed provides a constant supply of undesired enantiomer to be converted by preferential crystallization, allowing full autonomous direct deracemization through crystallization under racemizing conditions in semi-continuous fashion (adapted from [84]).

racemization for recycling of the undesired enantiomer, such as in the industrially relevant cases of galantamine and calcium (*R*)-pantothenate.[188–190] A more autonomous version of such a cyclic process was featured by Engwerda et al. for the deracemization of the Antimalaria Drug Mefloquine, where continuous feedback-loops between the crystallizer, racemization reactor, and feed tank were introduced to affect deracemization.[191]

Drawing from their work integrating biocatalytic racemization with chromatography,[192] Lorenz and Seidel-Morgenstern combined separation via Fluidized Bed Crystallization and racemization to affect the continuous production of enantiomers (Fig. 3.12a).[193–195] The concept is as follows: a racemic feed is continuously dissolved into a feed tank. The feed first passes through a crystallizer that preferentially crystallizes the undesired enantiomer. Having obtained a feed maximally (i.e. within the bounds of the metastable zone) enriched in the desired

enantiomer, the desired enantiomer is then obtained through a second preferential crystallization in the following crystallizer. Note that the undesired enantiomer crystals that are separated from the racemic feed in the first crystallizer are reintroduced into the feed tank. Through racemization in an inline racemization reactor the undesired enantiomer is then partially converted into the desired enantiomer, constituting the effective chemical component of the deracemization.

Rather than using an inline racemization reactor to effectively recycle the undesired enantiomer, one can also apply racemization directly in tandem with preferential crystallization (Fig. 3.12b). In such preferential crystallization under racemizing conditions, seed crystals of the desired handedness are used to induce the growth of enantiopure crystals from a supersaturated racemizing solution. Because the supersaturations of the two enantiomers are coupled through the racemization equilibrium, undesired enantiomer molecules are directly converted into the desired enantiomer. Deep cooling is possible to attain high yields, since much less supersaturation builds up in the undesired enantiomer as compared to the approach in Fig 12a and the risk of nucleation is thus low (i.e. as long as appropriate cooling rates are maintained). In batch mode, only one crystallizer is required. After the enantiopure material is collected, the reactor can be heated and fresh racemic feed introduced. Through such cycles of preferential crystallization under racemizing conditions semi-continuous deracemization of a racemic feed can be achieved, although the process can be relatively slow.

Hein and Rougeot reviewed such preferential crystallization processes featuring in-situ racemization.[84] An important next innovation to be considered is the introduction of a dissolution process in tandem with the preferential crystallization (Fig. 3.12c). By continuously dissolving a racemic feed in a first reactor, continuously crystallizing the desired enantiomer in the second, and circulating the racemizing liquid between the reactors, full consumption and deracemization of the feed is readily achieved and under within much shorter times. Simultaneous dissolution and growth can be achieved through grinding in the first reactor (i.e. using the Gibbs-Thomson effect) or through a temperature difference (i.e. maintaining a higher temperature in the first reactor). This implementation could allow for steady-state operation, facilitating true continuous deracemization.

A challenge in combining preferential crystallization and racemization directly in the same reactor is the compatibility of conditions, which is in fact a more general problem already eluded to in our introduction to reactive crystallization in chapter 2. Kellogg and co-workers faced this issue for a Praziquantel derivative which could be racemized through dehydrogenation-hydrogenation cycles—an interconversion commonly considered incompatible with crystallization (Fig. 3.13). To solve this incompatibility successfully, they used a loop to perform in-tandem racemization outside of the crystallizer in a flow reactor (essentially a packed bed of Pd on carbon

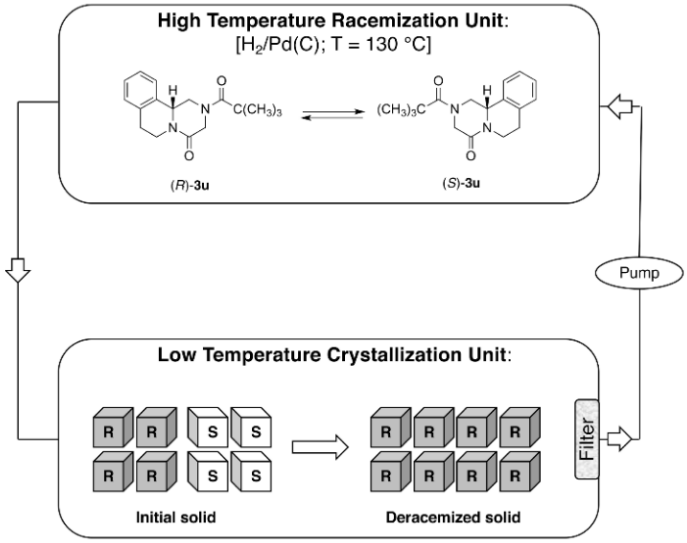


**Figure 3.13.** Racemization in-tandem with crystallization under incompatible conditions through a flow-reactor loop, as reported by Kellogg and co-workers for a Praziquantel derivative in ref. [46].

activated with $H_2$ at 130 °C).[46] This work importantly showed the possibility of spatially decoupling the racemization and crystallization conditions while still upholding the essential kinetic link between the two processes. Not much later, a medicinally-relevant benzopyran was even racemized through photochemistry via a type of retro-Claisen pathway within an oscillating flow reactor loop connected to a crystallizer.[196] Although less intrinsically problematic, similar work was performed to combine the racemization of e.g. amines and amino acids with crystallization through racemization loops.[182,197,198] Through such racemization-loops, one could in principle unleash the full potential of the wide array of racemization reactions discussed in the previous section on the preferential crystallization of chiral molecules to affect their deracemization.

In this section, we have gradually transitioned from isolated preferential crystallization for separation, to continuous deracemization through combining in-situ racemization with crystallization. Intrinsically, however, all these processes have featured one or more crystallizers in which only crystal growth occurs. The kinetics of dissolution and growth were technically coupled but not fully integrated. Indeed, the innovation of using continuous dissolution to fully and steadily required a separate dissolution reactor. The final innovation to discuss, therefore, is combining all three processes—crystal growth, dissolution, and racemization—within the same reactor. This will yield the purest form of crystallization-induced deracemization, and as such will be explored in the final sections of this chapter.

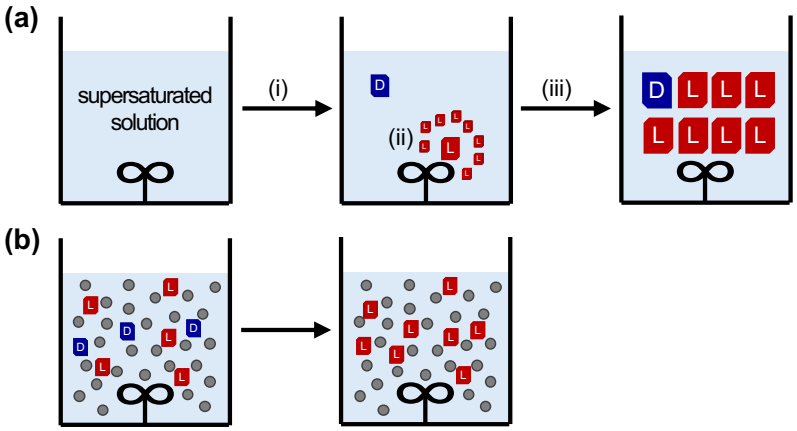


**Figure 3.14.** Spontaneous symmetry breaking (panel a) and the solid-state deracemization of achiral salts (panel b). In panel a, vigorous stirring induces the nucleation of a supersaturated solution (step i), followed by autocatalytic secondary nucleation to induce symmetry breaking (step ii), which then yields a virtually enantiopure solid upon growth (step iii). Although a point of contention, secondary nucleation by itself likely cannot fully explain the results observed by Kondepudi and McBride.[204] In panel b, glass beads induce strong attrition and continuous cycles of dissolution and growth to achieve deracemization of a racemic solid-phase slightly enriched through e.g. a symmetry breaking event.

## Crystallization-Induced Deracemizations

Let us wind back the clock to 1954 and recall a fascinating post-war experiment by Dutch scientist E. Havinga in Leiden.[199] Challenging the pertaining view at that time that a chiral racemic system does not spontaneously break symmetry, he reported on quaternary ammonium iodide salts crystallizing consistently as chiral crystals with a net optical activity—indicating spontaneous symmetry breaking!

Decades later, in the 1990's, Kondepudi and McBride again reported on such spontaneous resolution by stirred crystallization, this time of achiral $NaClO_3$ solutions.[200,201] It was Cristobal Viedma who then discovered, in the early 2000's, that cyclic crystal growth and dissolution via attrition can be used to fully deracemize such a $NaClO_3$-system initially comprised of both left- and right-handed crystals.[202,203] An overview of these experiments is provided in Figure 3.14. Later, attrition-enhanced deracemization was also demonstrated for achiral organic molecules that form chiral conglomerate crystals.[6]

Viedma's seminal deracemization experiments pertained to a system with strong attrition through grinding. Such grinding breaks up crystals into smaller fragments and thereby both promotes secondary nucleation and provides a driving force for dissolution through the Gibs-Thomson effect. Attrition moves the system out of equilibrium: Solute molecules originate from very small crystal fragments whose solubility surpasses the equilibrium solubility. As a consequence, the system becomes locally supersaturated and simultaneously experiences a driving force for growth. Attrition therefore can be a very effective method to enact continuous cycles

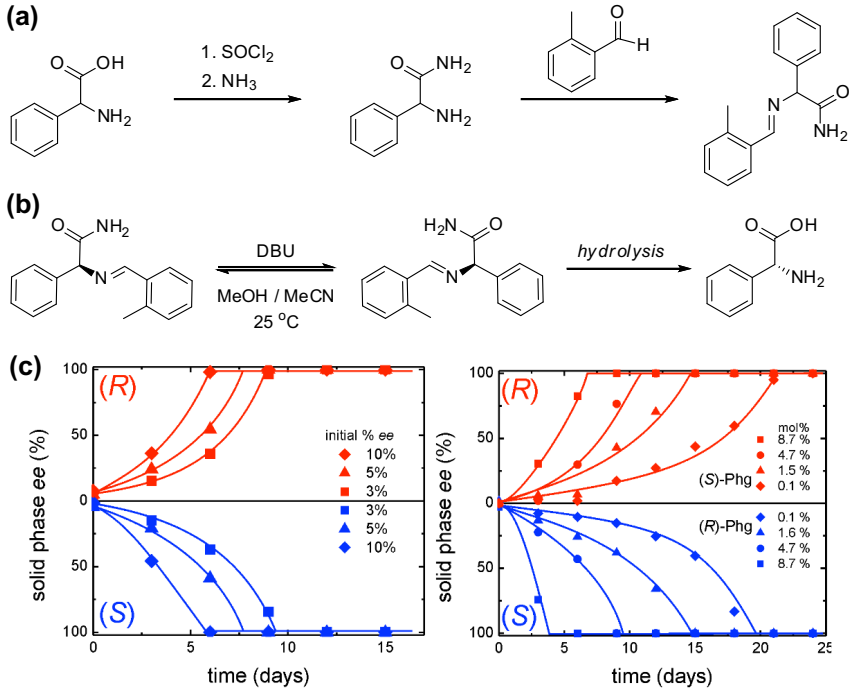


**Figure 3.15.** Solid-state deracemization of a phenylglycine Schiff-base derivative by Noorduin and co-workers:[209] (a) phenylglycine is converted into a conglomerate by forming the amide and derivatizing with an aldehyde to form a racemizable Schiff-base;† (b) the conglomerate Schiff-base is racemized using DBU (organic base)—note that the amino acid can be reacquired after deracemization through hydrolysis with retention of stereochemistry; (c) solid-state deracemization was achieved through grinding a slurry with glass beads under racemizing conditions, with the direction of chiral amplification directed by an initial enantiomeric excess (left) or addition of an enantiopure additive (right; panel c is reproduced from [209]).

of crystal dissolution and growth.[205] It has been shown that increasing the rate of attrition increases the deracemization kinetics.[206] Note, however, that attrition is not required for continuous dissolution and growth. In fact, the growth and dissolution of crystals always takes place, even without explicit fluctuations in temperature or concentration and even without explicit attrition.[207] This is a key notion underpinning thermodynamic ripening processes such as Ostwald-ripening.[208]

Following the discovery of attrition-enhanced deracemization, Noorduin and co-workers attempted to apply the same principles to the deracemization of a chiral organic molecule.[209] They opted for the pharmaceutically relevant amino acid phenylglycine (Phg) and used Schiff-base formation to generate a library of derivatives, of which one formed a conglomerate (Fig. 3.15). They then achieved the common solution resource pool inherent to achiral salts by affecting fast interconversion of enantiomers in solution through a base-catalysed racemization

† In the industrial process realized at DSM, the Phg-amide Schiff-base was directly formed through Strecker synthesis followed by selective aminonitril hydrolysis in the presence of 2-methylbenzaldehyde.

reaction. Finally, continuous nucleation, growth and dissolution was implemented through grinding—analogous to Viedma—by stirring the racemic slurry in the presence of glass beads. Starting with 10% *ee* in (*R*)- or (*S*) of the Phg-conglomerate derivative, the result was a spontaneous deracemization over the course of 5 days, after which the enantiopure resulting solid was obtained by filtration. This process for deracemizing chiral organic molecules can also be implemented differently to achieve much faster deracemization kinetics, e.g. mechanochemically,[210] using sonication,[206,211] or using an industrial bead mill.[212]



Besides continuous attrition, the cycles of growth and dissolution driving such crystallization-induced deracemization can also be achieved through spatial or temporal temperature cycling.[213–215] Such a methodology has advantages and disadvantages in respect to—among others—deracemization time, scalability, and compatibility with racemization conditions. Interesting to note is the use of an immobilized enzyme to affect racemization in deracemization through temperature cycling.[182] Palmans has provided a very useful summary of the first developments in crystallization-induced and other deracemizations under kinetic and thermodynamic control.[216]

Although conglomerate formation is rare and finding compatible racemization conditions might seem tedious—two aspects generally considered essential prerequisites for crystallization-induced deracemization to be feasible—numerous successful examples have been reported in literature to date, among which a wide array of chiral organic molecules. Figure 3.16 shows a selection of such successful examples (note that molecules mentioned previously in this introduction have not been repeated here). The diversity among the deracemized entries is quite remarkable. The interested reader is also directed to an early overview of molecules deracemized through more conventional SOATs compiled by Yoshioka.[185]

Also worth mentioning is CID during the in-situ formation of a (racemizable) conglomerate as a result of synthesis, such as in the famous case of naproxen as well as other reports.[224–227] These examples have also been submitted as being relevant to discussion on the origin of biological homochirality, when the in-situ deracemized chiral conglomerate emerges as a product from achiral reactants. Besides biological relevance, such processes are also very efficient and take away the disadvantage of a separate deracemization process step. Crystallization-induced deracemization combined with in-situ (conglomerate) product formation is indeed a reactive crystallization in the most elegant sense.

This introduction will not discuss all the practical considerations of executing crystallization-induced deracemizations. An important point is that primary nucleation should be avoided and secondary nucleation is generally beneficial.[228] Useful to know is that deracemization kinetics generally increases linearly with

racemization kinetics and is similarly slowed by increased solid loading (slurry density) and growth-dissolution cycling intensity (i.e. the amount of material cycled between solid and liquid phase per unit time).[206,229] Also a particularly common feature of deracemization kinetics is the sigmoidal shape of the curve, especially for temperature cycling: deracemization slows down when reaching higher enantiopurity in the solid phase. The origins of this effect have not yet been very well understood, but may be related to changes in the crystal size distribution. The presence of impurities—also from previous deracemizations!—can greatly affect the deracemization process, as with any crystallization.[230–232] Finally, the order of process steps (e.g. starting attrition, choosing whether to begin growth or dissolution, when to add the racemization catalyst, etc.) can have effects on the course of the deracemization.[233]



Although we have mainly discussed crystallization-induced deracemization as pertaining to conglomerates, the process can also be applied to diastereomers and co-crystals,[123,234–237] solid-solutions,[238,239] and isotopes.[240] Moreover, epitaxial conglomerates can also be deracemized by crystallization-induced deracemization

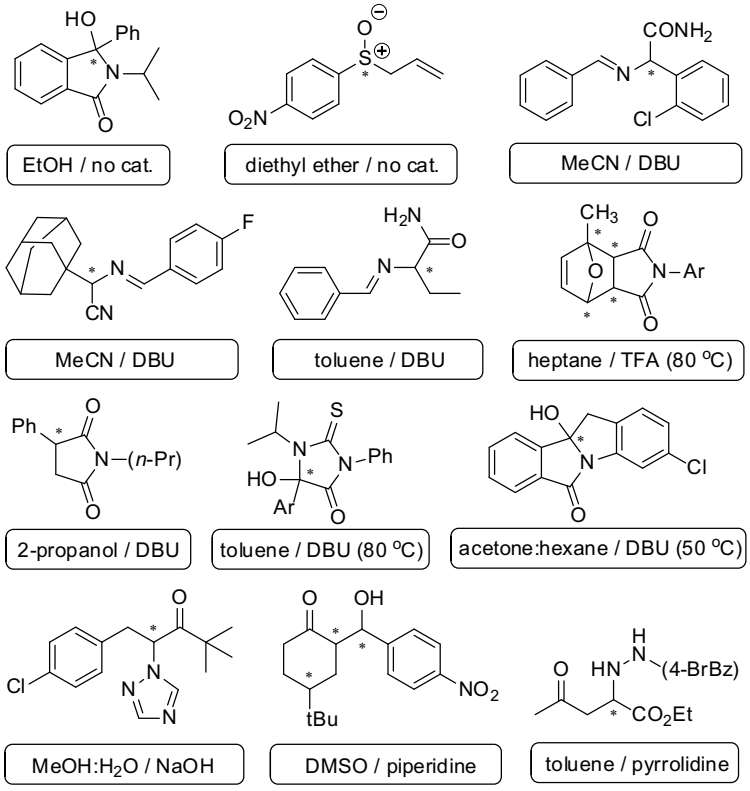


**Figure 3.16.** Selection of 12 chiral organic molecules deracemized through crystallization-induced deracemization (in arbitrary order) from refs. [41,43–45,135,217–223]. The conditions of racemization have been indicated for each entry as well as the chiral centre(s) using an asterisk (*).

under conditions of heavy attrition, such as imposed by grinding, since this effectively gives crystallization access to the individual enantiopure domains.[99] Beyond organic molecules, also chiral metal clusters and complexes,[241–243] supramolecular chiral polymer assemblies,[244,245] and nanocrystals[246] can be deracemized through a similar mechanism.

## Mechanistic Musings

A plethora of reports have observed, implemented or aimed to even optimize crystallization-induced deracemizations. A lingering question yet remains: what is the fundamental driver behind this fascinating process? In the section on reactive crystallization in chapter 2, we noted the general criterion that the product of the coupled equilibria of solubility and interconversion is deterministic for convergence. For crystallization-induced deracemizations of conglomerates, however, the inherent solubilities and reaction and crystallization rates of the two populations are the same. We will therefore end this final introductory chapter by summarizing the main mechanistic explanations that have been offered so far to address this puzzling phenomenon. This canvass will also clarify some of the key experimental questions addressed in this thesis.

Importantly, deracemization requires some form of asymmetry, causing a ratcheting effect that compounds chiral amplification. Indeed, without any such asymmetry, the cycles of growth and dissolution would be fully reversible, and there would be no possibility to achieve chiral amplification. We therefore classify the proposed mechanisms by the asymmetry on which they rely: (1) autocatalytic enantiospecific agglomeration or incorporation of clusters; (2) autocatalytic enantiospecific secondary nucleation; (3) a difference in stability between the enantiomer crystal populations; (4) a difference in the mechanisms of growth and dissolution; and (5) a difference in the rates of growth and dissolution.

Before discussing these mechanisms, we note that most work in this regard has been theoretical or has relied heavily on simulations. Indeed, relatively little experimental work has been published that really homes in on the mechanism of crystallization-induced deracemizations. Most studies tend to derive a hypothesis consistent with the characteristic exponential kinetics of deracemization, but unfortunately such exponential behaviour is insufficient to discriminate between the various models.[247] Some other aspects, like crystal size distributions and the solution enantiomeric excess, have given some further clues but all still are relatively indirect forms of evidence. One critical notion not often voiced is the possibility that multiple valid mechanisms may be at play under different conditions of deracemization, some perhaps even acting at the very same time and amplifying each other. These introductory remarks serve as general caution when discussing the ‘the mechanism’.

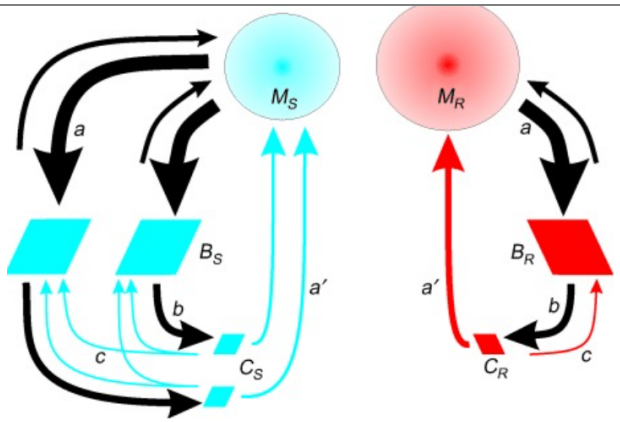


**Figure 3.17.** Schematic overview of the cluster model during attrition-induced (process *b*) continuous dissolution and growth (process *a*) reproduced from ref. [247]. The reincorporation of small clusters occurs statistically more frequently for the major population (*S*, left and blue) in the solid phase (process *c*), leading to an asymmetry between growth and dissolution rates of the populations that amplifies the majority chirality in the solid-state.

The first mechanism we should discuss is rooted in the formation of chiral clusters and their enantiospecific incorporation or agglomeration. Endeavouring to explain the emergence of homochiral $NaClO_3$ during abrasive grinding observed by Viedma and test Viedma's idea of clusters being involved in the mechanism, he proposed a set of equations that described (Fig. 3.17, visualized for a racemizing conglomerate).[248–250] In this model, a cluster is smaller than the critical nucleus of the crystal and therefore exhibits a fleeting presence. The statistically more frequent incorporation of majority clusters rescues those more often from rapid dissolution and racemization. Note that this mechanism effectively favours the growth of the majority enantiomer and thus relatively increases the growth rate of the majority enantiomer compared to the minor enantiomer, all the while not altering the balance in their dissolution rates. The resulting asymmetry then explains the chiral amplification and observed non-linear kinetics.[251] Recalling the discussion on Frank's view on autocatalytic chiral amplification introduced in chapter 1,[252] we note that Ribo has classified this mechanism as autocatalytic, as he regards the dissolution of chiral clusters into effectively achiral monomers as a form of mutual inhibition.[253,254]

The cluster mechanism has been contentious, as the 'subcritical clusters' are often said to be hard or impossible observe experimentally, so that direct evidence is lacking. Countering this objection, Iggland and Mazzotti used simulations to show that the same mechanism also works on the level of macroscopic enantiospecific agglomeration.[255] Experiments by Noorduin also further argued in favour of the cluster mechanism, as it could explain a persistent solution-phase enantiomeric excess during grinding present under conditions without racemization.[247] More complicated is the situation without explicit attrition or high supersaturation, as this would require the existence of thermodynamically omnipresent clusters.[256,257] This idea of stable 'thermodynamic' clusters is perhaps unconventional, but definitely not

new in discussions on non-classical nucleation and crystal growth.[258–262] Recent advances in experimental methodology have only strengthened the evidence for clusters and agglomerative crystal-growth as common non-classical pathways.[263–266] Interesting further experimental evidence comprises reports of deracemization on the cluster level,[267] enantiomer-specific oriented attachment (ESOA) of $NaBrO_3$ and $NaClO_3$,[268] enantioselective facet recognition in millimeter-sized gypsum crystals,[269] and ESOA in organic molecules.[270–272]



Another autocatalytic mechanism to explain deracemization was proposed based on enantiospecific secondary nucleation. Saito and Hyuga introduced the theoretical concept of enhanced chirality changes on the crystalline surface.[273] In that model, the crystals act quite classically as auto-catalysts and induce chiral amplification. The idea that the chirality of an enantiomer is more easily flipped on or near the surface a crystal of that opposite enantiomer inspired Skrdla to propose enantiospecific secondary nucleation as a different implementation of that idea.[274] Rather than the chemical conversion (i.e. the interconversion of enantiomers—which is also notably absent in achiral conglomerate systems) occurring in a different fashion near or on a crystal surface, Skrdla proposed that parts of crystals are continuously chopped off (i.e. the formation of secondary nuclei) and that this occurs more often for the major enantiomer because it is present in larger amounts after initial symmetry breaking. These nuclei then grow further, providing a sink for their source enantiomer. Rather than involving cluster formation and enantiospecific incorporation or agglomeration, the mechanism focusses on fast-growing enantiopure satellites.

Building on the argument that secondary nucleation is the main nucleation mechanism in suspensions and can be autocatalytic,[275] experimental work showed that deracemization kinetics were co-optimized by optimizing the conditions for secondary nucleation and the authors also found further evidence in the evolution of particle size distributions.[228] Surface-catalysed secondary nucleation processes have also been used to explain chiral amplification in polymer systems.[276] Secondary nucleation, however, is controversial if conditions that promote breakage (such as attrition or stirring) are absent. De Vrieze has recently shown, through very systematic study, that crystal breeding under such calm conditions is not observed.[277] A further experimental investigation into the conditions under which stereoselective secondary nucleation could be a valid mechanism for chiral amplification should thus tested by studying the deracemization kinetics with and without mixing or attrition present.

A mechanism very different to dynamic autocatalysis is one that hinges on differences in stability between the two enantiomer crystal populations, effectively banking on a thermodynamic driving force that favours the enantioconvergent transformation into the more stable population. We will neglect the origins of

symmetry breaking, and start with two enantiomeric crystals populations that are identical in all aspects but their number: The population with more crystals is the major enantiomer. One may then wonder how these two populations have thermodynamically different stabilities? Through the detachment from and re-attachment of molecules onto other crystals—a microscopically continuous stochastic process—the crystals will inevitably exhibit a shift in size distribution and grow into fewer but larger crystals. Because the number of majority crystals is higher, this shift occurs more rapidly for them, and a disparity in sizes between the populations ensues. Now, ripening mechanisms may take over and provide a thermodynamic driving force for deracemization, as the majority enantiomer population of larger crystals is thermodynamically more stable (Gibbs-Thomson effect).



Although simulations show the viability of this mechanism for deracemization,[278] a criticism often voiced is that specific experimental features seen in attrition-induced deracemization are not reproduced.[279] Indeed, the typical sigmoidal behaviour of deracemization kinetics seen under such conditions requires a chiral feedback mechanism in the model, that is lacking for simple ripening.[251,280,281] This may not necessarily be an actual issue and reason to discount thermodynamic ripening as a deracemization mechanism: some mechanisms may be more prevalent under certain conditions than others and transitions could be observed. Indeed, ripening could be a major source of amplification at low supersaturation, while clusters or enantiospecific agglomeration drive the process at high supersaturation. Besides, many variants of ripening mechanisms exist, and they can also be sped up through active cycles of growth and dissolution.[208]

Another thermodynamic notion that is little explored is that of non-ideal solution behaviour of enantiomers. Molecular interactions in solution may cause asymmetric driving forces for crystal growth and dissolution when mixed in unequal amounts. It is well known that the solubility rule is not always strictly adhered to for conglomerates, providing prime indications that non-ideal solution behaviour is on the horizon. Of course this is not a fundamental driver of deracemization as its prevalence will differ from molecule to molecule and has no place in systems containing achiral conglomerates.

Another question that has not been explored particularly well in the context of deracemization mechanisms is that of asymmetries between the mechanisms of crystal growth and dissolution. Hysteresis in crystal growth/dissolution cycles has been well-established, with impact on particle counts, size distribution, and crystal shapes.[282–285] Such cycles can lead to very different outcomes than ripening effects and *ab initio* equilibrium crystallization.[286,287] Although this holds for many if not all crystals, an special feature of non-centrosymmetric growth units are the stable and unstable edges, which can lead to asymmetric growth spirals on their surfaces.[288] The

irreversibility of the mechanisms of growth and dissolution might be an interesting, universal, starting point for an asymmetry that can lead to chiral amplification. Especially interesting is the consideration of stochastic effects such as those resulting from growth-rate dispersion, which has seen some attention on the modelling front.

Growth-rate dispersion (GRD) pertains to the phenomenon that crystals which are initially seemingly identical, at least of shape and size, can exhibit different growth rates under the same growth conditions.[289] Although the origins of this phenomenon are elusive, it is often encountered and quite an intrinsic effect. One explanation is that the growth rates of facets are continuously oscillating and stochastics related to dislocations can greatly affect the average growth rate observed. An effect often related to GRD is the frequent observation that small crystals do not grow at all under conditions that does induce growth of their larger neighbours, an effect described as 'size-dependent growth'.[289] These effects have been integrated into models through rate diffusivity factors and have been attempted in modelling crystallization-induced deracemization processes through cycles of growth and dissolution.[290,291] Although these models leave out breakage, agglomeration and nucleation, they still predict full deracemization (cycles of growth and dissolution are induced through temperature fluctuations). To explain these findings, we note that such dispersive effects do not occur during dissolution like they do during growth, creating an intrinsic asymmetry that can allow chiral amplification. Critically, we note that, in these simulations based on GRD as a mechanism, different extends of GRD were required for the enantiomer populations to affect full deracemization (but notably not different mean growth rates), which might be practically caused by stochastics in nucleation and growth, minor additive effects, or the preparation history of the solids (especially the excess seeds added or spontaneously formed). Recently observed experimental phenomena like chiral flipping might indeed require stochastic factors in crystal growth and dissolution to be explained, perhaps through fluctuations in crystal size distribution or growth rate dispersion.[292]

The last class of proposed mechanisms relies on an intrinsic asymmetry between the rates of crystal growth and dissolution, as recently argued by Uwaha and Katsuno.[279] They noted that, during dissolution, the majority enantiomer dissolves more than the minority, due to their different cumulative crystal surface areas. Because supersaturations are coupled through the racemization reaction, this means that major enantiomer is converted into minor enantiomer during dissolution. During growth, however, the reverse process occurs and the majority grows faster than the minority. Because the rates of crystal growth and dissolution are unequal, and dissolution is faster than growth, this cycle is not reversible and favours the amplification of the major enantiomer during growth, rather than its erosion during dissolution. A recent study by Deck and co-workers used population balance



(eq. 3.2)

modelling to show the viability of this hypothesis.[293] Importantly, this mechanism relies on the difference between the relative rates of growth ($k_g$) and dissolution ($k_d$) compared to the racemization rate ($k_r$) and requires that for deracemization:

$$\frac{k_d}{k_r} > \frac{k_g}{k_r}$$

Therefore, this mechanism can be an apt driver for deracemization under conditions where the rate of racemization is comparable to the kinetics of crystallization, but it will not suffice to explain chiral amplification when racemization is non-limiting ($k_r \rightarrow \infty$), such as for achiral molecules or salts crystallizing as conglomerates. Indeed, we foresee that the interplay between the rates of racemization and crystallization can be a powerful amplifier of chirality, but cannot not constitute a fundamental driver of deracemization. An interesting question therefore is whether the increasing deracemization efficiency experimentally observed with increasing racemization rate has a limit and which process then limits it.[206]



The aforementioned summary of mechanistic musings exposes two key open experimental questions that have so far been left wholly unanswered: (i) under which conditions does crystallization-induced deracemization occur, and (ii) is the asymmetry affecting deracemization located in the growth or dissolution step. Moreover, aspects like crystal size have received little experimental attention among the few studies on this topic. This thesis will therefore dive into those questions, beginning with a disentanglement of the growth and dissolution steps (Chapter 4 and 6) and a thorough consideration of size effects in crystallization-induced deracemizations (Chapter 5). Ultimately, we will show that the key in achieving enantiopurity lies in combining the right conditions and processes to leverage kinetic insight and control.[294,295] We foresee such a perspective is imperative in expanding the scope of crystallization-induced deracemizations from mere conglomerates to stable racemic compounds. It is that mission which motivates this thesis.

## References


(1) Jacques, J.; Collet, A.; Wilen, S. H. *Enantiomers, Racemates, and Resolutions*, Reissue with corr.; Krieger: Malabar, Fla, 1994.

(2) Intaraboonrod, K.; Lerdwiriyanupap, T.; Hoquante, M.; Coquerel, G.; Flood, A. E. Temperature Cycle Induced Deracemization. *Mendeleev Commun.* **2020**, *30* (4), 395–405. https://doi.org/10.1016/j.mencom.2020.07.002.

(3) Putman, J. I.; Armstrong, D. W. Recent Advances in the Field of Chiral Crystallization. *Chirality* **2022**, *34* (10), 1338–1354. https://doi.org/10.1002/chir.23492.

(4) Saseendran, A. S. K.; Jayaraj, H.; Kartha Kalathil, K.; Sarala, A. S. Crystallisation Based Deracemisation and Chiral Resolution of Small Molecules. *Chem. – Asian J.* **2025**, *20* (7), e202401465. https://doi.org/10.1002/asia.202401465.

(5) Kostyanovsky, R. G. Impossible Things in Stereochemistry. *Mendeleev Commun.* **2004**, *14* (6), 229–230. https://doi.org/10.1070/MC2004v014n06ABEH002104.
(6) McLaughlin, D. T.; Nguyen, T. P. T.; Mengnjo, L.; Bian, C.; Leung, Y. H.; Goodfellow, E.; Ramrup, P.; Woo, S.; Cuccia, L. A. Viedma Ripening of Conglomerate Crystals of Achiral Molecules Monitored Using Solid-State Circular Dichroism. *Cryst. Growth Des.* **2014**, *14* (3), 1067–1076. https://doi.org/10.1021/cg401577m.
(7) Brock, C. P.; Dunitz, J. D. Towards a Grammar of Crystal Packing. *Chem. Mater.* **1994**, *6* (8), 1118–1127. https://doi.org/10.1021/cm00044a010.
(8) Filippini, G.; Gavezzotti, A. A Quantitative Analysis of the Relative Importance of Symmetry Operators in Organic Molecular Crystals. *Acta Crystallogr. B* **1992**, *48* (2), 230–234. https://doi.org/10.1107/S0108768191011977.
(9) Pidcock, E. Achiral Molecules in Non-Centrosymmetric Space Groups. *Chem. Commun.* **2005**, No. 27, 3457. https://doi.org/10.1039/b505236j.
(10) Kikkawa, S.; Okayasu, M.; Hikawa, H.; Azumaya, I. Effect of Halogen Bonding on Chiral Assemblies of Achiral Sulfonamide Molecules in the Crystalline Phase. *Cryst. Growth Des.* **2021**, *21* (2), 1148–1158. https://doi.org/10.1021/acs.cgd.0c01469.
(11) Kikkawa, S.; Maeno, I.; Katagiri, K.; Murayama, Y.; Nozawa, M.; Hikawa, H.; Azumaya, I. High Proportion of Chiral Crystallization of Achiral Indolyl Sulfonamides: Effect of Intermolecular Interactions. *Cryst. Growth Des.* **2021**, *21* (8), 4380–4389. https://doi.org/10.1021/acs.cgd.1c00305.
(12) Killalea, C. E.; Amabilino, D. B. Stereochemistry and Twisted Crystals. *Isr. J. Chem.* **2021**, *61* (9–10), 629–644. https://doi.org/10.1002/ijch.202100063.
(13) Matsuura, T.; Koshima, H. Introduction to Chiral Crystallization of Achiral Organic Compounds. *J. Photochem. Photobiol. C Photochem. Rev.* **2005**, *6* (1), 7–24. https://doi.org/10.1016/j.jphotochemrev.2005.02.002.
(14) Chen, D.; Porada, J. H.; Hooper, J. B.; Klittnick, A.; Shen, Y.; Tuchband, M. R.; Korblova, E.; Bedrov, D.; Walba, D. M.; Glaser, M. A.; Maclennan, J. E.; Clark, N. A. Chiral Heliconical Ground State of Nanoscale Pitch in a Nematic Liquid Crystal of Achiral Molecular Dimers. *Proc. Natl. Acad. Sci.* **2013**, *110* (40), 15931–15936. https://doi.org/10.1073/pnas.1314654110.
(15) Oswald, S.; Seifert, N. A.; Bohle, F.; Gawrilow, M.; Grimme, S.; Jäger, W.; Xu, Y.; Suhm, M. A. The Chiral Trimer and a Metastable Chiral Dimer of Achiral Hexafluoroisopropanol: A Multi-Messenger Study. *Angew. Chem. Int. Ed.* **2019**, *58* (15), 5080–5084. https://doi.org/10.1002/anie.201813881.
(16) Xiao, W.; Ernst, K.-H.; Palotas, K.; Zhang, Y.; Bruyer, E.; Peng, L.; Greber, T.; Hofer, W. A.; Scott, L. T.; Fasel, R. Microscopic Origin of Chiral Shape Induction in Achiral Crystals. *Nat. Chem.* **2016**, *8* (4), 326–330. https://doi.org/10.1038/nchem.2449.
(17) Morrow, S. M.; Bissette, A. J.; Fletcher, S. P. Transmission of Chirality through Space and across Length Scales. *Nat. Nanotechnol.* **2017**, *12* (5), 410–419. https://doi.org/10.1038/nnano.2017.62.
(18) Cheng, Z.; Jones, M. R. Assembly of Planar Chiral Superlattices from Achiral Building Blocks. *Nat. Commun.* **2022**, *13* (1), 4207. https://doi.org/10.1038/s41467-022-31868-2.
(19) Popov, I. Is Chiral Crystal Shape Inherited or Acquired? *Science* **2021**, *372* (6543), 688–688. https://doi.org/10.1126/science.abh1213.
(20) Ben-Moshe, A.; Da Silva, A.; Müller, A.; Abu-Odeh, A.; Harrison, P.; Waelder, J.; Niroui, F.; Ophus, C.; Minor, A. M.; Asta, M.; Theis, W.; Ercius, P.; Alivisatos, A. P. The Chain of Chirality Transfer in Tellurium Nanocrystals. *Science* **2021**, *372* (6543), 729–733. https://doi.org/10.1126/science.abf9645.
(21) Zhao, Y.; Jin, S. Stacking and Twisting of Layered Materials Enabled by Screw Dislocations and Non-Euclidean Surfaces. *Acc. Mater. Res.* **2022**, *3* (3), 369–378. https://doi.org/10.1021/accountsmr.1c00245.

(22) Putze, P.; Ritschel, T.; Chekhonin, P.; Geck, J.; Wolf, D.; Popov, A. A.; Büchner, B.; Schmidt, P.; Hampel, S. Creating Chirality in $WSe_2$ through Screw Dislocations by Chemical Vapor Transport. *Nanoscale Horiz.* **2025**, *10* (5), 944–956. https://doi.org/10.1039/D4NH00567H.

(23) Steed, K. M.; Steed, J. W. Packing Problems: High $Z'$ Crystal Structures and Their Relationship to Cocrystals, Inclusion Compounds, and Polymorphism. *Chem. Rev.* **2015**, *115* (8), 2895–2933. https://doi.org/10.1021/cr500564z.

(24) Bredikhin, A. A.; Zakharychev, D. V.; Gubaidullin, A. T.; Fayzullin, R. R.; Pashagin, A. V.; Bredikhina, Z. A. Crystallization Features of the Chiral Drug Timolol Precursor: The Rare Case of Conglomerate with Partial Solid Solutions. *Cryst. Growth Des.* **2014**, *14* (4), 1676–1683. https://doi.org/10.1021/cg4017905.

(25) Lusi, M. A Rough Guide to Molecular Solid Solutions: Design, Synthesis and Characterization of Mixed Crystals. *CrystEngComm* **2018**, *20* (44), 7042–7052. https://doi.org/10.1039/C8CE00691A.

(26) Bishop, R.; Scudder, M. L. Multiple Molecules in the Asymmetric Unit ( $Z' > 1$) and the Formation of False Conglomerate Crystal Structures. *Cryst. Growth Des.* **2009**, *9* (6), 2890–2894. https://doi.org/10.1021/cg9002143.

(27) Wang, Y.; Chen, A. M. Enantioenrichment by Crystallization. *Org. Process Res. Dev.* **2008**, *12* (2), 282–290. https://doi.org/10.1021/op700239a.

(28) Rietveld, I. B.; Painsecq, F.; Jandl, C.; Stam, D.; Coquerel, G. In the Footsteps of Pasteur: Finding Conglomerates by Using State-of-the-Art Electron Diffraction. *Cryst. Growth Des.* **2024**, *24* (14), 5893–5897. https://doi.org/10.1021/acs.cgd.4c00513.

(29) Galland, A.; Dupray, V.; Berton, B.; Morin-Grognet, S.; Sanselme, M.; Atmani, H.; Coquerel, G. Spotting Conglomerates by Second Harmonic Generation. *Cryst. Growth Des.* **2009**, *9* (6), 2713–2718. https://doi.org/10.1021/cg801356m.

(30) Herman, C.; Haut, B.; Aerts, L.; Leyssens, T. Solid–Liquid Phase Diagrams for the Determination of the Solid State Nature of Both Polymorphs of (RS)-2-(2-Oxo-Pyrrolidin-1-Yl)-Butyramide. *Int. J. Pharm.* **2012**, *437* (1–2), 156–161. https://doi.org/10.1016/j.ijpharm.2012.07.047.

(31) Coquerel, G. Crystallization of Molecular Systems from Solution: Phase Diagrams, Supersaturation and Other Basic Concepts. *Chem Soc Rev* **2014**, *43* (7), 2286–2300. https://doi.org/10.1039/C3CS60359H.

(32) Klussmann, M.; White, A. J. P.; Armstrong, A.; Blackmond, D. G. Rationalization and Prediction of Solution Enantiomeric Excess in Ternary Phase Systems. *Angew. Chem. Int. Ed.* **2006**, *45* (47), 7985–7989. https://doi.org/10.1002/anie.200602520.

(33) Green, B. S.; Lahav, M.; Rabinovich, D. Asymmetric Synthesis via Reactions in Chiral Crystals. *Acc. Chem. Res.* **1979**, *12* (6), 191–197. https://doi.org/10.1021/ar50138a001.

(34) Conley, N.; Compton, R. N.; Pagni, R. M. The Conversion of Achiral Molecules in Chiral Crystals to Chiral Molecules. *Mendeleev Commun.* **2004**, *14* (6), 296–297. https://doi.org/10.1070/MC2004v014n06ABEH002010.

(35) Li, J.; Alezra, V. Enantiopure Chiral Crystals: A Powerful Tool for Absolute Asymmetric Synthesis. *Asian J. Org. Chem.* **2025**, *14* (8), e00267. https://doi.org/10.1002/ajoc.202500267.

(36) Wallach, O. Zur Kenntniss Der Terpene Und Der Ätherischen Oele. *Justus Liebigs Ann. Chem.* **1895**, *286* (1), 90–118. https://doi.org/10.1002/jlac.18952860105.

(37) Brock, C. P.; Schweizer, W. B.; Dunitz, J. D. On the Validity of Wallach's Rule: On the Density and Stability of Racemic Crystals Compared with Their Chiral Counterparts. *J. Am. Chem. Soc.* **1991**, *113* (26), 9811–9820. https://doi.org/10.1021/ja00026a015.

(38) Kuzmenko, I.; Weissbuch, I.; Gurovich, E.; Leiserowitz, L.; Lahav, M. Aspects of Spontaneous Separation of Enantiomers in Two- and Three-Dimensional Crystals. *Chirality* **1998**, *10* (5), 415–424. https://doi.org/10.1002/(SICI)1520-636X(1998)10:5%253C415::AID-CHIR7%253E3.0.CO;2-4.

(39) Clevers, S.; Rougeot, C.; Simon, F.; Sanselme, M.; Dupray, V.; Coquerel, G. Detection of Order–Disorder Transition in Organic Solids by Using Temperature Resolved Second Harmonic Generation (TR-SHG). *J. Mol. Struct.* **2014**, *1078*, 61–67. https://doi.org/10.1016/j.molstruc.2014.04.007.

(40) Mbodji, A.; Gbabode, G.; Sanselme, M.; Couvrat, N.; Leeman, M.; Dupray, V.; Kellogg, R. M.; Coquerel, G. Family of Conglomerate-Forming Systems Composed of Chlocyphos and Alkyl-Amine. Assessment of Their Resolution Performances by Using Various Modes of Preferential Crystallization. *Cryst. Growth Des.* **2019**, *19* (9), 5173–5183. https://doi.org/10.1021/acs.cgd.9b00568.

(41) Van Der Meijden, M. W.; Leeman, M.; Gelens, E.; Noorduin, W. L.; Meekes, H.; Van Enckevort, W. J. P.; Kaptein, B.; Vlieg, E.; Kellogg, R. M. Attrition-Enhanced Deracemization in the Synthesis of Clopidogrel - A Practical Application of a New Discovery. *Org. Process Res. Dev.* **2009**, *13* (6), 1195–1198. https://doi.org/10.1021/op900243c.

(42) Leeman, M.; De Gooier, J. M.; Boer, K.; Zwaagstra, K.; Kaptein, B.; Kellogg, R. M. Attrition-Enhanced Total Resolution Leads to Homochiral Families of Amino Acid Derivatives. *Tetrahedron Asymmetry* **2010**, *21* (9–10), 1191–1193. https://doi.org/10.1016/j.tetasy.2010.04.007.

(43) Baglai, I.; Leeman, M.; Wurst, K.; Kaptein, B.; Kellogg, R. M.; Noorduin, W. L. The Strecker Reaction Coupled to Viedma Ripening: A Simple Route to Highly Hindered Enantiomerically Pure Amino Acids. *Chem. Commun.* **2018**, *54* (77), 10832–10834. https://doi.org/10.1039/C8CC06658B.

(44) Baglai, I.; Leeman, M.; Kellogg, R. M.; Noorduin, W. L. A Viedma Ripening Route to an Enantiopure Building Block for Levetiracetam and Brivaracetam. *Org. Biomol. Chem.* **2019**, *17* (1), 35–38. https://doi.org/10.1039/C8OB02660B.

(45) Uemura, N.; Toyoda, S.; Shimizu, W.; Yoshida, Y.; Mino, T.; Sakamoto, M. Absolute Asymmetric Synthesis Involving Chiral Symmetry Breaking in Diels–Alder Reaction. *Symmetry* **2020**, *12* (6), 910. https://doi.org/10.3390/sym12060910.

(46) Valenti, G.; Tinnemans, P.; Baglai, I.; Noorduin, W. L.; Kaptein, B.; Leeman, M.; Ter Horst, J. H.; Kellogg, R. M. Combining Incompatible Processes for Deracemization of a Praziquantel Derivative under Flow Conditions. *Angew. Chem. Int. Ed.* **2021**, *60* (10), 5279–5282. https://doi.org/10.1002/anie.202013502.

(47) Nashawi, A. A. The Synthesis of Single Enantiomer Thiolactomycin Analogues Utilising Deracemisation by Crystallisation, University of Strathclyde, 2025. https://doi.org/10.48730/1M7B-5673.

(48) Taylor, C. R.; Butler, P. W. V.; Day, G. M. Predictive Crystallography at Scale: Mapping, Validating, and Learning from 1000 Crystal Energy Landscapes. *Faraday Discuss.* **2025**, *256*, 434–458. https://doi.org/10.1039/D4FD00105B.

(49) Plass, K. E.; Grzesiak, A. L.; Matzger, A. J. Molecular Packing and Symmetry of Two-Dimensional Crystals. *Acc. Chem. Res.* **2007**, *40* (4), 287–293. https://doi.org/10.1021/ar0500158.

(50) Dutta, S.; Gellman, A. J. Enantiomer Surface Chemistry: Conglomerate *versus* Racemate Formation on Surfaces. *Chem. Soc. Rev.* **2017**, *46* (24), 7787–7839. https://doi.org/10.1039/C7CS00555E.

(51) Carpenter, J. E.; Grünwald, M. Pre-Nucleation Clusters Predict Crystal Structures in Models of Chiral Molecules. *J. Am. Chem. Soc.* **2021**, *143* (51), 21580–21593. https://doi.org/10.1021/jacs.1c09321.

(52) Carpenter, J. E.; Grünwald, M. Heterogeneous Interactions Promote Crystallization and Spontaneous Resolution of Chiral Molecules. *J. Am. Chem. Soc.* **2020**, *142* (24), 10755–10768. https://doi.org/10.1021/jacs.0c02097.

(53) D'Oria, E.; Karamertzanis, P. G.; Price, S. L. Spontaneous Resolution of Enantiomers by Crystallization: Insights from Computed Crystal Energy Landscapes. *Cryst. Growth Des.* **2010**, *10* (4), 1749–1756. https://doi.org/10.1021/cg9014306.

(54) Hylton, R. K.; Tizzard, G. J.; Threlfall, T. L.; Ellis, A. L.; Coles, S. J.; Seaton, C. C.; Schulze, E.; Lorenz, H.; Seidel-Morgenstern, A.; Stein, M.; Price, S. L. Are the Crystal Structures of Enantiopure and Racemic

Mandelic Acids Determined by Kinetics or Thermodynamics? *J. Am. Chem. Soc.* **2015**, *137* (34), 11095–11104. https://doi.org/10.1021/jacs.5b05938.

(55) Jiang, Q.; Hu, C.; Ward, M. D. Stereochemical Control of Polymorph Transitions in Nanoscale Reactors. *J. Am. Chem. Soc.* **2013**, *135* (6), 2144–2147. https://doi.org/10.1021/ja312511v.

(56) Seibel, J.; Parschau, M.; Ernst, K.-H. From Homochiral Clusters to Racemate Crystals: Viable Nuclei in 2D Chiral Crystallization. *J. Am. Chem. Soc.* **2015**, *137* (25), 7970–7973. https://doi.org/10.1021/jacs.5b02262.

(57) Resel, R.; Jones, A. O. F.; Schweicher, G.; Fischer, R.; Demitri, N.; Geerts, Y. H. Polymorphism of Terthiophene with Surface Confinement. *IUCrJ* **2018**, *5* (3), 304–308. https://doi.org/10.1107/S2052252518003949.

(58) Tauvel, G.; Sanselme, M.; Coste-Leconte, S.; Petit, S.; Coquerel, G. Structural Studies of Several Solvated Potassium Salts of Tenatoprazole Crystallizing as Conglomerates. *J. Mol. Struct.* **2009**, *936* (1–3), 60–66. https://doi.org/10.1016/j.molstruc.2009.07.014.

(59) Choobdari, E.; Fakhraian, H.; Peyrovi, M. H. Anion Effect on the Binary and Ternary Phase Diagrams of Chiral Medetomidine Salts and Conglomerate Crystal Formation. *Chirality* **2014**, *26* (3), 183–188. https://doi.org/10.1002/chir.22299.

(60) Spix, L.; Alfring, A.; Meekes, H.; Van Enckevort, W. J. P.; Vlieg, E. Formation of a Salt Enables Complete Deracemization of a Racemic Compound through Viedma Ripening. *Cryst. Growth Des.* **2014**, *14* (4), 1744–1748. https://doi.org/10.1021/cg4018882.

(61) Shemchuk, O.; Grepioni, F.; Leyssens, T.; Braga, D. Chiral Resolution via Cocrystallization with Inorganic Salts. *Isr. J. Chem.* **2021**, *61* (9–10), 563–572. https://doi.org/10.1002/ijch.202100049.

(62) Kaviani, R.; Jouyban, A.; Shayanfar, A. Chiral Resolution Methods for Racemic Pharmaceuticals Based on Cocrystal Formation. *CrystEngComm* **2023**, *25* (44), 6120–6131. https://doi.org/10.1039/D3CE00853C.

(63) Harfouche, L. C.; Brandel, C.; Cartigny, Y.; Petit, S.; Coquerel, G. Resolution by Preferential Crystallization of Proxyphylline by Using Its Salicylic Acid Monohydrate Co-Crystal. *Chem. Eng. Technol.* **2020**, *43* (6), 1093–1098. https://doi.org/10.1002/ceat.202000040.

(64) Buol, X.; Caro Garrido, C.; Robeyns, K.; Tumanov, N.; Collard, L.; Wouters, J.; Leyssens, T. Chiral Resolution of Mandelic Acid through Preferential Cocrystallization with Nefiracetam. *Cryst. Growth Des.* **2020**, *20* (12), 7979–7988. https://doi.org/10.1021/acs.cgd.0c01236.

(65) Li, W.; De Groen, M.; Kramer, H. J. M.; De Gelder, R.; Tinnemans, P.; Meekes, H.; Ter Horst, J. H. Screening Approach for Identifying Cocrystal Types and Resolution Opportunities in Complex Chiral Multicomponent Systems. *Cryst. Growth Des.* **2021**, *21* (1), 112–124. https://doi.org/10.1021/acs.cgd.0c00890.

(66) Rapeenun, P.; Gerard, C. J. J.; Pinètre, C.; Cartigny, Y.; Tinnemans, P.; De Gelder, R.; Flood, A. E.; Ter Horst, J. H. Searching for Conglomerate Cocrystals of the Racemic Compound Praziquantel. *Cryst. Growth Des.* **2024**, *24* (1), 480–490. https://doi.org/10.1021/acs.cgd.3c01158.

(67) Harmsen, B.; Leyssens, T. Enabling Enantiopurity: Combining Racemization and Dual-Drug Co-Crystal Resolution. *Cryst. Growth Des.* **2018**, *18* (6), 3654–3660. https://doi.org/10.1021/acs.cgd.8b00438.

(68) Wang, L.; Wang, N.; Sui, J.; Sun, S.; Feng, Z.; Li, G.; Hao, H.; Zhou, L. Case of Chiral Resolution through Converting Two Racemic Compounds into a Conglomerate. *Cryst. Growth Des.* **2023**, *23* (8), 5641–5650. https://doi.org/10.1021/acs.cgd.3c00311.

(69) Habgood, M. Analysis of Enantiospecific and Diastereomeric Cocrystal Systems by Crystal Structure Prediction. *Cryst. Growth Des.* **2013**, *13* (10), 4549–4558. https://doi.org/10.1021/cg401040p.

(70) Molajafari, F.; Li, T.; Abbasichaleshtori, M.; Hajian Z. D., M.; Cozzolino, A. F.; Fandrick, D. R.; Howe, J. D. Computational Screening for Prediction of Co-Crystals: Method Comparison and Experimental Validation. *CrystEngComm* **2024**, *26* (11), 1620–1636. https://doi.org/10.1039/D3CE01252B.

(71) Sarjeant, A.; Abourahma, H.; Thomas, S.; Cook, C.; Yin, Z. On the Road to Cocrystal Prediction: A Screening Study for the Validation of In Silico Methods. *Cryst. Growth Des.* **2024**, *24* (13), 5486–5493. https://doi.org/10.1021/acs.cgd.4c00220.

(72) Liang, X.; Larsen, A. S.; Hans, P.; Xu, D.; Li, Y.; Martins, I. C. B.; Rades, T.; Jiang, Y. Recent Developments on Co-Crystal Polymorphs: From Formation to Prediction. *CrystEngComm* **2025**, *27* (39), 6415–6432. https://doi.org/10.1039/D5CE00652J.

(73) Song, Y.; Ding, Y.; Su, J.; Li, J.; Ji, Y. Unlocking the Potential of Machine Learning in Co-crystal Prediction by a Novel Approach Integrating Molecular Thermodynamics. *Angew. Chem. Int. Ed.* **2025**, *64* (21), e202502410. https://doi.org/10.1002/anie.202502410.

(74) Kellogg, R. M.; Kaptein, B.; Vries, T. R. Dutch Resolution of Racemates and the Roles of Solid Solution Formation and Nucleation Inhibition. In *Novel Optical Resolution Technologies*; Sakai, K., Hirayama, N., Tamura, R., Eds.; Topics in Current Chemistry; Springer Berlin Heidelberg: Berlin, Heidelberg, 2007; Vol. 269, pp 159–197. https://doi.org/10.1007/128_2006_095.

(75) Kellogg, R. M. Practical Stereochemistry. *Acc. Chem. Res.* **2017**, *50* (4), 905–914. https://doi.org/10.1021/acs.accounts.6b00630.

(76) Vries, T.; Wynberg, H.; Van Echten, E.; Koek, J.; Ten Hoeve, W.; Kellogg, R. M.; Broxterman, Q. B.; Minnaard, A.; Kaptein, B.; Van Der Sluis, S.; Hulshof, L.; Kooistra, J. The Family Approach to the Resolution of Racemates. *Angew. Chem. Int. Ed.* **1998**, *37* (17), 2349–2354. https://doi.org/10.1002/(SICI)1521-3773(19980918)37:17%253C2349::AID-ANIE2349%253E3.0.CO;2-I.

(77) Faigl, F.; Fogassy, E.; Nógrádi, M.; Pálovics, E.; Schindler, J. Strategies in Optical Resolution: A Practical Guide. *Tetrahedron Asymmetry* **2008**, *19* (5), 519–536. https://doi.org/10.1016/j.tetasy.2008.02.004.

(78) Pasteur, L. C. R. Transformation Des Acides Tartriques En Acide Racémique. Découverte de l'acide Tartrique Inactif. Nouvelle Méthode de Séparation de l'acide Racémique En Acides Tartriques Droit et Gauche. *Acad Sci Paris* **1853**, *37* (5), 162–166.

(79) Zaugg, H. E. A Mechanical Resolution of Dl-Methadone Base. *J. Am. Chem. Soc.* **1955**, *77* (10), 2910–2910. https://doi.org/10.1021/ja01615a084.

(80) Avalos, M.; Babiano, R.; Cintas, P.; Jiménez, J. L.; Palacios, J. C. Chiral Autocatalysis: Where Stereochemistry Meets the Origin of Life. *Chem. Commun.* **2000**, No. 11, 887–892. https://doi.org/10.1039/a908300f.

(81) Blackmond, D. G.; Klussmann, M. Spoilt for Choice: Assessing Phase Behavior Models for the Evolution of Homochirality. *Chem. Commun.* **2007**, No. 39, 3990. https://doi.org/10.1039/b709314b.

(82) Noorduin, W. L.; Bode, A. A. C.; Van Der Meijden, M.; Meekes, H.; Van Etteger, A. F.; Van Enckevort, W. J. P.; Christianen, P. C. M.; Kaptein, B.; Kellogg, R. M.; Rasing, T.; Vlieg, E. Complete Chiral Symmetry Breaking of an Amino Acid Derivative Directed by Circularly Polarized Light. *Nat. Chem.* **2009**, *1* (9), 729–732. https://doi.org/10.1038/nchem.416.

(83) Collet, A.; Brienne, M. J.; Jacques, J. Optical Resolution by Direct Crystallization of Enantiomer Mixtures. *Chem. Rev.* **1980**, *80* (3), 215–230. https://doi.org/10.1021/cr60325a001.

(84) Rougeot, C.; Hein, J. E. Application of Continuous Preferential Crystallization to Efficiently Access Enantiopure Chemicals. *Org. Process Res. Dev.* **2015**, *19* (12), 1809–1819. https://doi.org/10.1021/acs.oprd.5b00141.

(85) Orehek, J.; Teslić, D.; Likozar, B. Continuous Crystallization Processes in Pharmaceutical Manufacturing: A Review. *Org. Process Res. Dev.* **2021**, *25* (1), 16–42. https://doi.org/10.1021/acs.oprd.0c00398.

(86) Ito, K.; Akashi, T.; Tatsumi, S. Method of Optically Resolving Racemic Amino Acids. US 3260744, 1966.

(87) Binev, D.; Seidel-Morgenstern, A.; Lorenz, H. Continuous Separation of Isomers in Fluidized Bed Crystallizers. *Cryst. Growth Des.* **2016**, *16* (3), 1409–1419. https://doi.org/10.1021/acs.cgd.5b01513.

(88) Elsner, M. P.; Ziomek, G.; Seidel-Morgenstern, A. Simultaneous Preferential Crystallization in a Coupled, Batch Operation Mode—Part I: Theoretical Analysis and Optimization. *Chem. Eng. Sci.* **2007**, *62* (17), 4760–4769. https://doi.org/10.1016/j.ces.2007.05.035.

(89) Elsner, M. P.; Ziomek, G.; Seidel-Morgenstern, A. Simultaneous Preferential Crystallization in a Coupled Batch Operation Mode. Part II: Experimental Study and Model Refinement. *Chem. Eng. Sci.* **2011**, *66* (6), 1269–1284. https://doi.org/10.1016/j.ces.2010.12.035.

(90) Levilain, G.; Eicke, M. J.; Seidel-Morgenstern, A. Efficient Resolution of Enantiomers by Coupling Preferential Crystallization and Dissolution. Part 1: Experimental Proof of Principle. *Cryst. Growth Des.* **2012**, *12* (11), 5396–5401. https://doi.org/10.1021/cg3009943.

(91) Temmel, E.; Eicke, M. J.; Cascella, F.; Seidel-Morgenstern, A.; Lorenz, H. Resolution of Racemic Guaifenesin Applying a Coupled Preferential Crystallization-Selective Dissolution Process: Rational Process Development. *Cryst. Growth Des.* **2019**, *19* (6), 3148–3157. https://doi.org/10.1021/acs.cgd.8b01660.

(92) Cascella, F.; Temmel, E.; Seidel-Morgenstern, A.; Lorenz, H. Efficient Resolution of Racemic Guaifenesin via Batch-Preferential Crystallization Processes. *Org. Process Res. Dev.* **2020**, *24* (1), 50–58. https://doi.org/10.1021/acs.oprd.9b00413.

(93) Chaaban, J. H.; Dam-Johansen, K.; Skovby, T.; Kiil, S. Separation of Enantiomers by Continuous Preferential Crystallization: Experimental Realization Using a Coupled Crystallizer Configuration. *Org. Process Res. Dev.* **2013**, *17* (8), 1010–1020. https://doi.org/10.1021/op400087g.

(94) Vetter, T.; Burcham, C. L.; Doherty, M. F. Separation of Conglomerate Forming Enantiomers Using a Novel Continuous Preferential Crystallization Process. *AIChE J.* **2015**, *61* (9), 2810–2823. https://doi.org/10.1002/aic.14934.

(95) Galan, K.; Eicke, M. J.; Elsner, M. P.; Lorenz, H.; Seidel-Morgenstern, A. Continuous Preferential Crystallization of Chiral Molecules in Single and Coupled Mixed-Suspension Mixed-Product-Removal Crystallizers. *Cryst. Growth Des.* **2015**, *15* (4), 1808–1818. https://doi.org/10.1021/cg501854g.

(96) Dunn, A. S.; Svoboda, V.; Sefcik, J.; Ter Horst, J. H. Resolution Control in a Continuous Preferential Crystallization Process. *Org. Process Res. Dev.* **2019**, *23* (9), 2031–2041. https://doi.org/10.1021/acs.oprd.9b00275.

(97) Van Enckevort, W. J. P. On the Crystallization of Epitaxial Racemic Conglomerates. *J. Phys. Chem. C* **2010**, *114* (49), 21593–21604. https://doi.org/10.1021/jp108527h.

(98) Zlokazov, M. V.; Pivnitsky, K. K. Lamellar Conglomerates. *Mendeleev Commun.* **2020**, *30* (1), 1–6. https://doi.org/10.1016/j.mencom.2020.01.001.

(99) Kaptein, B.; Noorduin, W. L.; Meekes, H.; van Enckevort, W. J. P.; Kellogg, R. M.; Vlieg, E. Attrition-Enhanced Deracemization of an Amino Acid Derivative That Forms an Epitaxial Racemic Conglomerate. *Angew. Chem. Int. Ed.* **2008**, *47* (38), 7226–7229. https://doi.org/10.1002/anie.200802468.

(100) Robin, A.; Iavicoli, P.; Wurst, K.; Dyer, M. S.; Haq, S.; Amabilino, D. B.; Raval, R. A Racemic Conglomerate Nipped in the Bud: A Molecular View of Enantiomer Cross-Inhibition of Conglomerate Nucleation at a Surface. *Cryst. Growth Des.* **2010**, *10* (10), 4516–4525. https://doi.org/10.1021/cg100806w.

(101) Parschau, M.; Fasel, R.; Ernst, K.-H. Coverage and Enantiomeric Excess Dependent Enantiomorphism in Two-Dimensional Molecular Crystals. *Cryst. Growth Des.* **2008**, *8* (6), 1890–1896. https://doi.org/10.1021/cg701100r.

(102) Weissbuch, I.; Lahav, M.; Leiserowitz, L. Toward Stereochemical Control, Monitoring, and Understanding of Crystal Nucleation. *Cryst. Growth Des.* **2003**, *3* (2), 125–150. https://doi.org/10.1021/cg0200560.

(103) Harfouche, L. C.; Clevers, S.; Coquerel, G.; Rietveld, I. B. Nucleation Behaviour of Racemic and Enantiopure Histidine. *CrystEngComm* **2021**, *23* (47), 8379–8385. https://doi.org/10.1039/D1CE01199E.

(104) Mughal, R. K.; Davey, R. J.; Blagden, N. Application of Crystallization Inhibitors to Chiral Separations. 1. Design of Additives to Discriminate between the Racemic Compound and the Pure Enantiomer of Mandelic Acid. *Cryst. Growth Des.* **2007**, *7* (2), 218–224. https://doi.org/10.1021/cg0605638.

(105) Mughal, R. K.; Davey, R. J.; Black, S. N. Application of Crystallization Inhibitors to Chiral Separations. 2. Enhancing the Chiral Purity of Mandelic Acid by Crystallization. *Cryst. Growth Des.* **2007**, *7* (2), 225–228. https://doi.org/10.1021/cg060565s.

(106) Gou, L.; Lorenz, H.; Seidel-Morgenstern, A. Investigation of a Chiral Additive Used in Preferential Crystallization. *Cryst. Growth Des.* **2012**, *12* (11), 5197–5202. https://doi.org/10.1021/cg300042q.

(107) Davey, R. J.; Sadiq, G.; Back, K.; Wilkinson, L.; Seaton, C. C. The Isolation of a Metastable Conglomerate Using a Combined Computational and Controlled Crystallization Approach. *Chem Commun* **2012**, *48* (14), 1976–1978. https://doi.org/10.1039/C1CC16173C.

(108) Sun, J.; Wang, Y.; Gao, Z.; Gong, J.; Tang, W. Additive-Assisted Preferential Crystallization of Racemic Component: A Case of Norvaline. *J. Ind. Eng. Chem.* **2022**, *110*, 206–216. https://doi.org/10.1016/j.jiec.2022.02.054.

(109) Klussmann, M.; Izumi, T.; White, A. J. P.; Armstrong, A.; Blackmond, D. G. Emergence of Solution-Phase Homochirality via Crystal Engineering of Amino Acids. *J. Am. Chem. Soc.* **2007**, *129* (24), 7657–7660. https://doi.org/10.1021/ja0708870.

(110) Springuel, G.; Leyssens, T. Innovative Chiral Resolution Using Enantiospecific Co-Crystallization in Solution. *Cryst. Growth Des.* **2012**, *12* (7), 3374–3378. https://doi.org/10.1021/cg300307z.

(111) Brandel, C.; Amharar, Y.; Rollinger, J. M.; Griesser, U. J.; Cartigny, Y.; Petit, S.; Coquerel, G. Impact of Molecular Flexibility on Double Polymorphism, Solid Solutions and Chiral Discrimination during Crystallization of Diprophylline Enantiomers. *Mol. Pharm.* **2013**, *10* (10), 3850–3861. https://doi.org/10.1021/mp400308u.

(112) Brandel, C.; Cartigny, Y.; Coquerel, G.; ter Horst, J. H.; Petit, S. Prenucleation Self-Assembly and Chiral Discrimination Mechanisms during Solution Crystallisation of Racemic Diprophylline. *Chem. – Eur. J.* **2016**, *22* (45), 16103–16112. https://doi.org/10.1002/chem.201602707.

(113) Harfouche, L. C.; Brandel, C.; Cartigny, Y.; Ter Horst, J. H.; Coquerel, G.; Petit, S. Enabling Direct Preferential Crystallization in a Stable Racemic Compound System. *Mol. Pharm.* **2019**, *16* (11), 4670–4676. https://doi.org/10.1021/acs.molpharmaceut.9b00805.

(114) Lorenz, H.; Le Minh, T.; Kaemmerer, H.; Buchholz, H.; Seidel-Morgenstern, A. Exploitation of Shifts of Eutectic Compositions in Crystallization-Based Enantioseparation. *Chem. Eng. Res. Des.* **2013**, *91* (10), 1890–1902. https://doi.org/10.1016/j.cherd.2013.08.013.

(115) Buchholz, H. K.; Hylton, R. K.; Brandenburg, J. G.; Seidel-Morgenstern, A.; Lorenz, H.; Stein, M.; Price, S. L. Thermochemistry of Racemic and Enantiopure Organic Crystals for Predicting Enantiomer Separation. *Cryst. Growth Des.* **2017**, *17* (9), 4676–4686. https://doi.org/10.1021/acs.cgd.7b00582.

(116) Faigl, F.; Fogassy, E.; Nógrádi, M.; Pálovics, E.; Schindler, J. Separation of Non-Racemic Mixtures of Enantiomers: An Essential Part of Optical Resolution. *Org. Biomol. Chem.* **2010**, *8* (5), 947. https://doi.org/10.1039/b917564d.

(117) Polenske, D.; Lorenz, H.; Seidel-Morgenstern, A. Potential of Different Techniques of Preferential Crystallization for Enantioseparation of Racemic Compound Forming Systems. *Chirality* **2009**, *21* (8), 728–737. https://doi.org/10.1002/chir.20672.

(118) Ebbers, E. J.; Ariaans, G. J. A.; Houbiers, J. P. M.; Bruggink, A.; Zwanenburg, B. Controlled Racemization of Optically Active Organic Compounds: Prospects for Asymmetric Transformation. *Tetrahedron* **1997**, *53* (28), 9417–9476. https://doi.org/10.1016/S0040-4020(97)00324-4.

(119) Yamada, S.; Hongo, C.; Yoshioka, R.; Chibata, I. Method for the Racemization of Optically Active Amino Acids. *J. Org. Chem.* **1983**, *48* (6), 843–846. https://doi.org/10.1021/jo00154a019.

(120) Reider, P. J.; Davis, P.; Hughes, D. L.; Grabowski, E. J. J. Crystallization-Induced Asymmetric Transformation: Stereospecific Synthesis of a Potent Peripheral CCK Antagonist. *J. Org. Chem.* **1987**, *52* (5), 955–957. https://doi.org/10.1021/jo00381a052.

(121) Konoike, T.; Matsumura, K.; Yorifuji, T.; Shinomoto, S.; Ide, Y.; Ohya, T. Practical Enantioselective Synthesis of Endothelin Antagonist S-1255 by Dynamic Resolution of 4-Methoxychromene-3-Carboxylic Acid Intermediate. *J. Org. Chem.* **2002**, *67* (22), 7741–7749. https://doi.org/10.1021/jo0261092.

(122) Openshaw, H. T.; Whittaker, N. The Synthesis of Emetine and Related Compounds. Part V. A Stereochemically Favourable Synthesis of Emetine. *J. Chem. Soc. Resumed* **1963**, *277*, 1461. https://doi.org/10.1039/jr9630001461.

(123) Brands, K. M. J.; Davies, A. J. Crystallization-Induced Diastereomer Transformations. *Chem. Rev.* **2006**, *106* (7), 2711–2733. https://doi.org/10.1021/cr0406864.

(124) Caddick, S.; Jenkins, K. Dynamic Resolutions in Asymmetric Synthesis. *Chem. Soc. Rev.* **1996**, *25* (6), 447. https://doi.org/10.1039/cs9962500447.

(125) Zhang, Y.; Zhang, Y.; Ramström, O. Dynamic Covalent Kinetic Resolution. *Catal. Rev.* **2020**, *62* (1), 66–95. https://doi.org/10.1080/01614940.2019.1664031.

(126) El Gihani, M. T.; Williams, J. M. J. Dynamic Kinetic Resolution. *Curr. Opin. Chem. Biol.* **1999**, *3* (1), 11–15. https://doi.org/10.1016/S1367-5931(99)80003-9.

(127) Turner, N. J. Enzyme Catalysed Deracemisation and Dynamic Kinetic Resolution Reactions. *Curr. Opin. Chem. Biol.* **2004**, *8* (2), 114–119. https://doi.org/10.1016/j.cbpa.2004.02.001.

(128) Ahn, Y.; Ko, S.-B.; Kim, M.-J.; Park, J. Racemization Catalysts for the Dynamic Kinetic Resolution of Alcohols and Amines. *Coord. Chem. Rev.* **2008**, *252* (5–7), 647–658. https://doi.org/10.1016/j.ccr.2007.09.009.

(129) Wuyts, S.; De Temmerman, K.; De Vos, D.; Jacobs, P. A Zeolite–Enzyme Combination for Biphasic Dynamic Kinetic Resolution of Benzylic Alcohols. *Chem Commun* **2003**, No. 15, 1928–1929. https://doi.org/10.1039/B305120J.

(130) Zhao, Z.; Wang, C.; Chen, Q.; Wang, Y.; Xiao, R.; Tan, C.; Liu, G. Phase Separation-Promoted Redox Deracemization of Secondary Alcohols over a Supported Dual Catalysts System. *ChemCatChem* **2021**, *13* (18), 4055–4063. https://doi.org/10.1002/cctc.202100738.

(131) Zhu, C.-J.; Yang, X.; Wang, J. Electrocatalytic Cyclic Deracemization Enabled by a Chemically Modified Electrode. *Nat. Catal.* **2024**, *7* (8), 878–888. https://doi.org/10.1038/s41929-024-01189-2.

(132) Walden, P. Ueber Die Gegenseitige Umwandlung Optischer Antipoden. *Berichte Dtsch. Chem. Ges.* **1896**, *29* (1), 133–138. https://doi.org/10.1002/cber.18960290127.

(133) Chen, J. G.; Zhu, J.; Skonezny, P. M.; Rosso, V.; Venit, J. J. Crystallization-Induced Chiral Inversion As the Key Step for Synthesis of (*S*)-2-Acetylthio-3-Phenylpropanoic Acid from L-Phenylalanine. *Org. Lett.* **2004**, *6* (19), 3233–3235. https://doi.org/10.1021/ol0489806.

(134) Oda, Y.; Ikeda, T.; Tada, K. A Facile Preparation of (*E*)-α-(1*H*-1,2,4-Triazol-1-Yl)Styryl Ketones Using Isomerization-Crystallization Method. *Synth. Commun.* **1994**, *24* (15), 2195–2202. https://doi.org/10.1080/00397919408010235.

(135) Steendam, R. R. E.; Brouwer, M. C. T.; Huijs, E. M. E.; Kulka, M. W.; Meekes, H.; van Enckevort, W. J. P.; Raap, J.; Rutjes, F. P. J. T.; Vlieg, E. Enantiopure Isoindolinones through Viedma Ripening. *Chem. – Eur. J.* **2014**, *20* (42), 13527–13530. https://doi.org/10.1002/chem.201404320.

(136) Clarkson, A. J.; Fremin, S. O.; Johnson, J. S. Crystallization-Induced Diastereomer Transformations of Donor–Acceptor Cyclopropanes. *J. Am. Chem. Soc.* **2025**, *147* (43), 39870–39878. https://doi.org/10.1021/jacs.5c14503.

(137) Sakamoto, M.; Mino, T. Total Resolution of Racemates by Dynamic Preferential Crystallization. In *Advances in Organic Crystal Chemistry*; Tamura, R., Miyata, M., Eds.; Springer Japan: Tokyo, 2015; pp 445–462. https://doi.org/10.1007/978-4-431-55555-1_22.

(138) Feringa, B. L.; Van Delden, R. A.; Koumura, N.; Geertsema, E. M. Chiroptical Molecular Switches. *Chem. Rev.* **2000**, *100* (5), 1789–1816. https://doi.org/10.1021/cr9900228.

(139) Corpas, J.; Mauleón, P.; Gómez Arrayás, R.; Carretero, J. C. *E*/*Z* Photoisomerization of Olefins as an Emergent Strategy for the Control of Stereodivergence in Catalysis. *Adv. Synth. Catal.* **2022**, *364* (8), 1348–1370. https://doi.org/10.1002/adsc.202200199.

(140) Meinhardt, J. M.; Kim, D. D.; Wu, E. J.; Murray, P. R. D.; Walker, D. P.; Knowles, R. R. Light-Driven Crystallization-Induced Dynamic Resolution of Amines. *J. Am. Chem. Soc.* **2025**, *147* (29), 25851–25857. https://doi.org/10.1021/jacs.5c07676.

(141) Uchikura, T.; Sato, M.; Kanno, Y.; Fukuda, Y.; Hara, Y.; Yamamoto, K.; Akiyama, T. Visible-Light-Driven Racemization of 1,1′-Binaphthyl-2,2′-Diamine (BINAM) Derivatives. *Org. Lett.* **2025**, *27* (8), 1912–1917. https://doi.org/10.1021/acs.orglett.5c00162.

(142) Zhang, J.; Wang, K.; Zhu, C. Deracemization of Atropisomeric Biaryls Enabled by Copper Catalysis. *JACS Au* **2024**, *4* (2), 502–511. https://doi.org/10.1021/jacsau.3c00623.

(143) DeHovitz, J. S.; Hyster, T. K. Photoinduced Dynamic Radical Processes for Isomerizations, Deracemizations, and Dynamic Kinetic Resolutions. *ACS Catal.* **2022**, *12* (15), 8911–8924. https://doi.org/10.1021/acscatal.2c02480.

(144) Shaw, M. H.; Twilton, J.; MacMillan, D. W. C. Photoredox Catalysis in Organic Chemistry. *J. Org. Chem.* **2016**, *81* (16), 6898–6926. https://doi.org/10.1021/acs.joc.6b01449.

(145) Rodriguez, O.; Morrison, H. Photosensitized Racemization of an Optically Active Allene. *J. Chem. Soc. Chem. Commun.* **1971**, No. 13, 679. https://doi.org/10.1039/c29710000679.

(146) Hölzl-Hobmeier, A.; Bauer, A.; Silva, A. V.; Huber, S. M.; Bannwarth, C.; Bach, T. Catalytic Deracemization of Chiral Allenes by Sensitized Excitation with Visible Light. *Nature* **2018**, *564* (7735), 240–243. https://doi.org/10.1038/s41586-018-0755-1.

(147) Stierle, M.; Bitterlich, D.; Westermayr, J.; Bach, T. Photochemical Deracemization of 2,3-Allenoic Acids Mediated by a Sensitizing Chiral Phosphoric Acid Catalyst. *Chem. Sci.* **2025**, *16* (42), 19711–19719. https://doi.org/10.1039/D5SC05356K.

(148) Roberts, B. P. Polarity-Reversal Catalysis of Hydrogen-Atom Abstraction Reactions: Concepts and Applications in Organic Chemistry. *Chem. Soc. Rev.* **1999**, *28* (1), 25–35. https://doi.org/10.1039/a804291h.

(149) Kizu, T.; Uraguchi, D.; Ooi, T. Independence from the Sequence of Single-Electron Transfer of Photoredox Process in Redox-Neutral Asymmetric Bond-Forming Reaction. *J. Org. Chem.* **2016**, *81* (16), 6953–6958. https://doi.org/10.1021/acs.joc.6b00445.

(150) Mondal, S.; Dumur, F.; Gigmes, D.; Sibi, M. P.; Bertrand, M. P.; Nechab, M. Enantioselective Radical Reactions Using Chiral Catalysts. *Chem. Rev.* **2022**, *122* (6), 5842–5976. https://doi.org/10.1021/acs.chemrev.1c00582.

(151) Sun, X.; Liu, Y.; Yin, Y.; Ban, X.; Zhao, X.; Jiang, Z. Asymmetric Photoredox Catalytic Formal de Mayo Reaction Enabled by Sensitization-Initiated Electron Transfer. *Nat. Chem.* **2024**, *16* (7), 1169–1176. https://doi.org/10.1038/s41557-024-01502-3.

(152) Liu, Y.; Yang, B.; He, H.; Gao, S. Development and Application of Radical-Mediated Stereochemical Epimerization in Natural Product Synthesis. *Angew. Chem. Int. Ed.* **2025**, *64* (45), e202516814. https://doi.org/10.1002/anie.202516814.

(153) Shin, N. Y.; Ryss, J. M.; Zhang, X.; Miller, S. J.; Knowles, R. R. Light - Driven Deracemization Enabled by Excited - State Electron Transfer. *Science* **2019**, *366* (6463), 364–369. https://doi.org/10.1126/science.aay2204.

(154) Wen, L.; Ding, J.; Duan, L.; Wang, S.; An, Q.; Wang, H.; Zuo, Z. Multiplicative Enhancement of Stereoenrichment by a Single Catalyst for Deracemization of Alcohols. *Science* **2023**, *382* (6669), 458–464. https://doi.org/10.1126/science.adj0040.

(155) Kim, S. F.; Sarpong, R. Interconverting Mirror-Image Molecules. *Science* **2023**, *382* (6669), 373–374. https://doi.org/10.1126/science.adk7116.

(156) Zhang, Z.; Hu, X. Visible-Light-Driven Catalytic Deracemization of Secondary Alcohols. *Angew. Chem. Int. Ed.* **2021**, *60* (42), 22833–22838. https://doi.org/10.1002/anie.202107570.

(157) Poulhès, F.; Vanthuyne, N.; Bertrand, M. P.; Gastaldi, S.; Gil, G. Chemoenzymatic Dynamic Kinetic Resolution of Primary Amines Catalyzed by CAL-B at 38–40 °C. *J. Org. Chem.* **2011**, *76* (17), 7281–7286. https://doi.org/10.1021/jo201256w.

(158) DeHovitz, J. S.; Loh, Y. Y.; Kautzky, J. A.; Nagao, K.; Meichan, A. J.; Yamauchi, M.; MacMillan, D. W. C.; Hyster, T. K. Static to Inducibly Dynamic Stereocontrol: The Convergent Use of Racemic β-Substituted Ketones. *Science* **2020**, *369* (6507), 1113–1118. https://doi.org/10.1126/science.abc9909.

(159) Yang, Q.; Zhao, F.; Zhang, N.; Liu, M.; Hu, H.; Zhang, J.; Zhou, S. Mild Dynamic Kinetic Resolution of Amines by Coupled Visible-Light Photoredox and Enzyme Catalysis. *Chem. Commun.* **2018**, *54* (100), 14065–14068. https://doi.org/10.1039/C8CC07990K.

(160) Wang, J. Y.; Villalona, E.; Knowles, R. R. Photocatalyst-Dependent Enantioselectivity in the Light-Driven Deracemization of Cyclic α-Aryl Ketones. *J. Am. Chem. Soc.* **2025**, *147* (18), 15307–15317. https://doi.org/10.1021/jacs.5c00847.

(161) Candish, L.; Collins, K. D.; Cook, G. C.; Douglas, J. J.; Gómez-Suárez, A.; Jolit, A.; Keess, S. Photocatalysis in the Life Science Industry. *Chem. Rev.* **2022**, *122* (2), 2907–2980. https://doi.org/10.1021/acs.chemrev.1c00416.

(162) Qiao, K.-K.; Feng, G.-S.; Shi, L. Nonenzymatic Catalytic Deracemization. *J. Catal.* **2023**, *422*, 99–116. https://doi.org/10.1016/j.jcat.2023.04.011.

(163) Wang, J.; Lv, X.; Jiang, Z. Visible-Light-Mediated Photocatalytic Deracemization. *Chem. – Eur. J.* **2023**, *29* (29), e202204029. https://doi.org/10.1002/chem.202204029.

(164) Wan, Q.; Wang, Z.; Sun, H.; Song, D.; Wang, X.; Liu, L. Enzymatic and Chemo–Catalytic Redox Deracemization: Recent Progress. *ChemCatChem* **2024**, *16* (14), e202301757. https://doi.org/10.1002/cctc.202301757.

(165) Loh, Y. Y.; Nagao, K.; Hoover, A. J.; Hesk, D.; Rivera, N. R.; Colletti, S. L.; Davies, I. W.; MacMillan, D. W. C. Photoredox-Catalyzed Deuteration and Tritiation of Pharmaceutical Compounds. *Science* **2017**, *358* (6367), 1182–1187. https://doi.org/10.1126/science.aap9674.

(166) Prakash, G.; Paul, N.; Oliver, G. A.; Werz, D. B.; Maiti, D. C–H Deuteration of Organic Compounds and Potential Drug Candidates. *Chem. Soc. Rev.* **2022**, *51* (8), 3123–3163. https://doi.org/10.1039/D0CS01496F.

(167) Tatoueix, K.; Lepron, M.; Barboux, C.; Scherrmann, M.-C.; Pieters, G.; Feuillastre, S. Unlocking the Potential of Hydrogen Deuterium Exchange via an Iterative Continuous-Flow Deuteration Process. *Nat. Commun.* **2025**, *16* (1), 1314. https://doi.org/10.1038/s41467-025-56600-8.

(168) Taglang, C.; Martínez-Prieto, L. M.; del Rosal, I.; Maron, L.; Poteau, R.; Philippot, K.; Chaudret, B.; Perato, S.; Sam Lone, A.; Puente, C.; Dugave, C.; Rousseau, B.; Pieters, G. Enantiospecific C□H Activation Using Ruthenium Nanocatalysts. *Angew. Chem. Int. Ed.* **2015**, *54* (36), 10474–10477. https://doi.org/10.1002/anie.201504554.

(169) Horn, E. J.; Rosen, B. R.; Baran, P. S. Synthetic Organic Electrochemistry: An Enabling and Innately Sustainable Method. *ACS Cent. Sci.* **2016**, *2* (5), 302–308. https://doi.org/10.1021/acscentsci.6b00091.
(170) Capaldo, L.; Quadri, L. L.; Ravelli, D. Merging Photocatalysis with Electrochemistry: The Dawn of a New Alliance in Organic Synthesis. *Angew. Chem. Int. Ed.* **2019**, *58* (49), 17508–17510. https://doi.org/10.1002/anie.201910348.
(171) Liu, J.; Lu, L.; Wood, D.; Lin, S. New Redox Strategies in Organic Synthesis by Means of Electrochemistry and Photochemistry. *ACS Cent. Sci.* **2020**, *6* (8), 1317–1340. https://doi.org/10.1021/acscentsci.0c00549.
(172) Zhang, S.; Findlater, M. Electrochemically Driven Hydrogen Atom Transfer Catalysis: A Tool for C($Sp^3$)/Si–H Functionalization and Hydrofunctionalization of Alkenes. *ACS Catal.* **2023**, *13* (13), 8731–8751. https://doi.org/10.1021/acscatal.3c01221.
(173) Reetz, M. T.; Qu, G.; Sun, Z. Engineered Enzymes for the Synthesis of Pharmaceuticals and Other High-Value Products. *Nat. Synth.* **2024**, *3* (1), 19–32. https://doi.org/10.1038/s44160-023-00417-0.
(174) May, O.; Verseck, S.; Bommarius, A.; Drauz, K. Development of Dynamic Kinetic Resolution Processes for Biocatalytic Production of Natural and Nonnatural L -Amino Acids. *Org. Process Res. Dev.* **2002**, *6* (4), 452–457. https://doi.org/10.1021/op020009g.
(175) Schnell, B.; Faber, K.; Kroutil, W. Enzymatic Racemisation and Its Application to Synthetic Biotransformations. *Adv. Synth. Catal.* **2003**, *345* (6–7), 653–666. https://doi.org/10.1002/adsc.200303009.
(176) Adams, E. Catalytic Aspects of Enzymatic Racemization. In *Advances in Enzymology - and Related Areas of Molecular Biology*; Meister, A., Ed.; Wiley, 1976; Vol. 44, pp 69–138. https://doi.org/10.1002/9780470122891.ch3.
(177) Hamed, R. B.; Gomez-Castellanos, J. R.; Sean Froese, D.; Krysztofinska, E.; Yue, W. W.; Schofield, C. J. Use of Methylmalonyl-CoA Epimerase in Enhancing Crotonase Stereoselectivity. *ChemBioChem* **2016**, *17* (6), 471–473. https://doi.org/10.1002/cbic.201500644.
(178) Musa, M. M. Enzymatic Racemization of Alcohols and Amines: An Approach for Bi-enzymatic Dynamic Kinetic Resolution. *Chirality* **2020**, *32* (2), 147–157. https://doi.org/10.1002/chir.23138.
(179) Fellechner, O.; Blatkiewicz, M.; Smirnova, I. Reactive Separations for In Situ Product Removal of Enzymatic Reactions: A Review. *Chem. Ing. Tech.* **2019**, *91* (11), 1522–1543. https://doi.org/10.1002/cite.201900027.
(180) Salami, H.; Lagerman, C. E.; Harris, P. R.; McDonald, M. A.; Bommarius, A. S.; Rousseau, R. W.; Grover, M. A. Model Development for Enzymatic Reactive Crystallization of β-Lactam Antibiotics: A Reaction–Diffusion-Crystallization Approach. *React. Chem. Eng.* **2020**, *5* (11), 2064–2080. https://doi.org/10.1039/D0RE00276C.
(181) Carneiro, T.; Wrzosek, K.; Bettenbrock, K.; Lorenz, H.; Seidel-Morgenstern, A. Immobilization of an Amino Acid Racemase for Application in Crystallization-based Chiral Resolutions of Asparagine Monohydrate. *Eng. Life Sci.* **2020**, *20* (12), 550–561. https://doi.org/10.1002/elsc.202000029.
(182) Intaraboonrod, K.; Harriehausen, I.; Carneiro, T.; Seidel-Morgenstern, A.; Lorenz, H.; Flood, A. E. Temperature Cycling Induced Deracemization of DL -Asparagine Monohydrate with Immobilized Amino Acid Racemase. *Cryst. Growth Des.* **2021**, *21* (1), 306–313. https://doi.org/10.1021/acs.cgd.0c01140.
(183) Noyori, R.; Tokunaga, M.; Kitamura, M. Stereoselective Organic Synthesis via Dynamic Kinetic Resolution. *Bull. Chem. Soc. Jpn.* **1995**, *68* (1), 36–55. https://doi.org/10.1246/bcsj.68.36.
(184) Patel, R.; Hanson, R.; Goswami, A.; Nanduri, V.; Banerjee, A.; Donovan, M.-J.; Goldberg, S.; Johnston, R.; Brzozowski, D.; Tully, T.; Howell, J.; Cazzulino, D.; Ko, R. Enzymatic Synthesis of Chiral Intermediates for Pharmaceuticals. *J. Ind. Microbiol. Biotechnol.* **2003**, *30* (5), 252–259. https://doi.org/10.1007/s10295-003-0032-6.

(185) Yoshioka, R. Racemization, Optical Resolution and Crystallization-Induced Asymmetric Transformation of Amino Acids and Pharmaceutical Intermediates. In *Novel Optical Resolution Technologies*; Sakai, K., Hirayama, N., Tamura, R., Eds.; Topics in Current Chemistry; Springer Berlin Heidelberg: Berlin, Heidelberg, 2007; Vol. 269, pp 83–132. https://doi.org/10.1007/128_2006_094.

(186) Steinreiber, J.; Faber, K.; Griengl, H. De-racemization of Enantiomers versus De-epimerization of Diastereomers—Classification of Dynamic Kinetic Asymmetric Transformations (DYKAT). *Chem. – Eur. J.* **2008**, *14* (27), 8060–8072. https://doi.org/10.1002/chem.200701643.

(187) Huang, M.; Pan, T.; Jiang, X.; Luo, S. Catalytic Deracemization Reactions. *J. Am. Chem. Soc.* **2023**, *145* (20), 10917–10929. https://doi.org/10.1021/jacs.3c02622.

(188) Shieh, W.-C.; Carlson, J. A. Asymmetric Transformation of Either Enantiomer of Narwedine via Total Spontaneous Resolution Process, a Concise Solution to the Synthesis of (-)-Galanthamine. *J. Org. Chem.* **1994**, *59* (18), 5463–5465. https://doi.org/10.1021/jo00097a060.

(189) Küenburg, B.; Czollner, L.; Fröhlich, J.; Jordis, U. Development of a Pilot Scale Process for the Anti-Alzheimer Drug (–)-Galanthamine Using Large-Scale Phenolic Oxidative Coupling and Crystallisation-Induced Chiral Conversion. *Org. Process Res. Dev.* **1999**, *3* (6), 425–431. https://doi.org/10.1021/op990019q.

(190) Synoradzki, L.; Hajmowicz, H.; Wisialski, J.; Mizerski, A.; Rowicki, T. Calcium Pantothenate. Part 3. Process for the Biologically Active Enantiomer of the Same via Selective Crystallization and Racemization. *Org. Process Res. Dev.* **2008**, *12* (6), 1238–1244. https://doi.org/10.1021/op800189g.

(191) Engwerda, A. H. J.; Maassen, R.; Tinnemans, P.; Meekes, H.; Rutjes, F. P. J. T.; Vlieg, E. Attrition-Enhanced Deracemization of the Antimalaria Drug Mefloquine. *Angew. Chem. Int. Ed.* **2019**, *58* (6), 1670–1673. https://doi.org/10.1002/anie.201811289.

(192) Harriehausen, I.; Wrzosek, K.; Lorenz, H.; Seidel-Morgenstern, A. Assessment of Process Configurations to Combine Enantioselective Chromatography with Enzymatic Racemization. *Adsorption* **2020**, *26* (7), 1199–1213. https://doi.org/10.1007/s10450-020-00231-6.

(193) Gänsch, J.; Huskova, N.; Kerst, K.; Temmel, E.; Lorenz, H.; Mangold, M.; Janiga, G.; Seidel-Morgenstern, A. Continuous Enantioselective Crystallization of Chiral Compounds in Coupled Fluidized Beds. *Chem. Eng. J.* **2021**, *422*, 129627. https://doi.org/10.1016/j.cej.2021.129627.

(194) Gänsch, J.; Oliynyk, K.; Potharaju, S.; Seidel-Morgenstern, A.; Lorenz, H. Continuous Chiral Inversion by Coupling Enzymatic Racemization with Enantioselective Fluidized Bed Crystallization. *Ind. Eng. Chem. Res.* **2024**, *63* (43), 18525–18535. https://doi.org/10.1021/acs.iecr.4c01970.

(195) Gänsch, J.; Gamm, I.; Seidel-Morgenstern, A.; Lorenz, H. Applicability of Fluidized Bed Crystallization for Separation of Enantiomers Forming Needle-Shaped Crystals. *Org. Process Res. Dev.* **2025**, *29* (2), 430–439. https://doi.org/10.1021/acs.oprd.4c00444.

(196) Williams, J. D.; Pöchlauer, P.; Okumura, Y.; Inami, Y.; Kappe, C. O. Photochemical Deracemization of a Medicinally-Relevant Benzopyran Using an Oscillatory Flow Reactor. *Chem. – Eur. J.* **2022**, *28* (29), e202200741. https://doi.org/10.1002/chem.202200741.

(197) Intaraboonrod, K.; Seidel-Morgenstern, A.; Lorenz, H.; Flood, A. E. Efficient Conversion of Threonine to Allothreonine Using Immobilized Amino Acid Racemase and Temperature Cycles. *Cryst. Growth Des.* **2021**, *21* (10), 5641–5650. https://doi.org/10.1021/acs.cgd.1c00484.

(198) Kwan, M. H. T.; Breen, J.; Bowden, M.; Conway, L.; Crossley, B.; Jones, M. F.; Munday, R.; Pokar, N. P. B.; Screen, T.; Blacker, A. J. Continuous Flow Chiral Amine Racemization Applied to Continuously Recirculating Dynamic Diastereomeric Crystallizations. *J. Org. Chem.* **2021**, *86* (3), 2458–2473. https://doi.org/10.1021/acs.joc.0c02617.

(199) Havinga, E. Spontaneous Formation of Optically Active Substances. *Biochim. Biophys. Acta* **1954**, *13*, 171–174. https://doi.org/10.1016/0006-3002(54)90300-5.

(200) Kondepudi, D. K.; Kaufman, R. J.; Singh, N. Chiral Symmetry Breaking in Sodium Chlorate Crystallization. *Science* **1990**, *250* (4983), 975–976. https://doi.org/10.1126/science.250.4983.975.
(201) McBride, J. M.; Carter, R. L. Spontaneous Resolution by Stirred Crystallization. *Angew. Chem. Int. Ed. Engl.* **1991**, *30* (3), 293–295. https://doi.org/10.1002/anie.199102931.
(202) Viedma, C. Chiral Symmetry Breaking During Crystallization: Complete Chiral Purity Induced by Nonlinear Autocatalysis and Recycling. *Phys. Rev. Lett.* **2005**, *94* (6), 065504. https://doi.org/10.1103/PhysRevLett.94.065504.
(203) Viedma, C. Chiral Symmetry Breaking and Complete Chiral Purity by Thermodynamic-Kinetic Feedback Near Equilibrium: Implications for the Origin of Biochirality. *Astrobiology* **2007**, *7* (2), 312–319. https://doi.org/10.1089/ast.2006.0099.
(204) Viedma, C. Experimental Evidence of Chiral Symmetry Breaking in Crystallization from Primary Nucleation. *J. Cryst. Growth* **2004**, *261* (1), 118–121. https://doi.org/10.1016/j.jcrysgro.2003.09.031.
(205) Madras, G.; McCoy, B. J. A Fragmentation Model for Crystal Attrition. *J. Cryst. Growth* **2007**, *305* (1), 211–217. https://doi.org/10.1016/j.jcrysgro.2007.04.019.
(206) Noorduin, W. L.; Meekes, H.; van Enckevort, W. J. P.; Millemaggi, A.; Leeman, M.; Kaptein, B.; Kellogg, R. M.; Vlieg, E. Complete Deracemization by Attrition-Enhanced Ostwald Ripening Elucidated. *Angew. Chem. Int. Ed.* **2008**, *47* (34), 6445–6447. https://doi.org/10.1002/anie.200801846.
(207) Hein, J. E.; Huynh Cao, B.; Viedma, C.; Kellogg, R. M.; Blackmond, D. G. Pasteur's Tweezers Revisited: On the Mechanism of Attrition-Enhanced Deracemization and Resolution of Chiral Conglomerate Solids. *J. Am. Chem. Soc.* **2012**, *134* (30), 12629–12636. https://doi.org/10.1021/ja303566g.
(208) Shtukenberg, A. G.; García-Ruiz, J. M.; Kahr, B. Punin Ripening and the Classification of Solution-Mediated Recrystallization Mechanisms. *Cryst. Growth Des.* **2021**, *21* (2), 1267–1277. https://doi.org/10.1021/acs.cgd.0c01545.
(209) Noorduin, W. L.; Izumi, T.; Millemaggi, A.; Leeman, M.; Meekes, H.; Van Enckevort, W. J. P.; Kellogg, R. M.; Kaptein, B.; Vlieg, E.; Blackmond, D. G. Emergence of a Single Solid Chiral State from a Nearly Racemic Amino Acid Derivative. *J. Am. Chem. Soc.* **2008**, *130* (4), 1158–1159. https://doi.org/10.1021/ja7106349.
(210) Gieling, J.; Wéry, G.; Lopes, C.; De Meester, J.; Brandel, C.; Cartigny, Y.; Leyssens, T.; Baier, D. M. Mechanochemical Deracemization: A Sustainable Approach to Enantiopurity. *Chem. – Eur. J.* **2025**, *31* (15), e202404120. https://doi.org/10.1002/chem.202404120.
(211) Xiouras, C.; Van Aeken, J.; Panis, J.; Ter Horst, J. H.; Van Gerven, T.; Stefanidis, G. D. Attrition-Enhanced Deracemization of $NaClO_3$: Comparison between Ultrasonic and Abrasive Grinding. *Cryst. Growth Des.* **2015**, *15* (11), 5476–5484. https://doi.org/10.1021/acs.cgd.5b01108.
(212) Noorduin, W. L.; Van Der Asdonk, P.; Bode, A. A. C.; Meekes, H.; Van Enckevort, W. J. P.; Vlieg, E.; Kaptein, B.; Van Der Meijden, M. W.; Kellogg, R. M.; Deroover, G. Scaling Up Attrition-Enhanced Deracemization by Use of an Industrial Bead Mill in a Route to Clopidogrel (Plavix). *Org. Process Res. Dev.* **2010**, *14* (4), 908–911. https://doi.org/10.1021/op1001116.
(213) Viedma, C.; Cintas, P. Homochirality beyond Grinding: Deracemizing Chiral Crystals by Temperature Gradient under Boiling. *Chem. Commun.* **2011**, *47* (48), 12786. https://doi.org/10.1039/c1cc14857e.
(214) Suwannasang, K.; Flood, A. E.; Rougeot, C.; Coquerel, G. Using Programmed Heating–Cooling Cycles with Racemization in Solution for Complete Symmetry Breaking of a Conglomerate Forming System. *Cryst. Growth Des.* **2013**, *13* (8), 3498–3504. https://doi.org/10.1021/cg400436r.
(215) Suwannasang, K.; Flood, A. E.; Coquerel, G. A Novel Design Approach To Scale Up the Temperature Cycle Enhanced Deracemization Process: Coupled Mixed-Suspension Vessels. *Cryst. Growth Des.* **2016**, *16* (11), 6461–6467. https://doi.org/10.1021/acs.cgd.6b01139.
(216) Palmans, A. R. A. Deracemisations under Kinetic and Thermodynamic Control. *Mol. Syst. Des. Eng.* **2017**, *2* (1), 34–46. https://doi.org/10.1039/C6ME00088F.

(217) Tsogoeva, S. B.; Wei, S.; Freund, M.; Mauksch, M. Generation of Highly Enantioenriched Crystalline Products in Reversible Asymmetric Reactions with Racemic or Achiral Catalysts. *Angew. Chem. Int. Ed.* **2009**, *48* (3), 590–594. https://doi.org/10.1002/anie.200803877.

(218) Flock, A. M.; Reucher, C. M. M.; Bolm, C. Enantioenrichment by Iterative Retro-Aldol/Aldol Reaction Catalyzed by an Achiral or Racemic Base. *Chem. – Eur. J.* **2010**, *16* (13), 3918–3921. https://doi.org/10.1002/chem.200903497.

(219) Rougeot, C.; Guillen, F.; Plaquevent, J.-C.; Coquerel, G. Ultrasound-Enhanced Deracemization: Toward the Existence of Agonist Effects in the Interpretation of Spontaneous Symmetry Breaking. *Cryst. Growth Des.* **2015**, *15* (5), 2151–2155. https://doi.org/10.1021/cg501765g.

(220) Nakamura, T.; Ban, K.; Yoshida, Y.; Mino, T.; Kasashima, Y.; Sakamoto, M. Asymmetric Synthesis of Indoline from Achiral Phthalimide Involving Crystallization-Induced Deracemization. *Chem. – Eur. J.* **2021**, *27* (66), 16338–16341. https://doi.org/10.1002/chem.202103345.

(221) Uemura, N.; Hosaka, M.; Washio, A.; Yoshida, Y.; Mino, T.; Sakamoto, M. Chiral Symmetry Breaking of Thiohydantoins by Attrition-Enhanced Deracemization. *Cryst. Growth Des.* **2020**, *20* (8), 4898–4903. https://doi.org/10.1021/acs.cgd.0c00829.

(222) Sanada, K.; Washio, A.; Nishihata, K.; Yagishita, F.; Yoshida, Y.; Mino, T.; Suzuki, S.; Kasashima, Y.; Sakamoto, M. Chiral Symmetry Breaking of Racemic 3-Phenylsuccinimides via Crystallization-Induced Dynamic Deracemization. *Cryst. Growth Des.* **2021**, *21* (11), 6051–6055. https://doi.org/10.1021/acs.cgd.1c01010.

(223) Engwerda, A. H. J.; Koning, N.; Tinnemans, P.; Meekes, H.; Bickelhaupt, F. M.; Rutjes, F. P. J. T.; Vlieg, E. Deracemization of a Racemic Allylic Sulfoxide Using Viedma Ripening. *Cryst. Growth Des.* **2017**, *17* (8), 4454–4457. https://doi.org/10.1021/acs.cgd.7b00828.

(224) Noorduin, W. L.; Kaptein, B.; Meekes, H.; van Enckevort, W. J. P.; Kellogg, R. M.; Vlieg, E. Fast Attrition-Enhanced Deracemization of Naproxen by a Gradual In Situ Feed. *Angew. Chem. Int. Ed.* **2009**, *48* (25), 4581–4583. https://doi.org/10.1002/anie.200901386.

(225) Sakamoto, M. Spontaneous Chiral Crystallization of Achiral Materials and Absolute Asymmetric Photochemical Transformation Using the Chiral Crystalline Environment. *J. Photochem. Photobiol. C Photochem. Rev.* **2006**, *7* (4), 183–196. https://doi.org/10.1016/j.jphotochemrev.2006.11.002.

(226) Steendam, R. R. E.; Verkade, J. M. M.; Van Benthem, T. J. B.; Meekes, H.; Van Enckevort, W. J. P.; Raap, J.; Rutjes, F. P. J. T.; Vlieg, E. Emergence of Single-Molecular Chirality from Achiral Reactants. *Nat. Commun.* **2014**, *5* (1), 5543. https://doi.org/10.1038/ncomms6543.

(227) Steendam, R. R. E.; Kulka, M. W.; Meekes, H.; Van Enckevort, W. J. P.; Raap, J.; Vlieg, E.; Rutjes, F. P. J. T. One-Pot Synthesis, Crystallization and Deracemization of Isoindolinones from Achiral Reactants. *Eur. J. Org. Chem.* **2015**, *2015* (33), 7249–7252. https://doi.org/10.1002/ejoc.201501191.

(228) Cameli, F.; Ter Horst, J. H.; Steendam, R. R. E.; Xiouras, C.; Stefanidis, G. D. On the Effect of Secondary Nucleation on Deracemization through Temperature Cycles. *Chem. – Eur. J.* **2020**, *26* (6), 1344–1354. https://doi.org/10.1002/chem.201904239.

(229) Breveglieri, F.; Mazzotti, M. Role of Racemization Kinetics in the Deracemization Process via Temperature Cycles. *Cryst. Growth Des.* **2019**, *19* (6), 3551–3558. https://doi.org/10.1021/acs.cgd.9b00410.

(230) Steendam, R. R. E.; Harmsen, B.; Meekes, H.; Van Enckevort, W. J. P.; Kaptein, B.; Kellogg, R. M.; Raap, J.; Rutjes, F. P. J. T.; Vlieg, E. Controlling the Effect of Chiral Impurities on Viedma Ripening. *Cryst. Growth Des.* **2013**, *13* (11), 4776–4780. https://doi.org/10.1021/cg400927m.

(231) Steendam, R. R. E.; Dickhout, J.; Van Enckevort, W. J. P.; Meekes, H.; Raap, J.; Rutjes, F. P. J. T.; Vlieg, E. Linear Deracemization Kinetics during Viedma Ripening: Autocatalysis Overruled by Chiral Additives. *Cryst. Growth Des.* **2015**, *15* (4), 1975–1982. https://doi.org/10.1021/acs.cgd.5b00127.

(232) Baglai, I.; Leeman, M.; Wurst, K.; Kellogg, R. M.; Noorduin, W. L. Enantiospecific Solid Solution Formation Triggers the Propagation of Homochirality. *Angew. Chem.* **2020**, *132* (47), 21071–21075. https://doi.org/10.1002/ange.202009719.

(233) Noorduin, W. L.; Meekes, H.; van Enckevort, W. J. P.; Kaptein, B.; Kellogg, R. M.; Vlieg, E. Enantioselective Symmetry Breaking Directed by the Order of Process Steps. *Angew. Chem. Int. Ed.* **2010**, *49* (14), 2539–2541. https://doi.org/10.1002/anie.200907231.

(234) Guillot, M.; De Meester, J.; Huynen, S.; Collard, L.; Robeyns, K.; Riant, O.; Leyssens, T. Cocrystallization-Induced Spontaneous Deracemization: A General Thermodynamic Approach to Deracemization. *Angew. Chem.* **2020**, *132* (28), 11399–11402. https://doi.org/10.1002/ange.202002464.

(235) Lerdwiriyanupap, T.; Belletti, G.; Tinnemans, P.; Meekes, H.; Rutjes, F. P. J. T.; Vlieg, E.; Flood, A. E. Combining Diastereomeric Resolution and Viedma Ripening by Using a Racemic Resolving Agent. *Eur. J. Org. Chem.* **2021**, *2021* (44), 5975–5980. https://doi.org/10.1002/ejoc.202101193.

(236) Oketani, R.; Shiohara, K.; Hisaki, I. Crystallization-Induced Diastereomeric Transformation of Chiral Ozanimod Key Intermediate Using Homogeneous Ir-Based Racemization Catalyst. *Cryst. Growth Des.* **2024**, *24* (13), 5397–5401. https://doi.org/10.1021/acs.cgd.4c00604.

(237) Su, X.; Sun, J.; Liu, J.; Wang, Y.; Wang, J.; Tang, W.; Gong, J. Bifunctional Chiral Agent Enables One-pot Spontaneous Deracemization of Racemic Compounds. *Angew. Chem. Int. Ed.* **2024**, *63* (22), e202402886. https://doi.org/10.1002/anie.202402886.

(238) Baglai, I.; Leeman, M.; Wurst, K.; Kellogg, R. M.; Noorduin, W. L. Enantiospecific Solid Solution Formation Triggers the Propagation of Homochirality. *Angew. Chem. Int. Ed.* **2020**, *59* (47), 20885–20889. https://doi.org/10.1002/anie.202009719.

(239) Pinètre, C.; Gendron, F.; Kuroda, R.; Oketani, R.; Aupetit, C.; Buffeteau, T.; Coquerel, G. Use of Conglomerate Mixed Crystals to Deracemize a Stable Racemic-Compound-Forming System. *Chem. – Eur. J.* **2023**, *29* (27), e202300441. https://doi.org/10.1002/chem.202300441.

(240) Murray, J. I.; Sanders, J. N.; Richardson, P. F.; Houk, K. N.; Blackmond, D. G. Isotopically Directed Symmetry Breaking and Enantioenrichment in Attrition-Enhanced Deracemization. *J. Am. Chem. Soc.* **2020**, *142* (8), 3873–3879. https://doi.org/10.1021/jacs.9b11422.

(241) Björemark, P. M.; Jönsson, J.; Håkansson, M. Absolute Asymmetric Synthesis: Viedma Ripening of $[Co(Bpy)_3]^{2+}$ and Solvent-Free Oxidation to $[Co(Bpy)_3]^{3+}$. *Chem. – Eur. J.* **2015**, *21* (30), 10630–10633. https://doi.org/10.1002/chem.201500876.

(242) Wang, Y.; Nieto-Ortega, B.; Bürgi, T. Amplification of Enantiomeric Excess by Dynamic Inversion of Enantiomers in Deracemization of Au38 Clusters. *Nat. Commun.* **2020**, *11* (1), 4562. https://doi.org/10.1038/s41467-020-18357-0.

(243) Deng, H.; Yuan, P.; Lao, K.; Fu, Q.; Teo, B. K.; Zheng, N. Glacial Acetic Acid as a Resolution Solvent for Growing Enantiopure Crystals from Racemic Mixtures. *Inorg. Chem. Front.* **2025**, *12* (1), 171–178. https://doi.org/10.1039/D4QI01944J.

(244) Wu, S.-T.; Zhang, Y.-S.; Zhang, B.; Hu, X.-L.; Huang, X.-H.; Huang, C.-C.; Zhuang, N.-F. Viedma Ripening of Chiral Coordination Polymers Based on Achiral Molecules. *Cryst. Growth Des.* **2019**, *19* (5), 2537–2541. https://doi.org/10.1021/acs.cgd.9b00235.

(245) Yang, S.; Geiger, Y.; Geerts, M.; Eleveld, M. J.; Kiani, A.; Otto, S. Enantioselective Self-Replicators. *J. Am. Chem. Soc.* **2023**, *145* (30), 16889–16898. https://doi.org/10.1021/jacs.3c05472.

(246) Hananel, U.; Moshe, A. B.; Markovich, G.; Alivisatos, A. P. Nanocrystals as Model Systems for Studying the Interplay Between Crystallization and Chirality. *Isr. J. Chem.* **2021**, *61* (11–12), 697–707. https://doi.org/10.1002/ijch.202100058.

(247) Noorduin, W. L.; van Enckevort, W. J. P.; Meekes, H.; Kaptein, B.; Kellogg, R. M.; Tully, J. C.; McBride, J. M.; Vlieg, E. The Driving Mechanism Behind Attrition-Enhanced Deracemization. *Angew. Chem. Int. Ed.* **2010**, *49* (45), 8435–8438. https://doi.org/10.1002/anie.201002036.
(248) Uwaha, M. A Model for Complete Chiral Crystallization. *J. Phys. Soc. Jpn.* **2004**, *73* (10), 2601–2603. https://doi.org/10.1143/JPSJ.73.2601.
(249) Saito, Y.; Hyuga, H. Chirality Selection in Crystallization. *J. Phys. Soc. Jpn.* **2005**, *74* (2), 535–537. https://doi.org/10.1143/JPSJ.74.535.
(250) Uwaha, M. Simple Models for Chirality Conversion of Crystals and Molecules by Grinding. *J. Phys. Soc. Jpn.* **2008**, *77* (8), 083802. https://doi.org/10.1143/JPSJ.77.083802.
(251) Ricci, F.; Stillinger, F. H.; Debenedetti, P. G. A Computational Investigation of Attrition-Enhanced Chiral Symmetry Breaking in Conglomerate Crystals. *J. Chem. Phys.* **2013**, *139* (17), 174503. https://doi.org/10.1063/1.4827478.
(252) Frank, F. C. On Spontaneous Asymmetric Synthesis. *Biochim. Biophys. Acta* **1953**, *11*, 459–463. https://doi.org/10.1016/0006-3002(53)90082-1.
(253) Blanco, C.; Crusats, J.; El-Hachemi, Z.; Moyano, A.; Veintemillas-Verdaguer, S.; Hochberg, D.; Ribó, J. M. The Viedma Deracemization of Racemic Conglomerate Mixtures as a Paradigm of Spontaneous Mirror Symmetry Breaking in Aggregation and Polymerization. *ChemPhysChem* **2013**, *14* (17), 3982–3993. https://doi.org/10.1002/cphc.201300699.
(254) Ribó, J. M.; Hochberg, D.; Crusats, J.; El-Hachemi, Z.; Moyano, A. Spontaneous Mirror Symmetry Breaking and Origin of Biological Homochirality. *J. R. Soc. Interface* **2017**, *14* (137), 20170699. https://doi.org/10.1098/rsif.2017.0699.
(255) Iggland, M.; Mazzotti, M. A Population Balance Model for Chiral Resolution via Viedma Ripening. *Cryst. Growth Des.* **2011**, *11* (10), 4611–4622. https://doi.org/10.1021/cg2008599.
(256) Spix, L.; Engwerda, A. H. J.; Meekes, H.; Van Enckevort, W. J. P.; Vlieg, E. Persistent Reverse Enantiomeric Excess in Solution during Viedma Ripening. *Cryst. Growth Des.* **2016**, *16* (8), 4752–4758. https://doi.org/10.1021/acs.cgd.6b00804.
(257) Katsuno, H.; Uwaha, M. Mechanism of Chirality Conversion by Periodic Change of Temperature: Role of Chiral Clusters. *Phys. Rev. E* **2016**, *93* (1), 013002. https://doi.org/10.1103/PhysRevE.93.013002.
(258) Dey, A.; Bomans, P. H. H.; Müller, F. A.; Will, J.; Frederik, P. M.; De With, G.; Sommerdijk, N. A. J. M. The Role of Prenucleation Clusters in Surface-Induced Calcium Phosphate Crystallization. *Nat. Mater.* **2010**, *9* (12), 1010–1014. https://doi.org/10.1038/nmat2900.
(259) Gebauer, D.; Cölfen, H. Prenucleation Clusters and Non-Classical Nucleation. *Nano Today* **2011**, *6* (6), 564–584. https://doi.org/10.1016/j.nantod.2011.10.005.
(260) Finney, A. R.; Rodger, P. M. Probing the Structure and Stability of Calcium Carbonate Pre-Nucleation Clusters. *Faraday Discuss.* **2012**, *159*, 47. https://doi.org/10.1039/c2fd20054f.
(261) Gebauer, D.; Kellermeier, M.; Gale, J. D.; Bergström, L.; Cölfen, H. Pre-Nucleation Clusters as Solute Precursors in Crystallisation. *Chem Soc Rev* **2014**, *43* (7), 2348–2371. https://doi.org/10.1039/C3CS60451A.
(262) Zahn, D. Thermodynamics and Kinetics of Prenucleation Clusters, Classical and Non-Classical Nucleation. *ChemPhysChem* **2015**, *16* (10), 2069–2075. https://doi.org/10.1002/cphc.201500231.
(263) Jin, B.; Liu, Z.; Tang, R. Recent Experimental Explorations of Non-Classical Nucleation. *CrystEngComm* **2020**, *22* (24), 4057–4073. https://doi.org/10.1039/D0CE00480D.
(264) Zong, S.; Wang, J.; Huang, X.; Wang, T.; Liu, Q.; Tian, B.; Xie, C.; Hao, H. Molecular Evolution Pathways during Nucleation of Small Organic Molecules: Solute-Rich Pre-Nucleation Species Enable Control over the Nucleation Process. *Phys. Chem. Chem. Phys.* **2020**, *22* (33), 18663–18671. https://doi.org/10.1039/D0CP03493B.

(265) Svärd, M. Mesoscale Clusters of Organic Solutes in Solution and Their Role in Crystal Nucleation. *CrystEngComm* **2022**, *24* (29), 5182–5193. https://doi.org/10.1039/D2CE00718E.

(266) Urquidi, O.; Brazard, J.; LeMessurier, N.; Simine, L.; Adachi, T. B. M. In Situ Optical Spectroscopy of Crystallization: One Crystal Nucleation at a Time. *Proc. Natl. Acad. Sci.* **2022**, *119* (16), e2122990119. https://doi.org/10.1073/pnas.2122990119.

(267) El-Hachemi, Z.; Crusats, J.; Ribó, J. M.; McBride, J. M.; Veintemillas-Verdaguer, S. Metastability in Supersaturated Solution and Transition towards Chirality in the Crystallization of $NaClO_3$. *Angew. Chem. Int. Ed.* **2011**, *50* (10), 2359–2363. https://doi.org/10.1002/anie.201007209.

(268) Viedma, C.; McBride, J. M.; Kahr, B.; Cintas, P. Enantiomer-Specific Oriented Attachment: Formation of Macroscopic Homochiral Crystal Aggregates from a Racemic System. *Angew. Chem. Int. Ed.* **2013**, *52* (40), 10545–10548. https://doi.org/10.1002/anie.201303915.

(269) Viedma, C.; Cuccia, L. A.; McTaggart, A.; Kahr, B.; Martin, A. T.; McBride, J. M.; Cintas, P. Oriented Attachment by Enantioselective Facet Recognition in Millimeter-Sized Gypsum Crystals. *Chem. Commun.* **2016**, *52* (78), 11673–11676. https://doi.org/10.1039/C6CC06353E.

(270) Sivakumar, R.; Kwiatoszynski, J.; Fouret, A.; Nguyen, T. P. T.; Ramrup, P.; Cheung, P. S. M.; Cintas, P.; Viedma, C.; Cuccia, L. A. Enantiomer-Specific Oriented Attachment of Guanidine Carbonate Crystals. *Cryst. Growth Des.* **2016**, *16* (7), 3573–3576. https://doi.org/10.1021/acs.cgd.6b00547.

(271) Li, J.; Liu, Y.; Guo, Z.; Han, D.; Gong, J. Tuning Organic Crystal Chirality by Enantiomer-Specific Oriented Attachment. *CrystEngComm* **2024**, *26* (37), 5278–5286. https://doi.org/10.1039/D4CE00546E.

(272) Huang, Z.; Hu, Y.; Sun, J.; He, Z.; Jiang, T.; Tian, H.; Ma, X. Visualization of Enantiorecognition by Excited-State Conformation Modulation. *Nat. Commun.* **2025**, *16* (1), 7788. https://doi.org/10.1038/s41467-025-63065-2.

(273) Saito, Y.; Hyuga, H. Chiral Crystal Growth under Grinding. *J. Phys. Soc. Jpn.* **2008**, *77* (11), 113001. https://doi.org/10.1143/JPSJ.77.113001.

(274) Skrdla, P. J. Kinetics and Thermodynamics of Efficient Chiral Symmetry Breaking in Nearly Racemic Mixtures of Conglomerate Crystals. *Cryst. Growth Des.* **2011**, *11* (5), 1957–1965. https://doi.org/10.1021/cg200116e.

(275) Anwar, J.; Khan, S.; Lindfors, L. Secondary Crystal Nucleation: Nuclei Breeding Factory Uncovered. *Angew. Chem. Int. Ed.* **2015**, *54* (49), 14681–14684. https://doi.org/10.1002/anie.201501216.

(276) Sarkar, S.; Sarkar, A.; Som, A.; Agasti, S. S.; George, S. J. Stereoselective Primary and Secondary Nucleation Events in Multicomponent Seeded Supramolecular Polymerization. *J. Am. Chem. Soc.* **2021**, *143* (30), 11777–11787. https://doi.org/10.1021/jacs.1c05642.

(277) De Vrieze, L.; Kuhn, S. The Overestimated Capability of Fluid Shear to Induce Secondary Nucleation: An Urgent Call for Diligently Executed Control Experiments. *CrystEngComm* **2025**, *27* (28), 4810–4815. https://doi.org/10.1039/D5CE00323G.

(278) Noorduin, W. L.; Meekes, H.; Bode, A. A. C.; Van Enckevort, W. J. P.; Kaptein, B.; Kellogg, R. M.; Vlieg, E. Explanation for the Emergence of a Single Chiral Solid State during Attrition-Enhanced Ostwald Ripening: Survival of the Fittest. *Cryst. Growth Des.* **2008**, *8* (5), 1675–1681. https://doi.org/10.1021/cg701211a.

(279) Uwaha, M.; Katsuno, H. Mechanism of Chirality Conversion of Crystals by Viedma Ripening and Temperature Cycling. *J. Cryst. Growth* **2022**, *598*, 126873. https://doi.org/10.1016/j.jcrysgro.2022.126873.

(280) Uwaha, M.; Katsuno, H. Mechanism of Chirality Conversion by Grinding Crystals: Ostwald Ripening vs Crystallization of Chiral Clusters. *J. Phys. Soc. Jpn.* **2009**, *78* (2), 023601. https://doi.org/10.1143/JPSJ.78.023601.

(281) Katsuno, H.; Uwaha, M. Monte Carlo Simulation of a Cluster Model for the Chirality Conversion of Crystals with Grinding. *J. Cryst. Growth* **2009**, *311* (17), 4265–4269. https://doi.org/10.1016/j.jcrysgro.2009.07.005.

(282) Shekunov, B. Yu.; Grant, D. J. W. *In Situ* Optical Interferometric Studies of the Growth and Dissolution Behavior of Paracetamol (Acetaminophen). 1. Growth Kinetics. *J. Phys. Chem. B* **1997**, *101* (20), 3973–3979. https://doi.org/10.1021/jp9639298.

(283) Snyder, R. C.; Studener, S.; Doherty, M. F. Manipulation of Crystal Shape by Cycles of Growth and Dissolution. *AIChE J.* **2007**, *53* (6), 1510–1517. https://doi.org/10.1002/aic.11174.

(284) Snyder, R. C.; Doherty, M. F. Faceted Crystal Shape Evolution during Dissolution or Growth. *AIChE J.* **2007**, *53* (5), 1337–1348. https://doi.org/10.1002/aic.11132.

(285) Eisenschmidt, H.; Bajcinca, N.; Sundmacher, K. Optimal Control of Crystal Shapes in Batch Crystallization Experiments by Growth-Dissolution Cycles. *Cryst. Growth Des.* **2016**, *16* (6), 3297–3306. https://doi.org/10.1021/acs.cgd.6b00288.

(286) Lovette, M. A.; Muratore, M.; Doherty, M. F. Crystal Shape Modification through Cycles of Dissolution and Growth: Attainable Regions and Experimental Validation. *AIChE J.* **2012**, *58* (5), 1465–1474. https://doi.org/10.1002/aic.12707.

(287) Neugebauer, P.; Cardona, J.; Besenhard, M. O.; Peter, A.; Gruber-Woelfler, H.; Tachtatzis, C.; Cleary, A.; Andonovic, I.; Sefcik, J.; Khinast, J. G. Crystal Shape Modification via Cycles of Growth and Dissolution in a Tubular Crystallizer. *Cryst. Growth Des.* **2018**, *18* (8), 4403–4415. https://doi.org/10.1021/acs.cgd.8b00371.

(288) Kuvadia, Z. B.; Doherty, M. F. Spiral Growth Model for Faceted Crystals of Non-Centrosymmetric Organic Molecules Grown from Solution. *Cryst. Growth Des.* **2011**, *11* (7), 2780–2802. https://doi.org/10.1021/cg101560u.

(289) Ulrich, J. Growth Rate Dispersion — a Review. *Cryst. Res. Technol.* **1989**, *24* (3), 249–257. https://doi.org/10.1002/crat.2170240302.

(290) Suwannasang, K.; Coquerel, G.; Rougeot, C.; Flood, A. E. Mathematical Modeling of Chiral Symmetry Breaking Due to Differences in Crystal Growth Kinetics. *Chem. Eng. Technol.* **2014**, *37* (8), 1329–1339. https://doi.org/10.1002/ceat.201400056.

(291) Uchin, R.; Suwannasang, K.; Flood, A. E. Model of Temperature Cycle-Induced Deracemization via Differences in Crystal Growth Rate Dispersion. *Chem. Eng. Technol.* **2017**, *40* (7), 1252–1260. https://doi.org/10.1002/ceat.201600746.

(292) Choi, H. S.; Oh, I. H.; Zhang, B.; Coquerel, G.; Kim, W.-S.; Park, B. J. Chiral Flipping in Viedma Deracemization. *J. Phys. Chem. Lett.* **2024**, *15* (16), 4367–4374. https://doi.org/10.1021/acs.jpclett.4c00558.

(293) Deck, L.-T.; Hosseinalipour, M. S.; Mazzotti, M. Exact and Ubiquitous Condition for Solid-State Deracemization in Vitro and in Nature. *J. Am. Chem. Soc.* **2024**, *146* (6), 3872–3882. https://doi.org/10.1021/jacs.3c11332.

(294) Carder, H. M.; Occhialini, G.; Bistoni, G.; Riplinger, C.; Kwan, E. E.; Wendlandt, A. E. The Sugar Cube: Network Control and Emergence in Stereoediting Reactions. *Science* **2024**, *385* (6707), 456–463. https://doi.org/10.1126/science.adp2447.

(295) Borsley, S.; Leigh, D. A.; Roberts, B. M. W. Molecular Ratchets and Kinetic Asymmetry: Giving Chemistry Direction. *Angew. Chem. Int. Ed.* **2024**, *63* (23), e202400495. https://doi.org/10.1002/anie.202400495.

Chapter 4

# Chiral Amplification through Asymmetric Crystal Growth under Racemizing Conditions.*

*Amplification of enantiomeric excesses (ee) is routinely observed during chiral crystallization of conglomerate crystals for which the enantiomers undergo racemization in solution. Although routes comprising a combination of crystal growth and dissolution are frequently used to obtain enantiopure molecules, crystal growth by itself has rather been considered as a source of enantiomeric erosion and discounted as a potential source of enantiomeric amplification. Counterintuitively, we here demonstrate striking enantiomeric amplification during crystal growth for clopidogrel and tert-leucine precursors. Based on a mechanistic framework, we identify that the interplay between racemization and crystal growth rates elicits this surprising effect. The asymmetric amplification of the solid-phase ee can be enhanced by increasing the mass of grown material relative to the product such that small amounts of seeds of only 60% ee already result in virtually exclusive growth of the majority phase. These results impact our understanding of asymmetric amplification mechanisms during crystallization and offer a tangible basis for practical production of enantiopure molecules.*



## Introduction

Asymmetric amplification phenomena are of fundamental interest for understanding the emergence of enantiopure building blocks for the origin of life. Moreover, they offer practical routes for synthesis of essential molecules such as agricultural compounds and pharmaceuticals.[1–18] Amplification has been observed in catalysis, in which the chiral product exhibits a larger enantiomeric excess (*ee*) than the enantiopurity of the catalysts.[3,19] In the unique case of the Soai reaction, the reaction product even feeds back to catalyze its own formation, thus resulting in auto-catalytic amplification.[3] In contrast, amplification of *ee* is routinely observed during crystallization processes when enantiomers undergo racemization in solution while crystallizing in separate crystals (so-called conglomerates).[16,20–33] In particular, slurries of left- and right-handed enantiomorphic crystals can convert into an enantiopure phase via continuous growth and dissolution using, for instance, temperature gradient deracemization,[34] temperature cycling induced

* This chapter has been published as S.W. van Dongen, I. Ahlal, M. Leeman, B. Kaptein, R.M. Kellogg, I. Baglai, W.L. Noorduin (2023). Chiral Amplification through the Interplay of Racemizing Conditions and Asymmetric Crystal Growth. *J. Am. Chem. Soc*. 145(1): 436–442.

deracemization (TCID)[35–42] or attrition-enhanced deracemization (Viedma ripening).[25,27,29,43–46] Already, these deracemization processes have been demonstrated for a wide range of molecules, including precursors of agricultural compounds and blockbuster pharmaceuticals.[27,42,44,46–51] Even though there is still debate over the details of the underlying mechanism in these remarkable processes,[52] there is general consensus that the interplay between growth and dissolution is essential for achieving enantioenrichment through crystallization.[30,37,40,53–56]

Indeed, it is not obvious if, and how, merely growth of crystals can lead to any form of enantioenrichment. To understand this commonly assumed tenet, we consider a population of left and right-handed conglomerate seed crystals that are in contact with a supersaturated racemizing solution. Based on classical crystal growth theory, there is a tacit understanding that each crystal—either left- or right-handed—has a prima facie equal probability to incorporate molecular building blocks from the racemizing solution. Consequently, it is believed that during crystal growth the masses of both crystal populations would grow proportional to their population size. The initial enantiomeric excess of the solid phase thus remains preserved and no enantioenrichment is expected. Moreover, racemization is not infinitely fast and perturbations of the supersaturated solution can lead to nucleation, both of which favor the minority enantiomer and therefore are expected to result in erosion instead of preservation—let alone amplification—of the chiral purity. Hence, motivated by arguments along these lines of thought, crystal growth is generally considered as a source of erosion of *ee* and has therefore been discounted as a potential route for chiral amplification.

Contrary to this line of reasoning, in this Chapter we experimentally demonstrate that large and systematic chiral amplification can occur during crystal growth, such that even seed crystals with low enantiopurity can yield final products with high enantiomeric purity. Using precursors of clopidogrel and tert-leucine (Scheme 4.1) as model compounds, which are known to be conglomerates,[47,49] we demonstrate that the interplay between the crystal growth rate and racemization rate can create an

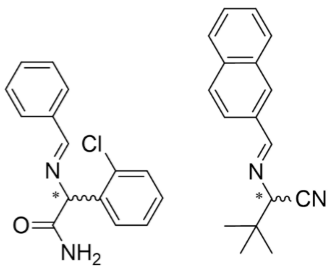


**1** **2**

**Scheme 4.1.** Racemizable conglomerates **1** and **2** used for demonstrating the mechanistic framework.

asymmetric form of crystal growth such that the majority phase grows faster than the minority phase (Fig. 4.1). We show that this surprising imbalance in the growth rates can give rise to amplification of the solid phase ee during crystallization. These results impact our fundamental understanding of crystal growth, the practical production of chiral molecules, and the discussion on the origin of homochirality.

## Results and Discussion

To guide the experiments, we define a framework to understand how the interplay between the crystallization rate and racemization rate can lead to this counterintuitive asymmetric amplification (Fig. 4.1). We consider seeding a clear supersaturated solution with crystals of low enantiomeric purity ($ee_0$) for three scenarios: (i) no racemization, (ii) relatively slow racemization compared to crystallization, and (iii) relatively fast racemization (Fig. 4.1A). We define the enantiomeric excess of the material deposited during growth onto the seed crystals as $ee_\Delta$. When no racemization is present, we expect erosion—essentially dilution—of the initial enantiomeric excess ($ee_\Delta = 0$), since equal amounts of both enantiomers are deposited, maintaining the eutectic composition in solution ($ee_{eu} = 0$) typical for conglomerate systems. When racemization is initiated, the enantiomers in solution become an increasingly common resource pool available to both populations of enantiomorphic crystals. For slow racemization, an initial enantiomeric excess can potentially be consolidated during growth ($ee_\Delta = ee_0$): the balancing of racemization and crystallization rates allows for the timely replenishment of the faster growing major enantiomer so that both crystal populations can grow proportionally to their initial composition. Indeed, the extent of amplification is racemization rate limited. When racemization is much faster than crystallization, the supply of major enantiomer is not limiting, and the balance can tip over: the faster growing major enantiomer draws away even more minor enantiomer in order to lower the supersaturation as fast as possible such that the initial enantiomeric excess is

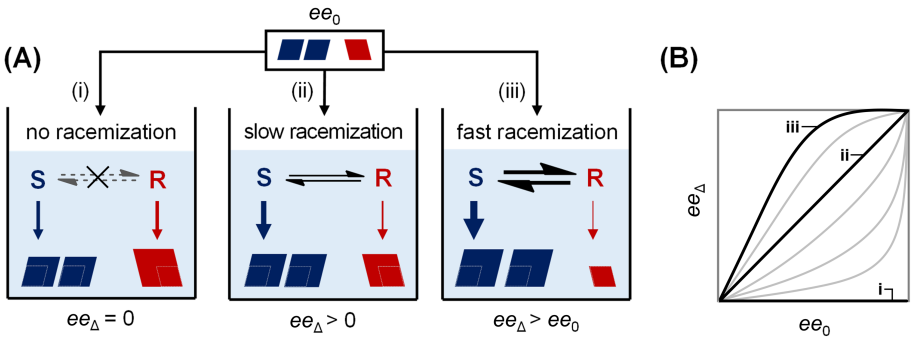


**Figure 4.1.** Mechanistic framework for amplification of the solid phase *ee* during crystal growth from a supersaturated racemic solution. (A) The balance between the crystallization and racemization rates determines if (i) erosion, (ii) consolidation, or (iii) amplification of the initial enantiomeric excess $ee_0$ of the seed crystals occurs: the solute resource pool is limited by the relative racemization rate. (B) The *ee* of the material deposited onto the seed crystals during growth ($ee_\Delta$) as function of the *ee* of the seed crystal $ee_0$ for the different scenarios.

amplified ($ee_\Delta > ee_0$). Visualizing $ee_\Delta$ for different starting $ee_0$'s (Fig. 4.1B),[57] this framework thus suggests that balancing racemization and crystallization rates can result in either erosion, consolidation or amplification of $ee_0$.

To demonstrate this experimentally, we study the growth of enantiomerically enriched seed crystals in contact with a supersaturated racemic solution in the absence and presence of a racemization catalyst using the compound 2-(benzylideneamino)-2-(2-chlorophenyl)acetamide (**1**, Scheme 4.1). This precursor to the cardiovascular drug Plavix (clopidogrel) is a conglomerate and can be easily racemized with tunable rate using the organic base 1,8-diazabicyclo[5.4.0]undec-7-ene (DBU) in acetonitrile. This compound has been used extensively to study both Viedma ripening and TCID, making **1** ideally suitable to study growth under racemizing conditions.[40,47,58,59]



To determine the experimental parameters for crystal growth, we establish the temperature-dependent solubility of (*RS*)-**1** (Fig. 4.2A), and determine the supersaturation at which spontaneous nucleation occurs, in order to define the metastable zone wherein merely growth takes place (Fig. 4.2A). The region between 20 and 30 °C in the phase diagram is within the metastable zone and suitable to grow substantial amounts of material. To grow in this region of the phase diagram, we first saturate a solution at 30 °C in the presence of various amounts of racemization catalyst (0, 1, 2, 5 or 10 µL/mL DBU). We then abruptly cool the solution down to 20 °C, to create a clear supersaturated solution, which is then added to a solid phase of enriched seed crystals (25 mg/mL of 20% $ee_0$ in (*R*)-**1**) to initiate growth (Fig. 4.2A). The resulting slurry is kept homogeneous using a shaking platform at the lowest possible setting (ca. 300 rpm). We use shaking—rather than stirring—to focus on crystal growth effects while avoiding undesired attrition and secondary nucleation. After 90 minutes, we determine the enantiomeric composition of the solid phase using chiral HPLC. To analyze the change of the solid phase composition as a result of growth, we calculate the enantiomeric excess of the grown material ($ee_\Delta$) using equation 4.1:

$$ee_\Delta = ee_P + \frac{m_0}{m_\Delta}(ee_P - ee_0) \qquad \text{(eq. 4.1)}$$

where $ee_P$ is the *ee* after growth, $m_0$ is the mass of seed crystals, $ee_0$ is the *ee* of the seed crystals, and $m_\Delta$ is the mass of grown material as determined by the difference in solubility between 20 and 30 °C.

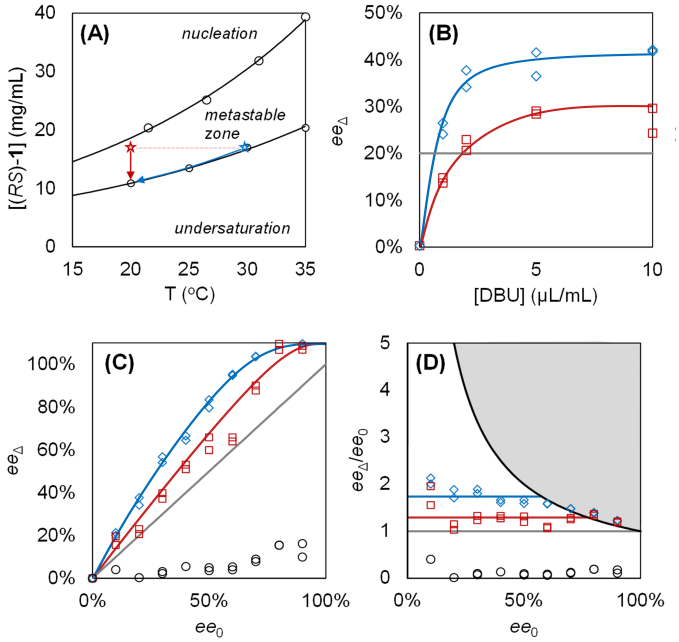


**Figure 4.2.** Erosion, consolidation and amplification of solid phase *ee* of **1** during crystal growth depends on the balance between the crystallization and racemization rate. (A) Temperature-dependent phase diagram with the metastable zone of (*RS*)-**1** in MeCN. The stars indicate the seeding conditions: abrupt (red, seed at 20 °C) or slow (blue, seed at 30 °C) cooling. (B, C) The enantiomeric excess of crystallized material $ee_\Delta$ is shown as function of (B) the amount of racemization catalyst DBU ($ee_0$ = 20%) and (C) as a function of the enantiomeric excess of the seed crystals $ee_0$ ([DBU] = 2 µL/mL) for abrupt cooling (red squares), slow cooling (blue diamonds), and no racemization (black circles, [DBU] = 0). (D) Experimental amplification factor $ee_\Delta/ee_0$ as function of $ee_0$ showing approximately constant amplification up to the theoretical limit 100%/$ee_0$ (grey zone). Blue and red lines (B, C, D) are guides to the eye.

After seeding, the phase diagram predicts that $m_\Delta$ = 6 mg/mL of **1** is grown on the seeds, i.e. the solid phase concentration increases to 31 mg/mL. We thus expect the average size of crystals to increase, which is confirmed by comparing scanning electron microscopy images of the crystals before and after growth (data shown in the Appendix). In the absence of racemization (0 µL/mL DBU), we observe erosion of the solid phase enantiopurity from $ee_0$ = 20% to $ee_P$ = 16%. This $ee_P$ corresponds to the precipitation of equal amounts of *R* and *S* (3 mg/mL of (*R*)-**1** and 3 mg/mL of (*S*)-**1**) yielding $ee_\Delta$ = 0 from equation 4.1 (Fig. 4.2B). Consistent with scenario (i) (Fig. 4.1), in the absence of racemization catalyst, disproportional growth of minority solid phase (*S*)-**1** thus results in erosion of the solid phase enantiopurity.

In the presence of 1 µL/mL racemization catalyst, however, we find that unequal amounts of (*R*)-**1** and (*S*)-**1** have precipitated. The grown material is slightly enriched in (*R*)-**1** with $ee_\Delta$ = 15% (Fig. 4.2B). Increasing the catalyst concentration further to 2 µL/mL DBU, results in growing even more enriched material with $ee_\Delta \approx 20\% = ee_0$, meaning no erosion of the solid phase enantiopurity has occurred at all during

growth (Fig. 4.2B). As described by scenario (ii) of our mechanistic framework (Fig. 4.1), under these relatively slow and limiting racemization conditions, both crystal populations grow proportionally to their concentration thereby consolidating the solid phase enantiopurity.

Strikingly, for high concentrations of the racemization catalyst (5 and 10 µL/mL DBU, *i.e.* fast racemization compared to crystallization), the solid phase enriches beyond the initial *ee* during growth, with $ee_{\Delta} = 30\% > ee_0$, thus demonstrating amplification of the solid phase *ee* (Fig. 4.2B). This asymmetric amplification implies that the majority crystal population (*R*)-**1** grows faster than the minority population (*S*)-**1**. Consistent with scenario (iii) (Fig. 4.1), the faster growth rate of (*R*)-**1** crystals results in a depletion of this enantiomer in the liquid phase, which is then replenished by the conversion of (*S*)-**1** to (*R*)-**1** through racemization. Since we only observe this enantioenrichment for high concentrations of the racemization catalyst, these results indicate that only high racemization rates allow for sufficiently fast conversion of the minor enantiomer to the major enantiomer to compensate for the disbalance in growth rates between the two crystal populations. For 10 µL/mL DBU no further enrichment is observed over 5 µL/mL DBU (Fig. 4.2B), demonstrating that there is a limit to the enrichment that can be achieved by increasing the racemization rate, as the rate of crystal growth cannot keep up with the rate of racemization. Increasing the racemization rate relative to the crystallization rate thus determines whether erosion, consolidation or amplification occurs during crystal growth.

Our framework suggests that tuning the crystallization rate compared to the racemization rate also enables control over the solid phase enrichment. Amplification is expected when racemization is fast compared to crystallization, prompting us to slow down the crystallization rate. To this aim, we seed a saturated solution and subsequently slowly increase the supersaturation by slow cooling (Fig. 4.2A), instead of seeding a cooled supersaturated solution directly (as in the previous abrupt cooling experiment). Specifically, we decrease the crystallization rate by slow linear cooling of the saturated solution from 30 °C to 20 °C in 90 minutes (0.11 °C/min) in the presence of the seed crystals (20% $ee_0$ in (*R*)-**1**) for the previously used racemization catalyst concentrations (0, 1, 2, 5 or 10 µL/mL DBU). We observe that slowing down the crystallization rate yields a systematic increase of the enrichment in the grown material compared to fast growth (Fig. 4.2B). Hence, maximizing the ratio of racemization rate to crystallization rate results in amplification of the initial solid phase enantiomeric excess during crystal growth.

We investigate how the amplification during growth is governed by the proportions of the initial crystal populations $ee_0$. For a fixed racemization catalyst amount (0 and 2 µL/mL DBU), we vary the initial enantiomeric excess of the seed crystals (10 – 90%) for both abrupt and slow cooling experiments (Fig. 4.2A), and plot the enrichment of the grown material $ee_{\Delta}$ as a function of the initial solid phase enrichment $ee_0$ (Fig.

4.2C). In the absence of racemization (0 µL/mL DBU), we find $ee_\Delta \approx 0$ for all initial *ee*'s, which is consistent with equal precipitation of both enantiomers as calculated from the phase diagram. In the presence of racemization (2 µL/mL DBU) and abrupt cooling (seeding at 20 °C), the initial *ee* is preserved during growth ($ee_\Delta \approx ee_0$) for all enantiomeric excesses of the seed. With racemization and slow cooling (seeding at 30 °C, linear cooling to 20 °C with 0.11 °C/min), we observe amplification for all initial *ee*'s ($ee_\Delta > ee_0$). In agreement with our framework (Fig. 4.1), increasing the racemization rate compared to the crystallization rate thus results in increased asymmetric crystal growth for all initial proportions of the crystal populations.

To quantify the extent of amplification, we define the experimental amplification factor $ee_\Delta/ee_0$: a relative measure for the enrichment in the grown material compared to the enrichment of the initial seed grown onto. Because $ee_\Delta$ is theoretically limited to 100%, the amplification factor is in turn limited to $100\%/ee_0$ and thereby constrains $ee_\Delta/ee_0$ for large $ee_0$. We plot $ee_\Delta/ee_0$ as a function of $ee_0$ for all experiments (Fig. 4.2D). In the absence of DBU, $ee_\Delta/ee_0$ is indeed equal to 0. In the presence of 2 µL/mL DBU, we find amplification factors of $ee_\Delta/ee_0 \approx 1.3 > 1$ (abrupt cooling) and $ee_\Delta/ee_0 \approx 1.7 > 1$ (slow cooling), corresponding to the enrichment of the solid phase beyond its initial enantiomeric excess. Moreover, $ee_\Delta/ee_0$ remains approximately constant for all $ee_0$ up to the theoretical limit, indicating that both small and large enantiomeric excesses in seeds can be amplified equally well.

We realize that—besides the rates of crystallization and racemization—we can further tune the amplification factor by controlling the mass of grown material ($m_\Delta$) relative to the mass of seed crystals ($m_0$). A smaller $m_\Delta/m_0$ results in less crystal growth and therefore less amplification of the enantiomeric excess. In contrast, a larger $m_\Delta/m_0$ results in more crystal growth and therefore a higher degree of amplification: consider using the product of a first crystallization experiment as a seed for a subsequent experiment. Such a recursive procedure would indeed lead to a net increased, and compounded, amplification factor. One effective way for increasing $m_\Delta/m_0$, is by decreasing the amount of seed crystals. To demonstrate this, we repeat the abrupt cooling experiment, with 2 µL/mL DBU, but using a 50 times smaller amount of seed crystals ($m_0$ = 0.5 instead of 25 mg/mL) (Fig. 4.3). We indeed find an increase in the amplification factor from 1.3 ($m_0$ = 25 mg/mL) to 2.2 ($m_0$ = 0.5 mg/mL) (Fig. 4.3B). In fact, seeds of only 60% *ee* already result in virtually exclusive growth of the majority phase ($ee_\Delta > 90\%$) (Fig. 4.3A). Hence, prolonged growth onto a seed with a small enantiomeric excess can lead to large chiral amplification and yield highly enantiopure product.

The mechanistic framework describing the observed amplification during growth of **1** is—to a large extent—compound independent, suggesting that these principles readily extent to other racemizable conglomerates. To show the generality of these chiral amplification phenomena, we perform a demonstration of amplification

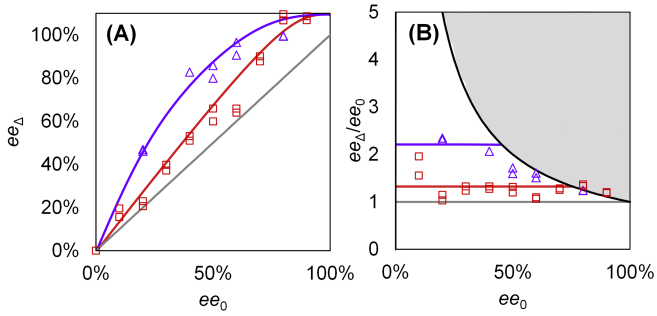


**Figure 4.3.** The amount of seed crystals controls the level of amplification of the enantiomeric excess. Decreasing $m_0$ from 25 (red squares) to 0.5 mg/mL (purple triangles) results in (A) higher enantiopurity of grown material $ee_\Delta$ and (B) increase of the amplification factor $ee_\Delta/ee_0$. Purple and red lines are guides to the eye.

4

during growth for *tert*-leucine precursor **2** (3,3-dimethyl-2-((naphthalen-2-ylmethylene)amino)butanenitrile) (Fig. 4.1C). Enantiopure *tert*-leucine is widely used in the synthesis of modified peptides and antiviral agents such as the HIV protease inhibitor atazanavir.[60,61] Compound **2** crystallizes as a conglomerate and also readily undergoes racemization the presence of DBU in methanol.[40,49,62] To demonstrate that the chiral amplification is also independent of the racemization catalyst, we use the organic base 1,1,3,3-tetramethylguanidine (TMG), which we show racemizes **2** as well (Fig. A11 of the Appendix). As a proof of generality, akin to the abrupt cooling experiments for **1**, we create a supersaturated solution of (*RS*)-**2** (30 mg/mL) in the presence of 100 µL/mL TMG at 20 °C. After seeding with 0.5 mg/mL of seed crystals with $ee_0$ = 60%, we obtain a solid phase with $ee_P$ = 92% and $ee_\Delta$ = 97% ($m_\Delta$ = 3 mg/mL). The resulting amplification factor $ee_\Delta/ee_0$ = 1.66 is close to the theoretical limit (100%/$ee_0$ = 1.70), demonstrating that large asymmetric amplification during crystal growth can be achieved with different choices of conglomerate, solvent and racemization catalyst.

Although the exact nature of the asymmetric crystal growth is still unclear, we anticipate that this mechanism could also play a decisive role during deracemization processes in which not only growth, but also dissolution plays a role. To explore these potential mechanistic analogies, we implemented the chiral amplification factor in a simple analytical model to describe both the kinetics of attrition-enhanced as well as temperature cycling induced deracemization (see the Appendix for details and the derivations). We assume that chiral amplification occurs during growth as described by a constant amplification factor $ee_\Delta/ee_0$. We further assume that dissolved material is racemic such that $ee_\Delta$ = 0 during dissolution steps. Combining these assumptions, we can describe the evolution of the ee for consecutive growth and dissolution steps by equation 4.2:

$$ee(t) = ee(0) \cdot \left(\frac{ee_\Delta \cdot m_\Delta}{ee_0 \cdot m_0} + 1\right)^{\frac{t}{\tau}} \qquad \text{(eq. 4.2)}$$

where we introduce a typical cycle time τ. To describe attrition-enhanced deracemization, where $m_\Delta$ and τ are less well-defined, equation 4.2 can be shown to simplify to the classical exponential description of equation 4.3:

$$ee(t) = ee(0) \cdot \exp(k \cdot t); \qquad \text{with} \quad k = \frac{ee_\Delta \cdot m_\Delta}{ee_0 \cdot m_0 \cdot \tau} \qquad \text{(eq. 4.3)}$$

We find that previously reported kinetic data from both temperature cycling induced and attrition-enhanced deracemization experiments are successfully described by equations 4.2 and 4.3 (fits included in the Appendix).[40,59] Moreover, trends for the deracemization rate *k* predicted by our model agree with those reported in literature from experiments.[28,40,63] This analysis shows that the introduction of an amplification factor to describe asymmetric crystal growth is sufficient to account for the kinetics of both deracemization methods. We therefore submit that a general mechanism involving chiral amplification during crystal growth may play an essential role in all these crystallization-induced deracemization methods.



## Summary and Outlook

In summary, guided by a mechanistic framework, we find that during crystal growth, the interplay between racemization and crystallization rates can result in either erosion, consolidation, or amplification of the enantiomeric excess of the seed crystals. The faster growth of the majority population of enantiomorphic seed crystals is at the core of this remarkable chiral amplification mechanism, and can lead to large chiral amplification even for seed crystals with a small enantiomeric excess. Surprisingly, solution phase racemization always leads to growing material with enantioenrichment ($ee_\Delta > 0$), regardless of the conditions under which growth is performed, and thus prevents the erosion observed without racemization.

The imbalance in crystallization rates observed in this Chapter reveals an intriguing form of asymmetric crystal growth that challenges our current understanding. The kinetics of temperature cycling induced and attrition-enhanced deracemization as well as the underlying nonlinear effects presented here appear to be well-described by the introduced experimental amplification factor. Our results thus suggest that asymmetric crystal growth effects play an essential part in driving deracemization processes of which crystal growth is an essential component, and can advance our understanding of the surprising amplification effects driving these deracemization processes.[25,27,28,30–32,35,41,45,52,64] Moreover, this form of asymmetric crystal growth might also explain why an enantiopure compound can grow at the expense of a stable racemic compound.[65] Nevertheless, the molecular mechanism remains elusive, and could involve processes at the crystal-liquid interface and non-classical crystallization mechanisms such as enantiomer-specific oriented attachment.[31,66] The next steps are aimed at further clarifying the roles of crystal size effects and the quantitative relation between the crystal growth and racemization rates to

ultimately unravel the molecular mechanism that lies at the core of this remarkable form of asymmetric crystal growth.

Our results also hold direct relevance for the practical production of enantiopure building blocks as they provide a tangible basis for the optimization of crystallization-based deracemization processes. We challenge the general consensus that large amounts of seed crystals with the highest enantiopurity are essential, which stems from the tacit understanding that the purity of the seeds determines the maximum achievable enantiomeric excess of the final product.[2,53–56] Counterintuitively, we show that the level of enantioenrichment can even be increased by decreasing the amount of seed crystals and that amplification of *ee* can even be achieved for small amounts of seed crystals of low enantiopurity. Specifically, we realize that industrial crystallizers are ideal to achieve the desired conditions for large enantioenrichment: small amounts of seed crystals, large amounts of grown material, and slow rates of crystallization combined with fast solution-phase racemization, hence outlining potential for practical production of chiral molecules.



More broadly, the asymmetric crystal growth process introduced in this Chapter may hold relevance for understanding the emergence and further amplification of enantiopure building blocks in origin of life scenarios. Specifically, we envision that asymmetric crystal growth induced amplification of enantiomeric excesses can play an essential role in amplifying minute chiral imbalances that are generated during spontaneous symmetry breaking processes, such as crystal nucleation from clear solutions as described by Havinga and Kondepudi.[20–23,58] In conclusion, the here-introduced chiral amplification process and mechanistic framework can guide the practical production of biologically active enantiopure molecules, and fit well in scenarios for the origin of single chirality in nature starting from (racemizable) conglomerates.

## References

(1) Frank, F. C. On Spontaneous Asymmetric Synthesis. Biochim. Biophys. Acta 1953, 11, 459–463. DOI: 10.1016/0006-3002(53)90082-1.

(2) Jacques, J.; Collet, A.; Wilen, S. H. Enantiomers, Racemates, and Resolutions; Wiley-VCH: Weinheim, 1981.

(3) Soai, K.; Shibata, T.; Morioka, H.; Choji, K. Asymmetric Autocatalysis and Amplification of Enantiomeric Excess of a Chiral Molecule. Nature 1995, 378 (6559), 767–768. DOI: 10.1038/378767a0.

(4) Avalos, M.; Babiano, R.; Cintas, P.; Jiménez, J. L.; Palacios, J. C. Chiral Autocatalysis: Where Stereochemistry Meets the Origin of Life. Chem. Commun. 2000, (11), 887–892. DOI: 10.1039/a908300f.

(5) Zepik, H.; Shavit, E.; Tang, M.; Jensen, T. R.; Kjaer, K.; Bolbach, G.; Leiserowitz, L.; Weissbuch, I.; Lahav, M. Chiral Amplification of Oligopeptides in Two-Dimensional Crystalline Self-Assemblies on Water. Science 2002, 295 (5558), 1266–1269. DOI: 10.1126/science.1065625.

(6) Weissbuch, I.; Lahav, M.; Leiserowitz, L. Toward Stereochemical Control, Monitoring, and Understanding of Crystal Nucleation. Cryst. Growth Des. 2003, 3 (2), 125–150. DOI: 10.1021/cg0200560.

(7) Brands, K. M. J.; Davies, A. J. Crystallization-Induced Diastereomer Transformations. Chem. Rev. 2006, 106 (7), 2711–2733. DOI: 10.1021/cr0406864.
(8) Blackmond, D. G.; Klussmann, M. Spoilt for Choice: Assessing Phase Behavior Models for the Evolution of Homochirality. Chem. Commun. 2007, (39), 3990–3996. DOI: 10.1039/b709314b.
(9) Novel Optical Resolution Technologies; Sakai, K., Hirayama, N., Tamura, R., Eds.; Springer: Berlin, Heidelberg, 2007; Vol. 269. DOI: 10.1007/978-3-540-46320-7.
(10) Viedma, C. Chiral Symmetry Breaking and Complete Chiral Purity by Thermodynamic-Kinetic Feedback Near Equilibrium: Implications for the Origin of Biochirality. Astrobiology 2007, 7 (2), 312–319. DOI: 10.1089/ast.2006.0099.
(11) Palmans, A. R. A. Deracemisations under Kinetic and Thermodynamic Control. Mol. Syst. Des. Eng. 2017, 2 (1), 34–46. DOI: 10.1039/C6ME00088F.
(12) Kolarovič, A.; Jakubec, P. State of the Art in Crystallization-Induced Diastereomer Transformations. Adv. Synth. Catal. 2021, 363 (17), 4110–4158. DOI: 10.1002/adsc.202100473.
(13) Sakamoto, M.; Uemura, N.; Saito, R.; Shimobayashi, H.; Yoshida, Y.; Mino, T.; Omatsu, T. Chirogenesis and Amplification of Molecular Chirality Using Optical Vortices. Angew. Chem. Int. Ed. 2021, 60 (23), 12819–12823. DOI: 10.1002/anie.202103382.
(14) Tsogoeva, S. B. A Noble Quest for Simplicity in the Chiral World. N. Engl. J. Med. 2021, 385 (27), 2579–2581. DOI: 10.1056/NEJMcibr2116228.
(15) Dutta, S.; Yun, Y.; Widom, M.; Gellman, A. J. 2D Ising Model for Adsorption-induced Enantiopurification of Racemates. ChemPhysChem 2021, 22 (2), 197–203. DOI: 10.1002/cphc.202000881.
(16) Buhse, T.; Cruz, J.-M.; Noble-Terán, M. E.; Hochberg, D.; Ribó, J. M.; Crusats, J.; Micheau, J.-C. Spontaneous Deracemizations. Chem. Rev. 2021, 121 (4), 2147–2229. DOI: 10.1021/acs.chemrev.0c00819.
(17) Smulders, M. M. J.; Filot, I. A. W.; Leenders, J. M. A.; van der Schoot, P.; Palmans, A. R. A.; Schenning, A. P. H. J.; Meijer, E. W. Tuning the Extent of Chiral Amplification by Temperature in a Dynamic Supramolecular Polymer. J. Am. Chem. Soc. 2010, 132 (2), 611–619. DOI: 10.1021/ja908053d.
(18) Caprice, K.; Pál, D.; Besnard, C.; Galmés, B.; Frontera, A.; Cougnon, F. B. L. Diastereoselective Amplification of a Mechanically Chiral [2]Catenane. J. Am. Chem. Soc. 2021, 143 (31), 11957–11962. DOI: 10.1021/jacs.1c06557.
(19) Guillaneux, D.; Zhao, S.-H.; Samuel, O.; Rainford, D.; Kagan, H. B. Nonlinear Effects in Asymmetric Catalysis. J. Am. Chem. Soc. 1994, 116 (21), 9430–9439. DOI: 10.1021/ja00100a004.
(20) Havinga, E. Spontaneous Formation of Optically Active Substances. Chem. Weekblad 1941, 38, 642–644.
(21) Havinga, E. Spontaneous Formation of Optically Active Substances. Biochim. Biophys. Acta 1954, 13, 171–174. DOI: 10.1016/0006-3002(54)90300-5.
(22) Kondepudi, D. K.; Kaufman, R. J.; Singh, N. Chiral Symmetry Breaking in Sodium Chlorate Crystallization. Science 1990, 250 (4983), 975–976. DOI: 10.1126/science.250.4983.975.
(23) McBride, J. M.; Carter, R. L. Spontaneous Resolution by Stirred Crystallization. Angew. Chem. Int. Ed. 1991, 30 (3), 293–295. DOI: 10.1002/anie.199102931.
(24) Viedma, C. Experimental Evidence of Chiral Symmetry Breaking in Crystallization from Primary Nucleation. J. Cryst. Growth 2004, 261 (1), 118–121. DOI: 10.1016/j.jcrysgro.2003.09.031.
(25) Viedma, C. Chiral Symmetry Breaking During Crystallization: Complete Chiral Purity Induced by Nonlinear Autocatalysis and Recycling. Phys. Rev. Lett. 2005, 94 (6), 065504. DOI: 10.1103/PhysRevLett.94.065504.

(26) Shan Monica Cheung, P.; Gagnon, J.; Surprenant, J.; Tao, Y.; Xu, H.; Cuccia, L. A. Complete Asymmetric Amplification of Ethylenediammonium Sulfate Using an Abrasion/Grinding Technique. Chem. Commun. 2008, (8), 987–989. DOI: 10.1039/b716977a.

(27) Noorduin, W. L.; Izumi, T.; Millemaggi, A.; Leeman, M.; Meekes, H.; van Enckevort, W. J. P.; Kellogg, R. M.; Kaptein, B.; Vlieg, E.; Blackmond, D. G. Emergence of a Single Solid Chiral State from a Nearly Racemic Amino Acid Derivative. J. Am. Chem. Soc. 2008, 130 (4), 1158–1159. DOI: 10.1021/ja7106349.

(28) Noorduin, W. L.; van Enckevort, W. J. P.; Meekes, H.; Kaptein, B.; Kellogg, R. M.; Tully, J. C.; McBride, J. M.; Vlieg, E. The Driving Mechanism Behind Attrition-Enhanced Deracemization. Angew. Chem. Int. Ed. 2010, 49 (45), 8435–8438. DOI: 10.1002/anie.201002036.

(29) Yagishita, F.; Ishikawa, H.; Onuki, T.; Hachiya, S.; Mino, T.; Sakamoto, M. Total Spontaneous Resolution by Deracemization of Isoindolinones. Angew. Chem. Int. Ed. 2012, 51 (52), 13023–13025. DOI: 10.1002/anie.201205097.

(30) Hein, J. E.; Huynh Cao, B.; Viedma, C.; Kellogg, R. M.; Blackmond, D. G. Pasteur's Tweezers Revisited: On the Mechanism of Attrition-Enhanced Deracemization and Resolution of Chiral Conglomerate Solids. J. Am. Chem. Soc. 2012, 134 (30), 12629–12636. DOI: 10.1021/ja303566g.

(31) Viedma, C.; McBride, J. M.; Kahr, B.; Cintas, P. Enantiomer-Specific Oriented Attachment: Formation of Macroscopic Homochiral Crystal Aggregates from a Racemic System. Angew. Chem. Int. Ed. 2013, 52 (40), 10545–10548. DOI: 10.1002/anie.201303915.

(32) Seibel, J.; Parschau, M.; Ernst, K.-H. From Homochiral Clusters to Racemate Crystals: Viable Nuclei in 2D Chiral Crystallization. J Am Chem Soc 2015, 137 (25), 7970–7973. DOI: 10.1021/jacs.5b02262.

(33) Walsh, M. P.; Barclay, J. A.; Begg, C. S.; Xuan, J.; Johnson, N. T.; Cole, J. C.; Kitching, M. O. Identifying a Hidden Conglomerate Chiral Pool in the CSD. JACS Au 2022. DOI: 10.1021/jacsau.2c00394.

(34) Viedma, C.; Cintas, P. Homochirality beyond Grinding: Deracemizing Chiral Crystals by Temperature Gradient under Boiling. Chem. Commun. 2011, 47 (48), 12786–12788. DOI: 10.1039/c1cc14857e.

(35) Suwannasang, K.; Flood, A. E.; Rougeot, C.; Coquerel, G. Using Programmed Heating–Cooling Cycles with Racemization in Solution for Complete Symmetry Breaking of a Conglomerate Forming System. Cryst. Growth Des. 2013, 13 (8), 3498–3504. DOI: 10.1021/cg400436r.

(36) Li, W. W.; Spix, L.; de Reus, S. C. A.; Meekes, H.; Kramer, H. J. M.; Vlieg, E.; ter Horst, J. H. Deracemization of a Racemic Compound via Its Conglomerate-Forming Salt Using Temperature Cycling. Cryst. Growth Des. 2016, 16 (9), 5563–5570. DOI: 10.1021/acs.cgd.6b01034.

(37) Breveglieri, F.; Maggioni, G. M.; Mazzotti, M. Deracemization of NMPA via Temperature Cycles. Cryst. Growth Des. 2018, 18 (3), 1873–1881. DOI: 10.1021/acs.cgd.7b01746.

(38) Cameli, F.; Xiouras, C.; Stefanidis, G. D. Intensified Deracemization via Rapid Microwave-Assisted Temperature Cycling. CrystEngComm 2018, 20 (21), 2897–2901. DOI: 10.1039/C8CE00575C.

(39) Maggioni, G. M.; Fernández-Ronco, M. P.; van der Meijden, M. W.; Kellogg, R. M.; Mazzotti, M. Solid State Deracemisation of Two Imine-Derivatives of Phenylglycine Derivatives via High-Pressure Homogenisation and Temperature Cycles. CrystEngComm 2018, 20 (27), 3828–3838. DOI: 10.1039/C8CE00356D.

(40) Breveglieri, F.; Baglai, I.; Leeman, M.; Noorduin, W. L.; Kellogg, R. M.; Mazzotti, M. Performance Analysis and Model-Free Design of Deracemization via Temperature Cycles. Org. Process Res. Dev. 2020, 24 (8), 1515–1522. DOI: 10.1021/acs.oprd.0c00266.

(41) Intaraboonrod, K.; Lerdwiriyanupap, T.; Hoquante, M.; Coquerel, G.; Flood, A. E. Temperature Cycle Induced Deracemization. Mendeleev Commun. 2020, 30 (4), 395–405. DOI: 10.1016/j.mencom.2020.07.002.

(42) Intaraboonrod, K.; Harriehausen, I.; Carneiro, T.; Seidel-Morgenstern, A.; Lorenz, H.; Flood, A. E. Temperature Cycling Induced Deracemization of DL-Asparagine Monohydrate with Immobilized Amino Acid Racemase. Cryst. Growth Des. 2021, 21 (1), 306–313. DOI: 10.1021/acs.cgd.0c01140.

(43) Uemura, N.; Toyoda, S.; Ishikawa, H.; Yoshida, Y.; Mino, T.; Kasashima, Y.; Sakamoto, M. Asymmetric Diels–Alder Reaction Involving Dynamic Enantioselective Crystallization. J. Org. Chem. 2018, 83 (16), 9300–9304. DOI: 10.1021/acs.joc.8b01273.

(44) Engwerda, A. H. J.; Maassen, R.; Tinnemans, P.; Meekes, H.; Rutjes, F. P. J. T.; Vlieg, E. Attrition-Enhanced Deracemization of the Antimalaria Drug Mefloquine. Angew. Chem. Int. Ed. 2019, 58 (6), 1670–1673. DOI: 10.1002/anie.201811289.

(45) Murray, J. I.; Sanders, J. N.; Richardson, P. F.; Houk, K. N.; Blackmond, D. G. Isotopically Directed Symmetry Breaking and Enantioenrichment in Attrition-Enhanced Deracemization. J. Am. Chem. Soc. 2020, 142 (8), 3873–3879. DOI: 10.1021/jacs.9b11422.

(46) Valenti, G.; Tinnemans, P.; Baglai, I.; Noorduin, W. L.; Kaptein, B.; Leeman, M.; ter Horst, J. H.; Kellogg, R. M. Combining Incompatible Processes for Deracemization of a Praziquantel Derivative under Flow Conditions. Angew. Chem. Int. Ed. 2021, 60 (10), 5279–5282. DOI: 10.1002/anie.202013502.

(47) van der Meijden, M. W.; Leeman, M.; Gelens, E.; Noorduin, W. L.; Meekes, H.; van Enckevort, W. J. P.; Kaptein, B.; Vlieg, E.; Kellogg, R. M. Attrition-Enhanced Deracemization in the Synthesis of Clopidogrel - A Practical Application of a New Discovery. Org. Process Res. Dev. 2009, 13 (6), 1195–1198. DOI: 10.1021/op900243c.

(48) Steendam, R. R. E.; Kulka, M. W.; Meekes, H.; van Enckevort, W. J. P.; Raap, J.; Vlieg, E.; Rutjes, F. P. J. T. One-Pot Synthesis, Crystallization and Deracemization of Isoindolinones from Achiral Reactants. European J. Org. Chem. 2015, 2015 (33), 7249–7252. DOI: 10.1002/ejoc.201501191.

(49) Baglai, I.; Leeman, M.; Wurst, K.; Kaptein, B.; Kellogg, R. M.; Noorduin, W. L. The Strecker Reaction Coupled to Viedma Ripening: A Simple Route to Highly Hindered Enantiomerically Pure Amino Acids. Chem. Commun. 2018, 54 (77), 10832–10834. DOI: 10.1039/C8CC06658B.

(50) Baglai, I.; Leeman, M.; Kellogg, R. M.; Noorduin, W. L. A Viedma Ripening Route to an Enantiopure Building Block for Levetiracetam and Brivaracetam. Org. Biomol. Chem. 2019, 17 (1), 35–38. DOI: 10.1039/C8OB02660B.

(51) Guillot, M.; Meester, J.; Huynen, S.; Collard, L.; Robeyns, K.; Riant, O.; Leyssens, T. Cocrystallization-Induced Spontaneous Deracemization: A General Thermodynamic Approach to Deracemization. Angew. Chem. Int. Ed. 2020, 59 (28), 11303–11306. DOI: 10.1002/anie.202002464.

(52) Uwaha, M.; Katsuno, H. Mechanism of Chirality Conversion of Crystals by Viedma Ripening and Temperature Cycling. J. Cryst. Growth 2022, 126873. DOI: 10.1016/j.jcrysgro.2022.126873.

(53) Wibowo, C.; Kelkar, V. v.; Samant, K. D.; Schroer, J. W.; Ng, K. M. Development of Reactive Crystallization Processes. In Integrated Chemical Processes; Sundmacher, K., Kienle, A., Seidel-Morgenstern, A., Eds.; Wiley-VCH Verlag GmbH & Co. KGaA: Weinheim, FRG, 2005; pp 339–358. DOI: 10.1002/3527605738.ch11.

(54) Oketani, R.; Hoquante, M.; Brandel, C.; Cardinael, P.; Coquerel, G. Resolution of an Atropisomeric Naphthamide by Second-Order Asymmetric Transformation: A Highly Productive Technique. Org. Process Res. Dev. 2019, 23 (6), 1197–1203. DOI: 10.1021/acs.oprd.9b00133.

(55) Breveglieri, F. Deracemization via Batch Temperature Cycles - Combining Racemization and Crystallization for Chiral Resolution. Ph.D. Dissertation, ETH Zurich, Zurich, 2021. DOI: 10.3929/ethz-b-000528254 (accessed 2022-10-04).

(56) Beletti, G. Solid State Deracemization. Viedma Ripening versus Temperature Cycling. Ph.D. Dissertation, Radboud University, Nijmegen, 2021. https://repository.ubn.ru.nl/handle/2066/236273 (accessed 2022-10-04).

(57) Plotting eeΔ as a function of ee0 is visually reminiscent to plotting the ee of the product against the ee of chiral auxilaries for nonlinear effects observed by Kagan during asymmetric catalysis, see ref. (19).
(58) Leeman, M.; Noorduin, W. L.; Millemaggi, A.; Vlieg, E.; Meekes, H.; van Enckevort, W. J. P.; Kaptein, B.; Kellogg, R. M. Efficient Havinga–Kondepudi Resolution of Conglomerate Amino Acid Derivatives by Slow Cooling and Abrasive Grinding. CrystEngComm 2010, 12 (7), 2051–2053. DOI: 10.1039/c0ce00140f.
(59) Noorduin, W. L.; van der Asdonk, P.; Bode, A. A. C.; Meekes, H.; van Enckevort, W. J. P.; Vlieg, E.; Kaptein, B.; van der Meijden, M. W.; Kellogg, R. M.; Deroover, G. Scaling Up Attrition-Enhanced Deracemization by Use of an Industrial Bead Mill in a Route to Clopidogrel (Plavix). Org. Process Res. Dev. 2010, 14 (4), 908–911. DOI: 10.1021/op1001116.
(60) Formaggio, F.; Baldini, C.; Moretto, V.; Crisma, M.; Kaptein, B.; Broxterman, Q. B.; Toniolo, C. Preferred Conformations of Peptides Containingtert-Leucine, a Sterically Demanding, Lipophilic Amino Acid with a Quaternary Side-Chain C Atom. Chem. – Eur. J. 2005, 11 (8), 2395–2404. DOI: 10.1002/chem.200400892.
(61) Skwarecki, A. S.; Nowak, M. G.; Milewska, M. J. Amino Acid and Peptide-Based Antiviral Agents. ChemMedChem 2021, 16 (20), 3106–3135. DOI: 10.1002/cmdc.202100397.
(62) Baglai, I.; Leeman, M.; Wurst, K.; Kellogg, R. M.; Noorduin, W. L. Enantiospecific Solid Solution Formation Triggers the Propagation of Homochirality. Angew. Chem. Int. Ed. 2020, 59 (47), 20885–20889. DOI: 10.1002/anie.202009719.
(63) Noorduin, W.L.; Meekes, H.; van Enckevort, W.J.P.; Millemaggi, A.; Leeman, M.; Kaptein, B.; Kellog, R.M.; Vlieg, E. Complete Deracemization by Attrition-Enhanced Ostwald Ripening Elucidated. Angew. Chem. Int. Ed. 2008, 47 (34), 6445–6447. DOI: 10.1002/anie.200801846.
(64) Uchin, R.; Suwannasang, K.; Flood, A. E. Model of Temperature Cycle-Induced Deracemization via Differences in Crystal Growth Rate Dispersion. Chem. Eng. Technol. 2017, 40 (7), 1252–1260. DOI: 10.1002/ceat.201600746.
(65) Viedma, C.; Ortiz, J.E. A New Twist in Eutectic Composition: Deracemization of a Racemic Compound Amino Acid by Viedma Ripening and Temperature Fluctuation. Isr. J. Chem. 2021, 61 (11–12), 758–763. DOI: 10.1002/ijch.202100075.
(66) De Yoreo, J.J.; Gilbert, P.U.P.A.; Sommerdijk, N.A.J.M.; Lee Penn, R.; Whitelam, S.; Joester, D.; Zhang, H.; Rimer, J.D.; Navrotsky, A.; Banfield, J.F.; Wallace, A.F.; Marc Michel, F.; Meldrum, F.C.; Cölfen, H.; Dove, P.M. Crystallization by particle attachment in synthetic, biogenic, and geologic environments. Science 2015, 349 (6247), aaa6760. DOI: 10.1126/science.aaa6760.

Chapter 5

# How Crystal Size and Number steer Asymmetric Crystallization.*

*Chiral amplification processes during crystallization can hinge on subtle asymmetries in crystal populations, yet the underlying kinetic drivers remain elusive. Here we experimentally investigate how size and mass imbalances between two enantiomeric crystal populations translate to asymmetric growth rates that determine asymmetric crystal growth. We find that the interplay between imbalances in size and mass can yield positive, linear or even negative, non-linear chiral amplification. Consequently, though small crystals have a thermodynamically higher solubility than large ones, a minority population of small crystals can collectively outgrow and ultimately dominate a majority of larger crystals. This amplification due to size effects can be further enhanced or dampened by controlling growth rates. Our findings uncover an intricate kinetic selection mechanism driven by population-level growth rates and governed by fundamental crystallization dynamics. Together, these results provide new insights into the origin of non-linear amplification phenomena and offer practical guidance for competitive asymmetric crystallization and self-assembly processes.*



## Introduction

Asymmetric crystallization processes are of profound importance for both fundamental science and practical applications with wide use in the pharmaceutical and fine chemical industries.[1–8] Especially interesting is the asymmetric crystallization of chiral molecules into enantiomerically pure crystals (so-called conglomerates).[9–20] Under racemizing conditions, the enantiomers can interconvert in the liquid phase and thereby form a common resource pool for asymmetric crystallization (Fig. 5.1a). An initial enantioenrichment in the solid phase can then be amplified through cycles of crystal growth and dissolution, allowing full deracemization. While the key prerequisites for such deracemizations are well-established, recent studies have revealed complex non-linear effects that can occur during asymmetric crystallization, which profoundly influence the selectivity and efficiency of chiral amplification.[21–25]

In particular, differences in the growth rates of enantiomeric crystal populations can spontaneously enrich one enantiomer over the other. It remains unclear, however, how such growth-rate asymmetries originate and how they can be leveraged and

* This chapter has been published as S.W. van Dongen*, P. Rang*, K.G.P. Dautzenberg, B. Kaptein, W. L. Noorduin (2026). Disparities in Seed Size Distributions can Drive or Hamper Chiral Amplification under Racemizing Conditions during Conglomerate Crystal Growth. *J. Phys. Chem. Lett.* 17(4):1129—1135.

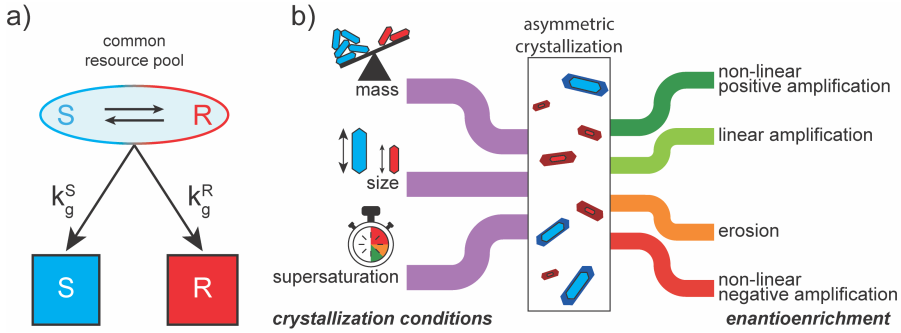


**Figure 5.1.** Asymmetric crystallization is dominated by the fastest growing population. (a) Conglomerates crystallize as two populations of enantiopure crystals with growth rates $k_g^R$ and $k_g^S$, respectively. Racemization in solution creates a common resource pool. (b) The outcome of asymmetric crystallization is determined by the balance of the collective growth rate of the crystal populations through the number of crystals (through mass), their size, and the crystallization conditions (supersaturation).

controlled. Several studies have shown that larger crystals generally grow faster and are thermodynamically more stable than their smaller counterparts, which has been proposed as a method to break symmetry and drive chiral amplification.[26–31] Moreover, it is known that crystal morphology and the evolution thereof can influence crystal growth rates.[32,33] Although the kinetics of individual crystal growth have been studied in detail[34], our understanding of how large, heterogeneous populations of interacting crystals behave collectively during crystallization is still limited. Such insights are of key importance for chiral crystallizations, as even minor differences in crystal size or morphology between enantiomeric populations can lead to significant divergence in their growth dynamics and, consequently, in the resulting chiral purity of the solid phase.

This raises an important question: how does the competition between two enantiomeric crystal populations for a common racemizing solute pool translate into asymmetric crystallization outcomes? More specifically, how do differences in initial mass and crystal size—two interrelated yet independently tunable parameters—govern the net growth rates of the enantiomer populations and determine the direction and extent of chiral amplification within a single growth step?

This question is particularly relevant because crystal size disparities frequently arise spontaneously through nucleation, Ostwald ripening, or growth-rate dispersion.[35,36] Such size disparities can also be introduced actively through seeding, mechanical grinding, or controlled crystallization conditions. Hence, understanding the consequences of size disparities on the growth rates of crystal population is not only essential to elucidate the fundamental principles of chiral crystallization, but also to develop rational strategies that steer deracemization toward the desired outcome.

In this work, we experimentally investigate how differences in crystal size and population mass affect the outcome of asymmetric crystal growth under racemizing

conditions (Fig. 5.1b). By carefully preparing enantiomeric seed mixtures that differ in either size or mass—or both—we can modulate the solid phase enantioenrichment and growth rate of each population independently. Moreover, motivated by fundamental insights on the mechanisms of crystal growth, we show that the effects of crystal size-disparities can be further manipulated through the applied supersaturation. Collectively, our findings highlight the domination of the fastest growing population, a core principle that prompts us to rethink how to understand, design, and control asymmetric crystallization processes.

## Results and Discussion

To investigate how size-differences between two otherwise identical crystal populations influence the population growth rates and the outcome of asymmetric crystallization, we prepared both small and large seed crystals of both the (*R*) and (*S*)-enantiomer of **1** (Scheme 5.1), a well-established racemizable conglomerate.[37] Small seed crystals (10-20 μm) were obtained by mechanical grinding assisted by ultrasonication in the presence of glass beads.[38] Large seed crystals (30-50 μm) were obtained by growing the small crystals (detailed procedures and characterization data for both small and large seed crystal batches are provided in the Appendix).



For our first experiment, using these small and large seed crystals, two types of racemic mixtures (i.e. no net solid-phase enantioenrichment) were prepared such that each enantiomer had equal mass, but a different crystal size compared to its counterpart. We combined (1) large (*S*)-enantiomer crystals with small (*R*)-enantiomer crystals, and (2) large *R* crystals mixed with small *S* crystals. These crystal mixtures were subsequently added as seed crystals to a saturated, racemizing solution of **1** in methanol, containing 50 μL/mL basic racemization catalyst 1,8-diazabicyclo[5.4.0]undec-7-ene (DBU), at 30 °C (Fig. 5.2a). Crystal growth was initiated by slowly cooling the solution with 0.22°C/min to 20 °C. To keep attrition effects to a minimum, during growth, the solution was shaken instead of stirred.

To determine how much of each enantiomer population crystallized, the resulting solids were isolated through vacuum filtration and their composition was

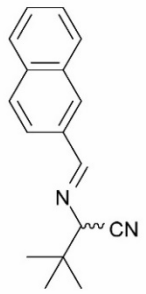


1

**Scheme 5.1.** Racemizable conglomerate **1**.

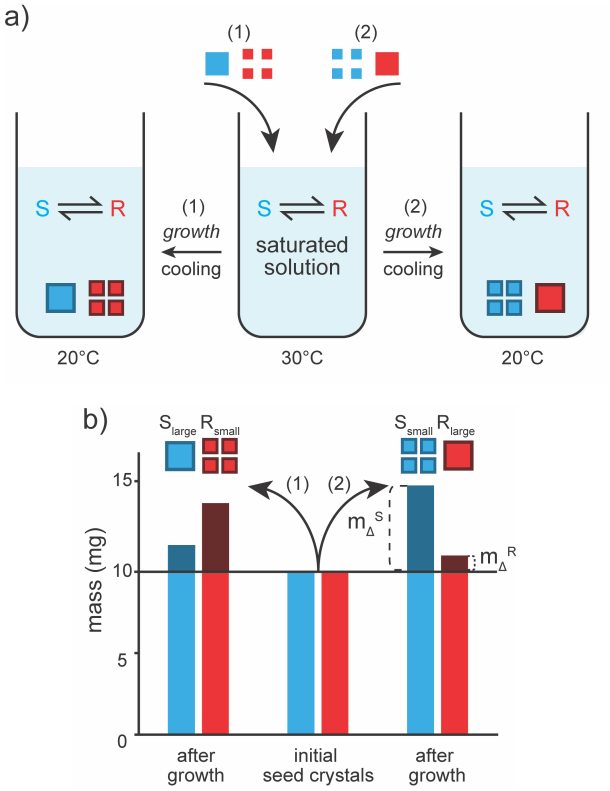


**Figure 5.2.** Chiral crystallization for equal mass but different crystal size of each enantiomer population. (a) Seeded growth of enantiomer populations under racemizing conditions from a saturated solution through cooling. (b) Crystal populations of equal mass but unequal size exhibit asymmetric growth rates, favoring the enantiomer population composed of smaller crystals.

determined using chiral HPLC. Importantly, the entire cooling trajectory was performed within the metastable zone, such that nucleation is minimized and precipitation from the supersaturated solution is dominated by growth of the seed crystals.

Before growth, both the population of small and large crystals have equal mass. After growth, as expected, both populations have gained mass, but not in equal amounts: the population with the smaller seed crystals grew more than the population with large seed crystals (Fig. 5.2b). Hence, the population of small crystals must have grown faster than the population of larger crystals. This size-dependency of enantioenrichment is non-trivial. The Gibbs-Thomson effect thermodynamically favors the growth of large crystals, such that the small crystals are individually less stable. However, under kinetic, out-of-equilibrium conditions the small crystal population can feature a higher collective growth rate because of a larger combined surface area[26,35].

For populations of equal mass, we thus find that a disparity in crystal size between two enantiomer populations breaks symmetry in favor of the smaller crystals. Commonly, however, chiral amplification is directed by breaking symmetry through unequal initial solid masses, such that the population with larger mass (the major enantiomer) wins at the cost of the population with smaller mass (the minor enantiomer). When chiral amplification is directed through mass imbalances, the sizes of crystal populations are oftentimes neglected or simply assumed to be the same. As we have just demonstrated, however, crystals sizes are important. Moreover, the imbalance of populations in mass can differ from the imbalance in size. We foresee the combined complex interplay of imbalances in mass and size can thus enhance but also diminish chiral amplification of the desired enantiomer.

To analyze how an interplay between size and mass affects chiral amplification, we determine the mass that is grown onto each population ($m_{\Delta}{}^{R}$ and $m_{\Delta}{}^{S}$), calculate the enantiomeric excess of the crystallized material ($ee_{\Delta} = (m_{\Delta}^{R} - m_{\Delta}^{S})/(m_{\Delta}^{R} + m_{\Delta}^{S})$), and define the amplification factor but $\alpha$ as $ee_{\Delta}$ relative to the initial mass imbalance ($ee_0$):

$$\alpha = \frac{ee_{\Delta}}{ee_0} \qquad \text{(eq. 5.1)}$$

Akin to Kagan's analysis of asymmetric catalysis,[39] this amplification factor classifies asymmetric crystallization into four distinct regimes. When $\alpha = 1$, both populations grow in proportion to their initial mass imbalance: the *ee* of grown material is equal to the starting *ee* resulting in linear amplification. When $\alpha > 1$, the major population in mass grows faster than the minority population, resulting in non-linear amplification of the major enantiomer. When $0 < \alpha < 1$, the major enantiomer grows faster than the minority, but insufficiently as to maintain its starting enantioenrichment, thus resulting in net erosion of the initial *ee*. When $\alpha < 0$, the minority enantiomer grows faster than the majority enantiomer, resulting in negative non-linear amplification.

Using a constant imbalance in seed mass (60 wt%, $ee_0$ = 20% in *R*), we prepared five experimental imbalances in size by mixing small and large crystals of the two enantiomers (see Appendix for details): (i) all majority enantiomer crystals are larger than the minority enantiomer crystals (i.e. majority larger), (ii) only the majority crystals that make up the enantiomeric excess are larger (i.e. excess larger), (iii) all crystals are of equal size, (iv) the excess crystals are smaller, and (v) all majority crystals are smaller than the minority enantiomer crystals (Fig. 5.3a). Subsequently, each mixture was used to seed a racemizing clear supersaturated solution to induce growth (see Appendix for details).

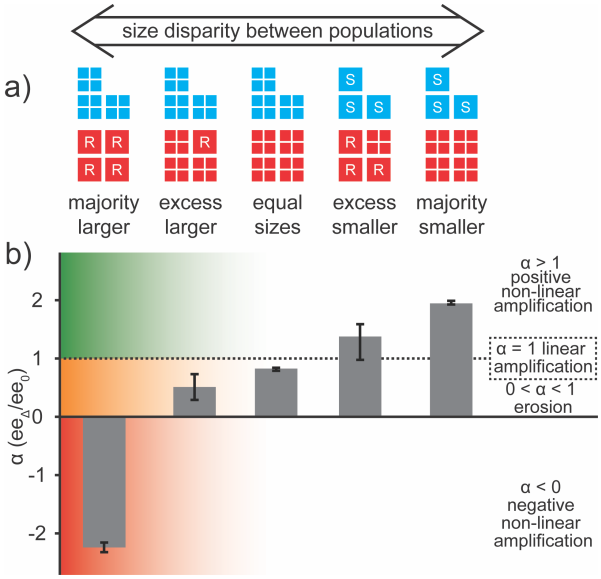


**Figure 5.3.** Asymmetric crystallization directed by crystal size-disparity. (a) Initial seeds are enriched in (*R*)-**1** by mass, but both enantiomer populations have different crystal sizes. (b) Maintaining the initial enantioenrichment in mass through growth constitutes expected linear amplification. However, crystal-size disparity in asymmetric crystallization can cause positive non-linear chiral amplification, linear amplification, erosion, or even negative non-linear amplification, characterized by amplification factor α.

The crystallized solid was analyzed as before and $\alpha$ was determined (Fig. 5.3b). For crystals of equal sizes, we observe near-linear amplification ($\alpha \approx 1$). Although nucleation and small inherent size disparities between seed crystals slightly suppress amplification (see Appendix for details), the populations grew with rates that are approximately proportional to their initial mass—as expected in the absence of any size imbalance. When all majority crystals are smaller than the minority crystals, we observe strong positive non-linear amplification ($\alpha >> 1$): the majority population grows much faster due to the smaller size of its constituting crystals.

Conversely, when the majority crystals are larger than the minority, we observe strong negative non-linear amplification ($\alpha << 0$): the minor enantiomer—through its larger collective surface area—has now completely outgrown the majority enantiomer. Despite the same significant initial *ee* in *R* by mass, switching the size imbalance from majority smaller to majority larger crystals thus fully reverses the outcome of chiral amplification: from amplifying the major ($\alpha \approx +2$, final *ee* = 80% in *R*) to amplifying the minor enantiomer ($\alpha \approx -2$, final *ee* = 3% in *R*). Hence, through the domination of the fast-growing population, the size imbalance completely determines the outcome of asymmetric crystallization.

Consistent with these findings, selectively changing only the size of the crystals constituting the excess (i.e. excess smaller vs. excess larger), yields similar relative effects of the size imbalance on chiral amplification, although less pronounced (Fig.

5.3). Smaller excess crystals still give positive non-linear amplification ($\alpha \approx 1.5$), but larger excess crystals now yield erosion ($\alpha \approx 0.5$), a much weaker effect than the negative non-linear amplification previously observed when all majority crystals were larger. These weaker effects on amplification observed when changing only the relative size of the excess crystals—rather than the whole population—can be explained by the smaller imbalances in the total surface area between the populations. These results demonstrate that strategic preparation of the initial solid phase—specifically, incorporating many small enantiopure seed crystals with large cumulative surface area—can achieve higher chiral amplification efficiency and thereby accelerate deracemization kinetics.

Fundamentally, the outcome of asymmetric crystallization is governed by differences in the growth rates of competing enantiomeric crystal populations. These growth rates are not only influenced by differences in size (r) and mass, but also by the growth mechanism, which in turn depends strongly on the supersaturation of the solution. At low supersaturation, often associated with spiral growth mechanisms, molecular attachment occurs predominantly at energetically favorable sites such as screw dislocations. In this regime, the number of active growth sites—proportional to the number of crystals (N)—determines the population growth rate ($k_g \sim N \sim 1/r^3$).[40] At high supersaturation, often associated with polynuclear and rough growth mechanisms, molecular attachment occurs across the entire surface. In this surface-integration-limited regime, the incorporation of molecules on the crystal surface (A) is rate-limiting ($k_g \sim \Sigma A \sim 1/r$). Indeed, calculations suggest that high supersaturation dampens the effects of size imbalances on population growth rates (Fig. 5.4a, details in the Appendix).[41] Furthermore, these calculations show that a small initial size disparity ratio between seed crystal populations has disproportionately large effects on the outcome of the asymmetric crystallization (Fig. A23 of the Appendix).

To test how these distinct growth regimes influence the effects of crystal size disparity, we performed asymmetric crystallization experiments under both low supersaturation (achieved by slow cooling from 30 °C to 20 °C at 0.22°C/min) and high supersaturation (achieved by fast cooling over the same temperature range at 2 °C/min). As shown in Figure 5.4b, under slow cooling strong size-dependent chiral amplification is observed, with populations of small crystals growing significantly faster and dominating the solid phase composition. However, under fast cooling, this amplification effect is markedly dampened. This confirms that size disparity effects are more pronounced under surface-integration-limited growth at low supersaturation compared to high supersaturation.

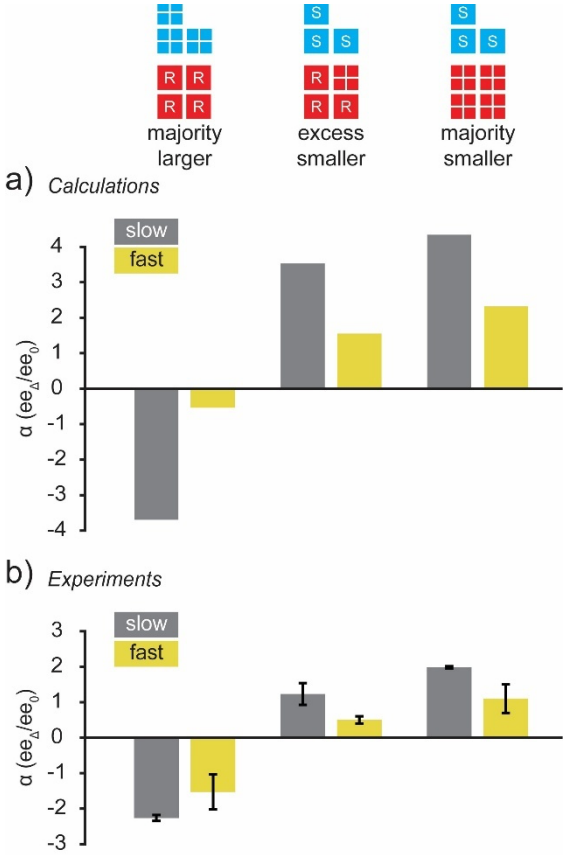


**Figure 5.4.** Asymmetric amplification by supersaturation through crystallization rate. (a) Calculations suggest that, for low supersaturation (slow growth, grey), population growth rate is proportional to the number of crystals. For high supersaturation (fast growth, yellow), population growth rate is surface-integration-limited. (b) Experiments confirm the effect of supersaturation and show that size-induced amplification effects are dampened through fast growth at high supersaturation.

## Summary and Outlook

In summary, this study experimentally reveals how subtle disparities in crystal size can decisively impact the outcome of asymmetric crystal growth when populations compete for the same resources. Populations of smaller crystals exhibit higher collective growth rates due to their greater cumulative surface area, enabling them to outcompete larger, thermodynamically more stable crystals. Consequently, disparities in crystal size and mass can enhance, diminish, or even reverse initial enantiomeric imbalances, resulting in regimes of positive, linear, and negative non-linear amplification.

In this study we have treated crystals as unidimensional and have not aimed to give a full quantitative description. Indeed, facet-dependent growth mechanisms and crystals undergoing morphological changes over time also likely influence the

degree of amplification, especially across different supersaturation regimes.[33,42,43] Future studies integrating *in situ* imaging for the tracking of shape and size of individual populations and population-balance modeling should therefore further clarify how size, shape, and growth mechanism interact to control chiral selection.[44,45]

Although this Chapter only studies chiral amplification during crystal growth, these results may also help to rationalize empirical trends in deracemization by growth/dissolution cycles such as temperature cycling-induced deracemization.[46] With each cycle, ripening phenomena shift the population size distributions, potentially giving rise to antagonistic size-disparities that slow the exponential deracemization kinetics. Multiple different routes exist to counteract this deceleration of deracemization. One known route to maintain the deracemization rate is progressively dampening the temperature swing with every cycle.[46] Our findings rationalize this strategy, which gradually transitions from classic temperature cycles, for which the emerging size-disparity increasingly disfavors the major enantiomer, to an accelerated Ostwald-ripening regime, where thermodynamics dominates and the remaining few minor enantiomer crystals are effectively converted. Counterintuitively, we propose exponential deracemization kinetics may also be maintained by progressively increasing crystallization rates during later cycles, as faster crystallization dampens antagonistic size-disparity effects.



Our results also serve as a practical guide for seeding and crystal size control. When a deracemization starts with racemization during growth, using an enantiopure excess comprised of small seed crystals is beneficial. The reverse is true for dissolution: small crystals dissolves faster than a population of large crystals and will thus experience negative amplification. A cyclic process starting with racemization during dissolution would thus benefit from an enantiopure excess comprised of large crystals and racemic bulk material comprised of small seed crystals. This lesson is also grounded in theory: if $ee_0 = 0$, the population with the greatest size deviation is enriched.[47] Similar is true for attrition-based deracemizations (Viedma ripening): if $ee_0 = 0$, the population with the larger crystals determines the outcome of deracemization.[48] Our results further imply that intermittent grinding could be effective to mitigate undesired ripening by resetting the crystal size distribution, which is even more powerful when combined with monitoring the crystal size distribution.[49,50] Finally, the use of small crystals may mitigate undesired growth inhibition from impurities.[51,52]

Overall, this work underscores that crystal size is a critical yet often overlooked kinetic parameter in asymmetric crystal growth. Size-disparities can be deliberate or accidental: many small crystals can for instance arise through nucleation and have a disproportionally big impact through to their high collective growth rate.[53] We also

note that any process mixing two or more sources of crystals (e.g. a racemic mixture of crystals and enantiopure crystals to establish an enantiomeric excess) invariably encounters size-disparities. Unfortunately, literature often lacks details on the preparation and origin of seed crystals used in crystallization experiments. Because subtle disparities quickly arise and can have major effects, this practice prevents comparing between studies and hampers benchmarking crystallization processes. At worst, neglecting seed design may even lead to confusing, inexplicable or irreproducible results. At best, deracemization is faster and completely reproducible. Furthermore, special care should be taken when re-using material from a completed batch in a subsequent crystallization, as dramatic changes in crystal properties (e.g. size, morphology) may occur. Hence, deliberate and well-reported seed design is essential for reproducibility and mechanistic understanding.

Finally, these findings on thermodynamically equal populations prompt a broader question: how does the kinetic domination of the fastest-growing population influence crystallization when the competing phases differ in thermodynamic stability?[54,55] This principle could be harnessed to deracemize the many chiral molecules that crystallize not as conglomerates but as racemic compounds.[56-58] In such systems, the enantiopure phase is typically less stable. However, enantiopure crystals might intrinsically grow faster than their racemic counterparts—a parameter so far seldomly considered—or could be actively favored through the choice of seed crystals, analogous to the experiments shown in this Chapter. To what extent cleverly exploiting crystal growth kinetics can overcome fundamental thermodynamic limitations is a compelling question. Beyond crystallization, these concepts may extend to the assembly of biological complexes and dynamic supramolecular systems.[59–63]



## References

1. Gellman, A.J.; Ernst, K. H. Chiral autocatalysis and mirror symmetry breaking. *Catal. Lett.* **2018**, *148*, 1610–1621.
2. Frank, F. C. On spontaneous asymmetric synthesis. *Biochim. Biophys. Acta* **1953**, *11*, 459–463.
3. Srisanga S.; Flood, A. E.; Galbraith S. C.; Rugmai, S.; Soontaranon S.; Ulrich, J. Crystal growth rate dispersion versus size-dependent crystal growth: appropriate modeling for crystallization processes. *Cryst. Growth Des.* **2015**, *15*, 2330–2336.
4. Klussmann, M.; Iwamura, H.; Mathew, S. P.; Wells, D. H.; Pandya, U.; Armstrong, A.; Blackmond, D.G. Thermodynamic control of asymmetric amplification in amino acid catalysis. *Nature* **2006**, *441*, 621–623.
5. Sacchi, P.; Wright, S. E.; Neoptolemou, P.; Lampronti, G. I.; Rajagopalan, A. K.; Kras, W.; Evans, C. L.; Hodgkinson, P.; Cruz-Cabeza, A. J. Crystal size, shape, and conformational changes drive both the disappearance and reappearance of ritonavir. *Proc. Natl. Acad. Sci. U. S. A.* **2024**, *121*, e2319127121.
6. Brands K. M. J.; Davies, A. J. Crystallization-induced diastereomer transformations. *Chem. Rev.* **2006**, *106*, 2711–2733.

7. Viedma, C.; Cuccia, L. A.; McTaggart, A.; Kahr, B.; Martin, A. T.; McBride, J. M.; Cintas, P. Oriented attachment by enantioselective facet recognition in millimeter-sized gypsum crystals. *Chem. Commun.* **2016**, *52*, 11673–11676.
8. Murakami, H. From racemates to single enantiomers - chiral synthetic drugs over the last 20 years. *Top. Curr. Chem.* **2006**, *269*, 273–299.
9. Choi, H. S.; Oh, I. H.; Zhang, B.; Coquerel, G.; Kim, W.; Park, B. J. Chiral flipping in Viedma deracemization. *J. Phys. Chem. Lett.* **2024**, *15*, 4367-4374.
10. Ma, A.; Du, W.; Wang, J.; Jiang, K.; Zhang, C.; Sheng, W.; Zhang, H.; Jin, R.; Wang, S. Transforming silver nanoclusters from racemic to homochiral via seeded crystallization. *J. Phys. Chem. Lett.* **2023**, *14*, 5095-5101.
11. Bak, S. Y.; Coquerel, G.; Kim, W.; Park, B. J. Solution volume effects on spontaneous chiral symmetry breaking of sodium chlorate crystals. *J. Phys. Chem. Lett.* **2023**, *14*, 785-790.
12. Fasel, R.; Parschau, M,; Ernst, K. H. Amplification of chirality in two-dimensional enantiomorphous lattices. *Nature* **2006**, *439*, 449–452.
13. Hein, J. E.; Huynh Cao, B.; Viedma, C.; Kellogg, R. M.; Blackmond, D. G. Pasteur's Tweezers revisited: On the mechanism of attrition-enhanced deracemization and resolution of chiral conglomerate. *J. Am. Chem. Soc.* **2012**, *134*, 12629–12636.
14. Ahn, J.; Kim, D. H.; Coquerel, G.; Kim, W. S. Chiral symmetry breaking and deracemization of sodium chlorate in Turbulent Flow. *Cryst. Growth Des.* **2018**, *18*, 297–306.
15. Srisanga, S.; ter Horst, J. H. Racemic compound, conglomerate, or solid solution: phase diagram screening of chiral compounds. *Cryst. Growth Des.*, **2010**, *10*, 1808–1812.
16. Sakamoto, M.; Fujita, K.; Yagishita, F.; Unosawa, A.; Mino, T.; Tsutomu, T. Kinetic resolution of racemic amines using provisional molecular chirality generated by spontaneous crystallization. *Chem. Commun.* **2011**, *47*, 4267–4269.
17. Ribó, J. M.; Hochberg, D.; Buhse, T.; Micheau, J. C. Viedma deracemization mechanisms in self-assembly processes. *Phys. Chem. Chem. Phys.* **2024**, *27*, 2516–2527.
18. Kondepudi, D. K.; Kaufman, R. J.; Singh, N. Chiral symmetry breaking in sodium chlorate crystallization. *Science* **1990**, *250*, 975–976.
19. Palmans, A. R. A. Deracemisations under kinetic and thermodynamic control. *Mol. Syst. Des. Eng.* **2017**, *2*, 34–46.
20. Breveglieri, F.; Maggioni, G. M.; Mazzotti, M. Deracemization of NMPA via temperature cycles. *Cryst. Growth Des.* **2018**, *18*, 1873–1881.
21. Zhang, B.; Coquerel G.; Kim, W. S. Isothermal deracemization of sodium chlorate in an agitated reactor: the effect of crystal size variables. *Cryst. Growth Des.* **2023**, *23*, 741–750.
22. Deck, L. T.; Hosseinalipour, M. S.; Mazzotti, M. Exact and ubiquitous condition for solid-state deracemization in Vitro and in Nature. *J. Am. Chem. Soc.* **2024**, *146*, 3872–3882.
23. Buhse, T.; Cruz, J. M.; Noble-Terán, M. E.; Hochberg, D.; Ribó, J. M.; Crusats, J.; Micheau, J. C. Spontaneous deracemizations. *Chem. Rev.* **2021**, *121*, 2147–2229.
24. van Dongen, S. W.; Ahlal, I.; Leeman, M.; Kaptein, B.; Kellogg, R. M.; Baglai, I; Noorduin, W. L. Chiral amplification through the interplay of racemizing conditions and asymmetric crystal growth. *J. Am. Chem. Soc.* **2023**, *145*, 436–442.
25. Uwaha, M. A model for complete chiral crystallization. *J. Phys. Soc. Jpn.* **2004**, *73*, 2601–2603.
26. Chernov. A.A. *Modern Crystallography III*. Springer Berlin, Heidelberg, 1st edn., **1984**.
27. Kile, D. E.; Eberl, D. D.; Hoch, A. R.; Reddy, M. M. An assessment of calcite crystal growth mechanisms based on crystal size distributions. *Geochim. Cosmochim. Acta* **2000**, *64*, 2937–2950.

28. van Rosmalen, G. M.; Daudey, P. J.; Marchee, W. G. J. An analysis of growth experiments of gypsum salts in suspension. *J. Cryst. Growth* **1981**, *52*, 801–811.
29. de Goede, R.; van Rosmalen, G. M. Modelling of crystal growth kinetics: a simple but illustrative approach. *J. Cryst. Growth* **1990**, *104*, 392–398.
30. Eek, R. A.; Dijkstra, S.; van Rosmalen, G. M. Dynamic modeling of suspension crystallizers, using experimental data. *AIChE J.* **1995**, *41*, 571–584.
31. Noorduin, W. L.; Vlieg, E.; Kellogg, R. M.; Kaptein, B. From Ostwald ripening to single chirality. *Angew. Chem. Int. Ed.* **2009**, *48*, 9600–9606.
32. Neugebauer, P; Cardona, J.; Besenhard, M. O.; Peter, A.; Gruber-Woelfler, H.; Tachtatzis, C; Cleary, A.; Andonovic, I.; Sefcik, J.; Khinast, J. G. Crystal shape modification via cycles of growth and dissolution in a tubular crystallizer. *Cryst. Growth Des.* **2018**, *18*, 4403-4415.
33. Snyder, R. C.; Doherty, M. F. Faceted crystal shape evolution during dissolution or growth. *AIChE J.* **2007**, *53*, 1337–1348.
34. di Gregorio, M.C.; Elsousou, M.; Wen, Q.; Shimon, L. J. W.; Brumfeld, V.; Houben, L.; Lahav, M.; van der Boom, M E. Molecular cannibalism: sacrificial materials as precursors for hollow and multidomain single crystals. *Nat. Commun.* **2021**, *12*, 957.
35. Srisanga, S.; Flood, A. E.; Galbraith, S. C.; Rugmai, S.; Soontaranon, S.; Ulrich, J. Crystal growth rate dispersion versus size-dependent crystal growth: appropriate modeling for crystallization processes. *Cryst. Growth Des.* **2015**, *15*, 2330–2336.
36. Shtukenberg, A. G.; García-Ruiz, J. M.; Kahr, B. Punin ripening and the classification of solution-mediated recrystallization mechanisms. *Cryst. Growth Des.* **2021**, *21*, 1267–1277.
37. Baglai, I.; Leeman, M.; Wurst, K.; Kaptein, B.; Kellogg R. M.; Noorduin, W. L. The Strecker reaction coupled to Viedma ripening: a simple route to highly hindered enantiomerically pure amino acids. *Chem. Commun.* **2018**, *54*, 10832–10834.
38. van Dongen, S. W.; Maeda, J.; Kaptein, B.; Cardinael, P.; Flood, A. E.; Coquerel, G.; Noorduin, W. L. Mechanistic dissymmetry between crystal growth and dissolution drives ratcheted chiral amplification. *J. Am. Chem. Soc.* **2025** *147*, 38508-38515.
39. Guillaneux, D.; Zhao, S. H.; Samuel, O.; Rainford, D.; Kagan, H. B. Nonlinear effects in asymmetric catalysis. *J. Am. Chem. Soc.* **1994**, *116*, 9430-9439.
40. Lewis, A.; Seckler, M. M.; Kramer, H. J. M.;van Rosmalen, G. M. *Industrial Crystallization: Fundamentals and Applications*; Cambridge University Press, **2015**. DOI: 10.1017/CBO9781107280427
41. The calculations overestimate the effects observed experimentally, since they do not account for size and shape evolution. Although all crystals grow, the smaller crystals grow incorporate relatively much more mass per crystal compared to larger crystals. Consequently, the size disparity shrinks over time. Hence the integrated effects of size disparity over time are lower than purely expected based on its initial imbalance.
42. Winn, D.; Doherty, M. F. Modeling crystal shapes of organic materials grown from solution. *AIChE J.* **2000**, *46*, 1348–1367.
43. Lu, F.; Zhang, Y.; Zhang, L.; Su, D.; Zhuang, Z.; Liu, M.; Chen; J. G.; Gang, O. Continuous encodable reshaping of gold nanocrystals through facet modulation. *J. Am. Chem. Soc.* **2025**, *147*, 25871-25882.
44. Sacchi, P.; Neoptolemou, P.; Davey, R. J.; Reutzel-Edens S. M.; Cruz-Cabeza, A. J. Do metastable polymorphs always grow faster? Measuring and comparing growth kinetics of three polymorphs of tolfenamic acid. *Chem. Sci.* **2023**, *14*, 11775–11789.
45. Ma, C. Y.; Wang, X. Z.; Roberts, K. J. Multi-dimensional population balance modeling of the growth of rod-like L-glutamic acid crystals using growth rates estimated from in-process imaging. *Adv. Powder Technol.* **2007**, *18*, 707–723.

46. Suwannasang, K.; Flood, A. E.; Rougeot, C.; Coquerel, G. Use of programmed damped temperature cycles for the deracemization of a racemic suspension of a conglomerate forming system. *Org. Process Res. Dev.* **2017**, *21*, 623–630.
47. Bodák, B.; Maggioni, G. M.; Mazzotti, M. Effect of initial conditions on solid-state deracemization via temperature cycles: a model-based study. *Cryst. Growth Des.* **2019**, *19*, 6552-6559.
48. Gherase, D.; Conroy, D.; Matar, O. K.; Blackmond, D. G. Experimental and theoretical study of the emergence of single chirality in attrition-enhanced deracemization. *Cryst. Growth Des.* **2014**, *14*, 928-937.
49. Noorduin, W. L.; Meekes, H.; van Enckevort, W, J. P.; Kaptein, B.; Kellogg R. M.; Vlieg, E. Enantioselective symmetry breaking directed by the order of process steps. *Angew. Chem. Int. Ed.* **2010**, *49*, 2539–2541.
50. Belletti, G.; Schuurman, J.; Meekes, H.; Rutjes, F. P. J. T.; Vlieg, E. Combining Viedma ripening and temperature cycling deracemization. *Cryst. Growth Des.* **2022**, *22*, 1874–1881.
51. Kondepudi, D. K.; Crook, K. E. Theory of conglomerate crystallization in the presence of chiral impurities. *Cryst. Growth Des.* **2005**, *5*, 2173–2179.
52. Sangwal, K. Effect of impurities on the processes of crystal growth. *J. Cryst. Growth*, **1993**, *128*, 1236–1244.
53. Cameli, F.; ter Horst, J. H.; Steendam, R. R. E.; Xiouras, C.; Stefanidis, G. D. On the effect of secondary nucleation on deracemization through temperature cycles. *Chem. Eur. J.* **2020**, *26*, 1344–1354.
54. Beckmann, W. Seeding the desired polymorph: background, possibilities, limitations, and case studies. *Org. Process Res. Dev.* **2000**, *4*, 372–383.
55. McDonald, M. A.; Salami, H.; Harris, P. R.; Lagerman, C. E.; Yang, X.; Bommarius, A. S.; Grover, M. A.; Rousseau, R. W. Reactive crystallization: a review. *React. Chem. Eng.* **2021**, *6*, 364-400.
56. Viedma, C.; Ortiz, J. E. A new twist in eutectic composition: deracemization of a racemic compound amino acid by Viedma ripening and temperature fluctuation. *Isr. J. Chem.* **2021**, *61*, 758–763.
57. Pinetre, C.; van Dongen, S. W.; Brandel, C.; Léonard, A. S.; Charpentier, M. D.; Dupray, V.; Oosterling, K.; Kaptein, B.; Leeman, M.; Kellogg, R. M.; ter Horst, J. H.; Noorduin, W. L. Enantiopurity by directed evolution of crystal stabilities and nonequilibrium crystallization. *J. Am. Chem. Soc.* **2025**, *147*, 8864-8870.
58. Katsuno, H.; Uwaha, M. How do most stable racemic crystals transform into metastable chiral crystals by grinding?. *Cryst. Growth Des.* **2025**, *25*, 3735-3741.
59. Ślęczkowski, M. L.; Mabesoone, M. F. J.; Ślęczkowski, P.; Palmans, A. R. A.; Meijer, E. W. Competition between chiral solvents and chiral monomers in the helical bias of supramolecular polymers. *Nat. Chem.* **2021**, *13*, 200-207.
60. Yang, S.; Geiger, Y.; Geerts, M.; Eleveld, M. J.; Kiani A.; Otto, S. Enantioselective self-replicators. *J. Am. Chem. Soc.* **2023**, *145*, 16889–16898.
61. Ernst, K. H. Supramolecular surface chirality. *Top. Curr. Chem.*, **2006**, *265*, 209–252.
62. Palmans, A. R. A.; Meijer, E. W. Amplification of chirality in dynamic supramolecular aggregates. *Angew. Chem. Int. Ed.* **2007**, *46*, 8948–8968.
63. Feringa, B. L.; van Delden, R. A. Absolute asymmetric synthesis: the origin, control, and amplification of chirality. *Angew. Chem. Int. Ed.* **1999**, *38*, 3418–3438.

Chapter 6

# On Mechanistic Ratchets driving Crystallization-Induced Deracemization.*

*Complete chiral amplification of the solid phase arises when mixtures of self-sorting enantiopure crystals undergo cycles of crystal growth and dissolution under solution-phase racemizing conditions. However, despite extensive studies and widespread use, the mechanism underlying such crystallization-induced deracemization remains insufficiently understood, hindering its optimization and broader application. Here, we experimentally dissect the individual contributions of crystal growth and dissolution and use a mass-balance to expose crystal dynamics. Regardless of the racemization rate, we always find a dissymmetry between the growth and the dissolution of the enantiomer populations. These experiments suggest that a fundamental difference between the mechanisms of crystal growth and dissolution enables a ratchet effect that drives chiral amplification. These insights advance our understanding of chiral crystallization mechanisms and provide guidance for optimizing crystallization-induced deracemizations, particularly by separately optimizing growth and dissolution steps to maximize the chiral amplification and deracemization efficiency.*



## Introduction

Chirality is a hallmark of life, and a key challenge in chemistry.[1-2] Isolating molecules of a desired chiral configuration is crucial for applications in pharmaceuticals, agrichemicals and materials.[3-7] The crystallization of racemic conglomerates,[8-9] where chiral molecules self-sort into enantiopure crystals, offers an intrinsically stereoselective strategy to separate or deracemize mixtures of enantiomers into a desired configuration.[10-13]

Deracemization of the solid-phase occurs when enantiopure crystals undergo cycles of crystal growth and dissolution while racemizing in solution (Fig. 6.1a).[14-19] The cycles of crystal growth and dissolution that drive deracemization may be implemented through temperature or solvent cycles or continuous attrition (Fig. 6.1b).[20-31] An initial enantioenrichment directs the deracemization process to an enantiomer of choice.

Although crystallization-induced deracemization has already been demonstrated for an array of bioactive chiral molecules,[23,28,32-36] the underlying mechanisms still pose questions of both fundamental and practical importance. Known is that each

* This chapter has been published as S.W. van Dongen*, J. Maeda*, B. Kaptein, P. Cardinael, A. Flood, G. Coquerel, W.L. Noorduin (2025). Mechanistic Dissymmetry between Crystal Growth and Dissolution drives Ratcheted Chiral Amplification. *J. Am. Chem. Soc.* 147(42): 38508–38515.

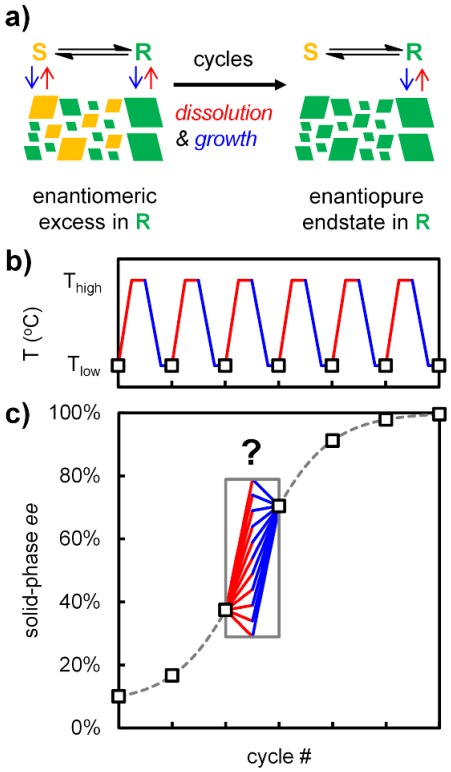


**Figure 6.1.** Crystallization-induced deracemization. (a) Crystal dissolution (red) and growth (blue) are coupled to racemization in solution to completely deracemize the solid-phase of a slurry with an initial solid enantiomeric excess (*ee*). (b) Cyclic growth and dissolution through temperature cycles. (c) Every cycle increases the solid-phase *ee* (squares), but the individual contributions of dissolution and growth to chiral amplification are unknown.

complete cycle of crystal growth and dissolution enantiomerically enriches the solid-phase and many theoretical models have been proposed.[37-50] Unknown, however, is what occurs during the individual segments of crystal growth or dissolution, as this question has not yet been studied experimentally, beyond a demonstration of chiral amplification during growth.[48] During crystal growth, the majority enantiomer has a higher growth rate, and racemization converts minority into majority to equalize supersaturation. It was recently hypothesized that the interplay between racemization and crystallization rate drives chiral amplification, as the inherently faster rate of dissolution compared to growth prevents racemization to fully neutralize the enantioenrichment obtained during growth.[47] Population balance modelling for an idealized system has recently shown deracemization through this mechanism.[50] Yet unclear, however, is how this mechanism can explain the deracemization for systems where racemization is very fast or instantaneous. Moreover, so far, no results have been reported to experimentally show the individual effects of crystal growth and dissolution for such unequal and competing populations of crystals.

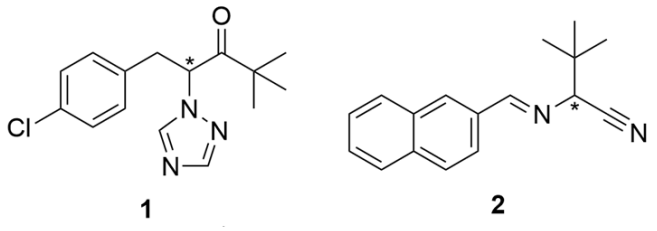


**Scheme 6.1.** Racemizable conglomerates **1** and **2** (* indicates chiral center).

This work aims to experimentally and systematically dissect the contributions of dissolution and growth and identify how these separately enrich, erode, or preserve the solid-phase enantiomeric excess (Fig. 6.1c). Using previously developed racemizable conglomerates Paclobutrazol precursor **1** and tert-leucine precursor **2** (Scheme 6.1),[23,48,51-54] we experimentally reveal the fundamental dissymmetry between asymmetric crystal growth and dissolution. This dissymmetry even exists when racemization kinetics are non-limiting and therefore is not caused by an interplay of crystallization and racemization rate alone, but likely results from a fundamental irreversibility between the mechanisms of crystal growth and dissolution. Through a full cycle of asymmetric dissolution and growth, this dissymmetry enables a ratchet-like effect that ultimately drives chiral amplification. This study challenges common tenets of crystallization-induced deracemization, shows that dissolution is antagonistic to chiral amplification, and exploits these insights to optimize deracemization processes.



## Results

To experimentally deconvolute cyclic dissolution and growth, we determined the evolution of the solid-phase enantiomeric excess (*ee*) after individual dissolution (heating) and growth (cooling) segments of a temperature cycle (Fig. 6.2). Low initial solid loading and high solubility differences between the low and high temperatures of the cycle were used to increase the sensitivity to subtle effects in asymmetric crystallization.[48] We prepared a slurry of conglomerate **1** at 40°C in MeOH:Water (60:40) with an initial ~25% *ee* in (*R*)-**1** in the solid-phase and started liquid-phase racemization by adding 0.1% w/v NaOH.[23,51-52] We cycled between 40°C and 55°C and analyzed the solid-phase *ee* via chiral HPLC after heating-induced dissolution (1.5°C/min) and after subsequent cooling-induced growth (0.5°C/min), both after 10 minutes isothermal hold to fully reach equilibrium. Experiments were repeated for slurries with an initial 50% and 90% *ee* in (*R*)-**1** in the solid-phase.

Figure 6.2c shows the solid-phase *ee* after dissolution and growth, starting with different degrees of initial solid-phase enantiomeric enrichment. As expected, the solid-phase *ee* increases over each full cycle, confirming net chiral amplification of the system. However, the extent of chiral amplification varies; cycles with low (~25%) and high (~90%) initial *ee* show lower enrichment than cycles with medium (~50%)

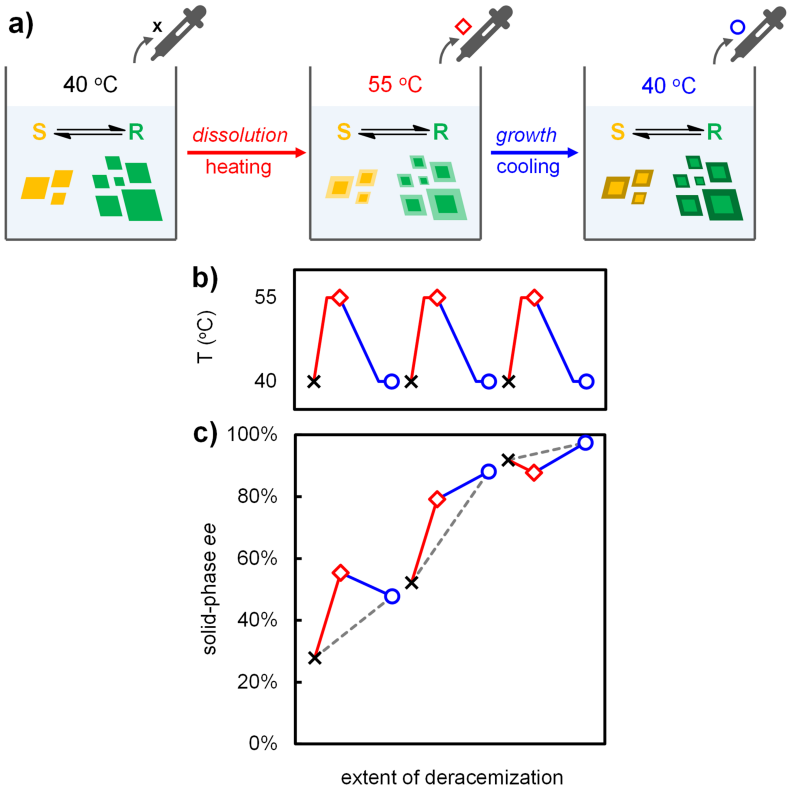


**Figure 6.2.** Deconvoluted temperature cycles for slurries with low, medium, and high initial *ee* in (*R*)-**1**. (a) Solid-phase *ee* is determined by sampling before dissolution (black cross), after dissolution (red diamond), and after subsequent growth (blue circle). (b) Temperature profile with sampling moments indicated. (c) Solid-phase *ee* increases for every cycle (grey dashed line), although individual contributions of dissolution and growth vary (solid lines). Lines are a guide to the eye.

initial *ee*, which is consistent with the sigmoidal characteristic of crystallization-induced deracemization kinetics.

The variation within cycles is profound. For low and medium initial *ee*, Figure 6.2c shows an increase in solid-phase *ee* after dissolution, as expected. For high initial *ee*, however, dissolution is shown to decrease solid-phase *ee*, which is in contrast to the common view that dissolution always enriches solid-phase *ee.* This surprising decrease in solid-phase *ee* during dissolution is not affected by the heating rate or the duration of the isothermal hold, and enhanced if the relative amount of dissolved solid is increased (see Appendix for details). Growth also allows for both enrichment and erosion: For low initial *ee*, the solid-phase *ee* decreases during growth, whereas for medium and high initial *ee* the solid-phase *ee* increases during growth. This experimental evidence for erosion during dissolution and enrichment during growth confirms that the major enantiomer may dissolve faster and grow faster than the minor enantiomer.[47,50]

Motivated by these results, we investigated how asymmetric crystallization causes the major enantiomer to dissolve and grow faster than the minor enantiomer. We therefore disentangled the deracemization process into two completely isolated dissolution and growth steps (Fig. 6.3a). Since crystals are only partly altered during dissolution and growth, we constructed a full mass balance, detailing exactly how much of each enantiomer is grown or dissolved. For this, we used conglomerate **2** (Scheme 6.1), which racemizes in the presence of 1,8-diazabicyclo[5.4.0]undec-7-ene (DBU) and exhibits clean racemization kinetics without side-reactions.[48,53-54] Since net chiral amplification is strongest at medium initial *ee* and boundary effects are minimized, we prepared initial solids with 50% *ee* in (*R*)-**2**. The initial solids were pre-ground to ensure a uniform initial crystal size distribution and morphology.

For dissolution, while at 20°C, a racemizing undersaturated solution of (*RS*)-**2** in MeOH (10 µL/mL DBU) was added to the pre-ground initial solid. The resulting slurry was shaken in the presence of soft PTFE spheres to homogenize while minimizing attrition and secondary nucleation effects.[29] After 90 minutes post-dissolution equilibration at 20°C, the solid-phase *ee* was analyzed. Simultaneously, liquid-phase samples were taken to track enantiomer concentrations. For growth, while at 30°C, a racemizing saturated solution of (*RS*)-**2** in MeOH was added to a new aliquot of pre-ground initial solid, which was slowly cooled back to 20°C (0.11°C/min) to avoid nucleation. Solid and liquid phases were sampled after 30 minutes post-growth equilibration at 20°C, when crystallization had completed as confirmed via mass-balance. Since both dissolution and growth experiments ended at room temperature (20°C), undesired crystallization during sampling was negligible.

Figure 6.3b shows the absolute solid-phase *ee* after independent dissolution and growth from identical pre-ground initial solids. At first glance, the experiment seems to confirm the common view that solid-phase *ee* increases during dissolution and decreases during growth. However, these absolute changes in solid-phase *ee* can be deceiving. For instance, dissolving more majority than minority enantiomer can still cause an increase in solid-phase *ee*, but effectively erodes the overall system *ee* through racemization. Exploiting our mass-balance, we therefore plot the initial mass and calculate the change in mass ($m_\Delta$) for both enantiomer populations using their initial and final liquid-phase concentrations (Fig. 6.3c, $m_\Delta$ indicated using arrows).

Figure 6.3c shows that both enantiomers decrease in total solid mass during dissolution and increase in solid mass during growth, but does not show how the initial imbalance between the enantiomer populations translates to asymmetric crystallization kinetics. To reveal this, we determined the *ee* of the portion of the crystals that is cumulatively removed from the crystals during dissolution and is cumulatively added to the crystals during growth (Fig. 6.3d, $ee_\Delta = (m_\Delta{}^R - m_\Delta{}^S) / (m_\Delta{}^R + m_\Delta{}^S)$).

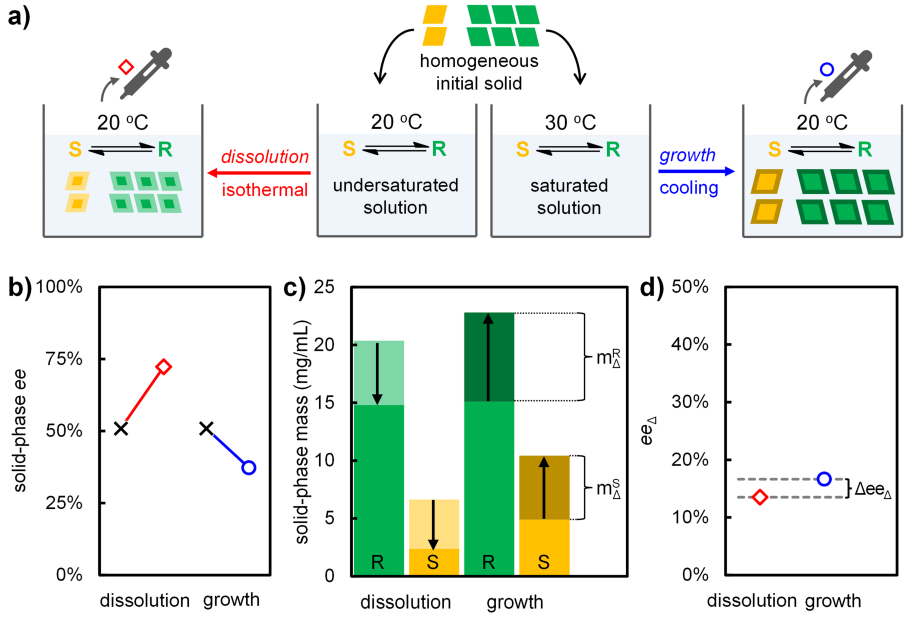


**Figure 6.3.** Dissymmetry between dissolution (red) and growth (blue) drives ratcheted chiral amplification. (a) Solid and liquid are analyzed after separate dissolution and growth starting from the same pre-ground initial solid of 50% *ee* in (*R*)-**2**. (b) Absolute solid-phase *ee* increases after dissolution and decreases after growth. (c) Mass-balance constructed from liquid-phase concentrations shows mass of grown and dissolved enantiomers ($m_\Delta$). (d) Positive *ee* of the dissolved and grown material ($ee_\Delta$) shows the major enantiomer dissolves and grows faster than the minor enantiomer. Enrichment during growth outweighs erosion during dissolution ($\Delta ee_\Delta > 0$); a dissymmetry that enables ratcheted chiral amplification. Data is provided in the Appendix.

To interpret $ee_\Delta$, we realize that when $ee_\Delta = 0$, growth and dissolution are racemic (i.e. equal amounts of R and S are grown onto or dissolved from the initial solid, as under non-racemizing conditions) and no net amplification occurs over a full cycle. When $ee_\Delta = ee_0 = 50\%$, growth or dissolution rates are proportional to the initial mass ratio of the enantiomers. Since the determined values of $ee_\Delta$ are positive for both dissolution and growth (Fig. 6.3d), the major enantiomer consistently dissolves and grows faster than the minor enantiomer. Despite the use of identical initial solids, however, Figure 6.3d also shows that the value of $ee_\Delta$ differs for dissolution and growth and shows that the asymmetry is actually stronger during growth: $ee_\Delta = 17\%$ for growth, while $ee_\Delta = 14\%$ for dissolution. This difference experimentally shows that liquid-phase racemization during growth enhances chiral amplification, while racemization during dissolution is counterproductive as the major enantiomer molecules are effectively racemized. Nevertheless, over a full cycle, growth-driven amplification outweighs dissolution-induced erosion. These results thus experimentally reveal how chiral dissolution and growth are dissymmetric processes, enabling a ratchet effect that drives net chiral amplification over a full cycle.

The origin of this dissymmetry could be the coupled kinetics of racemization and crystallization, when crystals dissolve faster than they grow,[47,50] but may also stem directly from fundamental differences between the mechanisms of crystal growth and dissolution. We therefore systematically varied the racemization rate to investigate how the observed effects depend on the interplay between rates of dissolution, growth and racemization. Since the racemization rate of **2** is linearly dependent on the catalyst concentration ([DBU]),[55] we repeated the previous experiment at various concentrations of DBU and plot the results (Fig. 6.4).

Without racemization, we observe the expected racemic growth and dissolution ($ee_\Delta = 0$). With racemization, we observe a continuously increasing $ee_\Delta$ for both growth and dissolution, with $ee_\Delta$ for growth always above that for dissolution. The larger the difference between the $ee_\Delta$ for dissolution and growth ($\Delta ee_\Delta$), the stronger the ratchet effect, resulting in higher chiral amplification efficiency. As expected from previous reports,[27,38,40,55-56] increasing the racemization rate will thus generally increase deracemization kinetics by increasing $\Delta ee_\Delta$.

Figure 6.4 shows that increasing the racemization rate increases $ee_\Delta$, until approaching a plateau. This effect has previously been reported for chiral crystal growth,[48] and thus also holds for dissolution. In this plateau, crystal growth and dissolution kinetics are much slower than racemization kinetics. Hence, akin to Michael-Menten kinetics in biochemistry, racemization has become non-limiting. The fact that Figure 6.4 shows that $ee_\Delta$ for growth is systematically higher than $ee_\Delta$ for dissolution, implies that amplification of the major enantiomer during growth always outweighs its erosion during dissolution: Net chiral amplification always occurs. This independence of racemization rate implies that the observed dissymmetry between chiral growth and dissolution is not merely caused by the kinetic interplay of racemization and crystallization, but—at its core—rooted in a fundamental difference between the mechanisms of crystal growth and dissolution.

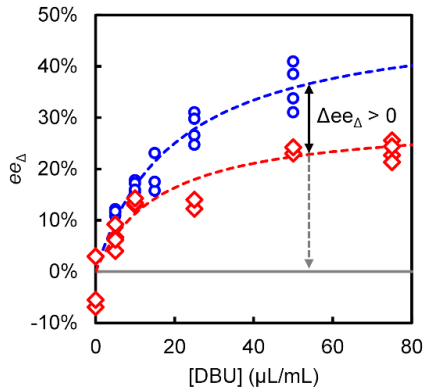


**Figure 6.4.** Dissolution (red) and growth (blue) are dissymmetric at every racemization rate (∝ [DBU]). Chiral amplification efficiency (∝ $\Delta ee_\Delta$, solid black arrow) increases with racemization rate. Chiral amplification efficiency can be maximized by switching off racemization during dissolution, such that $ee_\Delta = 0$ (dashed grey arrow). Lines are a guide to the eye.

This would explain why the dissymmetry that drives deracemization persists even when racemization kinetics are no longer limiting.

The plateau in Figure 6.4 has practical consequences: there is a limit to the beneficial effects that can be gained by increasing racemization kinetics. We realize, however, that increasing the racemization rate is not the only way to increase the efficiency of chiral amplification. Counterintuitively, chiral amplification efficiency can be increased further by switching racemization off entirely during dissolution. Without racemization, $ee_\Delta$ becomes 0 during dissolution, while the original $ee_\Delta$ during growth is retained, thereby maximizing $\Delta ee_\Delta$. To explore this idea, we extended a basic model previously introduced for asymmetric crystal growth,[48] by including a contribution for asymmetric dissolution. In short, we used the values of $ee_\Delta$ in Figure 6.4 to express asymmetric crystallization through empirical amplification factors for growth and dissolution (see Appendix for details). Although this qualitative model ignores many complexities of the deracemization process, it indeed predicts that switching off racemization during dissolution markedly increases deracemization efficiency (Fig. 6.5a). Moreover, the model visualizes that switching off racemization during growth would lead to complete loss of the initial solid-phase enantiomeric excess. These predictions thus suggest that individually optimizing growth and dissolution can maximize chiral amplification efficiency.



Repetitively switching on and off racemization is thus highly desirable, but often hardly possible or practical. However, switching off racemization once, e.g. by quenching the catalyst, is generally feasible. Since deracemization kinetics slow down significantly near the end, it may be beneficial to switch off racemization before a final dissolution step. To experimentally demonstrate this idea, we used

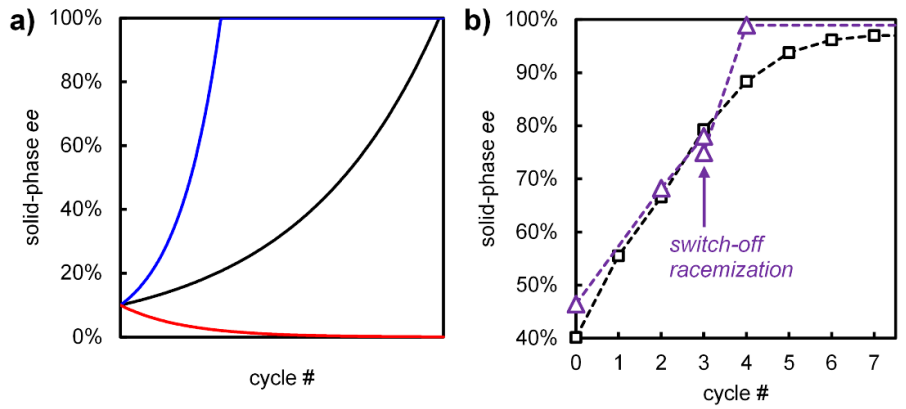


**Figure 6.5.** Increased deracemization efficiency through on/off-switching of racemization. (a) Compared to a regular cycle (black), racemizing only during growth accelerates deracemization (blue), while racemizing only during dissolution causes racemization of the solid-phase (red). (b) One-time switching off racemization before the final dissolution step (purple triangles; racemization is on during final growth step) in the temperature cycling of **1** increases deracemization efficiency compared to regular cycles (black squares).

conglomerate **1**, because racemization catalyst NaOH can be quenched by the addition of HCl. Starting with a solid-phase of 40–45% *ee* in (*R*)-**1** and 0.1% w/v NaOH, we performed three cycles to reach 75% *ee* in the solid. We then switched off racemization by adding 1.1 eq. 6 M HCl before performing a final dissolution step. After re-adding the racemization catalyst (0.2% w/v NaOH) a virtually enantiopure solid-phase was obtained after growth (99% *ee* in (*R*)-**1**, Figure 6.5b). In contrast, the experiment wherein we kept racemization switched on required four more cycles to reach a similar solid-phase *ee* (97%). Hence, even switching off racemization only once already yields a higher enantiopurity within less cycles and decreases the time to deracemization by about 25% (Fig. 6.5b).

## Discussion, Summary and Outlook

Our findings bring surprising new insights to the fundamental mechanistic understanding of crystallization-induced deracemizations.

First, our results impact the debate on the mechanistic role of crystal-size. Crystal-size effects and size-dependent solubility have been often proposed as central driving forces for chiral amplification,[39,41,44,49,57] although these mechanisms have received criticism from other theorists.[47,58] In this Chapter, we have minimized the effect of crystal-size effects by using constant and homogeneous seeds. Nonetheless, we do observe the dissymmetric growth and dissolution that drives chiral amplification. Our results thus suggest that chiral amplification is not a result of crystal size effects alone, although such effects can surely modulate the degree of amplification.

Second, for the first time, we experimentally reveal the individually different contributions of crystal growth and dissolution and show that their dissymmetry causes a ratcheting effect that drives chiral amplification. Paradoxically, although dissolution may increase and growth may decrease the absolute solid-phase *ee*, a full mass-balance shows that growth amplifies and dissolution erodes the enantiomeric enrichment of the entire system. These experimental results emphasize the proposed role of crystallization dynamics[47-48,50] and contrast with previous views rooted in equilibrium-thermodynamics.[45,59] As such, our study demonstrates how experimentally deconvoluting the effects of crystal growth and dissolution for populations of crystals under racemizing conditions may not only help to validate assumptions on the mechanism,[37,39,41-47,49-50] but may also bring new mechanistic insights in asymmetric crystallization.

Third, we zoom in on the source of the dissymmetry between growth and dissolution that enables ratcheted chiral amplification. Although the interplay between rates of racemization and crystallization indeed modulates the degree of chiral amplification when racemization is relatively slower during dissolution than during growth,[47,50] we experimentally find that chiral amplification also occurs when racemization is very

fast and non-limiting. This finding suggests that it is the fundamental difference between the mechanisms of growth and dissolution—not just their interplay with the rate of racemization—that is the core driver of crystallization-induced chiral amplification. Such a mechanistic dissymmetry could also explain deracemization in achiral systems (e.g. $NaClO_3$ and $(H_2NCH_2CH_2NH_2)\cdot H_2SO_4$), where racemization is instantaneous.[17-18]

The mechanistic differences between crystal growth and dissolution are manifold. Beyond modes of attachment and detachment of molecules at crystal surfaces,[60-63] important factors to consider are stereoselective incorporation of clusters and oriented attachment,[37,40,64-66] ripening and agglomeration mechanisms,[39,67-68] and a form of stereoselective secondary nucleation.[69-71] Also population-level effects such as stochasticity (e.g. chiral flipping and growth rate dispersion) and nonideal solution behavior of enantiomers may cause asymmetric crystallization.[44,70,72] The predominant dissymmetry may depend on the crystallization conditions (e.g. supersaturation and attrition) and crystallization characteristics of the species (e.g. morphology, surface tension and binding strength). In this study, primary and secondary nucleation were aimed to be minimal and crystallization proceeded at low supersaturation. Growth and dissolution of crystals always occurs, even without attrition or explicit fluctuations in temperature or concentration,[42] and the effects demonstrated in this Chapter will be prevalent for all chiral crystals under racemizing conditions. Understanding growth and dissolution processes on the surface of a single crystal and translating those across interacting populations of many crystals will be key in unravelling the whole mechanism of chiral amplification through asymmetric crystallization.

Our results hold important practical lessons for designing and performing crystallization-induced deracemizations: (1) optimize dissolution and growth separately for maximum efficiency; (2) minimize racemization during dissolution and dissolve as fast as possible; (3) maximize racemization during growth. The implementation of the cycles ideally should optimize the amount of cycled material per unit time.[73] An effective approach would be to push the system away from equilibrium, thereby achieving simultaneous and continuous growth/dissolution cycles, as in the case of grinding and spatial temperature cycling.[22,74-75] Moreover, we confirm a potential trap:[50] Racemization reactions that proceed at different rates during growth and dissolution, e.g. due to strong temperature dependence of its reaction kinetics, can hinder chiral amplification and may even lead to solid-phase racemization rather than deracemization (i.e. when $\Delta ee_\Delta < 0$).

These insights can also aid in comparing and choosing between different deracemization strategies. Solvent cycling,[29,30] for instance, follows many of these practical lessons: The dissolution rate is maximized through instant re-addition of solvent; racemization is maximized during growth through slow evaporation; both

growth and dissolution occur at equal temperatures and thus experience equal racemization rates.

To maximize chiral amplification, however, it will be required to sequentially switch on and off racemization. We therefore foresee the development of mechanical or chemical on-off switches, racemization based on electrochemistry and photochemistry, and exploiting gradients in experimental reactors. Also, flow chemistry or immobilized (bio)catalysts could be utilized in a separate racemization loop that is activated or deactivated on demand.[28,76-77] A ratchet effect may then also be exploited to deracemize thermodynamically stable racemic compounds.[13,78-80]

## References


(1) Noyori, R., Asymmetric catalysis: science and opportunities (Nobel lecture). *Angew. Chem. Int. Ed.* **2002,** *41* (12), 2008-2022. https://doi.org/10.1002/1521-3773(20020617)41:12<2008::AID-ANIE2008>3.0.CO;2-4

(2) *Comprehensive Chirality*, 1st ed.; Carreira, E. M., Yamamoto, H., Eds.; Elsevier: Amsterdam, 2012.

(3) List, B.; Yang, J. W., The organic approach to asymmetric catalysis. *Science* **2006,** *313* (5793), 1584-1586. https://doi.org/10.1126/science.1131945

(4) Palmans, A., Deracemisations under kinetic and thermodynamic control. *Mol. Syst. Des. Eng.* **2017,** *2* (1), 34-46. https://doi.org/10.1039/C6ME00088F

(5) Banerjee-Ghosh, K.; Ben Dor, O.; Tassinari, F.; Capua, E.; Yochelis, S.; Capua, A.; Yang, S.-H.; Parkin, S. S.; Sarkar, S.; Kronik, L., Separation of enantiomers by their enantiospecific interaction with achiral magnetic substrates. *Science* **2018,** *360* (6395), 1331-1334. https://doi.org/10.1126/science.aar4265

(6) Crassous, J.; Fuchter, M. J.; Freedman, D. E.; Kotov, N. A.; Moon, J.; Beard, M. C.; Feldmann, S., Materials for chiral light control. *Nat. Rev. Mater.* **2023,** *8* (6), 365-371. https://doi.org/10.1038/s41578-023-00543-3

(7) McVicker, R. U.; O'Boyle, N. M., Chirality of new drug approvals (2013–2022): trends and perspectives. *J. Med. Chem.* **2024,** *67* (4), 2305-2320. https://doi.org/10.1021/acs.jmedchem.3c02239

(8) Jacques, J.; Collet, A.; Wilen, S. H.; Collet, A., *Enantiomers, racemates, and resolutions*. Wiley New York: 1981.

(9) Walsh, M. P.; Barclay, J. A.; Begg, C. S.; Xuan, J.; Johnson, N. T.; Cole, J. C.; Kitching, M. O., Identifying a hidden conglomerate chiral pool in the CSD. *JACS Au* **2022,** *2* (10), 2235-2250. https://doi.org/10.1021/jacsau.2c00394

(10) Brands, K. M.; Davies, A. J., Crystallization-induced diastereomer transformations. *Chem. Rev.* **2006,** *106* (7), 2711-2733. https://doi.org/10.1021/cr0406864

(11) Lorenz, H.; Seidel-Morgenstern, A., Processes to separate enantiomers. *Angew. Chem. Int. Ed.* **2014,** *53* (5), 1218-1250. https://doi.org/10.1002/anie.201302823

(12) Buhse, T.; Cruz, J.-M.; Noble-Teran, M. E.; Hochberg, D.; Ribo, J. M.; Crusats, J.; Micheau, J.-C., Spontaneous deracemizations. *Chem. Rev.* **2021,** *121* (4), 2147-2229. https://doi.org/10.1021/acs.chemrev.0c00819

(13) Pinetre, C.; van Dongen, S. W.; Brandel, C.; Léonard, A.-S.; Charpentier, M. D.; Dupray, V.; Oosterling, K.; Kaptein, B.; Leeman, M.; Kellogg, R. M., Enantiopurity by directed evolution of crystal stabilities and nonequilibrium crystallization. *J. Am. Chem. Soc.* **2025,** *147* (10), 8864-8870. https://doi.org/10.1021/jacs.5c00569

(14) Havinga, E., Spontaneous formation of optically active substances. *Biochim. Biophys. Acta* **1954,** *13*, 171-174. https://doi.org/10.1016/0006-3002(54)90300-5

(15) Kondepudi, D. K.; Kaufman, R. J.; Singh, N., Chiral symmetry breaking in sodium chlorate crystallization. *Science* **1990,** *250* (4983), 975-976. https://doi.org/10.1126/science.250.4983.975
(16) McBride, J. M.; Carter, R. L., Spontaneous resolution by stirred crystallization. *Angew. Chem. Int. Ed.* **1991,** *30* (3), 293-295. https://doi.org/10.1002/anie.199102931
(17) Viedma, C., Chiral Symmetry Breaking During Crystallization: Complete Chiral Purity Induced by Nonlinear Autocatalysis and Recycling. *Phys. Rev. Lett.* **2005,** *94* (6), 065504. https://doi.org/10.1103/PhysRevLett.94.065504
(18) Cheung, P. S. M.; Gagnon, J.; Surprenant, J.; Tao, Y.; Xu, H.; Cuccia, L. A., Complete asymmetric amplification of ethylenediammonium sulfate using an abrasion/grinding technique. *Chem. Commun.* **2008,** 987(989), 987. https://doi.org/10.1039/B716977A
(19) Noorduin, W. L.; Izumi, T.; Millemaggi, A.; Leeman, M.; Meekes, H.; Van Enckevort, W. J.; Kellogg, R. M.; Kaptein, B.; Vlieg, E.; Blackmond, D. G., Emergence of a single solid chiral state from a nearly racemic amino acid derivative. *J. Am. Chem. Soc.* **2008,** *130* (4), 1158-1159. https://doi.org/10.1021/ja7106349
(20) Leeman, M.; Noorduin, W. L.; Millemaggi, A.; Vlieg, E.; Meekes, H.; van Enckevort, W. J.; Kaptein, B.; Kellogg, R. M., Efficient Havinga–Kondepudi resolution of conglomerate amino acid derivatives by slow cooling and abrasive grinding. *CrystEngComm* **2010,** *12* (7), 2051-2053. https://doi.org/10.1039/C0CE00140F
(21) Noorduin, W.; Van Der Asdonk, P.; Bode, A.; Meekes, H.; Van Enckevort, W.; Vlieg, E.; Kaptein, B.; Van Der Meijden, M.; Kellogg, R.; Deroover, G., Scaling up attrition-enhanced deracemization by use of an industrial bead mill in a route to Clopidogrel (Plavix). *Org. Process Res. Dev.* **2010,** *14* (4), 908-911. https://doi.org/10.1021/op1001116
(22) Viedma, C.; Cintas, P., Homochirality beyond grinding: deracemizing chiral crystals by temperature gradient under boiling. *Chem. Commun.* **2011,** *47* (48), 12786-12788. https://doi.org/10.1039/C1CC14857E
(23) Suwannasang, K.; Flood, A.; Rougeot, C.; Coquerel, G., Using programmed heating–cooling cycles with racemization in solution for complete symmetry breaking of a conglomerate forming system. *Cryst. Growth. Des.* **2013,** *13* (8), 3498-3504. https://doi.org/10.1021/cg400436r
(24) Li, W. W.; Spix, L.; De Reus, S. C.; Meekes, H.; Kramer, H. J.; Vlieg, E.; Ter Horst, J. H., Deracemization of a racemic compound via its conglomerate-forming salt using temperature cycling. *Cryst. Growth. Des.* **2016,** *16* (9), 5563-5570. https://doi.org/10.1021/acs.cgd.6b01034
(25) Breveglieri, F.; Maggioni, G. M.; Mazzotti, M., Deracemization of NMPA via temperature cycles. *Cryst. Growth. Des.* **2018,** *18* (3), 1873-1881. https://doi.org/10.1021/acs.cgd.7b01746
(26) Cameli, F.; Xiouras, C.; Stefanidis, G. D., Intensified deracemization via rapid microwave-assisted temperature cycling. *CrystEngComm* **2018,** *20* (21), 2897-2901. https://doi.org/10.1039/C8CE00575C
(27) Intaraboonrod, K.; Lerdwiriyanupap, T.; Hoquante, M.; Coquerel, G.; Flood, A. E., Temperature cycle induced deracemization. *Mendeleev Commun.* **2020,** *30* (4), 395-405. https://doi.org/10.1016/j.mencom.2020.07.002
(28) Valenti, G.; Tinnemans, P.; Baglai, I.; Noorduin, W. L.; Kaptein, B.; Leeman, M.; Ter Horst, J. H.; Kellogg, R. M., Combining incompatible processes for deracemization of a Praziquantel derivative under flow conditions. *Angew. Chem.* **2021,** *133* (10), 5339-5342. https://doi.org/10.1002/ange.202013502
(29) van Dongen, S. W.; Baglai, I.; Leeman, M.; Kellogg, R. M.; Kaptein, B.; Noorduin, W. L., Rapid deracemization through solvent cycling: proof-of-concept using a racemizable conglomerate clopidogrel precursor. *Chem. Commun.* **2023,** *59* (26), 3838-3841. https://doi.org/10.1039/D3CC00332A
(30) Intaraboonrod, K.; Flood, A. E., A Novel Strategy for Deracemization Using Periodic Fluctuations of Concentration. *Chem. Eng. Technol.* **2023,** *46* (11), 2310-2315. https://doi.org/10.1002/ceat.202200624

(31) Gieling, J.; Wéry, G.; Lopes, C.; de Meester, J.; Brandel, C.; Cartigny, Y.; Leyssens, T.; Baier, D. M., Mechanochemical Deracemization: A Sustainable Approach to Enantiopurity. *Chem. Eur. J.* **2025,** *31* (15), e202404120. https://doi.org/10.1002/chem.202404120

(32) van der Meijden, M. W.; Leeman, M.; Gelens, E.; Noorduin, W. L.; Meekes, H.; van Enckevort, W. J.; Kaptein, B.; Vlieg, E.; Kellogg, R. M., Attrition-enhanced deracemization in the synthesis of clopidogrel-a practical application of a new discovery. *Org. Process Res. Dev.* **2009,** *13* (6), 1195-1198. https://doi.org/10.1021/op900243c

(33) Noorduin, W. L.; Kaptein, B.; Meekes, H.; van Enckevort, W. J.; Kellogg, R. M.; Vlieg, E., Fast attrition-enhanced deracemization of naproxen by a gradual in situ feed. *Angew. Chem. Int. Ed.* **2009,** *121* (25), 4651-4653. https://doi.org/10.1002/anie.200901386

(34) Baglai, I.; Leeman, M.; Kellogg, R. M.; Noorduin, W. L., A Viedma ripening route to an enantiopure building block for Levetiracetam and Brivaracetam. *Org. Biomol. Chem.* **2019,** *17* (1), 35-38. https://doi.org/10.1039/C8OB02660B

(35) Shimizu, W.; Uemura, N.; Yoshida, Y.; Mino, T.; Kasashima, Y.; Sakamoto, M., Attrition-enhanced deracemization and absolute asymmetric synthesis of flavanones from prochiral precursors. *Cryst. Growth. Des.* **2020,** *20* (9), 5676-5681. https://doi.org/10.1021/acs.cgd.0c00955

(36) Oketani, R.; Naito, R.; Hisaki, I., Semicontinuous temperature cycle-induced deracemization using an axially chiral naphthamide. *Org. Process Res. Dev.* **2024,** *28* (9), 3570-3577. https://doi.org/10.1021/acs.oprd.4c00091

(37) Uwaha, M., A model for complete chiral crystallization. *J. Phys. Soc. Jpn* **2004,** *73* (10), 2601-2603. https://doi.org/10.1143/JPSJ.73.2601

(38) Noorduin, W. L.; Meekes, H.; van Enckevort, W.; Millemaggi, A.; Leeman, M.; Kaptein, B.; Kellogg, R.; Vlieg, E., Complete Deracemization by Attrition-Enhanced Ostwald Ripening Elucidated. *Angew. Chem. Int. Ed.* **2008,** 47 (34), 6445-6447. https://doi.org/10.1002/anie.200801846

(39) Noorduin, W. L.; Meekes, H.; Bode, A. A.; van Enckevort, W. J.; Kaptein, B.; Kellogg, R. M.; Vlieg, E., Explanation for the emergence of a single chiral solid state during attrition-enhanced Ostwald ripening: survival of the fittest. *Cryst. Growth. Des.* **2008,** *8* (5), 1675-1681. https://doi.org/10.1021/cg701211a

(40) Noorduin, W. L.; van Enckevort, W. J.; Meekes, H.; Kaptein, B.; Kellogg, R. M.; Tully, J. C.; McBride, J. M.; Vlieg, E., The driving mechanism behind attrition-enhanced deracemization. *Angew. Chem. Int. Ed.* **2010,** *49* (45), 8435-8438. https://doi.org/10.1002/anie.201002036

(41) Iggland, M.; Mazzotti, M., A population balance model for chiral resolution via Viedma ripening. *Cryst. Growth. Des.* **2011,** *11* (10), 4611-4622. https://doi.org/10.1021/cg2008599

(42) Hein, J. E.; Huynh Cao, B.; Viedma, C.; Kellogg, R. M.; Blackmond, D. G., Pasteur's tweezers revisited: on the mechanism of attrition-enhanced deracemization and resolution of chiral conglomerate solids. *J. Am. Chem. Soc.* **2012,** *134* (30), 12629-12636. https://doi.org/10.1021/ja303566g

(43) Suwannasang, K.; Coquerel, G.; Rougeot, C.; Flood, A. E., Mathematical modeling of chiral symmetry breaking due to differences in crystal growth kinetics. *Chem. Eng. Technol.* **2014,** *37* (8), 1329-1339. https://doi.org/10.1002/ceat.201400056

(44) Uchin, R.; Suwannasang, K.; Flood, A. E., Model of Temperature Cycle-Induced Deracemization via Differences in Crystal Growth Rate Dispersion. *Chem. Eng. Technol.* **2017,** *40* (7), 1252-1260. https://doi.org/10.1002/ceat.201600746

(45) Belletti, G. Solid state deracemization. Viedma ripening versus temperature cycling. Radboud University Nijmegen, 2021.

(46) Dutta, S.; Yun, Y.; Widom, M.; Gellman, A. J., 2D Ising Model for Adsorption-induced Enantiopurification of Racemates. *ChemPhysChem* **2021,** *22* (2), 197-203. https://doi.org/10.1002/cphc.202000881

(47) Uwaha, M.; Katsuno, H., Mechanism of chirality conversion of crystals by Viedma ripening and temperature cycling. *J. Cryst. Growth* **2022,** *598*, 126873. https://doi.org/10.1016/j.jcrysgro.2022.126873

(48) van Dongen, S. W.; Ahlal, I.; Leeman, M.; Kaptein, B.; Kellogg, R. M.; Baglai, I.; Noorduin, W. L., Chiral amplification through the interplay of racemizing conditions and asymmetric crystal growth. *J. Am. Chem. Soc.* **2022,** *145* (1), 436-442. https://doi.org/10.1021/jacs.2c10584

(49) Zhang, B.; Coquerel, G.; Kim, W.-S., Isothermal deracemization of sodium chlorate in an agitated reactor: the effect of crystal size variables. *Cryst. Growth. Des.* **2023,** *23* (2), 741-750. https://doi.org/10.1021/acs.cgd.2c00871

(50) Deck, L.-T.; Hosseinalipour, M. S.; Mazzotti, M., Exact and Ubiquitous Condition for Solid-State Deracemization in Vitro and in Nature. *J. Am. Chem. Soc.* **2024,** *146* (6), 3872-3882. https://doi.org/10.1021/jacs.3c11332

(51) Black, S.; Williams, L.; Davey, R.; Moffatt, F.; Jones, R.; McEwan, D.; Sadler, D., The preparation of enantiomers of paclobutrazol: a crystal chemistry approach. *Tetrahedron* **1989,** *45* (9), 2677-2682. https://doi.org/10.1016/S0040-4020(01)80097-1

(52) Maeda, J.; Cardinael, P.; Flood, A.; Coquerel, G., Improved Experimental Yield of Temperature-Cycle-Induced Deracemization (TCID) with Cooling and Crystal Washing: Application of TCID for the Industrial Scale. *Crystals* **2024,** *14* (7), 588. https://doi.org/10.3390/cryst14070588

(53) Baglai, I.; Leeman, M.; Wurst, K.; Kaptein, B.; Kellogg, R. M.; Noorduin, W. L., The Strecker reaction coupled to Viedma ripening: a simple route to highly hindered enantiomerically pure amino acids. *Chem. Commun.* **2018,** *54* (77), 10832-10834. https://doi.org/10.1039/C8CC06658B

(54) Breveglieri, F.; Baglai, I.; Leeman, M.; Noorduin, W. L.; Kellogg, R. M.; Mazzotti, M., Performance analysis and model-free design of deracemization via temperature cycles. *Org. Process Res. Dev.* **2020,** *24* (8), 1515-1522. https://doi.org/10.1021/acs.oprd.0c00266

(55) Breveglieri, F.; Mazzotti, M., Role of racemization kinetics in the deracemization process via temperature cycles. *Cryst. Growth. Des.* **2019,** *19* (6), 3551-3558. https://doi.org/10.1021/acs.cgd.9b00410

(56) Oketani, R.; Hoquante, M.; Brandel, C.; Cardinael, P.; Coquerel, G., Practical role of racemization rates in deracemization kinetics and process productivities. *Cryst. Growth. Des.* **2018,** *18* (11), 6417-6420. https://doi.org/10.1021/acs.cgd.8b01263

(57) Bodák, B.; Maggioni, G. M.; Mazzotti, M., Population-based mathematical model of solid-state deracemization via temperature cycles. *Cryst. Growth. Des.* **2018,** *18* (11), 7122-7131. https://doi.org/10.1021/acs.cgd.8b01292

(58) Ricci, F.; Stillinger, F. H.; Debenedetti, P. G., A computational investigation of attrition-enhanced chiral symmetry breaking in conglomerate crystals. *J. Chem. Phys.* **2013,** *139* (17), 174503. https://doi.org/10.1063/1.4827478

(59) Coquerel, G., Solubility of chiral species as function of the enantiomeric excess. *J. Pharm. Pharmacol.* **2015,** *67* (6), 869-878. https://doi.org/10.1111/jphp.12395

(60) Weissbuch, I.; Addadi, L.; Lahav, M.; Leiserowitz, L., Molecular recognition at crystal interfaces. *Science* **1991,** *253* (5020), 637-645. https://doi.org/10.1126/science.253.5020.637

(61) Horvath, J. D.; Koritnik, A.; Kamakoti, P.; Sholl, D. S.; Gellman, A. J., Enantioselective separation on a naturally chiral surface. *J. Am. Chem. Soc.* **2004,** *126* (45), 14988-14994. https://doi.org/10.1021/ja045537h

(62) Snyder, R. C.; Doherty, M. F., Faceted crystal shape evolution during dissolution or growth. *AIChE J.* **2007,** *53* (5), 1337-1348. https://doi.org/10.1002/aic.11132

(63) Snyder, R. C.; Studener, S.; Doherty, M. F., Manipulation of crystal shape by cycles of growth and dissolution. *AIChE J.* **2007,** *53* (6), 1510-1517. https://doi.org/10.1002/aic.11174

(64) Spix, L.; Engwerda, A. H.; Meekes, H.; van Enckevort, W. J.; Vlieg, E., Persistent reverse enantiomeric excess in solution during Viedma ripening. *Cryst. Growth. Des.* **2016,** *16* (8), 4752-4758. https://doi.org/10.1021/acs.cgd.6b00804

(65) Viedma, C.; McBride, J. M.; Kahr, B.; Cintas, P., Enantiomer-specific oriented attachment: formation of macroscopic homochiral crystal aggregates from a racemic system. *Angew. Chem. Int. Ed.* **2013,** *52* (40), 10545-10548. https://doi.org/10.1002/anie.201303915

(66) Katsuno, H.; Uwaha, M., Mechanism of chirality conversion by periodic change of temperature: Role of chiral clusters. *Phys. Rev. E* **2016,** *93* (1), 013002. https://doi.org/10.1103/PhysRevE.93.013002

(67) Zhang, B.; Park, B. J.; Coquerel, G.; Kim, W.-S., Agglomeration of Homochiral sodium chlorate crystals under near-equilibrium conditions. *Powder Technol.* **2025,** *458*, 121004. https://doi.org/10.1016/j.powtec.2025.121004

(68) Shtukenberg, A. G.; García-Ruiz, J. M.; Kahr, B., Punin Ripening and the Classification of Solution-Mediated Recrystallization Mechanisms. *Cryst. Growth. Des.* **2021,** *21* (2), 1267-1277. https://doi.org/10.1021/acs.cgd.0c01545

(69) Saito, Y.; Hyuga, H., Chiral crystal growth under grinding. *J. Phys. Soc. Jpn* **2008,** *77* (11), 113001. https://doi.org/10.1143/JPSJ.77.113001

(70) Skrdla, P. J., Kinetics and thermodynamics of efficient chiral symmetry breaking in nearly racemic mixtures of conglomerate crystals. *Cryst. Growth. Des.* **2011,** *11* (5), 1957-1965. https://doi.org/10.1021/cg200116e

(71) Cameli, F.; Ter Horst, J. H.; Steendam, R. R.; Xiouras, C.; Stefanidis, G. D., On the effect of secondary nucleation on deracemization through temperature cycles. *Chem. Eur. J.* **2020,** *26* (6), 1344-1354. https://doi.org/10.1002/chem.201904239

(72) Choi, H. S.; Oh, I. H.; Zhang, B.; Coquerel, G.; Kim, W.-S.; Park, B. J., Chiral Flipping in Viedma Deracemization. *J. Phys. Chem. Lett.* **2024,** *15* (16), 4367-4374. https://doi.org/10.1021/acs.jpclett.4c00558

(73) Wu, Z.; Yang, S.; Wu, W., Application of temperature cycling for crystal quality control during crystallization. *CrystEngComm* **2016,** *18* (13), 2222-2238. https://doi.org/10.1039/C5CE02522B

(74) Viedma, C., Chiral symmetry breaking and complete chiral purity by thermodynamic-kinetic feedback near equilibrium: implications for the origin of biochirality. *Astrobiology* **2007,** *7* (2), 312-319. https://doi.org/10.1089/ast.2006.0099

(75) Suwannasang, K.; Flood, A. E.; Coquerel, G., A novel design approach to scale up the temperature cycle enhanced deracemization process: coupled mixed-suspension vessels. *Cryst. Growth. Des.* **2016,** *16* (11), 6461-6467. https://doi.org/10.1021/acs.cgd.6b01139

(76) Intaraboonrod, K.; Harriehausen, I.; Carneiro, T.; Seidel-Morgenstern, A.; Lorenz, H.; Flood, A. E., Temperature cycling induced deracemization of dl-asparagine monohydrate with immobilized amino acid racemase. *Cryst. Growth. Des.* **2020,** *21* (1), 306-313. https://doi.org/10.1021/acs.cgd.0c01140

(77) Kwan, M. H.; Breen, J.; Bowden, M.; Conway, L.; Crossley, B.; Jones, M. F.; Munday, R.; Pokar, N. P.; Screen, T.; Blacker, A. J., Continuous flow chiral amine racemization applied to continuously recirculating dynamic diastereomeric crystallizations. *J. Org. Chem.* **2021,** *86* (3), 2458-2473. https://doi.org/10.1021/acs.joc.0c02617

(78) Viedma, C.; Ortiz, J. E., A new twist in eutectic composition: deracemization of a racemic compound amino acid by Viedma ripening and temperature fluctuation. *Isr. J. Chem.* **2021,** *61* (11-12), 758-763. https://doi.org/10.1002/ijch.202100075

(79) Borsley, S.; Gallagher, J. M.; Leigh, D. A.; Roberts, B. M., Ratcheting synthesis. *Nat. Rev. Chem.* **2024,** *8* (1), 8-29. https://doi.org/10.1038/s41570-023-00558-y

(80) Borsley, S.; Leigh, D. A.; Roberts, B. M., Molecular ratchets and kinetic asymmetry: giving chemistry direction. *Angew. Chem. Int. Ed.* **2024,** *63* (23), e202400495. https://doi.org/10.1002/anie.202400495

# Chapter 7
# Deracemization through Solvent Cycling.*

*We demonstrate that a conglomerate-forming clopidogrel precursor undergoing solution phase racemization can be deracemized through cyclic solvent removal and re-addition. We establish that the combination of slow growth and fast dissolution of crystals is ideal for rapid deracemization, which we achieve by repurposing a Soxhlet apparatus to realize the slow removal and fast re-addition of solvent autonomously.*

## Introduction

Crystallization-based deracemization processes involving continuous or alternative growth and dissolution of crystals have gained much attention as practical routes for obtaining bioactive enantiopure molecules and as plausible schemes towards prebiotic chiral building blocks.[1–12] These processes require enantiomers to interconvert via a solution phase racemization reaction while both enantiomers crystallize into separate crystals (*i.e.* as racemic conglomerate). When a scalemic mixture of such *R* and *S* crystals undergoes continuous growth and dissolution, the enantiomorphs in minority in the solid phase are converted into the majority phase via solution phase racemization. Such asymmetric crystallization processes only stop once full solid-phase enantiopurity has been reached.

In the first crystallization-induced deracemizations, continuous growth and dissolution was achieved by grinding slurries of crystals.[2] Spatial heat gradients and temporal heat fluctuations have subsequently been exploited to grow and dissolve crystals for deracemization.[3,4,10,11,13,5] The deracemization process can be sped up by applying more intense grinding, metastable compounds or steeper heating/cooling cycles.[4,6,7,10,11,14,15] Although grinding is simple and fast, deracemization by temperature cycling may offer the advantage that the growth and dissolution steps are disentangled and can therefore be separately optimized. Specifically, we showed in a previous Chapter that slow growth and deep cooling result in large asymmetric crystallization with virtually exclusive growth of the majority phase.[16] In addition, we realize in this Chapter that fast heating should be favourable to keep the overall cycle time short. Hence, we hypothesize that a process combining slow crystal growth and fast dissolution would be ideal to achieve rapid deracemization. This is challenging, as the quick and homogenous heating of volumes is often difficult to achieve practically.



* This chapter has been published as S.W. van Dongen, I. Baglai, M. Leeman, R.M Kellogg, B. Kaptein, W.L. Noorduin (2023). Rapid Deracemization through Solvent Cycling: Proof-Of-Concept using a Racemizable Conglomerate Clopidogrel Precursor. *Chem. Commun.* 59: 3838–3841.

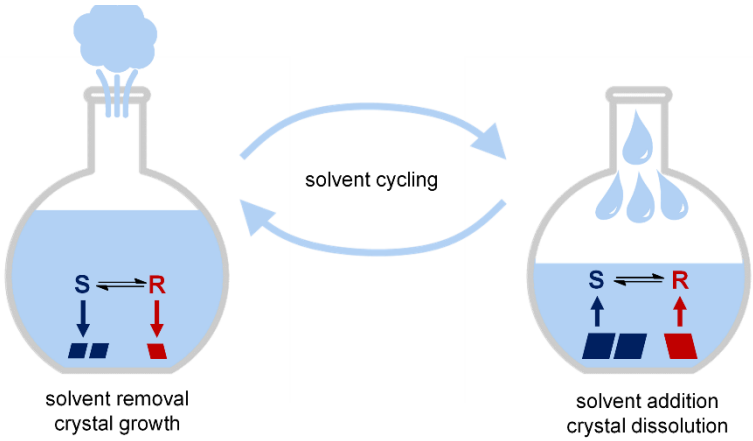


**Figure 7.1.** Solvent cycling-induced deracemization relies on alternating removal of solvent (e.g. evaporation), during which crystals grow, and re-addition (e.g. condensation) of solvent, during which crystals dissolve.

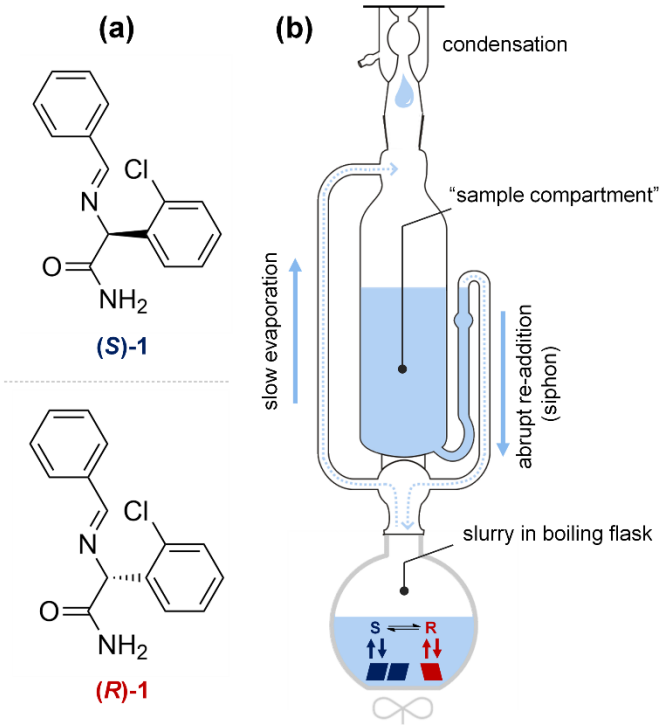


**Figure 7.2.** Model compound **1** (shown in panel a) is deracemized through autonomous solvent cycling by repurposing a Soxhlet apparatus (as depicted in panel b). A slurry of R and S crystals is stirred in a boiling flask containing racemization catalyst. On heating, solvent evaporates and condenses in the sample compartment traditionally used for extraction. When the critical volume is reached, the condensed solvent is abruptly re-added to the boiling flask through a siphoning effect. This results in the desired slow removal and fast re-addition of solvent.

Motivated by the above, we propose to grow and dissolve crystals during crystallization-induced deracemization by the removal and re-addition of solvent (Fig. 7.1). Unlike previously developed deracemization methods, independent control over the rate of solution addition/removal in the presented solvent cycling approach should in principle allow for the desirable slow growth and fast dissolution for practical rapid deracemization.

## Results and Discussion

To demonstrate the proof-of-principle of deracemization through solvent cycling, we use the clopidogrel-precursor 2-(benzylideneamino)-2-(2-chlorophenyl)acetamide (**1**, Fig. 7.2a). Compound **1** crystallizes as a conglomerate and represents a large class of amino acid Schiff base derivatives that can straightforwardly be racemized in solution using an organic base for crystallization-induced deracemization.[17] Since **1** has been studied extensively in various crystallization-induced deracemizations, this is an ideal model compound to demonstrate the proof-of-principle and benchmark the performance with previously developed methods.[6,11,16,17]

To realize solvent cycling-induced deracemization experimentally, we repurpose a Soxhlet apparatus (Fig. 7.2b). Traditionally, a Soxhlet apparatus is used for the continuous extraction of soluble components from solid material placed in the sample compartment.[18] In this Chapter, the Soxhlet apparatus is exploited for the autonomous removal and re-addition of solvent to the slurry. To cycle the solvent, the slurry is gently stirred under reflux, enabling slow solvent evaporation. The evaporated solvent is temporarily collected in the empty sample compartment of the Soxhlet until the maximum level of solvent is collected (<5 min.) and the entire volume of evaporated solvent is abruptly re-added (<10 sec.) to the refluxing slurry. The intrinsic design of a Soxhlet apparatus is thus ideally suited for autonomous solvent cycling with optimal conditions for deracemization: The slow evaporation of solvent results in slow crystal growth which is ideal for large asymmetric crystal growth, while the abrupt addition of solvent causes fast dissolution and therefore shortens deracemization cycles.

The choice of solvent is crucial to achieve successful deracemization by solvent cycling. Usually, **1** is deracemized in MeCN, but the relatively high boiling point of this solvent (82 °C) has multiple drawbacks. Specifically, at high temperatures, **1** is more prone to undesired side-reactions. Moreover, the solubility is increased to such an extent that large amounts of material are in the liquid phase–rather than the solid phase–thereby lowering yield and efficiency, since liquid phase molecules are not deracemized. Finally, the supersaturation increases rapidly at high temperatures, leading to undesired primary nucleation and fast growth with low chiral enrichment by asymmetric crystal growth.[16] These considerations highlight the importance of the choice of solvent for solvent cycling-induced deracemization.

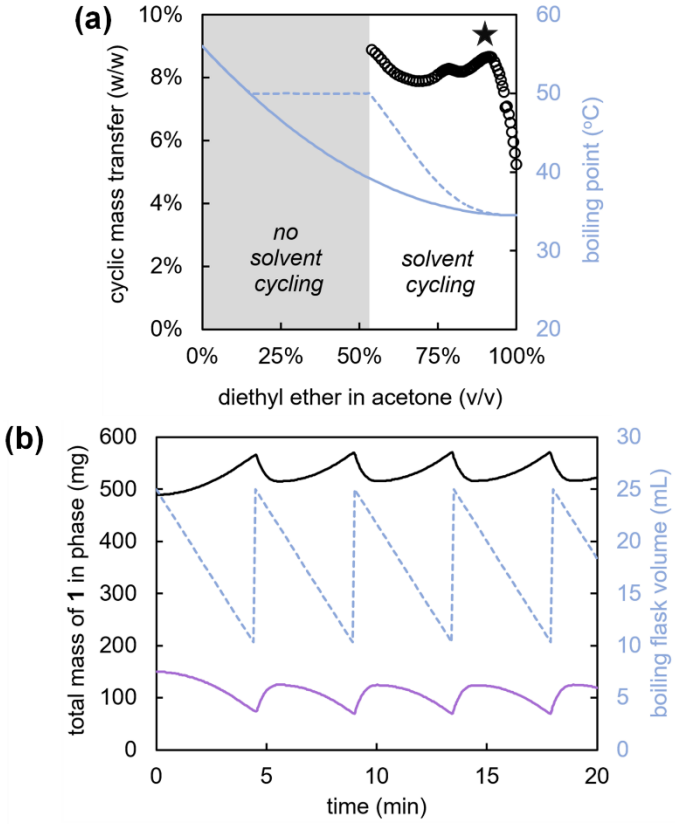


**Figure 7.3.** Computer simulation of solvent cycling using a binary solvent mixture at 50 °C. Cyclic mass transfer (black spheres) is computed for a solvent containing various compositions of diethyl ether and acetone (a). The optimal solvent composition (90 vol% diethyl ether) is indicated by a star. The initial and maximum boiling point during the cycle are indicated by solid and dotted blue lines respectively. A sample solvent cycling run with this optimal solvent was simulated and the total mass of **1** in the solid phase (black solid line) and liquid phase (purple solid line) was plotted as function of time (b). Cycle time is approximately 4.5 minutes. The cycling solvent volume of the boiling flask is indicated with a blue grey line.

In view of the above, we select a binary solvent mixture of diethyl ether and acetone for the deracemization of **1**. Although diethyl ether has the lowest boiling point of all common organic solvents (b.p. = 35 °C), the addition of acetone (b.p. = 56 °C) increases both the solubility and racemization rate. To judiciously balance the solubility and boiling point, we simulate solvent cycling processes with different ratios of solvents based on empirical data that we collect on the boiling points, vapour compositions and solubilities of various binary acetone-diethyl ether solvent mixtures (Fig. 7.3), (full simulation details provided in the Appendix). Specifically, in these simulations we modulate the ratio between the two solvents to maximize the mass transfer that occurs during each cycle: *i.e.* the amount of solid that is grown during evaporation and subsequently redissolved by re-addition of the solvent, to maximize the deracemization rate.

For a solvent cycling process operating at 50 °C, we compute the expected mass transfer per cycle as a function of solvent composition (Fig. 7.3a).[†] From the simulated runs (Fig. 7.3b), we project that for low concentrations of acetone in diethyl ether the mixture will lead to insufficient solvation of **1**, and therefore less possible total mass transfer between cycles. In contrast, for high concentrations of acetone, we find that the boiling point increases so much that an insufficient amount of solvent evaporates. A mixture of 90 vol% diethyl ether and 10 vol% acetone provides the desired balance between a low boiling point and a large mass transfer per cycle (Fig. 7.3a).

Guided by the simulations, we experimentally demonstrate solvent cycling-induced deracemization. We first suspend 800 mg of **1** with 10% *ee* in (*R*)-**1** in 10 mL of the designed binary solvent mixture (90 vol% diethyl ether and 10 vol% acetone). This suspension is sonicated for 30 minutes to obtain a homogenous slurry. The slurry is then transferred to a 50 mL round-bottom flask, containing 15 mL more solvent as well as PTFE spheres to avoid uneven boiling and caking. The flask is immersed in a water bath, gentle stirring is applied, and the flask is fitted with a Soxhlet apparatus with condenser (15 mL sample compartment volume), allowing for cyclic condensation and immediate re-addition of the evaporated solvent every 4 to 5 minutes. After heating the water bath to 50 °C and addition of the racemization catalyst (40 µL of 1,8-diazabicyclo[5.4.0]undec-7-ene (DBU)), we already observe virtually complete deracemization of the solid within 18 hours, from initially 10% to 99% *ee* in (*R*)-**1** with 90% yield.

We determine the deracemization kinetics by performing solvent cycling experiments starting with 10%, 20% and 50% initial *ee* in (*R*)-**1** (Fig. 7.4). These kinetics show that full deracemization can be achieved within 2, 3.5, and 6 hours respectively. The enantiomeric enrichment of the solid phase follows sigmoidal amplification of the *ee*, which is typical for this type of crystallization-induced enantiomeric transformations. As expected, starting with 50% *ee* in (*S*)-**1** also leads to complete deracemization in (*S*)-**1** with matching deracemization kinetics, indicating that the process has no substantial (kinetic) bias towards any of the two enantiomers (Fig. 7.4).

To validate that the fast deracemization kinetics are not caused by metastable crystal transformations or attrition, we perform several control experiments.[2,15] First, comparing powder crystal patterns of the equilibrated slurry and the final product shows identical patterns, indicating that the presence of metastable polymorphs or solvates as key intermediates in the deracemization can be excluded (diffractograms provided in the Appendix). Second, comparing the kinetics of an experiment with

[†] This operating temperature was selected to fit well between the boiling points of the low boiling component (diethyl ether, 35 °C) and high boiling component (acetone, 56 °C).

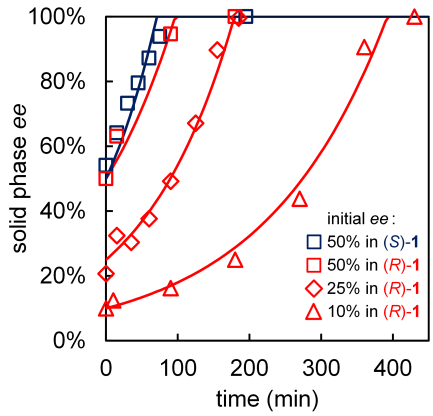


**Figure 7.4.** Deracemization kinetics of **1** by solvent cycling-induced deracemization (800 mg in 25 mL solvent (9:1 diethyl ether/acetone) containing 40 µL DBU at 50 °C) for various initial *ee*. Exponential kinetic fits are represented by solid lines.

and without Soxhlet apparatus (but with condenser and PTFE beads), shows that virtually no deracemization is observed over the relevant timelines without the Soxhlet apparatus. This suggests that neither attrition by stirring, nor the presence of the PTFE beads, but solvent cycling instead induces the observed deracemization (data shown in the Appendix).

We benchmark the performance of the here-introduced solvent cycling process against well-established deracemization by attrition-enhanced deracemization and temperature cycling. Typically, using attrition-enhanced deracemization and temperature cycling, deracemizes starting material of 20% *ee* in **1** in approximately 10 hours.[‡,6,11,17] In contrast, using solvent cycling, starting material of 20% *ee* completely deracemizes in only 3.5 hours (Fig. 7.4). Hence, even without any extensive optimization, solvent cycling-induced deracemization can readily outperform well-established deracemization processes.

## Summary and Outlook

In summary, we introduce solvent cycling as a robust and rapid deracemization method. Based on the key insight that slow and long crystal growth, and fast crystal dissolution are desirable for efficient deracemization, we implement solvent cycling autonomously and efficiently through repurposing a Soxhlet apparatus. To demonstrate the proof-of-principle, we develop a simulation-guided solvent design strategy to tailor a binary solvent mixture that maximizes mass transfer while maintaining a low boiling point during the deracemization. By combining these insights, we show that solvent cycling-induced deracemization—even in

[‡] Attrition-enhanced deracemization has been achieved within 45 minutes using a bead mill setup, but such equipment is oftentimes not readily accessible, and not all compounds can withstand the associated vigorous grinding conditions.[6]

nonoptimized form—is simple and more efficient in execution than most reported crystallization-induced deracemization techniques.

Our results emphasize the importance and potential of individually controlling the rates of crystal growth and dissolution for crystallization-induced deracemizations. We foresee new and synergistic opportunities for our solvent-tailoring strategy to accurately control and optimize key deracemization parameters (*e.g.* crystal growth and dissolution rates, amount of cyclic mass transfer, racemization rate), allowing the design of new deracemization systems that were previously ineffective or impossible. Preferentially cycling a 'good' solvent would be especially interesting to explore, exploiting an inverse anti-solvent effect.

The versatility and tunability of solvent cycling readily allow for extending these principles to other chiral compounds by tailoring the solvent, racemization catalyst or—if necessary—inserting a racemization loop.[6,8,9,12] Moreover, optimization can for instance be achieved by implementing flow control technologies or similar physical mechanisms for fine-tuning the regulation of solvent removal and re-addition rates. Besides optimization, many variants on the practical realizations of the removal and re-addition of solvent may be realized. In fact, during the preparation of this work, Flood et al. developed an alternative form of solvent cycling using evaporation by reduced pressure.[§,19] In addition, we foresee that solvent cycling processes can readily be scaled-up in conventional equipment, adapted in a continuous fashion, and implemented for the practical production of enantiopure molecules.[13,20,21]

Many types of stimuli can be exploited for crystallization-induced deracemizations; oscillating electrochemical potentials, alternating pressures or pH, photo-switchable reactions, and electromagnetic oscillations are just some of the many ways to induce continuous or alternating crystal growth and dissolution. Also, our results show the importance of cyclic physical chemical processes in synthesizing chiral molecules for practical purposes as well as in origin of life scenarios.



## References

1 M. Avalos, R. Babiano, P. Cintas, J. L. Jiménez and J. C. Palacios, *Chem. Commun.*, 2000, 887–892; E. Fogassy, M. Nógrádi, D. Kozma, G. Egri, E. Pálovics and V. Kiss, *Org. Biomol. Chem.*, 2006, **4**, 3011–3030; K. M. J. Brands and A. J. Davies, *Chem. Rev.*, 2006, **106**, 2711–2733; D. G. Blackmond and M. Klussmann, *Chem. Commun.*, 2007, 3990–3996; K. Sakai, N. Hirayama and R. Tamura, Eds., *Novel Optical Resolution Technologies*, Springer, Berlin, Heidelberg, 2007, vol. 269; I. Weissbuch and M. Lahav, *Chem. Rev.*, 2011, **111**, 3236–3267; A. R. A. Palmans, *Mol. Syst. Des. Eng.*, 2017, **2**, 34–46; I. Baglai, M. Leeman, K. Wurst, B. Kaptein, R. M. Kellogg and W. L. Noorduin, *Chem. Commun.*, 2018, **54**, 10832–10834; I. Baglai, M. Leeman, R. M. Kellogg and W. L. Noorduin, *Org. Biomol. Chem.*, 2019, **17**, 35–38; R. Oketani, M. Hoquante, C. Brandel, P. Cardinael and G. Coquerel, *Org. Process Res. Dev.*, 2019, **23**, 1197–1203; M. Guillot, J. Meester, S.

§ Both the study of Flood et al. and this work were performed independently and both studies were completed without each other's knowledge. Only during the preparation did the authors of both manuscripts become aware of the related work.[19]

Huynen, L. Collard, K. Robeyns, O. Riant and T. Leyssens, *Angew. Chem., Int. Ed.*, 2020, **59**, 11303–11306; T. Buhse, J.-M. Cruz, M. E. Noble-Terán, D. Hochberg, J. M. Ribó, J. Crusats and J.-C. Micheau, *Chem. Rev.*, 2021, **121**, 2147–2229; M. Uwaha and H. Katsuno, *J. Cryst. Growth*, 2022, 126873.

2 C. Viedma, *Phys. Rev. Lett.*, 2005, **94**, 065504; W. L. Noorduin, T. Izumi, A. Millemaggi, M. Leeman, H. Meekes, W. J. P. van Enckevort, R. M. Kellogg, B. Kaptein, E. Vlieg and D. G. Blackmond, *J. Am. Chem. Soc.*, 2008, **130**, 1158–1159; P. Shan Monica Cheung, J. Gagnon, J. Surprenant, Y. Tao, H. Xu and L. A. Cuccia, *Chem. Commun.*, 2008, 987–989; C. Viedma, J. E. Ortiz, T. de Torres, T. Izumi and D. G. Blackmond, *J. Am. Chem. Soc.*, 2008, **130**, 15274–15275.

3 C. Viedma and P. Cintas, *Chem. Commun.*, 2011, **47**, 12786–12788.

4 K. Suwannasang, A. E. Flood, C. Rougeot and G. Coquerel, *Cryst. Growth Des.*, 2013, **13**, 3498–3504.

5 W. W. Li, L. Spix, S. C. A. de Reus, H. Meekes, H. J. M. Kramer, E. Vlieg and J. H. ter Horst, *Cryst. Growth Des.*, 2016, **16**, 5563–5570; F. Breveglieri, G. M. Maggioni and M. Mazzotti, *Cryst. Growth Des.*, 2018, **18**, 1873–1881; G. M. Maggioni, M. P. Fernández-Ronco, M. W. van der Meijden, R. M. Kellogg and M. Mazzotti, *CrystEngComm*, 2018, **20**, 3828–3838; F. Cameli, C. Xiouras and G. D. Stefanidis, *CrystEngComm*, 2018, **20**, 2897–2901; K. Intaraboonrod, I. Harriehausen, T. Carneiro, A. Seidel-Morgenstern, H. Lorenz and A. E. Flood, *Cryst. Growth Des.*, 2021, **21**, 306–313.

6 W. L. Noorduin, P. van der Asdonk, A. A. C. Bode, H. Meekes, W. J. P. van Enckevort, E. Vlieg, B. Kaptein, M. W. van der Meijden, R. M. Kellogg and G. Deroover, *Org. Process Res. Dev.*, 2010, **14**, 908–911.

7 M. Leeman, W. L. Noorduin, A. Millemaggi, E. Vlieg, H. Meekes, W. J. P. van Enckevort, B. Kaptein and R. M. Kellogg, *CrystEngComm*, 2010, **12**, 2051–2053.

8 F. Yagishita, H. Ishikawa, T. Onuki, S. Hachiya, T. Mino and M. Sakamoto, *Angew. Chem., Int. Ed.*, 2012, **51**, 13023–13025.

9 N. Uemura, S. Toyoda, H. Ishikawa, Y. Yoshida, T. Mino, Y. Kasashima and M. Sakamoto, *J. Org. Chem.*, 2018, **83**, 9300–9304.

10 K. Intaraboonrod, T. Lerdwiriyanupap, M. Hoquante, G. Coquerel and A. E. Flood, *Mendeleev Commun.*, 2020, **30**, 395–405.

11 F. Breveglieri, I. Baglai, M. Leeman, W. L. Noorduin, R. M. Kellogg and M. Mazzotti, *Org. Process Res. Dev.*, 2020, **24**, 1515–1522.

12 G. Valenti, P. Tinnemans, I. Baglai, W. L. Noorduin, B. Kaptein, M. Leeman, J. H. ter Horst and R. M. Kellogg, *Angew. Chem., Int. Ed.*, 2021, **60**, 5279–5282.

13 B. Bodák and M. Mazzotti, *Cryst. Growth Des.*, 2022, **22**, 1846–1856.

14 W. L. Noorduin, B. Kaptein, H. Meekes, W. J. P. van Enckevort, R. M. Kellogg and E. Vlieg, *Angew. Chem., Int. Ed.*, 2009, **48**, 4581–4583.

15 A. H. J. Engwerda, H. Meekes, B. Kaptein, F. P. J. T. Rutjes and E. Vlieg, *Chem. Commun.*, 2016, **52**, 12048–12051.

16 S. W. van Dongen, I. Ahlal, M. Leeman, B. Kaptein, R. M. Kellogg, I. Baglai and W. L. Noorduin, *J. Am. Chem. Soc.*, 2023, **145**, 436–442.

17 M. W. van der Meijden, M. Leeman, E. Gelens, W. L. Noorduin, H. Meekes, W. J. P. van Enckevort, B. Kaptein, E. Vlieg and R. M. Kellogg, *Org. Process Res. Dev.*, 2009, **13**, 1195–1198; J. I. Murray, J. N. Sanders, P. F. Richardson, K. N. Houk and D. G. Blackmond, *J. Am. Chem. Soc.*, 2020, **142**, 3873–3879.

18 F. Soxhlet, *Dinglers Polytech. J.*, 1879, **232**, 461–465.

19 K. Intaraboonrod and A. Flood, presented in part at BIWIC 2022, Espoo, September, 2022.

20 R. R. E. Steendam and J. H. ter Horst, *Cryst. Growth Des.*, 2017, **17**, 4428–4436.

21 A. J. Kukor, N. Depner, I. Cai, J. L. Tucker, J. C. Culhane and J. E. Hein, *Chem. Sci.*, 2022, **13**, 10765–10772.

Chapter 8

# Enantiopurity through Nonequilibrium Crystallization.*

*Crystallization is a powerful method to isolate enantiopure molecules from racemates if enantiomers self-sort into separate enantiopure crystals. Unfortunately, this behaviour is unpredictable and rare (5–10%), as both enantiomers predominantly crystallize together to form racemic crystals, hindering any such chiral sorting. These unfavourable statistics might be overcome using nonequilibrium conditions. Therefore, we systematically characterize energy differences (ΔGΦ) between racemic and enantiopure crystal phases for libraries of target molecules (phenylglycine, praziquantel) with different chemical modifications. Surprisingly, these libraries reveal wide but similar continuous distributions of ΔGΦ, wherein similar chemical modifications group together. This grouping allows a directed evolution strategy to discover racemic crystals with low ΔGΦ for isolating desired enantiomers by crystallization under nonequilibrium conditions. Comparison with ca. hundred previously reported compounds suggests that as many as half of all chiral molecules may kinetically form enantiopure crystals (~50%). These insights open new previously unconsidered possibilities for isolating enantiopure molecules.*

## Introduction

Crystallization is a simple, direct, and therefore common method to separate chiral molecules and isolate their pure enantiomers.[1–7] However, chiral purification by crystallization has one fundamental requirement: enantiomers must spontaneously sort into separate enantiopure crystals (*i.e.* racemic conglomerates) (Fig. 8.1a).[8] Unfortunately, such self-sorting behaviour is rare and unpredictable:[9,10] the overwhelming majority of enantiomeric mixtures crystallize together into thermodynamically favoured racemic compounds (90-95%), which complicates the use of direct crystallization for chiral separations.[11,12] Overcoming the fundamental underlying thermodynamic limitations would not only open novel systematic and general approaches for discovering and utilizing conglomerates, but also potentially allows development of new strategies to resolve directly or even deracemize racemic compounds.



* This chapter has been published as C. Pinetre*, S.W. van Dongen*, C. Brandel, A.S. Léonard, G. Valenti, M. Charpentier, V. Dupray, K. Oosterling, B. Kaptein, M. Leeman, R.M. Kellogg, J.H. ter Horst, W.L. Noorduin (2025). Enantiopurity by Directed Evolution of Crystal Stabilities and Nonequilibrium Crystallization. *J. Am. Chem. Soc.* 147(10): 8864–8870. Following the later discovery of errors in the supplementary information and the literature dataset used for analysis, this Chapter contains some changes with respect to the associated publication; an author correction is under preparation.

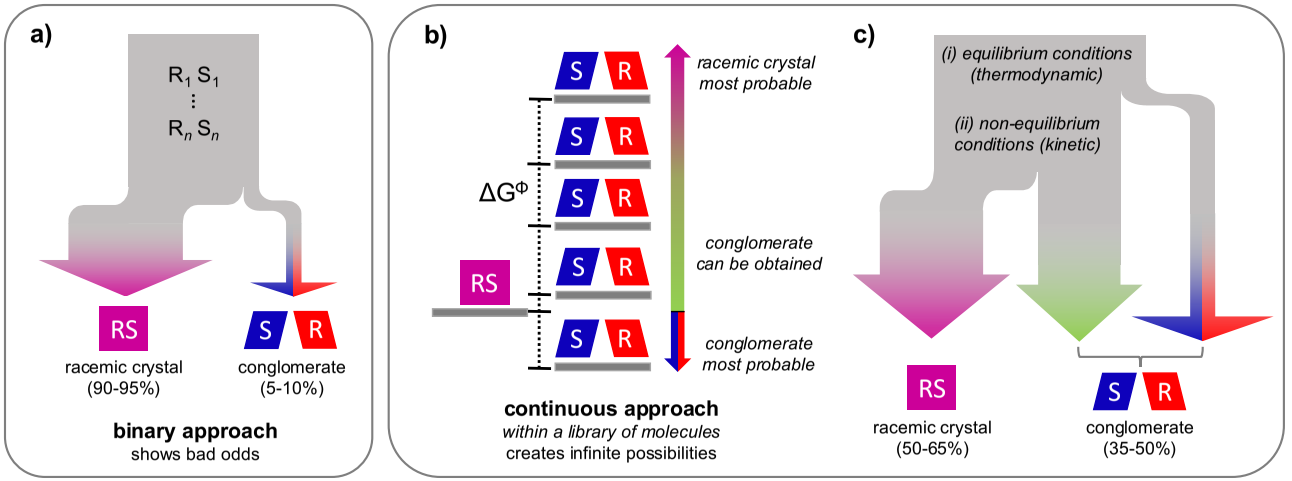


**Figure 8.1.** Stability of racemic compounds and conglomerates under thermodynamic and kinetic conditions. a) Current binary approach: thermodynamics dictates whether chiral molecules form either racemic (90-95%) or conglomerate (5-10%) crystals. b) Derivatives of a common chiral centre yield a library that screens a continuous energy difference ($\Delta G^{\Phi}$) between racemic and enantiopure crystal forms. c) For small positive $\Delta G^{\Phi}$, non-equilibrium conditions can (kinetically) stabilize enantiopure crystals of a thermodynamically stable racemic compound, such that an estimated 35-50% of chiral molecules may be accessible as either kinetic or thermodynamic conglomerates.

In this Chapter, we suggest that these thermodynamic limitations may be overcome by exploiting non-equilibrium conditions to kinetically favour the formation of conglomerates. Under such conditions, nucleation and crystal growth rates, rather than thermodynamic stabilities, may determine which crystalline phase dominates, akin to phenomena in polymorphism.[13,14] This opens the potential to exploit non-equilibrium conditions for favouring kinetic conglomerates at the cost of thermodynamically stable racemic compounds. Supporting this idea, there have already been reports of racemic compounds converting into enantiopure crystals under far-from equilibrium conditions by grinding of crystals or by applying steep temperature gradients during cooling crystallizations.[15–20] Although promising, it remains unclear if such cases are incidental reports on systems with specific traits, or if there are general guidelines that can be exploited to extend these principles for the systematic isolation of enantiomers by crystallization.

The conversion from racemic crystal phases into their enantiopure crystal counterparts may be feasible when the energy difference $\Delta G^{\Phi}$ between both phases is small (Fig. 8.1b).[21] Indeed, for polymorphic transformations it is commonly accepted that when $\Delta G^{\Phi} < 0.5$ kcal mol$^{-1}$ (2.1 kJ mol$^{-1}$) thermodynamically stable phases may be converted into kinetically stable crystal phases.[22–24] Previously, $\Delta G^{\Phi}$ has been analysed for many chiral compounds, and has been used as indicator for identifying thermodynamically stable racemic conglomerates.[25–27] However, these earlier analyses concern incidental reports and are based on molecules that bear no structural resemblance. What has been missing so far is a systematic analysis of $\Delta G^{\Phi}$ between racemic crystal phases and their enantiopure counterparts for structurally related compounds. Such analysis might not only enable the systematic discovery of crystal structures that can be kinetically stabilized, but may also guide rational experimental design to systematically exploit non-equilibrium conditions for destabilizing racemic compounds into their (kinetic) conglomerate counterparts (Fig. 8.1c).



Motivated by these insights, we here systematically analyse $\Delta G^{\Phi}$ between racemates and their enantiopure counterparts for two libraries of biorelevant target molecules with different chemical modifications. These libraries are found to exhibit a broad and continuous distribution for $\Delta G^{\Phi}$, in which similar chemical modifications group together. Akin to directed evolution in catalysis,[28] we foresee that the relationship between $\Delta G^{\Phi}$ and the chemical structure can be exploited by systematically selecting chemical modifications with the lowest $\Delta G^{\Phi}$ to guide the synthesis of a next generation (Fig. 8.2).[29–31] Such an evolutionary method may efficiently identify metastable enantiopure crystal phases for isolating desired enantiomers under non-equilibrium conditions. Analysis of ca. hundred chiral molecules in the literature supports that our findings are general and ca. 50% of all chiral molecules are prone to be isolated in enantiopure form under non-equilibrium conditions (Fig. 8.1c).

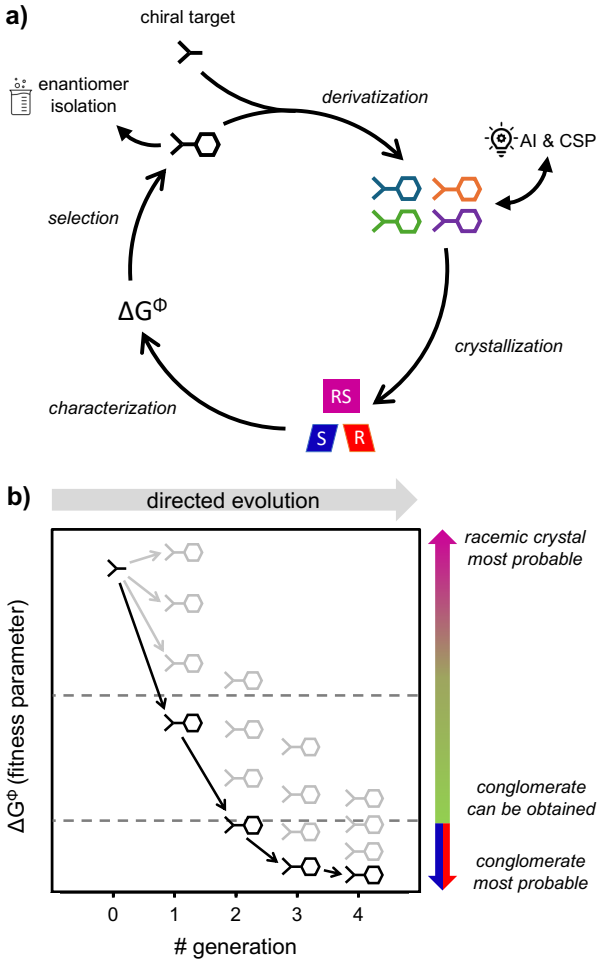


**Figure 8.2.** Concept of directed evolution for (kinetic) conglomerate discovery and rational library design. a) Development of (kinetic) conglomerates of chiral targets by iterate cycles of chemical derivatization, crystallization, characterization and selection. $\Delta G^{\Phi}$ serves as a fitness parameter for selecting the input for the next generation. Artificial Intelligence (AI) or Crystal Structure Prediction (CSP) could synergistically inform the choice of derivatives, leveraging the results from previous generations. b) Subsequent generations of target derivatives systematically evolve towards lower $\Delta G^{\Phi}$. Due to diminishing returns with each additional iteration, the fitness parameter typically plateaus following a power law or exponential decay.[31,32] Such directed evolution quickly discovers (meta)stable enantiopure crystal phases for isolating target enantiomers.

## Results & Discussion

We investigate $\Delta G^{\Phi}$ between enantiopure and racemic crystal forms for a library of chemically analogous chiral molecules. As chiral core we select the Schiff base of phenylglycine amide **1**, an amino acid derivative that serves as building block in several pharmaceutical compounds, and which has previously been deracemized as conglomerate **1a**.[33,34] These Schiff base derivatives can be formed straightforwardly

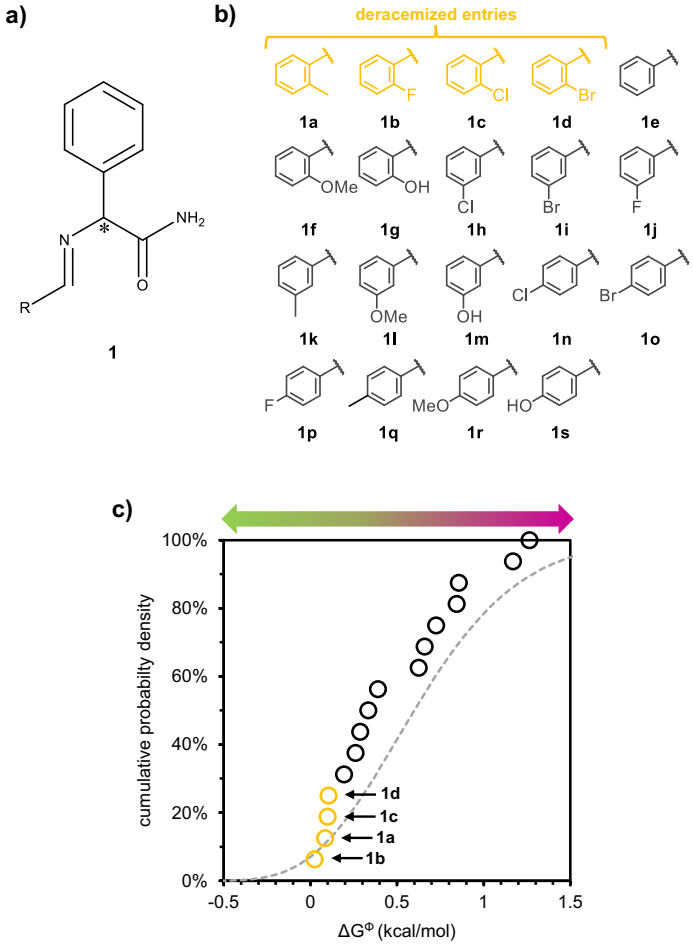


**Figure 8.3.** Analysis of free energy differences ($\Delta G^{\Phi}$) between racemic (*RS*) and enantiopure (*R*) crystals of a library with common chiral centre (full data in Appendix). a) Schiff-base derivatives of phenylglycinamide (**1**), chiral centre indicated with *. b) Synthesized library entries for **1**. c) The cumulative probability distribution of free energy differences shows a wide variation in $\Delta G^{\Phi}$ (dotted grey line is fitted gamma distribution based on the literature dataset in Fig. 8.5b). Low $\Delta G^{\Phi}$ entries **1a-d** (yellow) have been successfully deracemized.

from aldehydes to yield a library (Fig. 8.3a).[35] Following this procedure, a library of 19 derivatives, enantiopure as well as racemic crystal form, with the same chiral core was obtained (Fig. 8.3b).

We determine $\Delta G^{\Phi}$ for each pair of enantiopure and racemic crystal forms in the library. Differential scanning calorimetry (DSC) provides the melting points and heats of fusion for both crystal forms, from which we compute $\Delta G^{\Phi}$ (see Appendix for details). Figure 8.3c shows the cumulative probability density of $\Delta G^{\Phi}$. Although small, library **1** already displays a broad distribution of $\Delta G^{\Phi}$, ranging from close to 0 to 1.5

kcal/mol. The stable conglomerate **1a** and derivatives **1b,c**—both having been identified as racemic compound but deracemized previously[17]—group together with similar values of $\Delta G^{\Phi} \approx 0.1$ kcal/mol. This grouping is consistent with our expectation that thermodynamically stable racemic compound entries with low $\Delta G^{\Phi}$ may be suitable for conversion into kinetic conglomerates.

To explore the predictive potential of $\Delta G^{\Phi}$ further, we attempt the deracemization of **1d**, since **1d** is the next entry in ascending order of $\Delta G^{\Phi}$ (Fig. 8.3c). A slurry of racemic **1d** was prepared, racemization was initiated using a base, and the mixture was subsequently seeded with enantiopure (*R*)-**1d** (see Appendix for details). After 3 hours of attrition, complete conversion of (*RS*)-**1d** into enantiopure (*R*)-**1d** was observed. This successful deracemization confirms that this compound had formed a (metastable) conglomerate and that $\Delta G^{\Phi}$ can be used to predict conversion into enantiopure crystals.

Entries **1a-d** not only show similar $\Delta G^{\Phi}$, but also have similar crystal structures,[36] with all crystal structures sharing a common hydrogen bonding motif. From a molecular structure, the possible crystal structures can be predicted, for which, in turn, one can predict a corresponding $\Delta G^{\Phi}$. However, our data suggest that $\Delta G^{\Phi}$ could even be directly predicted from the molecular structure (without intervening considerations on the crystal structures). Revealing such a relationship would enable rational and methodical library design of molecules with low $\Delta G^{\Phi}$.

Akin to directed evolution in catalysis,[28] we envisage that iterative selection of low $\Delta G^{\Phi}$ molecules can systematically direct design of modifications around a chiral centre towards low $\Delta G^{\Phi}$. Because of its continuous character, as opposed to the binary classification of conglomerates and racemic compounds, we foresee that $\Delta G^{\Phi}$ can be a convenient fitness parameter in directed evolution.



To assess the potential of such an evolutionary approach to molecular design, a library based on the chiral core Praziquantel **2** was synthesized (Fig. 8.4a). Praziquantel **(2h)** is a racemic drug against parasitic worms, and there is wide interest for isolating the bioactive (*R*)-**2h** enantiomer.[37–39] To investigate trends in chemical structures and $\Delta G^{\Phi}$ systematically, we prepared 25 derivatives that group into four distinct modification classes (Fig. 8.4b): alkyls (**2a-e**); carbocycles (**2f-h**); aromatic alkyls (**2i-o**), aromatic halides and other substituted aromatics (**2p-v**), as well as three unclassified derivatives (**2w-y**).

We determined and plotted the cumulative probability density distribution $\Delta G^{\Phi}$ (Fig. 8.4c). With few exceptions, library entries cluster along $\Delta G^{\Phi}$ according to the predetermined modification classes, enabling an evolutionary strategy for library design (Fig. 8.2). Specifically, starting with only four entries (one per modification class) as the first generation, the alkyl derivative can be immediately identified as most promising, since that entry shows the lowest $\Delta G^{\Phi}$. Subsequently preparing a

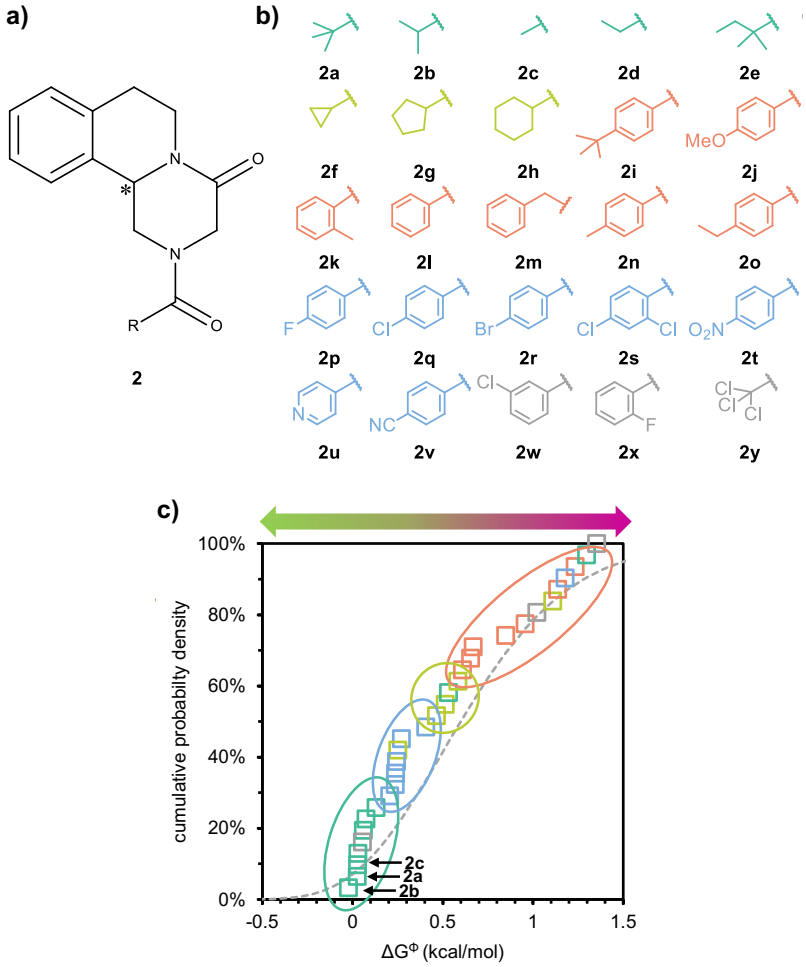


**Figure 8.4.** Potential of library design by directed evolution. a) Praziquantel derivatives **2**, chiral centre indicated with *. b) Synthesized library entries for **2**, classified as alkyls (dark green), carbocycle (light green), aromatic alkyls (orange), halogen and other substituted aromatics (light blue), non-classified (grey). c) Cumulative probability distribution of free energy differences (full data in Appendix; dotted grey line is fitted gamma distribution based on the literature dataset in Fig. 8.5b). Derivatives cluster by chemical classification (coloured ellipses), enabling rational library design by directed evolution.

second generation of four additional alkyl derivatives already yields the stable conglomerate **2a**. Hence, rather than preparing 25 quasi-arbitrary derivatives, we can find conglomerates and low $\Delta G^{\Phi}$ entries within just two generations and with less than a third of the total number of library entries (8 instead of 25), showing the potential of library design through directed evolution.

The clustering of chemical classes not only enables library design through directed evolution but may also group racemic compounds within the $\Delta G^{\Phi}$-distribution that are suitable for isolating enantiopure crystals through kinetically stabilized conglomerates.

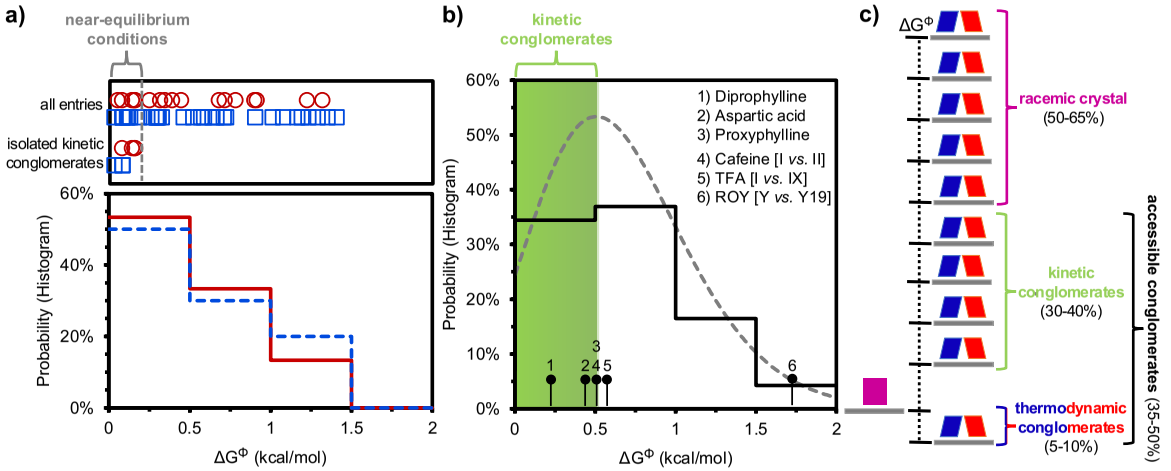


**Figure 8.5.** Generality of trends, and potential of non-equilibrium conditions for isolating enantiopure crystals. a) Despite their chemical differences, library entries of **1** (red solid histogram) and **2** (blue dashed histogram) show similar probability distributions. Entries isolated as kinetic conglomerates under near-equilibrium conditions fall within $\Delta G^{\Phi} < 0.2$ kcal/mol region. b) Probability histogram of $\Delta G^{\Phi}$ for the racemic compounds among ~100 unrelated chiral molecules from literature (black solid histogram). Histograms from libraries **1**, **2**, and literature data are similar and well-described by the same gamma-distribution (grey dotted line), supporting the generality of these trends. Region of $\Delta G^{\Phi} < 0.5$ kcal/mol (shaded green) contains kinetic conglomerates (1–3) and unstable polymorphs (4,5), which indicates that ca. 30-40% of the racemic compounds may be kinetically stabilized as enantiopure crystals under near- or far-from-equilibrium conditions. c) Predicted distribution between thermodynamic conglomerates, kinetic conglomerates, and racemic crystals.

To investigate this idea, we explore whether racemic compounds **2b** and **2c**, whichare situated in the same low $\Delta G^{\Phi}$-region as the known stable conglomerate **2a**, can be isolated as enantiopure crystals. To this aim, we prepare supersaturated racemic solutions of **2b** and **2c**, seed with (*R*)-**2b** and (*R*)-**2c** respectively, and obtain the desired enantiomers in good yield and enantiopurity (> 95% ee, see Appendix for details).

The chemical core of both libraries is very different: **1** is small and flexible and can undergo H-bonding, whereas **2** is large and stiff without possibilities for H-bonding.[40] To understand how these differences impact the distribution of $\Delta G^{\Phi}$, we plot the probability histograms of $\Delta G^{\Phi}$ for **1** and **2** (Fig. 8.5a). Comparison of both histograms shows that, despite the difference in molecular structure, their distribution in $\Delta G^{\Phi}$ is strikingly similar. Also, for both libraries we find that near-equilibrium conditions already allow for the straightforward isolation of enantiopure crystals from racemic compounds (when $\Delta G^{\Phi}$ < 0.2 kcal/mol, Fig. 8.5a). These commonalities prompt two questions. First, how general are these trends? Second, how much further can we push the threshold of $\Delta G^{\Phi}$ for which racemic compounds convert into kinetic conglomerates by exploiting far-from-equilibrium conditions?

To address the question of generality, we collect thermodynamic data for near a hundred chiral organic racemic compounds that have been previously investigated (see Appendix).[11,41] This literature catalogue of molecules is very diverse, ranging from salts to molecules with multiple chiral centres and covering a wide breadth of functional groups featuring several heteroatoms (S, N, O). Moreover, in contrast to our two libraries, the entries in the literature set are—to a large extent—structurally not related, thus forming a representative reference set for assessing generality. We find that the literature data are well-described by a gamma distribution (Fig. 8.5b). A statistical comparison (Kolmogorov-Smirnov test) shows that both libraries **1** and **2** follow the same gamma-distribution (see Appendix), as visualized in Fig. 8.3c and 4c. These similarities suggest that the trends for the two libraries can be generalized to a large diverse set of unrelated chiral organic molecules.

Based on this analysis, we also assess the general potential of non-equilibrium conditions to kinetically stabilize enantiopure crystals. We identify three chiral molecules (diprophylline, aspartic acid, proxyphylline) for which the racemic compound has previously been kinetically converted to enantiopure crystals,[15,18,19] calculate their $\Delta G^{\Phi}$ (0.24, 0.45, and 0.48 kcal/mol respectively), and mark them for comparison with the energy difference distribution in Fig. 8.5b. We realize that all three conversions require crystallization conditions that favour kinetic phases, suggesting that far-from-equilibrium conditions are essential.

$\Delta G^{\Phi}$ of these compounds is close to the thermal energy $k_B T$ (0.6 kcal/mol), suggesting that transitions between crystal phases with such energy differences ($\Delta G^{\Phi} \leq$ 0.5

kcal/mol) are kinetically probable. This idea is consistent with observations beyond chiral crystallization, where polymorphic transitions are often reported when energy differences are below 0.5 kcal/mol.[22,24] Notable examples include caffeine ($\Delta G^{\Phi}$ = 0.5 kcal/mol)[42] and tolfenamic acid (TFA, $\Delta G^{\Phi}$ = 0.55 kcal/mol)[43] (Fig. 8.5b). For some reported transformations the energy differences are even much larger, as exemplified by the archetypical polymorphic system known as ROY, with a $\Delta G^{\Phi}$ as large as 1.7 kcal/mol).[23,44] Hence, we estimate that 30-40% of thermodynamically stable racemic compounds ($\Delta G^{\Phi} \leq$ 0.5 kcal/mol) can likely be kinetically obtained as enantiopure crystals under near- or far-from-equilibrium conditions (Fig. 8.5b). Additionally, 5-10% of chiral compounds already crystallize as stable conglomerates. Consequently, we predict that 35-50% of all chiral compounds can be isolated as desired enantiomers through crystallization under either equilibrium or non-equilibrium conditions (Fig. 8.5c).

## Summary and Outlook

In summary, by systematically investigating the energy differences between the racemic and enantiopure crystal forms of structurally related molecules, we outline how combining directed evolution and combinatorial chemistry enables the expedient discovery of metastable enantiopure crystal phases that can be kinetically stabilized for isolating enantiomers of the desired handedness. Until now, hindered by thermodynamic limitations, it was generally understood that merely 5-10% of chiral molecules were accessible as enantiopure crystals. In contrast, we here estimate that ca. 50% of all chiral molecules are accessible as enantiopure crystals through non-equilibrium crystallization.

These insights can be implemented directly for the rational discovery of chiral compounds that can be separated by crystallization. Even though the change of only a single atom can drastically change the stability of crystal phases, we observe clustering of similar derivatives within a library which enables methodological library design. Specifically, we envision the autonomous construction of chemical libraries in self-driven labs,[45,46] following an iterative manner, in which a rapid assessment of $\Delta G^{\Phi}$ serves as diagnostic guide for the design of new library entries and the efficient discovery of targets for resolution or deracemization. Analogous to directed evolution in catalysis,[29–31] we propose to synthesize a small library with very diverse entries that are ranked according to $\Delta G^{\Phi}$ as fitness parameter, after which the most favourable entry is selected for synthesis of the next generation of entries. This evolutionary strategy prevents that only unfavourable zones with high $\Delta G^{\Phi}$ are screened, and instead iterate towards favourable low $\Delta G^{\Phi}$ within only a few cycles. We foresee that making informed design choices may be further aided by integrating Crystal Structure Prediction (CSP) methodologies.[47,48]

For entries with low $\Delta G^{\Phi}$, we have shown in this Chapter that enantiopure crystals can successfully be isolated from racemic mixtures by applying near-equilibrium conditions. The key next step is to systematically exploit far-from-equilibrium conditions, under which crystallization rates—instead of thermodynamic stabilities alone—determine which crystalline phase is favoured such that for instance, the desired kinetic conglomerate grows faster than the undesired racemic compound. Alternatively, specific non-equilibrium conditions can be exploited to supress the nucleation and growth rate of stable racemic compound crystals, such that the desired enantiopure crystals can be isolated. Importantly, the crystallization process offers a large parameter space that can be exploited to achieve these favourable rates of nucleation and growth, ranging from choice of solvent, confinements such as microdroplets, and (chiral) additives to temperature gradients and mechanochemistry. Indeed, mechanical grinding and temperature gradients have also been used to achieve deracemization of solid phases,[1–3,49] suggesting possibilities to yield non-equilibrium conditions that destabilize racemic compounds and simultaneously convert racemic (or partially enriched) solid phases into the desired enantiomer. Ultimately, especially with the rise of machine learning techniques and self-driven laboratories to design and execute the synthesis of chiral molecules,[50] evaluating the potential for resolving or deracemizing key intermediates should become an integrated aspect of synthesizing enantiopure molecules.

## References


(1) Viedma, C. Chiral Symmetry Breaking During Crystallization: Complete Chiral Purity Induced by Nonlinear Autocatalysis and Recycling. *Phys. Rev. Lett.* **2005**, *94* (6), 065504. https://doi.org/10.1103/PhysRevLett.94.065504.

(2) Viedma, C. Chiral Symmetry Breaking and Complete Chiral Purity by Thermodynamic-Kinetic Feedback Near Equilibrium: Implications for the Origin of Biochirality. *Astrobiology* **2007**, *7* (2), 312–319. https://doi.org/10.1089/ast.2006.0099.

(3) Suwannasang, K.; Flood, A. E.; Coquerel, G. A Novel Design Approach To Scale Up the Temperature Cycle Enhanced Deracemization Process: Coupled Mixed-Suspension Vessels. *Crystal Growth & Design* **2016**, *16* (11), 6461–6467. https://doi.org/10.1021/acs.cgd.6b01139.

(4) Oketani, R.; Marin, F.; Tinnemans, P.; Hoquante, M.; Laurent, A.; Brandel, C.; Cardinael, P.; Meekes, H.; Vlieg, E.; Geerts, Y.; Coquerel, G. Deracemization in a Complex Quaternary System with a Second-Order Asymmetric Transformation by Using Phase Diagram Studies. *Chem. Eur. J.* **2019**, *25* (61), 13890–13898. https://doi.org/10.1002/chem.201903338.

(5) Hein, J. E.; Huynh Cao, B.; Viedma, C.; Kellogg, R. M.; Blackmond, D. G. Pasteur's Tweezers Revisited: On the Mechanism of Attrition-Enhanced Deracemization and Resolution of Chiral Conglomerate Solids. *J. Am. Chem. Soc.* **2012**, *134* (30), 12629–12636. https://doi.org/10.1021/ja303566g.

(6) Sui, J.; Wang, N.; Wang, J.; Huang, X.; Wang, T.; Zhou, L.; Hao, H. Strategies for Chiral Separation: From Racemate to Enantiomer. *Chem. Sci.* **2023**, *14* (43), 11955–12003. https://doi.org/10.1039/D3SC01630G.

(7) Pasteur, L. Memoires Sur La Relation Qui Peut Exister Entre La Forme Crystalline et al Composition Chimique, et Sur La Cause Dela Polarization Rotatoire. *C R Acad Sci* **1848**, *26*, 535–538.

(8) Collet, A.; Brienne, M. J.; Jacques, J. Optical Resolution by Direct Crystallization of Enantiomer Mixtures. *Chem. Rev.* **1980**, *80* (3), 215–230. https://doi.org/10.1021/cr60325a001.

(9) Carpenter, J. E.; Grünwald, M. Pre-Nucleation Clusters Predict Crystal Structures in Models of Chiral Molecules. *J. Am. Chem. Soc.* **2021**, *143* (51), 21580–21593. https://doi.org/10.1021/jacs.1c09321.

(10) Goodall, R. E. A.; Lee, A. A. Predicting Materials Properties without Crystal Structure: Deep Representation Learning from Stoichiometry. *Nat Commun* **2020**, *11* (1), 6280. https://doi.org/10.1038/s41467-020-19964-7.

(11) Jacques, J.; Collet, A.; Wilen, S. H. *Enantiomers, Racemates, and Resolutions*; Krieger Publishing Company: Malabar, 1994.

(12) Pinètre, C.; Gendron, F.; Kuroda, R.; Oketani, R.; Aupetit, C.; Buffeteau, T.; Coquerel, G. Use of Conglomerate Mixed Crystals to Deracemize a Stable Racemic-Compound-Forming System. *Chemistry A European J* **2023**, e202300441. https://doi.org/10.1002/chem.202300441.

(13) Sacchi, P.; Wright, S. E.; Neoptolemou, P.; Lampronti, G. I.; Rajagopalan, A. K.; Kras, W.; Evans, C. L.; Hodgkinson, P.; Cruz-Cabeza, A. J. Crystal Size, Shape, and Conformational Changes Drive Both the Disappearance and Reappearance of Ritonavir Polymorphs in the Mill. *Proceedings of the National Academy of Sciences* **2024**, *121* (15), e2319127121. https://doi.org/10.1073/pnas.2319127121.

(14) Kocevska, S.; Burcham, C. L.; Nordstrom, F.; Maggioni, G. M. A Changing Paradigm in Industrial Pharmaceutical Crystallization. *Nat Chem Eng* **2024**, *1* (5), 327–329. https://doi.org/10.1038/s44286-024-00068-8.

(15) Viedma, C.; Ortiz, J. E. A New Twist in Eutectic Composition: Deracemization of a Racemic Compound Amino Acid by Viedma Ripening and Temperature Fluctuation. *Israel Journal of Chemistry* **2021**, *61* (11–12), 758–763. https://doi.org/10.1002/ijch.202100075.

(16) Hoquante, M.; Sanselme, M.; Rietveld, I. B.; Coquerel, G. Disappearing Conglomerates, Assessment of the Threat. *Crystal Growth & Design* **2019**, *19* (12), 7396–7401. https://doi.org/10.1021/acs.cgd.9b01316.

(17) Engwerda, A. H. J.; Meekes, H.; Kaptein, B.; Rutjes, F. P. J. T.; Vlieg, E. Speeding up Viedma Ripening. *Chem. Commun.* **2016**, *52* (81), 12048–12051. https://doi.org/10.1039/C6CC06766B.

(18) Brandel, C.; Amharar, Y.; Rollinger, J. M.; Griesser, U. J.; Cartigny, Y.; Petit, S.; Coquerel, G. Impact of Molecular Flexibility on Double Polymorphism, Solid Solutions and Chiral Discrimination during Crystallization of Diprophylline Enantiomers. *Mol. Pharmaceutics* **2013**, *10* (10), 3850–3861. https://doi.org/10.1021/mp400308u.

(19) Harfouche, L. C.; Brandel, C.; Cartigny, Y.; ter Horst, J. H.; Coquerel, G.; Petit, S. Enabling Direct Preferential Crystallization in a Stable Racemic Compound System. *Mol. Pharmaceutics* **2019**, *16* (11), 4670–4676. https://doi.org/10.1021/acs.molpharmaceut.9b00805.

(20) Spix, L.; Meekes, H.; Blaauw, R. H.; van Enckevort, W. J. P.; Vlieg, E. Complete Deracemization of Proteinogenic Glutamic Acid Using Viedma Ripening on a Metastable Conglomerate. *Crystal Growth & Design* **2012**, *12* (11), 5796–5799. https://doi.org/10.1021/cg301343a.

(21) Otero-de-la-Roza, A.; Hein, J. E.; Johnson, E. R. Reevaluating the Stability and Prevalence of Conglomerates: Implications for Preferential Crystallization. *Crystal Growth & Design* **2016**, *16* (10), 6055–6059. https://doi.org/10.1021/acs.cgd.6b01088.

(22) Borchardt-Setter, K. A.; Yu, L. Assessing the Potential for Chiral Separation by Crystallization Using Crystal Energies. *Crystal Growth & Design* **2023**, *23* (5), 3615–3622. https://doi.org/10.1021/acs.cgd.3c00077.

(23) Beran, G. J. O.; Sugden, I. J.; Greenwell, C.; Bowskill, D. H.; Pantelides, C. C.; Adjiman, C. S. How Many More Polymorphs of ROY Remain Undiscovered. *Chem. Sci.* **2022**, *13* (5), 1288–1297. https://doi.org/10.1039/D1SC06074K.

(24) Nyman, J.; Day, G. M. Static and Lattice Vibrational Energy Differences between Polymorphs. *CrystEngComm* **2015**, *17* (28), 5154–5165. https://doi.org/10.1039/C5CE00045A.

(25) Li, Z. J.; Zell, M. T.; Munson, E. J.; Grant, D. J. W. Characterization of Racemic Species of Chiral Drugs Using Thermal Analysis, Thermodynamic Calculation, and Structural Studies. *Journal of Pharmaceutical Sciences* **1999**, *88* (3), 337–346. https://doi.org/10.1021/js980205u.

(26) Collet, A.; Ziminski, L.; Garcia, C.; Vigné-Maeder, F. Chiral Discrimination in Crystalline Enantiomer Systems: Facts, Interpretations, and Speculations. In *Supramolecular Stereochemistry*; Siegel, J. S., Ed.; Springer Netherlands: Dordrecht, 1995; pp 91–110. https://doi.org/10.1007/978-94-011-0353-4_12.

(27) Wang, Y.; Chen, A. M. Enantioenrichment by Crystallization. *Org. Process Res. Dev.* **2008**, *12* (2), 282–290. https://doi.org/10.1021/op700239a.

(28) Leveson-Gower, R. B.; Mayer, C.; Roelfes, G. The Importance of Catalytic Promiscuity for Enzyme Design and Evolution. *Nat Rev Chem* **2019**, *3* (12), 687–705. https://doi.org/10.1038/s41570-019-0143-x.

(29) Arnold, F. H. Directed Evolution: Bringing New Chemistry to Life. *Angewandte Chemie International Edition* **2018**, *57* (16), 4143–4148. https://doi.org/10.1002/anie.201708408.

(30) Yang, K. K.; Wu, Z.; Arnold, F. H. Machine-Learning-Guided Directed Evolution for Protein Engineering. *Nat Methods* **2019**, *16* (8), 687–694. https://doi.org/10.1038/s41592-019-0496-6.

(31) Romero, P. A.; Arnold, F. H. Exploring Protein Fitness Landscapes by Directed Evolution. *Nat Rev Mol Cell Biol* **2009**, *10* (12), 866–876. https://doi.org/10.1038/nrm2805.

(32) Viering, T.; Loog, M. The Shape of Learning Curves: A Review. *IEEE Transactions on Pattern Analysis and Machine Intelligence* **2023**, *45* (6), 7799–7819. https://doi.org/10.1109/TPAMI.2022.3220744.

(33) Watkins, J. C.; Collingridge, G. L. Phenylglycine Derivatives as Antagonists of Metabotropic Glutamate Receptors. *Trends in Pharmacological Sciences* **1994**, *15* (9), 333–342. https://doi.org/10.1016/0165-6147(94)90028-0.

(34) Noorduin, W. L.; Meekes, H.; van Enckevort, W. J. P.; Millemaggi, A.; Leeman, M.; Kaptein, B.; Kellogg, R. M.; Vlieg, E. Complete Deracemization by Attrition-Enhanced Ostwald Ripening Elucidated. *Angewandte Chemie International Edition* **2008**, *47* (34), 6445–6447. https://doi.org/10.1002/anie.200801846.

(35) Noorduin, W. L.; Izumi, T.; Millemaggi, A.; Leeman, M.; Meekes, H.; Van Enckevort, W. J. P.; Kellogg, R. M.; Kaptein, B.; Vlieg, E.; Blackmond, D. G. Emergence of a Single Solid Chiral State from a Nearly Racemic Amino Acid Derivative. *J. Am. Chem. Soc.* **2008**, *130* (4), 1158–1159. https://doi.org/10.1021/ja7106349.

(36) George, F.; Norberg, B.; Wouters, J.; Leyssens, T. Structural Investigation of Substituent Effect on Hydrogen Bonding in (S)-Phenylglycine Amide Benzaldimines. *Crystal Growth & Design* **2015**, *15* (8), 4005–4019. https://doi.org/10.1021/acs.cgd.5b00621.

(37) Valenti, G.; Tinnemans, P.; Baglai, I.; Noorduin, W. L.; Kaptein, B.; Leeman, M.; ter Horst, J. H.; Kellogg, R. M. Combining Incompatible Processes for Deracemization of a Praziquantel Derivative under Flow Conditions. *Angew. Chem.* **2021**, *133* (10), 5339–5342. https://doi.org/10.1002/ange.202013502.

(38) Gerard, C. J. J.; Pinetre, C.; Cercel, H.; Charpentier, M. D.; Sanselme, M.; Couvrat, N.; Brandel, C.; Cartigny, Y.; Dupray, V.; ter Horst, J. H. Phase Diagrams of Praziquantel and Vanillic Acid Cocrystals: Racemic Compound and Conglomerate System. *Crystal Growth & Design* **2024**, *24* (8), 3378–3387. https://doi.org/10.1021/acs.cgd.4c00114.

(39) D'Abbrunzo, I.; Procida, G.; Perissutti, B. Praziquantel Fifty Years on: A Comprehensive Overview of Its Solid State. *Pharmaceutics* **2023**, *16* (1), 27. https://doi.org/10.3390/pharmaceutics16010027.

(40) Borrego-Sánchez, A.; Viseras, C.; Aguzzi, C.; Sainz-Díaz, C. I. Molecular and Crystal Structure of Praziquantel. Spectroscopic Properties and Crystal Polymorphism. *European Journal of Pharmaceutical Sciences* **2016**, *92*, 266–275. https://doi.org/10.1016/j.ejps.2016.04.023.

(41) Charpentier, M. D. Crystallization in Multicomponent Chiral Systems: Thermodynamic Characterization and Guidelines for Chiral Resolution of Racemic Compounds with Cocrystallization, University of Strathclyde, 2023. https://stax.strath.ac.uk/concern/theses/6q182k65j.

(42) Pinto, S. S.; Diogo, H. P. Thermochemical Study of Two Anhydrous Polymorphs of Caffeine. *The Journal of Chemical Thermodynamics* **2006**, *38* (12), 1515–1522. https://doi.org/10.1016/j.jct.2006.04.008.

(43) Sacchi, P.; Neoptolemou, P.; J. Davey, R.; M. Reutzel-Edens, S.; J. Cruz-Cabeza, A. Do Metastable Polymorphs Always Grow Faster? Measuring and Comparing Growth Kinetics of Three Polymorphs of Tolfenamic Acid. *Chemical Science* **2023**, *14* (42), 11775–11789. https://doi.org/10.1039/D3SC02040A.

(44) Lévesque, A.; Maris, T.; Wuest, J. D. ROY Reclaims Its Crown: New Ways To Increase Polymorphic Diversity. *J. Am. Chem. Soc.* **2020**, *142* (27), 11873–11883. https://doi.org/10.1021/jacs.0c04434.

(45) Abolhasani, M.; Kumacheva, E. The Rise of Self-Driving Labs in Chemical and Materials Sciences. *Nat. Synth* **2023**, *2* (6), 483–492. https://doi.org/10.1038/s44160-022-00231-0.

(46) MacLeod, B. P.; Parlane, F. G. L.; Morrissey, T. D.; Häse, F.; Roch, L. M.; Dettelbach, K. E.; Moreira, R.; Yunker, L. P. E.; Rooney, M. B.; Deeth, J. R.; Lai, V.; Ng, G. J.; Situ, H.; Zhang, R. H.; Elliott, M. S.; Haley, T. H.; Dvorak, D. J.; Aspuru-Guzik, A.; Hein, J. E.; Berlinguette, C. P. Self-Driving Laboratory for Accelerated Discovery of Thin-Film Materials. *Science Advances* **2020**, *6* (20), eaaz8867. https://doi.org/10.1126/sciadv.aaz8867.

(47) L. Price, S.; E. Braun, D.; M. Reutzel-Edens, S. Can Computed Crystal Energy Landscapes Help Understand Pharmaceutical Solids? *Chemical Communications* **2016**, *52* (44), 7065–7077. https://doi.org/10.1039/C6CC00721J.

(48) Hylton, R. K.; Tizzard, G. J.; Threlfall, T. L.; Ellis, A. L.; Coles, S. J.; Seaton, C. C.; Schulze, E.; Lorenz, H.; Seidel-Morgenstern, A.; Stein, M.; Price, S. L. Are the Crystal Structures of Enantiopure and Racemic Mandelic Acids Determined by Kinetics or Thermodynamics? *J. Am. Chem. Soc.* **2015**, *137* (34), 11095–11104. https://doi.org/10.1021/jacs.5b05938.

(49) Lopes, C.; Cartigny, Y.; Brandel, C.; Dupray, V.; Body, C.; Shemchuk, O.; Leyssens, T. A Greener Pathway to Enantiopurity: Mechanochemical Deracemization through Abrasive Grinding. *Chemistry – A European Journal* **2023**, *29* (35), e202300585. https://doi.org/10.1002/chem.202300585.

(50) Segler, M. H. S.; Preuss, M.; Waller, M. P. Planning Chemical Syntheses with Deep Neural Networks and Symbolic AI. *Nature* **2018**, *555* (7698), 604–610. https://doi.org/10.1038/nature25978.

# Appendix.

## Remarks belonging to all Chapters

These first remarks present a methodology shared between most chapters and apply unless indicated otherwise.

### General remarks

Chiral HPLC analyses were performed using an Agilent Technologies Infinity 1260 HPLC system.

To be able to experiment with multiple solutions at the time, a block from aluminium with milled holes for vials was fabricated in-house by the AMOLF Precision Manufacturing Department (suitable for either 2 mL or 7 mL vials). The block was temperature controlled using water, circulated by a thermostat manufactured by Huber (Huber Heat Regulator RS2232, range: 5 – 60 °C). When shaking, a VWR Standard vortex mixer was used. When stirring, 6x3mm cylindrical PTFE stirring bars (VWR) combined with a standard VWR hotplate were used. In some experiments, when shaking or stirring, 3 mm diameter PTFE coated beads were used (VWR). When used, glass beads (2 mm glasschrot, Assistent) were ordered through VWR.

For sample preparation and analysis, 0.2 µm PTFE syringe filter (VWR Internationals) and 2 mL HPLC vials (29651-U Supelco, Merck) were used. The 7 mL vials used in experiments were sourced from Merck (27150-U Supelco).

All solvents used (n-heptane, 1-propanol, acetonitrile and methanol) were HPLC grade (≥ 99%) and obtained from VWR chemicals. The racemization catalysts typically used are 1,8-Diazabicyclo[5.4.0]undec-7-ene (DBU, Across Organics) and 1,1,3,3-tetramethylguanidine (TMG, Sigma-Aldrich).



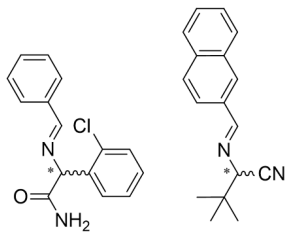


**1** **2**

**Scheme A1.** The two model conglomerates used frequently in this thesis: **1**) Clopidogrel (Plavix) precursor 2-(benzylideneamino)-2-(2-chlorophenyl)acetamide and **2**) tert-leucine precursor 3,3-dimethyl-2-((naphthalen-2-ylmethylene)amino)butanenitrile. As Schiff-bases derived from amino acids, both conglomerates racemize under basic conditions.

## On the two model conglomerates mainly used

The two model conglomerates used often in this thesis are depicted in Scheme A1 and were obtained over the course of previous research in the group where the work was carried out. The synthesis is detailed elsewhere.[1,2]

Note: in chapter-specific remarks, the numbering of compounds introduced in the main text or previous remarks belonging to that chapter.

## Sample Analysis through HPLC

For liquid phase samples: 50 – 100 µL of liquid was mixed with 1 mL of IPA by vortex.

For solid phase samples: 0.5 – 1.0 mg of solid material was dissolved in 1.5 mL of IPA by vortex and subsequent ultrasonication (10 minutes).

HPLC analysis was performed on a chiral column (CHIRALPAK IA (250 x 4.6 mm, 5µm)) with a mobile phase consisting of n-heptane and 1-propanol. For compound **1** (Fig. A1), the eluent is mixed in a 7:3 ratio (heptane:IPA). For compound **2** (Fig. A2), the eluent ratio is 95:5 (heptane:IPA). The flow rate was 0.7 mL/min, injection volume 4 µL, and detection was performed by UV-detector (wavelength: 220 nm). Each run had a total time of 10 to 12 minutes.

All experiments were run in MeCN or MeOH with an added 0.2 wt% anisole. The anisole acts as internal standard. By constructing calibration curves, the concentration of (*R*) and (*S*) in each liquid phase sample could be determined (Fig. A3).

# Remarks specific to Chapter 4

## Seed crystal preparation

Seed crystals of a specific enantiomeric excess (e.e.) were prepared from racemic and enantiopure source crystals as follows. First, the amount of required racemic ($m_{RS}$) and enantiopure crystals ($m_R$) was calculated using the following formulae ($m_{R+RS}$ is the total required seed weight):

$$m_R = ee \cdot m_{R+RS}$$

$$m_{RS} = (1 - ee) \cdot m_{R+RS}$$

[1] Van Der Meijden, M. W.; Leeman, M.; Gelens, E.; Noorduin, W. L.; Meekes, H.; Van Enckevort, W. J. P.; Kaptein, B.; Vlieg, E.; Kellogg, R. M. Attrition-Enhanced Deracemization in the Synthesis of Clopidogrel - A Practical Application of a New Discovery. *Org. Process Res. Dev.* **2009**, *13* (6), 1195–1198.

[2] Baglai, I.; Leeman, M.; Wurst, K.; Kaptein, B.; Kellogg, R. M.; Noorduin, W. L. The Strecker Reaction Coupled to Viedma Ripening: A Simple Route to Highly Hindered Enantiomerically Pure Amino Acids. *Chem. Commun.* **2018**, *54* (77), 10832–10834.

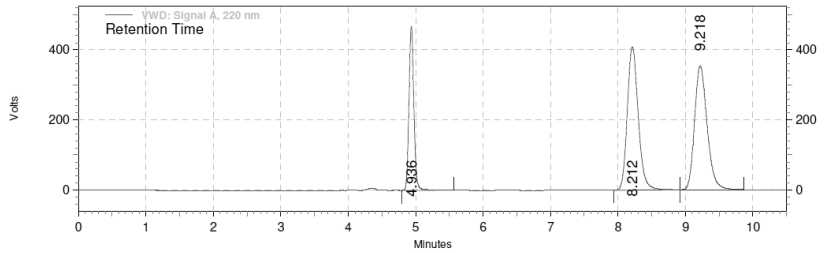


**Figure A1.** Typical chromatogram with retention times for 1: 4.94 min for anisole, 8.12 min for (*R*)-**1**, and 9.12 min for (*S*)-**1**.

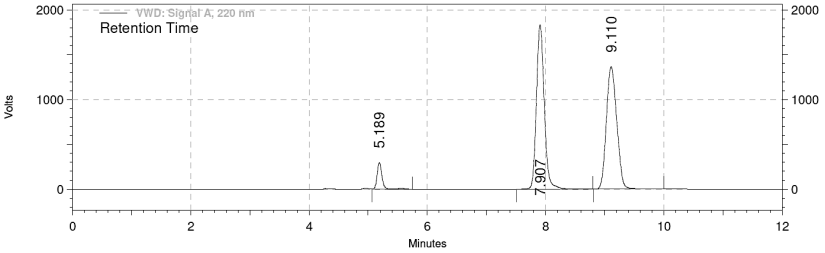


**Figure A2.** Typical chromatogram with retention times for 2: 5.19 min for anisole, 7.91 min for (*S*)-**2**, and 9.11 min for (*R*)-**2**.

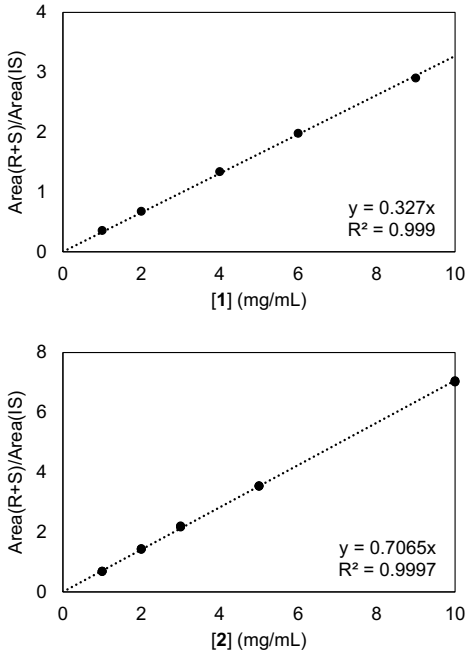


**Figure A3.** Calibration curves for **1** (top graph, in MeCN) and **2** (bottom graph, in MeOH) with 0.2wt% anisole.

These amounts of racemic and enantiopure crystals were then weighed and combined in a mortar and mixed with a spatula. Following the initial mixing, the powder was vigorously mixed using the pestle to form a homogeneous powder. By taking and analysing various samples of the resulting powder, the seed crystal enantiomeric excess was validated by HPLC.

The following seeds were prepared for **1**: 10%, 20%, 30%, 40%, 50%, 60%, 70%, 80% and 90% ee in R. The following seed was prepared for **2**: 60% ee in R.

To assess the size and physical characteristics of the seed crystals, SEM micrographs were taken of all batches (FEI Verios 460; 6nm Cr). Seed crystals were, on average, between 5 and 50 µm in size (Fig. A4). The seeds were reproducible and consistent between batches.

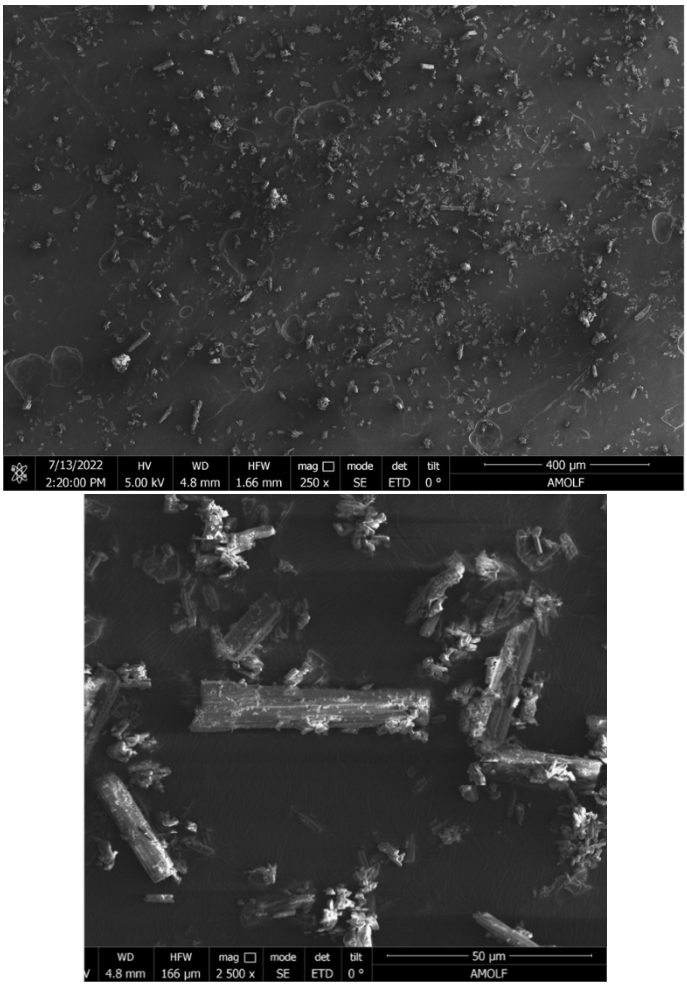


**Figure A4.** Representative SEM micrographs of seed crystals at lower (top) and higher (bottom) magnification. Example micrographs displayed originate from seeds of 20% ee in R for compound **1**.

## Growth experiments for compound 1

### Temperature dependent solubility

The temperature dependent solubility of **1** was determined by heating a slurry of (*RS*)-**1** in MeCN (with 0.2 wt% anisole) to the desired temperature (20, 25, 30, 35 °C) in a 7 mL vial under magnetic stirring. After three hours, a liquid phase sample was taken and submitted for HPLC analysis. The resulting temperature solubility data are given in Figure 4.2 (i.e. in the Chapter).

Furthermore, we validated that the solubility is independent of the concentration of racemization catalyst (DBU) at both 20 and 30 °C (Fig. A5).

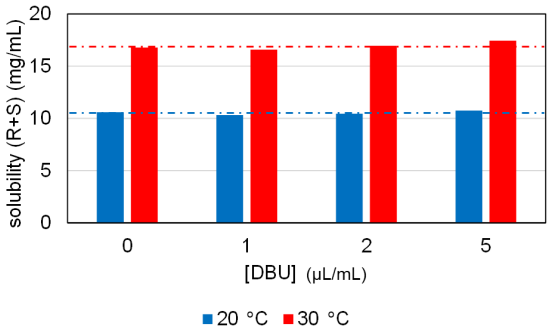


**Figure A5.** Solubility of (*RS*)-**1** at 20 °C (left-side blue bars) and 30 °C (right-side red bars) for various concentrations of DBU. The dotted lines indicate the level for no (zero) amount of catalyst.

### Metastable zone determination

To probe the metastable zone of **1**, saturated solutions were prepared at temperatures of 35, 40, 45 and 50 °C in 20 mL vials (10 mL solution; the smaller volumes used in growth experiments would correspond to even wider metastable zones than those measured here). These solutions were placed in a pre-heated water bath and the thermostat was switched off. Under mild magnetic stirring, the temperature of the solution was monitored while it slowly lowered towards room temperature (20 °C). As soon as nucleation was observed, the temperature was noted, corresponding to the critical supersaturation for that initial concentration. The resulting metastable zone is displayed in Figure 2(a) of the Chapter.

Independently, we verified that a solution saturated at 30 °C remains clear of nucleation for over 2 weeks at 20 °C (without stirring), after which single crystals slowly emerge.

To assess the validity of the metastable zone determination and the dependability on racemization catalyst (DBU) concentration, we checked the nucleation time for 1 mL (in 2 mL HPLC vials) and 5 mL (in 7 mL vials) solutions (identical preparation as

above) with varying concentrations of DBU (Table A1) under stirring. No nucleation was observed during the experimental timescales (max. 3 hours) and the MSZ width appears DBU-independent.

**Table A1.** Metastable zone validation for compound **1** under experimental conditions. Cross (x) indicates that nucleation was observed. Supersaturated solution prepared at 30 °C, cooled to 20 °C.

| V (mL) | [DBU] (µL/mL) | 1.5 hr | 3.0 hr | 24 hr |
|---|---|---|---|---|
| 1 | 2 | | | |
| 1 | 5 | | | x |
| 1 | 10 | | | |
| 5 | 2 | | | x |
| 5 | 5 | | | x |
| 5 | 10 | | | |

**General remarks on growth experiments**

Unless stated otherwise, growth experiments were carried out in 2 mL vials, placed in a custom-made multi-vial holder which was thermoregulated to 20 °C by a Huber thermostat (setting 19.8 °C). The multi-vial holder was placed on top of a shaker and shaken throughout the entire experiment at medium velocity (ca. 300 rpm).

Generally, for each growth experiment, 25 mg of seed crystals were weighed into a 2 mL vial. A supersaturated solution was prepared by mixing 200 mg (*RS*)-**1** with 5 mL internal standard solution in a 7 mL vial equipped with a magnetic stirring rod at 30 °C. In case of experiments under racemizing conditions, DBU was added as well. The mixture was stirred for 30 to 60 minutes. Then, the stirring was stopped to allow the suspension to sediment and the clear supernatant was filtered (2 µm PTFE syringe filter). The filtrate was cooled back to 20 °C over the course of 15 minutes and used as 'supersaturated solution' directly afterwards.

Note: Whenever vortexing suspensions, make sure to lower the speed gently as to avoid crystals sticking to the vial walls.



**Reference experiments (without racemization)**

The vial with the seed crystals was placed in the vial holder. The reference experiments (not under racemizing conditions) were initiated by adding 1 mL of supersaturated solution to the vial containing the seed crystals under shaking (T = 20 °C). The vial was then closed, swiftly vortexed, and placed back in the multi-vial holder. After 90 to 120 minutes, the liquid phase was sampled by filtering 125 µL through a 2 µm PTFE syringe filter and the filtrate was analysed further as the 'liquid phase'. Then, the remaining suspension was cast on top of filter paper laid down on glass filter connected to a vacuum filtration set-up (whilst under active vacuum). Two separate samples of the solids were taken using a Pasteur pipette analysed further as the 'solid phase' (Fig. A6).

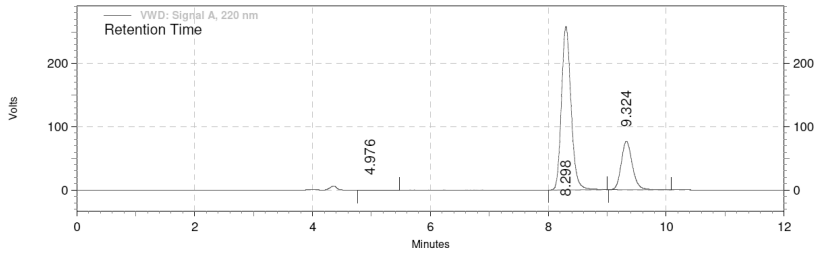


**VWD: Signal A, 220 nm Results**

| Retention Time | Area | Area % | Height | Height % |
|---|---|---|---|---|
| 4.976 | 32227 | 0.05 | 1903 | 0.03 |
| 8.298 | 48892148 | 74.48 | 4332637 | 77.11 |
| 9.324 | 16716244 | 25.47 | 1284520 | 22.86 |

**Figure A6.** Typical solid phase chromatogram following a reference experiment ($ee_0$ = 60%).

## Growth under racemization conditions

The vial with the seed crystals was placed in the vial holder. The seminal experiments under racemizing conditions were then initiated by adding 1 mL of supersaturated solution (now also containing DBU) to the vial containing the seed crystals under shaking (T = 20 °C). The vial was then closed, swiftly vortexed, and placed back in the multi-vial holder. After 90 to 120 minutes, sampling proceeded identically to the procedure stated above under 'reference experiments' (Fig. A7).

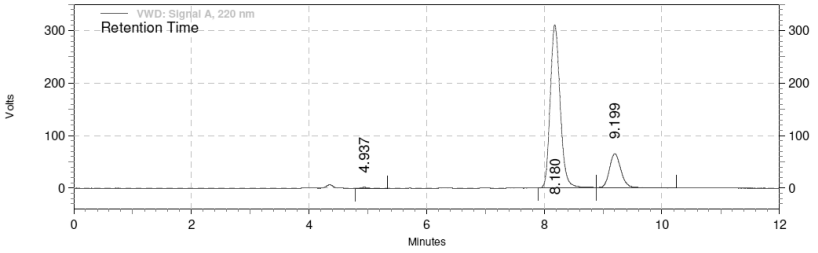


**VWD: Signal A, 220 nm Results**

| Retention Time | Area | Area % | Height | Height % |
|---|---|---|---|---|
| 4.937 | 150362 | 0.20 | 25888 | 0.41 |
| 8.180 | 61282845 | 79.94 | 5219307 | 82.26 |
| 9.199 | 15226482 | 19.86 | 1099570 | 17.33 |

**Figure A7.** Typical solid phase chromatogram following an abrupt growth experiment ([DBU] = 2 µL/mL, $ee_0$ = 60%).

## Slow growth

The thermostat of the multi-vial holder was set to 31 °C (actual temperature 30 °C). The vial with the seed crystals was placed in the vial holder and equilibrated for 30 minutes, under continuous shaking. The experiments (under racemizing conditions)

were initiated by adding 1 mL of supersaturated solution (containing the DBU) to the vial containing the seed crystals under shaking. The vial was then closed, swiftly vortexed, and placed back in the multi-vial holder. A cooling ramp was started, in which the thermostat temperature was linearly decreased to 20 °C over the course of 90 minutes as to allow for gradual growth. The system remained at 20 °C for 30 more minutes. Sampling proceeded after approximately 120 minutes (counted from the mixing between seeds and solution), identically to the procedure stated above under 'reference experiments' (Fig. A8).

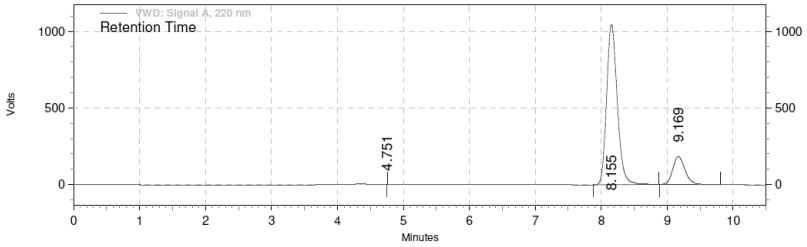


**VWD: Signal A, 220 nm Results**

| Retention Time | Area | Area % | Height | Height % |
|---|---|---|---|---|
| 4.751 | 105 | 0.00 | 196 | 0.00 |
| 8.155 | 197431306 | 83.42 | 17574501 | 85.20 |
| 9.169 | 39231656 | 16.58 | 3053171 | 14.80 |

**Figure A8.** Typical solid phase chromatogram following a slow growth experiment ([DBU] = 2 µL/mL, $ee_0$ = 60%).

## Growth kinetics

Samples after growth are taken after 90 to 120 minutes. To verify that growth has indeed completed after this period of time and the composition of the solid phase does not change afterwards, the experiment under 'Growth under racemization conditions' was performed for seeds with 20% ee in R and sampled after 90 and 200 minutes. Both solid and liquid phase samples had identical concentration and ee, respectively, indicating that growth is completed after 90 minutes and sampling can occur at any time afterwards.

## Prolonged growth of small seed crystal amounts

For the experiments in which small amounts of seed crystals are used to enable prolonged growth, the following altered procedure was followed, based on that for abrupt growth ("Growth under racemization conditions"). A 7 mL vial containing a stirring rod was now placed in the vial holder on a stirring plate (T = 20 °C). Identical to previous experiments, a supersaturated solution was prepared in the presence of DBU. After adding 2 mL of supersaturated solution to the 7 mL vial, 1 mg of seed crystals were added as well under stirring conditions. The vial was then quickly vortexed, swiftly closed and placed back in the vial holder. Mild stirring continued

throughout the experiment. Sampling proceeded after approximately 3 hours, counted from the mixing between seeds and the supersaturated solution, identically to the procedure stated above under 'reference experiments' (Fig. A9).

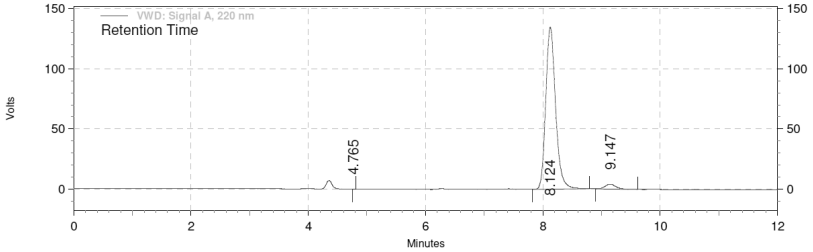


**VWD: Signal A, 220 nm Results**

| Retention Time | Area | Area % | Height | Height % |
|---|---|---|---|---|
| 4.765 | 763 | 0.00 | 439 | 0.02 |
| 8.124 | 26350299 | 96.72 | 2262468 | 97.02 |
| 9.147 | 893759 | 3.28 | 68954 | 2.96 |

**Figure A9.** Typical solid phase chromatogram following the use of a small amount of seed crystals for prolonged growth ([DBU] = 2 µL/mL, $ee_0$ = 60%).

## Growth experiments for compound 2

### Racemization of compound 2

To verify the racemization of compound **2** using the organic base TMG, a solution of (*R*)-**2** was prepared in MeOH (0.5 mg/mL) in the presence of 0.2wt% anisole in a 2 mL HPLC vial. The vial was sampled using the HPLC directly (t = 0, Figure A10). Then, 1 µL/mL TMG was added and sampling was performed at regular time intervals (1, 15, 30, 45, 60, 90 minutes) directly by the HPLC. After 30 minutes, racemization was complete (Fig. A10). The full racemization kinetics are displayed in Figure A11.

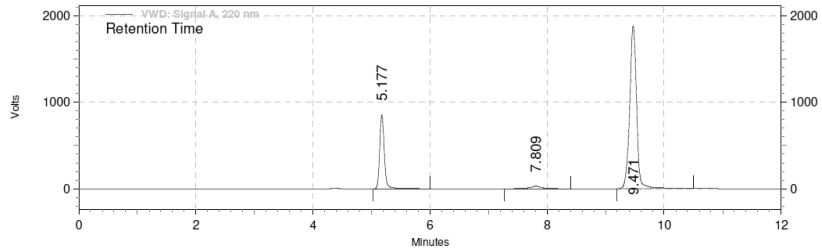


**VWD: Signal A, 220 nm Results**

| Retention Time | Area | Area % | Height | Height % |
|---|---|---|---|---|
| 5.177 | 78149149 | 22.72 | 14307525 | 30.86 |
| 7.809 | 6946303 | 2.02 | 449308 | 0.97 |
| 9.471 | 258801222 | 75.26 | 31599652 | 68.17 |

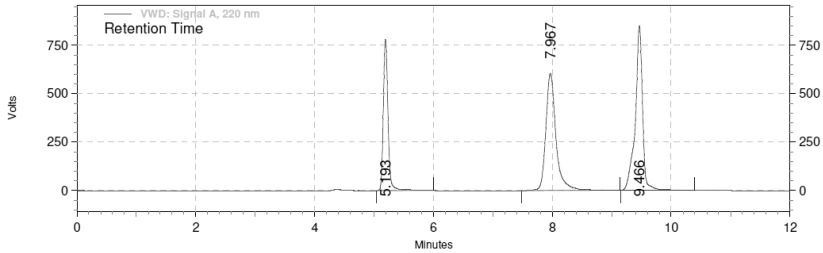


**VWD: Signal A, 220 nm Results**

| Retention Time | Area | Area % | Height | Height % |
|---|---|---|---|---|
| 5.193 | 71472543 | 22.83 | 13099190 | 34.91 |
| 7.967 | 120275073 | 38.41 | 10152153 | 27.06 |
| 9.466 | 121357044 | 38.76 | 14270691 | 38.03 |

**Figure A10.** Chromatograms of the solution at t = 0 (virtually enantiopure in R-**2**, top) and t = 30 minutes (virtually racemic 2, bottom) of racemization with TMG (t=0: 0.5 mg/mL (*R*)-**2** and 1 µL/mL TMG in MeOH).



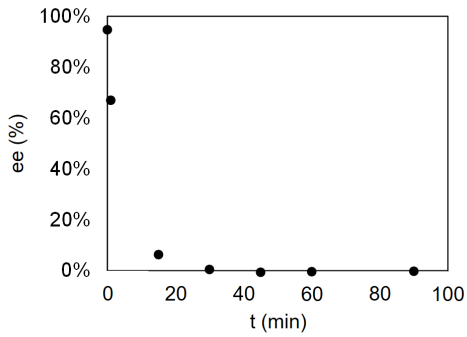


**Figure A11.** Racemization kinetics for compound **2** using TMG, starting from a virtually enantiopure solution (t=0: 0.5 mg/mL (*R*)-**2** and 1 µL/mL TMG in MeOH).

**Temperature dependent solubility**

The temperature dependent solubility of **2** was determined by heating a slurry of (*RS*)-**2** in MeOH (with 0.2 wt% anisole and 100 µL/mL TMG) to the desired temperature (20, 25, 30 °C) in a 7 mL vial under magnetic stirring. After three hours, a liquid phase sample was taken and submitted for HPLC analysis. The resulting data are given in Figure A12.

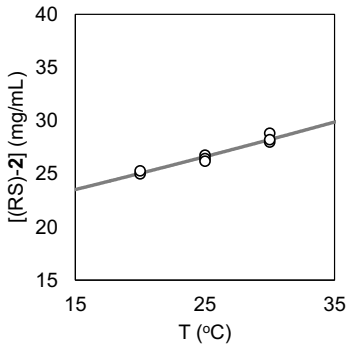


**Figure A12.** Temperature dependent solubility for **2** (in MeOH) in the presence of 100 µL/mL TMG.

**Metastable zone**

To validate that growth experiments take place within the metastable zone of **2**, it was visually verified that a solution saturated at 40 °C with [(*RS*)-**2**] = 30.4 mg/mL in MeOH, containing 100 uL/mL TMG and 0.2 wt% anisole, remains clear of nucleation for at least a day after having been cooled to 20 °C (no stirring). The solubility difference (30.4 – 25.1 = 5.3 mg/mL) is similar to that imposed for compound **1**.

**Growth experiment**

A solution of (*RS*)-**2** was prepared in MeOH at 40 °C (30.4 mg/mL) in the presence of 100 µL/mL TMG and 0.2 wt% anisole. The solution was cooled down to 20 °C. Similar to the experiment described under "Prolonged growth of small seed crystal amounts" for compound **1**, in a 7 mL vial, 1 mg of seed crystals (60% ee enriched in R) was added to 2 mL of supersaturated solution under the mildest of stirring conditions. After 3 hours, both solid and liquid phase were sampled (Fig. A13).

## Comparison of crystals before and after growth

Seed crystals of 20% ee (25 mg/mL) in *R* of compound **1** were subjected to the growth conditions listed under 'Growth under racemization conditions' in the presence of 2 µL/mL DBU. Before and after growth, solid phase samples were deposited on carbon stickers adhered to 1 $cm^2$ aluminium substrates by a sprinkling method. Excess crystals, that did not adhere to the sticker, were removed using $N_2$ flow. The samples

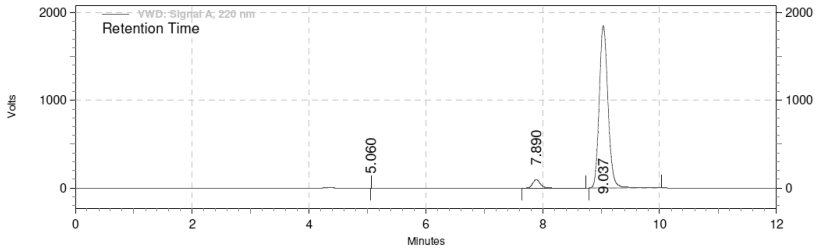


**VWD: Signal A, 220 nm Results**

| Retention Time | Area | Area % | Height | Height % |
|---|---|---|---|---|
| 5.060 | 95 | 0.00 | 267 | 0.00 |
| 7.890 | 13877683 | 4.10 | 1561720 | 4.78 |
| 9.037 | 324260793 | 95.90 | 31081405 | 95.21 |
| Totals | | | | |
| | 338138571 | 100.00 | 32643392 | 100.00 |

**Figure A13.** Solid phase chromatogram following the growth experiment for compound **2** ([TMG] = 100 µL/mL, $ee_0$ = 60%).

were then coated with a 11.3 nm layer of Chrome and directly imaged on a FEI Verios 460 Scanning Electron Microscope in immersion mode.

An increase in average crystal size, consistent with growth, can be observed from the resulting scanning electron micrographs (Fig. A14). Moreover, initially present satellite crystals could no longer be observed after growth, possibly due to dissolution, growth, coalescence and/or ripening phenomena. Also note the change in the aspect ratio to more elongated crystals, which could indicate preferential growth or attachment on the tip, or be caused by the breaking of crystals due to collisions with other crystals, the vessel walls, or shearing.

## Kinetic model based on the amplification factor

In the Chapter, we define the experimental amplification factor α:

$$\alpha = \frac{ee_\Delta}{ee_0} \tag{1}$$

where $ee_\Delta$ is the enantiomeric excess of the grown material during crystallization and $ee_0$ is the enantiomeric excess of the seed material. Here, we will use this definition to derive a simple model for deracemization kinetics under the assumption that nonlinear amplification (α > 0) only occurs during crystal growth. The model can be shown to lead to an exponential relationship under realistic assumptions, a hallmark of all deracemization kinetics. The applicability of this model will then be demonstrated for the two major forms of CIET: Temperature Cycling (TCID) and attrition-induced Ostwald ripening (Viedma Ripening). We conclude that the mechanistic framework and experimental amplification factor are in agreement with current theory and kinetic experiments.

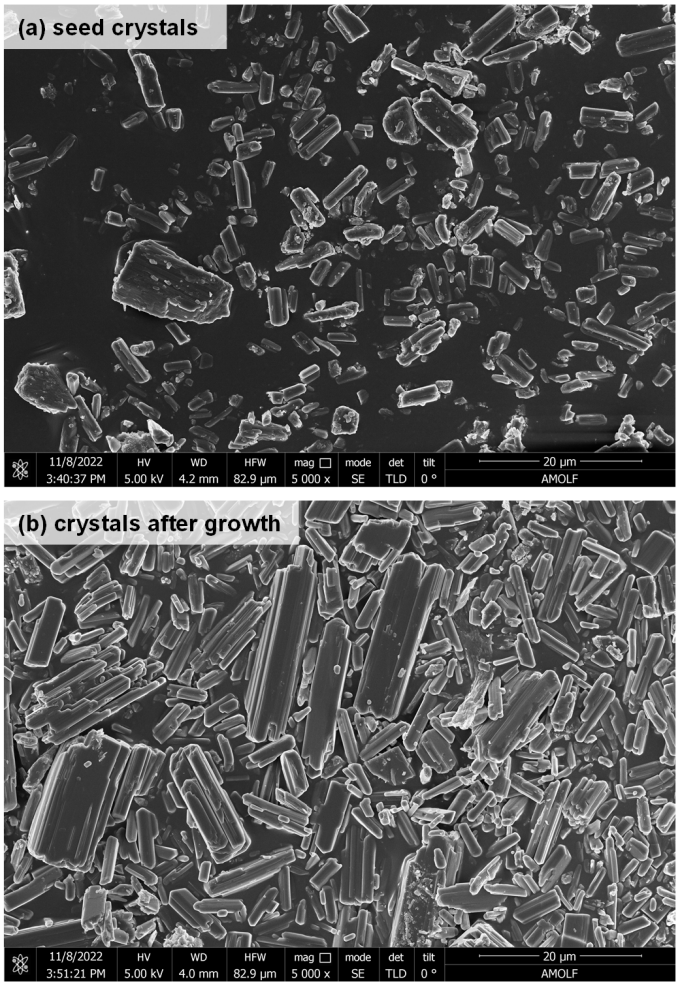


**Figure A14.** Scanning electron micrographs (SEM) of crystals of compound **1** (a, top) before (20% ee in R) and (b, bottom) after growth under racemizing conditions (2 µL/mL).

A

## Derivation of a kinetic model based on the experimental amplification factor

We start by recalling the definition of the enantiomeric excess (ee):

$$ee = \frac{[R] - [S]}{[R] + [S]} = \frac{[R] - [S]}{m} \tag{2}$$

where [X] is the mass fraction of X and m is the total mass fraction of both R and S enantiomers combined. We can than note that

$$ee \cdot m = [R] - [S] \tag{3}$$

so that the enantiomeric excess after crystal growth ($ee_P$) is given by

$$ee_P = \frac{ee_0 \cdot m_0 + ee_\Delta \cdot m_\Delta}{m_0 + m_\Delta} \tag{4}$$

This equation (eq. 4) is described, in altered form, in the main text of the Chapter for the calculation of $ee_\Delta$ from experimental samples.

Deracemization consists of crystal growth and crystal dissolution steps. By using eq. 1 (so that $ee_\Delta = \alpha \cdot ee_0$), we can write for crystal growth:

$$ee_{P,\text{growth}} = \frac{\alpha \cdot ee_0 + \frac{m_0}{m_\Delta} \cdot ee_0}{1 + \frac{m_0}{m_\Delta}} = \left(\frac{\alpha + \frac{m_0}{m_\Delta}}{1 + \frac{m_0}{m_\Delta}}\right) \cdot ee_0 \tag{5}$$

To describe the effect of crystal dissolution, we can adapt equation 4. First, we set $\alpha = 0$ (since $ee_\Delta = 0$ assumes no amplification during dissolution). To account for the mass balance, we further substitute $m_0 \rightarrow m_0 + m_\Delta$ and $m_\Delta \rightarrow - m_\Delta$ so that

$$ee_{P,\text{dissolution}} = \left(\frac{\frac{m_0+m_\Delta}{m_\Delta}}{\frac{m_0+m_\Delta}{m_\Delta} - 1}\right) \cdot ee_0 \tag{6}$$

In the combined cycle, we move from crystal growth to crystal dissolution (and back again), so that we can combine eq's 5 and 6 by using

$$ee_{P,\text{cycle}} = \frac{ee_{P,\text{growth}} \cdot ee_{P,\text{dissolution}}}{ee_0} = \left(\frac{\alpha + \frac{m_0}{m_\Delta}}{1 + \frac{m_0}{m_\Delta}}\right) \cdot \left(\frac{\frac{m_0+m_\Delta}{m_\Delta}}{\frac{m_0+m_\Delta}{m_\Delta} - 1}\right) \cdot ee_0 = \left(\frac{\alpha \cdot m_\Delta}{m_0} + 1\right) \cdot ee_0 \tag{7}$$

Now we can define the deracemization process as a number of these cycles (n) for which the enantiomeric excess of the solid phase at the end of each cycle $ee_n$ is given by

$$ee_n = \left(\frac{\alpha \cdot m_\Delta}{m_0} + 1\right) \cdot ee_{n-1} \tag{8}$$

,

which (if we consider α invariant with n) is a geometric sequence so that

$$ee_n = ee_0 \cdot \left(\frac{\alpha \cdot m_\Delta}{m_0} + 1\right)^n \tag{9}$$

In reality, the question naturally rises whether α is indeed constant between cycles. Our experiments have shown, however, that his assumption is reasonable and α does not very much depend on $ee_0$, barring theoretical constraints (α is limited to $1/ee_0$).

For application in describing deracemization kinetics, we can define a typical cycle time $\tau$ so that $t = n \cdot \tau$. This leads to the time-dependent deracemization kinetics as

$$ee(t) = ee(0) \cdot \left( \frac{\alpha \cdot m_{\Delta}}{m_0} + 1 \right)^{\frac{t}{\tau}} \qquad (10)$$

To demonstrate the kinetic model based on the experimental amplification factor, we will show a fit to the two main types of experimental deracemization data: Temperature Cycling (TCID) and Viedma Ripening (attrition-enhanced).

**Application to Temperature Cycling**

Mazzotti and co-workers performed an optimization study on the temperature cycling of clopidogrel precursor BCA (compound **1** in the Chapter).[40] They measured the kinetics of temperature cycles while they varied the cooling rate during the crystal growth (cooling) step. After we calculated the $m_0$ and $m_\Delta$ based on the given experimental details and solubility data in [40 of Chapter], we were able to fit the kinetic data presented by the Mazzotti group to our kinetic model (eq. 9) based on the experimental amplification factor. The results (points) and our fit (lines) are shown in Figure A15. There is a good agreement between our fit and the experimental results, implying that the kinetic model based on the experimental amplification factor is reasonable for deracemization via temperature cycles. This is in line with the proposed exponential behaviour of the process in literature. Moreover, the fitted values for the amplification factor, varying from 0.2 to 0.3 (depending on the cooling rate), are reasonable based on our own experimental results. The actual amplification factor will probably be higher, since the model assumes constant α, independent of ee and the changing crystallization kinetics, and fitting using the exponential in that way does not take into account the theoretical limit of $\alpha_n \leq 1/ee_{n-1}$.

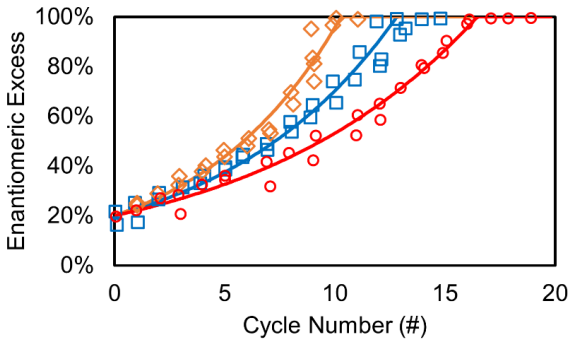


**Figure A15.** Fitting of temperature cycling data from Breveglieri et al. based on eq. 9 using actual values of $ee_0$, $m_\Delta$, and $m_0$. The resulting (fitted) amplification factors are in the range of 0.2 to 0.3. Original caption: Evolution of the BCA ee with the number of cycles at increasing cooling rate in going from experiment c3 (0.22 °C/min, orange markers) to c4 (0.43 °C/min, blue markers) to c5 (1.30 °C/min, red markers). Figure and caption adapted from ref. [40 of Chapter].

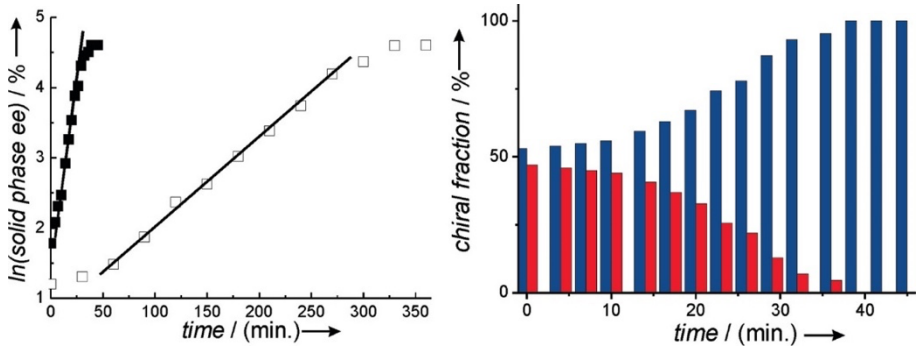


**Figure A16.** Progression of the enantiomeric excess in the solid phase during the grinding-induced transformation on a 10-mL scale using a thermostatted ultrasonic cleaning bath (open symbols) and on a 400-mL scale using the bead mill (closed symbols). The straight lines are a fit of the data to eq. 11. The right graph shows the increase of the chiral purity in the solids of the latter experiment (blue (*S*)-1, red (*R*)-1). The initial ee values after dissolution were 3.40% for the ultrasonic and 5.96% in the beadmill experiment. Figure and caption reprinted from ref. [59 of Chapter].

**Application to attrition-enhanced Ostwald ripening (Viedma Ripening)**

During Viedma Ripening, the concept of cyclic growth and dissolution fades, as there is a continuum of attrition that imposes continuous dissolution and growth. However, since crystal growth and crystal dissolution still appear as separate microscopic events, the model could still be applied to Viedma Ripening. Of course, under such conditions $m_\Delta$ gets a different meaning. Indeed, $m_\Delta$ will then pertain to the constant supersaturation imposed by the increased solubility of ground down crystals by virtue of the Gibbs-Thompson effect. This concept has been experimentally confirmed and it has been reported that the system is not in thermodynamic equilibrium, but in a kinetic equilibrium.[3] Also, the typical cycle time $\tau$ would better be re-interpreted via $1/\tau$ which then serves as a measure for the rates of crystal growth and dissolution under such grinding conditions (i.e. the frequency of microscopic growth and dissolution events). Both $m_\Delta$ and $1/\tau$ will, of course, vary with the strength of attrition and resulting kinetically stabilized crystal size distributions.



To apply the model to Viedma Ripening, we can rewrite eq. 10 by using the identity $x = \exp(\log(x))$ to yield

$$ee(t) = ee(0) \cdot \exp\left(\frac{\log\left(\frac{\alpha \cdot m_\Delta}{m_0} + 1\right)}{\tau} \cdot t\right) = ee(0) \cdot \exp(k \cdot t) \qquad (11)$$

where $k$ is a generic kinetic constant. Here, the deracemization rate constant $k$ is

[3] Noorduin, W. L.; van Enckevort, W. J. P.; Meekes, H.; Kaptein, B.; Kellogg, R. M.; Tully, J. C.; McBride, J. M.; Vlieg, E. The Driving Mechanism Behind Attrition-Enhanced Deracemization. *Angew. Chem. Int. Ed.* **2010**, *49* (45), 8435–8438. DOI: 10.1002/anie.201002036.

formally defined as

$$k = \frac{\log\left(\frac{\alpha \cdot m_\Delta}{m_0} + 1\right)}{\tau} \approx \frac{\alpha \cdot m_\Delta}{m_0 \cdot \tau} \qquad (12)$$

under the approximation that $\log(x+1) = x$ for small $x$ (i.e. $x < ½$), which is generally valid in the slurry regime where $m_0$ is substantially bigger than $m_\Delta$.

It has been well established that Viedma Ripening follows such exponential kinetics described by eq. 11. Amongst others, an example is that reproduced in Figure A16 (also for compound **1**, the clopidogrel-precursor BCA).[4] Moreover this form has been theoretically advocated in other works as well and the description of $k$ (eq. 12) predicts trends observed in other experimental work.[5,6,7] Therefore, a kinetic model based on the experimental amplification factor that we have introduced is in agreement with previous theoretical and experimental reports on deracemization via Viedma Ripening processes.

# Remarks specific to Chapter 5

## Origin of the material used

Racemic **1** was obtained by synthesis as described in previous research.[8] Enantiopure **1** was obtained through attrition based deracemization (98% ee) of racemic **1**, followed by deep temperature cycling induced deracemization for increased enantiopurity (99%+) and sonication assisted attrition to retrieve small, homogeneous enantiopure crystals.

[4] Noorduin, W. L.; van der Asdonk, P.; Bode, A. A. C.; Meekes, H.; van Enckevort, W. J. P.; Vlieg, E.; Kaptein, B.; van der Meijden, M. W.; Kellogg, R. M.; Deroover, G. Scaling Up Attrition-Enhanced Deracemization by Use of an Industrial Bead Mill in a Route to Clopidogrel (Plavix). *Org. Process Res. Dev.* **2010**, *14* (4), 908–911. DOI: 10.1021/op1001116.

[5] Noorduin, W. L.; van Enckevort, W. J. P.; Meekes, H.; Kaptein, B.; Kellogg, R. M.; Tully, J. C.; McBride, J. M.; Vlieg, E. The Driving Mechanism Behind Attrition-Enhanced Deracemization. *Angew. Chem. Int. Ed.* **2010**, *49* (45), 8435–8438. DOI: 10.1002/anie.201002036.

[6] Breveglieri, F.; Baglai, I.; Leeman, M.; Noorduin, W. L.; Kellogg, R. M.; Mazzotti, M. Performance Analysis and Model-Free Design of Deracemization via Temperature Cycles. *Org. Process Res. Dev.* **2020**, *24* (8), 1515–1522. DOI: 10.1021/acs.oprd.0c00266.

[7] Noorduin, W.L.; Meekes, H.; van Enckevort, W.J.P.; Millemaggi, A.; Leeman, M.; Kaptein, B.; Kellog, R.M.; Vlieg, E. Complete Deracemization by Attrition-Enhanced Ostwald Ripening Elucidated. *Angew. Chem. Int. Ed.* **2008**, *47* (34), 6445–6447. DOI: 10.1002/anie.200801846.

[8] Baglai, I.; Leeman, M.; Wurst, K.; Kaptein, B.; Kellogg R. M.; Noorduin, W. L. The Strecker reaction coupled to Viedma ripening: a simple route to highly hindered enantiomerically pure amino acids. *Chem. Commun.* **2018**, *54*, 10832–10834.

# Seed crystal preparation

## Small seeds

Small seed crystals of a specific enantiomeric excess (e.e.) were prepared from racemic and enantiopure crystals obtained from previous syntheses as follows. First, the amount of required racemic ($m_{RS}$) and enantiopure crystals ($m_R$) was calculated using the following formulae ($m_{R+RS}$ is the total required seed weight):

$$m_R = ee \cdot m_{R+RS}$$

$$m_{RS} = (1 - ee) \cdot m_{R+RS}$$

These amounts of racemic and enantiopure crystals were then weighed and combined in a 20 mL screw cap vial alongside 10 mL MeOH and 10 g glass beads and briefly vortexed. The vial was placed in an actively cooled ultrasonication bath for 24 hours. The vial was left to equilibrate at room temperature for 30 minutes. Consequently, the slurry was removed from the vial and filtered under vacuum on a paper filter pore size 11µm. By analysing various samples of the resulting powder, the seed crystal enantiomeric excess was validated by HPLC. The size and morphology were validated by optical microscopy and scanning electron microscopy. Following this procedure, small seeds with enantiomeric excess of 0% (racemic), 100% in (*R*)-**1**, 100% in (*S*)-**1**, and 18.0% in (*R*)-**1** were obtained.

## Large seeds

Large enantiopure crystals were obtained by growing the resulting enantiopure small seeds in the following manner. A slightly undersaturated enantiopure solution of (*R*)-**1** or (*S*)-**1** was prepared at 40 °C containing 20 mg/mL of **1** and charged with 0.75 g/mL PTFE beads. The vials were placed on a shaker and gently shaken (ca. 300 rpm). The solution was seeded using 17 mg/mL of (*R*)-**1** and/or (*S*)-**1** small seeds obtained by the above-described method. The solution was cooled down to 20 °C over

A

**Table A2.** Preparation of experimental size and mass imbalances.

| Scenario | $RS_{small}$ of ee=0 (rac.) (mg/mL) | $R_{small}$ (mg/mL) | $S_{small}$ (mg/mL) | $R_{large}$ (mg/mL) | $S_{large}$ (mg/mL) | $RS_{small}$ of ee=18% (mg/mL) |
|---|---|---|---|---|---|---|
| **Majority larger** | - | - | 8 | 12 | - | - |
| **Excess larger** | 12 | - | - | 8 | - | - |
| **Equal sizes** | - | - | - | - | - | 20 |
| **Excess smaller** | - | 8 | - | 6 | 6 | - |
| **Majority smaller** | - | 12 | - | - | 8 | - |
| **$S_{large}$ $R_{small}$ for ee=0** | - | 10 | - | 10 | - | - |
| **$R_{large}$ $S_{small}$ for ee=0** | - | - | 10 | - | 10 | - |

the course of 90 minutes to grow the small seeds into large seeds, characterization shown in the corresponding section of this Appendix.

**Mixing various seed compositions**

The scenarios described in the main text are constructed by mixing various sizes of racemic or enantiopure crystals. Throughout the experiments, the same batch was used for each of the bulk crystals to mitigate batch specific irregularities. Table A2 shows the amounts used in the experiments.

## Size comparison of small and large seed crystals

**Scanning electron microscopy**

SEM micrographs, shown as Figure A17, were taken of the small and large seeds using a FEI Verios 460; sputter-coated samples with 15nm Cr. Generally, the small seed crystals were around 10 µm, while the large seed crystals were substantially larger, ranging from around 10 µm to >60 µm.

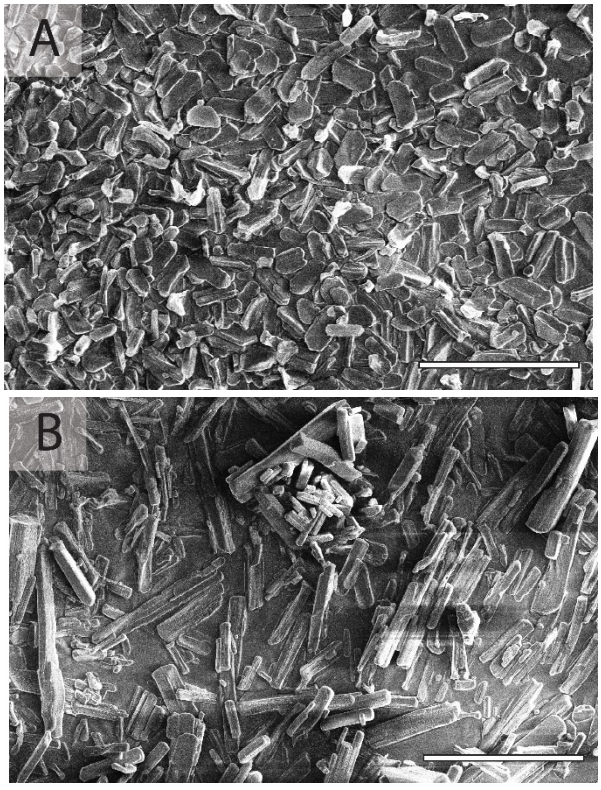


**Figure A17.** SEM micrographs of A) $RS_{small}$ seeds and B) $R_{large}$ seeds. Similar size distributions were found for the remaining batches. Scale bars: 50 µm.

## Optical Microscopy

The seed crystals were sandwiched between two glass slides and analyzed by optical microscopy, using a Canon EOS 850D camera attached to a Leica DMPA microscope with a N PLAN L 50x/0,50 / 566036 objective. The mean size of the large seed crystals is significantly larger than the small seed crystals (Fig. A18). Most small seed crystals are <10 µm, while the large seed crystals are commonly >20 µm. These findings are consistent with SEM analysis. Although SEM provides more details, optical microscopy offers faster and easier characterization of larger numbers of crystals.

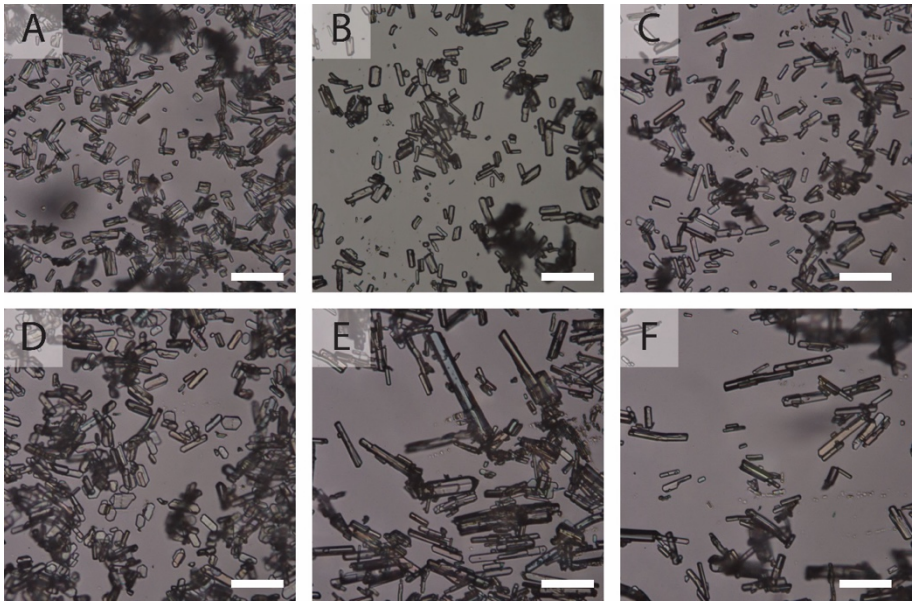


**Figure A18.** Optical microscopy images of seed crystals A) $R_{small}$, B) $S_{small}$, C) $RS_{smal}$ with 18% ee in R, D) $RS_{small}$, E) $R_{large}$ F) $S_{large}$. Scale bars: 50 µm.

## Laser particle analysis

The small and large seed crystal sizes were characterized before the start of the experiment through laser particle analysis using a Mastersizer 3000 laser particle size analyzer (Malvern Instruments Ltd., Malvern, UK). This method allows characterizing a large ensemble of crystals indirectly, as opposed to studying a smaller sample under the microscope. An aliquot of crystals was dispersed in a few drops of 2-propanol and inserted into the continuous water dispersant phase of the particle size analyser. The results are shown in Figure A19. The mean size of the crystals shifted from ~14-16 µm for small seed crystals to ~28-32 µm for large seed crystals. Furthermore, the crystal size distribution of the large seed crystals is narrower, which may be caused by slight dissolution before their growth from the small crystals (see the corresponding section of this Appendix).

These high-throughput ensemble measurements are quite consistent with those by SEM and optical microscopy. It should be emphasized laser particle analysis has some limitations. Laser particle analysis shows volume density, which is biased toward larger particles. This explains why the average size determined from laser particle analysis is inflated compared to electron and light microscopy. Furthermore, we note that laser particle analysis accounts for equivalent spherical diameters, instead of the non-equivalent x, y and z dimensions of the needle-like crystals. The small shoulder peak around ~2-3 µm for the large seed crystals is explained by this anisotropy.

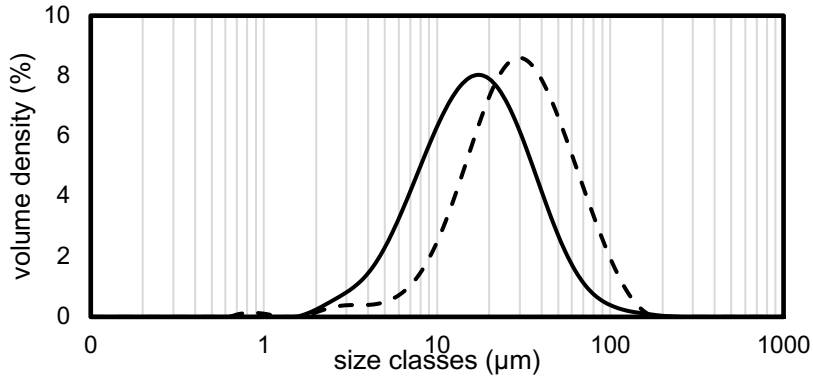


**Figure A19.** Crystal size distribution of small (solid) and large (dashed) seed crystals from laser particle analysis with a Malvern Mastersizer 3000.

## Growth experiments

**Experimental**

Growth experiments were carried out in 7 mL vials, placed in a custom-made multi-vial holder which was thermoregulated by a Huber thermostat. The multi-vial holder was placed on top of a shaker and shaken throughout the entire experiment at medium velocity (ca. 300 rpm).

Generally, for each growth experiment, 40 mg of seed crystals were weighed into a 7 mL vial along with 1.5g PTFE coated beads. The vial was heated to 30 °C (thermostat set at 31 °C). In a separate vial a saturated solution was prepared by adding 750 mg of a racemic mixture of (*R*) and (*S*)-**1** to 17.1 mL internal standard solution and 900 µL DBU (50 µL/mL) in a 20 mL vial equipped with a magnetic stirring rod at 30 °C. The mixture was stirred for 60 minutes. Then, the stirring was stopped to allow the suspension to sediment and the clear supernatant was transferred to a new 20 mL vial and allowed to heat until 30 °C once more. Using a glass Pasteur pipette, a liquid sample (ca. 10 µL) was removed from the solution and submitted for HPLC analysis as 'prestock', to determine the starting concentration for mass-balance determination. 2 mL of the clear saturated solution was added to the previously

heated 7 mL vial with the seeds. The vial was swiftly vortexed and placed back into the heating block. The temperature was lowered to 20 °C (thermostat set at 19.8 °C) over 90 or 10 minutes for slow or fast growth, respectively.

Note: Whenever vortexing suspensions, make sure to lower the speed gently as to avoid crystals sticking to the vial walls.

The suspensions were left at 20°C for 45 minutes, after which the vial was removed from the vial holder and swiftly vortexed. 50-100 µL of the slurry was removed and filtered through a 0.22 µm PTFE syringe filter. The filtrate was collected, diluted with IPA, and submitted for HPLC analysis as the 'liquid phase'. After briefly vortexing the vial again, the remaining suspension was removed from the vial using a glass Pasteur pipette and deposited dropwise onto the center of a paper filter pore size 11 µm and filtered under vacuum. The filter was left undisturbed for 10 minutes, after which solid samples (0.5 – 1 mg) were collected by insertion of a Pasteur pipette in three separate places of the filter cake. In total, 3 solid phase samples were collected, dissolved in IPA, and submitted for HPLC analysis as 'solid phase'. Typical chromatograms of the liquid and solid phases are displayed below (Fig. A20).

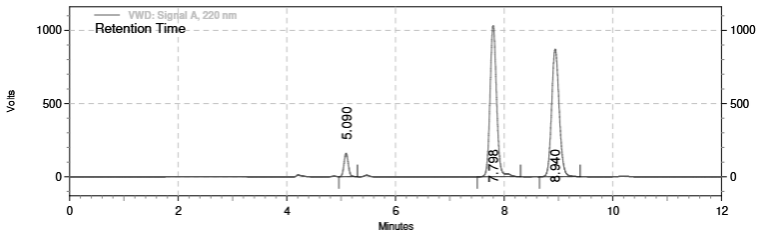


**VWD: Signal A, 220 nm Results**

| Retention Time | Area | Area % | Height | Height % |
|---|---|---|---|---|
| 5.090 | 14707808 | 4.89 | 2679552 | 7.74 |
| 7.798 | 144914066 | 48.14 | 17320240 | 50.04 |
| 8.940 | 141412294 | 46.98 | 14612002 | 42.22 |

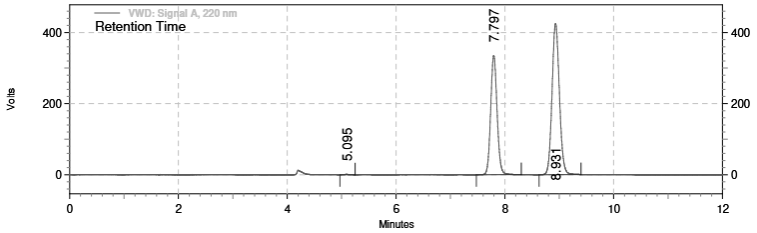


**VWD: Signal A, 220 nm Results**

| Retention Time | Area | Area % | Height | Height % |
|---|---|---|---|---|
| 5.095 | 64713 | 0.06 | 11231 | 0.09 |
| 7.797 | 45918829 | 40.62 | 5625921 | 44.07 |
| 8.931 | 67059780 | 59.32 | 7129461 | 55.84 |

**Figure A20.** Typical liquid phase (top) and solid phase (bottom) chromatogram following an experiment.

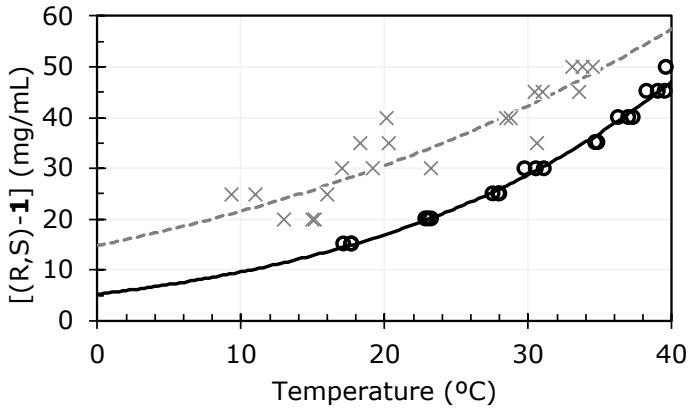


**Figure A21.** Temperature dependent solubility (circles) and metastable zone (crosses) for **1** in MeOH with Van 't Hoff fit shown with solid black and grey dashed lines respectively.

**Temperature dependent solubility**

The temperature dependent solubility was determined by heating a slurry of a racemic mixture of (*R*) and (*S*)-**1** in MeOH in a 2 mL vial under magnetic stirring. Using a Crystal 16 multireactor crystallizer, the temperature of clear points at various concentrations were measured. The resulting data are given in Figure A21.

**Mass balance**

From the concentrations in solution before and after growth, a mass balance can be constructed. Generally, the concentrations of the growth solutions before and after growth closely follow the solubility curve as seen in Figure A21, albeit slightly elevated due to the presence of DBU. Typically, concentrations decreased from 35 mg/mL to 25 mg/mL, leading to growth onto the seed crystals of about 10 mg/mL.

## Comparison of crystal surface before and after growth

SEM micrographs of the crystals before and after growth show the roughness at the crystal growth front (Fig. A22). Before growth, all seed crystals of the same size-class had similar growth fronts. After growth, the growth front morphology is quite rough for high supersaturation experiments, while for low supersaturation experiments, the growth fronts were much smoother. Similar results were found for the remaining batches and experiments. This is in accordance with previous findings, where growth mechanism is found to be strongly dependent on the degree of supersaturation.[9]

[9] Lewis, A.; Seckler, M. M.; Kramer, H. J. M.;van Rosmalen, G. M. *Industrial Crystallization: Fundamentals and Applications*; Cambridge University Press, **2015**. DOI: 10.1017/CBO9781107280427.

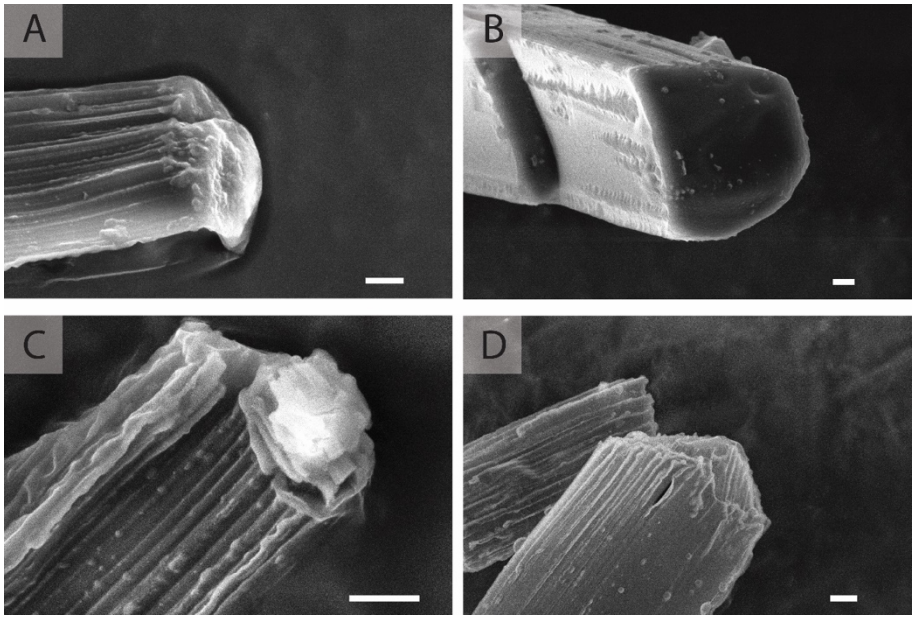


**Figure A22.** SEM micrographs of the crystal growth front of initial seed crystals A) $RS_{small}$ and B) $S_{large}$, and fully grown crystals of a C) fast and D) slow growth experiment. Scale bars: 1 µm.

## Calculation details

The theoretical predictions for the effects of supersaturation where based on computations that defined the enantiomeric excess of the grown material based on the growth rates of the enantiomeric populations

$$ee_{\Delta} \approx (G_R - G_S)/(G_R + G_S)$$

Here, we defined those growth rates as follows:

- For slow growth at low supersaturation, we assumed the population growth rate to be proportional to the number of crystals in the population: $G \sim N$.
- For fast growth at high supersaturation, we assumed the population growth rate to be proportional to the cumulative surface area of crystals in the population (cuboid approximation): $G \sim \Sigma A$.

These assumptions have been rationalized and explained in the main text.

Based on this theoretical framework, multiple calculations can be straightforwardly performed to explore the predicted effect of size-disparities between the seed crystals of populations on the outcome of crystallization. An example calculation is shown below, where a size-ratio effect was explored using an implementation in programming language *R*. The results of this calculation are shown as Figure A23.

```
# R-Script for Calculation of the Size-Ratio Effect.

# Growth Velocity Ratio: LENGTH / WIDTH = 10
# ee0 = 10%
# Steps of +5%
# initial size: 5 um x 5 um x 5 um

ee0 = 0.1
iterationgrowthfactor = 1.05
velocityratio = 0.1
width0 = 5 #um
length0 = 5 #um
lengthFin = 5000 #um
iterationsN = ceiling(log(lengthFin/length0)/log(iterationgrowthfactor))

# 1) Perform basecalculations
mR = (ee0 + 1)/2
mS = 1-mR
excessR = mR - mS
RsmallNormal = excessR
SsmallNormal = 0
RsmallInverse = mS
SsmallInverse = mS
RlargeNormal = mS
SlargeNormal = mS
RlargeInverse = excessR
SlargeInverse = 0
A0 = width0*width0*2 + width0*length0*4
V0 = width0*width0*length0

# 2) Define dataframe [iteration, lengthX, widthX, aArea, aAreaInv, aNum, aNumInv]
df <- data.frame(
  iteration = integer(iterationsN + 1),  # Integer column for iteration
  lengthX = numeric(iterationsN + 1),    # Numeric column for lengthX
  widthX = numeric(iterationsN + 1),     # Numeric column for widthX
  aArea = numeric(iterationsN + 1),      # Numeric column for aArea
  aAreaInv = numeric(iterationsN + 1),   # Numeric column for aAreaInv
  aNum = numeric(iterationsN + 1),       # Numeric column for aNum
  aNumInv = numeric(iterationsN + 1)     # Numeric column for aNumInv
)

# 3) Run iterations
for (iterationX in 0:iterationsN) {
  df$iteration[iterationX+1] = iterationX
  if (iterationX>0){
    # I. Grow the crystal ...
    lengthC = iterationgrowthfactor*df$lengthX[iterationX]
    widthC = df$widthX[iterationX] + lengthC*((iterationgrowthfactor-
1)/iterationgrowthfactor)*velocityratio
    df$lengthX[iterationX+1] = lengthC
    df$widthX[iterationX+1] = widthC
    # ... and calculate its dimension numbers
    Acryst = widthC*widthC*2 + widthC*lengthC*4
    Vcryst = widthC*widthC*lengthC
  }else{
    df$lengthX[iterationX+1] = length0
    df$widthX[iterationX+1] = width0
    Acryst = A0
```

```
  Vcryst = V0
 }

 # II. Calculate Relative Rates for Area cases
 # IIa. Normal Case
 kRsmall = A0*RsmallNormal/V0
 kSsmall = A0*SsmallNormal/V0
 kRlarge = Acryst*RlargeNormal/Vcryst
 kSlarge = Acryst*SlargeNormal/Vcryst
 kee = ((kRsmall+kRlarge) - (kSsmall+kSlarge))/(sum(c(kRsmall,kSsmall,kRlarge,kSlarge)))
 ampf = kee/ee0
 df$aArea[iterationX+1] = ampf

 # IIb. Inverse Case
 kRsmall = A0*RsmallInverse/V0
 kSsmall = A0*SsmallInverse/V0
 kRlarge = Acryst*RlargeInverse/Vcryst
 kSlarge = Acryst*SlargeInverse/Vcryst
 kee = ((kRsmall+kRlarge) - (kSsmall+kSlarge))/(sum(c(kRsmall,kSsmall,kRlarge,kSlarge)))
 ampf = kee/ee0
 df$aAreaInv[iterationX+1] = ampf

 # III. Calcluate Relative Rates for Number cases
 # IIIa. Normal Case
 kRsmall = RsmallNormal/V0
 kSsmall = SsmallNormal/V0
 kRlarge = RlargeNormal/Vcryst
 kSlarge = SlargeNormal/Vcryst
 kee = ((kRsmall+kRlarge) - (kSsmall+kSlarge))/(sum(c(kRsmall,kSsmall,kRlarge,kSlarge)))
 ampf = kee/ee0
 df$aNum[iterationX+1] = ampf

 # IIIb. Inverse Case
 kRsmall = RsmallInverse/V0
 kSsmall = SsmallInverse/V0
 kRlarge = RlargeInverse/Vcryst
 kSlarge = SlargeInverse/Vcryst
 kee = ((kRsmall+kRlarge) - (kSsmall+kSlarge))/(sum(c(kRsmall,kSsmall,kRlarge,kSlarge)))
 ampf = kee/ee0
 df$aNumInv[iterationX+1] = ampf
}

write.csv(df, file = "output_sizeratioeffect.csv", row.names = FALSE)
```

In this example calculation, we start with two initial crystal populations of different size and mass (i.e. giving an enantiomeric excess). The chosen initial *ee* by mass is 10%. The small crystals are taken as cuboids of 5 x 5 x 5 µm and are made to grow into needles by using a 1:1:10 growth velocity ratio for the growth axes. This is a crude approximation of the experimental system studied here, based on the presented microscopy data. Naturally, different sizes of large crystals are used in the calculations to predict the 'size-ratio effect'. These different sizes of large crystals are run as iterations in the script. Those iterations are iterations in increasing the initial size of the large crystal population, not iterations as in time-marching steps for simulating growth kinetics. Note also, that in these calculations only the excess

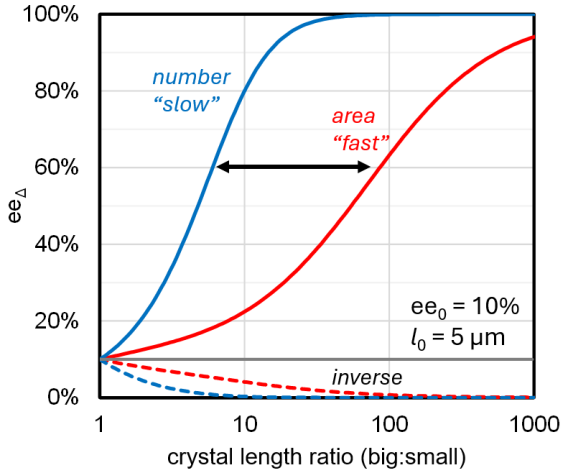


**Figure A23.** Predicted effect of the size-ratio between the small and large crystals using the computational approach outlined for both growth rates based on number ratio (G ~ N, for slow growth at low supersaturation) and area ratios (G ~ ΣA, for fast growth at higher supersaturations) of the crystals.

is made up of small ('normal case') or large crystals ('inverse case') and the racemic portion is the opposite (both cases are calculated). After these initial settings of the calculation, we proceed with a calculation of the expected ratio in growth rates of the two populations, giving an expected value of $ee_{\Delta}$. For this we use the equation and assumptions presented at the beginning of this section of the Appendix.

# Remarks specific to Chapter 6

## General Materials and Methods

### Materials

Paclobutrazol precursor **1** (1-(4-Chlorophenyl)-4,4-dimethyl-2-(1H-1,2,4-triazol-1-yl)pentan-3-one, called Cl-TAK) was synthesized as per previously reported methods.[10,11,12] Tert-leucine precursor **2** (3,3-dimethyl-2-((naphthalen-2-ylmethylene)amino)butanenitrile) was obtained over the course of previous

[10] Lopes, C.; Cartigny, Y.; Brandel, C.; Shemchuk, O.; Leyssens, T. A Greener Pathway to Enantiopurity: Mechanochemical Deracemization through Abrasive Grinding. *Chem. Eur. J.* **2023**, 29 (40), e202300585. DOI: 10.1002/chem.202300585.

[11] Bovonsombat, P.; Teecomegaet, P.; Kulvaranon, P.; Pandey, A.; Chobtumskul, K.; Tungsirisurp, S.; Sophanpanichkul, P.; Losuwanakul, S.; Soimaneewan, D.; Kanjanwongpaisan, P.; Siricharoensang, P.; Choosakoonkriang, S. Regioselective Monobromination of Aromatics via a Halogen Bond Acceptor-Donor Interaction of Catalytic Thioamide and N-Bromosuccinimide. *Tetrahedron* **2017**, 73 (46), 6631–6639. DOI: 10.1016/j.tet.2017.10.005.

[12] Qizhou, J. (Green Chemical Co., Ltd). Preparation Method of Chlorazolam. Chinese Patent CN 111777565 A, **2020**.

research.[13] Solvents, reagents, and analytical-grade chemicals were purchased from commercial suppliers and used as received unless otherwise specified. Sodium hydroxide pellets (85.0–100.5%, VWR Chemicals), 1,8-diazabicyclo[5.4.0]undec-7-ene (98+%, Acros Organics), anisole (99%, Thermo Scientific Chemicals), methanol (99%, Thermo Scientific Chemicals), and demineralized water were used in this study.

**HPLC Analysis**

Enantiomeric excess of **1** was determined using a Thermo Scientific UltiMate 3000 chiral HPLC system equipped with a Chiralcel OD-H column (4.6 mm × 250 mm, 5 µm) and UV detection at 220 nm. The mobile phase consisted of n-heptane:2-propanol (80:20, v/v) at a flow rate of 1.0 mL/min, with retention times of 7.4 min for (*R*)-**1** and 9.2 min for (*S*)-**1**. Chiral HPLC analyses of **2** were performed using an Agilent Technologies Infinity 1260 HPLC system equipped with a CHIRALPAK IA column (250 x 4.6 mm, 5µm) and UV detection at 220 nm. The mobile phase consisted of n-heptane:2-propanol (95:5, v/v) at a flow rate of 0.7 mL/min, with retention times of 5.2 min for anisole (internal standard), 7.9 min for (*S*)-**2**, and 9.1 min for (*R*)-**2**. All solvents used (n-heptane, 2-propanol) were HPLC grade (≥ 99%) and obtained from VWR chemicals.

**Solubility of 1**

The solubility of racemic **1** in MeOH:Water (60:40, v/v) was determined using a Technobis Crystal16 instrument (Alkmaar, The Netherlands) and is displayed in Figure A24.

Masses ranging from 5 to 62 mg of racemic **2** were placed in approximately 900 mg of 60 wt% methanol-water. Controlled temperature ramps from −5 °C to 60 °C were performed and repeated three times, while the turbidity was monitored to determine the clear points (solubility curve). The Van 't Hoff equation was fitted to the data between 10 °C and 60 °C.

Specifically, all samples were fully dissolved at 60 °C, where the temperature program began by cooling to -5 °C at a rate of 0.5 °C/min (2 hours and 10 minutes), followed by an isothermal hold for 5 hours. The temperature was then increased to 60 °C at 0.3 °C/min (3 hours and 36 minutes) with a final isothermal hold of 30 minutes. The solubility temperature for each sample was determined as the temperature at which transmissivity reached 100% (clear solution) during the heating cycle.

This experiment was conducted both with and without NaOH (0.1 wt% of solvent), and no significant differences in solubility temperatures were observed between the

[13] Baglai, I.; Leeman, M.; Wurst, K.; Kaptein, B.; Kellogg, R.M.; Noorduin. W.L. The Strecker reaction coupled to Viedma ripening: a simple route to highly hindered enantiomerically pure amino acids. *Chem. Commun.* **2018**, 54, 10832–10834. DOI: 10.1039/C8CC06658B.

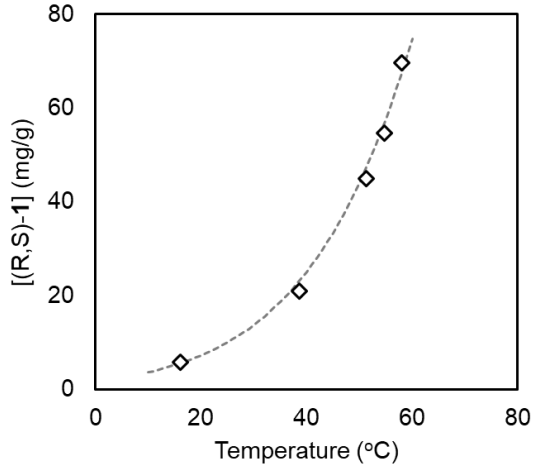


**Figure A24.** Temperature dependent solubility (diamonds) of racemic **1** in MeOH:Water (60:40, v/v). Van 't Hoff fit shown with grey dotted line.

two conditions. Additionally, no significant variations were detected across the three repeated temperature cycles, demonstrating the robustness of the measurements.

**Solubility of 2**

The solubility curve and metastable zone of racemic **2** in MeOH were similarly determined using the Technobis Crystal16 instrument and are displayed in Figure A25 (temperature range: 15 – 40 °C). The metastable zone was determined by also monitoring the cloud points (nucleation indicates end of metastable zone). The effect of racemization catalyst DBU was also assessed, showing constant elevated solubility due to the formed racemization intermediates (Fig. A25; figure on the next page).

## Deconvoluted temperature cycles

**Experimental set-up and sampling**

All experiments were conducted in 50 mL jacketed round-bottom flasks equipped with a magnetic stir bar and connected to a LAUDA ECO RE 630 S thermostat for precise temperature control. The stirring rate was set at 500 rpm. Methanol/water (60 wt% methanol) was chosen as the solvent system due to its optimal solubility profile of **1**. Racemization was achieved by adding NaOH (0.1 wt% of solvent).

Samples were taken at specific time points during the TCID (temperature cycling-induced deracemization, i.e. cycles of heating and cooling to induce dissolution and growth) cycles: (1) before initiating heating to determine the initial solid phase enantiomeric excess, (2) after the isothermal hold following dissolution, and (3) after

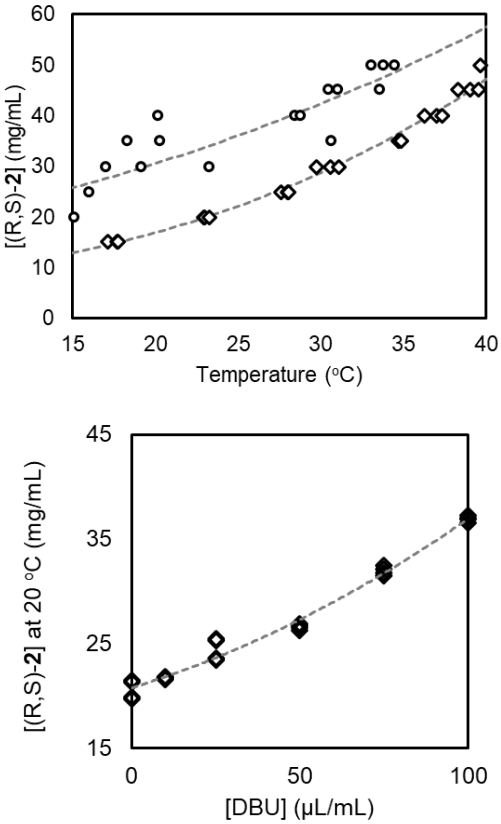


**Figure A25.** Temperature dependent solubility (diamonds) and metastable zone (circles) for racemic **2** in MeOH (top) and effect of [DBU] on the room temperature solubility (bottom). Van 't Hoff fit shown with grey dotted line.

the isothermal hold following growth. Approximately 0.3 mL of suspension was withdrawn using a plastic pipette. To prevent racemization during analysis, the solids were rapidly filtered, washed with aqueous HCl (6 M), and subsequently dissolved in methanol for analysis.

The seeds for temperature cycling are prepared by dissolving a mixture of racemic and enantiopure **1** (total 2.7 g) in methanol (18 g) preheated to 40 °C. Deionized water (11.8 g) was then added dropwise to induce antisolvent crystallization. Racemization was initiated by introducing NaOH to the system (0.1 wt% of solvent).

**Deconvoluted temperature cycles for low, medium, high initial ee**

The deconvoluted temperature cycle is initiated by starting the temperature program. The temperature cycle consisted of sampling, heating from 40 °C to 55 °C at 1.5 °C/min, holding isothermally for 10 minutes, sampling, cooling back to 40 °C at 0.5 °C/min, and holding isothermally for 10 minutes, and sampling; resulting in a

total cycle time of 60 minutes. During a cycle, 50% of the initial solids dissolve and regrow.

The effects of the initial solid phase ee were investigated by varying the initial enantiomeric excess of the seed-slurry of **1** in each experiment. Three levels of initial ee were used: low (weighed 25%, resulting in an initial 20–30% after antisolvent crystallization), medium (50, resulting in 50–55% after antisolvent crystallization), and high (90%, resulting in 80–90% after antisolvent crystallization).

**Heating rate and isothermal hold**

To exclude any effect from the heating rate, we repeated the cycle step for slurries starting with high initial ee but with fast (3 °C/min) and slow (0.25 °C/min) heating rate during the dissolution step (Table A3). The effect of different heating rate was negligible, showing that choice of heating rate did not significantly affect the asymmetric dissolution or growth.

**Table A3.** Effect of heating rate on cycling of 1, starting with high initial *ee* in (*R*)-**1**.

| | **5 min. (3 ˚C/min)** | **60 min. (0.25 ˚C/min)** |
|---|---|---|
| **Before Heating** | 98.72% | 98.92% |
| **After Heating** | 91.79% | 89.62% |
| **After Cooling** | 98.92% | 99.00% |

In addition, we investigated the effect of the length of the isothermal hold after the dissolution segment. In this experiment, we tested a short (5 min) and long (55 min) isothermal hold at 55 °C and measured the solid phase *ee* in both experiments (Table A4). No significant difference is observed between the experiments, and a sharp decrease in *ee* due to antagonistic effects of dissolution is observed immediately.

**Table A4.** Effect of isothermal hold on dissolution of 1, starting with high initial *ee* in (*R*)-**1**.

| | solid *ee* (%) |
|---|---|
| Before heating (40 °C) | 99.1 |
| 5 minutes after reaching 55°C | 91.6 |
| 55 minutes after reaching 55°C | 92.1 |
| After cooling (40°C) | 99.8 |

**Relative amount of seed crystals**

We also varied the total mass of **1** in each experiment while keeping the total solvent mass constant. This approach ensured control over the percentage of the suspension that underwent dissolution and crystallization at the start of each experiment. Three groups were defined based on the percentage of the suspension exchanged per temperature cycle: low (30%), medium (50%), and high (80%). The total mass of **1** was

adjusted to achieve these percentages, with 4.00 grams used for the low group, 2.70 grams for the medium group, and 1.95 grams for the high group.

We expect that increasing the relative amount of material that is dissolved and grown makes the asymmetric effects more pronounced.[14] We repeated the deconvoluted temperature cycle experiments wherein we dissolve and regrow 80% of the solids rather than the 50% in the previous experiments. As shown in Table A5, the asymmetric effects become more pronounced if the relative cyclic mass transfer is increased. Dissolution has a stronger antagonistic effect and growth has a stronger agonistic effect on chiral amplification when the relative amount of dissolved and grown material is increased.

**Table A5.** Effect of relative amount of seed crystals on asymmetric dissolution and growth of **1**, controlled through varying the relative amount of solids that dissolve and grow (cyclic mass transfer) during the deconvoluted temperature cycle experiment.

| | low initial ee | | medium initial ee | | high initial ee | |
|---|---|---|---|---|---|---|
| rel. cyclic mass transfer | 50% | 80% | 50% | 80% | 50% | 80% |
| ee before dissolution (%) | 27.9 | 31.8 | 56.6 | 51.3 | 91.9 | 85.8 |
| ee after dissolution (%) | 55.4 | 39.7 | 80.8 | 43.0 | 87.8 | 66.7 |
| ee after growth (%) | 47.8 | 66.8 | 84.3 | 97.4 | 97.5 | 96.2 |

## Dissymmetry between dissolution and growth

### Experimental set-up and sampling

Experiments were conducted in 7 mL vials sourced from Merck (27150-U Supelco). An aluminum block with milled holes for vials was fabricated in-house and placed on top of a shaker (VWR Standard vortex mixer). Temperature was controlled through a thermostat (Huber Heat Regulator RS2232, range: 5 – 60 °C). To ensure homogenization and minimize attrition and secondary nucleation, we used PTFE beads (3 mm PTFE balls, BOLA). To the solvent (MeOH), we added an internal standard (0.2 wt% anisole) to allow the determination of liquid phase concentration in samples to ascertain a full mass balance.

For seed crystal preparation, a 20 mL vial was charged with 5 g of glass beads (2 mm glasschrot, through VWR), 750 mg of **2** (~50% ee in (*R*)-**2**, by mixing enantiopure (*R*)-**2** and racemic **2**), and 5 mL 2-propanol. The vial was sonicated for 5 hours at low temperature (10 °C). After sonication, the vail was allowed to equilibrate in the fridge, before filtration over a P4 glass filter afforded a fine and homogeneous white solid. The *ee* of the obtained seed crystals was determined by HPLC analysis to be 50.89% in (*R*)-**2**.

[14] Van Dongen, S. W., et al. Chiral Amplification through the Interplay of Racemizing Conditions and Asymmetric Crystal Growth. *J. Am. Chem. Soc.* **2023** 145 (1), 436–442.

For sampling, we now discriminated between liquid and solid phase sampling. For liquid phase samples: 50 – 100 µL of liquid was obtained by filtering 125 µL of slurry over a syringe filter (0.2 µm PTFE, VWR International) and mixing it with 1 mL of 2-propanol by vortex. The solution was then submitted for HPLC analysis. For solid phase samples, aliquots of 0.5 – 1.0 mg of solid material were collected from the solids obtained by filtering 250 µL slurry over a P4 glass filter under vacuum. The solids were dissolved in 1.5 mL of 2-propanol by vortex and subsequent ultrasonication (10 minutes) and then submitted for HPLC analysis.

**Isolated dissolution**

For isolated dissolution, a 7 mL vial was charged with 27 mg of seed crystals and 0.7 g of PTFE spheres. Subsequently, an undersaturated solution of racemic **2** was prepared by dissolving 12 mg (*RS*)-**2** in 1 mL of MeOH (with 0.2 wt% anisole) at 20 °C in 1 mL and adding 10 µL/mL racemization catalyst (DBU). The liquid phase of the solution was analyzed. The vial with the crystal was placed in the shaker and shaking was initiated. The 1 mL solution was added to the crystals under shaking to induce instantaneous dissolution. After 90 minutes, the solid and liquid phases of the resulting slurry were analyzed.

**Isolated growth**

For isolated growth, a 7 mL vial was charged with 20 mg of seed crystals and 0.7 g of PTFE spheres. Subsequently, a saturated solution of racemic **2** was prepared at 30 °C in the presence of 10 µL/mL racemization catalyst (DBU). The liquid phase of the solution was analyzed. The vial with the crystal was placed in the shaker, kept at 30 °C, and shaking was initiated. The 1 mL solution was added to the crystals under shaking. The shaker was cooled back to 20 °C over the course of 90 minutes to induce growth. After 30 minutes, the solid and liquid phases of the resulting slurry were analyzed.

**Mass balance and $ee_\Delta$**

As shown in Chapter 4, the enantiomeric excess of grown (or dissolved) material ($ee_\Delta$) can be calculated if one knows the *ee* of the initial solid (seed crystals) denoted $ee_0$, the *ee* of the material after growth (or dissolution) denoted $ee_P$, the mass of the seed crystals (denoted $m_0$), and the mass change during growth or dissolution (denoted $m_\Delta$). The equation to calculate $ee_\Delta$ is as follows:

$$ee_\Delta = ee_P + \frac{m_0}{m_\Delta}(ee_P - ee_0) \qquad \text{(eq. 1)}$$

In our experiments, $m_0$ (weighed seed amount) and $ee_0$ (seed composition) are known at the start of the experiment. After growth or dissolution, $ee_P$ is determined by analyzing the resulting solids through chiral HPLC. Finally, $m_\Delta$ is obtained by comparing liquid phase concentration of the initial solution ($c_{\text{initial}}$) that is added to

the seed crystals and the concentration of the liquid phase of the slurry after growth or dissolution ($c_{final}$) as follows:

$$m_{\Delta} = c_{initial} - c_{final} \qquad \text{(eq. 2)}$$

We determine these concentrations through quantitative HPLC. The solvent contains anisole as internal standard, so that the concentration of (*R*)-**2** and (*S*)-**2** in solution can be quantified (Fig. A26).

This full mass balance (Table A6) hence allows calculating the exact $ee_{\Delta}$ after growth and dissolution to yield insight in what happens to the crystals during the process, rather than only viewing the initial and final *ee*.

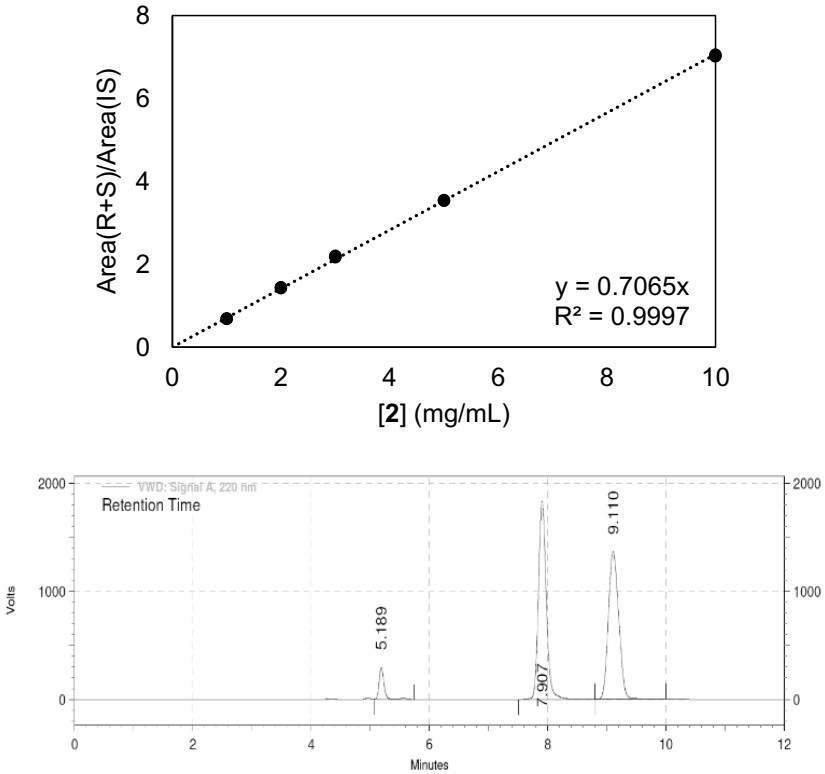


**Figure A26.** Calibration curve (top) for racemic **2** in MeOH with 0.2wt% anisole as internal standard, obtained from chiral HPLC (bottom). A quantifier for concentration is achieved by taking the peak areas of the enantiomers (7.9 min for (*S*)-2, and 9.1 min for (*R*)-2) relative to the peak area of the internal standard (5.2 min for anisole).

**Table A6.** Full mass balance results with determined values of $ee_0$, $ee_\Delta$, and final ee. Figure numbers refer to the main text of the Chapter.

| | | dissolution | | |
|---|---|---|---|---|
| | | solid mass R (mg/mL) | solid mass S (mg/mL) | *ee* |
| | initial (0) | 20.37 | 6.63 | 50.9% |
| [Fig. 3b] | final | 14.80 | 2.38 | 72.3% |
| [Fig. 3d] | change (Δ) | -5.57 | -4.25 | 13.5% |

| growth | | |
|---|---|---|
| solid mass R (mg/mL) | solid mass S (mg/mL) | *ee* |
| 15.09 | 4.91 | 50.9% |
| 22.80 | 10.43 | 37.2% |
| 7.71 | 5.52 | 16.6% |

**Effect of racemization rate**

To assert the effect of racemization rate, the isolated dissolution and growth experiments were repeated at various concentrations of racemization catalyst (DBU): 0, 10, 25, 50, 75 µL/mL for dissolution and 5, 15, 25, 50 µL/mL for growth. The initial amount of seed crystals was as described previously, but the concentration of the undersaturated solution for dissolution was adapted to the changed solubility due to changed DBU concentration (11, 13.5, 16, 18.5 mg/mL for 10, 25, 50, 75 µL/mL DBU respectively).

## One-time switching off racemization in a temperature cycle

Two identical TCID experiments of **1** were set up with an initial solid phase ee of 20% in (*R*)-**1** and temperature cycling was induced for three full cycles to reach a solid phase ee of 40 – 45% in (*R*)-**1**. After four more temperature cycles (parameters as before), one experiment proceeded without modification, while in the other, racemization was switched off. To achieve this, the temperature program was paused at 40 °C, and 6 mL of 6 M aq. HCl solution was added in excess to fully neutralize NaOH and ensure no racemization occurred. Neutralization was confirmed by a color change from dark blue to red on pH paper. The suspension was then stirred isothermally for 10 minutes before resuming the temperature program (heating segment for final non-racemizing dissolution step). Before the cooling segment to induce the final growth step, racemization catalyst was re-added (0.2 wt% NaOH).

## Thermodynamic Analysis using Phase Diagrams

To evaluate the applicability of conventional thermodynamic models to TCID, experimental results were compared to predictions based on ternary phase diagrams. These diagrams describe the phase behavior of enantiomers under equilibrium conditions, assuming ideal mixing and no kinetic effects.

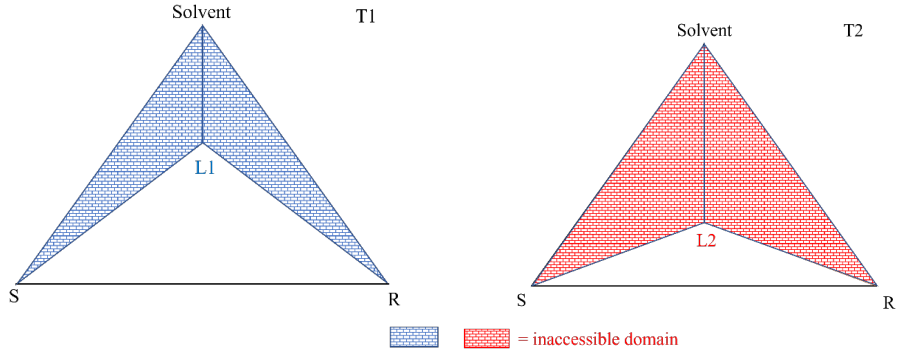


**Figure A27.** Theoretical Ternary Isotherms of a conglomerate forming system at T1 and T2 with T2>T1 and instant racemization in the solution. Due to the instant racemization in solution, phases can only exist along the segment represented by the pure solvent and point L1/L2 and in the white triangle L1/L2—<S>—<R>.

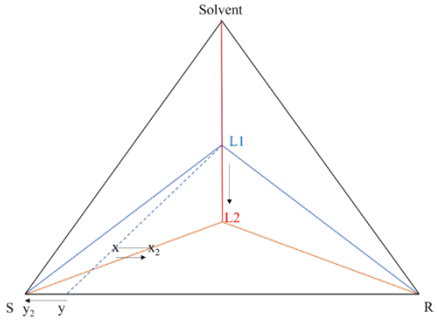


**Figure A28.** Theoretical evolution on heating described by the superimposition of two ternary isotherms at T1 and T2 where T2 > T1 and instant racemization in the liquid state. The overall composition of x at T1 gives solid composition of y, and shifts to x2 and y2 (pure enantiomer) at T2.

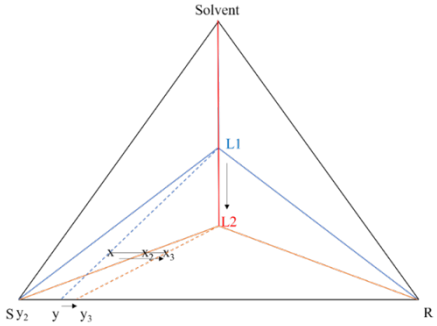


**Figure A29.** Experimentally observed evolution on heating described by the superimposition of two ternary isotherms at T1 and T2 where T2>T1 and instant racemization in the liquid state. The overall composition of x at T1 shifts to x3 instead of x2, resulting in a decreased solid composition of y3.

In a non-racemizing solution, both enantiomers dissolve according to their solubilities at a given temperature. If a scalemic solid mixture is heated, dissolution

occurs until the system reaches equilibrium with the saturated solution phase. In some cases, if the minor enantiomer dissolves completely before equilibrium is reached, the remaining solid phase consists entirely of the major enantiomer, and the solution exhibits an excess of the major enantiomer after dissolution. Conventional ternary phase diagrams predict that heating a scalemic mixture should generally result in an increase in enantiomeric excess of the solid phase as dissolution progresses.

However, experimental results show significant and repeatable deviations from these predictions in the presence of instantaneous racemization. In a racemizing solution, the solution cannot sustain an enantiomeric excess, as racemization continuously interconverts enantiomers in solution (Fig. A27). This fundamentally alters the accessible phase space in the ternary system, preventing the expected increase in enantiomeric excess upon heating (Fig. A28). Instead, in several observed cases, a decrease in enantiomeric excess occurs experimentally, demonstrating that ternary phase diagrams alone cannot always accurately describe systems undergoing active racemization (Fig. A29).

*Note*: The inaccessible domains in Figures A28 and A29 are not shaded to improve legibility.

## Model for asymmetric growth and dissolution

We adapt the empirical model for chiral amplification through asymmetric crystal growth under racemizing conditions presented in Chapter 4, that is based on a so-called amplification factor and makes no further assumptions on the underlying source of chiral amplification.

In short, the model empirically describes the extent of asymmetry during a growth or dissolution step using the amplification factor α defined by

$$\alpha = \frac{ee_{\Delta}}{ee_0} \qquad \text{(eq. 3)}$$

One then rewrites eq. 1 and 3 to yield a description of the evolution of solid phase *ee* after a dissolution or growth step as:

$$ee_P = ee_0 \cdot \left( \frac{\frac{m_0}{m_{\Delta}} + \alpha}{\frac{m_0}{m_{\Delta}} + 1} \right) \qquad \text{(eq. 4)}$$

This equation was numerically implemented by calculating the evolution of *ee* as a function of cycles consisting of an initial dissolution segment (with a specific value of $\alpha$ for dissolution) and a subsequent growth segment (with a specific value of $\alpha$ for growth). The final *ee* of the growth segment was taken as the $ee_0$ for the next cycle. Note that for the growth segment, $m_0 \rightarrow m_0 - m_{\Delta}$.

As values for the two amplification factors (which were assumed to be independent of $ee_0$, since this was the case in Chapter 4), we used the predicted plateaus of **2** to estimate $\alpha_{\text{disolution}} = 0.6$ and $\alpha_{\text{growth}} = 0.8$. These were the closest values we could relate to our experiments here. Of course, in reality, a sigmoidal shape would be expected for kinetics since size distributions change and $\alpha$ will disperse with evolving crystal populations and *ee*. We then ran numerical calculations using $ee_0$ = 0.1, $m_0$ = 27 and $m_\Delta$ = 7, although these only affect scaling.

To assess the effect of switching on and off racemization during dissolution or growth segments, we set $\alpha_{\text{disolution}} = 0$ or $\alpha_{\text{growth}} = 0$ respecitvely.

The script used to perform the numerical calculations, using software package "R",[15] is provided below as Script S-1.

**Script S-1.** Numerical implementation of the adapted model in R.

```
# Functions
calculateEE <- function(R, S){
  return((R - S)/(R + S))
}
calculateR <- function(ee, m){
  return(0.5*(ee + 1)*m)
}
calculateS <- function(ee, m){
  return(m - calculateR(ee, m))
}

# Parameters
ee0 = 0.1
m0 = 27
mD = 7
alfaG = 0.8
alfaD = 0.6
steps = 30

# Simulation
df <- data.frame(
  iteration = numeric(steps*2+ 1),  # Iteration
```

[15] R Core Team (**2021**). R: A language and environment for statistical computing. R Foundation for Statistical Computing, Vienna, Austria. https://www.R-project.org/.

```
  regR = numeric(steps*2+ 1),    # R for regular TC
  regS = numeric(steps*2+ 1),     # S for regular TC
  regee = numeric(steps*2+ 1),     # ee for regular TC
  grOnlyR = numeric(steps*2+ 1),      # R for TC with racemization during growth only
  grOnlyS = numeric(steps*2+ 1),   # S for TC with racemization during growth only
  grOnlyee = numeric(steps*2+ 1),   # ee for TC with racemization during growth only
  disOnlyR = numeric(steps*2+ 1),       # R for TC with racemization during dissolution only
  disOnlyS = numeric(steps*2+ 1),     # S for TC with racemization during dissolution only
  disOnlyee = numeric(steps*2+ 1)     # ee for TC with racemization during dissolution only
)

# Initial conditions
df$iteration = seq(0, steps, 0.5)
R0 = calculateR(ee0, m0)
S0 = calculateS(ee0, m0)
df[1,c(4,7,10)] <- ee0
df[1,c(2,5,8)] <- R0
df[1,c(3,6,9)] <- S0

for (i in 2:(steps*2 + 1)) {
  if(i %% 2 == 0){
    # B. Growth Step
    # Regular TC
    eeD = alfaG*df$regee[i-1]
    if(eeD > 1){
      eeD = 1
    }
    R0 = calculateR(df$regee[i-1], m0-mD)
    S0 = calculateS(df$regee[i-1], m0-mD)
    deltaR = calculateR(eeD, mD)
    deltaS = calculateS(eeD, mD)
    Rnew = R0 + deltaR
    Snew = S0 + deltaS
    eenew = calculateEE(Rnew, Snew)
    df$regR[i] = Rnew
    df$regS[i] = Snew
    df$regee[i] = eenew
```

A

```
  # Rac. Growth only
  eeD = alfaG*df$grOnlyee[i-1]
  if(eeD > 1){
    eeD = 1
  }
  R0 = calculateR(df$grOnlyee[i-1], m0-mD)
  S0 = calculateS(df$grOnlyee[i-1], m0-mD)
  deltaR = calculateR(eeD, mD)
  deltaS = calculateS(eeD, mD)
  Rnew = R0 + deltaR
  Snew = S0 + deltaS
  eenew = calculateEE(Rnew, Snew)
  df$grOnlyR[i] = Rnew
  df$grOnlyS[i] = Snew
  df$grOnlyee[i] = eenew

  # Rac. Dissolution only
  eeD = 0
  R0 = calculateR(df$disOnlyee[i-1], m0-mD)
  S0 = calculateS(df$disOnlyee[i-1], m0-mD)
  deltaR = calculateR(eeD, mD)
  deltaS = calculateS(eeD, mD)
  Rnew = R0 + deltaR
  Snew = S0 + deltaS
  eenew = calculateEE(Rnew, Snew)
  df$disOnlyR[i] = Rnew
  df$disOnlyS[i] = Snew
  df$disOnlyee[i] = eenew

}else{
  # A. Dissolution Step
  # Regular TC
  eeD = alfaD*df$regee[i-1]
  if(eeD > 1){
    eeD = 1
  }
  R0 = calculateR(df$regee[i-1], m0)
  S0 = calculateS(df$regee[i-1], m0)
```

```
deltaR = calculateR(eeD, mD)
deltaS = calculateS(eeD, mD)
if(deltaR > R0){
  deltaS = deltaS + deltaR - R0
  deltaR = R0
}
if(deltaS > S0){
  deltaR = deltaR + deltaS - S0
  deltaS = S0
}
Rnew = R0 - deltaR
Snew = S0 - deltaS
eenew = calculateEE(Rnew, Snew)
df$regR[i] = Rnew
df$regS[i] = Snew
df$regee[i] = eenew

# Rac. Growth only
eeD = 0
R0 = calculateR(df$grOnlyee[i-1], m0)
S0 = calculateS(df$grOnlyee[i-1], m0)
deltaR = calculateR(eeD, mD)
deltaS = calculateS(eeD, mD)
if(deltaR > R0){
  deltaS = deltaS + deltaR - R0
  deltaR = R0
}
if(deltaS > S0){
  deltaR = deltaR + deltaS - S0
  deltaS = S0
}
Rnew = R0 - deltaR
Snew = S0 - deltaS
eenew = calculateEE(Rnew, Snew)
df$grOnlyR[i] = Rnew
df$grOnlyS[i] = Snew
df$grOnlyee[i] = eenew
```

```
    # Rac. Dissolution only
    eeD = alfaD*df$disOnlyee[i-1]
    if(eeD > 1){
      eeD = 1
    }
    R0 = calculateR(df$disOnlyee[i-1], m0)
    S0 = calculateS(df$disOnlyee[i-1], m0)
    deltaR = calculateR(eeD, mD)
    deltaS = calculateS(eeD, mD)
    if(deltaR > R0){
      deltaS = deltaS + deltaR - R0
      deltaR = R0
    }
    if(deltaS > S0){
      deltaR = deltaR + deltaS - S0
      deltaS = S0
    }
    Rnew = R0 - deltaR
    Snew = S0 - deltaS
    eenew = calculateEE(Rnew, Snew)
    df$disOnlyR[i] = Rnew
    df$disOnlyS[i] = Snew
    df$disOnlyee[i] = eenew

  }
}

# Create Export
dfExport <- df[df$iteration %% 1 == 0, !(names(df) %in% c("regR", "regS", "grOnlyR",
"grOnlyS", "disOnlyR", "disOnlyS"))]
write.csv(dfExport, "exportedDataSimulation.csv", row.names = TRUE)
```



# Remarks specific to Chapter 7

## Binary solvent-mixture

Solvent for the binary solvent mixture (acetone, diethyl ether) was AR-grade (biosolve, VWR).

## Soxhlet-apparatus

The used Soxhlet-apparatus has a nominal chamber size of 30 mL, which was decreased to 15 mL by inserting a 22 mL vial inside the sample compartment (vial: 22 mL (27172-U Supelco); Soxhlet: 30 mL (537-0047 VWR)).

## Sampling

Two distinct sampling methods were used. One method for system sampling and one method for solid phase sampling. For both methods, samples are always taken at the end of each solvent cycle (i.e. directly after re-addition, when the solvent in the boiling flask is at maximum).

**System sampling**

A 1 mL syringe fitted with a long needle is used to collect ~ 50 µL of slurry from the boiling flask. This system sample is then dissolved in 7 mL of IPA. After brief ultrasonication (5 minutes), 1 mL is transferred to a 2 mL HPLC vial and directly submitted for HPLC analysis.

**Solid phase sampling**

A 1 mL syringe fitted with a long needle is used to collect ~ 250 µL of slurry from the boiling flask. The collected suspension was cast on top of filter paper laid down on glass filter connected to a vacuum filtration set-up (whilst under active vacuum). Two separate samples of the solids were taken using a Pasteur pipette, dissolved in 1.5 mL of IPA by vortex and ultrasonication (10 minutes, 2 mL HPLC vial) and subsequently analysed by HPLC.

## Solvent Cycling-Induced Deracemization using a Soxhlet-Apparatus

**Preliminaries**

For the solvent cycling experiments, we use a two-neck round bottom flask of 50 mL, to which we attach a Soxhlet-apparatus and a tap-water cooled condenser. The other neck is closed with a septum to allow sampling during the solvent cycling process. The Soxhlet-apparatus has a nominal volume of 30 mL, which is decreased to 15 mL by adding a closed glass vial to the sample compartment. Aluminium foil is used to prevent unwanted cooling of the glassware by air during the experiments. A batch of 250 mL of the binary solvent mixture (225 mL diethyl ether and 25 mL acetone) was prepared for use throughout the various experiments. During the solvent cycling experiments, unless stated otherwise, 28 g of PTFE beads and a stirring bar are present in the round-bottom flask (boiling flask) and stirring is performed on the highest possible setting. Experiments are performed under slight nitrogen pressure

(Schlenk line) to reduce the possibility of solvent evaporation out of the system as far as possible.

**Slurry preparation**

Starting material of **1** of a certain enantiomeric composition was prepared by mixing the required amounts of enantiopure **1** and racemic **1** in a pestle and mortar and ground until homogenous. The resulting *ee* of the starting material was always confirmed by HPLC (an example is shown in Fig. A30).

To prepare the slurry, a 20 mL vial is charged with 800 mg of compound **1**, in the desired enantiomeric composition. Subsequently, 10 mL of the solvent is added and the resulting suspension is sonicated for 30 minutes to obtain a homogenous slurry. The slurry is then transferred to the 50 mL round-bottom flask and an extra 15 mL of solvent is added to the flask.

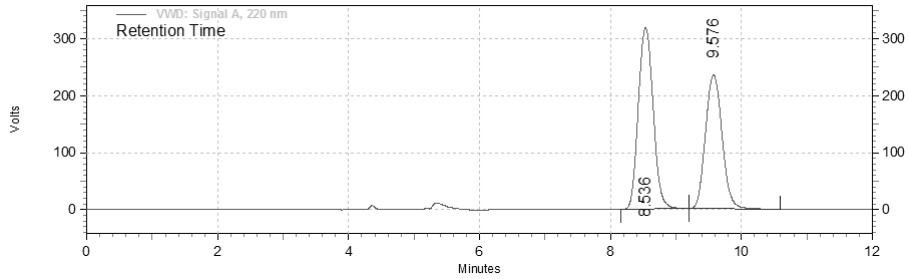


**VWD: Signal A, 220 nm Results**

| Retention Time | Area | Area % | Height | Height % |
|---|---|---|---|---|
| 8.536 | 84766089 | 54.88 | 5338022 | 57.53 |
| 9.576 | 69683447 | 45.12 | 3940171 | 42.47 |
| Totals | 154449536 | 100.00 | 9278193 | 100.00 |

**Figure A30.** Typical solid phase chromatogram of the initial seed material ($ee_0$ = 10%).

**Seminal solvent cycling experiment**

Starting material of 10% *ee* in (*R*)-**1** was used to prepare the slurry. The round-bottom flask was connected to the Soxhlet-apparatus and the condenser as described and lowered into a water bath set at 50 °C on a hotplate (maximum stirring setting). Once the solvent cycles attained a consistent time-interval (approximately 4 to 5 minutes per cycle), 40 µL of racemization catalyst (DBU) was added in 2.5 mL of solvent by syringe through the septum. After 18 hours, the solid phase and system were sampled as previously described. The seminal solvent cycling experiment was deemed successful, since virtually all material had converted to the major enantiomer. The final solid phase chromatogram is displayed as Figure A31 (>99% ee

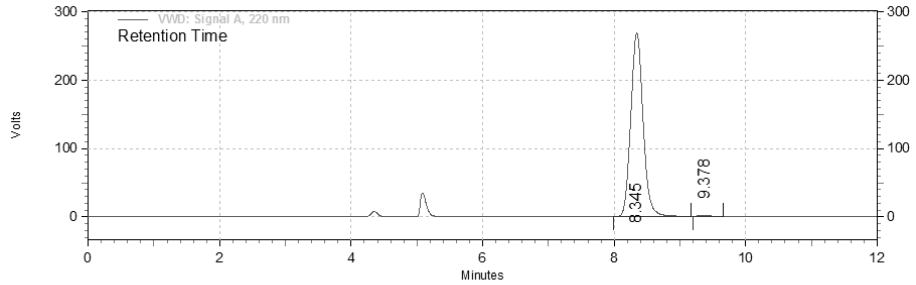


**VWD: Signal A, 220 nm Results**

| Retention Time | Area | Area % | Height | Height % |
|---|---|---|---|---|
| 8.345 | 58620914 | 99.56 | 4504637 | 99.55 |
| 9.378 | 260804 | 0.44 | 20425 | 0.45 |
| Totals | 58881718 | 100.00 | 4525062 | 100.00 |

**Figure A31.** Typical final solid phase chromatogram following a successful solvent cycling-induced deracemization experiment (t = 18 hrs, $ee_0$ = 10%).

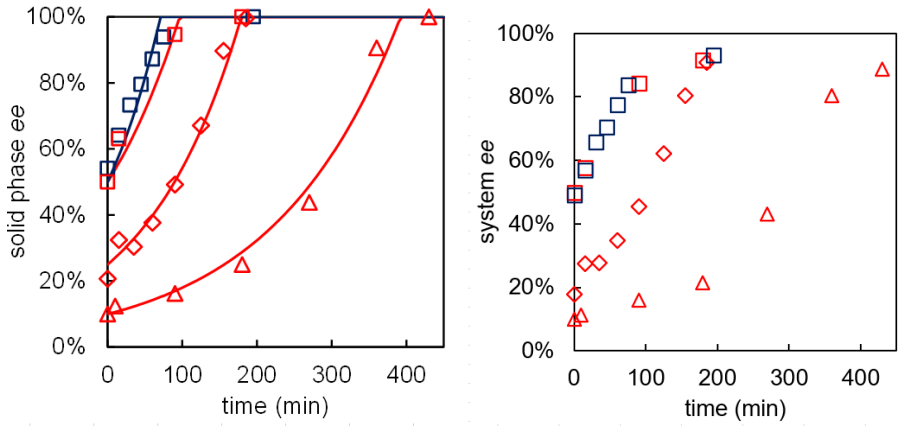


**Figure A32.** Deracemization kinetics of **1** by solvent cycling-induced deracemization. Initial *ee*: 10% (triangles), 20% (diamonds) and 50% (squares) in R (red) or S (blue). Exponential kinetic fits are represented by solid lines. The left graph shows the solid phase *ee* and the right graph shows the system *ee*.

in (*R*)-**1**). After cooling back to 20 °C, the contents of the boiling flask were filtered to afford virtually enantiopure material with 90% yield as a white residue.

## Kinetics of Solvent Cycling-Induced Deracemization

Having demonstrated the potential of Solvent Cycling-Induced Deracemization, the experiment was repeated with starting material of 10%, 20% and 50% ee in (*R*)-**1** and 50% in (*S*)-**1**. At various points after starting the experiment, solid phase and system samples were taken (Fig. A32). These experiments show that full deracemization can be achieved within 2, 3.5, and 6 hours respectively.

N.B. The system phase *ee* is always lower than the solid phase *ee* since a number of molecules is in the racemic liquid phases (soluble). This is also a reason why solubility should not be too high while cyclic mass transfer should be optimized.

**Control experiments**

In order to confirm that solvent cycling is the cause of the enantiomeric enrichment observed, and not–for example–attrition by the PTFE beads or stirring or ripening phenomena accelerated at higher temperatures, we conducted two specific control experiments. The kinetic solvent cycling experiment was repeated starting with material 10% *ee* in (*R*)-**1**.

In both experiments, the Soxhlet-apparatus is removed and the condenser is placed directly on top of the boiling flask. In this way, no–or only minimal trough refluxing–solvent cycling is achieved. These experiments were then performed in the presence of either the PTFE spheres or glass beads, since glass beads were used in the first demonstration of attrition-enhanced deracemization.[16]

The results are shown in Figure A33. Comparing of these experiments clearly demonstrates that solvent cycling, using the Soxhlet-apparatus, is vastly superior in kinetics to the two control experiments. In fact, on the relevant timescales of deracemization through solvent cycling, almost no enrichment is produced by the control experiment with PTFE beads and refluxing alone. This shows that it is the removal and re-addition of the solvent that is responsible for the enantiomeric enrichment reported here. Moreover, attrition by glass beads clearly outperforms the PTFE spheres (but still does not reach the kinetics of solvent cycling by any stretch). This shows that the soft PTFE beads are no strong source of attrition as compared to glass beads, the standard in attrition-enhanced deracemization experiments, and their impact is indeed minimal.



[16] Noorduin, Wim L., et al. "Complete Deracemization by Attrition-Enhanced Ostwald Ripening Elucidated." *Angewandte Chemie* 120.34 (2008): 6545-6547.

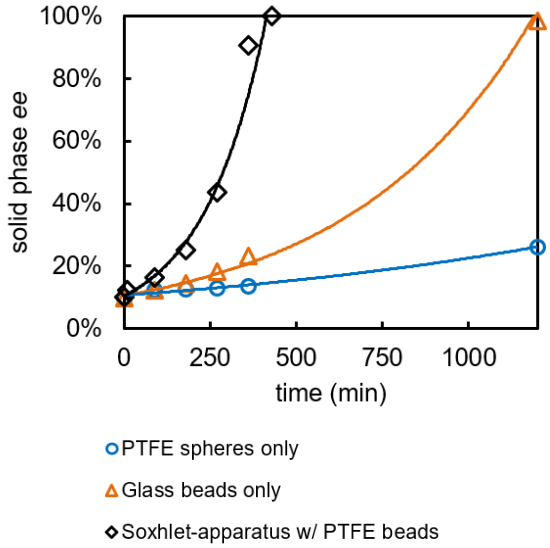


**Figure A33.** The deracemization kinetics were determined (starting with 10% *ee* in the solid phase) for three experiments: solvent cycling with a Soxhlet apparatus containing PTFE beads in the boiling flask (black diamonds), refluxing (no actual solvent cycling) with glass beads only (orange triangles), and refluxing with PTFE spheres only (blue circles). The solid lines are exponential kinetic fits.

## X-Ray Powder Diffraction Analyses

In order to exclude the presence of metastable polymorphs or solvates as key intermediates in the deracemization and confirm that no new polymorphs were formed as a starting material or final product during solvent cycling in the designed solvent, X-Ray Powder Diffraction analyses were performed on racemic reference material of **1** (unexposed), the sonicated initial slurry (before starting the solvent cycling experiment, but having been exposed to the solvent) and the final deracemized product (having been exposed to the process). For each sample, 20 – 50 mg of powder was placed on a 1 $cm^2$ aluminium square and pressed into a cake. X-Ray powder diffraction patterns of each sample were measured using a Bruker D2 Phaser with a Cu X-ray source (Cu K-α, λ = 1.5418 Å). The resulting patterns are displayed in Figure A34. These patterns are identical for all three samples, indicating that the presence of metastable polymorphs or solvates as key intermediates in the deracemization can be excluded and no new polymorphs were formed as a starting material or final product during solvent cycling in the designed solvent.

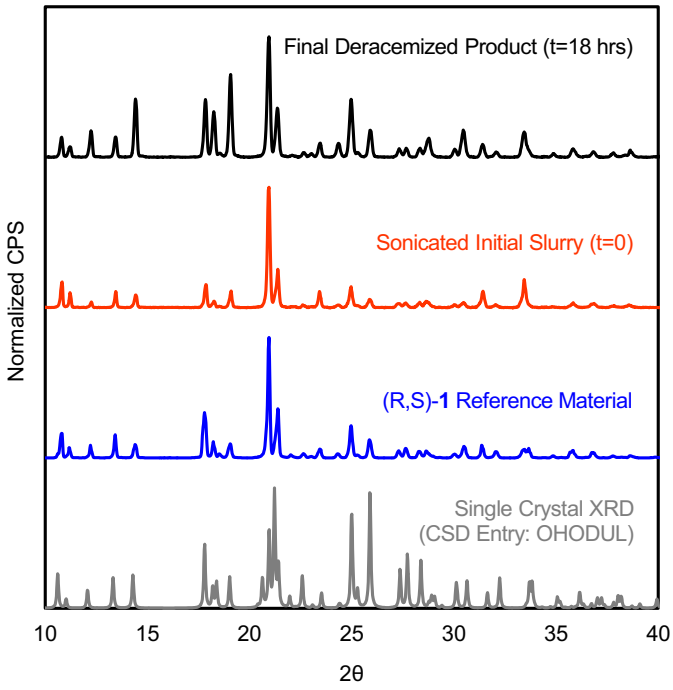


**Figure A34.** XRPD patterns for the three samples of interest: reference material of (*RS*)-**1**, the sonicated initial slurry (before starting the solvent cycling experiment, but having been exposed to the solvent) and the final deracemized product (having been exposed to the process). We have also included a Single Crystal XRD (simulated XRPD) reference from the existing CSD entry OHODUL.[17]

## Simulations for the Design of the Binary Solvent Mixture

In order to design a solvent with tailor-made composition which has a low boiling point and relatively low solubility at the boiling point, while still providing reasonably fast racemization kinetics, we use a binary solvent mixture of diethyl ether and acetone. To guide our choice in composition, we have simulated solvent cycles for various compositions, boiling points and solvent cycling geometries.

Our model consists of two compartments: the boiling flask, from which solvent is removed by evaporation, and the sample compartment, which adds all solvent condensed back to the boiling flask once a critical volume is reached—analogous to the Soxhlet-apparatus set-up.

[17] Van der Meijden, Maarten W., et al., CCDC 734087: Experimental Crystal Structure Determination, 2010, DOI: 10.5517/ccsmw7h.

**Premise and Assumptions**

In our model, we take a range of considerations into account. Not only the properties of the bare solvent are relevant. Since the solvent composition changes during the process, also the properties during the deracemization process should be considered. This means that:

- ✓ We consider that the composition of the vapour (the evaporated solvent) depends on the composition of the solvent that is boiling (in the boiling flask).
- ✓ We consider that the composition in the boiling flask changes as a result.
- ✓ We consider that the actual solubility of compound **1** and the boiling point of the solvent in the boiling flask changes over time as the composition of the solvent changes.
- ✓ We consider that that changes in solubility and volume mean that crystals have to grow or dissolve, but these processes are not instantaneous and have a mass transfer rate.

The relative amount of cyclic mass transfer is small compared to the total concentration in the solvent. We assume that changes in the boiling point and vapour pressure as a function of solute concentration can thus be neglected for these simulations.

**Underlying Datasets**

In order to accurately simulate the solvent cycling experiment for the binary diethyl ether – acetone system, we required solubility data as a function of solvent composition. Therefore, we determined the solubility for various compositions and temperatures of the solvent using the method previously reported in Chapter 4. The data, shown in Figure A35, were taken as empirical basis for the simulations.

Apart from solubility, we also required knowledge on the composition of the vapour of solvent that is boiling and the actual boiling point as a function of solvent composition. This data is modelled based on literature values and visualized in Figure A36.[18]

[18] Sameshima, Jitsusaburo. "On The System Acetone—Ethyl Ether." *Journal of the American Chemical Society* 40.10 (1918): 1482-1503.

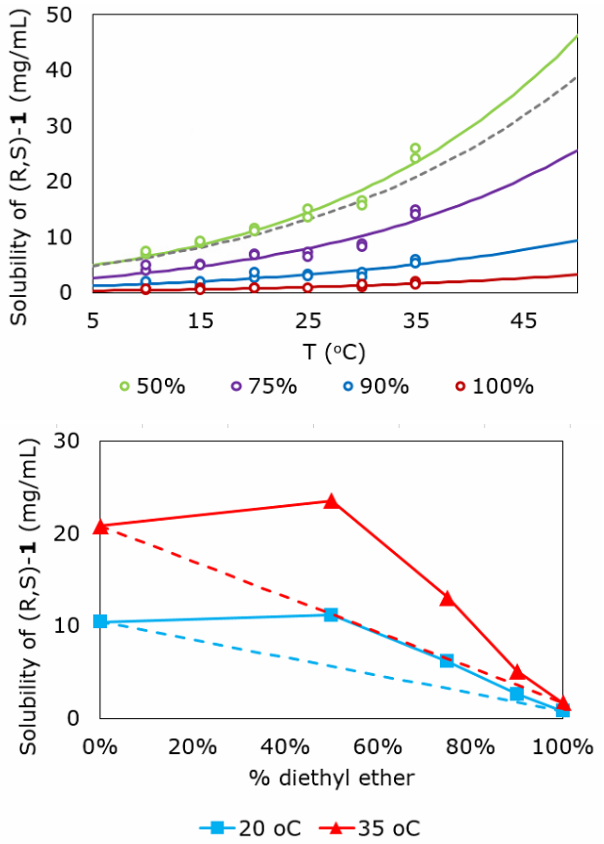


**Figure A35.** The solubility of (*RS*)-**1** was determined as a function of temperature (10 – 35 °C) and composition (0, 50, 75, 90, 100% diethyl ether in acetone; top graph). Data was fitted based on the Van 't Hoff equation (solid lines). As visualized in the bottom graph, the relationship as a function of composition is nonlinear: a certain degree of agonism is present. The grey dotted line indicates pure acetone.

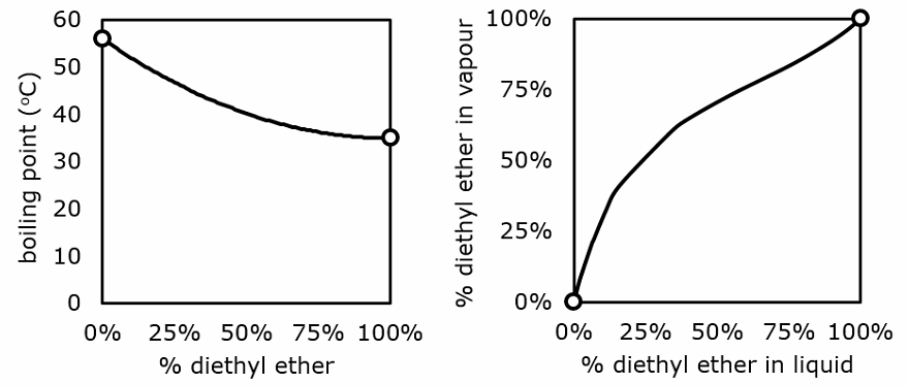


**Figure A36.** The boiling point (left) and vapour-liquid equilibrium (VLE) (right) of the diethyl ether – acetone system are shown, calculated based on literature values from Sameshima (1918).

**Equations and Implementation**

The simulation was implemented in R by following a time-marching approach.[19] To this aim, the following equations and methods were used to calculate the various variables at each time-step.

**Liquid-Vapour Equilibrium**

Composition of the vapour (solvent removed *via* evaporation) was calculated from the composition of the liquid (solvent in the boiling flask) based on an interpolation of the VLE data shown in Figure A36. Interpolation was performed using the `splinefun` method in R using a `monoH.FC` method.

**Boiling point**

To calculate the boiling point of the solvent in the boiling flask, we use the approximation:

$$\text{boiling point} = (H - L) \cdot \varphi^2 - 2 \cdot (H - L) \cdot \varphi + L$$

where H is the boiling point of the high boiling solvent (acetone), L is the boiling point of the low boiling solvent (diethyl ether) and φ is the binary solvent composition (between 0 and 1).

**Solubility**

First, composition dependent ΔH and ΔS were extracted from the solubility data shown in Figure A35. Second, the ΔH and ΔS for the actual composition of the solvent in the boiling flask was calculated by interpolation between the known values (similar method as above for VLE). Then, the solubility was predicted based on the calculated ΔH and ΔS for the actual composition. The relationship between solubility and the thermodynamic parameters ΔH and ΔS is given by the Van 't Hoff relationship:

$$\text{solubility} = \rho \cdot \exp\left( (-\Delta H/(R \cdot T)) + (\Delta S/R) \right)$$

where ρ is the density of the solvent (function of composition), R is the gas constant and T is the temperature in K.

**Removal and re-addition of solvent**

Material is removed from or re-added to the boiling flask using the following mass transfer equation:

$$dV/dt = \text{rate of mass transfer}$$

[19] R Core Team (2021). R: A language and environment for statistical computing. R Foundation for Statistical Computing, Vienna, Austria. URL https://www.R-project.org/.

where the rate is either that of removal or re-addition. The addition or removal in case of the sample compartment follows the negative sign to uphold the mass balance.

**Dissolution and Growth of crystals**

For crystal dissolution and growth, the supersaturation is first calculated based on solubility:

$$S = [(RS)\text{-}\mathbf{1}] \,/\, \text{solubility}$$

If $S < 1$, dissolution will take place. If $S > 1$, growth will take place. These processes are modelled following the approximation

$$dm/dt = rate_{growth} \cdot (S - 1)/(S_{max} - 1) \qquad \text{[for growth, if } S < S_{max}\text{]}$$

$$dm/dt = rate_{growth} \qquad \text{[for growth, if } S > S_{max}\text{]}$$

$$dm/dt = rate_{dissolution} \cdot S \qquad \text{[for dissolution]}$$

where $S_{max}$ is the so-called 'maximum supersaturation' at which the steady-state growth rate is reached and dm/dt is the mass transfer rate between solid and liquid phase.

**Time-marching implementation**

Separate volumes are tracked for acetone and diethyl ether for each of the two compartments in the implementation. At time-step 0, all parameters in the system are initialized and initial compositions are set. For each new time-step, the procedure is as follows.

First, we calculate the boiling point. If the boiling point is below or equal to the system temperature, we execute a solvent removal step. The amount of solvent to be removed is calculated and the composition of the removed solvent is based on the VLE. The removed solvent is then added to the sample compartment.

Second, we check whether the volume in the sample compartment is above the critical volume or if re-addition was busy in the previous step (if the volume of the sample compartment is at or below the 'zero-volume', we stop re-addition). If re-addition is required, we move part of the solvent from the sample compartment back into the boiling flask.

Third, we recalculate compositions of the boiling flask and the sample compartment. Based on this new data, we calculate the solubilities and execute crystal growth or dissolution.

**Simulation parameters**

Simulations were nominally performed with the following parameters. Temperature of the system was set at 50 °C. We used a sample compartment of 15 mL, initial solvent volume in the boiling flask of 25 mL and 1 mL of zero-volume (vapour lost in the system). We routinely used a maximum growth rate of 0.1 mg/s, dissolution rate of 1 mg/s, maximum supersaturation of 1.5 (c/c*), 1 mL/s solvent re-addition rate and 0.01 mL/s solvent removal rate. The amount of compound in the simulations was set at 800 mg. For time-marching, we used 15000 timesteps and each timestep was 0.5 seconds.

# Remarks specific to Chapter 8

## General Materials & Methods

**Chemicals**

Library **1** was kindly provided by InnoSyn (Geleen, NL) in both racemic and enantiopure form and used as is. For the deracemization of **1d**, the racemization catalyst was 1,8-Diazabicyclo[5.4.0]undec-7-ene (DBU, Across Organics) and the solvent was methanol sourced from Thermo Scientific Chemicals (99.9%, for spectroscopy). Library **2** was kindly provided by Symeres (Groningen, NL) in both racemic and enantiopure form and used as is. For the preferential crystallization of **2b** and **2c**, 2-propanol from VWR chemical (≥ 99%, HPLC grade) was used.

**DSC characterization method**

Thermal analyses were performed on a Netzsch DSC 214 Polyma or a DSC Q20 V24.11 Build 124 apparatuses. DSC runs were performed with ~4–5 mg of the solid sample in pierced aluminium pans and using heating rates of 5 or 10 $K.min^{-1}$. The atmosphere of the analyses was regulated by a nitrogen flux (40$mL.min^{-1}$). The Netzsch Proteus Software was used for data processing.

**HPLC analysis method**

For the determination of enantiomeric composition of samples from library **1**, chiral HPLC analyses were performed using an Agilent Technologies Infinity 1260 HPLC system. HPLC analysis was performed on a chiral column (CHIRALPAK IA (250 x 4.6 mm, 5µm)) with a mobile phase consisting of n-heptane and 2-propanol, where the eluent is mixed in a 7:3 ratio (heptane:IPA). All solvents used in these HPLC analysis (n-heptane, 1-propanol) were HPLC grade (≥ 99%) and obtained from VWR chemicals. The flow rate was 0.7 mL/min, injection volume 4 µL, and detection was performed by UV-detector (wavelength: 220 nm). Each run had a total time of 12 minutes.

For the determination of enantiomeric composition of samples from library **2**, chiral HPLC analyses were performed using an Ultimate 3000 HPLC (ThermoFisher Scientific). HPLC analysis was performed on a Phenomenex Lux Cellulose 4 column (3.0 x 150 mm x 3 µm), Chiracel OJ-H, OD-H columns (4.6 x 250 mm, 5µm) or CHIRALPAK IC column (4.6 x 250 mm, 5µm) with a UV detection at a wavelength of 220 nm with a mobile phase consisting of n-heptane and 2-propanol at flow rate of 1 mL.min−1. All solvents used in these HPLC analysis (n-heptane, 1-propanol) were HPLC grade (≥ 99%) and obtained from VWR chemicals.

## Computation of $\Delta G^{\phi}$

Melting point temperature and enthalpy of fusion were measured for the racemic ($T_m^{RS}$ and $\Delta H_f^{RS}$) and enantiopure crystals ($T_m^{R}$ and $\Delta H_f^{R}$) using DSC. Using these data, the free energy difference ($\Delta G^{\phi}$) was computed following previously developed approaches by Collet and Wilen:[20]

$$\text{if: } T_m^{RS} > T_m^{R} \Rightarrow \Delta G = \left[\Delta H_f^{RS} \cdot \left(\frac{T_m^{R}}{T_m^{RS}} - 1\right)\right] - [T_m^{R} \cdot R \cdot \ln 2] \qquad \text{(eq. 1a)}$$

$$\text{else: } T_m^{R} > T_m^{RS} \Rightarrow \Delta G = \left[\Delta H_f^{R} \cdot \left(1 - \frac{T_m^{RS}}{T_m^{R}}\right)\right] - [T_m^{RS} \cdot R \cdot \ln 2], \qquad \text{(eq. 1b)}$$

where $R$ is defined as the gas constant.

## Library 1

### Synthesis of library 1

The library **1** composed of Schiff-base derivatives of phenylglycinamide was provided by Innosyn and synthesized following the literature procedure.[21] In short, phenylglycinamide was first obtained from phenyl glycine. Subsequently, phenylglycinamide was reacted with a series of aldehydes to give library **1** (Table A7).

### DSC characterization of library 1

Racemic and enantiopure solids from library **1** were analysed using DSC following the procedure described in a previous section. From the DSC measurements we obtained the melting point and enthalpy of fusion of the racemic solid ($T_m^{RS}$ and $\Delta H_f^{RS}$) and the enantiopure solid ($T_m^{R}$ and $\Delta H_f^{R}$). Using equation 1, we computed the free energy difference ($\Delta G^{\phi}$) (Table A7).

[20] Jacques, J.; Collet, A.; Wilen, S. H. *Enantiomers, Racemates, and Resolutions*; Krieger Publishing Company: Malabar, 1994.

[21] Noorduin, W. L.; Izumi, T.; Millemaggi, A.; Leeman, M.; Meekes, H.; Van Enckevort, W. J. P.; Kellogg, R. M.; Kaptein, B.; Vlieg, E.; Blackmond, D. G. Emergence of a Single Solid Chiral State from a Nearly Racemic Amino Acid Derivative. J. Am. Chem. Soc. 2008, 130 (4), 1158–1159. https://doi.org/10.1021/ja7106349.

**Table A7:** DSC measurements of melting temperatures and enthalpies of fusion for racemates ($T_m^{RS}$ and $\Delta H_f^{RS}$) and enantiopure solids ($T_m^R$ and $\Delta H_f^R$) of library **1**, and the computed free energy differences ($\Delta G^{\Phi}$).

| Entry | Compound | $T_m^{RS}$ (K) | $\Delta H_f^{RS}$ (kcal/mol) | $T_m^R$ (K) | $\Delta H_f^R$ (kcal/mol) | $\Delta G^{\Phi}$ (kcal/mol) |
|---|---|---|---|---|---|---|
| **1b** | (E)-2-((2-fluorobenzylidene)- amino)-2-phenylacetamide | 403 | - | 430 | 8.39 | 0.03 |
| **1a** | (E)-2-((2-methylbenzylidene)-amino)-2-phenylacetamide | 430 | 8.20 | 453 | 9.59 | 0.09 |
| **1c** | (E)-2-((2-chlorobenzylidene)-amino)-2-phenylacetamide | 427 | 9.32 | 451 | 9.00 | 0.10 |
| **1d** | (E)-2-((2-bromobenzylidene)-amino)-2-phenylacetamide | 413 | - | 436 | 8.57 | 0.11 |
| **1e** | (E)-2-(benzylideneamino)-2-phenylacetamide | 399 | 7.63 | 419 | 7.40 | 0.19 |
| **1o** | (E)-2-((4-bromobenzylidene)-amino)-2-phenylacetamide | 430 | 9.70 | 446 | 9.25 | 0.26 |
| **1n** | (E)-2-((4-chlorobenzylidene)-amino)-2-phenylacetamide | 413 | 8.41 | 427 | 8.41 | 0.29 |
| **1i** | (E)-2-((3-bromobenzylidene)-amino)-2-phenylacetamide | 396 | 8.41 | 407 | 8.34 | 0.33 |
| **1h** | (E)-2-((3-chlorobenzylidene)-amino)-2-phenylacetamide | 390 | 8.80 | 397 | 7.89 | 0.39 |
| **1f** | (E)-2-((2-methoxybenzylidene)- amino)-2 phenylacetamide | 461 | 7.31 | 462 | 10.07 | 0.62 |
| **1j** | (E)-2-((3-fluorobenzylidene)- amino)-2-phenylacetamide | 393 | 7.26 | 386 | 7.26 | 0.66 |
| **1s** | (E)-2-((4-hydroxybenzylidene)- amino)-2-phenylacetamide | 425 | 4.86 | 410 | 4.38 | 0.73 |
| **1l** | (E)-2-((3-methoxybenzylidene)- amino)-2-phenylacetamide | 415 | 9.49 | 402 | 12.12 | 0.84 |
| **1g** | (E)-2-((2-hydroxybenzylidene)- amino)-2-phenylacetamide | 429 | 7.90 | 413 | 7.78 | 0.86 |
| **1r** | (E)-2-((4-methoxybenzylidene)- amino)-2-phenylacetamide | 404 | 6.86 | 364 | 5.58 | 1.17 |
| **1p** | (E)-2-((4-fluorobenzylidene)- amino)-2-phenylacetamide | 427 | 9.40 | 394 | 9.40 | 1.26 |
| **1q** | (E)-2-((4-methylbenzylidene)-amino)-2-phenylacetamide | 403 | 7.96 | 428 | 9.47 | - |



**Remarks on Table A7**

**1b)** Exothermic phase transition upon melting. $\Delta G^{\Phi}$ has been estimated following its linear correspondence to $\Delta T^{(RS-R)}$, as shown in Figure A37.

**1d)** Exothermic phase transition upon melting. $\Delta G^{\Phi}$ has been estimated following its linear correspondence to $\Delta T^{(RS-R)}$, as shown in Figure A37.

**1k)** Could not be crystallized, was not characterized by DSC, and is therefore not included in Table A7.

**1m)** Could not be crystallized, was not characterized by DSC, and is therefore not included in Table A7.

**1q)** Stable racemic compound which shows non-ideal thermodynamic behavior due to interactions between the two enantiomers in the melt and solution phase. This non-ideality invalidates the assumptions made underlying eq. 1 so that $\Delta G^{\phi}$ would not reflect the actual energy difference between the crystal phases.

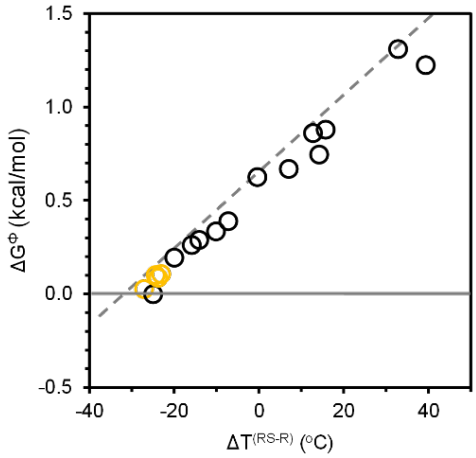


**Figure A37:** Difference in free energy between the racemate and the enantiopure form ($\Delta G^{\Phi}$) as a function of the difference in the temperature between the racemate and the enantiopure form $\Delta T^{(RS\text{-}R)}$ (°C) showing a linear relationship. Fitted equation: $\Delta G^{\Phi} \approx 0.02 \cdot \Delta T^{(RS\text{-}R)} + 0.6$.

**Deracemization of 1d**

A 7 mL vial (27150-U Supelco, Merck) was charged with 20 mg of (*R*)-**1d** and 100 mg of racemate (Fig. A38a), to yield a starting composition of the solid with 17% enantiomeric excess in *R*. Subsequently, a stirring bar (6x3mm cylindrical PTFE stirring bar, VWR), 1 g of glass beads (borosilicate, 2 mm diam.), and 1 mL of methanol (MeOH) were added to the solid, and the vial was briefly vortexed. To start the conversion, 20 µL of DBU was added and the slurry was stirred vigorously for 3 hours. After these 3 hours, the enantiomeric excess of the solid was determined by casting the slurry on top of filter paper laid down on a P5 glass filter connected to a vacuum filtration set-up (whilst under active vacuum). A sample of the solid (~1 mg) was then taken using a Pasteur pipette, dissolved in 1.5 mL of 2-propanol by ultrasonication, and submitted to HPLC analysis (Fig. A38b). The HPLC analysis showed a final composition of the solid of 97.9% enantiomeric excess in *R*, implying virtually full deracemization of 1d towards the desired *R*-enantiomer.

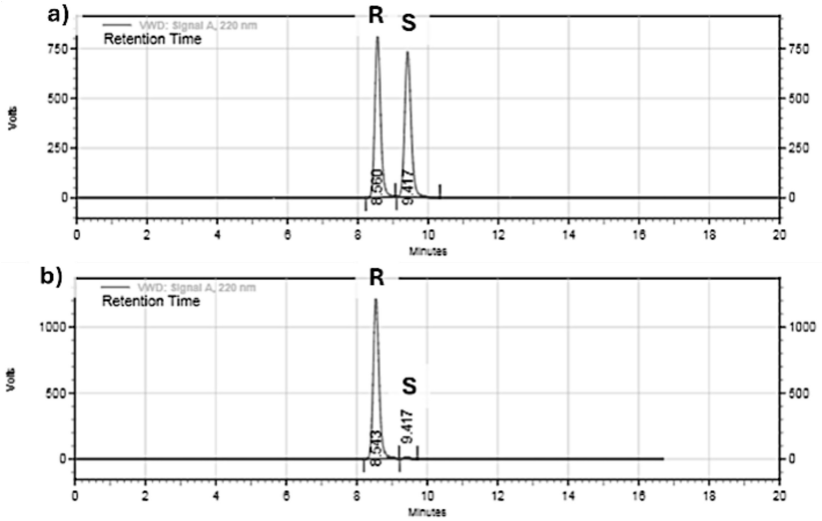


**Figure A38:** HPLC chromatograms of (a, top) the racemate of **1d**, showing peaks for both (*R*)-**1d** and (*S*)-**1d** in equal amounts, and (b, bottom) the solid obtained after the deracemization procedure, showing virtually only (*R*)-**1d** remaining.

# Library 2

## Synthesis of Library 2

The library **2** composed Praziquantel derivatives was provided by Symeres and synthesized following the literature procedure.[22] In short, different library entries were created by reacting praziquanamine with various acyl chlorides to give library **2** (Table A8).

## DSC characterization of library 2

Racemic and enantiopure solids from library **2** were analysed using DSC following the procedure described in a previous section. From the DSC measurements we obtain the melting point and enthalpy of fusion of the racemic solid ($T_m^{RS}$ and $\Delta H_f^{RS}$) and the enantiopure solid ($T_m^R$ and $\Delta H_f^R$). Using equation 1, we compute the free energy difference ($\Delta G^{\phi}$) (Table A8).

[22] Valenti, G.; Tinnemans, P.; Baglai, I.; Noorduin, W. L.; Kaptein, B.; Leeman, M.; ter Horst, J. H.; Kellogg, R. M. Combining Incompatible Processes for Deracemization of a Praziquantel Derivative under Flow Conditions. *Angew. Chem.* **2021**, *133* (10), 5339–5342. https://doi.org/10.1002/ange.202013502.

**Table A8.** DSC measurements of melting temperatures and enthalpies of fusion for racemates ($T_m^{RS}$ and $\Delta H_f^{RS}$) and enantiopure solids ($T_m^R$ and $\Delta H_f^R$) of library **2**, and the computed free energy differences ($\Delta G^{\phi}$).

| Entry | Compound | $T_m^{RS}$ (K) | $\Delta H_f^{RS}$ (kcal/mol) | $T_m^R$ (K) | $\Delta H_f^R$ (kcal/mol) | $\Delta G^{\phi}$ (kcal/mol) |
|---|---|---|---|---|---|---|
| **2a** | 2-pivaloyl-1,2,3,6,7,11b-hexahydro-4H-pyrazino[2,1-a]isoquinolin-4-one | 425 | 7.94 | 454 | 8.79 | 0.03 |
| | | 428 | 7.30 | | | 0.08 |
| **2b** | 2-isobutyryl-1,2,3,6,7,11b-hexahydro-4H-pyrazino[2,1-a]isoquinolin-4-one | 388 | 5.54 | 419 | 7.42 | -0.02 |
| | | 391 | 6.25 | | | 0.03 |
| **2c** | 2-acetyl-1,2,3,6,7,11b-hexahydro-4H-pyrazino[2,1-a]isoquinolin-4-one | 415 | 6.14 | 454 | 6.28 | 0.03 |
| | | 417 | 6.60 | | | 0.06 |
| | | 421 | 5.36 | | | 0.13 |
| **2d** | 2-propionyl-1,2,3,6,7,11b-hexahydro-4H-pyrazino[2,1-a]isoquinolin-4-one | 421 | 8.54 | 423 | 7.67 | 0.53 |
| **2e** | 2-(2,2-dimethylbutanoyl)-1,2,3,6,7,11b-hexahydro-4H-pyrazino[2,1-a]isoquinolin-4-one | 438 | 8.51 | 400 | 6.62 | 1.30 |
| **2f** | 2-(cyclopropanecarbonyl)-1,2,3,6,7,11b-hexahydro-4H-pyrazino[2,1-a]isoquinolin-4-one | 400 | 4.95 | 422 | 5.57 | 0.25 |
| | | 418 | 9.81 | | | 0.51 |
| | | 422 | 5.89 | | | 0.58 |
| **2g** | 2-(cyclopentanecarbonyl)-1,2,3,6,7,11b-hexahydro-4H-pyrazino[2,1-a]isoquinolin-4-one | 407 | 7.88 | 413 | 6.18 | 0.47 |
| **2h** | 2-(cyclohexanecarbonyl)-1,2,3,6,7,11b-hexahydro-4H-pyrazino[2,1-a]isoquinolin-4-one | 414 | 8.14 | 384 | 5.64 | 1.11 |
| **2i** | 2-(4-(tert-butyl)benzoyl)-1,2,3,6,7,11b-hexahydro-4H-pyrazino[2,1-a]isoquinolin-4-one | 476 | 8.59 | 458 | 8.07 | 0.96 |
| **2j** | 2-(4-methoxybenzoyl)-1,2,3,6,7,11b-hexahydro-4H-pyrazino[2,1-a]isoquinolin-4-one | 491 | 9.78 | 482 | 12.5 | 0.85 |
| **2k** | 2-(2-methylbenzoyl)-1,2,3,6,7,11b-hexahydro-4H-pyrazino[2,1-a]isoquinolin-4-one | 390 | 5.25 | 379 | 4.01 | 0.67 |
| **2l** | 2-benzoyl-1,2,3,6,7,11b-hexahydro-4H-pyrazino[2,1-a]isoquinolin-4-one | 438 | 8.27 | 408 | 4.88 | 1.14 |
| **2m** | 2-(2-phenylacetyl)-1,2,3,6,7,11b-hexahydro-4H-pyrazino[2,1-a]isoquinolin-4-one | 394 | 6.06 | 389 | 4.88 | 0.61 |
| **2n** | 2-(4-methylbenzoyl)-1,2,3,6,7,11b-hexahydro-4H-pyrazino[2,1-a]isoquinolin-4-one | 460 | 8.70 | 459 | 8.96 | 0.65 |
| **2o** | 2-(4-ethylbenzoyl)-1,2,3,6,7,11b-hexahydro-4H-pyrazino[2,1-a]isoquinolin-4-one | 447 | 9.15 | 414 | 6.07 | 1.24 |
| **2p** | 2-(4-fluorobenzoyl)-1,2,3,6,7,11b-hexahydro-4H-pyrazino[2,1-a]isoquinolin-4-onecc | 460 | 7.35 | 479 | 9.78 | 0.24 |
| **2q** | 2-(4-chlorobenzoyl)-1,2,3,6,7,11b-hexahydro-4H-pyrazino[2,1-a]isoquinolin-4-onebbr | 491 | 11.7 | 510 | 12.4 | 0.21 |

| | | | | | | |
|---|---|---|---|---|---|---|
| **2r** | 2-(4-bromobenzoyl)-1,2,3,6,7,11b-hexahydro-4H-pyrazino[2,1-a]isoquinolin-4-one | 487 | 10.8 | 511 | 8.55 | 0.27 |
| **2s** | 2-(2,4-dichlorobenzoyl)-1,2,3,6,7,11b-hexahydro-4H-pyrazino[2,1-a]isoquinolin-4-one | 411 | 5.90 | 431 | 7.39 | 0.24 |
| **2t** | 2-(4-nitrobenzoyl)-1,2,3,6,7,11b-hexahydro-4H-pyrazino[2,1-a]isoquinolin-4-one | 485 | 9.58 | 498 | 9.84 | 0.41 |
| **2u** | 2-isonicotinoyl-1,2,3,6,7,11b-hexahydro-4H-pyrazino[2,1-a]isoquinolin-4-one | 413 | 6.90 | 437 | 6.13 | 0.24 |
| **2v** | 4-(4-oxo-1,3,4,6,7,11b-hexahydro-2H-pyrazino[2,1-a]isoquinoline-2-carbonyl)benzonitrile | 490 | 8.25 | 458 | 6.53 | 1.18 |
| **2w** | 2-(3-chlorobenzoyl)-1,2,3,6,7,11b-hexahydro-4H-pyrazino[2,1-a]isoquinolin-4-one | 457 | 8.88 | 435 | 7.53 | 1.02 |
| **2x** | 2-(2-fluorobenzoyl)-1,2,3,6,7,11b-hexahydro-4H-pyrazino[2,1-a]isoquinolin-4-one | 401 | 6.64 | 436 | 6.14 | 0.06 |
| **2y** | 2-(2,2,2-trichloroacetyl)-1,2,3,6,7,11b-hexahydro-4H-pyrazino[2,1-a]isoquinolin-4-one | 459 | 8.29 | 416 | 5.50 | 1.35 |

**Remarks on Table A8**

**2a)** A racemic compound with a higher melting point than the reported conglomerate was detected. Further experiments highlighted the thermodynamic stability of the conglomerate at room temperature while the racemic solid phase becomes thermodynamically stable at elevated temperatures. $\Delta G^{\Phi}$ has been calculated for the two solid phases.

**2b)** The racemic conglomerate and the racemic compound could be grown from its racemic mixture. Further experiments highlighted the thermodynamic stability of the racemic compound, at least for temperatures greater than -30 °C. $\Delta G^{\Phi}$ has been calculated for the two solid phases.

**2c)** Two polymorphic forms of the racemic compound and the racemic conglomerate could be crystallized and characterized by DSC. $\Delta G^{\Phi}$ has been calculated for the three solid phases.

**2f)** Three polymorphic forms of the racemic compound exhibiting an enantiotropic relationship.[23] $\Delta G^{\Phi}$ has been calculated for the three solid phases.

[23] Pinètre, C.; Ritou, L.; Gerard, C. J. J.; Cercel, H.; Leeman, M.; Kellogg, R. M.; Tinnemans, P.; Sanselme, M.; Brandel, C.; Dupray, V.; ter Horst, J. H. Rare Case of Polymorphism in the Binary System of Enantiomers of a Praziquantel Derivative. *Org. Process Res. Dev.* **2024**. https://doi.org/10.1021/acs.oprd.4c00035.

**Resolution of 2b and 2c**

*SIPC method*

~ 800 mg of racemic **2b** and **2c** was dissolved in 10 mL and 30 mL IPA using a 20 mL and 50 mL vials respectively by heating the resulting stirred mixture (cross-shaped PTFE magnetic stirring bars (BOHLC369-25, VWR) and standard stirring plate at 700rpm) until a clear solution is obtained (double-jacketed flasks connected to a circulating cryostat (F34-HE, Julabo)). The clear solution was then filter through 0.22 µm syringe filter and cooled to reach a supersaturation $\beta$ = 2 (15 °C and 20 °C respectively) with respect to the solubility of the racemic compound (Fig. A39) and seeded with 40 mg of pure enantiomer.

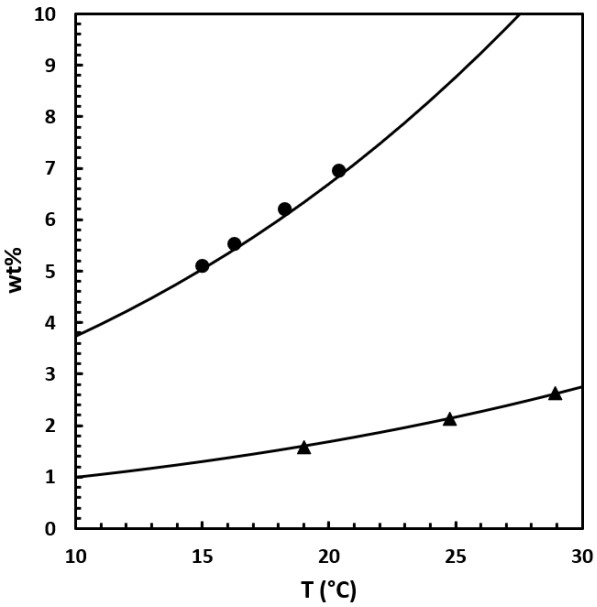


**Figure A39:** Temperature dependent solubility of **2b** (circle) and **2c** (triangle) in IPA. Solubility lines are theoretical modelling using Van't Hoff equation.

A

*Sampling methods and sample preparation*

For compound **2b** and **2c**, the chiral resolution via preferential crystallization was monitored by sampling ~ 0.5mL of the slurry from the crystallization flask using a single channel mechanical pipettor (613-0155, VWR). The solid and liquid phases were isolated from the collected suspension following two procedures :

- By casting it on top of filter papier laid down on glass filter connected to a vacuum filtration setup
- By centrifuge filtration using standard micro centrifuge (Fisherbrand) and 0.22µm cellulose acetate centrifuge tube filter (525-0017, VWR)

~1.5 mg of the solid phase was dissolved in 1.5 mL of a n-Heptane/IPA mixture (80/20; v/v) with subsequent ultrasonication while the liquid phase was diluted 9 times with the same solvent mixture prior to HPLC analyses.

*HPLC methods and SIPC monitoring*

Enantioselective HPLC analyses for compound 2b and 2c were performed on a Chiracel OD-H column (4.6 x 250 mm, 5µm) with a mobile phase consisting of n-heptane and 2-propanol (85/15 and 60/40 v:v respectively) at flow rate of 1 mL.min-1 with a UV detection at 220 nm. Each run had a total time of 60 minutes (Fig. A40).

The crystallized mass was obtained by (i) weighing the total amount of enantiopure solid recovered or (ii) determining the concentration of the solute based on the calibration curve in Figure A41. The evolution of the crystallized mass and its associated enantiomeric excess (e.e.) are summarized in Table A9.

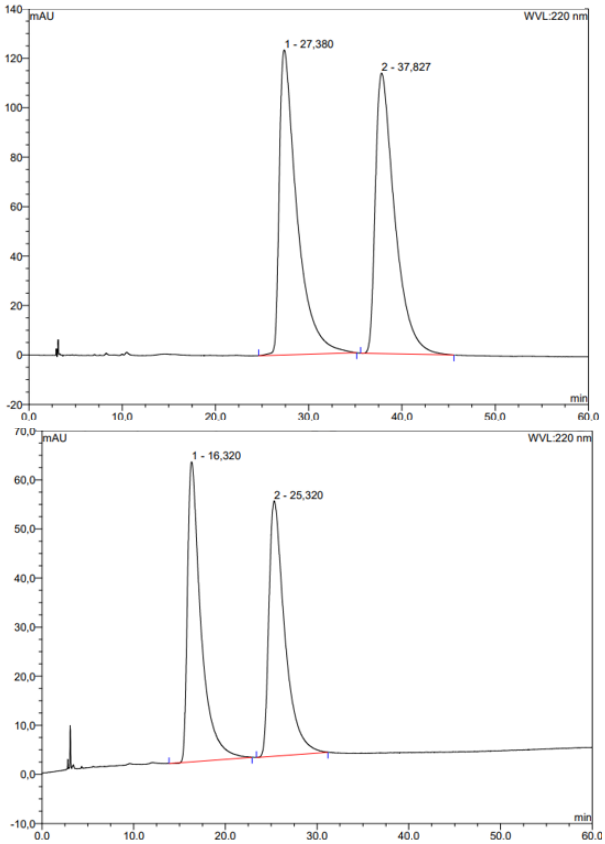


**Figure A40:** Typical chromatogram of racemic **2b** (top) and racemic **2c** (bottom). Retention time (min) for **2b**: (*R*)-**2b**: 27.38 (*S*)-**2b**: 37.83 and **2c**: (*R*)-**2c**: 16.32 (*S*)-**2c**: 25.32.

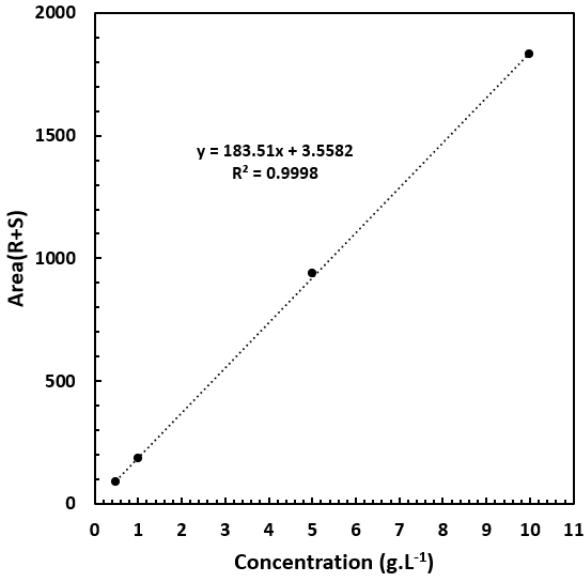


**Figure A41:** Calibration curve for derivative **2b**.

**Table A9:** SIPC monitoring result of compounds **2b** and **2c** giving the crystallized mass (mass of initial seed already deducted) and the enantiomeric excess of both the solid and liquid phases. The *e.e.* positive sign is arbitrary attributed to the (*R*) enantiomer.

| | **2b** | | | **2c** | | |
|---|---|---|---|---|---|---|
| Sampling time (min) | Crystallized mass (mg) | *e.e.* (%) | | Crystallized mass (mg) | *e.e.* (%) | |
| | | Solid | liquid | | Solid | liquid |
| 5 | 43.6 | 95.7 | - 6.3 | 14.8 | 99.4 | - 0.9 |
| 15 | 131.1 | 98.7 | - 6.6 | 46.9 | 98.4 | - 1.2 |
| 30 | 151.4 | 95.6 | -7.6 | 77.0 | 98.9 | - 1.5 |
| 60 | | | | 87.1 | 97.2 | - 1.9 |
| 120 | | | | 96.8 | 94 | - 2.4 |

# Literature dataset

## Thermochemical data compiled from literature

The melting point and enthalpy of fusion of racemic solids ($T_m^{RS}$ and $\Delta H_f^{RS}$) and enantiopure solids ($T_m^R$ and $\Delta H_f^R$) were obtained from literature.[24,25,26] Using equation 1, we computed the free energy difference ($\Delta G^{\phi}$) (Table A10).

**Table A10:** Literature dataset of melting temperatures and enthalpy of fusion for racemates ($\boldsymbol{T_m^{RS}}$ and $\boldsymbol{\Delta H_f^{RS}}$) and enantiopure solids ($\boldsymbol{T_m^R}$ and $\boldsymbol{\Delta H_f^R}$), and computed difference in free energy ($\boldsymbol{\Delta G^{\phi}}$).

| No. | Compound | $T_m^{RS}$ (K) | $\Delta H_m^{RS}$ (kcal/mol) | $T_m^R$ (K) | $\Delta H_m^R$ (kcal/mol) | $\Delta G^{\phi}$ (kcal/mol) |
|---|---|---|---|---|---|---|
| | **Conglomerates** | | | | | |
| **1** | (3S)-(3-Fluorophenyl)-3-hydroxy propanoic acid (3-(3-fluorophenyl)hydracrylic acid) | 290 | 4.90 | 311 | 5.80 | 0.008 |
| **2** | (+)-3-(4-chlorophenyl)-3-hydroxypropanoic acid (3-(4-Chlorophenyl)-hydracrylic acid) | 357 | 6.70 | 385 | 7.10 | -0.025 |
| **3** | (S)-3-(4-Bromophenyl)-3-hydroxypropanoic acid (3-(4-Bromophenyl)-hydracrylic acid) | 371 | 6.90 | 398 | 8.50 | -0.066 |
| **4** | 1(R),2(R)-1,2-diphenylethane-1,2-diol (Hydrobenzoin) | 394 | 7.20 | 420 | 8.00 | 0.056 |
| **5** | (S)-Fluoro-methyl-naphtalen-phenyl-1-ysilane | 312 | 5.40 | 341 | 5.60 | -0.039 |
| **6** | (R,S)-N-Methylephedrine (Methylephedrine) | 336 | 6.36 | 361 | 7.30 | -0.049 |
| **7** | (S)-2-Hydroxy-3-phenylpropanoic acid (3-Phenyllactic acid) | 368 | 7.29 | 395 | 7.29 | 0.003 |
| **8** | (2S)-1-butyl-N-(2,6-dimethylphenyl)piperidine-2-carboxamide (Levobupivacaine/Bupivacaine) | 376 | 4.62 | 413 | 6.27 | -0.044 |
| **9** | 2-(4-methoxyphenyl)-1-phenylpropan-1-one (a-methyl-4-methoxydeoxybenzoin) | 326 | 5.20 | 353 | 6.30 | -0.033 |
| **10** | (1S,2S)-1,2-dichloro-1,2-dihydroacenaphthylene | 339 | 4.90 | 375 | 5.10 | -0.023 |
| **11** | (R)-3-Hydroxy-3-phenylpropanoic acid (3-Phenyl hydracrylic acid) | 366 | 7.10 | 391 | 7.80 | 0.005 |
| **12** | 1,7,7-trimethyl-3-[(4-methoxyphenyl)methylidene]bicyclo[2.2.1]heptan-2-one (Anisylidene-camphor) | 372 | 6.30 | 400 | 7.20 | 0.007 |
| **13** | (S)-4-Hydroxy-2-pyrrolidone | 395 | 6.39 | 430 | 6.81 | -0.011 |
| **14** | (3S)-3-hydroxy-2,2-dimethyl-3-phenylpropanoic acid | 407 | 8.90 | 431 | 9.50 | 0.032 |
| **15** | (2S,3S)-2acetamido-N,3-dimethylpentanimde (N-acetyl-isoleucine-N'-methylamide) | 482 | 6.48 | 525 | 9.11 | -0.082 |

[24] Jacques, J.; Collet, A.; Wilen, S. H. *Enantiomers, Racemates, and Resolutions*; Krieger Publishing Company: Malabar, 1994.

[25] Li, Z. J.; Zell, M. T.; Munson, E. J.; Grant, D. J. W. Characterization of Racemic Species of Chiral Drugs Using Thermal Analysis, Thermodynamic Calculation, and Structural Studies. *Journal of Pharmaceutical Sciences* **1999**, *88* (3), 337–346. https://doi.org/10.1021/js980205u.

[26] Charpentier, M. D. Crystallization in Multicomponent Chiral Systems: Thermodynamic Characterization and Guidelines for Chiral Resolution of Racemic Compounds with Cocrystallization, University of Strathclyde, 2023. https://stax.strath.ac.uk/concern/theses/6q182k65j.

| | | | | | | |
|---|---|---|---|---|---|---|
| **16** | (1S,2S)-2-methylamino-1-phenylpropan-1-ol; hydrosulfide (Pseudoephedrine) | 381 | 7.77 | 404 | 8.75 | 0.027 |
| **17** | (S)-1-[2-(3,4-dimethoxyphenyl)ethylamino]-3-(3-methylphenoxy)propan-2-ol; hydrochloride (Bevantolol) | 408 | 9.68 | 428 | 11.0 | 0.041 |
| | **Racemic Compounds** | | | | | |
| **18** | (2S)-2-acetamido-3-methylbutanoic acid (N-acetyl-valine-N'-methylamide) | 497 | 8.90 | 531 | 8.14 | 0.154 |
| **19** | (-)5-(2-Hydroxypropan-2-yl)-2-methylcyclohex-2-en-1-ol (cis-Sobrerol) | 379 | 6.18 | 383 | 5.54 | 0.464 |
| **20** | (2R)-2-(4-Fluorophenyl)-2-hydroxyacetic acid (4-Fluoro mandelic acid) | 406 | 7.08 | 426 | 6.90 | 0.235 |
| **21** | 2-(4-(2-methylpropyl)-phenyl) propanoic acid (Ibuprofen) | 346 | 6.06 | 320 | 4.47 | 0.903 |
| **22** | (1R,2S)-2-amino-1-phenyl-1-propanol (Norephedrine) | 374 | 6.24 | 324 | 3.79 | 1.279 |
| **23** | (1S,4S)-4-(3,4-Dichlorophenyl)-N-methyl-1,2,3,4-tetrahydronaphtalen-1-amine (Sertraline) | 343 | 5.12 | 340 | 5.86 | 0.513 |
| **24** | 1-Naphthalen-1-yloxy-3-(propan-2-ylamino)propan-2-ol (Propranolol) | 367 | 9.75 | 344 | 8.37 | 1.072 |
| **25** | (2R)-2-Phenoxypropionic acid | 388 | 7.90 | 359 | 5.40 | 1.085 |
| **26** | (2R)-(2-Fluorophenyl)-2-hydroxyacetic acid (2-fluoromandelic acid) | 389 | 7.30 | 362 | 4.78 | 1.002 |
| **27** | (2R)-(2-Chlorophenyl)(hydroxy)acetic acid (2-chloromandelic acid) | 392 | 5.70 | 363 | 5.98 | 0.914 |
| **28** | (-)-2-hydroxybutanedioic acid (Malic acid) | 402 | 7.63 | 373 | 6.33 | 1.055 |
| **29** | (S)-(3-chlorophenyl)(hydroxy)acetic acid (3-chloromandelic acid) | 389 | 6.25 | 380 | 5.92 | 0.668 |
| **30** | (3R)-3-(4-Fluorophenyl)-3-hydroxypropanoic acid (3-(4-fluorophenyl)hydracrylic acid) | 362 | 6.60 | 381 | 7.40 | 0.130 |
| **31** | (S)-2-(2-oxopyrrolidin-1-yl)butanamide (Levetiracetam) | 393 | 7.44 | 389 | 6.51 | 0.597 |
| **32** | (2R)-2-(3-fluorophenyl)-2-hydroxyacetic acid (3-Fluoromandelic acid) | 369 | 5.46 | 394 | 5.56 | 0.157 |
| **33** | (S)-(+)-2-Hydroxy-2-phenylacetic acid (Mandelic acid) | 393 | 6.18 | 405 | 5.86 | 0.377 |
| **34** | (+)-2-(6-methoxynaphthalen-2-yl) propanoic acid (Naproxen) | 429 | 7.93 | 429 | 7.58 | 0.584 |
| **35** | (S)-7-(2,3-Dihydroxypropyl)-1,3-dimethylpurine-2,6-dione (Diprophylline) | 433 | 7.84 | 438 | 7.58 | 0.520 |
| **36** | 4-[(2S)-2-(3,5-dioxopiperazin-1-yl)propyl]piperazine-2,6-dione (Dexrazoxane) | 507 | 10.75 | 468 | 9.04 | 1.487 |
| **37** | (2R)-1-Naphthalen-1-yloxy-3-(propan-2-ylamino)propan-2-ol . HCl (Propranolol) | 436 | 7.13 | 468 | 7.96 | 0.057 |
| **38** | (1R,2S)-2-(Methylamino)-1-phenylpropan-1-ol (Ephedrine) | 351 | 6.95 | 313 | 4.14 | 1.180 |
| **39** | (2S)-2-(3-benzoylphenyl)propanoic acid (Ketoprofen) | 367 | 5.01 | 345 | 3.51 | 0.773 |
| **40** | (+)-(2S,3S)-Phenylglyceric acid | 395 | 7.50 | 372 | 5.60 | 0.958 |
| **41** | (+)-2-Methylamino-1-phenylpropan-1-ol (Pseudoephedrine) | 391 | 8.15 | 392 | 7.64 | 0.513 |
| **42** | N-[[(2S)-1-ethylpyrrolidin-2-yl]methyl]-2-methoxy-5-sulfamoylbenzamide (Sulpiride) | 451 | 11.03 | 460 | 10.04 | 0.433 |
| **43** | 1-(Propan-2-ylamino)-3-(2-prop-2-enyphenoxy)propan-2-ol (Alprenolol) | 331 | 8.51 | 299 | 5.68 | 1.249 |
| **44** | alpha-2-(1-Naphthyl)propanoic acid | 423 | 7.30 | 342 | 3.40 | 1.862 |
| **45** | (3R)-(2-Fluorophenyl )-3- hydroxy propanoic acid | 342 | 6.50 | 348 | 5.40 | 0.378 |
| **46** | (-)-1-[2-(3,4-Dimethoxyphenyl)ethylamino]-3-(3-methylphenoxy)propan-2- ol (Bevantolol) | 361 | 10.97 | 348 | 10.57 | 0.854 |

| | | | | | | |
|---|---|---|---|---|---|---|
| **47** | 3-(3-Bromo-3-phenyl)-3-hydroxy propanoic acid (3-(3-Bromophenyl)hydracrylic acid) | 349 | 6.40 | 350 | 5.70 | 0.464 |
| **48** | 1,5-Dichloro-9,10-dihydro-9,10-ethano anthracene | 424 | 6.60 | 354 | 3.00 | 1.584 |
| **49** | (S,S)-3,5- Dimercaptoheptanedioic acid (2',6'-pipecoloxylidide) | 429 | 9.40 | 355 | 5.00 | 2.110 |
| **50** | beta-3-Hydroxy-3-phenylbutanoic acid | 330 | 4.70 | 357 | 5.40 | 0.046 |
| **51** | 2R-Chloro-3-methyl-2-phenoxy propionic acid | 392 | 7.30 | 360 | 5.30 | 1.092 |
| **52** | 4-Nitro 2-phenoxy propionic acid | 412 | 7.70 | 362 | 5.00 | 1.425 |
| **53** | 9,10-Dihydro-9,10ethano-11,12-dicarbomethoxyanthracene | 380 | 5.60 | 363 | 4.00 | 0.750 |
| **54** | 2-(3-Chlorophenyl)-2-hydroxy acetic acid (3-chloromandelic acid) | 380 | 5.01 | 367 | 5.07 | 0.674 |
| **55** | 2-(m-Chlorophenoxy) propanoic acid | 386 | 7.90 | 368 | 7.10 | 0.885 |
| **56** | 3-(m-Chlorophenyl)-3-hydroxy propanoic acid (3-(m-Chlorophenyl)hydracrylic acid) | 340 | 5.70 | 368 | 6.70 | -0.041 |
| **57** | (+)-2-(2-Chlorophenoxy)-propionic acid | 388 | 7.70 | 369 | 6.40 | 0.885 |
| **58** | (1S,3E,4R)-3-benzylidene-1,7,7-trimethylbicyclo[2.2.1]heptan-2-one (Benzylidene camphor) | 351 | 5.50 | 371 | 5.60 | 0.173 |
| **59** | 2S-Dimethyl-diacetyl tartaric acid | 358 | 6.60 | 378 | 6.50 | 0.148 |
| **60** | (3R)-3-Hydroxy-3-phenylpentanoic acid | 384 | 8.40 | 379 | 7.40 | 0.631 |
| **61** | 2-(4-Chlorophenyl)-2-hydroxy acetic acid (4-chloromandelic acid) | 384 | 5.48 | 379 | 4.69 | 0.585 |
| **62** | 2-(2-Chlorophenyl)-2-hydroxy acetic acid (2-chloromandelic acid) | 346 | 4.76 | 380 | 4.94 | 0.028 |
| **63** | (2R)-2-(4-bromo phenoxy) propanoic acid | 385 | 7.60 | 380 | 6.60 | 0.622 |
| **64** | (R,S)-2-[(2-aminoethoxy)methyl]-4-(2-chlorophenyl)-ethoxycarbonyl-5-methoxycarbonyl-6-methyl-1,4-dihydropyridine (Amlodipine) | 414 | 4.83 | 384 | 4.03 | 0.880 |
| **65** | 9,10-Dimethyl-9,10 dihydro-9,10- ethano-11,12-dicarbomethoxyanthracene trans | 465 | 9.80 | 393 | 4.50 | 2.059 |
| **66** | 2-(2-chlorophenyl)-2-hydroxy acetic acid (2-chloromandelic acid) | 364 | 5.70 | 394 | 5.97 | 0.047 |
| **67** | (2R)-2-(4-Chlorophenyl )-2-hydroxy acetic acid (4-chloromandelic acid) | 395 | 6.51 | 395 | 5.03 | 0.544 |
| **68** | (S)-N-(2,6-dimethylphenyl)-1-piperidine-2-carboxamide | 385 | 5.53 | 403 | 5.78 | 0.272 |
| **69** | 11,12-Di(hydroxymethyl)-9,10-dihydro-9,10-ethanoanthracene | 475 | 9.85 | 406 | 5.70 | 1.991 |
| **70** | (2S)-N-(2,6-dimethylphenyl)-1-ethylpiperidine-2-carboxamide | 405 | 4.33 | 408 | 4.76 | 0.523 |
| **71** | Dibenzoylmethyl-tartaric acid | 423 | 11.70 | 409 | 11.00 | 0.937 |
| **72** | (2S)-N-(2,6-dimethylphenyl)-1-propylpiperidine-2-carboxamide (Ropivacaine) | 391 | 5.69 | 414 | 10.64 | -0.051 |
| **73** | 1,2-Dibromoacenaphtene/5,6-Dibromoacenaphthene | 397 | 6.00 | 416 | 6.30 | 0.259 |
| **74** | 5-O-ethyl 3-O-methyl (4R)-4-(2,3-dichlorophenyl)-2,6-dimethyl-1,4-dihydropyridine-3,5-dicarboxylate (Felodipine) | 417 | 7.53 | 417 | 6.07 | 0.566 |
| **75** | 5-(2-Hydroxypropan-2-yl)-2-methylcyclohex-2-en-1-ol (trans-Sobrerol) | 405 | 8.22 | 424 | 8.29 | 0.191 |
| **76** | 1,5-Dichloro-9,10-dihyro-9,10 ethano- 11,12-dicarbomethoxyanthracene (exo) | 465 | 8.80 | 424 | 5.55 | 1.360 |

| | | | | | | |
|---|---|---|---|---|---|---|
| **77** | (2R)-N-(2,6-dimethylphenyl)-1-methylpiperidine-2-carboxamide (Mepivacaine) | 423 | 4.05 | 426 | 4.25 | 0.553 |
| **78** | 1,5-Dichloro-9,10-dihyro-9,10-ethano-11,12dicarbomethoxyanthracene (endo) | 436 | 6.30 | 427 | 5.90 | 0.718 |
| **79** | (S)-2-acetamido-N,4-dimethylpentanamide (N-acetyl-leucine-N'-methylamide) | 432 | 6.49 | 428 | 5.54 | 0.648 |
| **80** | (2R)-5-[2-(3,4-Dimethoxyphenyl)ethyl](methyl)amino}-2-isopropyl-2-(3,4,5-trimethoxyphenyl)pentanenitrile (Gallopamil) | 427 | 12.27 | 434 | 13.00 | 0.357 |
| **81** | 1,5-Dichloro-11,12-dihydroxymethyl-9,10-dihydro-9,10ethanoanthracene trans (endo) | 441 | 7.90 | 435 | 4.70 | 0.707 |
| **82** | (2R)-2-[(3-amino-2,4,6-triiodophenyl)methyl]butanoic acid (Iopanoic acid) | 427 | 6.62 | 439 | 6.21 | 0.421 |
| **83** | (3R)-2,2,3-Triphenylpentanoic acid | 480 | 8.90 | 442 | 6.40 | 1.322 |
| **84** | 2-acetamido-N-methylacetamide (N-acetyl-alanine-N'-methylamide) | 412 | 3.80 | 455 | 5.65 | 0.034 |
| **85** | (2R)-2-(1-Nitronaphthalen-2-yl)oxypropanamide | 431 | 7.00 | 462 | 7.30 | 0.111 |
| **86** | 1-(1-Phenylethyl)thiourea | 411 | 7.90 | 472 | 8.60 | -0.547 |
| **87** | (2S)-2-[4-(3-oxo-1H-isoindol-2-yl)phenyl]butanoic acid (Indobufen) | 455 | 9.42 | 472 | 7.98 | 0.346 |
| **88** | Naphtoxy-2 propionamide | 445 | 9.00 | 475 | 9.10 | 0.038 |
| **89** | (2R)-2-[4-(3-oxo-1H-isoindol-2-yl)phenyl]propanoicacid (Indoprofen) | 486 | 10.02 | 483 | 12.35 | 0.711 |
| **90** | 11,12-Di(iodo-methyl)-9,10-dihydro-9,10-ethanoanthracene | 469 | 8.00 | 491 | 8.40 | 0.260 |
| **91** | 1,5-Dichloro-11,12 dihydroxymethyl-9,10 dihydro-9,10ethanoanthracene trans (exo) | 520 | 12.80 | 527 | 12.80 | 0.533 |
| **92** | 2-Amino-1-phenylpropan-1-ol; hydrosulfide (Norephedrine) | 391 | 7.12 | 375 | 5.56 | 0.808 |
| **93** | (2S)-2-(3,4-Dimethoxyphenyl)-5-[2-(3,4-dimethoxyphenyl)ethyl-methylamino]-2-propan-2-ylpentanenitrile . HCl (Verapamil) | 417 | 15.39 | 408 | 9.72 | 0.873 |
| **94** | 2-(Methylamino)-1-phenylpropan-1-ol; napsylate (Ephedrine; napsylate) | 444 | 9.20 | 444 | 7.88 | 0.607 |
| **95** | (1S,2S)-2-amino-1-phenyl-1-propanol . HCl (Norephedrine) | 469 | 6.92 | 446 | 4.84 | 0.955 |
| **96** | (+)-2-methylamino-1-phenylpropan-1-ol . HCl (Pseudoephedrine) | 439 | 5.24 | 456 | 5.45 | 0.403 |
| **97** | 2-(Methylamino)-1-phenylpropan-1-ol (Ephedrine) | 464 | 8.35 | 492 | 7.58 | 0.202 |
| **98** | 2-(cyclohexanecarbonyl)-3,6,7,11b-tetrahydro-1H-pyrazino[2,1-a]isoquinolin-4-one (Praziquantel) | 409 | 6.15 | 384 | 4.42 | 0.913 |

A

## Fitting of the gamma distribution

The CDF of the literature data were fitted to a cumulative gamma-distribution (Fig. A42). The gamma-distribution was first corrected for the physical reality that $\Delta G^{\phi}$ protrudes in the negative domain. Therefore, we establish the adapted gamma-distribution γ (eq. 2):

$$\gamma\left(\Delta G^{\phi}, \mathrm{k}, \theta\right) = \frac{1}{\theta^{\mathrm{k}}\,\Gamma(\mathrm{k})}\left(\Delta G^{\phi}+\delta\right)^{\mathrm{k}-1} \mathrm{e}^{-(\Delta G^{\phi}+\delta)/\theta} \text{ where } \Delta G^{\phi}+\delta > 0 \qquad \text{(eq. 2)}$$

wherein γ is the probability density, Γ is the gamma function, $k$ and $\theta$ serve as fitting parameters and $\delta$ provides the introduced offset. The cumulative gamma-distribution (CDF) then is calculated as eq. 3:

$$\mathrm{CDF}(\Delta G^{\phi}, \mathrm{k}, \theta) = \int_{-\delta}^{\Delta G^{\phi}} \gamma(G, \mathrm{k}, \theta)\, \mathrm{dG} \qquad \text{(eq. 3)}$$

We subsequently fitted the cumulative gamma-distribution (CDF, eq. 3) to the literature data by minimizing the sum of errors (least squares) through GRG nonlinear gradient descent. This provided the final fit shown in Figure A42 for which we found $k$ = 12.15, $\theta$ = 0.138, $\delta$ = 1.03.

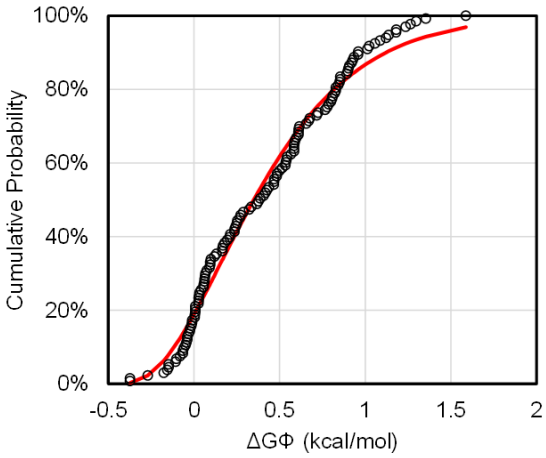


**Figure A42:** The cumulative probability distribution of the literature dataset of $\Delta G^{\phi}$ (black circles) fitted with an adapted gamma-distribution (eq. 2) through a GRG nonlinear gradient descent algorithm (red line).

## Statistical tests

First, a Goodness-of-Fit analysis (Chi-Square) was performed to assess whether the gamma-distribution accurately fitted the CDF of the combined dataset. The calculated value of $\chi^2$ = 0.723 under 80 degrees of freedom led to a p-value < α = 0.01 (***). Therefore, we have established that the fit is good.

Second, two-sided Kolmogorov-Smirnov tests were performed to assess whether the data from the individual $\Delta G^{\phi}$-distributions (library **1**, library **2**, literature dataset) could indeed be inferred to originate from the fitted gamma distribution. Here, we found: D = 0.267 and a p-value of 0.1478 for library **1**, D = 0.224 and a p-value = 0.0765 for library **2**, and D = 0.056 and a p-value = 0.9519 for the literature dataset. Under a typical α of 0.05, these results significantly accept the null-hypothesis, to mean that, indeed, all three individuals $\Delta G^{\phi}$-distributions can be inferred to match the fitted gamma distribution and could originate from this mother distribution.

# Summary.

## Introduction

Just like our hands, many molecules occur in two mirrored forms called enantiomers. Molecular chirality is concerned with discriminating such three-dimensional stereochemical molecular forms. The amplification of molecular chirality is at the core of discussions on the origin of life and is key in the production of essential enantiopure pharmaceutical and agrochemical building blocks. Indeed, administering the wrong enantiomeric form of a drug can have no therapeutic effect or, at worst, even cause severe side-effects.

One of the most promising methods to achieve full chiral amplification is crystallization-induced deracemization, in which even minute chiral imbalances can already be amplified to complete enantiomeric purity. This process relies on three elements: (i) enantiomers self-sort into enantiopure crystals called conglomerates, providing a physiochemical mechanism for stereochemical specificity; (ii) enantiomers racemize in solution, providing a pathway for interconversion that is required in deracemization; (iii) the crystalline solid-phase undergoes repeated cycles of growth and dissolution to drive the solid-state deracemization.

This thesis will explore the fundamental mechanism of this crystallization-induced deracemization process, provide tangible guides for its practical implementation, and pave the way to expanding its scope beyond the statistically limited group of thermodynamically favoured conglomerates. A theoretical background on chirality, crystal growth, and chiral crystallization is presented in **Chapters 1**, **2**, and **3** respectively. The Summary Figure provides a graphical collection of the main findings presented in this work, which will now be textually elaborated.

## Chiral Amplification through Asymmetric Crystal Growth under Racemizing Conditions

A poor mechanistic understanding of crystallization-induced deracemization deters further advances and effective implementation of the process. Up to now, there has been a widespread general consensus that enantiomeric enrichment occurs during the dissolution of crystals, while crystal growth may give undesired erosion of enantiopurity. This assumption, stemming from equilibrium thermodynamics, has led crystal growth to be disregarded and unstudied as a source of enantioenrichment by itself.

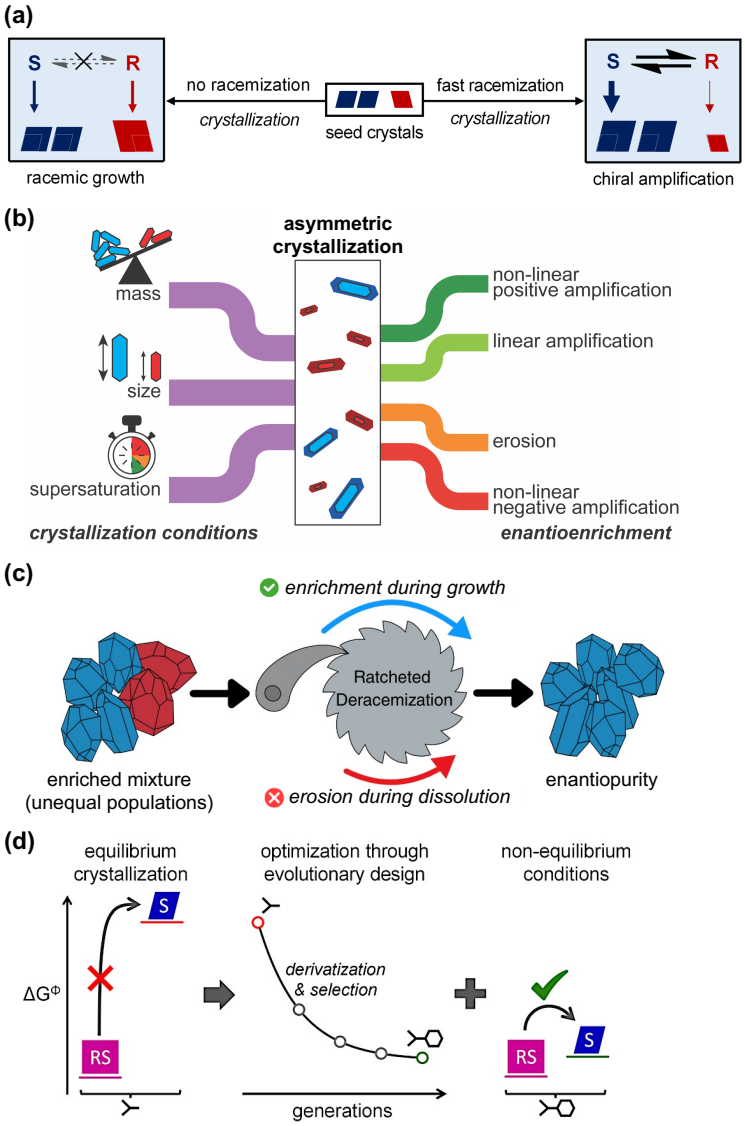


**Summary Figure.** Asymmetric Amplification and Deracemization during the Reactive Crystallization of Chiral Molecules. (a) Chiral amplification can occur during crystal growth under racemizing conditions, so that tiny amounts of low enantiopurity seeds yield high enantiopurity products. (b) The number and size crystals decisively govern asymmetric crystallization: subtle size-disparities in seeds exert strong non-linear effects that outweigh initial enantioenrichment in directing the outcome of chiral amplification. (c) Deconvoluting the roles of growth and dissolution in asymmetric crystallization uncovers a fundamental hysteresis effect driving ratcheted deracemization: growth-driven enantioenrichment consistently exceeds dissolution-induced erosion. (d) Conglomerate crystals are generally (90-95% of cases) less stable than their racemic compound equivalents, but a directed evolution strategy that systematically introduces chemical modifications can rapidly favour enantiopure crystallization over the formation of racemic crystals. Moreover, non-equilibrium conditions may allow obtaining kinetically stable conglomerates for ca. 50% of all crystalline chiral organic molecules.

In **Chapter 4**, we answer a question of both fundamental and practical importance: is enantiomeric amplification during crystal growth really to be discounted? For the first time, we study crystal growth under racemizing conditions for seed crystals of low enantiopurity and demonstrate that, defying currently prevalent views, amplification of enantioenrichment can occur during crystal growth. Guided by a mechanistic framework, we show that the interplay between racemization and crystallization rates can result in either erosion, consolidation or amplification of the enantiomeric excess of the seed crystals. We identify that the faster growth of the majority population of enantiomorphic seed crystals is at the core of this remarkable chiral amplification mechanism. Moreover, contrary to the common belief that large amounts of seed crystals are generally beneficial, we demonstrate that the level of chiral amplification can be further increased by decreasing the amount of seed crystals: small amounts of seeds of only 60% ee can already result in virtually exclusive growth of the enantiomer that constitutes the majority population of the solid phase.

## How Crystal Size and Number steer Asymmetric Crystallization

Having revealed complex non-linear effects during crystal growth that can greatly affect the outcome of chiral crystallization under racemizing conditions, we now know that differences in the growth rates of enantiomeric crystal populations are essential in our understanding and control of chiral amplification. So far it has remained unclear, however, where such growth rate asymmetries originate and how they can be leveraged and controlled.

In **Chapter 5**, we investigate how size and mass imbalances between two enantiomeric crystal populations translate to asymmetric growth rates that determine asymmetric crystal growth. By carefully preparing enantiomeric seed mixtures with controlled imbalances in size and mass, we were able to disentangle their contributions and quantify their impact on the extent and direction of amplification. We find that the interplay between imbalances in size and mass can yield positive, linear or even negative, non-linear chiral amplification. Consequently, though small crystals have a thermodynamically higher solubility than large ones, we show that a minority population of small crystals can collectively outgrow and ultimately dominate a majority of larger crystals. Furthermore, by tuning the crystallization rate through supersaturation, we demonstrate that these size-induced effects can be enhanced, dampened, or even inverted, depending on the fundamental mechanism of crystal growth.

These results provide a conceptual advance in understanding the kinetic drivers of symmetry breaking and offer a practical guide for controlling deracemization processes. We can now rationalize several existing empirical strategies for the

execution of crystallization-induced deracemizations, suggest novel approaches, and provide ideas that extend asymmetric amplification to stable racemic compounds (i.e. molecules that thermodynamically do not favour conglomerate crystallization). These findings further apply beyond chirality in other asymmetric crystallization processes of profound importance to industry.

## On Mechanistic Ratchets driving Crystallization-Induced Deracemization

So far, we have focussed on asymmetric crystal growth under racemizing conditions to study chiral amplification. Full crystallization-induced deracemization processes, however, combine crystal growth and dissolution steps. The cyclic interplay between crystal growth and dissolution ultimately drives deracemization, urging the experimental study of their individual contributions to further elucidate the mechanistic details of crystallization-induced deracemization.

In **Chapter 6**, we dissect the individual contributions of asymmetric crystal growth and dissolution on chiral amplification and use a mass-balance to expose the underlying crystal dynamics. Regardless of the racemization rate, we consistently find a dissymmetry between the growth and dissolution of the enantiomer populations: despite the major enantiomer growing and dissolving faster than the minor enantiomer, growth-driven enantioenrichment consistently surpasses dissolution-induced erosion. This dissymmetry between chiral crystal growth and dissolution enables a ratchet effect that drives chiral amplification. Contrary to the prevailing view in the field, we also show that dissolution can even reduce initial enantioenrichment of the solid phase, whereas crystal growth can absolutely increase it—in agreement with our findings presented in Chapter 4 and 5.

The experiments reported in Chapter 6 suggest that a fundamental difference between the mechanisms of crystal growth and dissolution underpins the fundamental workings of crystallization-induced deracemization. Besides fundamental impact, these insights provide further guidance for optimizing crystallization-induced deracemizations, particularly by separately optimizing growth and dissolution steps to maximize chiral amplification and deracemization efficiency. Specifically, we demonstrate how switching off racemization during crystal dissolution maximizes the hysteresis between growth and dissolution, thereby maximizing chiral amplification efficiency.

## Deracemization through Solvent Cycling

Whereas the previous Chapter was concerned with the fundamental roles of crystal growth and dissolution in chiral amplification, it only marginally discussed how different conditions for growing and dissolving crystals may have a profound impact on the efficiency and application potential of this chiral amplification. So far,

attrition (i.e. continuous dissolution and growth through size-dependent solubility and ripening) and spatiotemporal temperature cycling have been the two approach for achieving repeated growth and dissolution cycles.

In **Chapter 7**, we present a novel method for implementing such growth-dissolution cycles that seeks to exploit the insights derived in previous Chapters. By now, we have established that slow growth but fast dissolution of crystals is ideal for stark non-linear chiral amplification and reduced antagonistic effects from dissolution. Moreover, Chapter 6 explained that the racemization rate should ideally be equal or lower during dissolution than during growth. Chapter 7 introduces a novel method for deracemization that implements all these lessons: growth occurs through slow solvent removal and instantaneous dissolution is achieved through re-addition. This approach of solvent cycling-induced deracemization is achieved autonomously by repurposing a Soxhlet apparatus and designing a binary solvent with desirable boiling point, racemization kinetics, and solubility (i.e. cyclic mass transfer).

As a proof-of-principle, we use the solvent-cycling approach to fully deracemize a chiral building block of blockbuster pharmaceutical Clopidogrel within 3.5 hours (20% initial enantiomeric excess), which is—even in its nonoptimized form—much faster than state-of-the-art crystallization-induced deracemization methods.

## Enantiopurity through Nonequilibrium Crystallization

Crystallization is clearly a powerful and cornerstone method for isolating enantiopure molecules, but it relies on the rare and unpredictable self-sorting of enantiomers into separate enantiopure crystals (i.e. conglomerates). Critically, this only occurs in 5-10% of all cases. The vast majority of chiral mixtures (90-95%) crystallize together into racemic compounds, making the separation of enantiomers extremely challenging.

Although cumbersome workarounds have been developed, these approaches fail to directly address the fundamental thermodynamic challenges underlying this low success rate in desirable crystallization behaviour. Recognizing this gap, we end this thesis by exploring the possibility that non-equilibrium crystallization conditions, which favour kinetic over thermodynamic stability, can overcome these challenges and potentially increase the likelihood of enantiopure crystal formation.

In **Chapter 8**, we systematically characterize energy differences ($\Delta G^{\Phi}$) between racemic and enantiopure crystal phases for libraries of target molecules (phenylglycine, praziquantel) with different chemical modifications. Surprisingly, these libraries reveal wide but similar continuous distributions of $\Delta G^{\Phi}$, wherein similar chemical modifications group together. This grouping allows a directed evolution strategy to discover crystals with low $\Delta G^{\Phi}$ for isolating desired enantiomers by crystallization under non-equilibrium conditions. By coupling

directed evolution, non-equilibrium strategies, and emerging AI-driven tools, our study paves a promising pathway toward scalable, automated isolation of essential enantiopure molecules in both academic and industrial applications.

To examine how broadly this strategy might apply, we analysed the energy differences between racemic and enantiopure crystal forms for ca. 100 previously reported chiral molecules. This analysis suggests that as many as half of all chiral molecules may kinetically form enantiopure crystals. Our finding that 40 to 50% of chiral molecules are potentially accessible by applying non-equilibrium conditions opens an exciting new pathway for accessing essential enantiopure compounds by pairing non-equilibrium crystallization with rational design grounded in crystal stability analysis.

# Samenvatting.

## Reactieve Kristallisatie van Chirale Moleculen:

*Asymmetrische Aanwas en Deracemizatie*

### Inleiding

Net zoals onze handen, komen ook veel moleculen in twee vormen voor die elkaars spiegelbeeld zijn; zulke moleculaire spiegelbeelden worden enantiomeren[1] genoemd. Het begrip chiraliteit[2] op moleculaire schaal draait dan ook om het onderscheiden van dergelijke driedimensionale stereochemische varianten van stoffen. Aan de ene kant speelt het ontstaan en versterken van de chiraliteit van een chemisch systeem op fundamenteel niveau een rol, bijvoorbeeld rond de oorsprong van het leven. Aan de andere kant is er ook een praktisch belang bij de vraag hoe de chiraliteit van een moleculair systeem kan worden versterkt: het is essentieel voor toepassingen van moleculen als geneesmiddel of als bioactieve stof in de land- en tuinbouw om een zuivere vorm van het juiste spiegelbeeld te produceren. Het gebruik van het verkeerde enantiomeer kan er namelijk toe leiden dat een middel geen werking heeft of kan zelfs de oorzaak zijn van (dodelijke) bijwerkingen.

Een veelbelovende methode om absolute chirale versterking te bewerkstelligen is deracemizatie[3] op basis van kristallisatie, waarbij zelfs een kleine onbalans tussen twee enantiomeren kan worden uitversterkt. Bij een dergelijke deracemizatie vindt een volledige omzetting van een (enigszins) verrijkt mengsel van enantiomeren plaats met een enantiozuiver product als resultaat. Het proces stoelt op drie belangrijke pijlers: (i) de enantiomeren scheiden zichzelf door te kristalliseren als aparte enantiozuivere kristallen (conglomeraten genoemd), hetgeen een intrinsiek fysisch-chemisch mechanisme voor stereoselectiviteit oplevert; (ii) de enantiomeren racemizeren in de oplossing, hetgeen een chemische route biedt voor de noodzakelijke uitwisseling tussen de twee enantiomeerpopulaties; (iii) de kristallen ondergaan voortdurend cycli van groei en oplossen, hetgeen de drijvende kracht vormt voor de deracemizatie van de vaste stof.

---

[1] Enantiomeren zijn dus elkaars spiegelbeeld, maar passen niet op elkaar. Vaak is een asymmetrisch koolstofatoom met 4 verschillende substituenten de oorzaak. Omdat enantiomeren in principe dezelfde fysische eigenschappen hebben, zijn ze niet met conventionele scheidingsmethoden uit elkaar te halen!

[2] Deze term is afgeleid van het Grieks voor 'hand' (GR: *chier*).

[3] Een racemaat is een 1:1 mengsel van beide enantiomeren. Met deracemizeren bedoelen we dus het omzetten van 1:1 of verrijkt mengsel naar een 100% enantiozuivere toestand. Racemizeren is het tegenovergestelde.

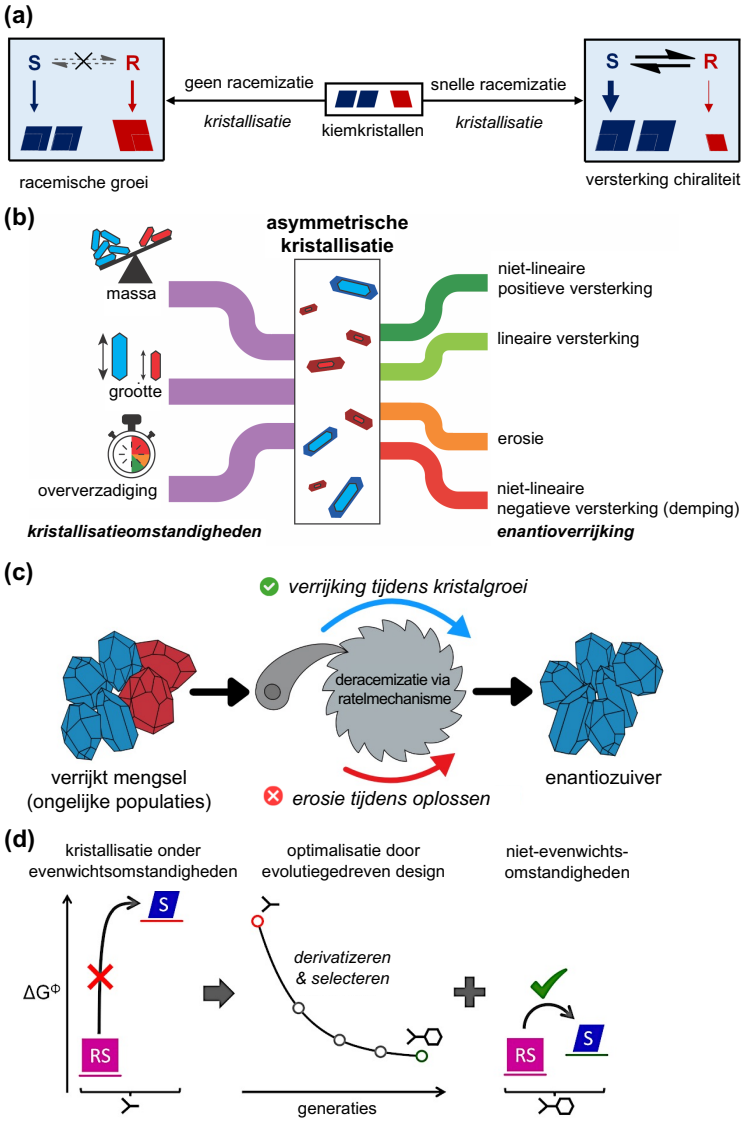


**Samenvattend Figuur.** Asymmetrische aanwas en deracemizatie bij de reactieve crystallizatie van chirale moleculen (enantiomeren: *S* en *R*). (a) Versterking van chiraliteit kan plaatsvinden tijdens kristalgroei onder racemizerende reactieomstandigheden, zodat kleine hoeveelheden kiemkristallen met lage enantiozuiverheid reeds tot producten met een hoge enantiozuiverheid kunnen leiden. (b) Het aantal en de grootte van kiemkristallen zijn doorslaggevend in het sturen van asymmetrische kristallisatie: subtiele grootteverschillen tussen kiemkristallen geven non-lineaire effecten die sterker wegen bij het bepalen van de uitkomst van het kristallisatieproces dan de aanvankelijke enantiomeersamenstelling van de kiemkristallen. (c) Het experimenteel ontwarren van de individuele rollen van groei en oplossen in asymmetrische kristallisatie legt een fundamentele hysterese bloot als drijvende kracht achter deracemizatie via een ratelmechanisme: enantioverrijking verkregen tijdens groei weegt consequent op tegen de afname tijdens oplossen. (d) De 'conglomeraat' kristalvorm is in het algemeen (nml. 90—95% van de gevallen) minder stabiel dan de 'racemische' kristalvorm van een chiraal molecuul. Een strategie van gestuurde evolutie, die systematisch chemische modificaties aanbrengt, kan in enkele generatiecycli tot een thermodynamisch begunstigde enantiozuivere kristalvorm leiden. Daarnaast kunnen procesomstandigheden die het systeem buiten evenwicht drijven vaak (~50%) ook kinetisch stabiele conglomeraatvormen geven van chirale organische moleculen.

Dit proefschrift onderzoekt fundamenteel het mechanisme van deze kristallisatiegedreven deracemizatie (in het Engels: 'Crystallization-Induced Deracemization', afgekort tot CID). Daarnaast bieden de resultaten in dit proefschrift praktische handvatten voor de implementatie van CID-processen. Tot slot bespreekt dit proefschrift hoe het bereik van CID kan worden uitgebreid voorbij de kleine klasse moleculen die kristalliseren als conglomeraat; deze groep is immers zowel statistisch als thermodynamisch in het nadeel, hetgeen het toepassingsbereik van CID beperkt.

Een theoretische achtergrond over chiraliteit, kristalgroei, en de kristallisatie van chirale moleculen is gegeven in resp. **Hoofdstuk 1**, **2** en **3**. Het Samenvattend Figuur biedt een grafische collage van de belangrijkste bevindingen die in dit proefschrift worden gepresenteerd. Deze samenvatting zal nu de inhoud van de verschillende experimentele hoofdstukken verder bespreken.

## Asymmetrische kristalgroei versterkt chiraliteit onder racemizerende reactieomstandigheden

Ons beperkte begrip van de mechanismen die ten grondslag liggen aan CID-processen belemmert zowel het effectief praktisch implementeren als verder innoveren op deze deracemizatiemethode. Tot op heden was er een brede consensus dat de verrijking van een gewenst meerderheidsenantiomeer[4] plaatsvindt tijdens het oplossen van kristallen uit de vaste stof, terwijl kristalgroei juist een contraproductieve daling van de enantiozuiverheid tot gevolg heeft. Deze aanname, die voortkomt uit de evenwichtsthermodynamica, heeft ertoe geleid dat kristalgroei als bron van enantioverrijking nagenoeg geheel is afgeschreven.

**Hoofdstuk 4** beantwoordt de vraag of verrijking van het meerderheidsenantiomeer ten gevolge van kristalgroei inderdaad buiten beschouwing mag worden gelaten—een vraag die zowel van praktisch als fundamenteel belang is. Voor het eerst bestuderen we kristalgroei van kiemkristallen[5] met een lage enantiozuiverheid[6] onder racemizerende reactieomstandigheden. We tonen aan dat—in strijd met de heersende opvatting—verrijking van het meerderheidsenantiomeer wel degelijk kan plaatsvinden door asymmetrische kristalgroei. Aan de hand van een mechanistisch raamwerk laten we daarnaast zien dat de dynamische wisselwerking tussen de kinetiek van racemizatie en kristallisatie tot verschillende regimes kan leiden:

[4] Er is in chirale kristallisatie niet altijd per definitie sprake van een meerderheidsenantiomeer, maar vaak wordt van het gewenste enantiomeer in ieder geval een overmaat toegevoegd waardoor zo'n meerderheidsenantiomeer ontstaat. Op fundamenteel niveau is het daarnaast welhaast onmogelijk om géén meerderheidsenantiomeer te hebben: dan zou men immers van elk enantiomeer exact evenveel moleculen moeten hebben!

[5] Kiemkristallen zijn kristallen die – vaak aan het begin – worden toegevoegd aan een (over)verzadigde oplossing om als startpunt voor kristalgroei te dienen. Dit is een belangrijke manier om kristallisatie te sturen.

[6] Formeel definiëren we dit als *e.e.* (EN: "enantiomeric enrichment"). Bij 100% is er maar één enantiomeer, bij 0% is het mengsel racemisch (d.z.w. het bestaat uit gelijke hoeveelheden van beide enantiomeren).

daling, behoud, of verrijking van de initiële enantiozuiverheid van de kiemkristallen. Snellere groei van de meerderheidspopulatie enantiozuivere kristallen is de kern van dit fenomeen, hetgeen tot asymmetrische aanwas leidt. Een verdere bevinding gaat in tegen het veelgehoord mantra dat meer kiemkristallen altijd beter zijn; dit hoofdstuk laat namelijk zien dat de mate van waargenomen verrijking toeneemt wanneer het aantal gebruikte kiemkristallen afneemt. Tot slot toont dit hoofdstuk de kracht van kristalgroei voor de versterking van chiraliteit: kleine hoeveelheden kiemkristallen met 60% enantiozuiverheid kunnen in de vaste stof reeds absolute—d.w.z. enantiozuivere—groei van het meerderheidsenantiomeer opleveren.

## De bepalende invloed van de kristalgrootte en het aantal kiemkristallen op de uitkomst van asymmetrische kristallisatie

In hoofdstuk 4 hebben we laten zien dat complexe niet-lineaire effecten tijdens kristalgroei een grote invloed kunnen uitoefenen op de uitkomst van chirale kristallisatie onder racemizerende reactieomstandigheden. Daarnaast is duidelijk geworden dat verschillen tussen de groeisnelheden van de enantiomere kristalpopulaties essentieel zijn in ons begrip van asymmetrische kristalgroei en voor controle over de versterking van chiraliteit. Tot dusverre is echter onduidelijk waar de verschillen in die groeisnelheden precies vandaan komen, hoe ze vervolgens te sturen, en te benutten.

In **Hoofdstuk 5** onderzoeken we het effect van ongelijke grootte en/of massa van twee enantiomere kristalpopulaties op hun relatieve groeisnelheden en het gevolg daarvan voor de uitkomst van asymmetrische kristalgroei. Door nauwkeurig mengsels van kiemkristallen te maken met een bepaalde grootte, massa, en zuiverheid, kunnen we de individuele en gezamenlijke invloed van de kristalgrootte en het aantal kiemkristallen op de richting en mate van chirale versterking bepalen. De experimenten laten zien dat de wisselwerking tussen de grootte van en het aantal kiemkristallen per populatie doorslaggevend is voor het bewerkstelligen van daling, behoud, of verrijking van de enantiozuiverheid van de kiemkristallen. Hoewel kleine kristallen thermodynamisch minder stabiel zijn en sneller oplossen, toont dit hoofdstuk aan hoe een collectief van kleine kristallen—zelfs als dit qua totale massa in het nadeel is—netto sneller kan groeien dan de andere enantiomeer die bestaat uit een populatie grotere kristallen; de snelstgroeiende kristalpopulatie domineert de uitkomst van het proces. Door experimenten te herhalen onder een andere oververzadiging[7], observeren we voorts dat de balans tussen de groeisnelheden van

[7] Met oververzadiging wordt het getal bedoeld dat weergeeft hoeveel meer moleculen er van een stof zijn opgelost dan volgens de thermodynamica in evenwicht in de oplossing passen (d.w.z. conform oplosbaarheid). De oververzadiging van een systeem is rechtstreeks gekoppeld aan de drijvende kracht voor kristallisatie.

ongelijke populaties kan worden gematigd, versterkt of zelfs omgekeerd door verandering van het vigerende kristalgroeimechanisme[8].

De resultaten in dit hoofdstuk geven een duidelijk inkijkje in de kritieke kinetische concepten die leidend zijn in asymmetrische kristallisatieprocessen. Deze concepten bieden een helpende hand bij het ontwerpen, implementeren en controleren van kristallisatiegedreven deracemizaties. Deze theorie stelt ons nu ook in staat een aantal empirische strategieën uit de literatuur en praktijk te verklaren. Tot slot geeft het gepresenteerde denkkader een richting voor geheel nieuwe vormen van asymmetrische kristallisatie, die mogelijk ook kunnen worden toegepast op thermodynamisch stabiele racemische kristallen, waarvoor CID-processen in principe ongeschikt zouden zijn. Daarnaast zijn deze bevindingen conceptueel ook van belang voor andere asymmetrische (kristallisatie)processen waarbij meerdere populaties in competitie zijn voor dezelfde bouwblokken, zowel in toepassingen binnen de industrie als op fundamenteel niveau binnen het academisch onderzoek.

## Ratelmechanismen als drijvende kracht achter kristallisatiegedreven deracemizatie

Tot dusverre heeft dit proefschrift een nadruk gelegd op het bestuderen van asymmetrische kristalgroei ten behoeve van de versterking van chiraliteit. In een volledig kristallisatiegedreven deracemizatieproces worden echter groeistappen gecombineerd met oplosstappen. Cyclische opeenvolging van dergelijke groei- en oplosstappen is uiteindelijk essentieel om deracemizatie te bewerkstelligen, hetgeen de experimentele vraag oproept wat hun beider rol in het mechanisme van kristallisatiegedreven deracemizatie precies is.

**Hoofdstuk 6** ontleedt de individuele bijdragen van asymmetrische kristalgroei en oplossen aan de versterking van chiraliteit en legt middels een massabalans de onderliggende kristaldynamica bloot. Ongeacht de snelheid van de racemizatiereactie meten we consistent een dissymmetrie tussen het groei- en het oplosgedrag van de twee enantiomeerpopulaties. We zien dat enantioverrijking verkregen tijdens groei consequent opweegt tegen de afname tijdens oplossen; dit ondanks de zowel snellere groei- als oploskinetiek van het meerderheidsenantiomeer vergeleken met het minderheidsenantiomeer. Deze dissymmetrie tussen het asymmetrisch groeien en oplossen van de chirale kristalpopulaties leidt tot een ratelmechanisme[9] dat de volledige deracemizatie van de gemengde enantiomeren tot gevolg heeft. In afwijking van de gangbare gedachte dat het oplossen van kristallen gunstig is voor enantioverrijking, laten we hier zien

[8] Zie **Hoofdstuk 2** voor een toelichting op de mechanismen achter kristalgroei.
[9] Met een ratelmechanisme bedoelen we hier een proces dat tijdens de eerste helft van een cyclus meer stapjes vooruit beweegt dan het tijdens de tweede helft terugdoet. Concreet: kristalgroei doet de nadelige effecten van oplossen op de enantiozuiverheid van de kristallen dus meer dan teniet.

dat dit oplossen zelfs in absolute zin de enantiozuiverheid van de vaste stof kan doen dalen; in vergelijkbare zin laten we zien—in lijn met hoofdstuk 4 en 5—dat kristalgroei een absolute toename van de enantiozuiverheid van de vaste stof kan bewerkstelligen.

De experimenten die in hoofdstuk 6 worden gepresenteerd impliceren dat een intrinsiek verschil tussen de mechanismen waarmee kristallen groeien en oplossen als fundament dient voor de werking van kristallisatiegedreven deracemizatie. Naast een duidelijke invloed binnen het academisch onderzoek hebben de inzichten uit dit hoofdstuk ook een toepassing als handvat bij het optimaliseren en implementeren van kristallisatiegedreven deracemizatieprocessen. In het bijzonder de notie dat groei- en oplosstappen elk individueel bezien en geoptimaliseerd moeten worden om de deracemizatie-effectiviteit te optimaliseren is vernieuwend. Een voorbeeld hiervan uit hoofdstuk 6 is het uitschakelen van de racemizatiereactie tijdens de oplosstap; het verschil tussen de chirale versterking tijdens groei- en oplossen wordt dientengevolge maximaal, met een uitzonderlijke mate van asymmetrische aanwas over de gehele cyclus tot gevolg.

## Deracemizatie via een oplosmiddelkringproces

Waar het voorgaande hoofdstuk gericht was op de fundamentele rollen van kristalgroei en oplossen bij het uitversterken van chiraliteit, is tot op heden slechts marginaal beschouwd hoe de verschillende praktische procesomstandigheden voor het groeien en oplossen van die kristallen invloed uitoefenen op de efficiëntie en het toepassingspotentieel van kristallisatiegedreven deracemizatieprocessen. In de literatuur zijn twee methodieken bekend om het kringproces van afwisselende groei- en oplosstappen te bewerkstelligen: (i) zgn. afslijten (EN: ‘attrition’), waarbij grootte-afhankelijke oplosbaarheid en een soort Ostwald-rijping[10] de cycli effectueren; (ii) zgn. temperatuurschommelingen[11] (EN: ‘temperature cycling’), waarbij de temperatuur-afhankelijke oplosbaarheid de cycli drijft.

In **Hoofdstuk 7** introduceren we een nieuwe methode voor het effectueren van groei/oplos-cycli, gebaseerd op de fundamentele inzichten die in de voorgaande hoofdstukken zijn opgedaan. In hoofdstuk 4, 5 en 6 is vastgesteld dat langzaam groeien en snel oplossen ideaal is voor een effectieve non-lineaire versterking van de chiraliteit van een systeem en voor het mitigeren van het inherent tegenwerkende karakter van het oplossen. Daarnaast liet hoofdstuk 6 zien dat de racemizatiesnelheid tijdens oplossen idealiter lager ligt dan tijdens groeien en in ieder geval niet hoger moet zijn. Hoofdstuk 7 presenteert een nieuwe aanpak voor

[10] Ostwald-rijping is een proces, gedreven door thermodynamica, waarbij kleine kristallen door hun hogere oppervlaktespanning oplossen en hun materiaal “afgeven” aan stabielere grotere kristallen. Het resultaat is dat de kleine deeltjes verdwijnen en de grote deeltjes nog groter worden. Chemische pac-man dus!

[11] In **Hoofdstuk 2** en **3** worden zulke temperatuurschommelingen toegelicht.

kristallisatiegedreven deracemizatie waarin we streven al deze lessen ter harte te nemen: het groeien doen we middels het langzaam verdampen van oplosmiddel, en het oplossen vervolgens middels het in één keer terug toevoegen van het verdampte oplosmiddel. Een dergelijk oplosmiddelkringproces kan autonoom worden uitgevoerd met een Soxhlet-apparaat[12] in combinatie met een binair oplosmiddel dat gunstig gebalanceerde eigenschappen heeft t.a.v. kookpunt, racemizatiekinetiek, en (schommelingen in absolute) oplosbaarheid.

Als eerste bewijs dat dit principe werkt gebruiken we een oplosmiddelkringproces om het chirale bouwblok van medicijn Clopidogrel volledig te deracemizeren: binnen 3,5 uur gaan we vanuit 20% aanvankelijke naar 100% uiteindelijke enantiozuiverheid. Dit resultaat, zelfs in niet-geoptimaliseerde vorm, is reeds sneller dan diverse vooraanstaande implementaties van de CID-technologie.

## Enantiozuiverheid via kristallisatie ver uit chemisch evenwicht

Het moge inmiddels duidelijk zijn dat kristallisatie een krachtige methode is om enantiozuivere moleculen te verkrijgen—een aanpak die tot het chirale kerngereedschap behoort. Problematisch is echter dat chirale kristallisatie als scheidingstechnologie uiteindelijk behoorlijk afhankelijk is van conglomeraatvorming, d.w.z. dat chirale moleculen zich scheiden in enantiozuivere kristallen, terwijl dat onvoorspelbaar en zeldzame gedrag is (5—10%). Veruit de meeste chirale moleculen kristalliseren racemisch (90—95%), wat een fundamenteel thermodynamisch obstakel oplevert om enantiomeren met kristallisatie te scheiden; een intrinsiek stereoselectiemechanisme ontbreekt dan immers.

Alhoewel er bewerkelijke en soms ook zeer moeizame alternatieven bestaan voor directe kristallisatie als chirale scheidingsmethode, wordt in dergelijke sluiproutes niet de fundamentele thermodynamische beperking aangepakt die hen wegens het natuurlijk spaarzame voorkomen van conglomeraten noodzakelijk maakt. Om dit gebrek te adresseren, eindigt dit proefschrift met een verkenning van het potentieel van niet-evenwichtsomstandigheden binnen chirale kristallisatie, waarbij kinetische factoren belangrijker zijn dan thermodynamische gegevens. De hoop is dat een dergelijke herbalans de statistische patstelling kan openbreken en de mogelijkheden om enantiozuivere kristallen te isoleren verruimt.

**Hoofdstuk 8** begint met een systematische analyse van de energieverschillen ($\Delta G^{\Phi}$) tussen de racemische en enantiozuivere ('conglomeraat') kristalvormen van twee derivatenbibliotheken van doelmoleculen (fenylglycine en praziquantel). We vormen zulke bibliotheken door systematisch diverse chemische veranderingen aan die doelmoleculen aan te brengen. Onverwachte bevindingen in dit hoofdstuk zijn de

[12] Een bijzonder stuk laboratoriumglaswerk dat normaal wordt gebruikt voor extracties met oplosmiddel.

brede maar onderling vergelijkbare verdeling van $\Delta G^{\Phi}$ voor de beide bibliotheken en de binnen die verdeling de clustering van derivaten met gelijksoortige chemische modificaties. Deze clustering staat een gestuurde evolutiestrategie toe, die systematisch chemische modificaties aanbrengt en in slechts enkele generatiecycli tot een derivaat met lage $\Delta G^{\Phi}$ kan komen[13], waarvan de enantiozuivere kristalvorm onder niet-evenwichtsomstandigheden zou kunnen worden geïsoleerd. Door gestuurde evolutie te koppelen met niet-evenwichtsomstandigheden en opkomende technologieën zoals AI wordt een beloftevolle weg gebaand naar schaalbare en geautomatiseerde scheiding van chirale moleculen met relevantie voor zowel de academische als industriële toepassingssfeer.

Om te onderzoeken hoe breed deze strategie zou kunnen worden toegepast hebben we de verdelingen in energieverschillen tussen racemische en enantiozuivere kristalvorm van onze experimentele bibliotheken vergeleken met data van circa 100 chirale moleculen uit de literatuur. Onze experimentele bevindingen blijken te veralgemeniseren en impliceren dat meer dan de helft van alle chirale moleculen kinetisch stabiele conglomeraten zouden kunnen vormen. Cruciaal is het inzicht om niet-evenwichtskristallisatie te combineren met principes voor molecuulontwerp gestoeld op een grondige analyse van kristalstabiliteit. Meer dan 50% van chirale moleculen zouden aldus onder niet-evenwichtsomstandigheden enantiozuiver kunnen worden geïsoleerd of zelfs gederacemizeerd. Deze beloftevolle conclusie besluit dit proefschrift.

[13] Lage energieverschillen tussen de kristalvormen laten het makkelijker toe om de metastabiele vorm te isoleren. Deze methode geeft een hogere kans om het conglomeraat als zo'n metastabiele vorm te pakken te krijgen. Daarnaast is het ook makkelijker om een absoluut stabiel conglomeraat te verkrijgen via deze methode.

# List of Publications.

This thesis is based on the following publications:

Chapter 4

**S.W. van Dongen**, I. Ahlal, M. Leeman, B. Kaptein, R.M. Kellogg, I. Baglai, W.L. Noorduin (2023). Chiral Amplification through the Interplay of Racemizing Conditions and Asymmetric Crystal Growth. *J. Am. Chem. Soc.* 145(1): 436–442.

Chapter 5

**S.W. van Dongen***, P. Rang*, K.G.P. Dautzenberg, B. Kaptein, W. L. Noorduin (2026). Disparities in Seed Size Distributions can Drive or Hamper Chiral Amplification under Racemizing Conditions during Conglomerate Crystal Growth. *J. Phys. Chem. Lett.* 17(4):1129—1135.

Chapter 6

**S.W. van Dongen***, J. Maeda*, B. Kaptein, P. Cardinael, A. Flood, G. Coquerel, W.L. Noorduin (2025). Mechanistic Dissymmetry between Crystal Growth and Dissolution drives Ratcheted Chiral Amplification. *J. Am. Chem. Soc.* 147(42): 38508–38515.

Chapter 7

**S.W. van Dongen**, I. Baglai, M. Leeman, R.M Kellogg, B. Kaptein, W.L. Noorduin (2023). Rapid Deracemization through Solvent Cycling: Proof-Of-Concept using a Racemizable Conglomerate Clopidogrel Precursor. *Chem. Commun.* 59: 3838–3841.

Chapter 8

C. Pinetre*, **S.W. van Dongen***, C. Brandel, A.S. Léonard, G. Valenti, M. Charpentier, V. Dupray, K. Oosterling, B. Kaptein, M. Leeman, R.M. Kellogg, J.H. ter Horst, W.L. Noorduin (2025). Enantiopurity by Directed Evolution of Crystal Stabilities and Nonequilibrium Crystallization. *J. Am. Chem. Soc.* 147(10): 8864–8870.

*The asterisk (*) indicates shared first-authorship. For all publications included in this thesis, the author has either sole or shared first-authorship.*

Other publications by the author:

- T. Heeremans*, **S.W. van Dongen***, J. Kapma, B. Kaptein, W.L. Noorduin. Understanding and Overcoming Inhibition Effects in Conglomerate Crystallization. *In preparation.*

- S.A. Rigter*, **S.W. van Dongen***, C.T. van Campenhout*, P. Schall, E.C. Garnett, W.L. Noorduin. Green Synthesis of Stable Processable Organic-Inorganic Lead Halide Perovskite Nanocrystals. *Submitted to ACS Omega.*
- A.S. Léonard*, M. Regnier*, S. Bertuletti, **S.W. van Dongen**, R. Listro, M. Leeman, R.M. Kellogg, T. Noël, W.L. Noorduin (2025). Deracemization by coupling electrochemically assisted racemization and asymmetric crystallization. *Chem. Commun.* 61: 18834–18837.
- E. Marino*, R.A. LaCour*, T.C. Moore, **S.W. van Dongen**, A.W. Keller, D. An, S. Yang, D.J. Rosen, G. Gouget, E.H.R. Tsai, C.R. Kagan, T.E. Kodger, S.C. Glotzer, C.B. Murray (2024). Crystallization of Binary Nanocrystal Superlattices and the Relevance of Short-Range Attraction. *Nature Synthesis* 3(1): 111–122.
- L. Helmbrecht, **S.W van Dongen**, A. van der Weijden, C.T. van Campenhout, W.L. Noorduin (2023). Direct Environmental Lead Detection by Photoluminescent Perovskite Formation with Nanogram Sensitivity. *Environ. Sci. & Tech.* 57(40): 20494–20500.
- L.S.D. Antony, **S.W. van Dongen**, G. Grimaldi, S. Mathew, L. Helmbrecht, A. van der Weijden, J. Borchert, I. Schuringa, B. Ehrler, W.L. Noorduin, E. Alarcon-Llado (2023). The Role of Pb-Oxidation State of the Precursor in the Formation of 2D Perovskite Microplates. *Nanoscale* 15(13): 6285–6294.
- E. Marino*, **S.W. Van Dongen***, S.J. Neuhaus, W. Li, A.W. Keller, C.R. Kagan, T.E. Kodger, C.B. Murray (2022). Monodisperse Nanocrystal Superparticles through a Source–Sink Emulsion System. *Chem. Mater.* 34(6): 2779–2789.
- G. Grimaldi, L.S.D. Antony, L. Helmbrecht, A. van der Weijden, **S.W. van Dongen**, I. Schuringa, J. Borchert, E. Alarcon-Llado, W.L. Noorduin, B. Ehrler (2021). Microstructuring of 2D Perovskites via Ion-Exchange Fabrication. *Appl. Phys. Lett.* 119(22): 223102.
- I. Baglai, **S.W. van Dongen**, M. Leeman, R.M. Kellogg, B. Kaptein, W.L. Noorduin (2021). Counteracting Enantiospecific Behavior of Tailor-Made Additives During Chiral Symmetry Breaking: Growth Inhibition versus Solid-Solution Formation. *Israel J. Chem.* 61(9–10): 645–649.
- E. Marino, A.W. Keller, D. An, **S.W. van Dongen**, T.E. Kodger, K.E. MacArthur, M. Heggen, C.R. Kagan, C.B Murray, P. Schall (2020). Favoring the Growth of High-Quality, Three-Dimensional Supercrystals of Nanocrystals. *J. Phys. Chem. C* 124(20): 11256–11264.
- L. Broers*, **S.W. van Dongen***, V. de Goederen*, M. Ton, J. Spaen, C. Boeriu, K. Schroën (2018). Addition of Chitin Nanoparticles improves Polylactic Acid Film Properties. *Nanotechnol. Adv. Mater. Sci.* 1(2): 1–8.

*The asterisk (*) indicates shared first-authorship.*

# About the Author.

Sjoerd Willem van Dongen was born in Eindhoven, grew up in the small village of Aarle-Rixtel, and completed VWO at the Jan van Brabant College in Helmond. Sjoerd already showed an early interest in science and travelled to Forschungszentrum Jülich (Germany) for his final research project together with his friend Patrick Barendse to study the extraction and antimicrobial properties of curcuminoids.

He went on to study Molecular Life Sciences at Wageningen University (the Netherlands) and rapidly developed a love for physical chemistry, pursuing a minor in macromolecular, supramolecular, and nanochemistry. In 2016, he won the Top Sector Chemistry Student Competition with the team Perfect Package, developing biopolymer nanocomposites with enhanced performance for food packaging applications. His BSc thesis featured the synthesis of ABA triblock co-polymers by first constructing bifunctional RAFT-agents. He also developed new coumarin monomers for RAFT-polymerization that enable dynamic photo-crosslinking and photo-curing when used as coacervate glues. The research was carried out under prof. Marleen Kamperman and Aljosha Filippov.

Continuing at Wageningen University for his MSc, Sjoerd further specialized in physical, organic, and surface chemistry. His final thesis with dr. Thomas Kodger concerned the synthesis and assembly of star polymers from silsesquioxane cubic molecular cores. As part of his MSc, he visited the Chemistry Department of the University of Pennsylvania (U.S.A.) to join the group of prof. Christopher B. Murray to work on the synthesis and characterization of responsive hybrid supercrystals by constructing binary or ternary colloidal superstructures through emulsion templated assembly together with dr. Emanuele Marino.

During his university studies, Sjoerd was also an active member of the Wageningen University Student Choir and Orchestra, served in an advisory committee to the Mayor of Wageningen Municipality, and co-founded ABACCI, an online accounting platform for non-profits.

Nearing the apex of the COVID-19 pandemic, in summer 2020, Sjoerd started a PhD at AMOLF in Amsterdam in the Self-Organizing Matter group (SOM) under prof. Wim Noorduin. Here, he performed the research that has been described in this thesis, focussing on asymmetries in chiral crystallization, their role in the mechanism of crystallization-induced deracemizations, and how understanding of these asymmetries may guide further process development. The PhD featured several fruitful international collaborations, especially with the University of Rouen Normandy (France). Staying on for an extra year after the completion of the bulk of

his PhD project, he also started new directions in chiral crystallization at AMOLF that are currently further explored by the next generation of SOM. Next to his PhD research, Sjoerd also contributed to several collaborative publications on perovskite materials, both pertaining to the fundamentals of their formation as well as novel applications in lead detection.

During his PhD, Sjoerd completed the first-year of an Ancient Greek degree through the Scholae-programme at Radboud University Nijmegen and the University of Amsterdam (2024 – 2025). As part of his interest in Classics, he participated in two instalments of the Amsterdam Classics Summer School. Sjoerd also served as Chief Technology Officer at Fortitudo Legal Concepts, responsible for in-house legal software development and the co-ordination of all matters related to IT and technology. Before building the tech side of the company (2020—2024), he had represented clients in cases on privacy, information and administrative law (2013—2018).

Currently, Sjoerd is employed as Scientist Chemistry & Materials at SolarFoil, a start-up from the University of Amsterdam in 2022. SolarFoil commercializes recent developments in nanomaterials research by bringing to market agricultural foils containing solar conversion pigments. Such pigments enable steering sunlight for greenhouse and horticultural applications and convert harmful and unused parts of the solar spectrum to light that is beneficial for photosynthesis and growth. In joining SolarFoil, Sjoerd returns to his academic roots in nanotechnology and supramolecular chemistry and works on the development and polymer processing of SolarFoil's nanocomposites.

# Acknowledgments.

Now is the moment to look back at the PhD as a journey. While most often tangible outputs like figures, published papers, and journal impact factors are emphasized, the most important aspect of the journey is the personal development. In my PhD-application to AMOLF I wrote 'I am looking forward to developing myself further as a scientist'. Only now, in hindsight, I fully appreciate that this development extends much further than 'as a scientist' and—regardless of what the future may bring — am very happy that I went on this incredibly rewarding journey. Although a PhD is often perceived as a lonely endeavour, the truth is I was never alone. Especially at AMOLF, a vibrant international and strong interdisciplinary community, nothing could be further from the truth.

In the full realization that my PhD is part of a larger collaborative and continuous building on top of previous inquisitive endeavours, I would like to the final pages of this thesis to thank all that have shaped my journey so far and have been there along the way. I will forget some—for sure, but in no way take any such lapse as a reflection of any lesser gratitude. Admittedly, I find writing these acknowledgments harder than the making of any of the preceding chapters, the scientific discussions, or diplomatic intricacies involved with publishing a paper.

First, let me thank you, Wim, my *promotor*. There is often much talk about taking charge and captaining one's PhD. However, in the end, I believe our journey together was much more one in which we sat side-by-side in a rowing boat, each of us holding a peddle. I much valued our writing sessions in which I learned a great deal and that brought out a very productive synergy. I don't think all of them were strictly necessary, but at least they were most fun. I have come away with the strong conviction that my tangible PhD-products indeed are very much shaped by our close co-operation. That having been said, in the end you always did encourage me to speak my mind and, after each discussion, let me decide what to do and which direction we would go. I greatly value that brilliant balance and the way I experienced freedom, trust, and never-ending enthusiasm under your kind guidance. Beyond the science I treasure the memories of our shared experiences, especially the trip to Rouen together, and look back with much pleasure on the way our weekly scientific discussion often evolved into discussions about food (esp. pans and the cooking of poultry and stews), books (esp. non-fiction), and whatever else randomly crossed our paths and we were taken by. Beyond science, I have learned a great deal from your leadership and mentoring. Thank you very much.

Next are obviously my *co-promotores*, Dick and Bernard; your involvement in the PhD I have also very much appreciated. Unfortunately, we did not speak much beyond the

occasional phone call or telecom, but your input and advice were there when it was most critical. I am sorry for surfing so close to the final few deadlines. Thank you very much for all your help and care!

My sincere gratitude also goes out to my *opponentes*, who have taken the time to sit on the committee and attend the defence, as well as to all the reviewers and editors of the various published manuscripts, and prof. Vetter for their valuable feedback. Not all pieces of criticism were necessarily pleasant or easy to deal with, but, in the end, I really value all such contributions in strengthening the science we all put out there and I learned a lot.

I would also like to thank all the direct colleagues in the Self-Organizing Matter group over the years. First there was Iarik; you set-up the chirality research in Amsterdam and gave me a great introduction to the topic and the tools of the trade. The first few months together with you will remain very fond memories and have greatly shaped my approach in the lab and outside ("you can do many experiments, but you also need time to think"). For most of my stay at AMOLF, Christiaan you were my office-mate. I of course loved our joint projects and grinding to bits some toasted clay, but much more did I enjoy the many little moments in which we took a step back and relaxed, from playing chess to daily talk or brainstorming the challenges we were facing in our research. I am very glad we could be each other's paranymph! Marloes, Arno, and Lukas, you also belonged to the first generations of SOM and your stay largely intersected with mine. It has been a pleasure to work with and alongside you, I have really enjoyed getting to know you and spending time together—also on the group retreats (and for Marloes: in the HANOS ☺). Ariane, you are very special and possess a virtually limitless empathy; although we had to find an equilibrium in humour and ways of doing things, I am glad we grew to be good friends and even unlikely scientific collaborators! I hope you will find a nice new challenge where you can harness all your many and diverse skills and interests. Kendra and Juan, it has been great to have some different backgrounds, stories and perspectives in the group, thank you for our shared time! Marius, *du warst ein sehr geselliger Kollege* and I have enjoyed our casual chats, hopefully you will soon find the data science position you deserve. Thanks also to you and Sandra for watering the plants ;).

To the other members of the chirality-gang: Anne-Sophie, Susanna, Pepijn, Tess, and Rutger. We have had a lot of great and inspiring conversations, it has been great to see you enter and grow into the chirality field, and I hope my work proves useful to you all. Anne-Sophie, what a journey you have made! So many different projects and events over the past few years, hats off; just the final sprint to bring it all together. It has been great to talk and brainstorm together. Pepijn, thank you so much for finalizing the work on size-disparities with me, I am really impressed by your diligence and patience with figures. Tess, it was great to have you in the office, some change to sit opposite a physicist after years with Christiaan! I hope you will be able

to combine the two worlds and trust you'll find your voice in the chirality field; don't let your creativity and unique perspective be dulled. Susanna, *grazie per essere nel gruppo*; it was great to be in the lab with you and amazing see how you do not compromise on exact an understanding of what is going on in a project and taking the time to clarify all the positions and opinions of the people involved. I am sure the metastable project is in safe hands with you!

I have had the pleasure to coach a few students during my time at AMOLF and I am greatly indebted to them for learning a lot about science and myself: Miriam, Joep, Ilias, it was an honour to supervise you and shape projects together. Miriam, your level of detail and desire to reach the highest degree of knowledge is astounding. Joep, the enthusiasm and energy you brought were great, I truly enjoyed every minute working on the project together. Joep and Miriam, I am very glad that both your projects have led to scientific work that is (about to be) published.

AMOLF is a unique place to do science, not least of all because of its amazing support staff. *Primus inter pares*: Hinco; the list of things for which to thank you would never fit in one of your inseparable little notebooks. Beyond a catalyst of scientific discovery, you also were key in organizing many activities and guarded over the SOM-flock as the social conscience of the group. Thank you for everything and I hope I may frequent the Boat in the years to come! Marc, you have solved many HPLC problems and kept my workhorse going, many thanks for your assistance and chemical management! Henk-Jan and the workshop: many thanks for designing and producing the Multi-Experimental Plate, I believe it was involved in almost all figures presented in this thesis and has achieved critical acclaim with many successive users! Chemists tend to order a huge amount of chemicals, consumables and other pieces of equipment; thank you Radjin & Remco for always taking care of that and showing a great interest in our scientific work along the way. Also thank you, Max, for designing the beautiful cover of our *ChemComm* paper, something I could never have achieved myself.

Over the course of the research, I have had the pleasure to collaborate with many fine and inspiring scientists. At AMOLF, I thank Gianluca, Esther, Susan, and Eric. Outside of AMOLF, many thanks to Clement P. & Clement B., Gerard, Adrian, Jin, Peter, Pascal, Valerie, Joost, and Maxime. Also I wish to give special thanks to Michel: you have been involved in the majority of chapters presented here and always given constructive criticism and feedback.

Besides pure academic collaboration, I also want to thank a few others that have made the time at AMOLF more memorable and social. First, Daphne we met during the 'taking charge' course at the beginning of our first-year and we met frequently, especially during the lonely COVID-times. It has been my honour to be your paranymph, and I hope we keep in touch and bake and cook many fine dishes and

desserts. Also, thanks to the many fond memories of the moments I shared with Imme, Anthony, Yifei, and SaFyre.

In the final phase of the PhD it is easy to get apathic, overwhelmed, or to lose track of the many loose ends that need to come together. Thank you, Derek, for your keen insights and our constructive conversations. Besides occasionally taking a step back and reflecting from a distance, doing something entirely different also sharpens the blade. Therefore, χάριν ἔχω καὶ τοῖς μὲν πραέσιν ἑταίροις μεθ' ὧν τὸν οἶμον εἰς τὸ τῆς Ἑλλάδος γλώττης κατανοῆσαι ἐπορεύθην, τῷ δὲ Kees, ὃς μακροθύμως τε καὶ σπουδῇ τοῦ πάντα τὰ ἐρωτήματα ἀποκρίνασθαι μελετῶν ἐδίδαξεν.

I also wish to extend my gratitude to the entire SolarFoil crew, Arnon, Yingying, Carlo, Jasmin, and Peter, for giving me a nice new place to continue the journey of discovery, creativity, learning and self-development. I have really enjoyed my time with you all so far.

Now, let me rewind and go back in time to where interest in chemistry started. As a kid I got the desire to know: how do you make an entirely new molecule on demand? The foundations to answering this question were laid at Jan van Brabant College in Helmond by the Science and Chemistry teachers there. Turning the spark into a smoulder was surely the enthusiastic presentation of mr. Meulendijks during a lunch break, explaining the exact mechanism by which the synthesis of the natural product curcumin had been achieved—of course way beyond the high school level! Nonetheless, this was the first real glimpse into the enigma of chemistry that had so long enticed me. Thank you to all the teachers at JvB for fuelling my interest in science and giving me and my classmates the freedom to experiment. Mr. Delhaye, your hypothesis that I could easily do the PhD in 3 years has remained unproven—sorry!

Moving to Wageningen for my university studies, there have been many friends and cherished moments along the way, and I can only name a few. Tom, it was great to work with you as a MSc student on star polymer synthesis. It was during this project that I was able to develop my independent research skills; I am very thankful for the feeling of trust and confidence you gave me, your kind and calm supervision, and the freedom to also pursue some other side-projects. Beyond your inspiring width and depth of knowledge, I want to acknowledge that you really taught me how to write when you agreed to tutor me for the research proposal writing course. Many thanks for the academic essentials you instilled in me and for being the linking pin to the next crucial step in my personal development and academic career.

Emanuele, you gave me the warmest welcome any internship student could hope for. The great experience was not only a result of synergy in the lab: I am also very grateful for the food truck visits and the activities you organized and took me along with, especially Thanksgiving (confession: I have still not finished the Irishman). The

trip to the synchrotron was also a very special experience and I often laugh when I remember you walking around with a dolly while I was making some last-minute calculations for ternary assemblies. Many thanks also to Egle and Leo for enriching the experience and receiving us in Sicily. It was a joy to see you all again (+Emilia!) in Artis and we hope to visit again soon.

Patrick, al sinds de eerste van de middelbare school trekken we in allerlei ondernemingen samen op. Van serieuze wetenschappers in de dop onder vlag van ASA tot een profielwerkstuk in Jülich, en van grootverbruikers van potgrond en buffer tot studiegenoten in Wageningen. Momenten om op te halen te over. Zo verhaal ik nog vaak hoe we tijdens het programmeren van monopolie samen een hele nacht op Skype hadden doorgehaald en jij tegen 6 uur 's ochtends zei: 'ik ga even naar de koelkast, Sjoerd, ik heb honger en volgens mij is er nog taart!'. Wat mooi dat we nu allebei gepromoveerd zijn en in het start-up wezen werken—en van elkaar begrijpen wat we doen en wat ons bezighoudt ook! Vincent, jij kwam bij de club tijdens Thermodynamica. Hoewel ik je eerst een vreemde voedselvogel vond, is dat beeld duizelingwekkend snel 180 graden gedraaid. Met mooie projecten tot gevolg, ABACCI er slechts een van. Ik heb nog steeds spijt dat ik mijn had brak en we niet samen aan nieuwe boorzuurderivaten konden werken. Heren, ik heb intens genoten van onze activiteiten, hackathons, ski-vakantie, en het vele andere samenzijn. Tot snel en veel dank voor jullie gezelschap van meneer Smaak.

Jaap en Lieke: als WSKOV-fossielen gaat onze vriendschap volgens mij al heel lang terug, we kwamen allemaal op hetzelfde moment in het orkest en steken graag de handen uit de mouwen. Het organiseren van de trip naar Spanje was ongetwijfeld een professioneel hoogtepunt, maar wat is het potverdorie toch altijd mooi gezellig, of we nou een sneeuwstorm doorbanjeren of een Italiaanse appeltaart bakken! Ons politiek en maatschappelijk discours waardeer ik eveneens elk maal zeer. Ik hoop aan onze samenkomsten nog heel vaak een gevolg te geven, of het nou kalm in de concertzaal is of tijdens een nieuw gedurfd avontuur.

Nick, toen ik ooit een vriend op de middelbare school adviseerde over geluidsoverlast ten gevolge van kattenverjagers, had ik nooit verwacht dat een reis door het informatierecht uiteindelijk tot een ontmoeting met jou en blijvende samenwerking zou leiden die ons langs vele zaken, rechtsvragen, en memorabele momenten heeft gevoerd. Ik geef toe, van de juristerij word ik nog steeds blij; wie weet hoe dat nog een staartje krijgt! Het ga je goed en ik hoop nog lang van dichtbij mee te maken hoe je knokt voor de burger zoals alleen jij dat kan, met een Haags vechtershart en Platoonse wijsheden op zak. Kevin, het was me een waar genoegen om in jou een collega te vinden om de IT op orde te krijgen en op te schalen. Opschalen is zeker gelukt, inmiddels staat er een heuse afdeling en heb jij je in de afgelopen jaren ook ongelooflijk ontwikkeld; ik vraag me elke keer weer af waar ik eigenlijk nog voor

nodig ben... Ik zeg er maar niets meer van: ons frequente onderhoud is veel te leuk en geeft me altijd nieuwe energie.

Making music has always played a central role in my life, although the intensity and frequency have invariably oscillated. I would like to thank my teachers and maestros Marco D., Marco vD., Daniel, Gerrit, Joop and Frank, and the several ensembles I have had the honour to be a part of: Harmonie de Goede Hoop, the UPenn Concert Band, Wageningen Studenten Koor- en Orkest, the VU Chamber Orchestra, and the Prinses Irene Concert Band Huizen. I have greatly enjoyed your inspiring company and the happiness of immersing oneself in music together.

Natuurlijk wil ik ook graag mijn familie bedanken: mijn ouders, Stanny, Fred, oma, At†, ooms en tante, Bert†, Nienke, Jack, en schoonfamilie, Stef, Karina, Aafke, Beppe, en natuurlijk mijn lieve Sabine. Jullie zijn er altijd voor mij geweest, ieder op zijn of haar eigen manier, *every step of the way*. Ik ben zekersteweten niet altijd de makkelijkste klant en volgens mij vaak lastig te begrijpen, maar hopelijk maken mijn enthousiasme over de minst relevante dingen, mijn niet-aflatend impuls om problemen aan te pakken en iedereen te helpen en de diverse culinaire versnaperingen die ik mettertijd pleeg aan te bieden veel goed. Ik ben jullie ieder dankbaarder dan ik hier met zwart pigment kan drukken. Hopelijk kunnen we nog lang in goede gezondheid van elkanders gezelschap genieten. Sabine, ik kijk er naar uit om samen aan ons nieuwe stekje te gaan bouwen; hopelijk kan ik er voor jou zijn zoals je mij altijd hebt ondersteund.

To conclude these acknowledgments, I would like to thank NWO for financing this research and acknowledge the root cause of our being in this business anyways: *Natura Artis Magister*.[*]

Sjoerd van Dongen
*Amsterdam, February 2026*

[*] Slogan of the Amsterdam Zoo. My translation: *Nature is the Master of all Art.*